

**Imperial College
London**

Faculty of Engineering
Department of Chemical Engineering

*En route to the industrial applications of ionic liquids for
metal oxide production and biomass fractionation:
A sustainable avenue to advanced materials*

Thesis submitted for the degree of
Doctor of Philosophy
By

Francisco José Malaret
Supervised by Professor Dr Jason P. Hallett

Declaration of originality

The entirety of the work described in this thesis was carried out at Imperial College London between February 2016 and July 2020. Unless otherwise stated the work presented in this thesis is my own and has not been submitted previously for a degree at any Academic Institution.

Copyright

The copyright of this thesis rests with the author and is made available under a Creative Commons Attribution Non-Commercial No Derivatives 4.0 International Licence (CC BY-NC-ND 4.0) [<https://creativecommons.org/licenses/by-nc-nd/4.0/>].

Under this License, you are free to copy and redistribute this thesis in any medium or format. You must give appropriate credit, provide a link to the license, and indicate if changes were made. You may do so in any reasonable manner, but not in any way that suggests that I endorse you or your use, unless prior written consent. If you remix, transform, modify or build upon the thesis, you may not distribute the modified version. You may not use the material for commercial purposes.

Contact information

E-mail: f.malaret@imperial.ac.uk

Web of Science ResearcherID: [AAK-3178-2020](https://orcid.org/0000-0002-5717-3629)

Orcid ID [0000-0002-5717-3629](https://orcid.org/0000-0002-5717-3629)

Abstract

In the context of climate change, it is essential to use renewable materials and to reduce the environmental footprint of industrial processes. This work focuses on the feasibility of implementing a low-cost Ionic Liquid (IL) in a large-scale biorefinery for bioethanol production (the ionoSolv process). The selected feedstock was *Eucalyptus red grandis*, a fast-growing hardwood. The lignocellulosic biomass was fractionated at laboratory scale, using aqueous *N,N,N*-trimethylammonium hydrogen sulfate (20 wt% water), at different temperatures and reaction times, to maximize glucose recovery (86%). Experiments under CO₂ atmospheres (sub and supercritical) revealed that the ionoSolv process is pressure insensitive.

A detailed Techno-Economic Analysis (TEA) for a biorefinery using the ionoSolv pretreatment was performed and compared to one using the acid-catalysed steam explosion pretreatment. With the ionoSolv pretreatment, the composition of the cellulose-rich pulps can be tailored and high-purity lignins can be recovered. The economic performance of both pretreatments are similar. From a sustainability perspective there are trade-offs: the ionoSolv process consumes 25% more energy (with potential for optimization) but consumes less chemicals and produces less waste. These results indicate that this process can be a competitive alternative.

During the development of this process, and other IL-based processes, the interaction of ILs (neat and aqueous) with metals was investigated to establish suitable materials of construction. It was observed that the corrosion behaviour of metals exposed to ILs is system dependent. Surprisingly, water can act either as a corrosion inhibitor or promoter. A semi-quantitative classification method for the different corrosion behaviours observed was developed.

Some metals exposed to aqueous ILs formed particles, resulting in the inadvertent development of a novel process for metal-based materials at large-scale: Oxidative Ionothermal Synthesis (OIS). A high-level TEA suggests that OIS offers economic and environmentally advantageous production of bulk and advanced metal-based materials, such as zinc oxide.

Acknowledgements

I want to thank my supervisor Professor Dr Jason Patrick Hallett for opening his research group and welcoming me after my journey in industry. I am very grateful for this life-changing experience, his trust, his advice, patience and for allowing me to explore my ideas.

I would like to thank Dr Kyra Sedransk Campbell, with whom I established a collaboration project to study the corrosion behaviour of metals exposed to ionic liquids. Studies that ultimately led to the discovery of new ways of manufacturing micro- and nano- particles.

Jason's and Kyra's advice and guidance have been vital to completing my PhD. I hope I can continue to work with them beyond my PhD in our quest for knowledge, solving problems and creating a positive impact.

Thanks to the Chemical Engineering Department (ChemEng) at Imperial College London (ICL) for their support in helping us explore the commercial aspects of one of the technologies that emerged from this research work.

To ICL academic and administrative staff for all their help. Special thanks to Professors Niall Mac Dowell, Tom Welton, Paul Fennell and Martin Trusler, to the ChemEng safety officer Severine Toson for keeping me safe throughout my research and the Analytical Suites team, Patricia Carry and Kaho Cheung for all their help using the analytical instruments. Thanks to the team of the centre for electron microscopy of the Material Department at ICL Mahmoud Ardakani and Cati Ware.

To my fellow PhD students. Special thanks to Anton Firth, Amir Al-Ghatta, Raul Aravena Contreras, Florence Gschwend, Clementine Chambon, Vivi Filippousi, Meng Chen (Angela), Min Yang (beautiful Shirley) and Aida R. Abouelela. Post-docs, Andreas Bröhl, Coby Clark, Agnieszka Brandt-Talbot, Joseph Yao and Pedro Verdia Barbara. MRes and MSc students: Angela Romano, Xingchen Li, Jonathan Woods, Katherine Moffa and Yurou Gao. Visiting students and academics: Everton Skoronski, Jesús Lemus Torres, Victor Dognin, Gwenaël Bonnavé and Joana M. Lopes.

To my family (Los Tirilines, Los Malaret and La Russianera) and friends for always being unconditionally supportive and available for me... I would not have made it this far without you.

Thank you! / ¡Gracias! / Merci!

Contents

Abstract.....	3
Acknowledgements.....	4
Chapter 1 - Introduction	14
1.1 Motivation.....	14
1.2 Background	14
1.2.1 Sustainability	14
1.2.2 Climate change and CO ₂ emissions.....	15
1.2.3 Green chemistry and engineering.....	16
1.3 Overall knowledge gaps	20
1.4 General objectives	21
1.5 Thesis outline	22
1.6 Publications and presentations.....	24
1.7 Acronyms and abbreviations	24
Chapter 2 - Ionic liquids – Synthesis, characterisation and physicochemical properties.....	27
2.1 Motivation.....	27
2.1.1 Objectives.....	27
2.2 Ionic liquids	27
2.2.1 Applications of ILs	31
2.2.2 Protic Ionic Liquids (PILs)	32
2.2.3 Thermodynamic considerations of PIL formation	33
2.2.4 Base:acid ratio.....	37
2.2.5 Molecular structure of IL and water systems	39
2.2.6 State-of-the-art for the physicochemical properties of hydrogen sulfate based IL and knowledge gaps	44
2.3 Methods.....	45
2.3.1 PIL lab-scale synthesis.....	45
2.3.2 PIL large-scale synthesis.....	47
2.3.3 Analytical techniques	49
2.4 Results and discussions.....	52
2.4.1 Determination of the base:acid ratio (β) of PILs by acid-base titration	52
2.4.2 Volumetric properties of alkylammonium hydrogen sulfate ($\beta=1$) and water mixtures.. ..	56
2.4.3 Volumetric properties of alkylammonium hydrogen sulfate ($\beta\neq 1$)	63
2.4.4 Viscosity of alkylammonium hydrogen sulfate ($\beta=1$) and water mixtures	64
2.4.5 Viscosity as a function of temperature and the base:acid ratio (β).....	67

2.4.6	Crystallization behaviour as a function of the base:acid ratio (β)	69
2.4.7	Thermal stability	69
2.5	Conclusions	71
2.5.1	Future research	72
Chapter 3 - Interactions between ionic liquids and metallic materials		73
3.1	Motivation.....	73
3.1.1	Objectives.....	73
3.2	Introduction	73
3.2.1	Types of corrosion.....	74
3.2.2	Corrosion rates.....	75
3.2.3	Corrosion rate quantification methods	76
3.2.4	Corrosion rate quantification – Immersion test	77
3.2.5	Mechanisms of corrosion.....	78
3.2.6	Corrosive medium.....	79
3.2.7	Mechanism of corrosion inhibition.....	80
3.2.8	Corrosion behaviour of metals in ILs - Knowledge gaps	83
3.3	Experimental methods.....	85
3.3.1	Materials	85
3.3.2	Corrosion rate measurements	89
3.3.3	Analytical techniques	95
3.4	Semiquantitative-categorization system for the corrosion behaviour of metals based on immersion tests	96
3.5	Results and discussions.....	104
3.5.1	Analysis of ILs	104
3.5.2	Corrosion behaviour of metals exposed to $[C_4C_{1im}][NTf_2]$	105
3.5.3	Corrosion behaviour of metals exposed to water-soluble ILs	120
3.5.4	Zinc exposed to $[C_4C_{1im}]Cl$ and water systems.....	120
3.5.5	Anion effect on IL-induced corrosion: $Cl^-/[NTF_2]^-/[HSO_4]^-$	135
3.5.6	Cation effect on IL-induced corrosion: protic Vs. aprotic ILs	137
3.5.7	Anion effect on IL-induced corrosion - protic ILs	137
3.5.8	Temperature effect on IL-induced corrosion.....	139
3.5.9	Water effect on IL-induced corrosion	140
3.5.10	Semiquantitative-categorization method.....	142
3.6	The Oxidative Ionothermal Synthesis (OIS)	144
3.6.1	Zinc oxide (ZnO)	144
3.6.2	Industrial ZnO production	145

3.6.3	OIS process – Products.....	147
3.6.4	OIS process – Sustainability considerations.....	148
3.6.5	OIS process – Economic potential.....	152
3.6.6	OIS process – Overall considerations.....	153
3.7	Conclusions and future work	154
3.7.1	Corrosion behaviour of metals exposed to ILs.....	154
3.7.2	Material selection	156
3.7.3	Semi-quantitative categorization method	157
3.7.4	Oxidative Ionothermal Synthesis (OIS)	158
3.7.5	Lessons learnt and recommendations for future work	159
3.7.6	Future work.....	160
Chapter 4 - Techno-economic analysis for an eucalyptus biorefinery using the IonoSolv Process....		161
4.1	Motivation.....	161
4.1.1	Eucalyptus fractionation using [N ₂₂₂₀][HSO ₄]	161
4.1.2	Objectives.....	162
4.2	Theoretical background	162
4.2.1	Lignocellulosic biomass	164
4.2.2	Hardwood	169
4.2.3	Second generation bioethanol.....	170
4.2.4	Biorefinery.....	171
4.2.5	Lignocellulosic biomass pretreatment	172
4.2.6	Ionic liquids for biomass fractionation.....	178
4.2.7	Techno-economic analysis for biorefineries	188
4.2.8	Knowledge gaps	190
4.3	Experimental methods.....	191
4.3.1	Materials	191
4.3.2	Biomass fractionation and characterisation	192
4.3.3	Biorefinery - Base case definition	197
4.3.4	Biorefinery - Reference project description.....	200
4.3.5	Biorefinery - Capital cost (CAPEX) estimation.....	201
4.3.6	Biorefinery – OPEX estimation	202
4.4	Results and discussion	203
4.4.1	Pretreatment experiment setup, temperature profiles and severity factors.....	203
4.4.2	Effect of intensified [N ₂₂₂₀][HSO ₄] on pretreatment	205
4.4.3	Predictive models.....	211
4.4.4	Influence of pressure and CO ₂ atmosphere on pretreatment.....	213

4.4.5	General CAPEX assessment for biorefineries.....	215
4.4.6	CAPEX ionoSolv vs. ACSE pretreatments.....	216
4.4.7	OPEX IonoSolv vs. ACSE pretreatments	220
4.4.8	MESP ionoSolv vs. ACSE pretreatments.....	222
4.4.9	Sensitivity analysis	223
4.5	Conclusions	232
4.5.1	Further work	234
Chapter 5 - Overall conclusions		237
5.1	Bioderived materials <i>via</i> the ionoSolv process	237
5.2	Corrosion of metals exposed to ILs.....	238
5.3	Oxidative Ionothermal Synthesis (OIS) for advanced materials production?.....	239
5.4	Challenges and future work	240
References		241
Appendix 1 - Supplementary information on ILs		261
A1.1.	IL cost	261
A1.2.	Toxicity of ILs and impact on the environment	262
A1.3.	Thermodynamic properties of [HSO ₄]-based ILs	264
Appendix 2 - [C ₄ C ₁ im]Cl-water system structures		267
Appendix 3 – Definition of terms.....		269
Appendix 4 – Surface analytical techniques for corrosion studies		272
Appendix 5 – Details on the interaction of metals exposed to ILs		273
A5.1.	Aluminium	273
A5.1.1.	Corrosion rates	273
A5.1.2.	XRD	274
A5.1.3.	XRF	275
A5.1.4.	SEM	276
A1.1.1.	Overall considerations	279
A5.1.4.1	Al corrosion in chloride media.....	281
A5.1.4.2	Al corrosion in sulfate media.....	283
A5.1.4.3	Al categorization system.....	283
A5.1.4.4	Al corrosion in other ILs.....	284
A5.2.	Copper	285
A5.2.1.	Corrosion rates	285
A1.1.2.	XRD	286
A1.1.3.	XRF	287
A1.1.4.	SEM	288

A5.2.2. Overall considerations.....	291
A5.2.2.1 Cu corrosion in chloride media.....	291
A5.2.2.2 Cu corrosion in sulfate media.....	295
A5.2.2.3 Cu categorization system.....	296
A5.2.2.4 Cu corrosion in other ILS.....	297
A5.3. Iron.....	297
A5.3.1. Corrosion rates	297
A5.3.2. XRD	298
A5.3.3. XRF	300
A5.3.4. SEM	300
A5.3.5. Overall considerations.....	302
A5.3.5.1 Fe corrosion in chloride media	303
A5.3.5.2 Fe corrosion in sulfate media	306
A5.3.5.3 Fe categorization system	306
A5.3.5.4 Fe corrosion in other ILS	307
A5.4. Molybdenum	307
A5.4.1. Corrosion rates	307
A5.4.2. XRD	308
A5.4.3. XRF	309
A5.4.4. SEM	309
A5.4.5. Overall considerations.....	311
A5.4.5.1 Mo categorization system	313
A5.4.5.2 Mo corrosion in other ILS.....	313
A5.5. Nickel	313
A5.5.1. Corrosion rates	314
A5.5.2. XRD	315
A5.5.3. XRF	316
A5.5.4. SEM	316
A5.5.5. Overall considerations.....	318
A5.5.5.1 Ni corrosion in chloride media	318
A5.5.5.2 Ni corrosion in sulfate media.....	320
A5.5.5.3 Ni categorization system	320
A5.5.5.4 Ni corrosion in other ILS.....	321
A5.6. Titanium.....	321
A5.6.1. Corrosion rates	321
A5.6.2. XRD	323

A5.6.3. XRF	323
A5.6.4. SEM	323
A5.6.5. Overall considerations	325
A5.6.5.1 Ti corrosion in chloride media	325
A5.6.5.2 Ti corrosion in sulfate media	326
A5.6.5.3 Ti categorization system	327
A5.6.5.4 Ti corrosion in other ILs	328
A5.7. Zinc.....	328
A5.7.1. Corrosion rates	328
A5.7.2. XRD	331
A5.7.3. XRF	331
A5.7.4. SEM	332
A5.7.4.1 SEM images of Zn in PILs	332
A5.7.4.2 SEM images of Zn in aprotic IL solutions and water	335
A5.7.5. Overall considerations	340
A5.7.5.1 Zn exposed to PILs	340
A5.7.5.2 Summary of classification method from Zn exposed to corrosive media	342
A5.7.5.3 Zn corrosion in other ILs	342
A5.8. Brass (Cu63/Zn37)	343
A5.8.1. Corrosion rates	343
A5.8.2. XRD	344
A5.8.2.1 XRF	345
A5.8.3. SEM	346
A5.8.4. Overall considerations	350
A5.8.4.1 Brass categorization system	351
A5.8.4.2 Brass corrosion in other ILs	351
A5.9. Stainless Steel 304	351
A5.9.1. Corrosion rates	352
A5.9.2. XRD	353
A5.9.3. XRF	354
A5.9.4. SEM	355
A5.9.5. Overall considerations	357
A5.9.5.1 304 SS corrosion in chloride media	357
A5.9.5.2 304 SS corrosion in sulfate media	358
A5.9.5.3 304 SS categorization system	360
A5.9.5.4 304 SS corrosion in other ILs	361

Appendix 6 - Corrosion rates	362
Appendix 7 – High-level techno-economic analysis for the Oxidative Ionothermal Process	371
A7.1. Motivation	371
A7.1.1. Objectives	371
A7.2. Introduction	371
A7.2.1. Toxicology	372
A7.2.2. Industrial grades	373
A7.2.3. Different production methods.....	374
A7.2.3.1 The American (Direct) Process	376
A7.2.3.2 The French (Indirect) Process	377
A7.2.3.3 Wet-process zinc oxide.....	379
A7.2.3.4 Other methods	380
A7.2.4. Metallic zinc feedstocks.....	381
A7.2.4.1 Special High Grade (SHG) zinc	381
A7.2.4.2 Secondary zinc	381
A7.3. From laboratory to commercial scale.....	382
A7.4. High-level laboratory assessment	384
A7.4.1. Oxidative Ionothermal Synthesis (OIS).....	384
A7.4.2. ZnO nanoparticles synthesis methods.....	385
A7.4.2.1 Chemical precipitation.....	388
A7.4.2.2 Sol-gel method.....	389
A7.4.3. Production cost – raw materials.....	389
A7.4.4. Environmental assessment.....	394
A7.4.4.1 Safety aspects of zinc precursors.....	396
A7.4.4.2 Overall considerations.....	397
A7.5. High-level OIS process evaluation	398
A7.5.1. CAPEX and OPEX estimations	398
A7.5.2. Process description for particles production.....	398
A7.5.2.1 Reaction unit.....	399
A7.5.2.2 Hydrogen management unit	402
A7.5.2.3 Particle recovery and purification unit.....	404
A7.5.2.4 Ionic liquid conditioning	408
A7.5.2.5 Water production unit.....	409
A7.5.2.6 Particle drying unit.....	411
A7.5.2.7 IL storage unit	412
A7.5.2.8 Packaging unit.....	413

A7.5.2.9 Other systems.....	413
A7.5.3. Process description for metal-nanoparticle composites.....	414
A7.5.4. Overall CAPEX and OPEX estimations.....	414
A7.5.4.1 CAPEX.....	414
A7.5.4.2 Overall OPEX - Variable cost.....	416
A7.5.4.3 Overall OPEX - Fixed cost.....	418
A7.5.4.4 Zinc oxide production cost	418
A7.6. Process uncertainties.....	420
A7.7. Overall considerations	422
A7.8. Conclusions.....	424
A7.8.1. Future research.....	424
Appendix 8 – Supplementary information on the high-level TEA for the OIS Process.....	425
A8.1. Energy calculations for OIS evaluation	425
A8.1.1. Laboratory heat losses – Convection oven.....	425
A8.1.2. Energy cost and CO ₂ emissions.....	426
A8.1.3. Energy calculations	426
A8.2. ZnO laboratory-scale cost.....	429
A8.3. CAPEX and OPEX estimations – OIS process.....	430
A8.3.1. Reactor.....	430
A8.3.1.1 Heat losses (reactor).....	431
A8.3.2. Centrifuge	432
A8.3.3. Vessels and tanks.....	433
Appendix 9 - Specific area and equivalent particle size relationships.....	435
Appendix 10 – Additional information on eucalyptus pretreatment	436
Appendix 11 - ANOVA analysis (saccharification yields of IL pretreatment under CO ₂ atmosphere).....	440
Appendix 12- FTIR <i>Eucalyptus red grandis</i> pulps and lignin	441
Appendix 13 - Supplementary information on the bioenergy assessment	450
A12.1. Process description - Reference project.....	450
A12.1.1. Section 1000 - Feedstock handling.....	450
A12.1.2. Section 100 – Pretreatment	450
A12.1.3. Section 200 - Steam explosion/wash.....	450
A12.1.4. Section 300 - Enzyme production.....	451
A12.1.5. Section 400 - Hydrolysis.....	451
A12.1.6. Section 500 - Evaporation.....	451
A12.1.7. Section 600 - Fermentation	451
A12.1.8. Section 700 – Distillation	452

A12.1.9. Section 800 - Anaerobic digestion	452
A12.1.10. Other units.....	452
A12.2. Process description - ionoSolv process.....	453
A12.2.1. Unit 100 - Fractionation.....	453
A12.2.2. Unit 2000 – Lignin recovery	455
A12.2.3. Unit 3000 - Ionic liquid conditioning	455
A12.3. Biomass fractionation modelling in HYSYS.....	456
A12.3.1. Model parameters.....	456
A12.3.2. Ionic liquid modelling	457
A12.3.3. Chemical reactions	457
A12.3.4. Components	458
Appendix 14 - Quick investment and operating cost estimation method for second generation bioethanol production plants	469
Appendix 15 – ESI - Quick investment and operating cost estimation method for second generation bioethanol production plants	489

Chapter 1 - Introduction

1.1 Motivation

Climate change is one of the major challenges facing society at the time this thesis was written. It is an extremely complex problem that will require the contribution of many solutions to solve it. One of the major contributors to climate change is CO₂ emissions from different industries. Chemical engineers need to revisit industrial processes, some of them, decades old, to improve their efficiency and reduce their environmental footprint by reducing their CO₂ emissions, energy consumption and amount of waste generated.

Ionic liquids (ILs) are substances, with interesting properties, believed to be green solvents mainly because of their extremely low boiling points ¹. Despite the great amount of research focused on the use of these solvents for different applications, only a few processes had found their way out of the laboratory and have been implemented in large scale processes ².

This thesis explores the use of these super solvents (ILs) in large scale processes focusing on the production of biofuels (bioethanol) using alkylammonium hydrogen sulfates, known as the IonoSolv Process ³.

1.2 Background

A general background is presented in this section to provide the context of this work and its importance. Detailed literature review and knowledge gaps relevant to each section are presented in their corresponding chapters.

1.2.1 Sustainability

Sustainable development has been defined by the World Commission on Environment and Development (Brundtland report) as “development that meets the needs of the present without compromising the ability of future generations to meet their own needs” ⁴. This report highlights the importance and strategies to achieve a sustainable future covering different aspects of human activities, including strategies for sustainable industrial development, with a focus on energy usage and raw materials.

Chemical engineers have been responsible for the development, design and operation of large-scale processes for the production of energy and products needed to support our way of life (e.g. energy, petrochemical, pharmaceutical, materials, fertilizers, food, etc.). However, many industrial processes are not considered sustainable ⁴. Some of the reasons include:

- High energy consumption.
- The use of fossil fuels releasing CO₂ into the atmosphere (therefore contributing to climate change).
- Waste generation.
- High water consumption.

There are several environmental concerns such as climate change, resource depletion and pollution ⁵. It has become critical tackling these issues to fight climate change, and for that, chemical engineers will play a major role. They need to find ways to minimize the environmental footprint of existing processes and develop new ways to produce energy and products using more sustainable materials. Improving the sustainability of chemical processes will preserve the environment and assure the future for the next generations.

1.2.2 Climate change and CO₂ emissions

Climate change is one of the major issues mankind is facing as an increase in the Earth's temperature will negatively impact society, the economy, and the environment. Some of the consequences of climate change include more extreme weather events, further widespread extinction of animal and plant species, coastal inundation due to sea-level rise (loss of coastal biodiversity and massive human migrations) and impact in agriculture due to shifting trends in precipitation and cropping patterns ⁵.

The link between CO₂ and global climate warming is the well-known "greenhouse effect". Solar radiation passes largely unhindered through the atmosphere, heating the Earth's surface. In turn, energy is re-emitted as infrared radiation, much of which is absorbed by atmospheric CO₂ and water vapour, which act like a blanket surrounding the Earth ⁶. Without this natural greenhouse effect, the average surface temperature would plummet to about -21 °C, rather less pleasant than the 14 °C experienced today ⁶.

Humans have influenced the environment for centuries; but, it is only since the beginning of the industrial revolution that the impact of human activities has begun to extend to a global scale ^{5,6}. Currently, environmental-related issues have become one of the biggest concerns of mankind. This is due to the scientific evidence about the increasing concentration of greenhouse gases in the atmosphere and their effects on Earth's climate ^{5,6}. At the United Nations Climate Change Conference held in Paris at the end of 2015, 195 countries agreed on a plan to reduce CO₂ and other greenhouse gases emissions, aiming to limit the global

temperature increase to below 2 °C (relative to pre-industrial climate, meaning a future warming of less than 1.4 °C because the temperature had already increased by 0.6 °C by the end of the twentieth century)⁶. This attests for the global efforts to achieve a more sustainable future. From an industrial point of view, some of the initiatives include the development of more energy-efficient and carbon-free processes (decarbonization of the economy and net-zero CO₂ emissions), the use of renewable energy and materials (pollution and resource depletion mitigation) and valorisation of waste (circular economy).

Currently, fossil fuels (oil, coal and gas) are the main sources of energy and chemicals. However, their use is not sustainable for several reasons: Firstly, they are non-renewable materials, meaning that they will deplete over time, and therefore cannot ensure the needs for future generations. Secondly, the use of fossil fuels leads to an increase of the CO₂ concentration in the atmosphere, causing global warming which can have catastrophic consequences as previously mentioned.

Therefore, to address the global climate change problem sustainable sources of energy and materials are needed, based on renewable sources and/or carbon-free technologies⁷⁻⁹. It is believed that the production of energy, fuels and chemicals using renewable sources, such as Lignocellulosic Biomass (LB), is essential to achieve a sustainable future⁷⁻⁹. This can be achieved through a biorefinery, which is analogous to a petroleum refinery for the production of fuel, heat, electricity and/or chemicals from biomass⁷⁻⁹.

1.2.3 Green chemistry and engineering

1.2.3.1 Green chemistry

Green chemistry has been defined by the IUPAC as “Design of chemical products and processes that reduce or eliminate the use or generation of substances hazardous to humans, animals, plants, and the environment. Green chemistry discusses the engineering concept of pollution prevention and zero waste both at laboratory and industrial scales. It encourages the use of economical and eco-compatible techniques that not only improve the yield but also bring down the cost of disposal of wastes at the end of a chemical process”¹⁰. Paul Anastas and John Warner developed guidelines on what would make a chemical process or product greener^{11,12}.

Prevention - It is better to prevent waste than to treat or clean up waste after it has been created^{11,12}.

Atom economy - Synthetic methods should be designed to maximize the incorporation of all materials used in the process into the final product^{11,12}.

Less hazardous chemical syntheses - Wherever practicable, synthetic methods should be designed to use and generate substances that possess little or no toxicity to human health and the environment ^{11,12}.

Designing safer chemicals - Chemical products should be designed to preserve the efficacy of function while reducing toxicity ^{11,12}.

Safer solvents and auxiliaries - The use of auxiliary substances (*e.g.* solvents, separation agents, etc.) should be made unnecessary wherever possible and, innocuous when used ^{11,12}.

Design for energy efficiency - Energy requirements should be recognized for their environmental and economic impacts and should be minimized. Synthetic methods should be conducted at ambient temperature and pressure ^{11,12}.

Use of renewable feedstocks - A raw material or feedstock should be renewable rather than depleting whenever technically and economically practicable ^{11,12}.

Reduce derivatives - Unnecessary derivatization (use of blocking groups, protection/deprotection, temporary modification of physical/chemical processes) should be minimized or avoided if possible because such steps require additional reagents and can generate waste ^{11,12}.

Catalysis - Catalytic reagents (as selective as possible) are superior to stoichiometric reagents ^{11,12}.

Design for degradation - Chemical products should be designed so that at the end of their function they break down into innocuous degradation products and do not persist in the environment ^{11,12}.

Real-time analysis for pollution prevention - Analytical methodologies need to be further developed to allow for real-time, in-process monitoring and control prior to the formation of hazardous substances ^{11,12}.

Inherently safer chemistry for accident prevention - Substances and the form of a substance used in a chemical process should be chosen to minimize the potential for chemical accidents, including releases, explosions, and fires ^{11,12}.

1.2.3.2 *Green engineering*

Green engineering focuses on how to achieve sustainability through science and technology by making greener chemical processes, systems or products ¹³. Different approaches with similar

goals have been developed, *e.g.* the 12 engineering principles formulated by Paul Anastas and Julie Zimmerman, and the Sandestin principles of green engineering.

Although it is certainly true that all human processes and actions will impact the environment to some extent, it is extremely important to minimize those effects that could irreversibly and significantly alter the environment by designing more sustainable products, processes, and systems ¹³. These principles have been taken into consideration in this work to design a biorefinery using a novel pretreatment technology based on ionic liquids (the *ionoSolv* process), presented in section 4.3.3. They have also been used to perform a high-level assessment of the environmental benefits of a novel synthetic method for metal oxide production, based on the direct oxidation of metals in aqueous ILs solutions (the *Oxidative Ionothermal Synthesis (OIS)*), presented in section 3.6.

1.2.3.2.1 The 12 principles of green engineering

These principles are not simply a listing of goals, but rather a set of methodologies to accomplish the goals of green design and sustainability ¹⁴.

Principle 1 - Inherent rather than circumstantial: Designers need to strive to ensure that all material and energy inputs and outputs are as inherently non-hazardous as possible ¹⁴.

Principle 2 - Prevention instead of treatment: It is better to prevent waste than to treat or clean up waste after it is formed ¹⁴.

Principle 3 - Design for separation: Separation and purification operations should be designed to minimize energy consumption and materials use ¹⁴.

Principle 4 - Maximize mass, energy, space, and time efficiency: Products, processes, and systems should be designed to maximize mass, energy, space, and time efficiency ¹⁴.

Principle 5 - Output-pulled versus input-pushed: Products, processes, and systems should be “output pulled” rather than “input pushed” through the use of energy and materials. This applies to chemical reactions or transformations at equilibrium, which can be “driven” to completion whether by adding more energy or materials (push) or by removing the products (pulled) to shift the equilibrium towards the desired output. By doing this, the amount of resources consumed to transform inputs into the desired outputs are minimized ¹⁴.

Principle 6 - Conserve complexity: Embedded entropy and complexity must be viewed as an investment when making design choices on recycling, reuse, or beneficial disposition. This

means that it is not always beneficial to recycle a composite material to recover its constitutive materials ¹⁴.

Principle 7 - Durability rather than immortality: Targeted durability, not immortality, should be a design goal in order to avoid the accumulation of undesirable materials in the environment ¹⁴.

Principle 8 - Meet need, minimize excess: Design for unnecessary capacity or capability (*e.g.* “one size fits all”) solutions should be considered a design flaw ¹⁴.

Principle 9 - Minimize material diversity: Material diversity in multicomponent products should be minimized to promote disassembly, recyclability and value retention ¹⁴.

Principle 10 - Integrate local material and energy flows: Design of products, processes, and systems must include integration and interconnectivity with available energy and materials flows. Doing this might significantly benefit the life cycle of a process by reducing the need for raw materials and energy acquisition and requiring less processing and disposal ¹⁴.

Principle 11 - Design for commercial “afterlife”: Products, processes, and systems should be designed for performance in a commercial “afterlife”. To reduce waste, components that remain functional and valuable can be recovered for reuse and/or reconfiguration ¹⁴.

Principle 12 - Renewable rather than depleting: Material and energy inputs should be renewable rather than depleting ¹⁴.

1.2.3.2.2 [The Sandestin Declaration: 9 principles of green engineering](#)

In 2003, approximately 65 chemists and engineers from industry, academia, and government met at the Sandestin Resort in Florida (USA) for a conference on “Green Engineering: Defining the Principles.” By the end of the conference, the scientists and engineers collectively agreed to a compiled set of nine principles, now known as The Sandestin Declaration ¹³.

1. Engineer processes and products holistically, use systems analysis and integrate environmental impact assessment tools ¹³.
2. Conserve and improve natural ecosystems while protecting human health and well-being ¹³.
3. Use life-cycle thinking in all engineering activities ¹³.
4. Ensure that all material and energy inputs and outputs are as inherently safe and benign as possible ¹³.

5. Minimize depletion of natural resources ¹³.
6. Strive to prevent waste ¹³.
7. Develop and apply engineering solutions, while being cognizant of local geography, aspirations, and cultures ¹³.
8. Create engineering solutions beyond current or dominant technologies; improve, innovate, and invent (technologies) to achieve sustainability ¹³.
9. Actively engage communities and stakeholders in the development of engineering solutions ¹³

1.3 Overall knowledge gaps

From the reviewed literature the importance of decreasing CO₂ emissions of industrial processes was evident. Efforts are being made to replace products obtained from the petrochemical industry (and fossil fuels) with more sustainable bio-derived products. Even though lignocellulosic biomass seems a viable candidate for sustainable chemical and fuel production, there is still a need for a cost-effective, flexible and efficient biomass conversion process that can be implemented at large scale.

There are a diversity of methods that have been developed to allow the conversion of cellulose into sugars, which can be then used as precursors for chemical and biofuels, such as bioethanol (details on these methods are discussed in section 4.2.5). Among biomass conversion processes, there are those based on ILs. These substances possess interesting properties, such as low vapour pressures, which would allow:

- Operating at high temperatures without developing high pressures, improving process safety and the need for expensive pressure resistance equipment.
- Solvent recovery with no losses to atmosphere, improving process safety and reducing atmospheric pollution.

There are a great number of possible ILs, for which their physicochemical properties can be adjusted by selecting the cation and the anion ¹⁵. Different types of ILs have already been used for the pretreatment of a variety of feedstocks (details in section 4.2.6). However, many IL-based pretreatments suffer from major challenges that make their industrial application unfeasible. In the quest for effective and cost-efficient alternatives for aprotic ionic liquids, Dr Agnieszka Brandt developed at Imperial College London a biomass pretreatment strategy based on acidic protic ILs (alkylammonium hydrogen sulfate ILs), which are low-cost and very

effective for biomass fractionation³. This process has been named the ionoSolv process³. Since its discovery, progress has been made in understanding the underlying science of the interactions of these ILs with different lignocellulosic biomass feedstocks, for the production of cellulose-rich pulp and lignin^{3,16}. However, despite the claims made about the potentials of implementing this technology in large scale processes, at the time this research work began, there was not a detailed Techno-Economic Analysis (TEA) to support such statements.

Several preliminary TEA, performed by Master students, showed the economic potential of the technology¹⁷⁻¹⁹. Many assumptions were made in the development of these preliminary assessments, therefore, there is a high uncertainty level associated with those models. For example, detailed physicochemical data (densities, viscosities, and heat capacities) for the aqueous ILs were not used to generate the heat and material balances or for equipment sizing.

Moreover, as ILs are not used extensively in industry, there is scarce data about the corrosion behaviour of metals exposed to these substances, and no data at all for the ILs used in the ionoSolv process. Selecting the right materials of construction is critical to evaluate the technical and economic feasibility of a process. More importantly, those assessments do not benchmark the ionoSolv process with other biomass pretreatment technologies, therefore, the benefits of implementing this process within a biorefinery are known.

It is extremely important to reduce the uncertainty of variables affecting the outcome of the TEA for the ionoSolv process, in order to establish if this is a viable solution for biomass processing, and if the implementation of this process can contribute to the development of more cost-effective and sustainable biorefineries.

It has also been noticed that most of the TEAs performed for the ionoSolv process limit their scope to the process being evaluated. As there are many uncertainties and assumptions made at an early stage, the usefulness of such studies is questionable. A more powerful approach is to perform the TEA on a novel process and compare it to established technologies, so that the actual benefits of a new technology can be established.

1.4 General objectives

It has been hypothesised that the ionoSolv process can be a viable alternative for lignocellulosic biomass fractionation in a large-scale biorefinery for bioethanol production. The general objective of this work is to test this hypothesis by comparing the economic performance of the ionoSolv pretreatment against the Acid Catalysed Steam Explosion (ACSE) within a biorefinery producing bioethanol using hardwood as feedstock, specifically *Eucalyptus red grandis*.

To achieve this, Eucalyptus fractionation using an IL (*N,N,N*-triethylammonium hydrogen sulfate) will be experimentally tested, and the process conditions (temperature and time) will be optimized to maximize cellulose conversion into glucose. The effect of using CO₂ atmospheres (sub and supercritical) on the ionoSolv pretreatment performance will be explored as a means to improve the pretreatment efficiency. The optimum conditions will be used to model the process in Aspen HYSYS. Once the Heat and Material Balances (HMBs) are completed, process equipment will be sized according to good engineering practice and costed using costing correlations. Sensitivity analysis will be performed to gain insight on how different process variables impact the investment costs (CAPEX) and operating cost (OPEX) of the ionoSolv process. Finally, the ionoSolv pretreatment will be compared to the Acid Catalysed Steam Explosion (ACSE) pretreatment method, which is one of the most studied biomass fractionation processes.

To improve the accuracy of the TEA, physicochemical data of hydrogen sulfate based ILs will be measured experimentally. Additionally, a systematic corrosion study of common metals (*e.g.* Al, Cu, Fe, Ni, Mo, Ti and Zn) and some alloys (*e.g.* brass and stainless steel 304 (304 SS)) in common ILs will be performed. The corrosion rates in neat and aqueous ILs will be quantified to gain some insight into possible materials of construction for IL-based chemical processes.

1.5 Thesis outline

This thesis has been separated into chapters which are intended to cover specific topics. They include a literature review at the beginning highlighting the most relevant information and knowledge gaps for the topic under consideration. They also include the method section and the results and discussions, conclusions, and future work. The last chapter is a summary of the main findings of this work.

Chapter 2 covers the definition of ILs, focussing on protic ILs, their synthesis, physicochemical properties of interest for process design, and the properties of their mixtures with water (page 27).

Chapter 3 covers the interactions of ILs with metals. As the use of ILs in industrial processes is relatively new, few data are available on the corrosion behaviour of metals exposed to these substances. Material selection plays a major role when evaluating the industrial implementation of processes as it will impact the cost. This chapter focuses on the corrosion processes of metals exposed to ILs with the aim of proper material selection for techno-economic assessments. A categorization method to classify the corrosion behaviour of metals

exposed to corrosive media was developed for ILs but can be extended to other systems. Additionally, it explored the economic potential of producing metal-based materials (nano and micro) *via* the Oxidative Ionothermal Synthesis (OIS) method (page 73).

Chapter 4 explores the use of low-cost ILs (hydrogen-sulfate based ILs) for *Eucalyptus red grandis* fractionation (ionoSolv process) and the techno-economic feasibility of implementing this process for bioethanol production (page 161).

Chapter 5 summarises the main findings of this thesis (page 237).

Supporting information, numeric results, a high-level techno-economic analysis of the OIS process for zinc oxide production and a method for the process and economic evaluation of a biorefinery are presented in the appendixes.

1.6 Publications and presentations

1. Malaret, F., Hallett, J. & Campbell, K. S. Oxidative ionothermal synthesis for micro and macro Zn-based materials. *Mater. Adv.*, **1**, 3597–3604 (2020). DOI: [10.1039/D0MA00660B](https://doi.org/10.1039/D0MA00660B)
2. Chen M, Malaret F, Firth AEJ, Verdía P, Abouelela AR, Chen Y, et al. Design of a combined ionosolv-organosolv biomass fractionation process for biofuel production and high value-added lignin valorisation. *Green Chem.*, **22**, 5161(2020) DOI: [10.1039/D0GC01143F](https://doi.org/10.1039/D0GC01143F)
3. Malaret, F., Gschwend, F. J. V., Lopes, J. M., Tu, W.-C. & Hallett, J. P. Eucalyptus red grandis pretreatment with protic ionic liquids: effect of severity and influence of sub/super-critical CO₂ atmosphere on pretreatment performance. *RSC Adv.*, **10**, 16050–16060 (2020). DOI: [10.1039/D0RA02040K](https://doi.org/10.1039/D0RA02040K)
4. Gschwend FJ V, Malaret F, Shinde S, Hallett JP. Rapid pretreatment of Miscanthus using the low-cost ionic liquid triethylammonium hydrogen sulfate at elevated temperatures. *Green Chem.*, **20**, 3486-3498 (2018). DOI: [10.1039/C8GC00837J](https://doi.org/10.1039/C8GC00837J)
5. Abouelela A.R., Gschwend F.V., Malaret F., Hallett J.P. (2020) Commercial Aspects of Biomass Deconstruction with Ionic Liquids. In: Shiflett M. (eds) Commercial Applications of Ionic Liquids. Green Chemistry and Sustainable Technology. Springer, Cham. DOI:[10.1007/978-3-030-35245-5_5](https://doi.org/10.1007/978-3-030-35245-5_5)
6. The 8th International Congress on Ionic Liquids (COIL-8). Oral presentation: Are Metallic Materials Suitable to Build Green Ionic-Liquids Based Processes? Beijing, China MAY 13-17, 2019

1.7 Acronyms and abbreviations

2SIP	Double solvent-separated ion pair
ACSE	Acid catalysed steam explosion
AFM	Atomic force microscopy
AIL	Aprotic ionic liquid
AInL	Acid insoluble lignin
APD	Average percent deviation
ASL	Acid soluble lignin
BOD	Biological oxygen demand
CAC	Critical aggregation concentration
CAPEX	Capital investment
CEMS	Conversion electron Moessbauer spectroscopy
CIP	Contact ion pair
COD	Chemical oxygen demand
CR	Corrosion rate
CrI	Crystallinity index
CS	Carbon steel
CSW	Chemical supercondensation by water
DAP	Diluted acid pretreatment
DBN	1,5-diazabicyclo[4.3.0]non-5-ene
DBU	1,8-diazabicyclo[5.4.0]undec-7-ene

DOSY	Diffusion-ordered spectroscopy
DSC	Differential scanning calorimetry
DZR	Dezincification-resistant (or DR)
ECHA	European Chemical Agency
EMF	Electromotive Force
EPMA	Electron probe microanalysis
FEP	Fluorinated ethylene propylene
FTIR	Fourier transform infrared
GDP	Gross domestic product
GHG	Greenhouse gas
GPC	Gel permeation chromatography
HMB	Heat and materials balance
HMF	Hydroxymethylfurfural
HPLC	High-performance liquid chromatography
IC	Ion chromatography
ICL	Imperial College London
ICP-MS	Inductively coupled plasma mass Spectrometry
ICP-OES	Coupled Plasma Optical Emission Spectrometry
IL	Ionic liquid
IMS	industrial methylated spirits
IRPD	infrared photodissociation
KF	Karl Fisher
KPFM	Kelvin probe force microscopy
LB	Lignocellulosic biomass
LCA	Life cycle analyses
MARD	Maximum absolute relative deviation
MCR	Mass change rate
MD	Molecular dynamic
MESP	Minimum ethanol selling price
MSDS	Material safety data sheet
MSW	Municipal solid waste
NREL	National Renewable Energy Laboratory
ODW	Oven-dried weight
OIS	Oxidative ionothermal synthesis
OPEX	Operating cost
PEEK	Polyether-ether-ketone
PFA	Perfluoroalkoxy alkane
PFD	Process flow diagram
PIL	Protic ionic liquids
PTFE	Polytetrafluoroethylene
PVC	Polyvinyl chloride
REACH	Registration, evaluation, authorisation and restriction of chemicals
RES	Relative standard deviation
RO	Reverse osmosis
SECM	Scanning electrochemical microscopy
SERI	Solar Energy Research Institute
SHG	Special high grade
SIMS	Secondary ion mass spectrometry
SIP	Solvent-shared ion pair
SRC	Sugar recovery coefficient
SS	Stainless steel

STEX	Steam explosion
STM	Scanning tunnelling microscopy
SWEC	Stone & Webster Engineering Corporation
TEA	Techno-economic analysis
TEG	Triethylene glycol
TIEC	Total installed equipment cost
TPES	Total primary energy supply
TRL	Technology Readiness Level
VBT	Volume-based thermodynamics
VC	Vapour-compression
VTF	Vogel–Tammann–Fulcher
WFI	Water for injection
XPS	X-ray photoelectron spectroscopy
XRD	X-ray diffraction
XRF	X-ray fluorescence
ZCAR	Zinc carbonate hydroxide ($\text{Zn}_5(\text{CO}_3)_2(\text{OH})_6\text{Cl}_2 \cdot \text{H}_2\text{O}$)
ZHC	Zinc chloride hydroxide monohydrate ($\text{Zn}_5(\text{OH})_8\text{Cl}_2 \cdot \text{H}_2\text{O}$)
β	Base:acid ratio

Chapter 2 - Ionic liquids – Synthesis, characterisation and physicochemical properties

2.1 Motivation

Research on different applications of Ionic Liquids (ILs) has increased over the last decades, mainly due to the tuneable properties of these solvents. Another reason for the increased interest around these substances is that they are considered “green” solvents due to their low volatilities¹. However, despite the great number of possible applications for ILs, there are only a few commercial processes using them to date. The main reason is their high cost, which makes their implementation in large scale industrial processes not economically viable^{20,21}. A relatively new type of low-cost ILs, such as the Protic Ionic Liquids (PILs) based on the hydrogen sulfate anion, may open the door for industrial applications, such as biomass fractionation (ionoSolv process)³.

These types of ILs have not been extensively used by the scientific community and therefore, little data on their properties is available. This chapter is intended as an introduction to ILs, with focus on the synthesis of hydrogen sulfate-based ILs and the physicochemical properties of these ILs and their mixtures with water. The use of experimental data for the physicochemical properties of fluids used in a chemical process is very important to improve the accuracy of any technical assessment. This data is used for the Techno-economic Analysis (TEA) of a biorefinery employing *N,N,N*-dimethylbutylammonium hydrogen sulfate $[N_{4110}][HSO_4]$ to fractionate *Eucalyptus red grandis* (Chapter 4).

2.1.1 Objectives

The main objective of this chapter is to introduce the topic of ionic liquids, with focus on the alkylammonium hydrogen sulfate ILs. Establish their synthesis methods, both at lab-scale and large-scale processes. The impact of base:acid ratio for this kind of ILs is discussed and an equation to determine such ratio through acid-base titrations is developed. Additionally, physicochemical properties of interest (*e.g.* density, viscosity, crystallisation temperature and thermal stability) for process design for one of these ILs ($[N_{4110}][HSO_4]$), anhydrous and aqueous, are measured to perform detailed process simulations and design.

2.2 Ionic liquids

Ionic Liquids (ILs) are ionic melts, generally defined as those with low melting point (100 °C and below). Some ILs are liquid at room temperature and are known as Room Temperature Ionic

Liquids (RTIL). Of particular interest is their low melting, a result of poor coordination amongst the constituent ions on ILs, thereby preventing the formation of a stable crystal lattice ²². However, this does not simply yield an ‘electrolytic-like’ solution; rather, ILs can form stable and structured polar and nonpolar regions in the liquid phase due to the interplay between the strong coulombic forces between cations and anions, van der Waals and π - π interactions, and hydrogen bonding ^{23,24}. ILs display several useful, and often tuneable, properties such as low vapour pressure, wide liquid region with respect to temperature, high thermal and chemical stability, low combustibility, just to name a few. For these reasons, they have been tagged as an environmentally-friendly alternative capable of replacing organic solvents industrially ¹.

The properties of ILs can be adjusted by alterations to their anion and/or cation components ²⁵. The terms “task-specific” ILs and “designer solvents” account for the fact that by changing the chemical structure of an IL, *i.e.*, their constituent cation and anion, its physicochemical properties can be adjusted to meet a specific application. Typical cations and anions are shown in Figure 1 and Figure 2 respectively. There are a great number of possible ILs that can be synthesized, in fact, this number has been estimated to be approximately one million (10^6), with one billion (10^{12}) binary combinations of these, and one trillion (10^{18}) ternary systems possible ^{21,26}. These numbers have been used systematically in the scientific literature to illustrate the huge amount of ILs, compared to the 750 organic solvents commonly used in industry. Nonetheless, the number of ILs studied and used is several orders of magnitude lower. For example, SCM software COSMO-RS contains a database for ILs (ADFCRS-IL-2014) with 80 cations and 56 anions (4480 ILs). The NIST Standard Reference Database #147 (Ionic Liquids Database – ILThermo (v2.0), contains 1826 references (Last updated June 11th, 2019). According to several sources, there are approximately 300 ILs commercially available ²¹. This shows that there are still many opportunities to be discovered.

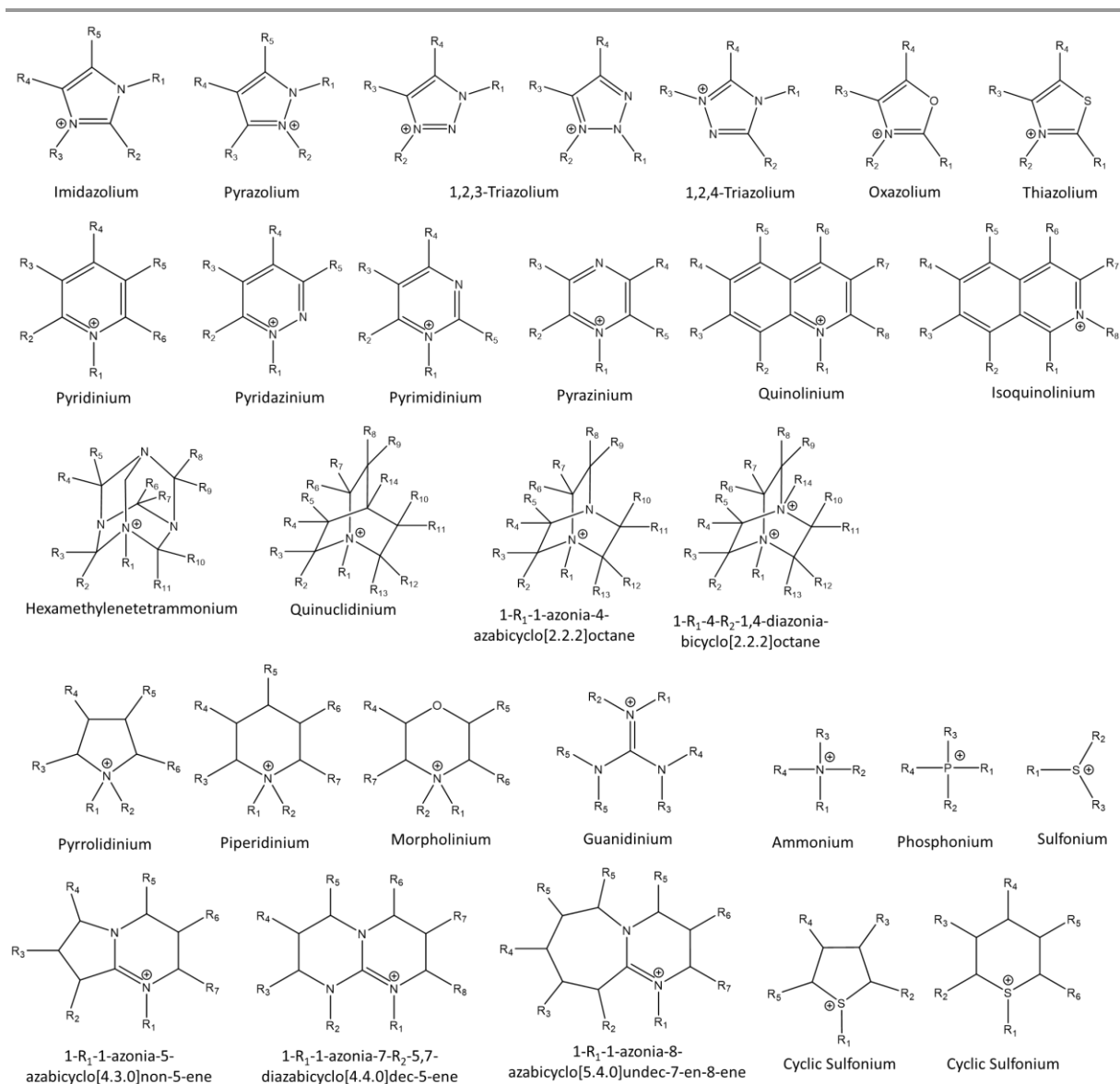


Figure 1. Common cations found in ILs. Wherein R₁ to R₁₄ are independently selected from H, a C₁ to C₂₄ alkyl chain, a C₁ to C₂₄ substituted alkyl chain, phenyl group, substituted phenyl groups, -OH, -OR₁, -SR₁, -SH, -CN, -NH₂, -NHR₁, -NR₁R₂, -SO₃H group, -OSO₃H group, -COH, -COOH, -NO₂, -Cl, -Br, -F, -I, -C≡N. The C₁ to C₂₄ alkyl chain can be linear, branched, cyclic and can contain one or several functional groups such as double bonds (-C=C-), triple bonds (-C≡C-), phenyl groups, substituted phenyl groups, -OH, -OR₁, -SR₁, -SH, -CN, -NH₂, -NHR₁, -NR₁R₂, -SO₃H group, -OSO₃H group, -COH, -COOH, -NO₂, -Cl, -Br, -F, -I, -C≡N.

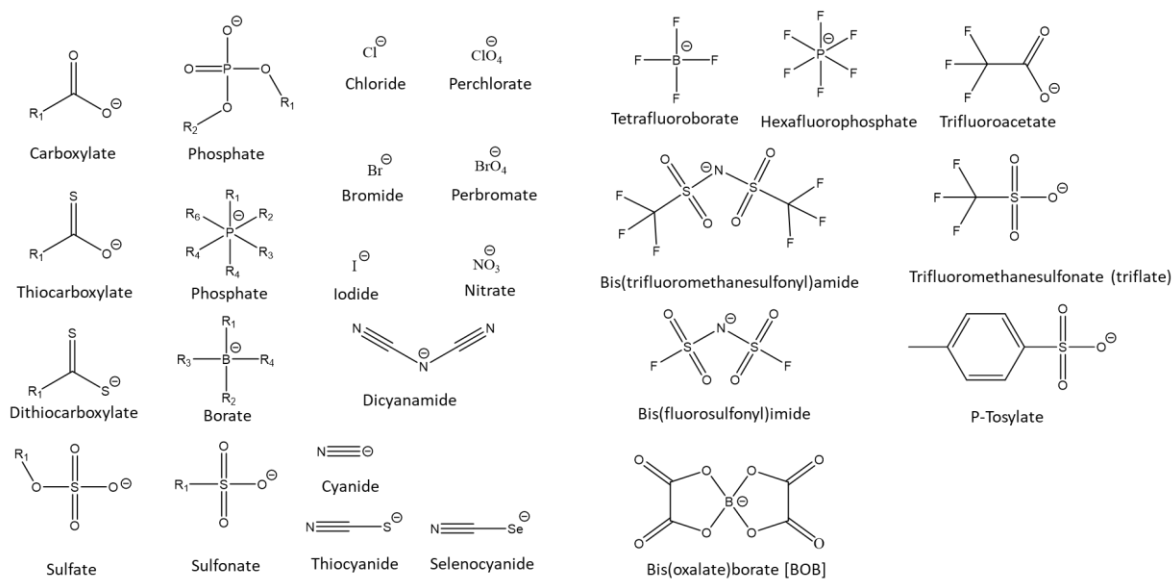


Figure 2. Commonly used anions found in ionic liquids. Common cations found in ILs. Wherein R_1 to R_{14} are independently selected from H, a C_1 to C_{24} alkyl chain, a C_1 to C_{24} substituted alkyl chain, phenyl group, substituted phenyl groups, -OH, -OR₁, -SR₁, -SH, -CN, -NH₂, -NHR₁, -NR₁R₂, -SO₃H group, -OSO₃H group, -COH, -COOH, -NO₂, -Cl, -Br, -F, -I, -C≡N. The C_1 to C_{24} alkyl chain can be linear, branched, cyclic and can contain one or several functional groups such as double bonds (-C=C-), triple bonds (-C≡C-), phenyl groups, substituted phenyl groups, -OH, -OR₁, -SR₁, -SH, -CN, -NH₂, -NHR₁, -NR₁R₂, -SO₃H group, -OSO₃H group, -COH, -COOH, -NO₂, -Cl, -Br, -F, -I, -C≡N.

Due to the great number of possible ILs generalizations regarding their properties should be avoided as they can be either toxic or benign, safe or hazardous, non-volatile or distillable. Despite their interesting properties, there are some limiting factors for their industrial implementation, such as their high viscosity, and more importantly, their high cost. Conventional Aprotic Ionic Liquids (AILs), which do not possess acidic protons, *e.g.* protonated amine, that can participate in acid-base reactions, are generally too costly for large scale industrial applications. The reason for their high cost is the number of different reaction steps needed for their synthesis and purification procedures²⁷. Protic Ionic Liquids (PILs), which are easily produced through the combination of a Brønsted acid and Brønsted base, can be substantially cheaper and therefore economically viable for large scale applications. The relatively low-cost starting materials, short and simple synthesis procedures and the lack of (or relatively fewer) purification steps radically reduces the price of this type of ILs^{28,29}. The bulk production cost for PIL have been estimated from 0.78-5.88 \$US/kg (based on 2014 chemical commodity prices) compared to 20-100 \$US/kg for 1-ethyl-3-methylimidazolium acetate [C₂C₁im][OAc]²⁷. One of the cheapest PILs are those made with sulfuric acid, such as *N,N,N*-triethylammonium hydrogen sulfate [N₂₂₂₀][HSO₄], which can be produced for as low as 1.24 \$US/kg²⁸. A recent estimation evaluated the cost of this PIL at 0.78 \$US/kg, making it one of the most economically viable candidates for industrial applications³⁰. Further information about the cost of ILs is presented in Appendix 1. The use of this IL for lignocellulosic biomass (LB) pretreatment will be explored in Chapter 4. An analogous IL, *N,N,N*-

dimethylbutylammonium hydrogen sulfate $[N_{4110}][HSO_4]$, have equal or better performance than $[N_{2220}][HSO_4]$ for hardwood and grass fractionation^{16,31,32}. Whereas $[N_{2220}][HSO_4]$ is suitable for the fractionation of hardwood and grass, it was found that it is not suitable for softwood, a more recalcitrant type of biomass (section 4.2.1)^{16,31}. However, an isomeric IL, $[N_{4110}][HSO_4]$, is very efficient for softwood fractionation^{16,31}. As process efficiency should be maximized, as well as the flexibility to treat different types of biomass, it is likely that large-scale ionoSolv-based biorefineries will use $[N_{4110}][HSO_4]$. For this reason, the $[N_{4110}][HSO_4]$ isomer has been selected for the corrosion study presented in Chapter 3. Additionally, based on the price of raw materials for the amine fabrication at large scale, it is suspected that $[N_{4110}][HSO_4]$ can be produced at the same or even at lower cost than $[N_{2220}][HSO_4]$, making it a better candidate for industrial applications. However, this amine is not yet produced at large scale, therefore its bulk cost remains known. Another PIL used in an industrial application is 1-methylimidazolium chloride $[HC_{1im}][Cl]$, employed in the BASIL (biphasic acid scavenging using ionic liquids) process by BASF. The corrosion behaviour of this IL is also studied in Chapter 3. Figure 3 presents the chemical structure and synthesis reactions for these PILs. Further details are provided in section 2.3.1.

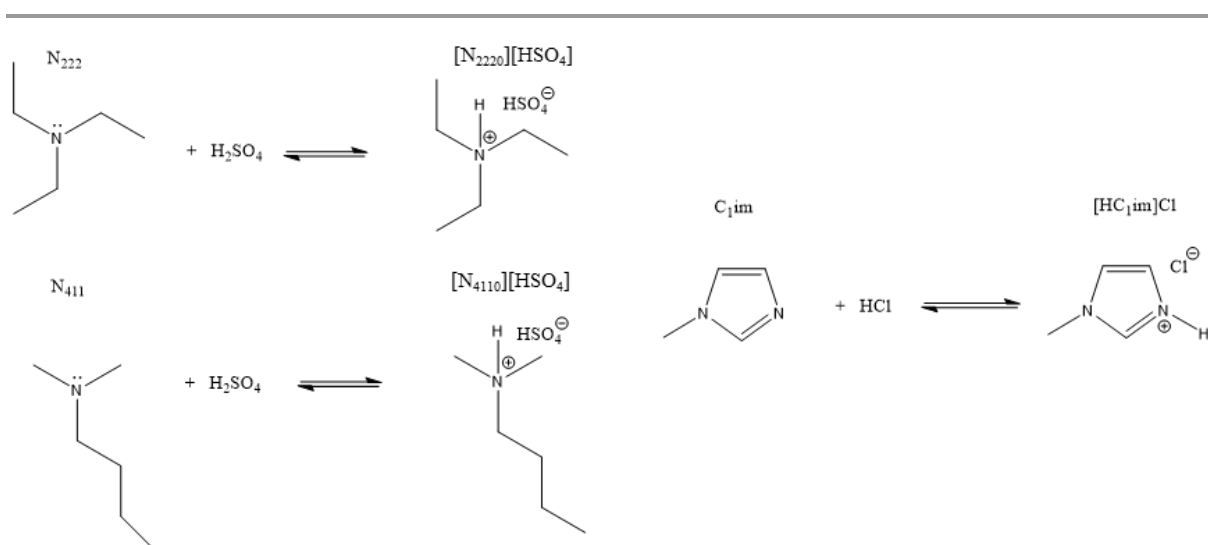


Figure 3. Example of protic ionic liquids.

2.2.1 Applications of ILs

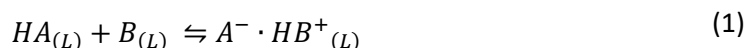
There are several reviews on the history, applications and perspectives of ILs^{15,20,21}. Many applications have been considered, some commercialized, and others remain under development²¹. ILs, as solvents for synthesis and catalysis, have been used in all sort of chemical reactions, including electron transfer, acid-base, substitutions, eliminations, additions, acid-catalysed, base/nucleophile catalysed, and transition-metal catalysed reactions

¹⁵. ILs have been also used for other applications, such as pharmaceuticals, aluminium plating, nuclear fuel reprocessing, solar thermal energy, waste recycling, batteries, dispersing agents in paints, carbon capture, tribology (lubricants) and cellulose processing, which will be discussed in detail in section 4.2.6.

Despite the great number of ILs and potential applications, their use in large-scale processes is still limited, being one of the key concerns on the feasibility of industrial use of ILs, their cost ^{2,21}. In a recent publication it has been identified 57 implemented ILs applications, compared to 13 in 2008, at different stages. *i.e.* 25 applications in pilot trials, 27 commercial applications, and 1 and 3 applications that went from pilot trials to commercial scale in 2019 and 2020 respectively ².

2.2.2 Protic Ionic Liquids (PILs)

Although PILs are very easy to form, just a neutralization reaction of a Brønsted acid with a Brønsted base as shown in Eq. 1, some of them may exhibit inferior properties to their equivalent aprotic versions, due to incomplete proton transfer from the Brønsted acid to the Brønsted base. For example, some PILs have relatively high vapour pressures and low conductivities ³³.



The mechanisms of proton transfer in protic ionic liquids are widely discussed in the literature, and it was found that the interaction of a Brønsted acid with a Brønsted base by the neutralization reaction does not always lead to a complete proton transfer from the acid to the base or formation of PIL, but rather leads to a more complex system, as illustrated in Figure 4 ³⁴.

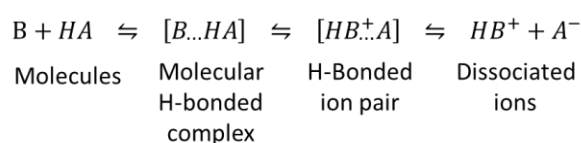


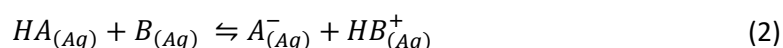
Figure 4. Proton transfer process in the formation of PIL³⁴.

The degree of proton transfer from the acid to the base can vary depending on the acid and base strength, and can be determined by the IR and NMR spectroscopy methods, quantum-chemical calculations, and other complex approaches combining theoretical and experimental research methods ³⁴. It is outside the scope of this thesis to present a detailed description of

the fundamental aspects of these systems, rather, the discussion is centred in relevant aspects for process design using these substances.

2.2.3 Thermodynamic considerations of PIL formation

There is extensive information on the equilibrium and energy involved in the proton transfer process between acid and bases in aqueous media. The relevance of the behaviour of the same acids and bases interacting in the absence of water has been studied, to establish if data in aqueous systems can be used to predict the formation of PIL^{33,35,36}. The work (energy) of proton transfer to restore the original molecular acid and base molecules from the IL should therefore be much greater in the absence of any dielectric, particularly a medium with a high dielectric constant such as water (Eq. 2). It has been concluded that estimations of the energy change during proton transfer for PIL formation can be estimated from proton free energy level diagrams but for accurate values it should be experimentally determined^{33,35}.



The behaviour of PIL have been studied as a function of ΔpK_a and it has been concluded that when the difference of the aqueous pK_a of the acid and the amine (ΔpK_a) is greater than 10, the equilibrium shown in Eq. 1 lies to the right, with the formation of a PIL with transport behaviour similar to AILs. When the difference in ΔpK_a is smaller than 10, the chemical species in Eq. 1 might be equilibrium with H-bonded complexes (Figure 4), which leads in some instances to high vapour pressures and low conductivities^{33,35,36}. The higher the difference in the ΔpK_a of the Brønsted acid with a Brønsted base, the closer the behaviour of a PIL to an AIL. The pK_a values of common acids and amines obtained from various sources, such as handbooks, databases and scientific publications, are given in Table 1.

Table 1. pK_a values for selected substances.

Name	Abbreviation	$pK_a(aq)$
Ammonia	N ₀₀₀	9.25 [A] ³⁷
<i>N,N,N</i> -Triethyl amine	N ₂₂₂	10.8 [A] ³⁶
<i>N,N,N</i> -Dimethyl-butyl amine	N ₄₁₁	10.2 [A] ³⁶
Methylimidazole	C _{1Im}	7.20 [A,B] ³⁸
Acetic acid	CH ₃ COOH	4.75 ³³
Sulfuric acid	H ₂ SO ₄	-9 ³³
Hydrogen sulfate	HSO ₄ ⁻	1.99 ³⁷
Hydrochloric acid	HCl	-5.9 ³⁹
Nitric acid	HNO ₃	-1.3 ³³ , -1.55 ⁴⁰
Hydrobromic acid	HBr	-8.8 ³⁹
Hydroiodic acid	HI	-9.5 ³⁹
Perchloric acid	HClO ₄	-15.4 ³⁹

- A. pKa of the protonated amine
- B. Average of 2 values reported in literature 7.21 and 7.19

From the values of pKa in Table 1 it can be seen that the protonated ammonium cations have higher pKa than the protonated imidazolium cations, almost 3 orders of magnitude, which makes them good candidates for the formation of PILs. Sulfuric acid has a lower pKa than hydrochloric acid, which makes it a good acid for PIL. Both *N,N,N*-triethylammonium and *N,N,N*-dimethylbutylammonium chlorides are solids at room temperature. *N,N,N*-Triethylammonium hydrogen sulfate is a solid at room temperature and *N,N,N*-dimethylbutylammonium hydrogen sulfate is a liquid. The importance in the difference of pKa in the formation of PIL can be illustrated with the case of *N,N,N*-triethylammonium acetate which was reported as an extreme case in which the acid and base do not even mix ³⁶.

This can be explained in terms of the free energy change in the proton transfer process. When it is large, the proton may become so firmly bound to the Brønsted base that the probability of reforming the acid molecule HA becomes negligible at ambient temperatures, and in some cases, it remains negligible even at temperatures as high as 300 °C. This probability is measured by the Boltzmann function $\exp(-\epsilon/kT)$, where $\epsilon = \Delta G^\circ/N_{Av}$ and ΔG° is the molar free energy change in the process that reverses the original proton transfer ³⁵.

The fact that the reverse proton transfer can yield two new species from the ionic liquid provides a thermodynamic (entropic) drive to generate a vapour phase. The entropic term must ultimately outweigh the enthalpic term as temperature increases because of the $T\Delta S$ component of the total free energy change (Eq. 3). For practical reasons, the relevant question is if vaporization of the ionic liquid occurs before its decomposition temperature ⁴¹.

$$\Delta G = \Delta H - T\Delta S \quad (3)$$

In summary, Brønsted acid-base neutralization processes can be highly exothermic, therefore it is important to measure experimentally the values of the energy changes involved in this process for the proper design of any synthesis reactor. In the absence of detailed experimental data, this energy can be estimated by several ways, for example using energy level diagrams (Belieres and Angell) ³³, Born–Haber–Fajans like cycle (Figure 5) or computational chemistry

^{34,42–46}

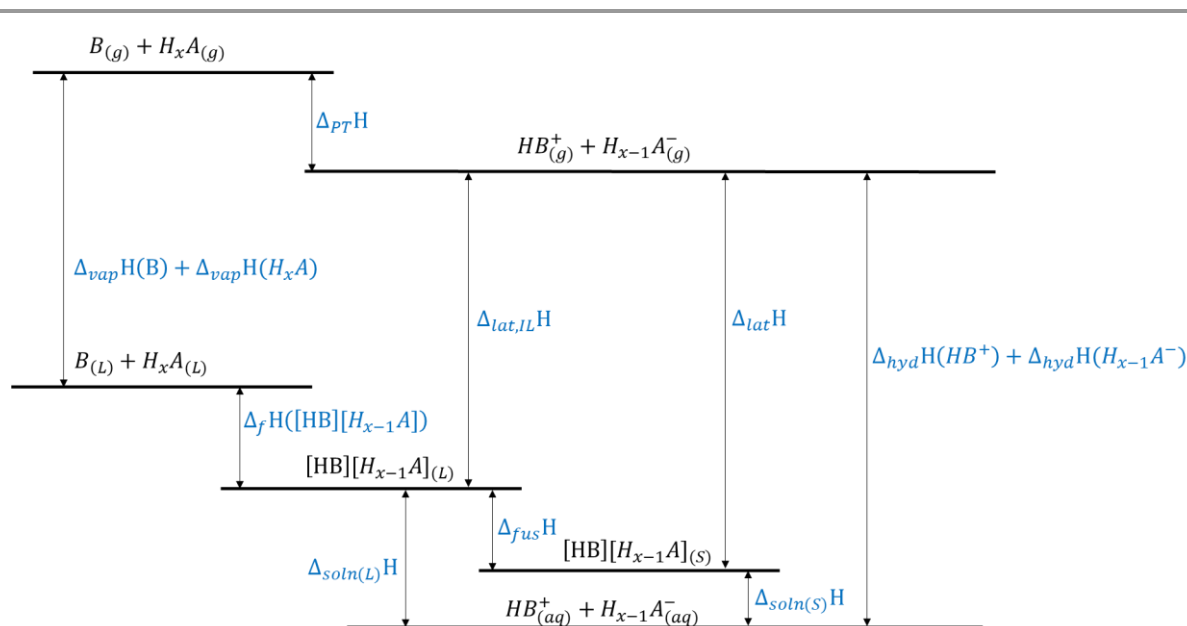


Figure 5. Born–Haber–Fajans cycle for ionic solids, PIL and their aqueous solutions, assuming the acid and base are liquid in standard conditions. $\Delta_{\text{vap}}H$, enthalpy of vaporization. $\Delta_{\text{PT}}H$, enthalpy of proton transfer in gas phase. $\Delta_{\text{lat}}H$ and $\Delta_{\text{lat,IL}}H$ lattice enthalpy of the ionic solid and the PIL respectively. $\Delta_f H$, enthalpy of formation. $\Delta_{\text{fus}}H$, enthalpy of fusion. $\Delta_{\text{hyd}}H$ enthalpy of hydration. $\Delta_{\text{sol,(S)}}H$ and $\Delta_{\text{sol,(L)}}H$ is the enthalpy of solution from the solid or liquid states respectively. The cycle can also be constructed using free energies (ΔG) or entropies (ΔS). However, most experimental data is available for enthalpies. Each of the different enthalpic changes shown in the diagram are described in detail in the literature specifically for ionic solids and AIL, with some shortcuts to estimate some of the quantities^{47,48}.

Surprisingly, up to date, the experimental heat of formation for PIL is not available in the scientific literature. Most of the data available are for AIL, for which some empirical formulae for the estimation of the heat of formation were developed^{49,50}. Some studies determined the heat of formations for acetic acid based IL, to assess the level of proton transfer⁵¹ or the vaporization energies.

There is also scarce thermodynamic data for the heat of neutralization of PIL. A conservative approach is then needed to estimate the energies of the neutralization process for PILs. To illustrate the order of magnitude of the energies involved in the neutralization process of common acid with different bases, the $\Delta_f H^\circ$ was calculated and tabulated in Table 2.

Table 2. Calculated neutralization enthalpy for common acids with different bases³⁷.

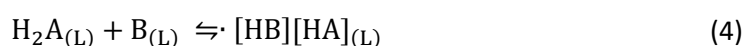
Acid	Salt	Neutralization Enthalpy		
		$\Delta_f H^\circ$ [kJ/mol]		
		NH ₃	NaOH	KOH
Hydrogen chloride	HCl	-176.2	-179.1	-205.4
Hydrogen bromide	HBr	-188.6	-185.0	-218.7
Hydrogen iodide	HI	-182	-174.5	-215.6
Acetic acid	HBAc	-	-84.7	-99.9
Oxalic acid	(HB) ₂ C ₂ O ₄	-209.5	-216.7	-246.7
Hydrogen cyanide	HBCN	-62.6	-56.6	-83.1
Nitric acid	HBNO ₃	-145.6	-154.0	-181.7
Nitrous acid	HBNO ₂	-131.1	-139.4	-151.5

Acid	Salt	Neutralization Enthalpy $\Delta_f H^\circ$ [kJ/mol]		
		NH ₃	NaOH	KOH
Sulfuric acid	HBHSO ₄	-167.1	-171.7	-207.8
Sulfuric acid	(HB) ₂ SO ₄	-275.1	-293.5	-346.2
Perchloric acid	HBClO ₄	-208.8	-202.9	-253.4
Phosphoric acid	HBH ₂ PO ₄	-	-	-145.1
Phosphoric acid	(HB) ₂ HPO ₃	-190.7	-184.1	-
Phosphoric acid	(HB) ₂ HPO ₄	-249.8	-	-249.4

It can be seen from Table 2 that the heat of neutralization of the acids with NaOH or NH₃ is extremely similar, the relative differences range from -6 to 11% with an average value of -0.2%. The neutralization values for KOH are on average 20% higher than NaOH, ranging from 9% to 47%. NH₄⁺ would be the smallest cation for alkylammonium PILs, however, all the salts shown in Table 2 are solids at room temperature. The liquid state has a higher enthalpy than the solid state, as explained before. Therefore, it would be expected that the neutralization process generating a liquid would have a lower $\Delta_f H^\circ$. A computational study on the ion-pair structures and hydrogen bonding in alkylammonium hydrogen sulfate ILs showed that there are 3 main interactions between the cation and the anion: electrostatics forces, hydrogen bonding and dispersion forces. The dispersion contribution to the interionic interaction in cation–anion pairs formation is smaller than that of electrostatic forces and H-bonding⁴⁵. The H-bonding is stronger in primary amines than in tertiary amines, and it decreases with increasing alkyl chain length. On the contrary, the dispersion forces increase with increasing alkyl chain length. However, the overall interaction decreases with increasing alkyl chain length. In that work, the smallest amine studied was methylamine, which had the strongest interionic interaction⁴⁵. In another study, the heat of formation of a series of amine was calculated and it was found that it decreased with increasing size, [N₂₂₀₀][HSO₄] = -141.8 kJ/mol, [N₁₁₁₀][HSO₄] = -98.5 kJ/mol, [N₂₂₂₀][HSO₄] = -109.8 kJ/mol⁵². All these values are smaller than the value for the [N₀₀₀₀][HSO₄] = -167.1 kJ/mol, shown in Table 2. Therefore, in the absence of detailed experimental data, as a conservative approach, the heat of neutralization reaction for PIL can be approximated as to heat of neutralization of the corresponding acid with NH₃ or NaOH. This generalization should hold true for the imidazolium-based PIL, which has lower pKa values than alkylammonium, but should be confirmed for exotic bases, such as the superbases 1,8-diazabicyclo(5.4.0)undec-7-ene (DBU), 1,5-diazabicyclo[4.3.0]non-5-ene (DBN) or guanidine (Figure 1) which have higher pKa in water, ranging from 11.5 to 13.6⁵³.

2.2.4 Base:acid ratio

In a typical PIL synthesis, an equimolar amount of acid and base, either neat or in an aqueous solution, are reacted together. In the scientific literature, it has been reported that when volatile amines are used with monoprotic acids, such as HCl, a slight excess of amine is added to the reaction medium, to ensure a complete reaction, followed by its removal, along with water if aqueous acids are used, by evaporation typically at 80 °C under vacuum using a rotary evaporator. When amines of higher molecular weight are employed, there is a risk of contamination of the product by residual amines³³. This strategy cannot be used for diprotic acids, such as sulfuric acid, as any excess of the amine, even if volatile, will be protonated by the [HSO₄]⁻ anions to form the protonated amine and [SO₄]²⁻ anions. The protonated amine cannot be removed by evaporation (Eqs. 4-5). Likewise, H₂SO₄ is a non-volatile acid, hence adding an excess of it will result in a mixture of the IL with H₂SO₄, which cannot be corrected via evaporation of the excess acid.



It follows that in order to obtain a base:acid ratio of 1:1 for the hydrogen sulfate based ILs, the amount of amine and acid need to be carefully controlled in the mixing step to guarantee an equimolar IL.

There are some examples in the scientific literature of PILs with an excess of acid that have been used for different catalytic applications⁵⁴⁻⁵⁶. Excess sulfuric acid has been added to different hydrogen sulfate based ILs to tune the acidity of the reaction medium to catalyse the Beckmann rearrangement of cyclohexanone oxime to ϵ -caprolactam⁵⁴ or Fischer esterification of acetic acid with 1-butanol⁵⁶. These works have shown that it is possible to tune the catalytic activity of PILs by modifying the base:acid ratio.

The effects of the base:acid ratio (β) of the PILs used in the IonoSolv process have been explored for biomass (hardwood willow) deconstruction with [N₂₂₂₀][HSO₄]⁵⁷. It has been shown that β has a significant influence in the outcome of the pretreatment process, *i.e.* pulp yield, composition and saccharification yields, as well as lignin yields and chemical structure. For example, a 2 mol% acid excess in the IL promotes the removal of the hemicellulosic fraction and induces the formation of pseudo-lignins at long pretreatment times, compared to pretreatment performed with a 2 mol% base excess. The saccharification yields with 2 mol% acid excess are higher than the ones obtained with 2 mol% base excess at short times, but at

longer pretreatment times they decrease dramatically, unlike the case with 2 mol% base excess⁵⁷. This shows the importance of controlling the base:acid ratio (β) in the ionoSolv process.

A study for biomass fractionation using another type of IL, monoethanolammonium acetate [MEA][OAc], concluded that there is also a significant effect of the base:acid ratio on the biomass pretreatment performance⁵⁸. Unlike the ionoSolv process, in which acid conditions improve the saccharification yields, in this pretreatment, the outcome is favourable with an excess base. This shows that the effect of base:acid ratio (β) on pretreatment performance is an important parameter for biomass processing with PIL, and its effect on the pretreatment outcome is system dependent.

As explained in section 2.2.3, acetic acid is not a strong acid and therefore might yield ILs in which the neutral species are present and at equilibrium with the IL. In the case of [MEA][OAc], the addition of excess base (monoethanolamine) forms a mixture with [MEA][OAc], as there are no additional protons for amine protonation.

A different situation occurs with the $[\text{HSO}_4]^-$ containing ILs, which can protonate excess amine, to form $[\text{SO}_4]^{2-}$ anions. The $[\text{HSO}_4]^-$ based ILs provide this additional region, in which the acidity of the mixture can be reduced, with the formation of anions with 2 negative charges in the system. The properties in such regions for the $[\text{HSO}_4]^-$ based ILs have been little explored in the literature. In the acidic region, it has been shown that H_2SO_4 forms clusters with the $[\text{HSO}_4]^-$ anion, to form $[\text{HSO}_4]^- (\text{H}_2\text{SO}_4)$ and $[\text{HSO}_4]^- (\text{H}_2\text{SO}_4)_2$ ⁵⁶. These complex systems offer opportunities for further tunability of the properties of this type of ILs. Another reason to understand the properties as a function of base:acid (β). The ionic structures present in the system as a function of the base:acid (β) have been represented schematically in Figure 6.

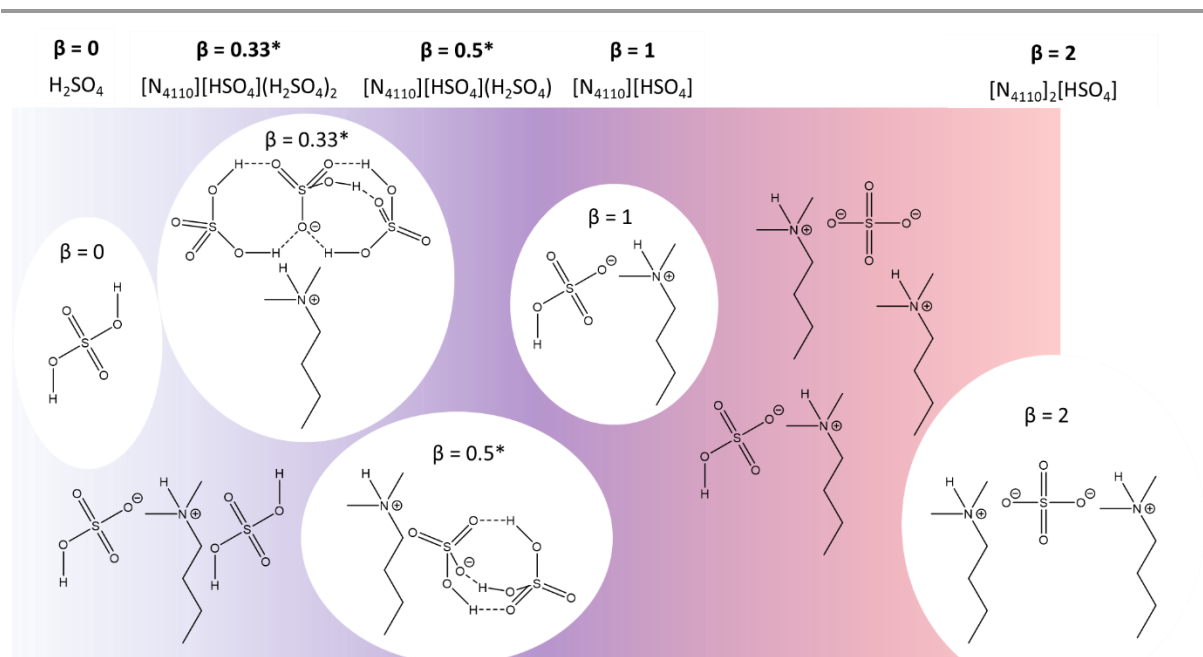


Figure 6. Structures of the $[\text{N}_{4110}][\text{HSO}_4]$ system at different base:acid ratios β . * $[\text{HSO}_4](\text{H}_2\text{SO}_4)_x$ clusters have been identified experimentally the base:acid ratio (β)⁵⁶.

2.2.5 Molecular structure of IL and water systems

As mentioned in the previous sections, IL might exhibit all sorts of interactions (coulombic, hydrogen bonding, van der Waal's forces, π - π interactions), which leads to the organization of the ionic pairs at molecular level (supramolecular solvents). The addition of water, or other molecular solvents to ILs, modifies their self-organization patterns, which can strongly affect their physical and chemical properties, such as density, surface tension, vapour pressure, viscosity conductivity, heat capacity as well as solvation and solubility properties⁵⁹. For example, hydrogen-sulfate-based ILs, such as $[\text{N}_{4110}][\text{HSO}_4]$ and $[\text{N}_{2220}][\text{HSO}_4]$ can be used for biomass fractionation. At low water content (below ~ 30 wt%), these ILs can dissolve lignin, but at high water content, lignin becomes insoluble. This difference in lignin solubility has been exploited as a method to isolate lignin in a biorefinery and will be discussed in detailed in Chapter 4.

The structural organization of IL-water systems have been studied through spectroscopic measurements^{23,24,60}, Molecular Dynamic (MD) simulations^{61,62} and physicochemical properties measurements⁶³. It is acknowledged that at low water contents, the system behaves as an IL and at high water contents, it behaves as an electrolyte aqueous solution. However, the boundary of this transition is not clear. In this section, experimental data taken from the literature will be used to try to understand where these transitions take place and

their implications. I do not intend to provide a detailed description of the nature of IL-water mixtures, but rather a high-level estimation.

Hydrogen bonds play an important role in the interaction between ILs and cosolvents, and some studies focused on hydrogen bonds have been carried out to understand the properties of ILs and structural changes induced when mixed with other solvents. Seddon's group was the first to report the existence of hydrogen bonds in imidazolium salts ^{59,64}.

One of the important features affecting the properties of ionic liquids in mixtures is ion pair formation. Ion pairing in solution is the result of a subtle balance between ion-solvent interaction and cation-anion interaction ^{65,66}, which is particularly true for IL due to the number of possible interactions as mentioned earlier.

When ILs are mixed with a solvent such as water, their organisation will be affected. At low water content, the anion-cation interactions are stronger than the interactions of the ions with the solvents, then Contact Ion Pairs (CIPs) would be the dominant structures in the mixtures and water molecules are dispersed in the polar regions on the IL structure ⁶⁷. On the other hand, at increasing water contents, the ionic liquid would first form a Solvent-shared Ion Pair (SIP), when a single solvent layer exists in the space between the ion partners of the pair. As the water concentration increases, it would form a Double Solvent-separated Ion Pair (2SIP), and beyond this point, the primary solvation shells of both ions remain essentially intact ⁶⁸. A schematic of the ion pair formation is shown in Figure 7. An excellent review of this topic is available in the scientific literature ⁶⁸.

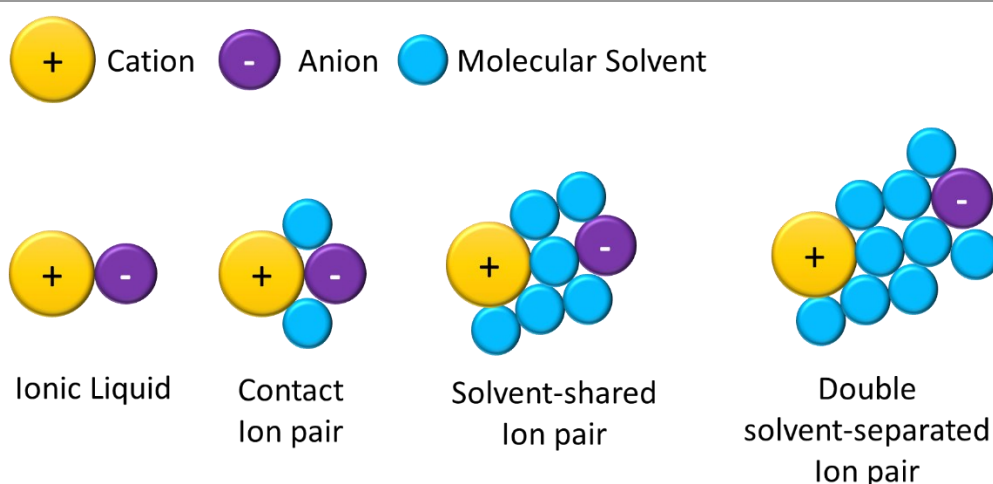


Figure 7. Schematic representation of ion-pair types.

For ALLs, it is well known that the addition of hydrophobic organic solvents, such as chloroform or benzene, leads to the disruption of the Coulombic network. In the highly diluted systems,

neutral aggregates and CIPs are formed resulting in a strong decrease of the electrical conductivity⁶⁹.

The situation for PILs can be completely different, as they possess proton acceptor and donor sites that can participate in hydrogen bonding. For studying the transition from CIPs to SIPs, strongly polar solvents such as water are needed to overcome the strong cation–anion interaction⁶⁶. Spectroscopic and density functional theory (DFT) methods have been used to determine how many water molecules are needed to disrupt the strong interactions in CIPs and how the transition from CIPs to SIPs occurs.

In a study using triethylammonium methylsulfonate $[\text{N}_{2220}][\text{CH}_3\text{SO}_3^-]$, not identical but a similar ion to $[\text{HSO}_4^-]$, revealed that the “magic number” of water molecules needed for the transition from CIPs to SIPs is four⁶⁶. In this study, it was shown that the addition of 1 water molecule to 1 ionic pair results in a strong interaction between water and the proton acceptors sites of the anion, *i.e.* negatively charged oxygen. If a second water molecule is added to the system, it also prefers to interact with the anion by the second available oxygen acceptor site. With these 2 water molecules, the contact ion pair is still stable but further weakened. If a third water molecule is added, it competes with the triethylammonium cation for one of the anion oxygen atoms. The addition of the fourth water molecule creates a SIP, as all of the proton-acceptor positions of the methylsulfonate anion are occupied⁶⁶. The SIPs are enthalpically favoured over the CIPs owing to increasing H-bond possibilities and cooperative effects⁶⁶. In that study was highlighted that the transition from contact to solvent-separated states strongly depends on the interaction power of the PIL anion. If the anion $[\text{CH}_3\text{SO}_3^-]$ is replaced by $[\text{CF}_3\text{SO}_3^-]$, the cation–anion interaction is weaker and the transition process may begin at lower water concentrations⁶⁶. Therefore, as the $[\text{HSO}_4^-]$ have an additional -OH group capable of forming hydrogen bonds, when compared to the $[\text{CH}_3\text{SO}_3^-]$ anion, the situation might be different, requiring possibly 5 water molecules to form the SIP. However, this should be investigated experimentally and with computational techniques.

Water is a unique substance with a complex phase space and unusual physicochemical properties, arising from its ability to form strong hydrogen-bond networks. Additionally, the extensive hydrogen bonding provides water with the ability to transfer protons rapidly between the water molecules and to produce positively charged hydrogen ions and negatively charged hydroxide ions⁷⁰.

When ions are present in water, the electric fields of the ions perturb the hydrogen network of water, causing water molecules to organise around the ions. The now-accepted model of a

hydrated ion in solution is a dynamic one. At any instant, the ion is surrounded by a first shell of suitably oriented water molecules (primary solvation number of the ion). Far away from the ion, there is the unperturbed structure of bulk water. In between, there is a secondary solvation shell, a few molecules thick, in which the structure of the solvent is modified to an intermediate extent ⁷¹.

In terms of the total hydration energy, the secondary solvation shell can contribute for as much as half the total hydration energy of a singly charged ion, which shows the great importance of the interactions beyond the primary hydration sphere in determining total hydration energies. Therefore, it is not possible to treat ion hydration on the basis of considering only the interaction of the ion and its immediate solvent neighbours ⁷¹.

Ions such as sulfate $[\text{SO}_4]^{2-}$ form a hydration shell from small rings of hydrogen-bonded water molecules. There are different values of the number of water molecules needed to complete the hydration shell for this ion. It has been reported that each sulfate oxygen is hydrogen-bonded to three water molecules and that these water molecules form small-looped chains. $[\text{SO}_4]^{2-}(\text{H}_2\text{O})_{12}$ or a symmetrical dodecahedral arrangement of $[\text{SO}_4]^{2-}(\text{H}_2\text{O})_{16}$ have been mentioned in the scientific literature ⁷²⁻⁷⁴. Hydrogen sulfate $[\text{HSO}_4]^-$ may also be hydrated similarly as $[\text{HSO}_4]^- (\text{H}_2\text{O})_{16}$. ⁷⁵.

The long-range interactions of the $[\text{SO}_4]^{2-}(\text{H}_2\text{O})_n$ anion have been studied with Infrared Photodissociation (IRPD) spectroscopy of up to 80 water molecules. It was shown that molecules with "free" OH groups similar to those at the surface of bulk water appeared at $n > 43$, indicating that the sulfate dianion has a long-range effect on water structure ⁷⁶. Interestingly, the heat of dilution for sulfuric acid almost reaches its limiting value after 5×10^5 molecules have been added to each molecule of acid. From these results, one might propose that each ion at such dilution is surrounded by a huge hydrate shell that seems to consist of thousands of layers of water molecules. However, this is not the case, and it has been reported that fewer than 30 water molecules could be lined up along the radius of a hydrate shell ⁷⁷.

The hydration shell for chloride anions is smaller. The first shell contains between 6 and 8 water molecules with their OH bond pointing directly at the chloride ion ^{74,78}. The second shell is much more disordered but generally consists of two water molecules donating hydrogen bonds to the first shell and one being an acceptor to the water in the first hydration shell ⁷⁹. Therefore, assuming 3 water molecules in the second shell, there should be 24 water molecules.

It has been reported that the hydration shell for ammonium presents some controversial features. For example, first studies on NH_4Cl concluded that a model in which chloride was

coordinated to 6 water molecules and $[\text{N}_{0000}]^+$ (or $[\text{NH}_4]^+$) to 4 water molecules was consistent with the X-ray diffraction results ⁸⁰. Another study concluded that there are between 10 and 11 water molecules coordinated to the $[\text{N}_{0000}]^+$ determined by neutron-diffraction on 5.0 molal NH_4Cl ⁸¹. Monte Carlo simulations yielded 14 water molecules present in the coordination shell ⁸². Finally, a cluster containing 20 water molecules around jointly constructing a deformed pentagonal dodecahedron cage structure with an NH_4^+ ion in its centre was reported ⁸³.

The situation when hydrogens in the $[\text{N}_{0000}]^+$ are replaced by alkyl chains is different as the alkyl chain has a hydrophobic character. Mass spectra in the gas phase of hydrated protonated amines and tetraalkylammonium ions with chain lengths greater than 2 exhibit magic number clusters, explained as clathrates of 20 water molecules ⁸⁴. 25 water molecules in the hydration shell $[\text{N}_{1111}]^+$ was reported ⁸⁵. A study assessing the water structure around $[\text{N}_{1110}]^+(\text{H}_2\text{O})_n$ ($n = 1-22$), it was shown that there was no proton transfer to the water, generating a neutral network but under the strong influence of the excess proton near the amine. The morphology of the water network is a function of the water content ⁸⁶. For methylimidazolium cation, the hydration number was reported to be 15.38 water molecules, oriented to the imidazole ring by oxygen atom ⁷⁸. This value is close to the reported hydration number of the imidazole ring of 14.6, and 18.9 for the C_4 tail of $[\text{C}_4\text{C}_{1\text{im}}]^+$ obtained by MD simulation for the diluted aqueous solution of imidazolium-based IL ⁷⁸.

Water-IL interactions when ILs contain hydrogen sulfate anions are of particular interest to this work as these ILs have proven to be an excellent solvent for biomass pretreatment, as it is discussed in Chapter 4. The interactions of water with imidazolium based ionic liquids had been studied by different methods, but no data had been reported for alkylammonium hydrogen sulfates.

Putting all the above together, the dry IL up to 3 water molecules should behave as an IL, with CIP the dominant structures. The addition of 4-5 water molecules will start generating SIP, the addition of 41 water molecules should be enough to complete the first hydration shell of the $[\text{N}_{4110}](\text{H}_2\text{O})_{25}[\text{HSO}_4](\text{H}_2\text{O})_{16}$ and reach the 2SIP state. Completion of the second shell for $[\text{HSO}_4]^-$ should be less than for the $[\text{SO}_4]^{2-}$ as it only has 1 charge. however, the proton can be transferred to the medium. Assuming the same hydration behaviour as per $[\text{SO}_4]^{2-}$, 43 molecules would be needed to complete the second shell for $[\text{HSO}_4]^-$. As for the cation, the second shell of the anion should be more disordered $[\text{N}_{4110}](\text{H}_2\text{O})_{25}[\text{HSO}_4](\text{H}_2\text{O})_{43}$. Figure 8 shows the proposed solvent structure for $[\text{N}_{4110}][\text{HSO}_4]$ water mixtures. Diamonds represent concentration points for which properties of the system are measured.

The scheme shown in Figure 8 is only for illustration purposes, as these systems are complex. For example, the addition of water molecules will not necessarily result in the hydration of the ionic species but the formation of water clusters as well, therefore, the solvent structure should be confirmed with experimental and simulation techniques.

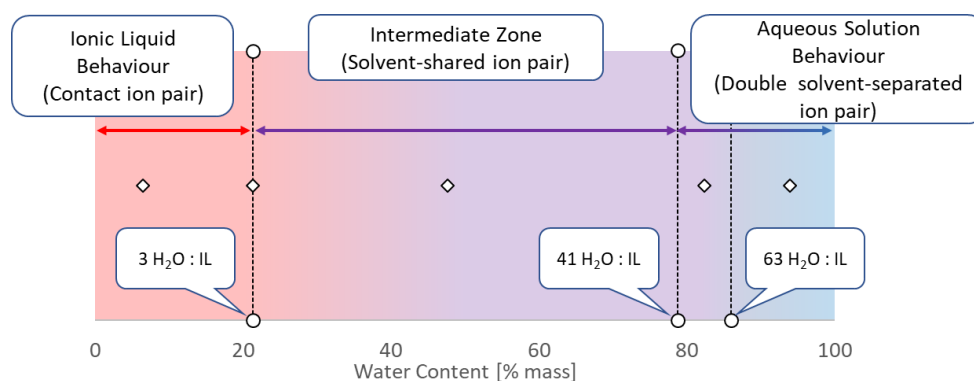


Figure 8. Proposed solvent structure for $[N_{4110}][HSO_4]$ /water mixtures. Diamonds represent concentration points for which properties of the system are measured.

2.2.6 State-of-the-art for the physicochemical properties of hydrogen sulfate based IL and knowledge gaps

There have been a few publications on the experimental physicochemical properties of hydrogen sulfate based ILs with either dry conditions at different temperatures or their dependency with water concentration at a fixed temperature. Some examples include the thermophysical properties of $[C_4C_{1im}][HSO_4]$, $[HC_{4im}][HSO_4]$ and $[HC_{1im}][HSO_4]$ as a function of temperature⁸⁷. Thermal transitions such as melting points, glass transition temperatures, and boiling point, were reported for a series of alkylammonium hydrogen sulfate ILs. The viscosities and densities for $[N_{2000}][HSO_4]$, $[N_{4000}][HSO_4]$ and $[N_{1100}][HSO_4]$ were reported³³. Additionally, the thermophysical properties for the mixtures of $[N_{2200}][HSO_4]$, $[N_{1110}][HSO_4]$, $[N_{2220}][HSO_4]$ with water at room temperature are reported⁵².

Despite the great amount of scientific research on ILs, there is still scarce experimental data for the hydrogen sulfate based ILs. As mentioned before, the available datasets on physicochemical properties of these types of ILs address dry conditions with temperature or constant temperature with varying concentration, therefore complete experimental datasets considering both variables do not yet exist. For this reason, it was decided to measure some properties of interest for process design for the system $[N_{4110}][HSO_4]$ and water at different concentrations and temperatures. Additionally, the effect of the base:acid ratio on these properties was also explored, since it plays an important role in the catalytic performance of these types of ILs, as discussed in section 2.2.4.

Probably the two most important physicochemical properties needed to evaluate an IL-based process at an early stage, using these substances as non-volatile solvents, are density and heat capacity. Density would allow the conversion of mass streams into volumetric ones, which are required for the sizing of volume-dependent process equipment, such as pumps, buffer vessels, tanks, reactors, etc. The heat capacity is required to establish the energy required to heat and/or cool process streams. Another property of importance that is needed for detailed equipment sizing is the viscosity. This property, is used for example, to establish dynamic pressure losses in the piping system and for equipment selection. It will also severely affect unit operations which are diffusion controlled, such as distillation columns or extraction systems. In this work, these properties have been measured and reported for $[\text{N}_{4110}][\text{HSO}_4]$, a low-cost IL which is used for efficient biomass deconstruction. The properties were measured on the dry ionic liquid with a base:acid ratio of one ($\beta = 1$), and as well with water mixtures and other base:acid ratios ($\beta \neq 1$).

The main challenges for measuring the physicochemical properties of this type of ILs is that they are extremely hygroscopic, and the presence of water will affect their properties. Ideally, they should be handled in gloveboxes to avoid moisture uptake. Moreover, these materials are corrosive toward metals typically found in laboratory instruments and it is difficult to obtain a base:acid ratio of 1 for these ILs.

2.3 Methods

2.3.1 PIL lab-scale synthesis

Hydrogen sulfate based IL synthesis was carried out by mixing the corresponding amount of sulfuric acid and base to reach a certain base:acid ratio, either neat or in an aqueous solution. Since PIL formation reactions are very exothermic (Section 2.2.3), the synthesis was carried out by dropwise addition of the acid into the amine. As amines can be volatile, the synthesis was carried out in a closed system as shown in Figure 9 to avoid amine loss. For practical reasons, the synthesis was performed by putting the acid into the dropping funnel and the amine in the bottom round flask. However, adding the acid to an excess of amine will release more energy as the 2 protons will be neutralized. The acid addition rate was slow (max 1 drop per second), under stirring and the amine cooled in an ice bath. Some groups reported the use of an acetone/dry ice bath ($-78\text{ }^\circ\text{C}$) for PIL synthesis³³. This extreme cooling is not required for the synthesis of alkylammonium hydrogen sulfates as shown in previous work^{88,89}, for which the quality of the product was confirmed with ^1H NMR. At the end of the synthesis, the IL can be dried under vacuum in a rotatory evaporator or Schlenk line. The water content is measured

by Karl Fisher (KF) titration (section 2.3.3.1) and the base:acid ratio is measured by acid-base titration (section 2.3.3.2). Unless otherwise stated, all chemicals were purchased from Sigma-Aldrich (Merk) and used as received without any further purification. *N,N,N*-triethylamine ($\geq 99\%$, CAS Number 121-44-8), *N,N,N*-dimethylbutylamine (99%, CAS Number 927-62-8) (product discontinued) and of 5 M H_2SO_4 .

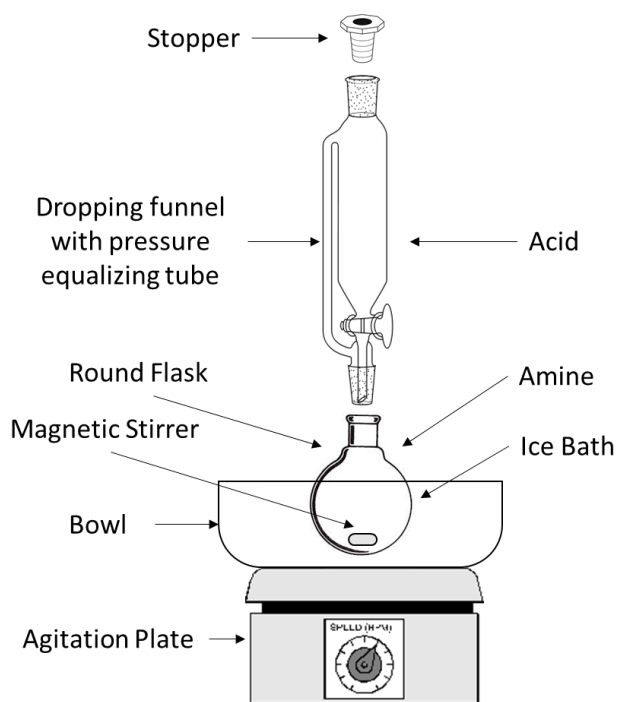


Figure 9. Schematic of experimental setup for PIL synthesis.

The procedure described in this section is suitable to produce a maximum amount of approximately 1 kg of IL, limited to the size of the labware. $[\text{N}_{2220}][\text{HSO}_4]$ recovered after drying as a white hygroscopic solid while $[\text{N}_{4110}][\text{HSO}_4]$ remains liquid. It was noticed that when concentrated sulfuric acid was used for the synthesis, the quality of the IL was poor and showed a pinkish colour. Additionally, when extreme drying was required, the ILs turned yellowish after 48h drying at 60 °C. ^1H NMR spectra of the dried IL did not show any detectable signals showing the degradation of the ILs.

Dry $[\text{N}_{4110}][\text{HSO}_4]$ with different base:acid ratios (β), were prepared in collaboration with Dr Vivi Filippousi, to determine the impact of β on the physicochemical properties of this IL. $[\text{N}_{4110}][\text{HSO}_4]$ with different β were prepared by adding an excess of dimethylbutylamine (N_{411}) or sulfuric acid (5 mol% or 10 mol%) to the 1:1 $[\text{N}_{4110}][\text{HSO}_4]$. Attempts to saturate the IL with N_{411} ($\beta = 2$) led to the formation of a biphasic mixture with poor mixing of the amine due to its low polarity. This was finally achieved by direct synthesis by adding 1 equivalent of 5M H_2SO_4

to 2 equivalents of amine, with a slight amine excess. As the amine is volatile and does not mix easily with the IL, it is recommended for $\beta > 1$, directly mixing the base and the acid rather than adding an excess amine to the IL.

$[\text{N}_{4110}]_2[\text{SO}_4]$ is a liquid at room temperature but due to limited time, it could not be included in this study. All ionic liquids were finally dried under vacuum to exclude the effect of residual water on the studied thermophysical properties. Varying the base:acid ratio (β) is expected to have a significant effect on the physicochemical properties of the IL compositions by modifying the interionic interactions. It is expected that a mixture of $[\text{HSO}_4]^-$ and $[\text{SO}_4]^{2-}$ ions will be present upon the addition of an excess of the base (N_{411}). Several thermophysical properties were investigated as a function of the composition at ambient pressure.

2.3.2 PIL large-scale synthesis

Bulk synthesis of alkylammonium hydrogen sulfate $[\text{N}_{xyz0}][\text{HSO}_4]$ was performed using a PTFE lined batch reactor operated in a similar way as described by A. Gariglia⁹⁰. The reactor consists of a jacketed carbon steel pipe element (nominal bore 4 inches and 65 cm length) with a Polytetrafluoroethylene (PTFE) liner supplied by Corrosion Resistant Products Ltd. Even though the presence of a polymer liner will decrease the overall heat transfer coefficient, it is required to avoid corrosion and metal contamination of the ILs. For the same reasons, all parts in contact with the IL, are made of inert polymers, such as Perfluoroalkoxy Alkane (PFA) tubing and fittings supplied by Swagelok. Two peristaltic pumps (Masterflex L/S[®] Easy-Load[®] II) are used to feed acid and amine into the reactor where they are mixed using a motorised (12V DC) PTFE stirrer. The tubing material is flexible Polyvinyl Chloride (PVC) for sulfuric acid handling and silicon for amine handling. As mentioned in section 2.2.3, the neutralization reaction is highly exothermic, therefore, the production rate is limited by the heat dissipation rate. Heat is removed by circulating a mixture of water and ethylene glycol (Sigma Aldrich) through the metal jacket which is cooled with an external chiller (Ministat 230 from Huber). The reactor was equipped with an internal overflow pipe, with a high of 18 cm, leading to a total working volume of $\sim 1.2\text{L}$. The reactor is equipped with a conductivity meter that can be used to monitor the base:acid ratio of the ILs. A schematic of the reactor is depicted in Figure 10.

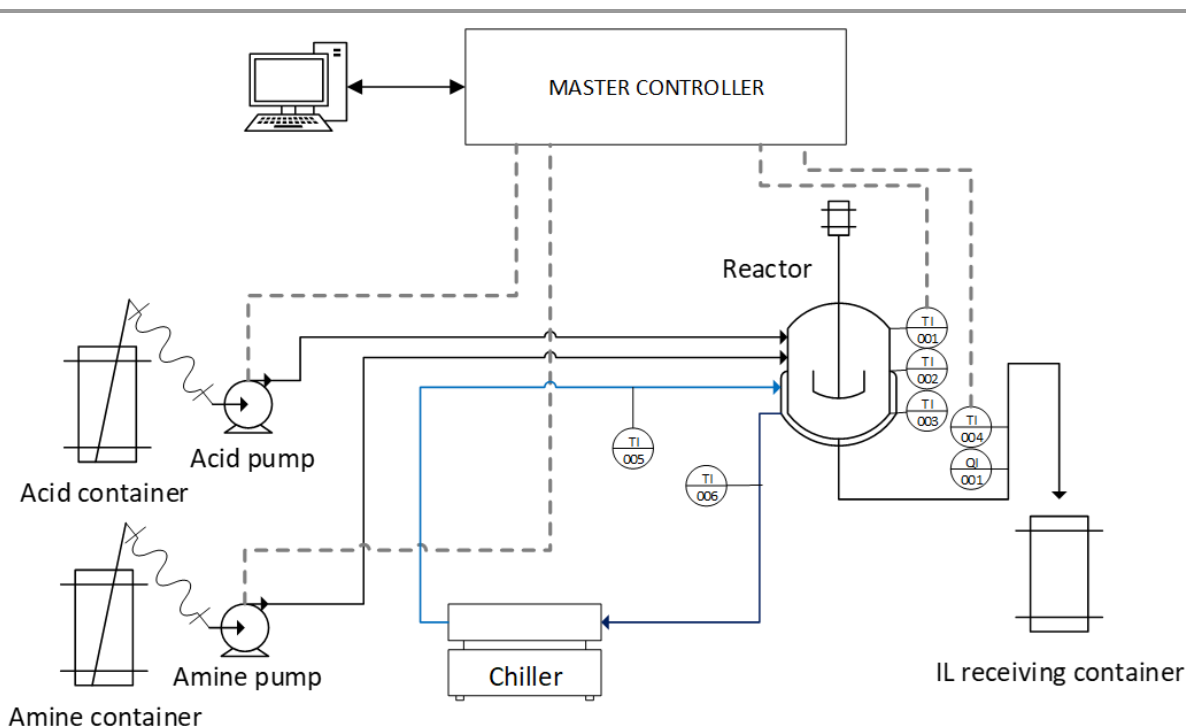


Figure 10. Schematic of the bulk synthesis reactor.

The reactor can be operated in batch mode, to produce ~1 L of IL, or continuously. When operated in batch mode, the acid is loaded first into the reactor and cooled down to near 0 °C. Once this is done, the amine is added into the reactor under agitation. The reason for this mixing sequence is that if acid is added to an excess of amine, 2 protons are neutralized, leading to a higher energy release during the neutralization process. The product is recovered by draining the reactor.

If operated continuously, first, it needs to be primed with IL to fill the total working volume, prior to amine and acid feed into the reactor. The product is continuously recovered by the outflow tube. At the end of the synthesis, the remaining IL inside the reactor is recovered by draining the reactor.

It is noteworthy to mention that the reactor was not completely sealed and therefore it was operated at atmospheric pressure. As N_{222} and N_{411} amines are volatile, there was a systematic amine loss to the environment, which resulted in ILs with an acid excess that needed to be corrected manually, by addition of amine.

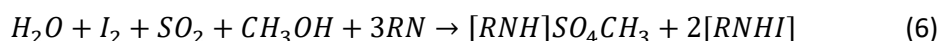
The reactor and the synthesis method described above was used to prepare $[N_{4110}][HSO_4]$ for the corrosion tests (Chapter 3) and $[N_{2220}][HSO_4]$ for biomass fractionation (Chapter 4). Briefly, the corresponding amine was added into the reactor with H_2SO_4 (66.3 wt%). Unless otherwise stated, the water content and the base:acid ratio was measured and adjusted when required.

In total, around 250 kg of alkylammonium hydrogen sulfate ILs were produced using this system.

2.3.3 Analytical techniques

2.3.3.1 Karl-Fischer titration

The water content in the ILs was measured by Karl Fisher (KF) titration, which is a moisture determination method specific for water. It is suitable for samples with high water content (titrimetry) and for samples with water content in the ppm range (coulometry)⁹¹. The method is based on the oxidation of sulfur dioxide by iodine in a methanolic hydroxide solution. The principle is illustrated by the chemical reaction shown in Eq. 6, where RN is an amine⁹¹:



In the volumetric method, a KF solution containing iodine is added until the first trace of excess iodine is present. The amount of iodine converted is determined from the burette volume of the iodine-containing KF solution⁹¹. In the coulometric procedure, the iodine participating in the reaction is generated directly in the titration cell by electrochemical oxidation of iodide until again a trace of unreacted iodine is detected. Faraday's law can be used to calculate the amount of iodine generated from the quantity of electricity required⁹¹.

The instruments used were Mettler Toledo Volumetric KF Titrator V20 for water contents >5 wt% and Mettler Toledo Coulometric KF Titrator C20 for water contents <5 wt%. For the KF determinations, HYDRANAL[®] titrant and solvents were used. For the volumetric KF titrations, calibration was performed using a standard solution of 0.1 wt% water (SIGMA-ALDRICH HYDRANAL[®]-Water Standard 1.0 mg/g (1000 ppm)) according to the manufacturer's recommendations.

2.3.3.2 Acid-base titrations

The base:acid ratio (β) for the hydrogen sulfate based ILs was determined by acid-base titration using a Mettler Toledo Compact Titrator G20S. The titrant used was a solution of 0.1 M sodium hydroxide (NaOH), standardized using about 100 mg potassium hydrogen phthalate (K phthalate) as a primary standard. The standardization was performed according to the manufacturer's recommendations.

To determine β , a known mass of the IL was weighted (~100 mg) in an analytical balance with a resolution of 0.1 mg or better in plastic cups suitable for the instrument. 50 ml of deionised water was then added to the sample. The cups were fitted into the instrument, where the

solution is automatically agitated for 1 minute before the titration began. At the end of the titration, the moles of NaOH consumed to reach the equivalence point determined automatically by the instrument were used to calculate the base:acid ratio (β) according to Eq. 19. Determinations were performed in triplicate and the average β value reported.

2.3.3.3 Density measurements

Density measurements were performed with a vibrating-tube densimeter from Mettler Toledo (Density Meter DM40) with a resolution of 0.0001 g/mL. Calibration was performed using Milli-Q water and dry air as density standards. It is important to mention that viscosity corrections are automatically made by the instrument, and they are needed for accurate results since ILs might have high viscosities. According to the manufacturer, the viscosity correction should be applied for accurate results for samples with a viscosity greater than 25 mPa·s. The maximum viscosities that can be handled by the instrument is 30000 mPa·s (which equals approximately liquid honey). Iglesias-Otero *et al.* pointed out that reported density values for ILs taken from the literature often exhibit differences as large as 0.005 g/mL and, if no viscosity correction is applied, the resulting density values depart by up to 0.0008 g/mL from the corrected values⁹². The viscosity correction might entail determining its experimental value, which is labour-intensive and expensive for systems containing RTILs^{92,93}.

Dissolved air and gas in the samples can interfere with the density measurements. For example, the instrument manufacturer recommends boiling water for at least 10 minutes, keep it under boiling until use and to introduce it to the measuring cell while hot. This procedure cannot be applied to the IL/water mixtures, as boiling the solutions, would change the water content. In an effort to remove dissolved gas in the IL solutions, the samples were placed in an ultrasonic bath at room temperature for 5 minutes.

2.3.3.4 Differential Scanning Calorimetry (DSC)

Differential Scanning Calorimetry (DSC) was performed in a calorimeter (Q2000, TA Instruments), equipped with liquid nitrogen cooling. Approximately 4 mg of the sample was enclosed in an aluminium hermetic pan whereas an empty pan was used as a reference. To achieve an equal heat transfer, nitrogen (50 mL/min) was used as purging gas.

The DSC measurement on dry samples was performed as follows. Each sample was tested by first equilibrating the temperature at 20 °C before cooling down to -150 °C (10 °C/min). The latter step was followed by ramping the temperature up to 100 °C. This cycle was repeated

three times, increasing the temperature to 250 °C for the last cycle. The glass transition temperatures were obtained from the thermograms by intercepting the baseline with the steepest gradient of the peak (onset temperature).

2.3.3.5 Viscosity

The viscosity of $[N_{4110}][HSO_4]$ ($\beta = 1$) was measured as a function of temperature, in triplicate, with a falling ball viscometer (Gilmont Falling Ball Viscometer). The time required for the ball to fall under gravity was measured in a sample-filled tube that was immersed in a temperature-controlled oil bath or ice bath. A tantalum ball was used for measurements from 200 cP to 2000 cP whereas a glass ball was applied for measurements ranging from 20 cP to 200 cP. The time of descent was used to calculate the viscosity according to Eq. 7, in centipoise [cP]. ρ_{ball} corresponds to the density of the ball: 2.53 g/cm³ and 16.6 g/cm³ for glass and tantalum, respectively, t refers to the time of descent [min] and K is the viscometer constant that was provided by the supplier ($K = 35$).

$$\eta = K \cdot (\rho_{ball} - \rho_{IL}(T)) \cdot t \quad (7)$$

According to the manufacturer, the repeatability with good technique varies from ± 0.2 to $\pm 1.0\%$. It is noteworthy to mention that the K value given by the vendor was used without any further calibration. As no calibration was performed as a function of temperature, it is expected higher uncertainties than the ones reported by the manufacturers, likely $\sim 3\%$, as reported for viscosities measurements with an equivalent method, the falling body viscometer⁹⁴.

2.3.3.6 Thermal Gravimetric Analysis (TGA)

Thermal Gravimetric Analysis (TGA) was performed in a NETZSCH Thermal Analysis instrument Jupiter STA 449 F5. The sample was placed in Al₂O₃ pans.

The short-term thermal stability of the ILs was carried out under nitrogen (40 mL/min) and the applied thermal cycling was as follows: the temperature was increased from room temperature to 120 °C at 10.0 K/min, with a 15 min isothermal at 120 °C in order to remove any residual adsorbed water during handling and followed by three temperature ramp-up stages [120 °C to 250 °C (10.0 K/min), 250 °C to 350 °C (5.0 K/min)], and 350 °C to 700 °C (10.0 K/min)].

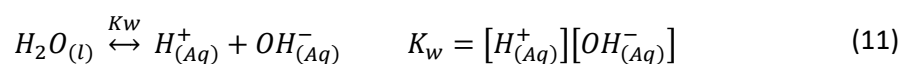
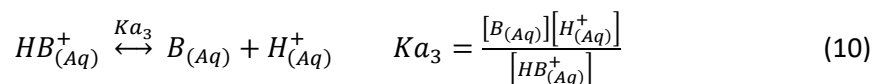
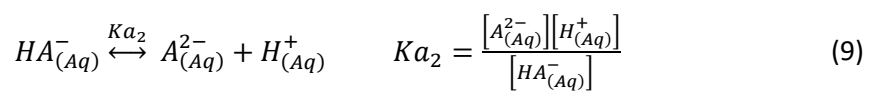
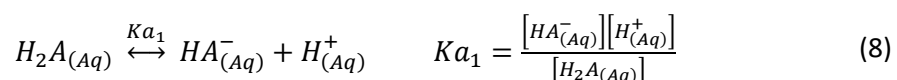
2.3.3.7 ¹H NMR measurements

¹H-NMR spectral data for the Diffusion Ordered Spectroscopy (DOSY) measurements were recorded on a Bruker AVANCE 500 MHz spectrometer with dimethyl sulfoxide (DMSO-*d*₆) in a capillary.

2.4 Results and discussions

2.4.1 Determination of the base:acid ratio (β) of PILs by acid-base titration

The base:acid ratio can then be determined by acid-base titration and corrected by adding additional base or acid as required. Eqs. 8-11 show the different equilibria of the species present in an aqueous diprotic-acid-based IL, such as the hydrogen sulfate, and the mathematical relationships of the concentrations of such species at equilibrium. Eq. 12 is the mass balance for the acid, Eq. 13 is the mass balance for the base, Eq. 14 is the charge balance and Eq. 15 is the definition of base:acid molar ratio.



$$[H_2A_{Total}] = [H_2A_{(Aq)}] + [HA_{(Aq)}^-] + [A_{(Aq)}^{2-}] \quad (12)$$

$$[B_{Total}] = [B_{(Aq)}] + [HB_{(Aq)}^+] \quad (13)$$

$$[OH_{(Aq)}^-] + [HA_{(Aq)}^-] + 2 \cdot [A_{(Aq)}^{2-}] = [HB_{(Aq)}^+] + [H_{(Aq)}^+] \quad (14)$$

$$\beta = \frac{[B_{Total}]}{[H_2A_{Total}]} \quad (15)$$

In Eqs. 8-15, the quantities $[X_{(Aq)}]$ represent the molar concentration of species X at equilibrium, A_{total} is the total molar concentration of acid, B_{total} the total molar concentration of base, Ka_1 , Ka_2 , Ka_3 and K_w are the dissociation constants of sulfuric acid (1st and 2nd proton), base and water respectively, and β is the base:acid ratio.

The activity coefficients have been ignored in Eqs. 8-11. A typical lab procedure involves the dissolution of 100 mg of IL in 50 ml of water, which corresponds to ~0.01 M, equivalent to a molar ionic strength ranging between 0.010 – 0.018 M depending on the base:acid ratio. The molar ionic strength is calculated with Eq. 16, where c is the molar concentration of an ion and z its charge.

$$I = \frac{1}{2} \left(\sum_i C_i z_i^2 \right) \quad (16)$$

For accurate determinations of the equilibrium concentration of all the chemical species involved in the different equilibria, the activity coefficient should be included in the equilibrium expressions. These activity coefficients are a function of the ionic strength (Eq. 16), higher the ionic strength, higher the deviation from ideal behaviour. Several models have been proposed to calculate the activity coefficients such as Debye–Hückel (up to $I = 0.001$ M), Davies equation, Pitzer equations and specific ion interaction theory^{95,96}.

By solving Eqs. 8-15 simultaneously, the equilibrium concentration of the different species in a diluted aqueous environment can be calculated for diluted systems. Additionally, equilibrium reaction between atmospheric CO_2 and the solution was not considered, but errors in acidic media should be minimum. It has been noticed that $[\text{N}_{4110}]_2[\text{SO}_4]$ is a liquid at room temperature and that addition of N_{411} amine yields to a second layer which does not mix with the IL. Therefore, the maximum β value for this system is 2. The complete proton transfer at $\beta = 2$ to form the $[\text{N}_{4110}]_2[\text{SO}_4]$ IL should be confirmed with experimental methods. The minimum value is 0 in the limit of infinite sulfuric acid addition, which corresponds to the pure acid.

Figure 11 shows the pH and ionic strength of 1 mM solutions of two hydrogen sulfate based ILs. For $[\text{N}_{4110}][\text{HSO}_4]$, the solutions are acidic in the whole range of β and increases abruptly to slightly acidic conditions near $\beta=2$. For $[\text{HC}_{1im}][\text{HSO}_4]$, the change in pH is gradual as the solutions are more acidic than $[\text{N}_{4110}][\text{HSO}_4]$, due to the difference in the pK_a of the amines. The calculated pH for a 1 mM solution of $[\text{HC}_{1im}]\text{Cl}$ is 6.57, which is just slightly acidic. Showing the strong acidity of the $[\text{HSO}_4]^-$ anion based IL. This acidic property makes these ILs good catalytic solvents. In Chapter 4, these types of ILs are used for biomass fractionation.

The acidity of non-aqueous systems can be measured in different ways, being the Hammett method one of the most well-established techniques, which uses a range of UV-vis active substances that are employed to generate the Hammett acidity function, H_0 ^{97,98}. The Hammett

acidity scale has been implemented to measure the acidity of ILs and of solutions of acids dissolved in them⁹⁹. These methods will not be further discussed here.

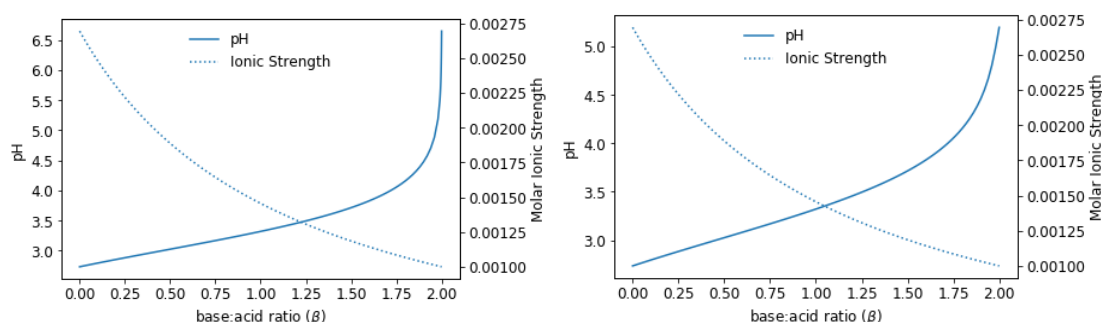


Figure 11. pH plots as a function of the base:acid ratio for a solution of 1 mM total (acid + base). Left: $[N_{4110}][HSO_4]$. Right: $[HC_{1im}][HSO_4]$. Ionic strength in M.

The titration curves for 1 L of a 0.01 mol of H_2SO_4 with different molar ratios of N_{411} amine, using a 0.01 M solution of NaOH, are shown in Figure 12. Even though H_2SO_4 is a diprotic acid, the titration curve of the pure acid ($\beta=0$) shows only 1 equivalence point that occurs at a titrant volume of 2L, which corresponds to the neutralization of both protons. As the base is added, the equivalence point is shifted to lower titrant volumes. A weak inflexion point in the curve, almost undetectable to the eye, takes place when the pH is around 10.2, which corresponds to the pK_a of the amine. This means that the proton attached to the amine is neutralized by NaOH at a pH around the pK_a value of the amine.

At the extreme case of ($\beta=2$), most of the acidic protons are attached to the amine, therefore, a small addition of NaOH provokes a rapid increase in the pH, with the gradual neutralization of the protons attached to the amine. Even in this situation, the inflexion point is not strong enough. For those titration curves it can be seen that to determine the base:acid ratio of the hydrogen sulfate ILs, it is not necessary to titrate the solution until the second equivalence point. In fact, when $[N_{4110}][HSO_4]$ is titrated with automatic titrator in the lab (refer to the experimental method section 2.3.3.2), the instrument is unable to detect the second inflexion point. Additionally, as the titration continues, once the amine is deprotonated in the strongly alkaline solution, it separates from the solution and volatilizes, generating a strong amine smell. As amine are toxic in general, reaching the second equivalence point should be avoided.

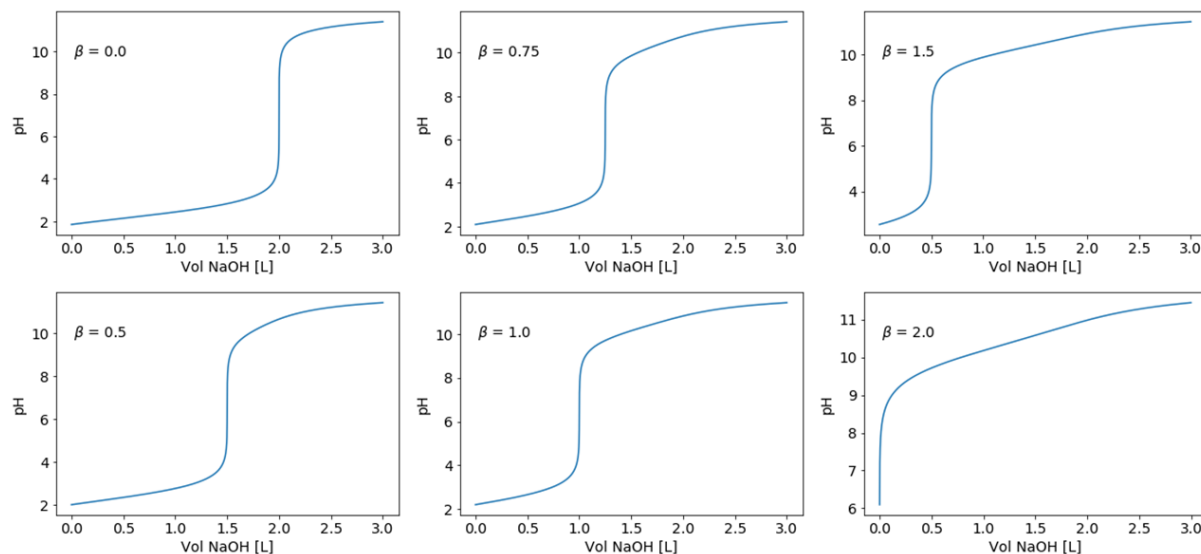


Figure 12. Simulated titrations curves of 1 L of 0.01 mol H_2SO_4 with different molar ratios of N_{411} amine, titrated with NaOH 0.01 M.

For monoprotic ILs, such as $[\text{HC}_1\text{im}]\text{Cl}$, the situation is different as seen in Figure 13. As explained before, for these ILs, the maximum β value is 1 for the 1:1 base:acid ratio. The pH of this IL is only slightly acidic; hence, the addition of the base will provoke an abrupt increase in the pH, in consequence, no acid-base titration can be done when $\beta = 1$. However, excess acid ($\beta < 1$) could be determined by this method.

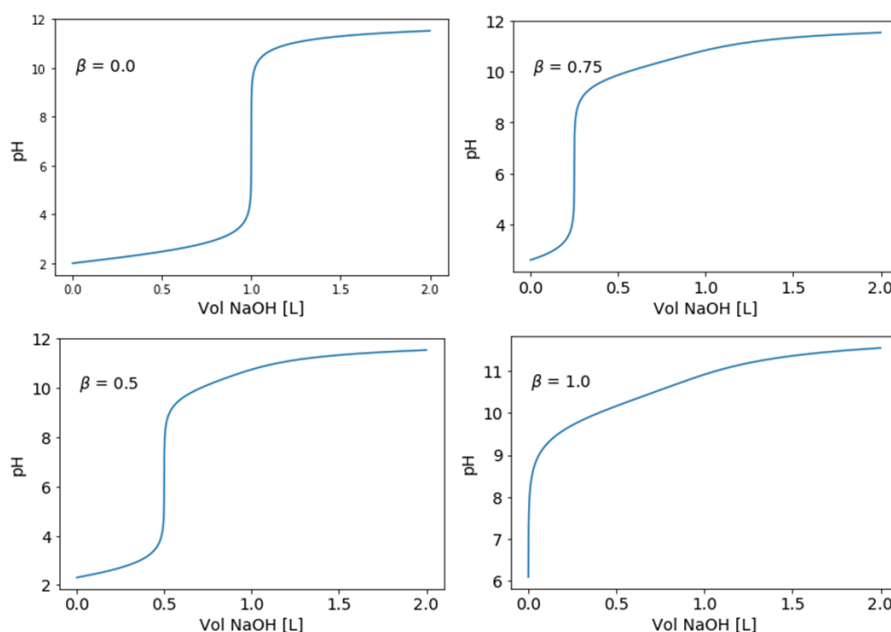


Figure 13. Simulated titrations curves of 1 L of 0.01 mol HCl with different molar ratios of C_1im amine, titrated with NaOH 0.01 M.

Finally, it is of interest to establish the relationship between the equivalence point and the β value for the hydrogen sulfate system. Any excess acid, given by the difference $A_{\text{total}} - B_{\text{total}}$,

where A_{total} is the total moles of acid and B_{total} is the total moles of base, will consume 2 equivalents of titrant. The $[HSO_4]^-$ anion will consume 1 equivalent of titrant, and for a mixture of acid and base, it will be equal to B_{total} . Putting all this together yields to Eq. 17. It can be seen that this equation reduces to $2 \cdot A_{total}$, when $\beta=0$, which corresponds to the pure acid, and for which 2 equivalents of titrant will be required, and to 0 equivalents when $\beta=2$. In a titration, the quantity of ionic liquid is known and it is related to the amount of acid and base by Eq. 18, where Mw_A and Mw_B are the molar weights of the acid and base of the PIL. Using the definition of β given in Eq. 15, and combining Eq. 17 and 18, the relationship between β and the moles of NaOH consumed at equivalence point can be established (Eq. 19).

$$NaOH_{mol} = 2 \cdot (A_{Total} - B_{Total}) + B_{Total} = 2A_{Total} - B_{Total} \quad (17)$$

$$IL_{mass} = A_{Total} \cdot Mw_A + B_{Total} \cdot Mw_B \quad (18)$$

$$\beta = \frac{2 \cdot IL_{mass} - Mw_A \cdot NaOH_{mol}}{IL_{mass} + Mw_B \cdot NaOH_{mol}} \quad (19)$$

The simulated results from solving the system of equations (Eqs. 8-15) to titrate 100 mg of IL dissolved in 50 ml, with different base:acid ratios, using a 0.1M NaOH solution were plotted against values calculated with Eq. 19 and shown Figure 14, where it can be seen that there is an excellent agreement between the simulated and calculated values in the whole range of β .

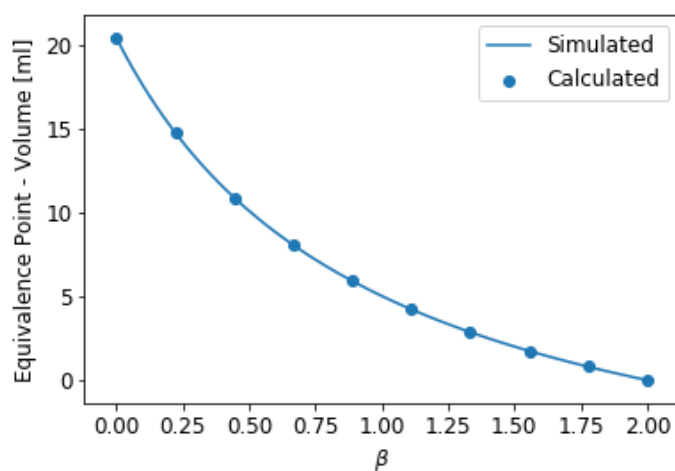


Figure 14. Volume of titrant (NaOH = 0.1 M) to neutralize 100mg of $[N_{4110}][HSO_4]$ with different base:acid ratios. Continuous line represents the values obtained by solving the system of equations (Eqs. 8-15) and the circles represent values calculated with Eq. 19.

2.4.2 Volumetric properties of alkylammonium hydrogen sulfate ($\beta=1$) and water mixtures
 The density as a function of temperature and water content for $[N_{4110}][HSO_4]$ was measured experimentally and several volumetric properties for this system were established. The excess properties were calculated using Eq. 20-25, where the superscript id denotes the property of

the ideal solution, the superscript E denotes the excess property, the superscript f denotes a property for a single IL pair, the subscript IL denotes a property for an IL, and z denotes the particular property under consideration. The subscript mix corresponds to the mixture, V_m and ρ are the molar volume and density, respectively. N_a is the Avogadro constant ($6.02214076 \times 10^{23} \text{ mol}^{-1}$).

$$z^E = z - z^{id} \quad (20)$$

$$\rho_{mix}^{id} = \left(\sum_i \left(\frac{w_i}{\rho_i} \right) \right)^{-1} \quad (21)$$

$$V_m^{id} = \sum_i x_i V_{m_i} \quad (22)$$

$$V_{m_i} = \frac{Mw_i}{\rho_i} \quad (23)$$

$$V_{m_{mix}} = \frac{\sum_i x_i Mw_i}{\rho_{mix}} \quad (24)$$

$$V_m^f = \frac{Mw_{IL}}{N_a \cdot \rho_{IL}} \cdot \frac{10^{21} \text{ nm}^3}{\text{cm}^3} = 1.6605 \cdot 10^{-3} \frac{Mw_{IL}}{\rho_{IL}} \quad (25)$$

The results are shown in Figure 15. The samples containing high water contents could not be measured as bubbles formed in the instrument. Various attempts were made to remove any dissolved gases from the mixtures by ultrasonication of the samples without success. The densities for water were measured until 50 °C and the values were compared with reported values³⁷, showing excellent agreement to the precision of the instruments (0.0001 gr/mL). The excess properties, calculated with Eq. 20, arises from differences in the interaction of different substances and provide a good estimate of the strength of unlike molecular interactions in the solution phase. The excess properties are almost always fitted with the following Redlich–Kister polynomial equation (Eq. 26):

$$z^E = x_1 x_2 \left(\sum_{i=0}^n a_i (x_1 - x_2)^i \right) \quad (26)$$

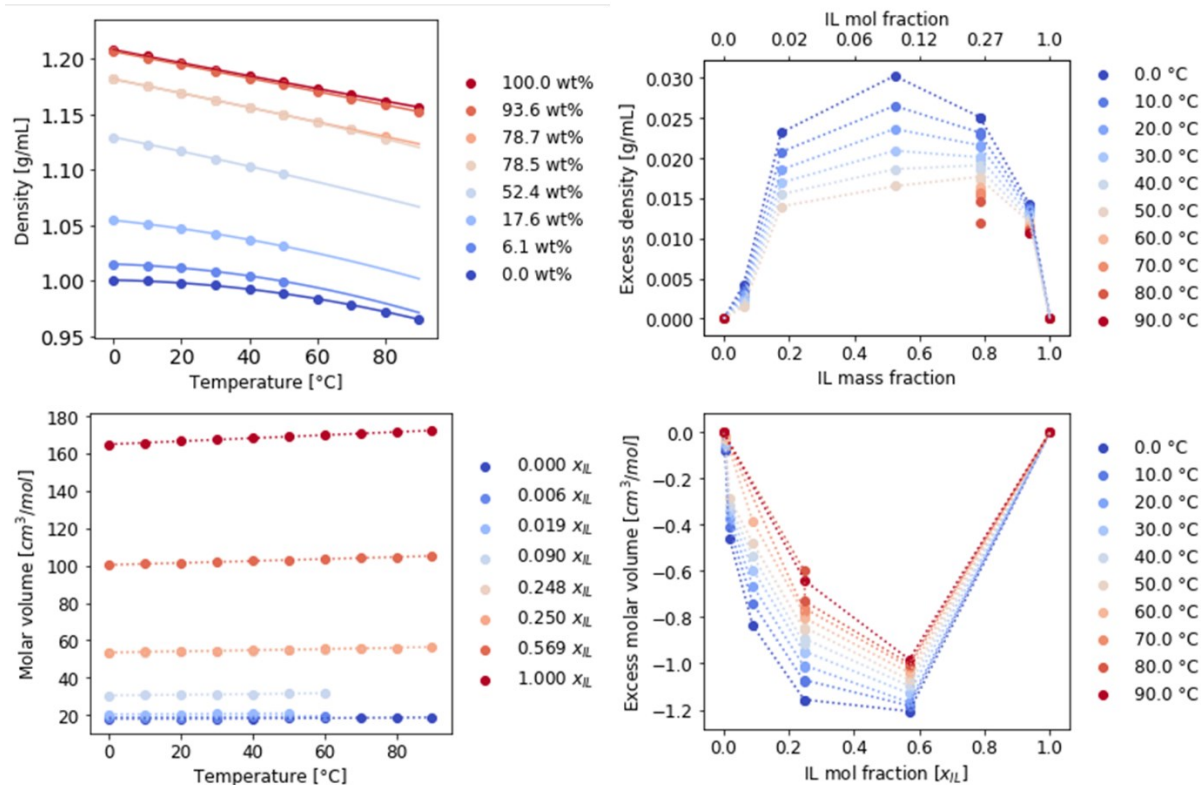


Figure 15. Experimental density values and molar volumes of $[N_{4110}][HSO_4]$ /water mixtures as a function of temperature and IL mass content. Water values from the literature³⁷.

In Figure 15, it can be seen that the excess molar volume (V_m^E) values are negative over the whole range of concentrations and temperatures studied. Several studies of water mixtures with some ammonium-based ILs have shown similar behaviours, *i.e.* negative V_m^E and asymmetric curves^{100–103}. The V_m^E negative values indicate higher attractive interactions in the mixtures than in the pure components, resulting in a strong packing effect by hetero-associations between water and IL molecules through hydrogen bonding. It has been proposed that the negative contribution to the free volume in the real mixtures, comprising ions and water molecules, might arise from the restriction of rotational motion when the water molecules are accommodated interstitially within the ions of ILs¹⁰⁰. The V_m^E depends on the interactions and on the size and shape of molecules of the system. In a study of the volumetric properties of several alkylammonium hydrogen sulfate ILs, it was found that the maximum deviations were observed for $[N_{2200}][HSO_4]$ ($V_m^E = -0.583 \text{ cm}^3/\text{mol}$ at $x_{IL} = 0.3912$), $[N_{1110}][HSO_4]$ ($V_m^E = -0.266 \text{ cm}^3/\text{mol}$ at $x_{IL} = 0.4781$) and $[N_{2220}][HSO_4]$ ($V_m^E = -0.204 \text{ cm}^3/\text{mol}$ at $x_{IL} = 0.3876$)¹⁰⁰. This study concluded that V_m^E values become less negative in higher alkyl length of the IL under the same experimental condition. According to this trend, it would be expected that $[N_{4110}][HSO_4]$ solutions would V_m^E values closer to its isomer, $[N_{2220}][HSO_4]$, however, the maximum V_m^E is $-1.1490 \text{ cm}^3/\text{mol}$ at $x_{IL} = 0.569$, which shows a higher deviation even when compared to a secondary ammonium analogue $[N_{2200}][HSO_4]$ ¹⁰⁰. This result is in contradiction

of what would be expected, that higher alkyl chain molecules would decrease the tendency for hydrogen bonding formation that would result in a lesser deviation from ideal solution behaviour¹⁰⁰. The $[\text{HSO}_4]^-$ anion has four accessible, negatively charged oxygen atoms to form hydrogen bonds with water molecules and protonated amines. This shows that ion–dipole interactions and packing effects between alkylammonium hydrogen sulfate and water are complex and that the nature of such interactions is highly dependent on the nature of the cation.

In many studies on the density variations with temperature for IL, it was found a linear relationship as seen in Figure 15 for dry and low water content mixtures^{100–103}. However, for water, the density dependency with temperature behaves as a second-order polynomial. IL with high water contents also follows a similar behaviour. This shows that the system transitions from an IL-like behaviour to aqueous solution behaviour, as discussed in Section 2.2.5. In order to predict the density of $[\text{N}_{4110}][\text{HSO}_4]$ mixtures with water, the density variations as a function of temperature, at constant water content, were adjusted to second-order polynomials (Eq. 27). Then the coefficients of such polynomial, *i.e.* a_0 , a_1 and a_2 , were in turn fitted to polynomials of second, third and second-order respectively (Eq. 28). The regressed parameters are shown in Table 3.

$$\rho(c) = a_0 + a_1T + a_2T^2 \quad (27)$$

$$\rho(c, T) = (b_0 + b_1c + b_2c^2) + (b_3 + b_4c + b_5c^2 + b_6c^3)T + (b_7 + b_8c + b_9c^2)T^2 \quad (28)$$

Table 3. Regressed parameter to calculate the density as a function of temperature [°C] and water content [wt%] (Eq. 28).

Coefficient	IL [N_{4110}] HSO_4
b_0	1.21121
b_1	-0.00122372
b_2	-8.89484e-06
b_3	-0.000592796
b_4	-1.6523e-06
b_5	-2.90688e-09
b_6	7.70021e-10
b_7	9.61887e-08
b_8	-1.55639e-08
b_9	-2.7471e-10

The Average Percent Deviation (APD), between the experimental measurements and the fitted polynomial (Eq. 28), calculated using Eq. 29 is 0.3%. The Maximum Absolute Relative Deviation (MARD) among all the experimental points was 1%.

$$APD = \frac{100}{n} \sum_1^n \left(\frac{|\rho_{experimental} - \rho_{model}|}{\rho_{experimental}} \right) \quad (29)$$

Using Eq. 28 and the data given in Table 3, the densities and the excess density were calculated and plotted (Figure 16) for the entire range of concentrations and temperatures from 0 to 90 °C. It can be seen from that data that at higher water contents and high temperatures the variations of density have a lesser gradient. Additionally, it can be seen the nonlinear dependence of density with the temperature at high water contents. Regarding the excess density plot, the maximum deviations from ideal solution behaviour are in the middle range of concentration, where the solvent-shared ion pairs predominate. The magnitude of the deviation decreases with temperatures, which is consistent with what would be expected for a gas phase. Mixtures of gases behave ideally at high temperatures, and the magnitude of the excess properties tend to zero.

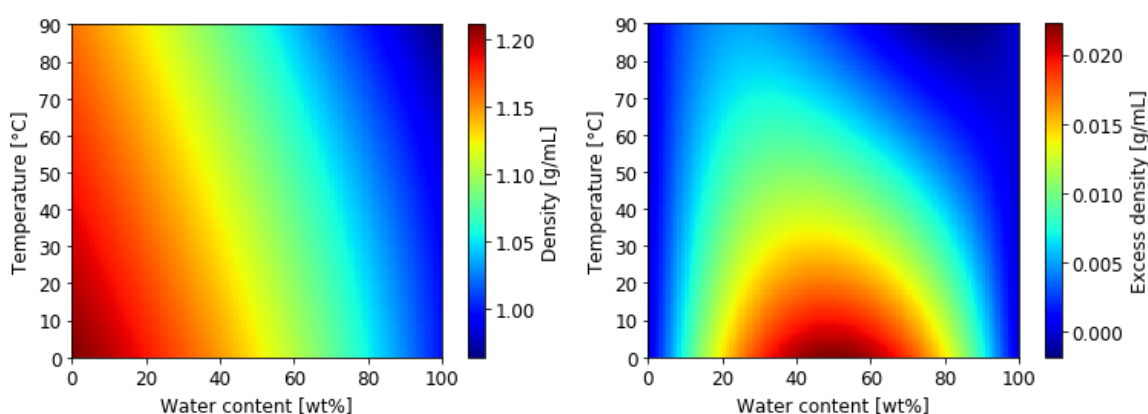


Figure 16. Left: Calculated density for $[N_{4110}][HSO_4]$ as a function of temperature and concentration (Eq. 28). Right: Calculated excess density

Finally, the volume for one IL pair was calculated with Eq. 25 and used to estimate a series of thermodynamic parameters with Volume-Based Thermodynamics (VBT). Glasser estimated a VBT-based entropy for ionic liquids (Eq. 30), derived from correlations for both inorganic solids and organic liquids, that can be used as a first approximation in the absence of direct measurements¹⁰⁴. Similarly, Gutowski *et al.*^{105,106} developed a lattice energy correlation for 1 : 1 ionic liquids, with amended constants for Eq. 31, with $l = 1$, $\alpha = 83.26$ kJ.nm/mol (19.9 kcal.nm/mol) and $\beta = 157$ kJ/mol (37.6 kcal/mol). Lattice energy is readily converted to lattice enthalpy (as it needs to be if it is to be included in an enthalpy-based thermochemical cycle such as that in Figure 5) using Eq. 32 where $\Delta_l H$ is the lattice enthalpy, n is the number of ion types in the formula unit, n_i is the number of ions of type i , and c_i is defined according to whether ion i is monatomic ($c_i = 3$), linear polyatomic ($c_i = 5$), or nonlinear polyatomic ($c_i = 6$)⁴⁷. The coulombic (or Madelung) energy, E_M , of a material of known structure is readily

calculated by means of standard computer programs, such as GULP and EUGEN⁴⁷. This energy corresponds to separating the constituent ions into independent gas phase ions against coulombic forces only, which is the major interaction in ILs. It has been observed that the resulting Madelung energy is closely related to the corresponding lattice energy, and their values have been correlated with a simple linear relationship shown in Eq. 33⁴⁷. The heat capacities can also be estimated *via* VBT (Eq. 34)⁴⁷. It was reported that the maximum mean absolute error for the Cp values obtained with this correlation was 24.5%. Additionally, it was reported that to avoid outliers, the minimum value between the value calculated with Eq. 34 and the approximate limiting Dulong–Petit value of $n \times 25$ J/K.mol, where n = number of atoms in the formula unit, should be used. It has been stated that this limiting value is for the C_v instead of the C_p , with $C_v = 3Nk_b$, which does not depend on any assumptions about the frequencies in a solid and that it corresponds to the theoretical value of the C_v of any monoatomic solid at high temperatures⁹⁶. When dealing with 1 mol of material, the $N = N_A$, and $N_Ak_b = R$ and $C_v = 3R \approx 25$ J/K.mol. At room temperature, the values of C_v are often less than the ideal value $3R$ ⁹⁶. The C_v value calculated by this approximations for $[N_{4110}][HSO_4]$ ($n=29$) is 725 J/mol.K which is 2.18 times higher than the value obtained by Eq. 34 of 333 J/mol.K, therefore values calculated by the empirical equation was retained. Some thermodynamic parameters calculated with the VBT correlations for a series of hydrogen sulfate ILs are given in Table 4. It is noteworthy to mention that many of these correlations were developed for large cations in AILs and/or limited number of PIL. It would be interesting to verify the validity of that approximation to hydrogen-sulfate based ILs.

$$S = 1246.5V_m^f + 29.5 \quad (30)$$

$$U_{POT} = 2I \left(\frac{\alpha}{V_m^{f\frac{1}{3}}} + \beta \right) = 2 \left(\frac{8326}{V_m^{f\frac{1}{3}}} + 157 \right) \quad (31)$$

$$\Delta_L H = U_{POT} + \sum_{i=1}^n n_i \left(\frac{c_i}{2} - 2 \right) RT \quad (32)$$

$$E_M = \frac{U_{POT} - 293.9}{0.8518} \quad (33)$$

$$C_p = 1037V_m^f + 45 \quad (34)$$

Table 4. Thermodynamic parameters calculated with VBT correlations.

IL	Mw [g/mol]	ρ [g/mL]	V_m^f [nm ³]	S [J/mol.K]	U _{POT} [kJ/mol]	$\Delta_L H$ [kJ/mol]	E _M [kJ/mol]	C _p [J/mol.K]
[N ₄₁₁₀]HSO ₄	199.27	1.1932 (A)	0.277	375.2	570	575	324	333
[N ₂₂₂₀]HSO ₄	199.27	1.14289 ¹⁰⁰	0.290	390.4	566	571	320	345
[N ₁₁₁₀]HSO ₄	157.19	1.46758 ¹⁰⁰	0.178	251.2	611	616	372	229
[N ₂₂₀₀]HSO ₄	171.22	1.28395 ¹⁰⁰	0.221	305.5	590	595	347	275
[N ₂₀₀₀]HSO ₄	143.16	1.4380 (B) ¹⁰⁷	0.165	235.6	618	623	381	216
[C ₄ C _{1im}]HSO ₄	236.29	1.284 ⁸⁷	0.306	410.4	562	567	315	362
[HC _{4im}]HSO ₄	222.26	1.294 ⁸⁷	0.285	385.0	568	573	321	341
[HC _{1im}]HSO ₄	180.18	1.468 ⁸⁷	0.204	283.5	598	603	357	256

A. This work.

B. At 27°C.

The data shown in Table 4 reveal that the ILs have lower lattice energies compared with normal alkali halides; for example, U_{POT}, for NaCl 769 kJ/mol and similar when compared to [N₁₁₁₁]Cl 566 kJ/mol. The lattice energies for sulfates are higher, for example, the values for (NH₃)₂SO₄ is 1766 kJ/mol³⁷. Low lattice energies render ILs liquid at room temperature. The low lattice energies of ILs in comparison with that of alkali chlorides (*e.g.* NaCl) are attributed to the asymmetric and bulky nature of the cation, which promotes steric hindrance and decreases interactions between the cation and anion⁸⁷.

There are other properties that can be calculated from this data set, however, as they were not used in this work, they were not computed and discussed. For example, the isobaric thermal expansion coefficient, α , [K⁻¹] is related to the variation of the density with temperature and is defined as shown in Eqs. 35-36¹⁰⁸.

Hepler showed that the change of C_p with pressure at constant temperature can be related with the term $\left(\frac{\partial^2 V}{\partial T^2}\right)_P$ according to Eq. 37, which in turn, is related to isobaric thermal expansion coefficient, α , according to Eq. 38¹⁰⁹. Hepler relations can provide qualitative information about the structure -making or -breaking ability of a solute in solution¹⁰⁹, and have been applied for some IL-water systems¹¹⁰.

$$\alpha_P = \frac{1}{\rho} \left(\frac{\partial \rho}{\partial T} \right)_P \quad (35)$$

$$\alpha = \frac{1}{V} \left(\frac{\partial V}{\partial T} \right)_P \quad (36)$$

$$\left(\frac{\partial C_p}{\partial P} \right)_T = -T \left(\frac{\partial^2 V}{\partial T^2} \right)_P \quad (37)$$

$$\left(\frac{\partial^2 V}{\partial T^2}\right)_P = \frac{M_w}{\rho} \left(\alpha^2 + \left(\frac{\partial \alpha}{\partial T}\right)_P \right) \quad (38)$$

Apparent molar volumes can be calculated and represented using Redlich–Mayer equation in dilute region, which can be used to calculate infinite dilution apparent molar volumes¹¹¹. In this region, theoretical approaches for dilute electrolytes, such as the Pitzer model, had been used for IL-water mixtures^{112,113}.

There are group contribution methods to calculate the volumetric properties for IL, but unfortunately, they don't include the $[\text{HSO}_4]^-$ or $[\text{SO}_4]^{2-}$ anions¹¹⁴. It has been established that mixtures of ILs can be treated as ideal with errors less than 1.5% on the molar volumes¹¹⁵. There are also correlations for the heat capacity¹¹⁶ and correlations for the relationship between density and refractive index^{92,117}.

2.4.3 Volumetric properties of alkylammonium hydrogen sulfate ($\beta \neq 1$)

The density (ρ) of dry $[\text{N}_{4110}][\text{HSO}_4]$ at different base:acid ratios (β) was measured as a function of temperature (0 – 90 °C) at atmospheric pressure and the results are shown in Figure 17. Numeric values can be found in Appendix 1.

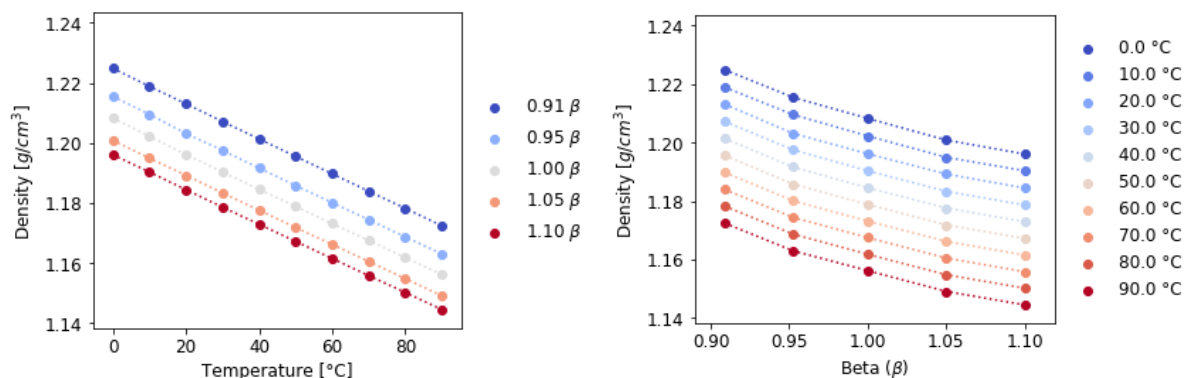


Figure 17: Density for different acid/base molar ratios (dry $[\text{N}_{4110}][\text{HSO}_4]$) as a function of temperature. Numeric values are given in Appendix 1.

The density was found to increase upon decreasing the base:acid ratio (β) across all temperatures with the potential of fine-tuning the density by adjusting the β value. The density of the system at $\beta = 0$ should approach the one of neat sulfuric acid. The highest value observed was 1.2248 g/cm^3 for $\beta = 0.91$ (10 mol% excess H_2SO_4). Comparing the density values of the studied IL, $[\text{N}_{4110}][\text{HSO}_4]$, against other $[\text{HSO}_4]^-$ -based ionic liquids, the measured values for $[\text{N}_{4110}][\text{HSO}_4]$ were within the range of literature-reported values for other $[\text{HSO}_4]^-$ ion based ionic liquids (Table 4 and Appendix 1). Moreover, $[\text{N}_{4110}][\text{HSO}_4]$ is approximately 4% denser

than the one containing an isomeric form of its cation: $[N_{2220}][HSO_4]$ (Table 4). The literature-based density values of ethylammonium hydrogen sulfate ($[N_{2000}][HSO_4]$) and trimethylammonium hydrogen sulfate ($[N_{1110}][HSO_4]$) appear to be the highest with values approximating 1.4 g/cm^3 (Table 4). Nonetheless, it should be noted that $[N_{2000}][HSO_4]$ is solid at temperatures below $31.9 \text{ }^\circ\text{C}$ whereas the lab-scale synthesis of $[N_{1110}][HSO_4]$ would not have been feasible due to the fact that one of the starting materials, trimethylamine, is a gaseous amine ³³.

As expected, the density of dry $[N_{4110}][HSO_4]$ showed a linear decrease with increasing temperature for all the tested base:acid (β) ratios. The data were fitted to a linear equation and the respective values of the correlation coefficients are given in Appendix 1, together with the R^2 and the standard error of the estimate σ_{est} , indicating the high accuracy of predictions.

Data reported for aqueous solutions of $[N_{2220}][HSO_4]$ at different base:acid ratios ($20 \text{ }^\circ\text{C}$) is presented in Figure 18 ¹¹⁸. The relative densities normalized with $\beta=1$ are also shown in Figure 18. It can be seen that the relative changes in density with changing base:acid ratio are very small to be used as a property for quality control. Additionally, it can be seen some scattering in the experimental data, due to experimental errors on both, water content and base:acid ratio, and the fact that the differences are small. For the dry $[N_{4110}][HSO_4]$, these relative curves overlap for all temperatures (not shown here), and the relative variations are also small in magnitude.

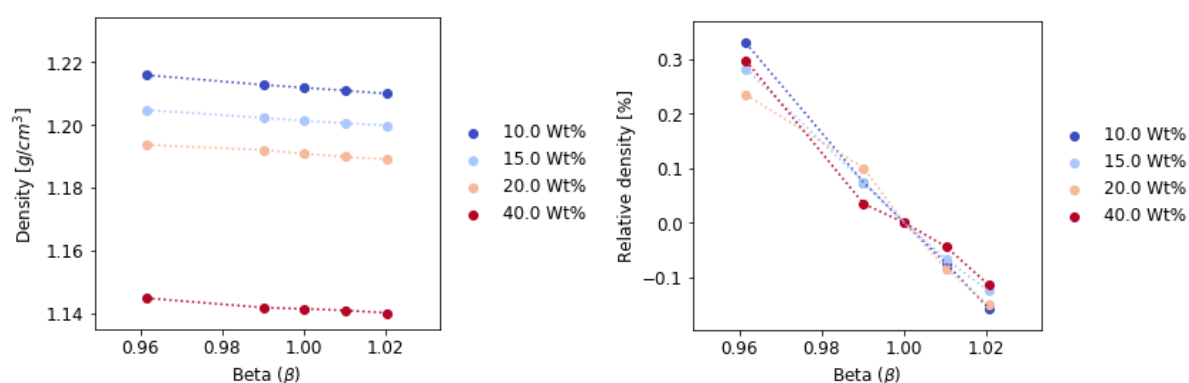


Figure 18. Density values for aqueous solutions of $[N_{2220}][HSO_4]$ at different base:acid ratios (20°C) ¹¹⁸.

2.4.4 Viscosity of alkylammonium hydrogen sulfate ($\beta=1$) and water mixtures

The viscosity of $[N_{4110}][HSO_4]$ ($\beta = 1$) was measured in triplicates with a falling ball viscometer as described in 2.3.3.5. The values are given in Appendix 1 and shown in Figure 19. The viscosity data were fitted to Vogel–Tammann–Fulcher (VTF) equations (Eq. 39), which has been used extensively to fit temperature-dependent data such as viscosity and conductivity ¹¹⁹. Water

viscosity values were taken from the literature and also fitted to VTF equation ¹²⁰. The meaning of the parameters of the VTF equation have been discussed in literature and will not be further explained here ¹¹⁹. However, for ILs it has been reported that a better fit is provided by the modified version of the VTF equation, which includes a term $T^{1/2}$ term (Eq. 40), used for glass-forming liquids ^{119,121}:

$$\eta = \eta_0 \cdot e^{\frac{B}{T-T_0}} \quad (39)$$

$$\eta = A \cdot T^{0.5} \cdot e^{\frac{B}{T-T_0}} \quad (40)$$

The fitting parameters to the VTF equation for $[N_{4110}][HSO_4]$ and water are given in Table 5 and the plots are given in Figure 19. As expected, the modified version of the VTF equation (Eq. 40) provides a better fit than the VTF model. These 2 models fit the experimental data for water extremely well.

Table 5. VTF correlation coefficients for the viscosity of $[N_{4110}][HSO_4]$ and water. APD - average percent deviation (Eq. 29). MARD - maximum absolute relative deviation.

Substance	Model	A	η_0	B	T_0	APD	MARD
$[N_{4110}][HSO_4]$	Eq. 39	-	8.62725	480.45	206.831	78%	223%
	Eq. 40	2.4827×10^4	-	2951.62	69.88	16%	44%
Water	Eq. 39	-	0.0428348	398.268	166.613	1%	5%
	Eq. 40	1.157×10^3	-	581.54	145.00	0.6%	2.7%

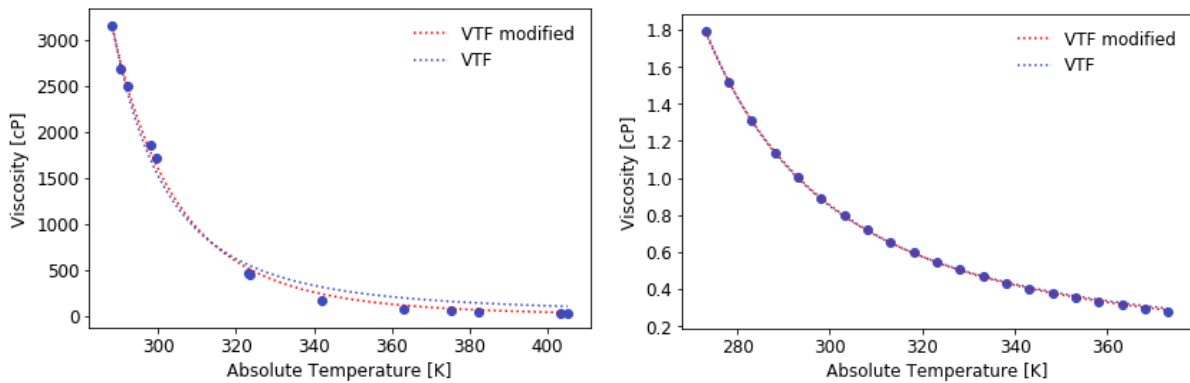


Figure 19: Experimentally determined viscosity of $[N_{4110}][HSO_4]$ ($\beta = 1$) and water ¹²⁰ as a function of temperature. Lines correspond to the fitting models VTF (Eq. 39) and VTF modified (Eq. 40).

There are various equations to calculate the viscosity of mixtures in terms of pure component data. Some of them contained no adjustable parameters and will be used here to evaluate the mixtures of $[N_{4110}][HSO_4]$ with water. These models include the Arrhenius mixing law for viscosity is given in (Eq. 41) ¹²². Kendall-Monroe derived Eq. 42 for calculating the viscosity of binary mixtures as the cubic-root average of the component viscosities ¹²³. Frenkel with the help of Eyring's model took into consideration the interaction between molecules and

developed the following logarithmic relation for nonideal binary mixtures (Eq. 43), where, η_{12} is a constant attributed to unlike pair interactions and can be calculated from Eq. 44. Other approaches include fitting the term η_{12} to experimental data. There exist many other correlations to calculate the viscosity of binary mixtures but they contained fitting parameters¹²⁴.

$$\ln(\eta_{mix}) = x_1 \cdot \ln(\eta_1) + x_2 \cdot \ln(\eta_2) \quad (41)$$

$$\eta_{mix} = \left(x_1 \eta_1^{\frac{1}{3}} + x_2 \eta_2^{\frac{1}{3}} \right)^3 \quad (42)$$

$$\ln(\eta_{mix}) = x_1^2 \cdot \ln(\eta_1) + x_2^2 \cdot \ln(\eta_2) + 2x_1x_2 \ln(\eta_{12}) \quad (43)$$

$$\eta_{12} = 0.5\eta_1 + 0.5\eta_2 \quad (44)$$

Using the VTF parameters for $[N_{4110}][HSO_4]$ and water, the viscosities of the IL-water mixtures were simulated using Eqs. 41-44 and the results are shown in Figure 20, where it can be seen that all these models predict different values for the viscosity of the mixture. The Kendall-Monroe model (Eq. 42) predicts higher viscosities than the other models. The values obtained with the Frenkel-Eyring model (Eq. 43-44) are very similar to the values predicted by Kendall-Monroe, at high IL concentrations, but diverge rapidly as the water concentration increases. Finally, the Arrhenius model predicts the lowest viscosity values for the mixture over the entire concentration range. In the absence of experimental data, the Kendall-Monroe model should be used as a conservative approach, as it yields the highest viscosity values. It would be interesting to verify experimentally these models, and the parametric ones, to establish which one predicts better the viscosities of alkylammonium hydrogen sulfate ILs with water, as a function of concentration and temperature.

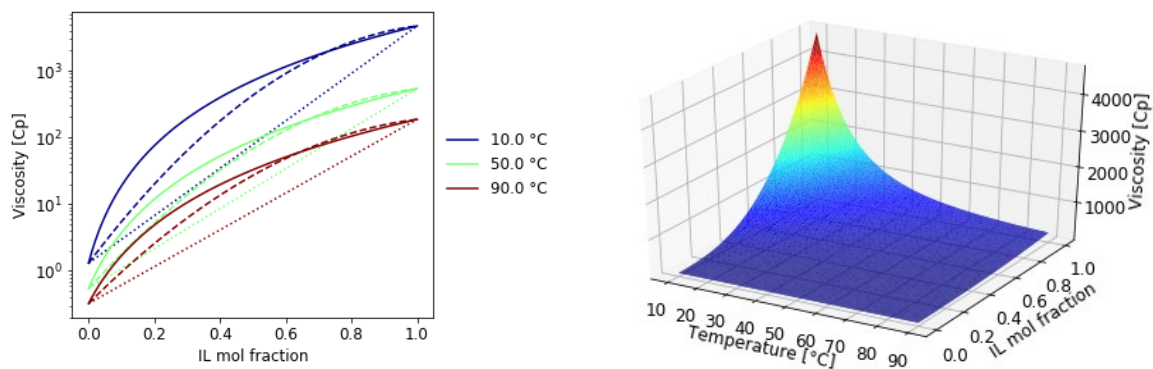


Figure 20. Simulated viscosity for the $[N_{4110}][HSO_4]$ water system. Left figure: solid line Kendall-Monroe model (Eq. 42), segmented line Frenkel-Eyring's model (Eq. 43-44) and dotted line Arrhenius mixing law (Eq. 41). Right: 3D view of the Kendall-Monroe model as a function of temperature and concentration.

2.4.5 Viscosity as a function of temperature and the base:acid ratio (β)

The average diffusion coefficient (D ; m^2/s) for $[\text{N}_{4110}][\text{HSO}_4]$ with different base:acid (β) ratios were obtained by Diffusion Ordered Spectroscopy (DOSY) at 25 °C, 50 °C and 90 °C. The DOSY data at 130 °C were inconclusive and thus they were not used for the calculation of the viscosity of the $[\text{N}_{4110}][\text{HSO}_4]$ -based samples bearing a different β value. Numerical values for the self-diffusivities are given in Appendix 1. The Stokes-Einstein equation (Eq.45) was applied given that it correlates the dynamic viscosity (η) with the diffusion constant (D) at different temperatures. In this equation, k_b is Boltzman constant, r corresponds to the hydrodynamic radius of the particle and c a geometric constant. It was assumed that c and r were independent of the base:acid ratios (β), and the viscosity (η) and the diffusion constant (D) of $[\text{N}_{4110}][\text{HSO}_4]$ ($\beta = 1$) were used as a reference to calculate the viscosity values for each sample with a varying β across different temperatures (Eq. 46). Self-diffusion values are given in Appendix 1. Examples of this technique to measure viscosity are described in literature^{125–127}. A variety of common laboratory solvents were analysed using acetone, chloroform and DMSO as reference systems, and the predicted viscosities through the DOSY experiments were accurate to ± 0.1 cP and consistent across multiple experiments¹²⁶.

$$D = \frac{k_B T}{c \pi \eta r} \quad (45)$$

$$\eta = \frac{D_{ref} \eta_{ref}}{D} \quad (46)$$

Plotting the calculated viscosity as a function of the base:acid ratio, it appears that an exponential curve fits the data with excellent R^2 values (> 0.99) for 25 °C and 50 °C whereas a relatively good fit ($R^2 > 0.94$) was achieved for 90 °C as well. Extrapolating to $\beta = 0$ (neat H_2SO_4) was also achieved as illustrated in Figure 21. Increasing the quantity of acid ($\beta < 1$) decreased the viscosity whereas an amine excess ($\beta > 1$) increased the viscosity, due to the formation of $[\text{SO}_4]^{2-}$ species.

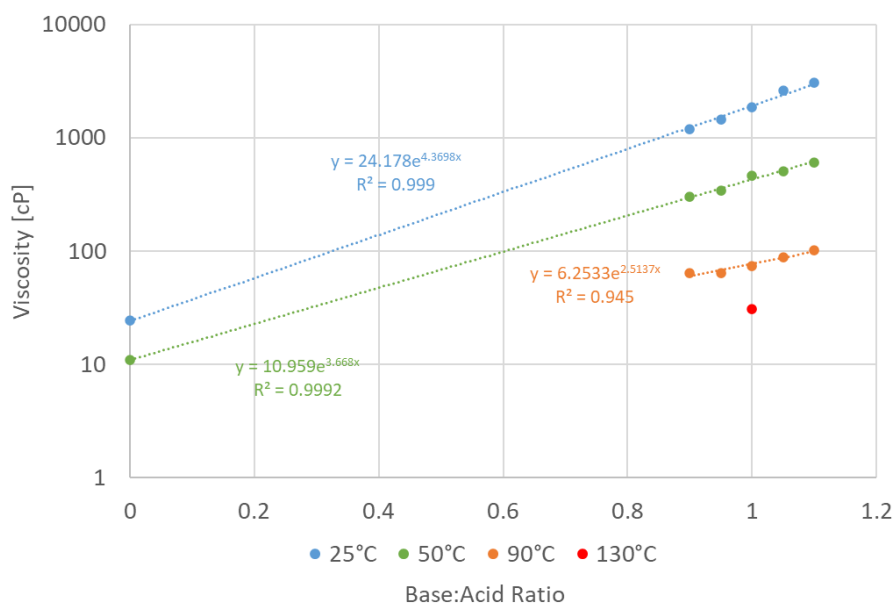


Figure 21: Viscosity (cP) calculated from the diffusion coefficients (DOSY experiments) as a function of the base:acid ratio. Self-diffusion values are given in Appendix 1.

Viscosity values for H_2SO_4 as a function of temperature taken from literature and fitted to the VTF equation. The results are given in Figure 22 and Table 6. The VTF equation is an excellent fit for the experimental data of H_2SO_4 .

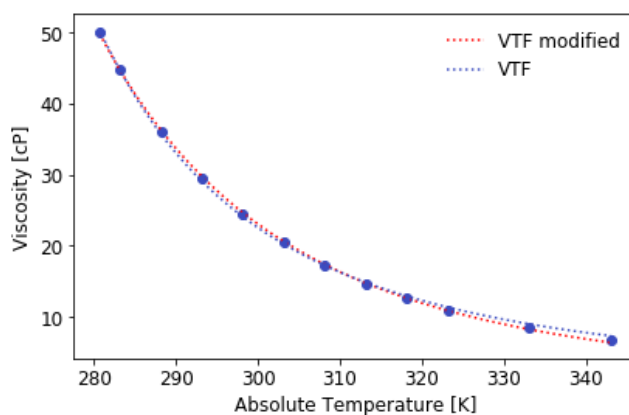


Figure 22: Viscosity values for H_2SO_4 as a function of temperature taken from literature and fitted to VTF equation¹²⁸. Lines correspond to the fitting models VTF (Eq. 39) and VTF modified (Eq. 40).

Table 6. VTF correlation coefficients; viscosity of H_2SO_4 as a function of temperature. APD - average percent deviation (Eq. 29). MARD - maximum absolute relative deviation.

Model	A	η_0	B	T	APD	MARD
Eq. 39	-	0.285948	543.269	175.623	2%	8%
Eq. 40	4.6662×10^{-4}	-	1676.70	89.26	1.1%	5.9%

The viscosity of mixtures of dry $[\text{N}_{4110}][\text{HSO}_4]$ with sulfuric acid was modelled using a similar approach as in section 2.4.4. For this system, the Kendall-Monroe model and Frenkel-Eyring's model predict very similar results.

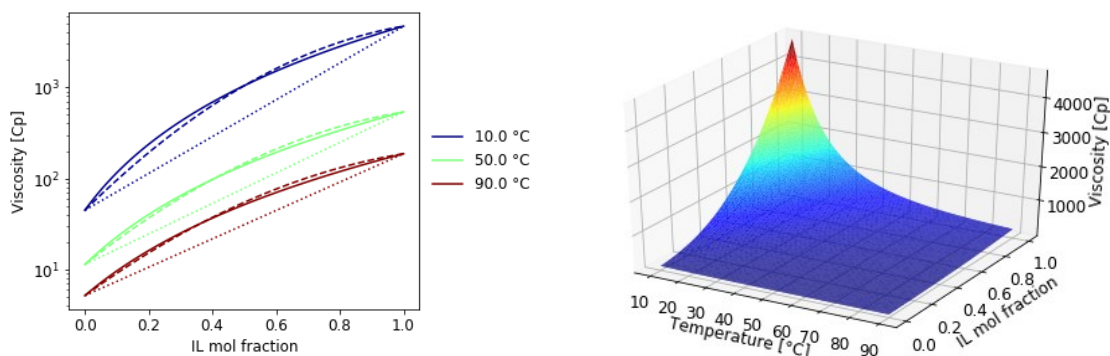


Figure 23. Simulated viscosity for the $[N_{4110}][HSO_4]$ water system. Left figure: solid line Kendall-Monroe model (Eq. 42), segmented line Frenkel-Eyring's model (Eq. 43-44) and dotted line Arrhenius mixing law (Eq. 41). Right: 3D view of the Kendall-Monroe model as a function of temperature and concentration.

2.4.6 Crystallization behaviour as a function of the base:acid ratio (β)

DSC measurements were performed on $[N_{4110}][HSO_4]$ with varying base:acid ratios. Unfortunately, the C_p data obtained from the thermograms is not conclusive, as it varied between cycles. Additionally, the magnitude of the C_p seemed correct, but the values do not seem accurate enough to be reported. This is probably due to calibration errors in the instrument. Therefore, the information from the thermograms is used only for qualitative purposes. To perform energy calculation with these ILs, the C_p values estimated via VBT will be used (Table 4) and their mixtures with other substances will be treated as ideal systems.

Glass transition temperatures were observed at around 189 K (-85 °C), with no subsequent crystallization or melting observed. It is therefore suggested that the liquid phase is the stable state at very low temperatures as the IL is too viscous when supercooled to allow nucleation and the formation of crystals. Some unknown phase transitions were observed at very low temperatures ~ 153 K (~ -120 °C).

Table 6: DSC measurements of $[N_{4110}][HSO_4]$ as a function of the base:acid ratio (β).

Base:Acid		
β	T_g [K]	Error T_g [K]
1.10	191	7.0
1.05	189.9	0.1
1.00	186.6	0.4
0.95	184.0	0.1
0.90	185.4	0.2

2.4.7 Thermal stability

The thermal stability of ILs is crucial for their use in high-temperature applications, as degradation of the IL will impact not only its physicochemical properties but also the economics of a process¹²⁹. Temperature-ramped thermogravimetric analysis (TGA) is an efficient method

for the rapid comparison of the thermal stability of ionic liquids by determining their onset decomposition temperature (T_{onset}), under comparable experimental conditions^{130–132}. The effect of the anion on thermal stability is known to be prominent with a reported increase of the T_{onset} by more than 100 °C in imidazolium-based ILs upon replacing halide ions with perfluorinated anions, that are associated with superior thermal stability^{130,132–139}. Even though the thermal decomposition of ILs has been thoroughly reviewed^{132,139}, showing that ILs generally have good thermal stability, there has been little emphasis on the thermal stability of acidic ionic liquids, such as the hydrogen sulfate based ILs. In this work, the short-term thermal stability of $[\text{N}_{4110}][\text{HSO}_4]$ was assessed via TGA to examine the relationship between the base:acid ratio and the short-term thermal stability. The temperature-ramped experiments monitored the weight loss (%) as a function of temperature, at a constant heating rate. The T_{onset} was extrapolated as the intersection of the baseline and the tangent of the weight dependence on the temperature curve as decomposition occurs. Additionally, the derivative curves were used to obtain the respective first derivative peak temperature (T_{peak}), indicating the point at which the sample undergoes maximum decomposition. Plotting the first derivative of weight loss (dw/dt) allows the distinction between subtle, overlapping weight loss processes that might not be evident by solely examining the TG curves. The T_{peak} value is therefore an additional parameter of the short-term thermal stability of the ionic liquids tested. The thermogram for $\beta = 1$ is shown in Figure 24.

The short-term thermal stability of the ionic liquids was carried out as described in 2.3.3.6. The estimated T_{onset} temperatures for $[\text{N}_{4110}][\text{HSO}_4]$ with different base:acids ratios ($0.9 < \beta < 1.1$) were all very similar (271 ± 2 °C). It is well established that T_{onset} dramatically overestimates the thermal stability of ILs, but is still a useful parameter for comparing the relative stabilities of ionic liquids¹⁴⁰. Further long-term thermal stability studies (isothermal studies at the large-scale application T) would be required to fully confirm the long-term thermal stability of these ILs. As the T_{onset} value is close to the boiling point of H_2SO_4 337 °C¹⁴¹, and the thermal decomposition of H_2SO_4 to sulphur trioxide (SO_3) and water, which increases rapidly at a temperature above 400 °C¹⁴², it is unclear whether TGA mass loss is due to decomposition or vaporization of the liquids, or a combination of these processes.

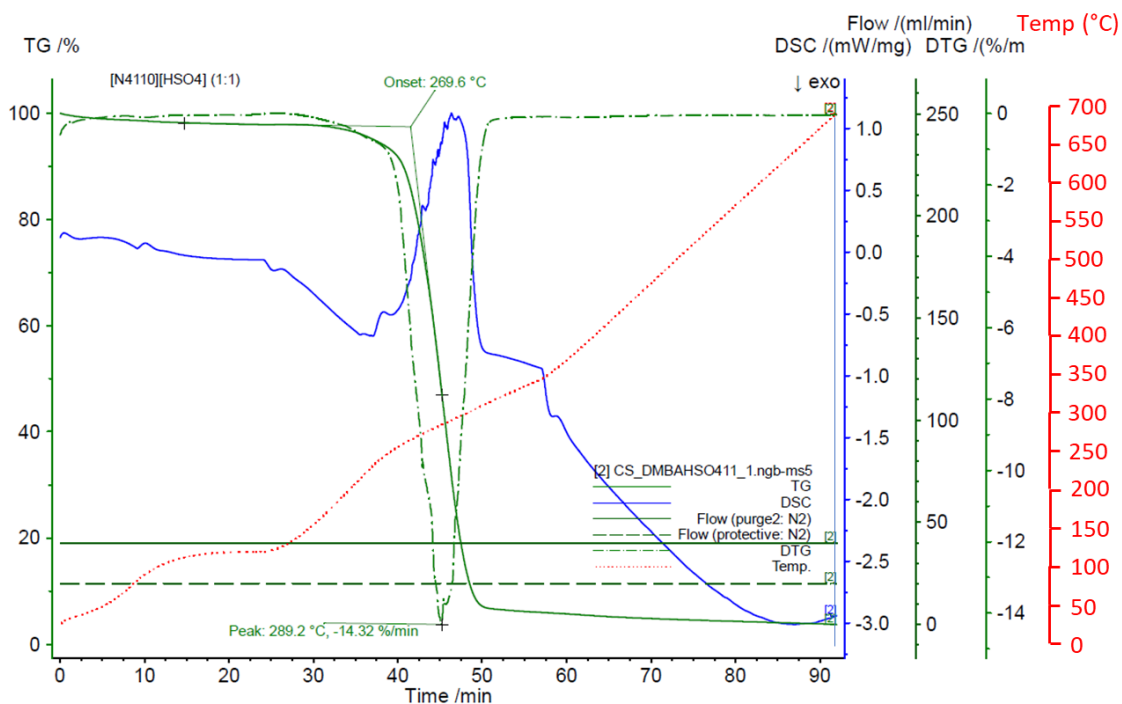


Figure 24. Thermogram for $[N_{4110}][HSO_4]$ ($\beta=1$). Created with NETZSCH Proteus software.

From an engineering point of view, unit operations using $[N_{4110}][HSO_4]$ should be operated lower than 271 °C to avoid decomposition of the ILs, and ideally, should be operated at the lowest possible temperature to ensure long-term stability of the IL.

2.5 Conclusions

Alkylammonium hydrogen sulfate ILs appear to be excellent candidates as solvents for industrial applications due to their low cost, their good thermal stability (up to 271 ± 2 °C) and their acidic nature which can be used to catalyse chemical reactions, such as biomass fraction. In this kind of ILs, it has been shown (by others) that the base:acid ratio plays a major role in their catalytic properties, which offers an additional way to tune the physicochemical properties of these solvents. For this reason, it is important to control the base:acid ratio. In this work, an equation to determine the base:acid ratio for diprotic ILs through acid-base titration was developed and tested.

Volumetric properties for $[N_{4110}][HSO_4]$ (neat and aqueous for $\beta=1$) were measured as a function of temperature, as well as the impact of the base:acid ratio and temperature on the volumetric properties of the neat IL. Regarding the density of $[N_{4110}][HSO_4]$ /water mixtures, the errors for treating these systems as ideal are relatively small (<3%). The deviations from ideal behaviour (excess properties) are maximum around a water content of 50 wt% and decrease

with temperature. Changes in base:acid ratio impacts the properties but not to a significant extent to be used to monitor the base:acid ratio.

Glass transition temperatures were detected at around $-85\text{ }^{\circ}\text{C}$ (189 K), with no subsequent crystallization or melting being observed. It is therefore suggested that the liquid phase is the stable state at very low temperatures, which might enable other applications that the ones explored in this work.

It seems that RTILs with the $[\text{SO}_4]^{2-}$ anion has not been reported. The fact that $[\text{N}_{4110}]_2[\text{SO}_4]$ is liquid at room temperature and might enable other applications that the ones explored in this thesis.

2.5.1 Future research

There is a lot of room to investigate the solvent structures and their relationship to macroscopic properties for PILs, especially for those containing the $[\text{HSO}_4]^-/[\text{SO}_4]^{2-}$ ions. It has been noticed that scarce data is available in the scientific literature covering the physicochemical properties of hydrogen sulfate based ILs, and their mixtures with water, or other solvents. It has also been noticed that many estimation methods based on group contribution or empirical formulae do not cover this family of ILs. It is, therefore, necessary to perform more measurements of the properties of these ILs, to expand those models to include these ILs. Additionally, the region ($\beta > 1$), where $[\text{SO}_4]^{2-}$ ions form, should be further explored, as an additional dimension to tune the acidity/properties of the ILs for catalytic applications.

The hydration behaviour of the PIL systems, specifically those containing the $[\text{HSO}_4]^-/[\text{SO}_4]^{2-}$ ions, should be further studied with detailed analytical and spectroscopic techniques, and computational methods, to elucidate the molecular structures of these systems and how these relate to macroscopic properties.

Chapter 3 - Interactions between ionic liquids and metallic materials

3.1 Motivation

Choosing the right materials of construction for a chemical process is critical, not only it is essential for safety, but also for its technical and economic feasibility. The field of Ionic Liquids (ILs) is emerging for a great number of applications. However, very little is currently known about how metallic materials behave when exposed to ILs, either alone or in aqueous mixtures. Therefore, to have some insight into possible materials of construction it is essential to perform a detailed evaluation.

3.1.1 Objectives

The main objective of this section is to perform a systematic study of the corrosion behaviour of metals and alloys exposed to different types of ILs, to identify possible materials of construction for IL-based processes. The assessment is performed by quantifying the corrosion rates using gravimetric methods. Surface analysis was also carried out to have a better understanding of the corrosion mechanisms taking place. Variables explored in this study include different types of ILs, water content and temperature.

The laboratory corrosion tests were carried out in accordance with the immersion test as described in the industrial standards ASTM G 31 “Standard Guide For Laboratory Immersion Corrosion Testing Of Materials”¹⁴³ and ISO 11845:2020 “Corrosion of metals and alloys — General principles for corrosion testing ISO”¹⁴⁴. Additionally, a comprehensive method to classify the different corrosion behaviours observed in this study was developed and discussed.

Definitive validation for industrial use of metallic materials in IL-based processes is excluded from this work as it would require a lot of additional testing.

3.2 Introduction

Corrosion is a natural process, by which a refined metal is converted to a more chemically stable form, such as its oxide, hydroxide, or sulfide. It is the gradual destruction of materials (usually metals) by chemical and/or electrochemical reactions with their environment, resulting in the degradation of their useful properties (such as strength). Corrosion processes are complex in nature and studies thereof have become an interdisciplinary research field, combining fundamental sciences and engineering. Corrosion can lead to structural and equipment failure in settings ranging from domestic and civil to industrial applications (such as oil, gas and chemical industries), leading to catastrophic consequences¹⁴⁵. To avoid these

situations, globally billions of dollars are spent each year to fight corrosion. In a 2-year study (1999-2001) to determine the economic impact of corrosion, it was estimated that the total annual direct cost of corrosion in the U.S.A. was 276 billion \$US, approximately 3.1% of the nation's Gross Domestic Product (GDP) ¹⁴⁶.

Corrosion tests are widely used to evaluate the durability of materials of construction exposed to reactive environments. Corrosion-test planning and design are different for each of the three stages in the evolution of a chemical process plant, *i.e.* research and development, plant design and plant operation. This is discussed in detail in the book “Corrosion Tests and Standards: Application and Interpretation” ¹⁴⁷.

Definitions for some of the terms used in this section can be found in Appendix 3.

3.2.1 Types of corrosion

There are several classifications of the various ways in which corrosion can damage metallic materials. It is possible in most cases to identify each form of corrosion by mere visual observation, being the naked eye sufficient, but sometimes magnification is helpful or required ¹⁴⁸. There are different categorisations for the types of corrosion which varies slightly from different authors, but generally speaking, the forms are: (1) uniform, or general attack, (2) galvanic, or two-metal corrosion, (3) crevice corrosion, (4) pitting, (5) intergranular corrosion, (6) selective leaching, or parting, (7) stress corrosion and (8) erosion-corrosion ^{148,149}. Not all these forms of corrosion were addressed in this work and therefore will not be discussed.

3.2.1.1 Uniform Attack

Uniform attack (or general overall corrosion) is the most common form of corrosion. It is normally characterized by a chemical or electrochemical reaction which proceeds uniformly over the entire exposed surface or over a large area ^{148,149}. When this type of corrosion manifests, the metal becomes thinner and eventually fails. It represents the greatest destruction of metal on a tonnage basis. This form of corrosion, however, is not of too great concern from the technical standpoint, because the life of equipment can be accurately estimated based on comparatively simple tests. Merely immersing specimens in the fluid involved is often sufficient. Uniform attack can be prevented or reduced by (1) proper materials, including coatings, (2) inhibitors, or (3) cathodic protection ¹⁴⁸. For example, a piece of steel or zinc immersed in dilute sulfuric acid will normally dissolve at a uniform rate over its entire surface ¹⁴⁸.

3.2.1.2 Pitting

Pitting is a form of extremely localized attack that results in holes in the metal ¹⁴⁸. The corrosion rate is greater in some areas than others ^{148,149}. If an appreciable attack is confined to a relatively small, fixed area of metal, acting as an anode, the resultant pits are described as deep. If the area of attack is relatively larger and not so deep, the pits are called shallow. Depth of pitting is sometimes expressed by the pitting factor, the ratio of deepest metal penetration to average metal penetration as determined by the weight loss of the specimen ¹⁴⁹. It is often difficult to detect pits because of their small size and because the pits are often covered with corrosion products. In addition, it is difficult to measure quantitatively and compare the extent of pitting because of the varying depths and numbers of pits that may occur under identical conditions ¹⁴⁹. Pitting is also difficult to predict by laboratory tests. Sometimes the pits require a long time, several months or years, to show up in actual service ¹⁴⁹. Pitting is particularly vicious because it is a localized and intense form of corrosion, and failures often occur with extreme suddenness ¹⁴⁹.

3.2.1.3 Selective leaching

Selective leaching (dealloying or parting) is the removal of one element from a solid alloy by corrosion processes ^{148,149}. The most common example is the selective removal of zinc in brass alloys (dezincification), in which zinc corrodes preferentially, leaving a porous residue of copper and corrosion products ¹⁴⁸. The alloy so corroded often retains its original shape and may appear undamaged except for surface tarnish, but its tensile strength and ductility are seriously reduced ¹⁴⁸. Dezincified brass pipe may retain sufficient strength to resist internal water pressures until an attempt is made to uncouple the pipe, or a water hammer occurs, causing the pipe to split open ¹⁴⁸. Similar processes occur in other alloy systems in which aluminium; iron, cobalt, chromium, and other elements are removed ^{148,149}.

3.2.2 Corrosion rates

The corrosion rate is typically expressed in millimetres of metal lost per year (mm/y). Other units used to express corrosion is mils (1 mil = 0.001 inches) per year (mpy). The suitability of a material for a given application will depend upon many factors. It is a common industrial practice to use low-cost materials with a thickness allowance for corrosion when metal contamination of the process streams is not an issue. If the presence of metals is not acceptable, then more corrosion-resistant metals or alloys with low corrosion rates should be used.

As a general guideline in corrosion handbooks, corrosion rates (CR) of metals in their operational environments are classified as follows: excellent ($CR < 0.05$ mm/y), very good ($0.05 < CR < 0.5$ mm/y), satisfactory ($0.5 < CR < 1.27$ mm/y), unsatisfactory (1.27 mm/y $< CR$)¹⁵⁰. In another reference the suitability of materials is classified as follows: resistant ($CR \leq 0.1$ mm/y), fairly resistant ($0.1 < CR < 1$ mm/y) and not resistant (1 mm/y $\leq CR$)¹⁴⁵. For reference, in a study about the corrosion behaviour of metals in ILs the corrosion target was 0.1 mm/y (3.94 mpy)¹⁵¹.

3.2.3 Corrosion rate quantification methods

The main approaches to study corrosion are gravimetric methods and electrochemical methods, which are not discussed in this work. The former technique is still the dominant method, where the mass loss measurement is achieved by immersing a sample of the metal on the corrosion media (immersion test). This is a simple and well-established method based in determining the difference in weight of the specimen under study before and after it is immersed in a corrosive medium for a certain amount of time¹⁵². However, this method presents some important limitations¹⁵²:

- It only provides the average corrosion rate over the immersion test duration, not allowing for differences in the oxidation kinetics to be determined.
- It can lead to inaccuracies in corrosion rate determination as a consequence of a poor or an excessive corrosion product removal post immersion.
- It does not provide information about the corrosion mechanisms.

Corrosion is, in nature, an electrochemical process and as such electrochemical methods represent a powerful tool for the study of the corrosion behaviour of metals exposed to a corrosive medium¹⁵². They have been used to estimate the Corrosion Rate (CR) and evaluate the viability of effective corrosion protection methods. In order to determine detailed corrosion mechanisms, a number of different and complementary techniques are required¹⁵².

One of the most frequently used electrochemical methods to quantify the corrosion rate of metals exposed to a corrosive medium is the Tafel extrapolation from a polarisation curve. Tafel extrapolation is a mathematical technique used to estimate either the corrosion current (i_{corr}) or the corrosion potential (E_{corr}) in an electrochemical cell, which in turn allows the estimation of the corrosion rate. These parameters are obtained by extrapolation of linear values within a Tafel plot^{152,153}. Despite the fact that that this technique is extensively used in research to estimate the CR, It has been shown that it does not always provide a good

estimation, *i.e.* the CR values predicted by this technique do not always agree with corrosion rates evaluated from weight loss and/or hydrogen evolution methods ¹⁵³. One example is the case of Mg corrosion, for which discrepancies up to 90% were observed between the gravimetric or electrochemical methods ¹⁵³. For this reason, it is common practice that these Tafel measurements are complemented by the use of other measurement methods, *e.g.* weight loss rate, hydrogen evolution rate, and rate of metal cations leaving the metal surface ¹⁵³.

In summary, gravimetric methods to quantify the corrosion rates are the simplest techniques and do not involve measurements of currents or voltages. Some electrochemical techniques, such as Tafel extrapolation method, require high anodic/ cathodic polarizing voltage, *e.g.* ± 250 mV, and thus might change the surface properties of an electrode ¹⁵⁴. The results obtained by such techniques do not represent the real conditions of metallic materials used as construction materials for industrial plants. For this reason, the corrosion phenomena in this work will be studied using gravimetric methods. Electrochemical methods can be useful, however, for understanding the fundamental mechanisms of corrosion and to evaluate trends.

3.2.4 Corrosion rate quantification – Immersion test

The following section provides a short description of the main method described in the literature used to quantify the corrosion rates through immersion experiments. Standard guidelines to study corrosion, such as ISO, ASME or NACE TM0169/G31 – 12a “Standard Guide for Laboratory Immersion Corrosion Testing of Metals” ¹⁴³, are broadly used by industry and academics. They describe methods to perform immersion test experiments and to quantify the corrosion rates of metals exposed to corrosive environments. However, these methods are not complete, and without demerits, of particular note is the lack of guidelines for post-exposure analysis of the as-obtained corroded samples. Post-exposure analysis provides useful information to understand the underlying physicochemical mechanisms of corrosion, but as the focus of the standards is less on the underlying phenomena this has been omitted. This knowledge, however, is useful for selecting the right materials of construction and to develop corrosion prevention strategies ^{155,156}. Upon completion of the immersion, a visual inspection of the metal sample is recommended followed by an extreme cleaning (mechanical, chemical or electrochemical) ¹⁴³. This process removes all corrosion products from the specimens, to quantify the corrosion rate, by the mass difference of the corrosion-products-free-corroded sample. In doing so, vital information is lost, for example, chemical nature and morphology of the chemical species forming on the metal.

Standard ISO 11845 : 2020 “Corrosion of metals and alloys — General principles for corrosion testing ISO”¹⁴⁴ also provide some guidelines to evaluate the corrosion rate by immersion

3.2.5 Mechanisms of corrosion

Metals (M) oxidise by losing electrons (e^-) as shown in Eq. 47. In the context of corrosion, this is known as the anodic reaction.



The Electromotive Force (EMF) series lists chemical species (atoms, molecules, and ions) in the order of their tendency to gain or lose electrons (be reduced or oxidized, respectively), expressed in volts and it is measured with reference to the hydrogen electrode, which is defined as a standard and arbitrarily assigned the voltage of zero (Eq. 48). The hydrogen electrode is defined as an aqueous solution containing hydrogen in its oxidized form (the hydrogen ion, H^+) in equilibrium with hydrogen in its reduced form (hydrogen gas, H_2) at a concentration of 1M, 25 °C and 1 atmosphere⁹⁶. In the context of corrosion, the reduction reaction is known as the cathodic reaction.



The EMF series for the metals used in this work are presented in Table 7.

Table 7. Standard reduction potential (E^0) for the metals used in this work (EMF series). Values taken from the CRC Handbook of Chemistry and Physics³⁷.

Reaction	Standard Reduction Potential (E^0) [V] ³⁷
$O_2 + 4H^+ + 4e^- \rightleftharpoons 2 H_2O$	1.229
$Cu^+ + e^- \rightleftharpoons Cu$	0.521
$O_2 + 2 H_2O + 4e^- \rightleftharpoons 4OH^-$	0.401
$Cu^{2+} + 2e^- \rightleftharpoons Cu$	0.3419
$2H^+ + 2e^- \rightleftharpoons H_2$	0
$Fe^{3+} + 3e^- \rightleftharpoons Fe$	-0.037
$Mo^{3+} + 3e^- \rightleftharpoons Mo$	-0.200
$Ni^{2+} + 2e^- \rightleftharpoons Ni$	-0.257
$Fe^{2+} + 2e^- \rightleftharpoons Fe$	-0.447
$Zn^{2+} + 2e^- \rightleftharpoons Zn$	-0.7618
$2H_2O + 2e^- \rightleftharpoons H_2 + 2OH^-$	-0.8277
$Ti^{3+} + 3e^- \rightleftharpoons Ti$	-1.209
$Ti^{2+} + 2e^- \rightleftharpoons Ti$	-1.628
$Al^{3+} + 3e^- \rightleftharpoons Al$	-1.676

Elements that have a greater tendency than hydrogen to lose electrons are considered as electropositive and those with a higher tendency to gain electrons, above hydrogen in the

series, are considered electronegative. Electropositive metals will replace hydrogen from acids⁹⁶.

The reaction shown in Eq. 48 is just one example of a cathodic reaction that can take place during a corrosion process. The cathodic reaction will depend on the nature of the corrosive medium. Corrosive media relevant to this work are briefly reviewed in the next sections.

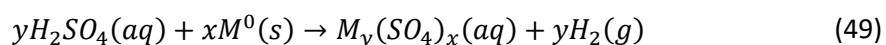
3.2.6 Corrosive medium

The corrosion rates of metal exposed to Protic Ionic Liquids (PIL) are compared to the corrosion rates of the corresponding acid used for the PIL synthesis. In this section general considerations on the corrosion behaviour of such acidic media is briefly discussed.

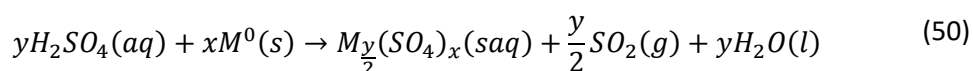
3.2.6.1 Sulfuric acid

Sulfuric acid (H_2SO_4) is considered a strong acid (section 2.4.1). Generally speaking, dilute sulfuric acid dissolves all metals below hydrogen in the EMF series. However, some metals like barium and lead produce insoluble layers of corrosion products attached to their surface, such as oxides and sulfates, preventing further dissolving of the metal¹⁴⁵. The propensity towards dissociation of H_2SO_4 explains its corrosiveness. The corrosion depends on the temperature and concentration, with a maximum on most materials in the concentration range between 40 and 80 wt%¹⁴⁵. The general corrosion behaviour of H_2SO_4 can be summarized as follows¹⁴⁵:

- 0–65 wt% H_2SO_4 : The acid reacts with metals to produce hydrogen gas and the corresponding metal sulfate (Eq. 49). This reaction takes place at all temperatures and is commonly referred to as “reducing” conditions.



- 65–85 wt% H_2SO_4 : Reducing at cold temperatures (Eq. 49) and oxidizing at high temperatures and the boiling point. Hot and concentrated sulfuric acid is a strong oxidizing agent and does not react with metals in the same way as described in (Eq. 49); instead, it forms sulfur dioxide, water and SO_4^{2-} , according to Eq. 50:



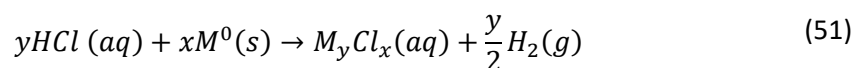
- 85–100 wt% H_2SO_4 : Oxidizing at all temperatures (Eq. 50).

Noble metals such as platinum and gold are not corroded by H₂SO₄. The metals above hydrogen in the electromotive series, such as copper, mercury and silver, for example, react in hot H₂SO₄ to form SO₂ without hydrogen formation ¹⁴⁵.

The corrosion rates of metallic materials in sulfuric acid and its solutions are mainly determined by the solubility of their corresponding metal sulfates as a function of the concentration and temperature ¹⁴⁵. Other parameters affecting the corrosion are the gas content, especially the oxygen content, the flow rate of the medium and the presence of substances that can promote or inhibit corrosion.

3.2.6.2 Hydrochloric acid

The corrosiveness of hydrochloric acid (HCl) towards metals is based on the oxidising effect of the hydrated proton H₃O⁺, which attacks metals that lie below hydrogen in the electrochemical series to form metal chlorides and liberate hydrogen gas according to Eq. 51.



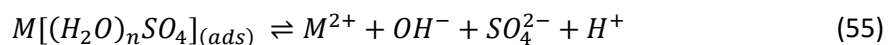
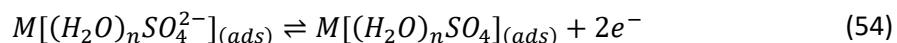
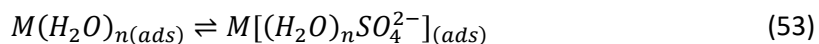
Furthermore, hydrochloric acid can dissolve passivating surface films (oxides and other compounds) leading to active corrosion. Additionally, chloride ions can form metal complexes that can lower the electrode potential of electropositive metals, *e.g.* copper, to below that of the hydrogen electrode so that corrosive attack can take place ¹⁴⁵.

3.2.7 Mechanism of corrosion inhibition

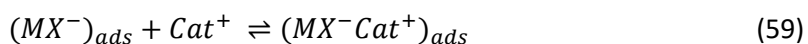
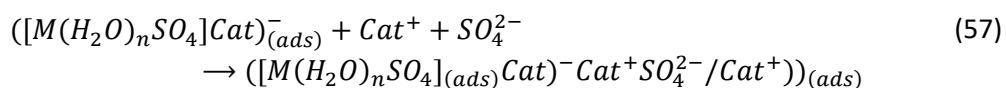
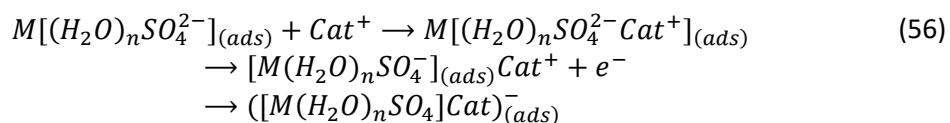
Interestingly, the use of ILs as corrosion inhibitors has been explored ¹⁵⁷. To understand the corrosion behaviour of these substances, the mechanisms of how they inhibit corrosion are discussed in this section.

Similar to most of the organic corrosion inhibitors, ILs inhibit metallic corrosion by blocking the anodic and cathodic sites present over the metallic surface ¹⁵⁷. Therefore, inhibition of metallic corrosion in the presence of ILs is believed to block anodic oxidative metallic dissolution as well as cathodic hydrogen evolution reactions. The mechanism of metallic corrosion inhibition by ILs in an aqueous acidic solution of H₂SO₄ for iron (Fe) has been reported by Likhanova *et al.* who described the anodic dissolution of metals in this medium in the absence of ILs as follows ¹⁵⁸:





However, in presence of ILs, it has been reported that the anodic reactions can be represented as shown in Eqs. 56-59: where, Cat^+ and X^- represent the cation (mostly organic) and anion of the IL, respectively ¹⁵⁸:



The mechanisms are given in Eqs. 56-57, are shown as reported in the original reference. However, the notation is not clear. These mechanisms have been cited many times in the scientific literature, including in the review on the corrosion inhibition by ILs ¹⁵⁷. However, the mechanisms have been modified and the step involving the electron is not shown ¹⁵⁷. In any case, the overall mechanism has been explained as the adsorption of the IL cation (Cat^+) on the metallic surface to form a “protective multilayer” of $Cat^+/[SO_4]^{2-}/Cat^+$ on the corrosion products $M[(H_2O)_nSO_4]_{ads}$ that restrain their dissolution and consequently this prevents iron dissolution to continue. As those experiments were conducted on sulfuric acid, the concentration of sulfate ions is much higher than the concentration of the anionic counterpart of the IL (X^-) that results into formation of $[M(H_2O)_nSO_4^{2-}]_{ads}$ in larger proportion than $[MX^-]_{ads}$ (Eq. 58). Nevertheless, these both anionic species attract the positively charged counterpart of the IL (Cat^+) by electrostatic force (physisorption) to form a monomolecular layer as an insoluble complex on the metallic surface ^{157,158}. The adsorption of the Cat^+ on the metallic surface causes a change in the surface polarity which induces the subsequent adsorption of a sulfate or X^- ions on the surface, resulting in a multimolecular layer ^{157,158}. The multimolecular layers are stabilized by Van der Waal’s cohesion force acting between the organic moiety of the IL which causes a more closely adsorbed film at the metal/electrolyte interfaces. Generally,

the charged part of the cation (Cat^+) interacts with the metallic surface to form the multimolecular layers while the rest of the cation, (hydrophobic part) can form hemi-micelles, ad-micelles and/or surface aggregation ^{157,158}. The adsorbed multimolecular layers of the ILs isolate the metal from the corrosive environment and protect it from corrosive attack (Figure 25) ^{157,158}. The inhibition mechanism of metallic corrosion by ILs in other protic acidic solutions, such as in HCl, should be similar.

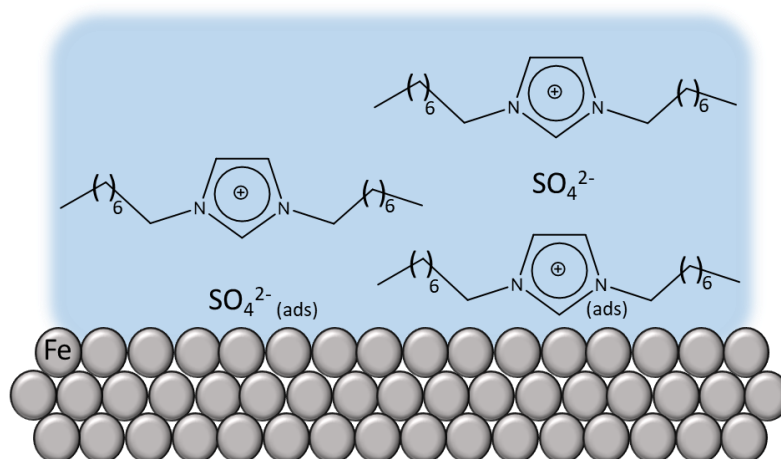
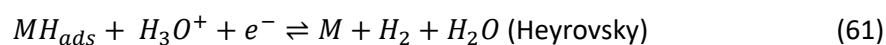
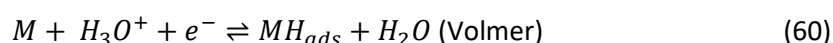


Figure 25. Schematic representation of the inhibition mechanism adapted from ref ¹⁴³. It is important to note that the positions of the alkyl chains are fictitious, and they do not necessarily display their real orientation in the system.

In aqueous environments, the cathodic hydrogen evolution reaction can be the reduction of water as shown in Table 7. Generally, the hydrogen evolution reaction follows two very common mechanisms, either the Volmer-Heyrovsky mechanism represented by Eqs. 60 and 61 or the Tafel hydrogen evolution mechanism represented by Eq. 62 ^{157,159}. These mechanisms, in acidic medium, are as follows ^{157,159}:



During the first step of cathodic reactions hydrogen ions (or hydronium ions) first adsorbed on the metallic surface by Volmer mechanism (Eq. 60) followed by discharge of hydrogen gas by Heyrovsky or Tafel mechanism represented by Eqs. (61-62). All these reactions do not occur with the same rate ^{157,159}. Generally, if the Volmer reaction is fast, then Heyrovsky and/or Tafel reactions occur with a slower rate and vice versa. Presence of the organic corrosion inhibitors, such as ILs, in the corrosive solution, may retard or slow down the formation of MH_{ads} , or retards the electron transfer to the hydronium ions and suppresses the Heyrovsky reactions (Eq. 61) ^{157,159}. In general, in a corrosive medium, the adsorbed hydrogen on the metallic

surface recombined and evolved as bubbles of hydrogen gas, which is the second step in the cathodic hydrogen evolution reaction. The formation of hydrogen gas either occurs through hydrogen atom-atom combination as denoted by Volmer-Tafel (Eq. 60 and 62) or may result through hydrogen atom-hydrogen ion combination as represented by Volmer-Heyrovsky (Eq. 60 and 61) ^{157,159}.

In the presence of inhibitors (ILs), cathodic can be represented as follows ¹⁵⁷:



At the cathode, the cations in the ILs (Cat^+) starts competing with hydrogen ions for electrons. In general, Cat^+ has a large molecular size and therefore can replace a greater number of water molecules from the metallic surface. After their adsorption, Cat^+ accepts electrons from the metal which results in the formation of electrically neutral species. These adsorbed species can donate electrons from heteroatoms and/or π -orbitals into the d-orbitals of metal. Further, as metals are already electron-rich species; this type of donation causes inter electronic repulsion which results in the transfer of electrons from d-orbitals of the metallic atoms on the surface back to the antibonding molecular orbitals of the ILs (retro-donation). Both donation and retro-donation strengthen each other through synergism ^{157,158,160}.

In a study addressing the corrosion behaviour of metals in ILs, it was shown that the use of corrosion inhibitors in IL media is also possible. It was also shown that what can be a corrosion inhibitor for a specific metal, can be a corrosion promotor for other metals ¹⁵¹.

3.2.8 Corrosion behaviour of metals in ILs - Knowledge gaps

A survey published in 2020, performed among 25 academic and industrial leaders in the field of ILs revealed that almost 60% of the participants disagreed that “material compatibility with ILs is challenging”, but 40% were not completely convinced ². The outcome of the survey is quite surprising for several reasons:

- Material compatibility of new compounds has always been a challenge for the chemical industry due to the high cost of corrosion as previously stated. One example of how IL-induced corrosion can impact industrial processes is the case of BASF, who replaced $[C_2C_1im]Cl$ by $[C_2C_1im][OAc]$ for their commercial CELLIONIC™ formulation of IL solutions of cellulose, due to the higher corrosivity of the chloride-containing IL ¹⁶¹.
- It has been highlighted that the high thermal stability of ILs opens the door for high-temperature applications ¹⁵. It is known that the corrosion phenomena will be enhanced

by temperature ^{148,149}, and therefore, material compatibility under those conditions should be a critical point.

- Due to the electrochemical nature of the corrosion phenomena, it is expected that the corrosion rate of metals exposed to ILs will be higher than when exposed to low-electrical-conductivity solvents, such as organic solvents used in the industry. This increase in corrosion has been noticed for metals, such as iron, exposed to electrolyte solutions ¹⁴⁸. For example, in distilled water having low conductivity, anodes and cathodes on the surface of the metal must be located relatively near each other for the corrosion phenomena to take place ¹⁴⁸. Consequently, OH⁻ ions forming at cathodes are in the proximity of Fe²⁺ ions forming at nearby anodes, resulting in a film of Fe(OH)₂ on the metal surface, which provides a protective barrier against further corrosion ¹⁴⁸. In sodium chloride solutions, the electrical conductivity is increased; hence, anodes and cathodes can operate at much further distances from each other ¹⁴⁸. At such cathodes, NaOH does not react immediately with FeCl₂ formed at anodes; instead, these substances diffuse into the solution and react to form Fe(OH)₂ away from the metal surface. Any Fe(OH)₂ so formed does not provide a protective barrier (passive layer) on the metal surface ¹⁴⁸. Hence, iron corrodes more rapidly in sodium chloride solutions than in water ¹⁴⁸.

Due to the above, it would be expected that material compatibility will be a major challenge for the industrial applications of ILs. ILs represent a large class of new liquid salts, with very different chemistries than molecular solvents and salt solutions as mentioned in Chapter 2. Despite the great number of scientific publications about ILs and their applications, there is scarce data about the corrosion behaviour of metallic materials exposed to these solvents. The focus has been centred around the fluorinated ILs, such as [NTf₂]-based ILs, with some minor work on other chemistries, and no information about the acidic protic ILs, such as the hydrogen sulfate based-IL, needed for the ionoSolv process for biomass pretreatment (Chapter 4). Moreover, the effects of different variables affecting the corrosion processes, *e.g.* water concentration, temperature, have not been addressed systematically. It has been also noticed that the corrosion of metals exposed to ILs has been studied from a tribology perspective, as some ILs have been used as lubricants ¹⁶²⁻¹⁶⁵. Reference to what is known about metal corrosion in ILs will be discussed in the relevant part in the results and discussions section of this chapter.

Overall, the published knowledge available today regarding the corrosion behaviour of metals exposed to ILs is scarce and insufficient for the proper selection of materials of constructions for IL-based processes. Therefore, in this chapter, a systematic study on the corrosion of

several metals and alloys exposed to different ILs (neat and aqueous) at different temperatures will be presented.

3.3 Experimental methods

3.3.1 Materials

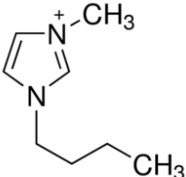
3.3.1.1 Ionic liquids

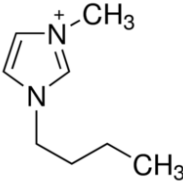
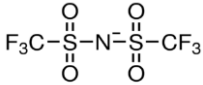
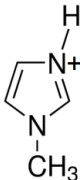
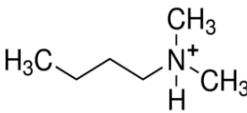
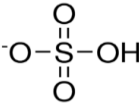
Starting materials for ionic liquid synthesis were purchased from Sigma Aldrich and used as received, unless stated otherwise. 1-Butyl-3-methylimidazolium chloride $[C_4C_1im]Cl$, purity $\geq 98.0\%$ HPLC (CAS: 79917-90-1), 1-butyl-3-methylimidazolium bis(trifluoromethylsulfonyl)imide $[C_4C_1im][NTf_2]$ purity $\geq 98\%$ (CAS: 174899-83-3) and 1-Methylimidazolium chloride $[HC_1im]Cl$ purity $>98\%$ (CAS: 35487-17-3) were purchased from Iolitec. *N,N,N*-dimethylbutylammonium hydrogen sulfate $[N_{4110}][HSO_4]$ was prepared using a reactor as explained in section 2.3.2 and the base:acid ratio was controlled by acid titration with the method described in section 2.3.3.2 (Mettler Toledo Compact Titrator G20S).

High purity water (Millipore 15 M Ω cm) was used throughout (IL dilutions, water control and sample cleaning). The solution water content was measured by Karl Fisher Titration (section 2.3.3.1). No effort was made to remove the carbon dioxide or oxygen from the water, the ILs and their mixtures. For the dry ILs, water was removed using first a rotary evaporator with further drying using the Schlenk line at 80 °C for 48 h at least.

Different cations and anions have been selected for this study to cover ILs with different properties. The cations selected include: $[C_4C_1im]^+$ (aromatic / aprotic), $[HC_1im]^+$ (aromatic / protic) and $[N_{4110}]^+$ (non-aromatic / protic). The anions selected include: Cl^- (neutral, hydrophilic and coordinating), $[NTf_2]^-$ (neutral, hydrophobic and non-coordinating) and $[HSO_4]^-$ (acidic and hydrophilic). The ILs selected for this study are shown in Table 8.

Table 8. Structure of ILs used in the corrosion study.

Name	Cation	Anion	Characteristics
$[C_4C_1im]Cl$ 1-Butyl -3-methylimidazolium chloride		Cl^-	<ul style="list-style-type: none"> • Aprotic IL • Miscible in water • Coordinating anion

Name	Cation	Anion	Characteristics
[C ₄ C ₁ im][NTf ₂] 1-Butyl-3-methylimidazolium bis(trifluoromethylsulfonyl)imide			<ul style="list-style-type: none"> • Aprotic IL • Immiscible in water • Non-coordinating anion
[HC ₁ im]Cl 1-Methylimidazolium chloride		Cl ⁻	<ul style="list-style-type: none"> • Protic IL • Miscible in water • Coordinating anion • Water solutions slightly acidic
[N ₄₁₁₀][HSO ₄] <i>N,N,N</i> -Dimethylbutylammonium hydrogen sulfate			<ul style="list-style-type: none"> • Protic IL • Miscible in water • Acidic

To assess the effect of coordination nature of the anion on corrosion, Cl⁻ and [NTf₂]⁻ were combined with [C₄C₁im]⁺, to form [C₄C₁im]Cl and [C₄C₁im][NTf₂] respectively. [C₄C₁im]Cl is hydrophilic and miscible with water at all proportions while [C₄C₁im][NTf₂] is hydrophobic and not miscible in water.

To establish the effect of the nature of cation (protic vs. aprotic), the corrosion behaviour in [C₄C₁im]Cl and [HC₁im]Cl will be tested. [HC₁im]Cl is a PIL while [C₄C₁im]Cl is an Aprotic Ionic Liquid (AIL), meaning that it does not have protons available to participate in chemical reactions. However, it has been shown that the proton in the C2 position of the imidazolium ring, is slightly acidic (with pKa values for simple 1,3-dialkylimidazolium cations in the range of 21–24¹⁶⁶), and can participate in chemical reactions¹⁶⁷.

Further, another IL has been included in the study, [N₄₁₁₀][HSO₄], as it has practical applications, such as biomass pretreatment (refer to Chapter 4). This PIL does not share any chemical structure with the other ones. However, comparing the corrosion rates of metals exposed to this IL with [HC₁im]Cl, another PIL, will provide information on the effect of the anion on PIL corrosion behaviour. The isomer [N₄₁₁₀][HSO₄] was chosen over [N₂₂₂₀][HSO₄] for the corrosion test for the reasons discussed in section 2.2. It is expected that the corrosion behaviour will be similar, as the effect of the acidic [HSO₄]⁻ anion should shadow any effects of the alkyl substituents in the cation for those isomers. Regarding the base:acid ratio (β) for the alkylammonium hydrogen sulfate ILs, it is expected that β will have a significant influence on

the corrosion behaviour of metals exposed to these ILs. Unfortunately, due to the size of the experimental matrix, the effect of β on the corrosion of metals exposed to $[\text{N}_{4110}][\text{HSO}_4]$ could not be included.

3.3.1.1.1 IL purity

The presence of metallic impurities in the ILs might impact the corrosion process. Therefore, the metal content in the IL was measured and expressed on a dry basis. The results are given in the results and discussion section 3.5.1 (Table 12).

The metal content in the ILs was calculated by measuring the mass ratio of the metal to a reference element present in the IL *via* XRF (section A5.7.3) (Eq. 64).

$$M_c = \frac{M_{XRF}}{\frac{X_{XRF}}{n \cdot MW_x} \cdot MW_{IL}} \quad (64)$$

Where M_{XRF} and X_{XRF} are the mass % detected in the sample by XRF for a particular metal and the reference element present in the IL. n is the number of moles of the reference element contained in 1 mol of IL. MW_x and MW_{IL} are the molecular weights of the reference element in the IL and the IL respectively. For the $[\text{NTf}_2]^-$ and $[\text{HSO}_4]^-$ based ILs, sulfur was used as a reference. For Cl^- based ILs, chlorine content was used for the calculation.

3.3.1.1.2 Water effect – Concentration

As mention in Section 2.2.5, the molecular structure of ionic liquids is affected by water concentration. Three concentrations have been chosen as representative of different regimes and controls in pure water were performed as well (results are shown in Appendix 5).

- *Residual-water* case: water molecules are dispersed in the polar regions on the IL structure⁶⁷, and the dominant structure is Contact Ion Pair (CIP).
- *IL-rich* case (75 mol%): 3 water molecules per IL pair. This is in the early part of the transition region between IL behaviour and aqueous solution behaviour, where MD simulations¹⁶⁸ indicate the formation of bigger water clusters beyond this point. Beyond this point, Solvent-shared Ion Pairs (SIP) start to form and become the dominant structure.
- *Water-rich* case (97.8 mol%): 45 water molecules per IL pair. This is in the final part of the transition region where full hydration of the ionic species is achieved. The predominant structure is Double Solvent-Separated Ion Pairs (2SIP).

A graphical representation of the different regimes for $[C_4C_{1im}]Cl$ is depicted in Figure 26 and further information presented in Appendix 2. The experimental water concentrations used in the corrosion studies are given in the results and discussion section 3.5.1 (Table 13).

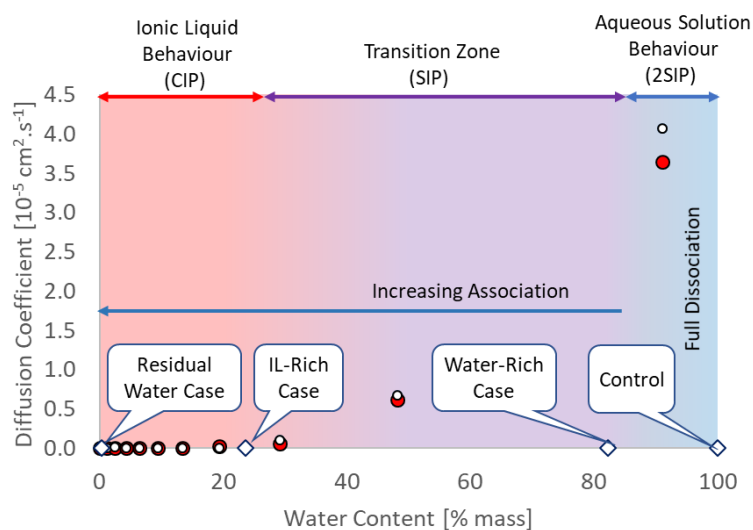


Figure 26. Structural and diffusion properties of $[C_4C_{1im}]Cl$ /water mixtures as a function of water concentration. Diffusion data calculated from MD simulations at 350 K ¹⁶⁸. White circle (○) chloride, red circle (●) $[C_4C_{1im}]^+$. Published by The Royal Society of Chemistry ¹⁶⁹.

3.3.1.2 Metal coupons

The metals selected for this study are shown in Table 9 and were obtained from Goodfellow Cambridge Limited. The samples were disks of around 18mm diameter and 0.125 mm thickness. The exact dimensions of each sample were determined with the help of a micrometre with a precision of 0.001 mm. A 0.8 mm hole was drilled on each sample for the immersion experiments. The metals were used as received. The cleaning protocol was as follows: the coupons were first washed with high purity water, then with Industrial Methylated Spirits (IMS), and finally with acetone at room temperature. The metals were dried for 45 min in an oven at 105 °C, cooled in a desiccator for 30 min, and weighed (AND GH-252 analytical balance with a resolution of 0.01 mg). The elemental composition is presented in the XRF section for each metal (Appendix 5).

Table 9. Metals used for the corrosion study obtained from Goodfellow Cambridge Limited. The samples were disks of around 18 mm diameter and 0.125 mm thickness.

Metal	CAS	Product N°	Purity	Temper	Density [g/cm ³] ^A
Aluminium	7429-90-5	AL000581/1	99.999%	Hard	2.70
Copper	7440-50-8	CU000591/4	99.9%	Hard	8.96
Iron	7439-89-6	FE000360	>99.99%	As rolled	7.87

Metal	CAS	Product N°	Purity	Temper	Density [g/cm ³] ^A
Molybdenum	7439-98-7	MO000330/31	99.9%	Annealed	10.22
Nickel	7440-02-0	NI000531/5	99.98%	Annealed	8.9
Titanium	7740-32-6	TI000385	99.99%	As rolled	4.5
Zinc	7440-66-6	ZN000270/3	>99.95%	As rolled	7.14
Brass	-	CU020270/8	Cu63/Zn37	Half hard	8.45
SS 304	-	FE220280/10	Fe/Cr18/Ni10	Annealed	8.0

A. Density at 20 °C.

3.3.2 Corrosion rate measurements

For the reasons discussed in section 3.2.3, the immersion test (gravimetric method) was chosen to quantify the corrosion rates in this work. It consists of the measurement of the mass loss of a material of known dimensions when immersed in a corrosive media for a given amount of time. The weight of the specimen is measured before and after the exposure. The procedure is outlined in ASTM G 31, “Standard Guide For Laboratory Immersion Corrosion Testing Of Materials”¹⁴³. Standard ISO 11845:2020 “Corrosion of metals and alloys — General principles for corrosion testing ISO”¹⁴⁴ also provide some guidelines to evaluate the corrosion rate by immersion. In both standards, the corrosion products need to be removed from the surface to quantify the corrosion rates and provide references to the cleaning procedure (ASTM G1¹⁷⁰ and ISO 8407¹⁷¹), which are aimed to remove all corrosion products from test specimens with minimum removal of sound metal. Standard ISO 11845:2020¹⁴⁴ recommends that specimens should also be weighed before corrosion product removal, and the mass of the corrosion products obtained by difference, however, does not established any protocols for the washing to guarantee removal of the corrosion media without removing the corrosion products.

In this work, a variation of the standard method ASTM G 31 was performed in order to study the corrosion products and morphological characteristics of the surface metal post-exposure, with the purpose of maximizing the information that could be obtained from the immersion test. The modification is as follows:

Before removing the corrosion products from the specimens in accordance with ASTM G1¹⁷⁰ and ISO 8407¹⁷¹ standards, they were cleaned using solvents in which the corrosion products were expected to be insoluble, *e.g.* acetone, alcohol and water, and not be very reactive with the metal. The use of abrasive materials or ultrasounds were not used to minimize the loses of corrosion products from the metal surface. The cleaning was done by submerging the coupons in various solvents (acetone, alcohol and water) followed by rising. Those steps were repeated as required in order to remove the corrosive medium. Once the cleaning step completed, the samples were let to dry in a desiccator. The use of towels for drying was avoided as it may

introduce an error through contamination of the specimens with grease or lint and might remove corrosion products. The test specimens were handled with gloves, and plastic tweezers to avoid contamination of the surface after cleaning.

After the dried-corroded test specimens had been cleaned by the method described above, their masses were measured with an accuracy corresponding to that of the original mass measurements, as recommended in ISO 11845:2020¹⁴⁴. The mass of loose corrosion products that detached and fell from the metal surface into the weighing boat or paper, was taken into account to quantify the final mass of the metal coupon. The mass loss or gain during the test period and the aspect of the sample were used to classify the system according to the method presented in Section 3.4.

3.3.2.1 Gravimetric methods - Mass balance

The mass balances for the corrosion rate determination by gravimetric methods are given in the expressions below:

$$M_{ini} = M_{final} + M_{solution} + M_{losses} \quad (65)$$

$$M_{final} = M_{metal-final} + M_{CP} \quad (66)$$

$$\Delta m_{MCR} = M_{ini} - M_{final} \quad (67)$$

$$\Delta m_{CR} = M_{ini} - M_{metal-final} \quad (68)$$

Where: M_{ini} , is the initial mass of the tested material, M_{final} is the final mass of the cleaned and dried tested material after the immersion test with the procedure described in this method, which includes the remaining metal ($M_{metal-final}$) and any corrosion products deposited on the surface (M_{cp}). $M_{solution}$ is the metal content in the solution which can be calculated from the total amount of solvent multiplied by the metal concentration, which can be determined by several analytical techniques, such as Inductively Coupled Plasma Mass Spectrometry (ICP-MS), Inductively Coupled Plasma Optical Emission Spectrometry (ICP-OES) or Ion Chromatography (IC). M_{losses} correspond to the metal present in crystals that did not grow in the surface of the metal, or in the corrosion products that fell during the immersion test or the washing steps, and the metal that might be adsorbed into the surface of containers and equipment where the corrosion experiment took place.

The mass change for the calculation of the Mass Change Rate (MCR), Δm_{MCR} , can be calculated by subtracting $M_{ini} - M_{final}$ (Eq. 67) and can be positive if the material is being dissolved in the medium at a higher rate than the corrosion products (if any) are depositing over the surface of

the metal or negative if the corrosion products are growing in significant quantities over the surface of the material. The mass change (Δm_{CR}) for the Corrosion Rate (CR) calculation according to ASTM G 31¹⁴³ and ISO 11845:2020¹⁴⁴ standard is calculated by subtracting M_{ini} - $M_{metal-final}$, for which further cleaning of the sample might be required to ideally selectively remove the corrosion (Eq. 68) products (M_{cp}) leaving the sound metal ($M_{metal-final}$). Eq. 68 should always lead to positive values of the CR as the mass change (Δm_{CR}) in standards ASTM G 31¹⁴³ and ISO 11845:2020¹⁴⁴, correspond to the cleaned sample after corrosion products have been removed and therefore it is expected to always be less than the original sample.

After the sample is weight containing the corrosion products, it can be categorised according to a method developed here (Section 3.4) and analysed. If the tests are non-destructive, the corrosion products could be mechanically removed by the methods described in ASTM G1¹⁷⁰ and ISO 8407¹⁷¹ standards, and the corrosion rates quantified as per ASTM G 31¹⁴³ and ISO 11845:2020¹⁴⁴ standard (Eq. 70).

3.3.2.2 Corrosion rate quantification

The Corrosion Rates (CRs) are generally expressed as a penetration rate [units of length/unit of time]. The Mass Change Rate (MCR) calculation proposed here is not expressed in such units as the presence of corrosion products might change the overall and/or local density of the material (Eq. 69). In some instances, the CR was expressed as a penetration rate only as a guide (Eq. 70). Differences in the MCR and CR could be used to estimate the formation kinetics of corrosion products on the surface of the material.

$$MCR = \frac{\Delta m_{MCR}}{A \cdot t} \quad (69)$$

$$CR = \frac{k \cdot \Delta m_{MCR}}{A \cdot t \cdot \rho} \quad (70)$$

Where Δm_{MCR} is the mass loss or gain [mg] by the metal in time t [d]. ρ is the density of the material (in g/cm^3). k is a constant [8.76×10^4 so that CR is in mm/y]. A is the surface area of the exposed material [cm^2]. For a flat disk with a hole for support, A is calculated with Eq. 71:

$$A = \pi/8 (d_1 + d_2)^2 + \pi/2 (d_1 + d_2)h - \pi/2 d_3^2 + \pi d_3 h \quad (71)$$

Where d_1 and d_2 are the disk diameter measured in 2 orthogonal axes. d_3 is the diameter of the hole used to suspend the samples (drilled using a 0.8 mm mesh) and h the thickness of the sample.

It should be mentioned that Eqs. 69 and 70 considered the initial area (not accounting for roughness).

The uncertainties (σ), calculated with the uncertainty propagation rules, for the MCR ($\sigma\Delta MCR$) and surface area A (σA) are given in Eq. 72 and Eq. 73 respectively:

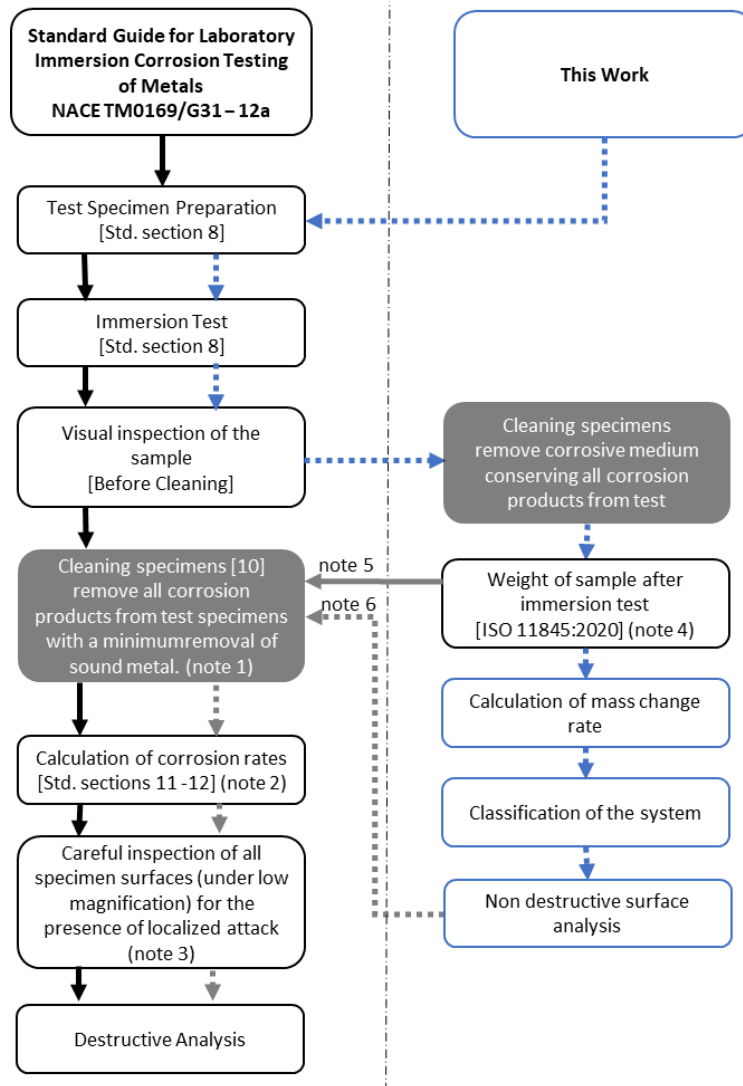
$$\sigma MCR = MCR \cdot \left(\frac{\sigma \Delta m_{MCR}}{\Delta m_{MCR}} + \frac{\sigma t}{t} + \frac{\sigma A}{A} \right) \quad (72)$$

$$\sigma A = \left| \frac{1}{2} \pi (d_1 + d_2 + 2h) \right| \cdot \sigma d_1 + \left| \pi (h - d_3) \right| \cdot \sigma d_3 + \left| \frac{1}{2} \pi (d_1 + d_2 + 2d_3) \right| \cdot \sigma h \quad (73)$$

Where:

- $\sigma\Delta MCR$: Technically should be twice the resolution of the balance used (0.02 mg). However, due to errors in the weighing process, the error was estimated as 0.05 mg.
- σt has been estimated to be 10s.
- σd_1 , is the resolution of the micrometre used to measure the disk (0.001 mm) and is equal to σd_2 .
- σd_3 , the uncertainty of the hole diameter, is estimated to be 0.2 mm.
- σh is 0.0125 mm according to the vendor data, the thickness of the disks is 0.125 mm with a max error of 10%.

Figure 27 shows the methodology used in this work.



Note 1. ASTM Practice G1 and ISO 8407

Note 2. If the variance between samples exceeds 10%, the causes of the reason for the disparity should be investigated and reported. If the reason for the disparity cannot be found, retesting should be considered.

Note 3. If pits are observed, they should be evaluated following the guidance of ASTM Guide G46.

Note 4. Standard ISO 11845 : 2020 recommends that specimens should also be weighed before corrosion product removal and the mass of the corrosion products obtained by difference.

Note 5. The path indicated in ISO 11845:2020

Note 6. Proposed path to continue the determination of the corrosion rates as per current standards.

Figure 27. Main steps to quantify the corrosion rates.

The metal substrates were prepared at room temperature by washing with demineralized water, industrial methylated spirits, and acetone, after which, the samples were dried for 45 min at 105 °C and then cooled in a desiccator for 30 min. Each metal coupon was immersed in the prepared solution and suspended by a fluorocarbon filament. The metallic surface area to liquid volume ratio was 0.2 mL mm² (NACE TM0169/G31 – 12a)¹⁴³.

The high-temperature experiments at 120 °C containing water were carried out inside custom-built aluminium / Polyether-ether-ketone (PEEK) containers. They were designed to withstand any pressure build-up due to water evaporation. To avoid solvent contaminations, the

containers were equipped with a Polytetrafluoroethylene (PTFE) liner and a PEEK rod used to hold the metal foils. The dry experiments at 120 °C were done in open containers in a vacuum oven (Binder VLD-53) with no further change in the water content. To ensure isothermal conditions for experiments at 70 °C and 120 °C (aqueous solutions), the metal foils and the solutions were preheated separately for 1 h and 2 h respectively (Thermo Scientific Heratherm).

High-temperature experiments in $[C_4C_1im][NTf_2]$ were performed at 150 °C. The metal coupons were attached to PTFE lids by a fluorocarbon filament, preheated, immersed in the IL contained in a beaker and placed in a vacuum oven (Binder VLD-53) for the duration of the experiment. Schematics of the containers used in the corrosion experiments are shown in Figure 28.

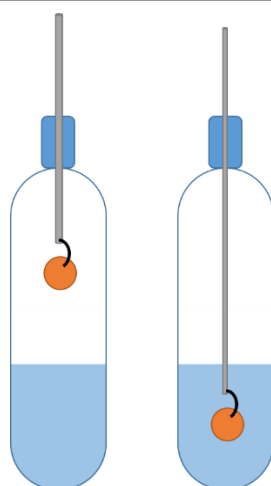


Figure 28. Schematics of containers used for the corrosion immersion test. . Left: during pre-heating. Right: during corrosion test.

To cope with differences in the oxidation rates of the different metals tested, the exposure times were adjusted according to the propensity of a specific metal to corrode and the severity of the experimental conditions. Conditions were selected to achieve a measurable mass change rate whilst avoiding the complete oxidation of the foils, *i.e.* longer exposure times at low temperatures and shorter exposure times with increased temperatures. At the conclusion of the experiments, the samples were removed from the solvent and quenched in demineralized water. The metal substrates were then washed, as previously described. A suite of *ex-situ* analyses were undertaken.

For each experimental condition and metal, two coupons were exposed at different times, then the mass change per surface area [mg/cm^2] was plotted against time and the corrosion rates [mg/cm^2d] were determined as the average of the two measurements.

3.3.3 Analytical techniques

It has been established that surface features of materials, such as texture and surface energy, along with defects dislocation related to their mechanical processing, impact the corrosion behaviour, and therefore it is helpful to characterise the surface of materials in order to gain a better understanding of the corrosion processes ¹⁴⁷. Further details on surface analysis methods are given in Appendix 4.

3.3.3.1 Scanning Electron Microscopy (SEM)

Surface morphology was analysed with a high-resolution field emission gun scanning electron microscope (FEGSEM) (LEO Gemini 1525 FEGSEM) coupled with an Oxford Instruments INCA energy dispersive and a wavelength dispersive x-ray spectrometer for EDX analysis. The acceleration voltage was taken for 5 kV for imaging only and 20kV when EDX was performed.

3.3.3.2 XRD

X-ray powder diffraction (XRD) was used for phase identification of the corrosion products (crystalline material) formed over the surface of the metal. Crystalline materials have a unique X-ray diffraction pattern that can be compared with a database for compound identification. The analysed samples, cleaned metal coupons, corroded or not, were mounted in the instrument without removing the corrosion products over the surface. The XRD spectra were obtained at room temperature with a PANanalytical X'Pert-PRO instrument using CuK α radiations. The scanning range for the sample was 2θ from 5° to 110°, step size $2\theta = 0.033$, Scan Step Time = 44.5 s, 40 kV and 20 mA. The instrument was regularly calibrated using certified Si disks. The reported accuracy of the instruments is $\pm 0.0025^\circ$ with an angular reproducibility $< 0.0002^\circ$. Spectra were analysed using HighScore suite - PANalytical's commercial powder diffraction analysis software

3.3.3.3 XRF

X-ray fluorescence (XRF) was used to analyse the elemental composition of metals and ILs. This technique is based on the measurement of the emission of characteristic "secondary" (or fluorescent) X-rays from a material that has been excited by being bombarded with high-energy X-rays. XRF analysis was carried out with a PANalytical's Epsilon 3XLE benchtop spectrometer equipped with a silver anode X-ray tube. The measurements were performed at room temperature and the instrument was flushed with He. Disposable XRF sample cups were used to analyse the metal coupons or liquids (5 g). The recorded spectra were analysed using

the Omnian software with the general Omnian method to calculate the elemental composition. The instrument is able to detect elements with atomic numbers higher than fluorine (Z=9) with a detection limit of the instrument is 1 ppm wt.

3.3.3.4 *Thermal Gravimetric Analysis (TGA)*

The thermal gravimetric analysis for the calcination of corrosion products was performed in a (TGA Q500 V20.13 Build 39) instrument, with platinum pans, and nitrogen as balance gas (40.0 ml/min) and sample gas (60.0 ml/min). The method was as follow:

- 1: Equilibrate at 30.00 °C
- 2: Ramp 5.00 °C/min to 650.00 °C
- 3: Isothermal for 1.00 min
- 4: Data storage Off
- 5: Jump to 30.00 °C
- 6: Isothermal for 20.00 min

3.4 **Semiquantitative-categorization system for the corrosion behaviour of metals based on immersion tests**

In this work, the corrosion behaviour of metals exposed to corrosive media has been classified into different types. Once the sample has been cleaned, the MRC calculated, and the metal sample visually inspected, the flow diagram (Figure 29) was used as a classification tool.

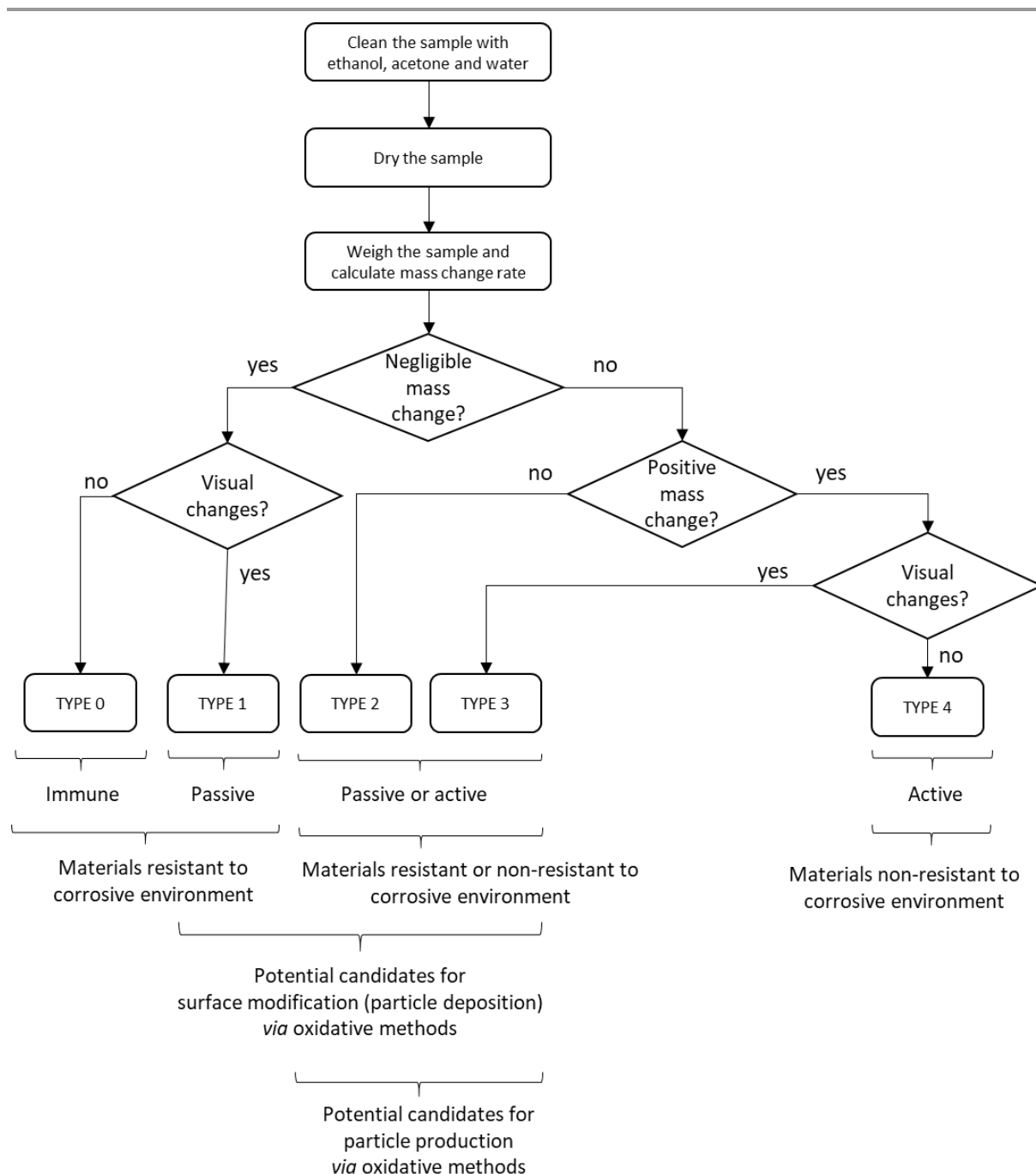


Figure 29. Flow diagram to classify the corrosion behaviour after the immersion test.

Immune metals: Immune metals (type-0) do not react with the corrosive medium. Metals within this category are the ideal materials of construction from a corrosion perspective.

Passive metals: The passive state is characterized by a contiguous “passivating film“ of solid corrosion products separating the metallic phase from the adjacent corrosive medium. Corrosion in the passive state involves the growth of the passivating film and/or transfer of metal ions through the film into the corrosive medium ¹⁷². A metal is passive if it substantially resists corrosion in a given environment despite a marked thermodynamic tendency to react

¹⁴⁹. A passive metal is one that is active in the EMF Series (Table 7), but that corrodes nevertheless at a very low rate ¹⁴⁹. Metals within this category forming thin films are classified as type-1 and those forming thick films as type-2S or type-3S. Passive metals might be used as construction materials under certain conditions.

Active metals: Corrosion in the active state occurs by direct transfer (which may involve one or several steps) of metal ions from the metallic phase to the adjacent corrosive medium ¹⁷². As the categorization method is based on gravimetric measurements without insights in the electrochemical phenomena and mechanisms taking place, an active metal in this context means the metal is either being transformed into corrosion products which do not form passive layers that can protect the material from corrosion (type-2 and type-3) or actively dissolving into the corrosive medium (type-4). Materials within this category are not suitable as materials of construction.

Figure 30 shows hypothetical curves for the mass change as a function of time for each corrosion-behaviour-classification type.

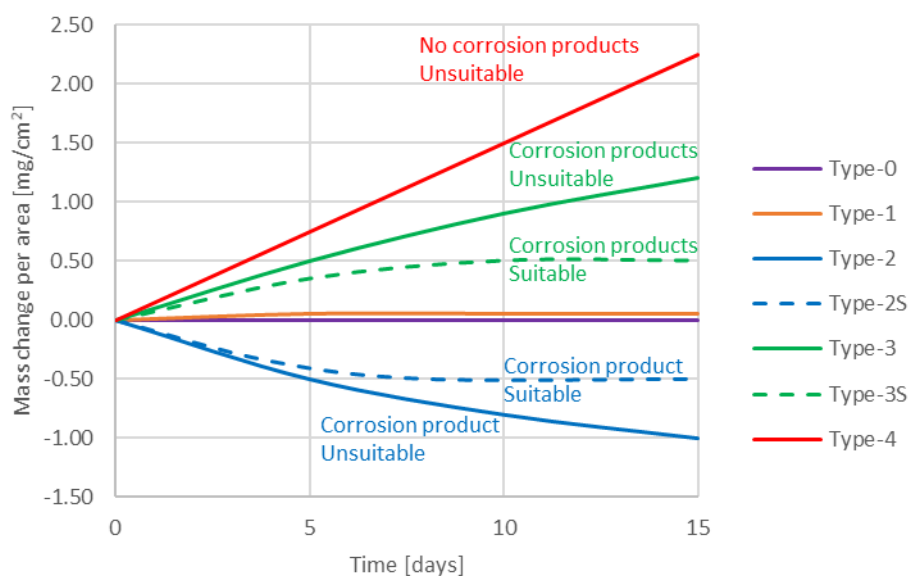


Figure 30. Hypothetical curves for the mass change as a function of time for each corrosion-behaviour-classification type.

3.4.1.1 Negligible mass changes

The magnitude of the corrosion rate is extremely small and close to the precision of the quantification method, *i.e.* precision of the balance and area determination, therefore it cannot be determined accurately. CMR data present considerable scatter, originating for errors in the weighting step. The magnitude of the mass change rate leads to $CR < 0.05$ mm/y. If the

exposure times were short, retesting a sample at longer exposure time could be used to confirm this behaviour.

3.4.1.2 Passivation

Passivation, in this context, refers to a material becoming less corroded by the corrosion environment at increasing exposure times. Passivation involves the creation of a stable outer layer of shield material, created by spontaneous chemical reaction with the material and the corrosion environment. Certain materials, such as lead exposed to sulfuric acid corrodes at an extremely high rate at first, while building this protective film; then the rate decreases considerably so that further corrosion is negligible¹⁴³.

3.4.1.3 Visual changes

Visual changes correspond to variations in the aspect of the sample before and after the immersion test. This corresponds to changes in colours or formation of corrosion products deposited on the surface of the metals and that remain attached after the cleaning process. If corrosion products are observed on the reaction medium but not on the surface of the metal, or if they are removed easily during the cleaning step, it can be considered that there are no changes. In some instances, if raw surfaces are used without any prior cleaning before the immersion test, the metals may look shining after the exposure to the corrosive medium. This can be due to the dissolution of an oxide layer, similar to a chemical cleaning, for the purpose of the classification system, in this case, it can be considered that there are no visual changes. Morphology changes on the surface detected at high magnifications do not account for the criteria of visual changes.

3.4.1.4 Categories

This section makes discussed the implications for each category.

3.4.1.4.1 TYPE 0

This represents the ideal case for which a material is not affected by its environment. Materials in this category exhibit negligible mass change rate during the immersion test method. An exposed piece cannot be distinguished from an untreated piece by visual inspection. Typically, samples under this category are also undisguisable between untreated samples by more detailed surface analysis such as SEM, XRF or EDX.

For metals type-0, mechanical cleaning is not required and the MCR and the CR should be identical. The metal content in solution and well as the metal losses are negligible and most likely below detection limits of common instrumental analysis.

It is likely that these systems will not be affected by the area:solvent ratio, and therefore, lesser quantities than the ones recommended in ASTM G 31 ¹⁴³ and ISO 11845:2020 ¹⁴⁴ standards, especially if the solvents are difficult to synthesized or expensive.

3.4.1.4.2 TYPE 1

As per materials type-0, metals in this category exhibit a very small mass change rate to be accurately quantified by the immersion test method, however, there are obvious changes in the appearance of the metal, *e.g.* colour changes.

Materials under this category form rapidly stable passive layers that protect the material from the further attack. As the layers form are very thin, overall mass changes are minor, and typically, samples under this category are also undisguisable between untreated samples by more detailed surface analysis such as SEM, XRF or EDX. Other techniques for thin-film analysis are needed to study the nature of the corrosion products, such as XPS.

For type-1 materials, it is expected that the CR is slightly higher than the MCR due to the removal of the layer during the cleaning process. The metal content in solution and well as the metal losses are negligible and most likely below detection limits of common instrumental analysis.

As per type-0 metals, it is likely that these systems will not be affected by the area:solvent ratio, and therefore, lesser quantities than the ones recommended in ASTM G 31 ¹⁴³ and ISO 11845:2020 ¹⁴⁴ standards, especially if the solvents are difficult to synthesized or expensive.

3.4.1.4.3 TYPE 2

Materials in this category exhibit active anodic reactions with the corrosive medium leading to the formation of corrosion products layers that results in a net mass gain. In these systems, the corrosion products exhibit very low solubilities in the corrosion medium and their crystals grow firmly on the surface of the metal. In these systems, system passivation is possible (type-2S) (see suitable materials, section 3.4.1.4.6). If the layers formed do not offer sufficient protection, the attack will continue until the material is destroyed. Typically, changes are detected by SEM, XRD, EDX or XRF (depending on the nature of the products).

The use of type-2 materials as construction materials is not recommended unless the material forms a stable passive layer (type-2S) (see suitable materials, section 3.4.1.4.6). Mechanical cleaning is required for CR quantification; with $CR > MCR$, due to the presence of deposition products. As per materials type-3, the metal concentration in the corrosion medium will depend on the solubility of the corrosion products in the solvent and the rate of formation of corrosion products. The solvents in these systems might reach saturation or not, depending on the amount of material used. M_{losses} can be significant as crystal might grow in the bulk solution (or other places) and/or can detach during the immersion test or cleaning step.

As the corrosion phenomenon takes place at the interphase between the material and the medium, it is expected that the presence of corrosion products which are being deposited on the surface will modify the effective area and therefore measurements of MCR and CR for this kind of materials will be less accurate.

3.4.1.4.4 TYPE 3

Similar to type-2 materials, metals in this category exhibit active anodic dissolution in the corrosive medium with the formation of corrosion products on the surface, but samples experience a net mass loss. In these systems, passivation is possible (type-3S, section 3.4.1.4.6) If the layers formed do not offer sufficient protection, the attack will continue until the material is destroyed. In these systems however, the corrosion products exhibit low-partial solubilities in the corrosion medium and their crystal might nucleate and grow in the bulk solution as well as in the surface of the metal. Typically, changes are detected by SEM, XRD, EDX or XRF (depending on the nature of the products).

The use of type-3 materials as construction materials is not recommended unless the material forms a stable passive layer (type-3S) (see suitable materials, section 3.4.1.4.6). Mechanical cleaning is required for CR quantification; with $CR > MCR$, due to the presence of deposition products. The metal concentration in the corrosion medium will depend on the solubility of the corrosion products in the solvent and the rate of formation of corrosion products. The solvents in these systems might reach saturation or not, depending on the amount of material used. M_{losses} can be significant as crystal might grow in the bulk solution or other places or can detach during the immersion test or cleaning step. Corrosion products are loosely adherent to the surface and do not form protective films.

As the corrosion phenomenon takes place at the interphase between the material and the medium, it is expected that the presence of corrosion products which are being deposited on

the surface will modify the effective area and therefore measurements of MCR and CR for this kind of materials will be less accurate.

3.4.1.4.5 TYPE 4

Materials in this category exhibit active anodic dissolution in the corrosive medium without the formation of corrosion products nor passive layers. In these systems, the corrosion products exhibit high solubilities in the corrosion medium. Typically, no changes are detected by XRD, EDX or XRF. However, in some instances, changes in the morphology of the surface could be detected by SEM.

The use of type-4 metals is to be avoided as construction materials. Mechanical cleaning for CR quantification is not required and the MCR and the CR should be identical as there are no corrosion products forming on the surface. The metal concentration in the corrosion medium is significant. The material mass change should be identical to the metal content in the solution if corrosion products are not growing on the bulk solution nor being adsorbed by the wetted parts of the corrosion testing apparatus.

3.4.1.4.6 Suitable materials (S-suffix)

Materials in this category exhibit active anodic dissolution with the formation of stable protective layers which offer sufficient protection against corrosion (system passivation), and therefore, these materials might be suitable materials of construction. This behaviour is characterised by an initial mass gain (type-2S), or an initial mass loss (type-3S), followed by a steady-state condition.

3.4.1.5 Summary

Table 10 and Table 11 summarise the main features of the semiquantitative classification system for the corrosion behaviour of metals exposed to corrosive media.

Table 10. Summary of the qualitative categorization system

TYPE	MCR	MCR magnitude	Visual Changes	Passivation	Corrosion product formation (surface)	CR MCR relationship
0	Negligible	+ / -	No	n/a	No	CR = MCR
1	Negligible	+ / -	Yes	Yes	Yes	CR \geq MCR
2	Significant	-	Yes	Possible	Yes	CR > MCR
3	Significant	+	Yes	Possible	Yes	CR > MCR
4	Significant	+	No	No	No	CR = MCR

Table 11. Summary of the mass balance parameters.

TYPE	M_{final}	$M_{metal-final}$	M_{CP}	$M_{Solution}$	M_{Losses}
0	$\approx M_{ini}$	$\approx M_{ini}$	0	0	0
1	$\approx M_{ini}$	$\approx M_{ini}$	≈ 0	≈ 0	≈ 0
2	$> M_{ini}$	$< M_{ini}$	> 0	$> \text{ or } \approx 0$	$> \text{ or } \approx 0$
3	$< M_{ini}$	$< M_{ini}$	> 0	$> \text{ or } \approx 0$	$> \text{ or } \approx 0$
4	$< M_{ini}$	$< M_{ini}$	0	$> \text{ or } \approx 0$	$> \text{ or } \approx 0$

3.4.1.6 Classification method disambiguation

As pointed out in the ASTM G 31¹⁴³ standard and other references¹⁴⁷, corrosion processes are complex in nature and are affected by many variables. As the corrosion behaviour of materials exposed to a corrosive environment may be affected by the conditions of the experiments, it is important a detailed recording of meaningful factors and conditions for proper interpretation of the results. Such factors include heat transfer (differences in temperature between the metal and corrosive environment), motion of the fluid, formation of corrosion products, nature of the specimen (*e.g.* chemical composition, presence of weldings, metal sample preparation, cast and wrought alloys) and solution properties (*e.g.* composition, dissolved oxygen, concentration of impurities, temperature and pH value).

Impact of geometry: The shape of the test specimen might influence the conclusion regarding the type of behaviour. For example, the use of thin samples minimizes errors in the CR or MCR calculations due to the assumption of constant area. However, thin samples are difficult to measure and handle, and the attack can continue and destroy the material before stable passive layers are formed. If the formation of passivation layers (materials type-2S and type-3S) is suspected, samples with a significant thickness should be used.

Impact of exposure time: The duration the corrosion test might influence the category for a given system, therefore it should be always stated the length of the test. Materials could be classified in one way at short exposure times and in another at long exposure time. For example, short tests of a material exhibiting passivation could result in an initial high corrosion rate, which might be misleading. Also, at short exposure times, there might not be enough formation of corrosion products (due to slow kinetics) and the system could be classified in another category. It has been mentioned in the ASTM G 31¹⁴³ standard that tests run for long periods are considerably more realistic than those conducted for short durations. It was also pointed out, that corrosion should not proceed to the point where the original specimen size or the exposed area is drastically reduced or where the material is perforated.

The author believes that with the guidelines provided in this work, systems can be categorized in one type. However, some systems might exhibit borderline behaviours. If this situation arises, it can be mentioned that the tests are inclusive to categorise the system or mention the

suspected categories, along with the reasons why a single category could not be assigned. Retesting the specimen with other conditions, *e.g.* another geometry or longer exposure times might be helpful to provide the correct category.

3.5 Results and discussions

3.5.1 Analysis of ILs

The initial metal content in the ILs, shown in Table 12, were determined by XRF (Eq. 64). Commercial ILs contain traces of aluminium, silicon and tellurium. As [HC₁im]Cl is a very hygroscopic IL which is difficult to handle, the metal content was not determined.

Table 12. Elemental content on mass and dry basis for the ILs determined by XRF.

	[C ₄ C ₁ im][NTf ₂]	[C ₄ C ₁ im]Cl	[N ₄₁₁₀][HSO ₄]
Silicon [Si]	386 ± 2 ppm	594 ppm	565 ppm
Tin [Sn]	46 ± 3 ppm	39 ppm	194 ppm
Tellurium [Te]	43 ± 1 ppm	37.4 ppm	178 ppm
Sulfur [S]	15.29 ± 0.01%	119 ppm	16.09 %
Sodium [Na]	-	83 ppm	-
Aluminium [Al]	270 ± 10 ppm	324.6 ppm	-
Chlorine [Cl]	-	20.30%	-
Bromide [Br]	-	3.8 ppm	-
Neodymium [Nd]	-	4.2 ppm	-

For the IL-rich and water-rich case, the same batch was used for consistency. Water content determined by KF titration (section 2.3.3.1) is shown in Table 13.

Table 13. Water concentrations used in the corrosion studies.

Ionic Liquid	Residual Water Case	IL-Rich Case (low water content)	Water Rich-Case (high water content)
[C ₄ C ₁ im]Cl	0.42 ± 0.01 wt%	23.7 ± 0.1 wt%	82.4 ± 0.4 wt%
	3.95 ± 0.04 mol%	75.1 ± 0.3 mol%	97.8 ± 0.1 mol%
[HC ₁ im]Cl	n.d. ^B	31.2 ± 0.2 wt%	87.0 ± 0.5 wt%
		74.9 ± 0.5 mol%	97.8 ± 0.6 mol%
[N ₄₁₁₀][HSO ₄] ^A	0.1009 ± 0.0008 wt%		
	1.105 ± 0.008 mol%	21.5 ± 0.1 wt%	80.4 ± 0.6 wt%
	0.57 ± 0.06 wt%	75.2 ± 0.5 mol%	97.8 ± 0.7 mol%
	6.0 ± 0.6 mol%		
[C ₄ C ₁ im][NTf ₂]	230 ± 30 ppm wt.	N.A.	N.A.

A. Water content range for the residual water case.

B. Not determined (refer to text).

[N₄₁₁₀][HSO₄], [HC₁im]Cl, and [C₄C₁im]Cl are extremely hygroscopic. A study in which different synthesis methods for PIL were explored to minimize the presence of water in the ILs, showed that even if handled under inert atmospheres, the lowest water content was ~100 ppm wt. for the majority of PILs, almost an order of magnitude lower than produced by solvent removal *in*

*vacuo*¹⁷³. Due to the hygroscopic nature of the ILs and the large quantities needed to be dried for the corrosion testing, for [C₄C₁im]Cl a 0.42 wt% and for [N₄₁₁₀][HSO₄] a 0.1009 wt% were the minimum water content achieved.

[C₄C₁im]Cl and [HC₁im]Cl are not Room Temperature ILs (RTILs). There are several values reported in the literature for the melting point of [C₄C₁im]Cl, ranging from 41 to 70 °C, and 74.3 °C for [HC₁im]Cl¹⁷⁴. Once melted, [C₄C₁im]Cl formed metastable liquids if cooled to room temperature while [HC₁im]Cl crystallised. For this reason, the water content of the residual case could not be determined for [HC₁im]Cl nor corrosion testing at room temperature was done. Samples could not be dried in large quantities, and therefore there were variations in the water content, especially for [N₄₁₁₀][HSO₄], that turned yellowish (amine browning) upon prolonged drying in a Schlenk line. As [HC₁im]Cl and [C₄C₁im]Cl are solid at room temperature, they were melted and weighted while in the liquid phase and warm temperatures, to minimize water uptake.

3.5.2 Corrosion behaviour of metals exposed to [C₄C₁im][NTf₂]

The corrosion behaviour of metals exposed to [C₄C₁im][NTf₂] is presented and discussed in this section. [C₄C₁im][NTf₂] is a hydrophobic IL considered to be weakly coordinating. Therefore, the corrosion rates of metals exposed to this IL is not expected to be as high as for the PIL or AIL containing the chloride anion.

3.5.2.1 Corrosion rates

The corrosion rates of metals exposed to [C₄C₁im][NTf₂] was determined from one observation, unless otherwise stated, due to the high cost of this IL, as mentioned in section A1.1. Cu, Fe, Zn and brass were exposed at 70 °C to [C₄C₁im][NTf₂] for 16 days. More resistant metals Al, Mo, Ni, Ti and 304 SS were exposed at 70 °C for 28 days. A repeat was performed at 70 °C and longer exposure time for the system Cu, Zn and brass in which they were immersed in the IL for 162, 165 and 165 days respectively. The corrosion rates were also tested at high temperatures at 150 °C for 68 days. The corrosion rates at 70 °C are shown in Figure 31 and Figure 32, and at 150 °C in Figure 33.

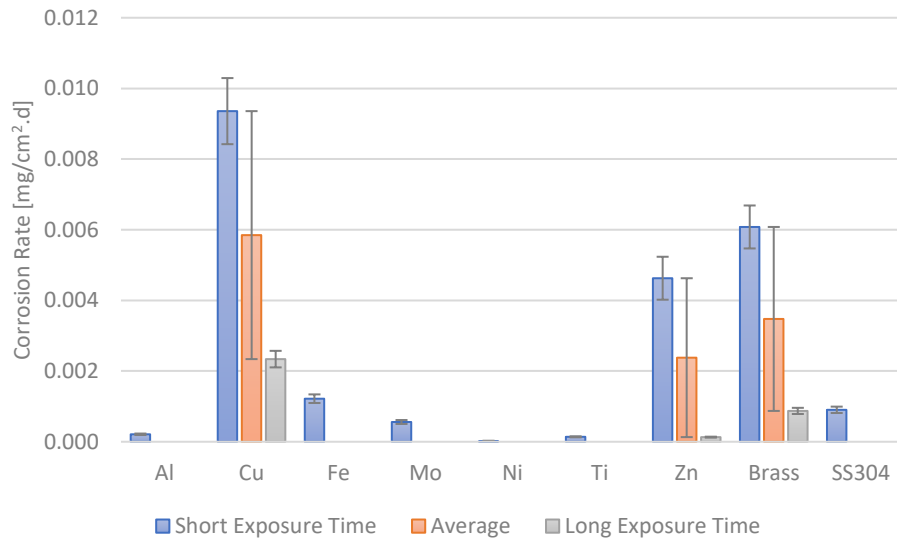


Figure 31. Mass change rates for metals exposed to $[C_4C_1im][NTf_2]$ at 70 °C. Short exposure time 16 d for Cu, Fe, Zn and brass and 28 d for Al, Mo, Ni, Ti and 304 SS. Long exposure time for Cu, Zn and brass 162, 165 and 165 days respectively.

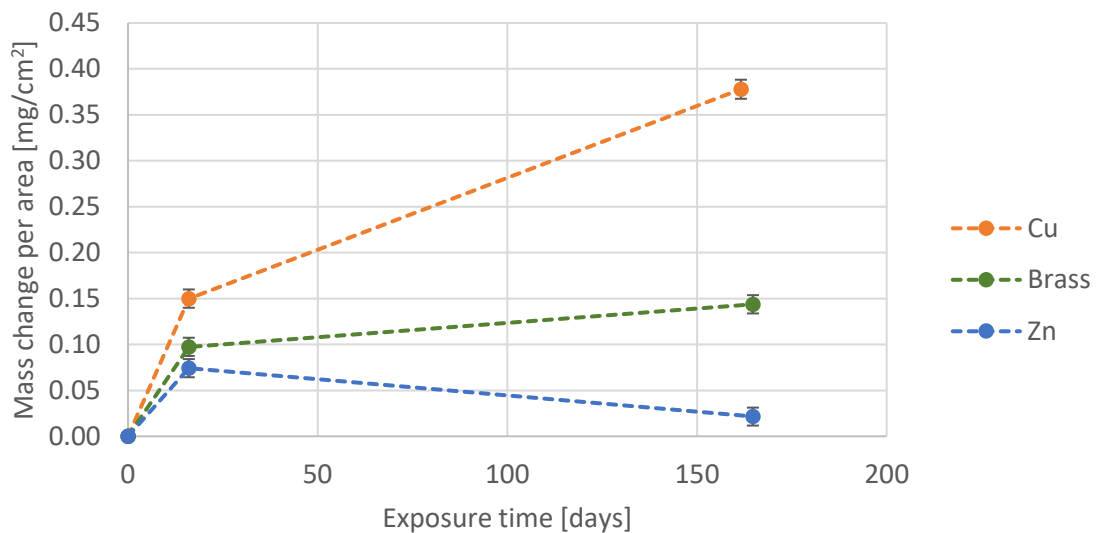


Figure 32. Mass change rates for Cu, Zn and brass exposed to $[C_4C_1im][NTf_2]$ at 70 °C. Lines have been added to guide the eye.

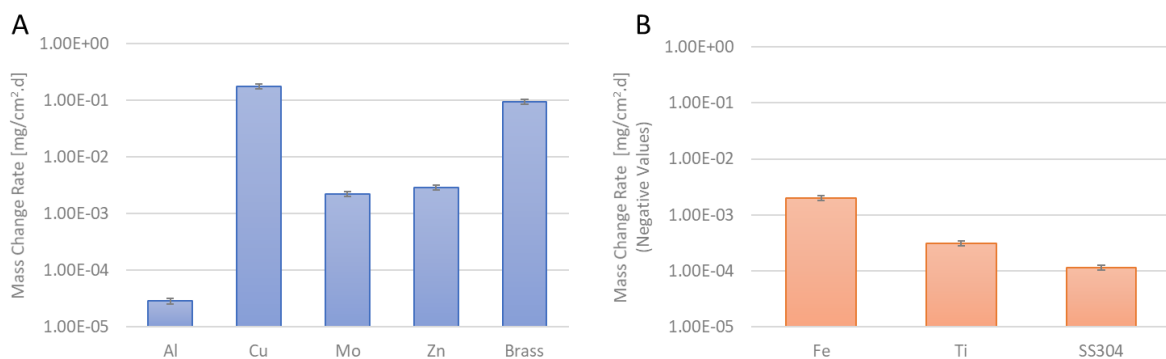


Figure 33. Mass change rates for metals exposed to $[C_4C_1im][NTf_2]$ at 150 °C for 68 days. [A] positive mass change. [B] Negative mass change.

At 70 °C, the most reactive metal is Cu, followed by brass and then Zn. The metals Fe, 304 SS and Mo had measurable MCR while it was extremely low for Al, Ni and Ti. When replicates were done, the MCR decreases at longer exposure time for Cu, Zn and Brass (Figure 31). Examining the mass change as a function of time (Figure 32A/B), the reduction in the apparent MCR for Cu and brass is due to a flattening on the curve. The reason for this behaviour might be explained by passivation of the surfaces, corrosion products deposition or a combination of both. For Zn however, there is a decreased in the MCR at a longer exposure time, which can only be explained by a corrosion product deposition.

When the metals are exposed at 150 °C (Figure 33), Cu and brass are again the most active metals followed by Zn. Fe, Ti and 304 SS experienced a negative MRC.

3.5.2.2 XRD

The XRD spectra for Cu, Zn and brass exposed to [C₄C₁im][NTf₂] are depicted in Figure 34. For Cu, there are no differences between the XRD pattern of the untreated metal and the metal exposed at 70 °C for 162 days, despite the formation of a green solid on the surface. When Cu was exposed for 68 days at 150 °C, a change in the relative intensity appeared but no new signals were detected, despite the formation of a green solid on the surface. Green residue from the surface was recovered but the XRD spectra did not show any signal (not shown here) suggesting that the material is not crystalline.

For Zn, no changes in the XRD were observed when exposed for 162 days at 70 °C or 68 days at 150 °C (Figure 34C/F). For brass, some foreign weak signals can be seen $2\theta < 40^\circ$ when exposed at 70 °C for 162 days (Figure 34B), which became significant when exposed for 68 days at 150 °C (Figure 34E). These signals were matched to ZnO (Zincite “Würtzite structure”, reference code 00-036-1451) using the HighScore suite (PANalytical’s commercial powder diffraction analysis software), however, a signal around $\sim 70^\circ$ could not be assigned.

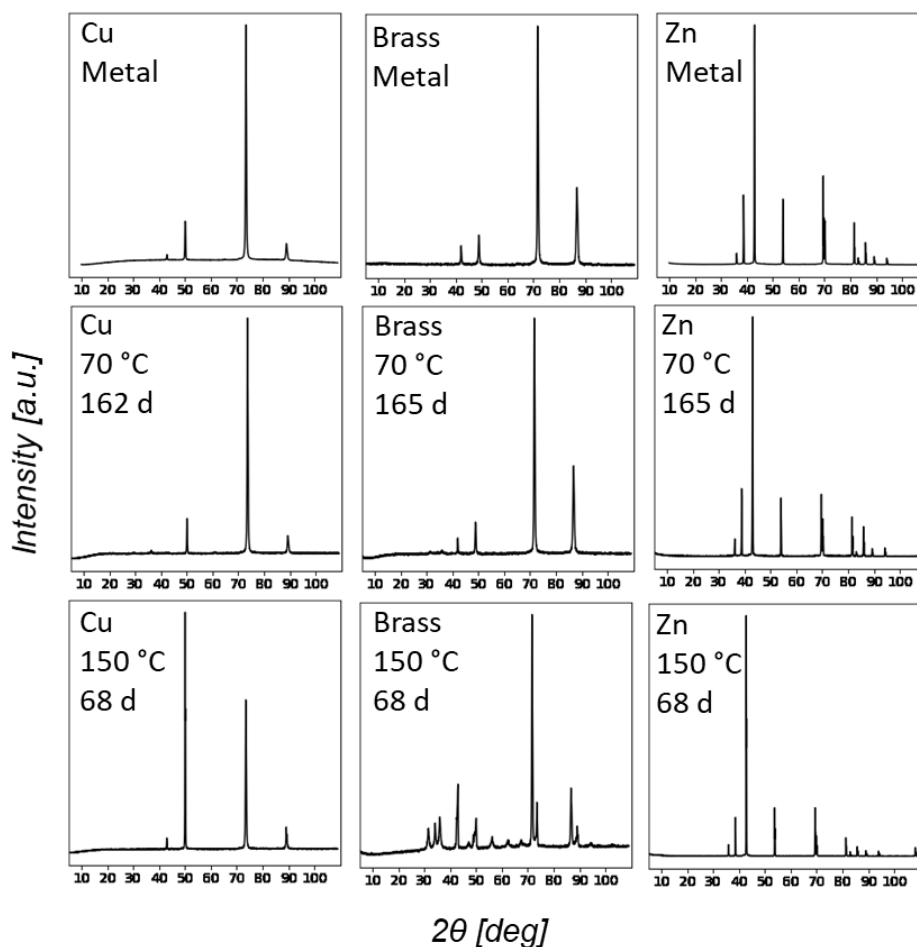


Figure 34. XRD patterns for Cu, brass and Zn exposed to $[C_4C_{1im}][NTf_2]$.

3.5.2.3 XRF

The XRF data summary for metals exposed to $[C_4C_{1im}][NTf_2]$ is given in Table 14. Cu and brass showed the presence of sulphur, as well as Fe when exposed at 150 °C.

Table 14. XRF results summary for metals exposed to $[C_4C_{1im}][NTf_2]$.

Metals	Comments
Al	No significant changes.
Cu	Sulphur detected (S=0.1-0.2%)
Fe	Some sulphur in the sample exposed at 150°C (S=0.768%)
Mo	No significant changes.
Ni	No significant changes.
Ti	No significant changes.
Zn	No significant changes.
Brass	Increased content of S.
304 SS	No significant changes.

The concentration of species in the IL after exposure experiments at 70 °C were calculated from the XRF data and Eq. 64 and given in Figure 35 for short exposure times and Figure 36 for long

exposure times. At a short exposure time, there are no significant variations in the IL composition except for the sample exposed to Cu, in which 18 ppm wt. of the metal can be detected. It should be noticed that the Sn signal present in the neat IL disappeared for the sample exposed to Mo. This phenomenon was observed in other situations and seems random in nature. When Cu, Zn and brass were exposed for longer times, the Si signal disappeared for the systems, while the Sn disappeared only from Cu and Zn. Zn was not detected in the IL exposed to the metal or brass. However, Cu was detected in the IL exposed to Cu and brass, and the metal content was estimated to 35 and 25 ppm respectively.

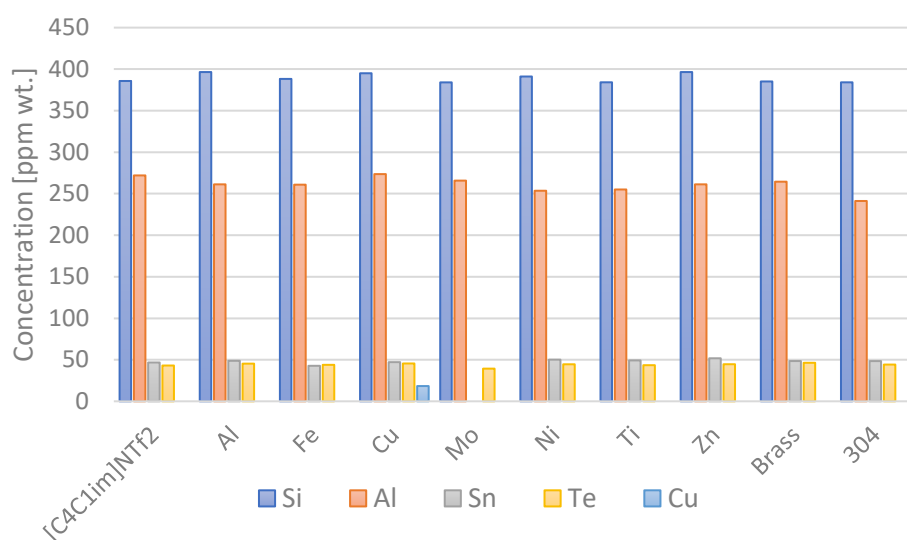


Figure 35. XRF measurements of $[C_4C_1im][NTf_2]$ after exposure experiments at 70 °C and short exposure times. Al, Mo, Ni, Ti, 304 SS 28 days and Cu, Fe, Z, brass 16 days. Error 1 ppm wt.

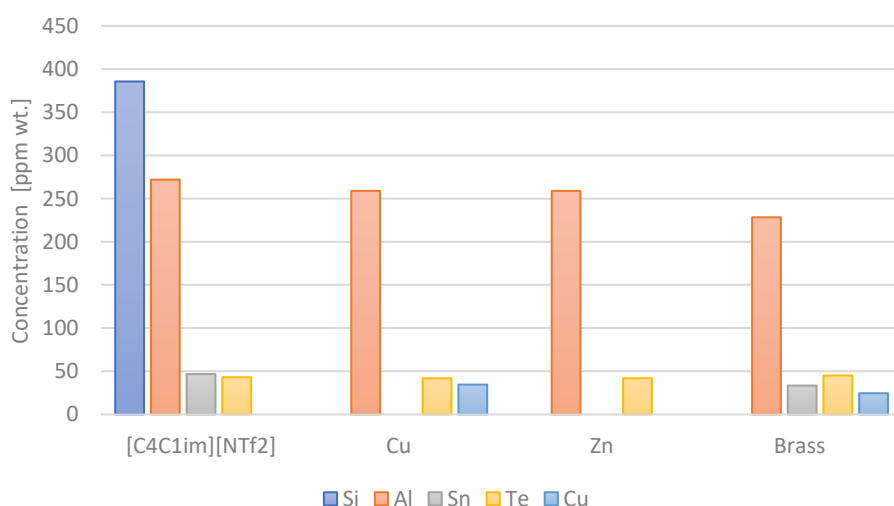


Figure 36. XRF measurements of $[C_4C_1im][NTf_2]$ after exposure experiments at 70 °C and long exposure times. Cu (162 days), Zn (165 days) and brass (165 days). Error 1 ppm wt.

The XRF measurements of $[C_4C_1im][NTf_2]$ after exposure experiments at 150 °C are given in Figure 37. In these experiments, the Si signals disappeared for all the metals except for Al and

304 SS, where traces could still be detected. The Sn signal was not detected in the IL in contact with Zn and 304 SS. Traces of Fe (0.4 ppm wt.), Zn (17 ppm wt.) and Mo (11 ppm wt.) were found in the IL where these metals were immersed. Cu was detected to a significant extent in the IL. The IL in contact with brass contained both Cu and Zn. When analysing the behaviour of Cu and Zn, it would be expected to find higher quantities of Cu than Zn in the IL exposed to brass, however, this is not the case, and the concentration of Zn (94 ppm wt.) is higher than Cu (75 ppm wt.). The reason why only traces of Zn were observed in the Zn sample might be due to the presence of the passive layers that is stable in the IL at 150 °C.

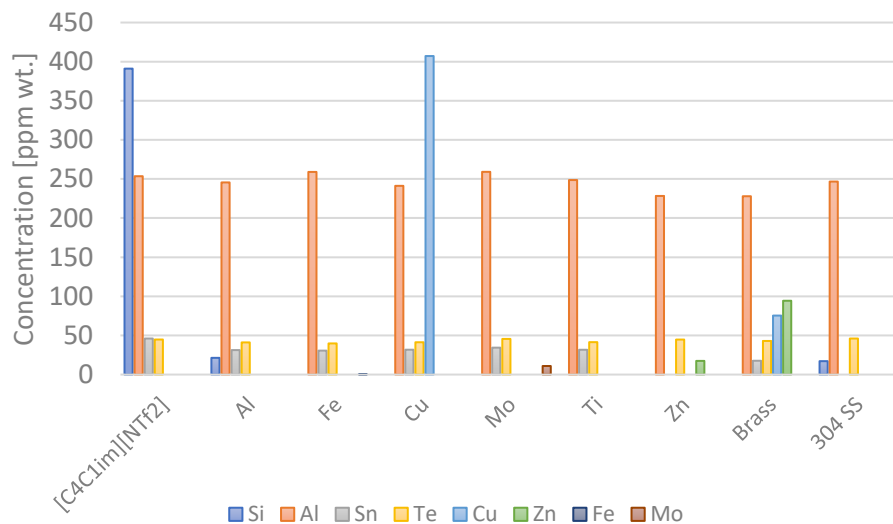


Figure 37. XRF measurements of [C₄C₁im][NTf₂] after exposure experiments at 150 °C (68 days). Error 1 ppm wt.

The corrosion rates were also calculated for the systems in which metal in solution could be detected by XRF (Cu and brass). It was found that the corrosion rates calculated from this method are higher than the MCR calculated by weight loss, ~2-4 times higher (Figure 38), suggesting deposition of corrosion material on the surface, which leads to underestimations of the true MCR.

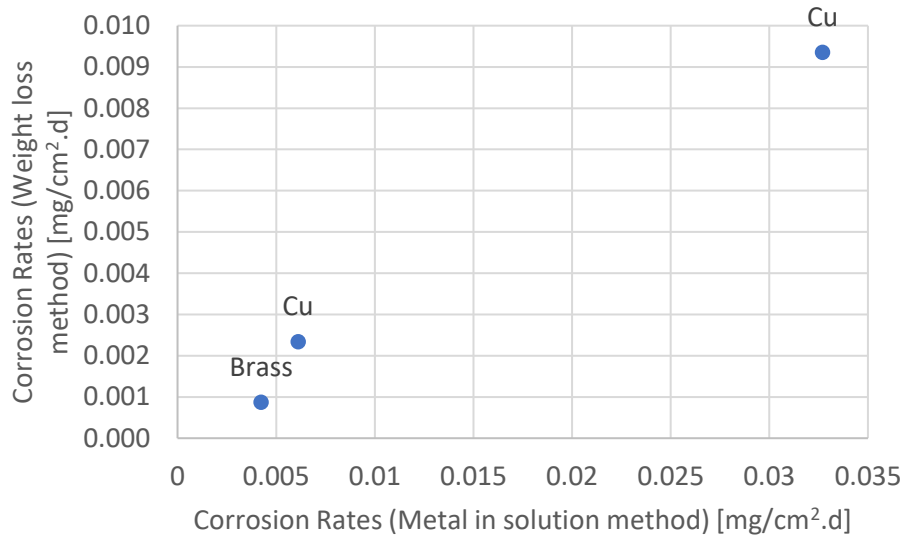


Figure 38. MCR calculated by weight loss and metal in solution methods.

3.5.2.4 SEM

The SEM/EDX images for selected system are shown in Figure 39 to Figure 41. Pure metals and water controls are given in Appendix 5.

The SEM/EDX images for Al, Fe and 304 SS exposed at 70 °C are given in Figure 39, Figure 40 and Figure 41 respectively, where no significant modifications are seen. Traces of oxygen were observed in Al and Fe, possibly from reaction with residual water present in the IL.

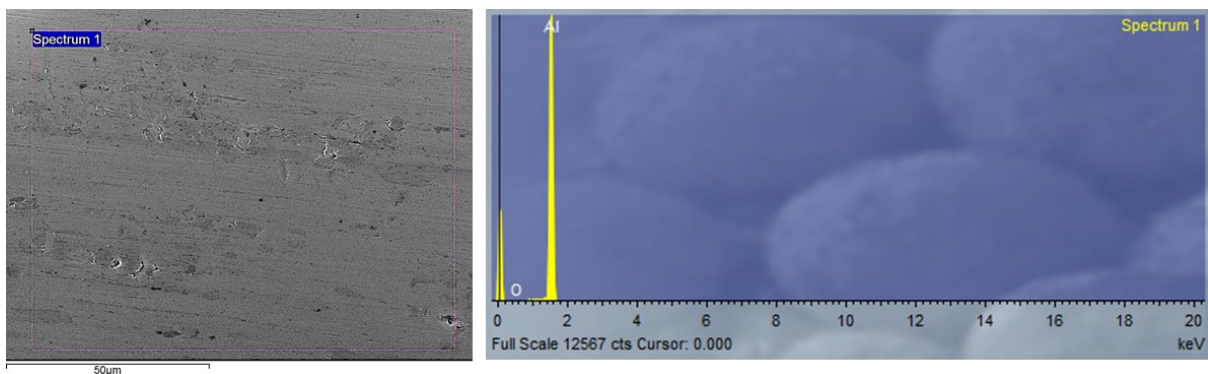


Figure 39. SEM/EDX of Al exposed to [C₄C₁im][NTf₂] (70 °C and 28 d). EDX Al:O atomic ratio 38.2:1.

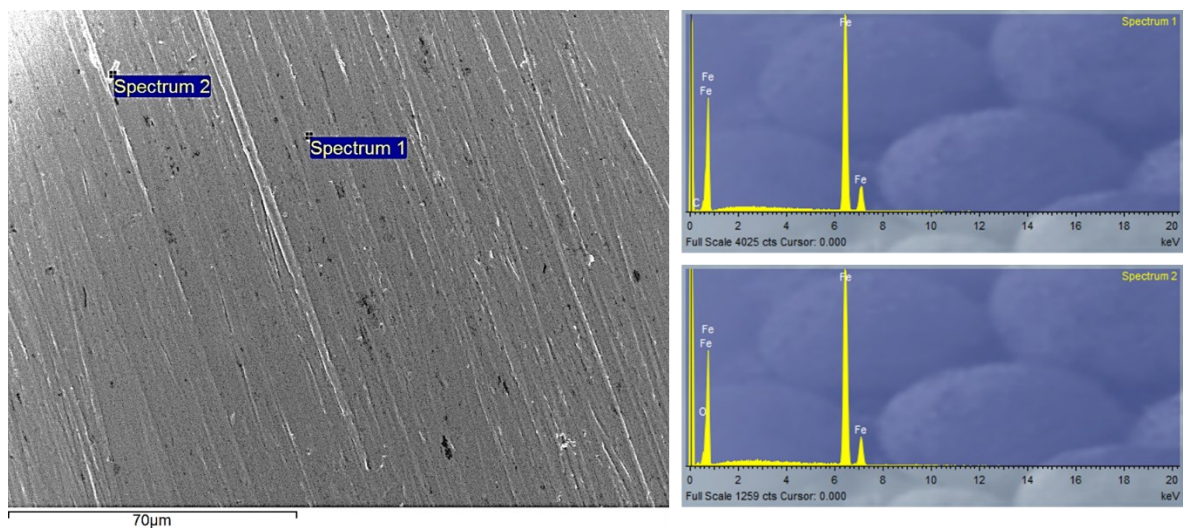


Figure 40. SEM/EDX of Fe exposed to $[C_4C_1im][NTf_2]$ (70 °C and 28 d). EDX Top figure. Fe:C atomic ratio 9:1. Bottom Figure. Fe:O atomic ratio 8.1:1.

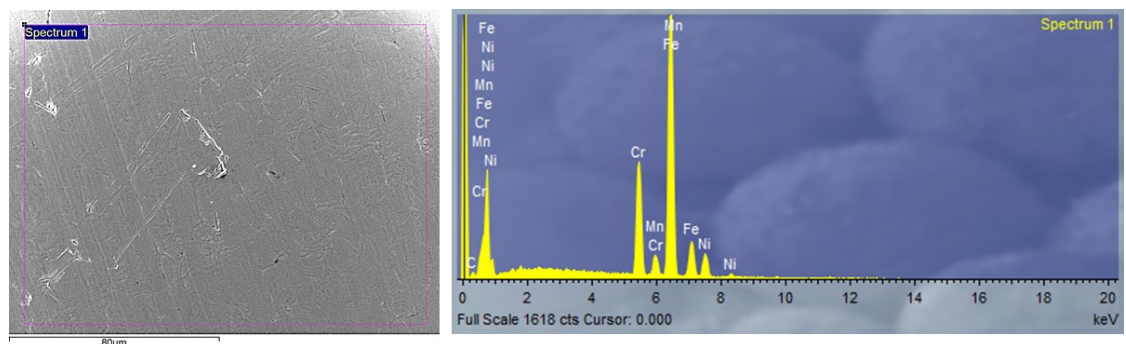


Figure 41. SEM/EDX of 304 SS exposed to $[C_4C_1im][NTf_2]$ (70 °C and 28 d). EDX Fr:Cr:Ni:Ma atomic ratio 35.6:10.1:4.6:1.

Cu SEM/EDX images are given in Figure 42 (70 °C and 16 d) and Figure 43 (150 °C and 68 d). There are no significant changes detected via SEM when the metal was exposed for (70 °C and 16 d), however, oxygen was detected in an atomic ratio $\sim 1:5$ O:Cu. When exposed at (150 °C and 68 d), large crystals were observed.

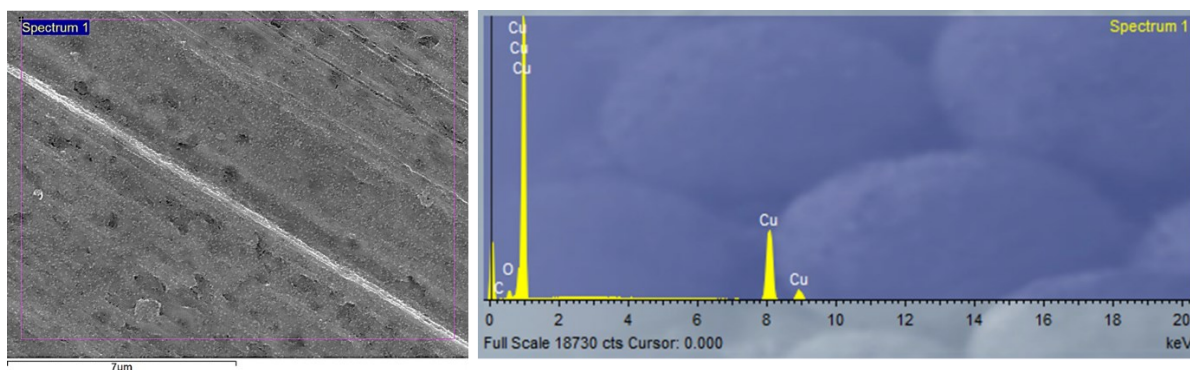


Figure 42. SEM/EDX of Cu exposed to $[C_4C_1im][NTf_2]$ (70 °C and 16 d). EDX Cu:O atomic ratio 4.8:1.

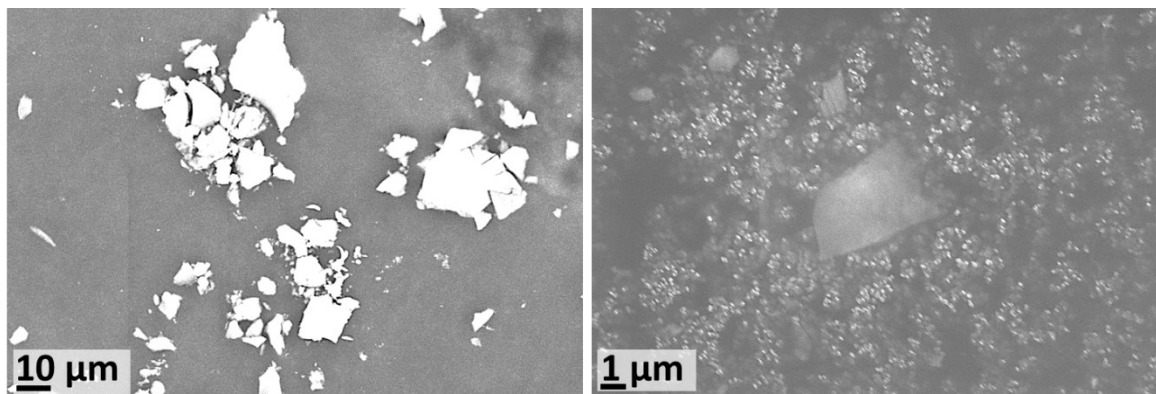


Figure 43. SEM of Cu exposed to $[C_4C_1im][NTf_2]$ (150 °C and 68 d).

The SEM/EDX images of Zn exposed to $[C_4C_1im][NTf_2]$ (150 °C and 68 d) are shown in Figure 44 and Figure 45. There was a change in the morphology of the Zn substrate, where oxygen was detected to a significant extent and traces of sulphur. Some areas (Figure 45) showed corrosion products containing N, F, S and O, elements found in the IL, which suggest the formation of $Zn(NTf_2)_2$ or other degradations products.

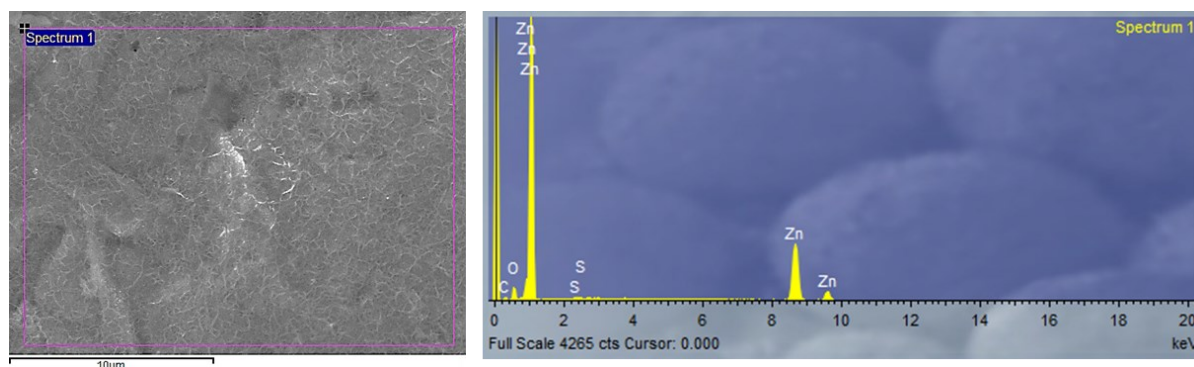


Figure 44. SEM/EDX of zinc exposed to $[C_4C_1im][NTf_2]$ (150 °C and 68 d). EDX Zn:O:S atomic ratio 121.9:41.8:1.

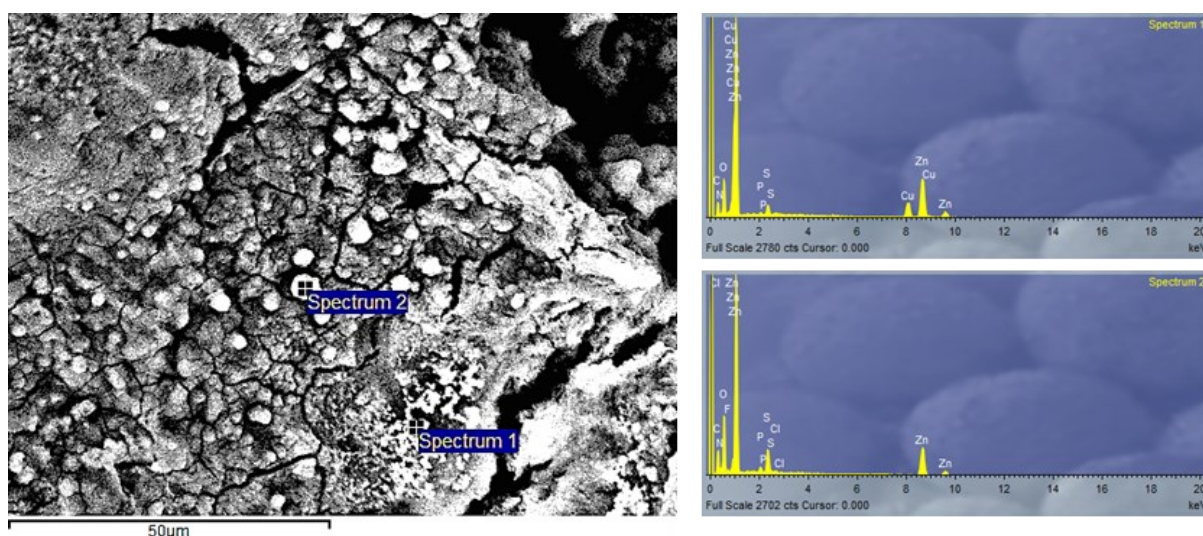


Figure 45. SEM/EDX of Zn exposed to $[C_4C_1im][NTf_2]$ (150 °C and 68 d). EDX: N:S:F:Zn:O atomic ratio 7.0:1:0:15.5:25.2 and 6.5:1:1.5:4.9:20.9 top and bottom spectra respectively.

The SEM/EDX images for brass exposed to $[C_4C_1im][NTf_2]$ are shown in Figure 46 to Figure 48. No significant changes are observed in the surface of brass when exposed at 70 °C for 16 d (Figure 46), except for the presence of traces of oxygen. Powder from the surface of the sample exposed to the IL at 150 °C for 68 days was recovered and analysed with SEM/EDX. Surprisingly, in Figure 47 it can be seen particles composed of metallic Zn with oxygen. Figure 48 shows another set of structures, for which the EDX revealed the presence of elements found in the anion of the IL. The particles showed in Figure 48 (top) contained significant amounts of Cu while those in Figure 48 (bottom) only contained traces of this metal.

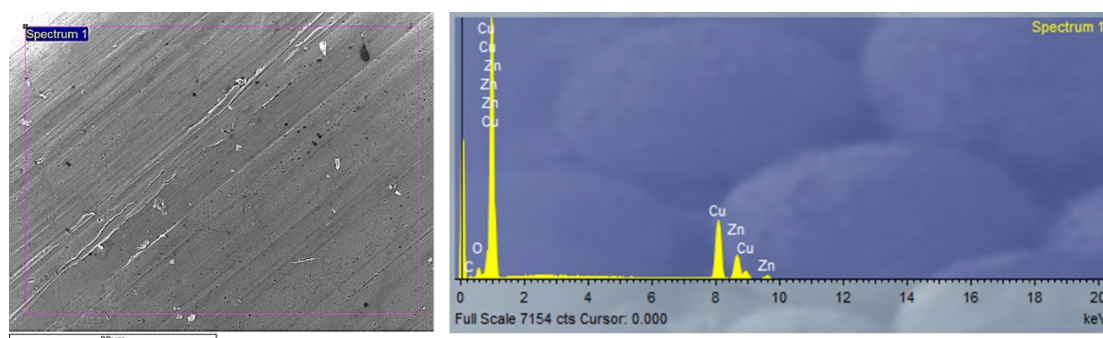


Figure 46. SEM/EDX of brass exposed to $[C_4C_1im][NTf_2]$ (70 °C and 16 d). EDX Cu:Zn:O atomic ratio 3.1:1.5:1.

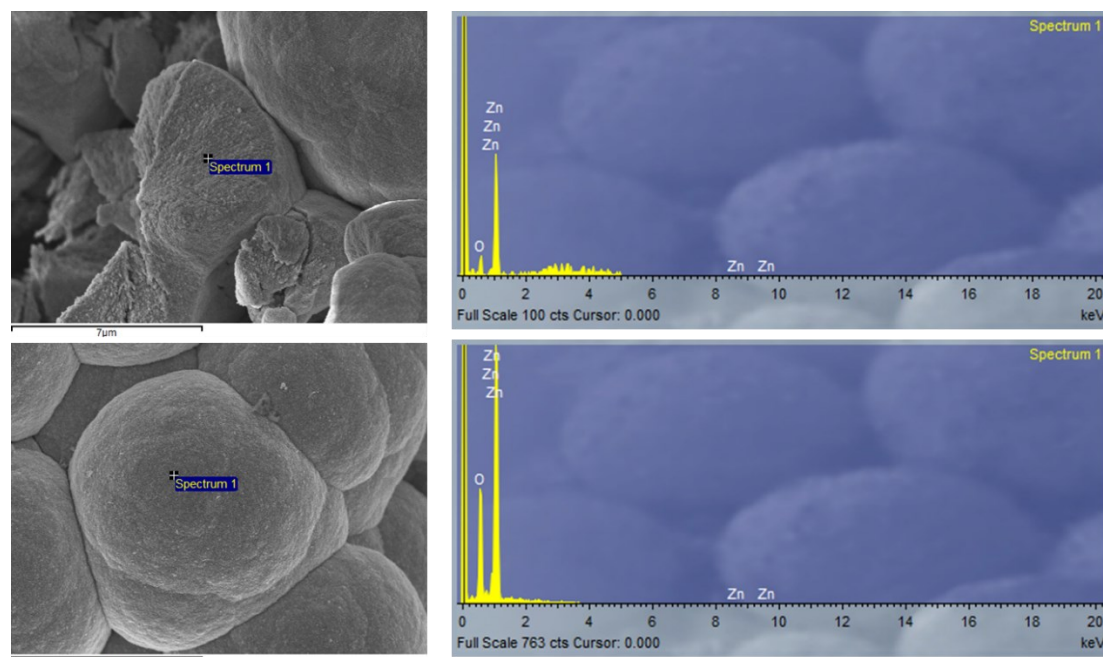


Figure 47. SEM/EDX of powder recovered from brass exposed to $[C_4C_1im][NTf_2]$ (150 °C and 68 d). EDX Zn:O atomic ratio 2.3:1 and 1:1.1 top and bottom spectra, respectively.

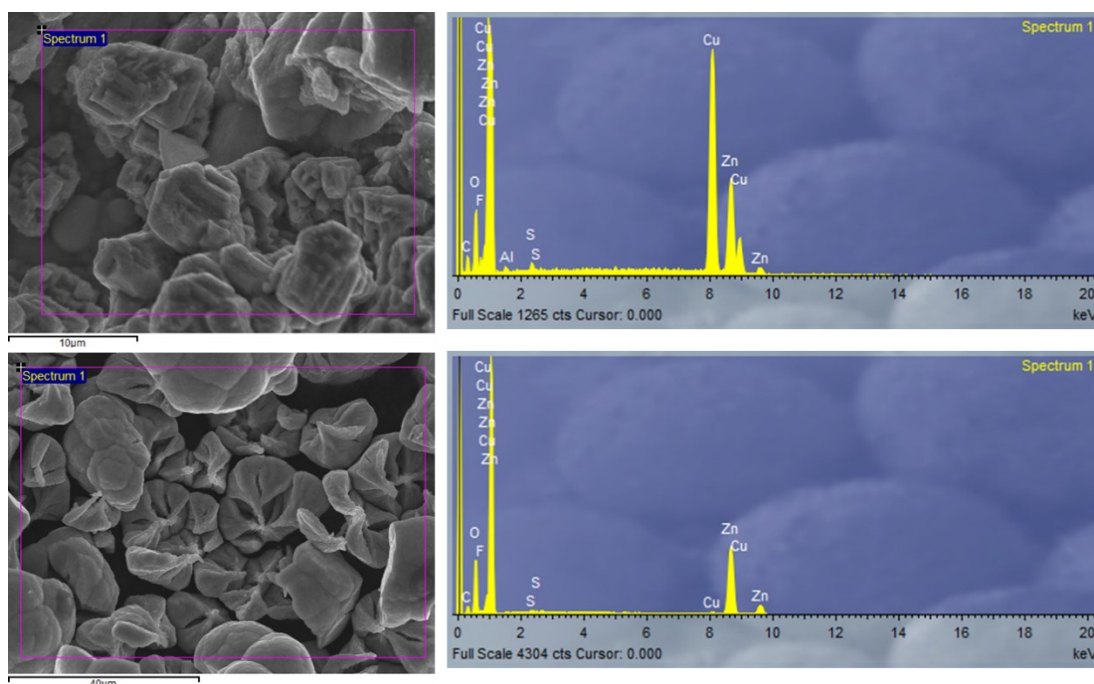


Figure 48. SEM/EDX of powder recovered from brass exposed to $[C_4C_{1im}][NTf_2]$ (150 °C and 68 d). EDX Cu:Zn:O:F:S atomic ratio 76.5:34.7:37.9:5.9:1 top spectrum. EDX Zn:O:F:S atomic ratio 122.9:145.7:6.0:1 bottom spectrum.

3.5.2.5 Overall considerations

ILs containing the bis(trifluoromethylsulphonyl) imide anion ($[NTf_2]^-$) are vastly used in scientific research. $[C_4C_{1im}][NTf_2]$ is hydrophobic, the water content determined by KF titration was 230 ± 30 ppm wt. In this system, it is not clear what the cathodic reaction is, as species that can be reduced, such as water and oxygen are not present to a significant extent. However, the corrosion of metals in this medium is clearly happening with quantifiable CRs (section 3.5.2.1). Aluminium was found in the neat IL with an unknown oxidation state. If present as Al^{3+} , it could be reduced to Al^0 with the corresponding oxidation of a metal. However, it can be seen from the EMF series (presented in Table 7) that Al has the lowest reduction potential at standard conditions, thus it is not expected that trivalent aluminium would be a strong oxidizing agent.

A colour change in the IL after the immersion test at 150 °C can be seen for Cu, brass and Fe (Figure 49). Cu formed a dark green solution; brass formed a light green solution and iron a dark orange solution. The presence of Cu in the IL exposed to Cu and brass confirms that the green colour is due to the presence of Cu complexes with the $[NTf_2]^-$ anion; as reported in an electrochemical study of $Cu[NTf_2]_2$ dissolved in $[C_2C_{1im}][NTf_2]$ ¹⁷⁵. It is unclear if the origin of the dark colour in the IL exposed to Fe is due to IL degradation or trace amounts of Fe complexes below the detection limit of the XRF instrument used. For the other metals, no colour change was perceived.

Cu and brass experienced the highest attack in this IL, an interesting result given that Cu is the only metal with a positive standard reduction potential (Table 7). This makes this metal, and its alloys, resistant to acids yet, they are prone to corrosion in $[C_4C_1im][NTf_2]$ considered as an “inert” IL. This result shows that the corrosion behaviour in aqueous solutions cannot always be extrapolated to ILs.

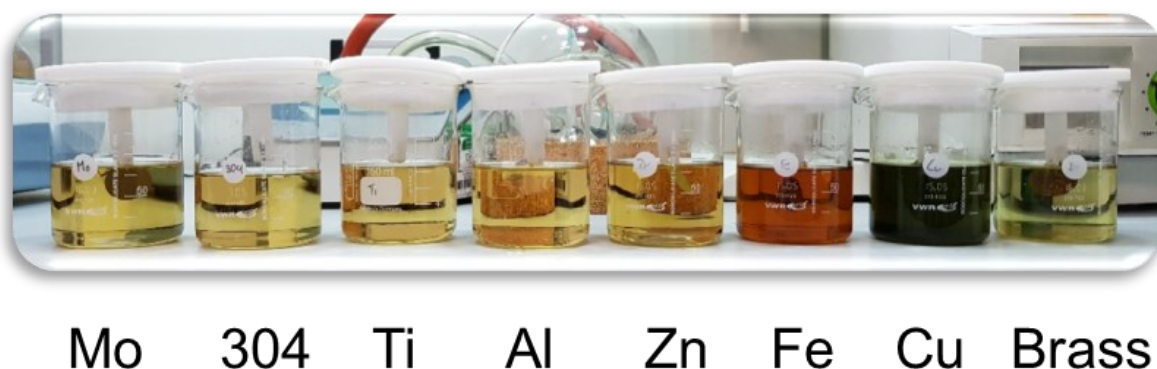


Figure 49. Picture of the $[C_4C_1im][NTf_2]$ after the immersion test at 150 °C.

Another result, that shows the tunability of ILs, is the fact that all ILs studied in this work induced a dezincification process on the brass (Figure 178 in Appendix 5), except for $[C_4C_1im][NTf_2]$, which induced decuprification of brass. Some examples of the brass surface after exposure to ILs are depicted in Figure 50.

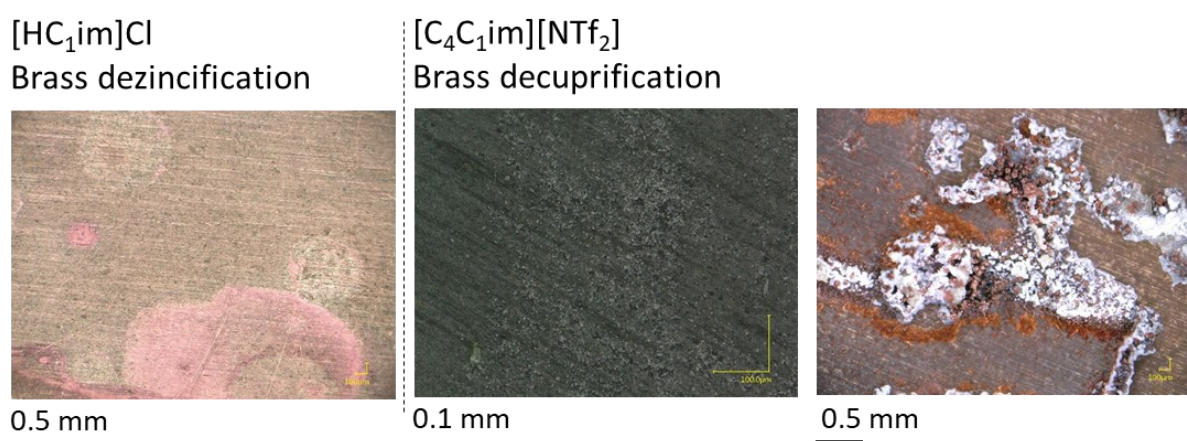


Figure 50. Pictures of the surface of brass exposed to $[HC_1im]Cl$ (120 °C, water 98 mol% and 13.18 h) and $[C_4C_1im][NTf_2]$ (70 °C, dry and 162 d).

At temperatures up to 70 °C, the decuprification of brass (Cu63/Zn37) is the main phenomenon, while at increased temperature (150 °C) decuprification and dezincification take place simultaneously, and the dissolution of zinc becomes more marked. Dezincification of brass is a commonly reported phenomenon while the preferential removal of Cu from Cu-

containing alloys, or decuprification, is rarely mentioned in the engineering literature. Interestingly, decuprification has been mentioned as a curiosity in archaeological (dating techniques and authentications) sciences and art conservation, and some references are made to prehistoric bronze artefacts and ancient Roman brass ^{176–179}.

In a review on the corrosion inhibition properties of several substances on brasses (70/30, 63/37, 60/40) exposed to different acidic media, it was shown that dezincification was the most common de-alloying mechanism. However, in acetic acid, Cu is preferentially dissolved from brass Cu63/Zn37. It was reported that decuprification was initially enhanced by pyrogallol, tannin, gum acacia, dextrin, agar-agar, but with increasing test duration, the selective dissolution of zinc becomes more marked ¹⁸⁰. It was also shown that in other acids, some inhibitors promoted brass decuprification ¹⁸⁰. The mechanisms of selective dealloying of brass in acidic media could not be found in the literature. In a work describing the effects of different corrosion inhibitors, where both dezincification and decuprification are mentioned, there is only a quick reference to the mechanisms of the overall corrosion inhibition of the different substances, which can add by inhibiting whether the cathodic or anodic reaction of the corrosion process, depending on the chemical nature of the corrosion inhibitor ¹⁸⁰. Another example of decuprification reported in the literature is brass (Cu80/Zn20) exposed in 0.5 M NaCl or Na₂SO₄, for which 2-mercaptobenzothiazole 0.05 mM was able to inhibit decuprification of 0.5 M NaCl ¹⁸¹.

3.5.2.5.1 Other studies on the corrosion of metals in [C₄C₁im][NTf₂]

Perissi *et al.* studied the corrosion behaviour of metals: Cu, carbon steel AISI 1018, Ni, brass naval alloy 464 (wt% 59–62 Cu, 36.7–40.2 Zn, 0.2 Pb, 0.1 Fe, 0.5–1 Sn, density 8.41 g/cm³) and Incomel, exposed to [C₄C₁im][NTf₂] at different temperatures from 150 °C to 325 °C ¹⁸². In this study, Cu showed the highest weight loss among all the tested metals, with a corrosion rate at 150 °C estimated at (373 g/cm².y). At higher temperature, it was reported that the Cu samples crumbled due to crevice corrosion after 48h immersion, and the CRs were not calculated. For CS, Ni and Incomel, no significant weight loss was reported until 250 °C with the formation of a black layer and uneven corrosion at higher temperatures. For brass (naval alloy 464), a dark layer appeared with no significant mass loss until 300 °C and uneven corrosion at 325 °C, making this the most resistant metal in those experiments.

These results are in general agreement with the observations of this study, in which Cu experienced the highest MCRs. However, brass (Cu63/Zn37) used in this work showed significant attack when exposed to this IL while the brass naval alloy 464 used by Perissi *et al.*

showed excellent resistance ¹⁸². These results indicate that alloying, can have significant effects on the corrosion behaviour of metals exposed to ILs.

The corrosion layers formed on the surface of different metals (Inconel 600, naval brass and carbon steel AISI 1018) after their long-term interaction (20 d) with [C₄C₁im][NTf₂] at 225 °C was investigated by Secondary Ion Mass Spectrometry (SIMS) and X-ray photoelectron spectroscopy (XPS) ¹⁸³. It is shown that intense decomposition of ILs, especially in the presence of Ni, and subsequent adsorption of decomposition products on the alloy surface can induce processes of surface corrosion ¹⁸³. It was reported that after the immersion test, the colour of the IL liquid also changed; the liquid in which Inconel samples were immersed acquired the darkest tint and the liquid in which brass samples were immersed retained the lightest colour ¹⁸³. The colour changes were associated with IL decomposition upon interaction with the alloy surface, especially in the presence of Ni ¹⁸³.

Those observations do not match the experimental results in this work, as the IL exposed to the Ni containing alloy (304 SS) did not show significant colour changes when exposed to the IL at 150 °C and another type of brass showed a green tint due to the presence of Cu in solution. This discrepancy shows that the exact nature of the alloy and the temperature plays a significant role in metal corrosion in ILs. The average specific loss values (g/cm²) were reported as 2.5 x 10⁻⁵ for Inconel, 1.3 x 10⁻² for naval brass and 2.0 x 10⁻² for Carbon Steel (CS) ¹⁸³. Using those values and the duration of the experiments, the CR (mg/cm².d) at 225 °C were calculated as 1.25 x 10⁻⁴ for Inconel, 0.065 for naval brass and 0.1 for CS respectively. For reference, the CR (mg/cm².d) obtained experimentally at 150 °C were 6.38 ± 0.02 for brass (Cu63/Zn37) and -0.13 ± 0.01 for Fe (Figure 33). It is noteworthy to mention that the dark layers reported that work (ref ¹⁸³) were not observed in this work, probably because of their appearance at temperatures higher than 150 °C.

In a study of 304 SS dissolution in weakly coordinating ILs ethyl-dimethyl-propyl-ammonium bis(trifluoromethylsulphonyl)imide [N₃₂₁₁][NTf₂] at 200 °C and 10 days, it was found that the concentration of Fe, Cr, and Ni in the ILs solution detected by ICP-OES was 181.7, 54.7 and 30 mg/kg IL ¹⁸⁴. Normalized according to the mass, 68.2% Fe, 20.5% Cr and 11.3% Ni, which roughly correspond to the composition of the alloy. However, the Cr and Ni concentration in solution are higher, suggesting that these metals leached at a higher rate. The corrosion rate reported for this metal in [N₃₂₁₁][NTf₂] is 1.23 x 10⁻² g/cm².y ¹⁸⁴. Compared to the results found in this work, no metals were detected in the solution of [C₄C₁im][NTf₂], at 150 °C and long exposure times (68 d). This could be explained that the active dissolution of the 304 SS in [NTf₂] containing ILs takes places at temperatures equals or higher than 220 °C. Another explanation

could be stronger interaction of the imidazolium ring with the metal surface, through the π orbitals electrons, resulting in higher corrosion inhibition.

The corrosion rate determined by corrosion current densities extrapolated from Tafel plots, showed the CS 1018 have a CR of 5.6 $\mu\text{m}/\text{y}$ when exposed to $[\text{C}_4\text{C}_1\text{im}]\text{Cl}$ and a higher CR of 11 $\mu\text{m}/\text{y}$ when exposed to $[\text{C}_4\text{C}_1\text{im}][\text{NTf}_2]$ ¹⁸⁵. Another study on the same system found similar values, 3.16 $\mu\text{m}/\text{y}$ and 11.0 $\mu\text{m}/\text{y}$ when exposed to $[\text{C}_4\text{C}_1\text{im}]\text{Cl}$ and $[\text{C}_4\text{C}_1\text{im}][\text{NTf}_2]$ respectively¹⁸⁶. These results are in contradiction with the general expectation that CR would be higher in chloride-containing environments than in $[\text{C}_4\text{C}_1\text{im}][\text{NTf}_2]$, which is considered an “inert” ILs. However, these trends were also observed in the experiments in this work, as 304 SS have higher MCR in $[\text{C}_4\text{C}_1\text{im}][\text{NTf}_2]$ than $[\text{C}_4\text{C}_1\text{im}]\text{Cl}$, at 70 °C and dry conditions. This is further discussed in section 3.5.5.

The corrosion behaviour of metals exposed to $[\text{C}_4\text{C}_1\text{im}][\text{NTf}_2]$ is summarised in Table 15, where it can be seen that most metals are resistant in this IL except for Cu and its alloy.

Table 15. Summary of the classification system (section 3.4) and corrosion type for metals exposed to $[\text{C}_4\text{C}_1\text{im}][\text{NTf}_2]$. Corrosion types: NC: no corrosion, PC: pitting corrosion, USC: uniform surface corrosion and NUSC: non-uniform corrosion.

Metal	Temperature [°C]	$[\text{C}_4\text{C}_1\text{im}][\text{NTf}_2]$	
		Classification System Type	Corrosion Type
Aluminium	70	0	NC
	150	0	NC
Copper	70	3	NUSC
	150	3	NUSC
Iron	70	0	NC
	150	0	NC
Molybdenum	70	1	UC
	150	1	UC
Nickel	70	0	NC
	150	0	NC
Titanium	70	0	NC
	150	0	NC
Zinc	70	0	NC
	150	0	NC
Brass	70	3	NUSC
	150	3	NUSC
304 SS	70	0	NC
	150	0	NC

Finally, it is noteworthy to mention that the cathodic reaction is not mentioned in any of the above-cited works on the corrosion of metals exposed to $[\text{C}_4\text{C}_1\text{im}][\text{NTf}_2]$, and the detailed corrosion mechanisms of Cu and its alloys awaits experimental determination.

3.5.3 Corrosion behaviour of metals exposed to water-soluble ILs

Detailed corrosion rate calculations, surface analyses and discussions for metals exposed to water-soluble ILs are given in Appendix 5.

It was observed that some metals and alloys, such as Zn, Cu, Fe and brass, oxidize in aqueous IL solution to yield nano and micro-sized particles with a diversity of morphologies. In particular, it has been noticed that Zn oxidises in [C₄C₁im]Cl and water to form a diversity of particles with different chemistries, shapes and sizes, all of which can be controlled by adjusting the process conditions, such as temperature, exposure time and water concentration. The following section provides a detailed description of the corrosion products formed in this system.

3.5.4 Zinc exposed to [C₄C₁im]Cl and water systems

3.5.4.1 XRD

XRD proved to be a powerful technique to detect crystalline phases formed from Zn exposed to corrosive media. A diversity of compounds were seen when exposed to [C₄C₁im]Cl and water systems. The XRD spectra are given in Figure 51 to Figure 55 and a summary of the detected species is presented in Table 16. The diffraction patterns of the detected species were matched to the following references compounds using HighScore suite, PANalytical's commercial powder diffraction analysis software:

- Zinc (Zn): Reference code 00-004-0831.
- Zinc carbonate hydroxide (Zn₅(CO₃)₂(OH)₆Cl₂·H₂O): (ZCAR). Reference code 00-019-1458.
- Zinc chloride hydroxide monohydrate (Zn₅(OH)₈Cl₂·H₂O): ZHC or Simonkolleite ¹⁸⁷. Reference code 00-007-0155.
- Zinc hydroxide (ε- Zn(OH)₂): (Wülfingite). Reference code 00-038-0385
- Zinc oxide (ZnO): Zincite "Würtzite structure". Reference code 00-036-1451

Table 16. Summary of the corrosion products crystalline phases detected on the zinc surface by XRD ¹⁶⁹.

Solvent	IL	Water Content [mol%]	Temp [°C]	Exposure Time [days]	Species detected by XRD				
					Zn	ZnO	ε-Zn(OH) ₂	ZHC	ZCAR
[C ₄ C ₁ im]Cl	1	Residual	70	14	X				
	2	Residual	120	12	X				
	2	Residual	120	16	X				

Solvent	IL	Water Content [mol%]	Temp [°C]	Exposure Time [days]	Species detected by XRD				
					Zn	ZnO	ϵ -Zn(OH) ₂	ZHC	ZCAR
	1	75	20	18	X	(Traces)			
	1	75	20	26	X	X			
	1	75	70	5	X	X			
	2	75	120	5.8	X	X			
	2	75	120	16h	X	X			
	2	98	20	6 [A]	X	X			(Traces)
	2	98	20	14	X	X		X	(Traces)
	1	98	20	18	X	X		X	
	1	98	20	44	X	X	X	X	
	2	98	20	48	X	X	X	X	
	1	98	70	3.5	X	X			
	1	98	70	15	X	X		(Traces)	
	2	98	120	16h	X	X			
Water	-	-	20	3	X	X			X
	-	-	20	6	X	X			X
	-	-	70	3	X	X			(Traces)
	-	-	70	6	X	X			(Traces)
	-	-	120	2.6	X	X			
	-	-	120	4.6	X	X			

A. [C₄C₁im]Cl (IL-2) and agitation (650 rpm).

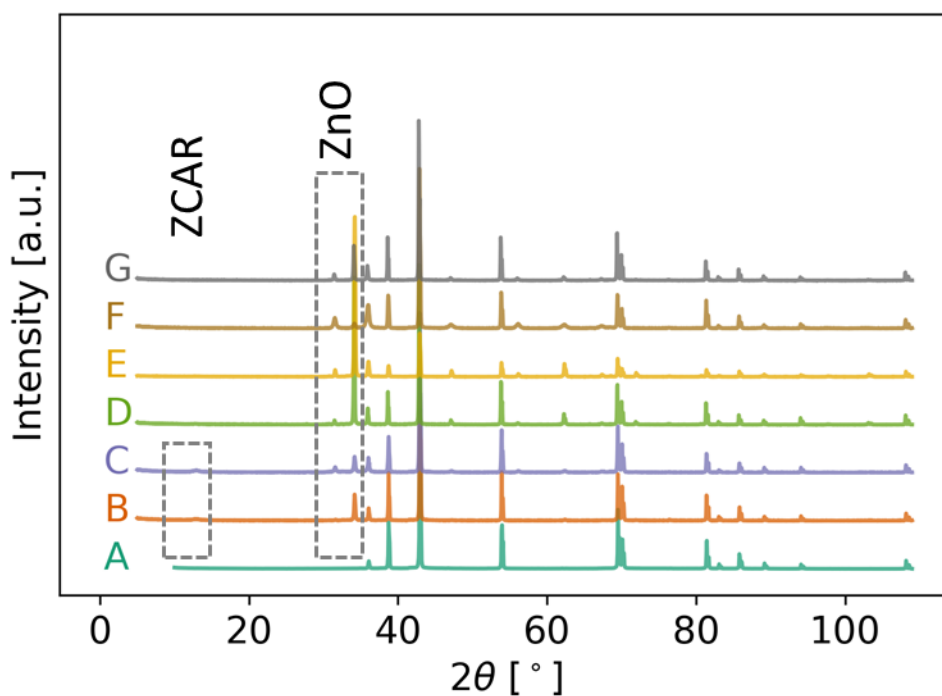


Figure 51. XRD pattern of zinc coupons (as prepared) exposed to water. [A] unexposed metal. [B] 20 °C and 3 days. [C] 20 °C and 6 days. [D] 70 °C and 3days. [E] 70 °C and 6 days. [F] 120 °C and 2.6 days. [G] 120 °C and 4.6 days. Published by The Royal Society of Chemistry ¹⁶⁹.

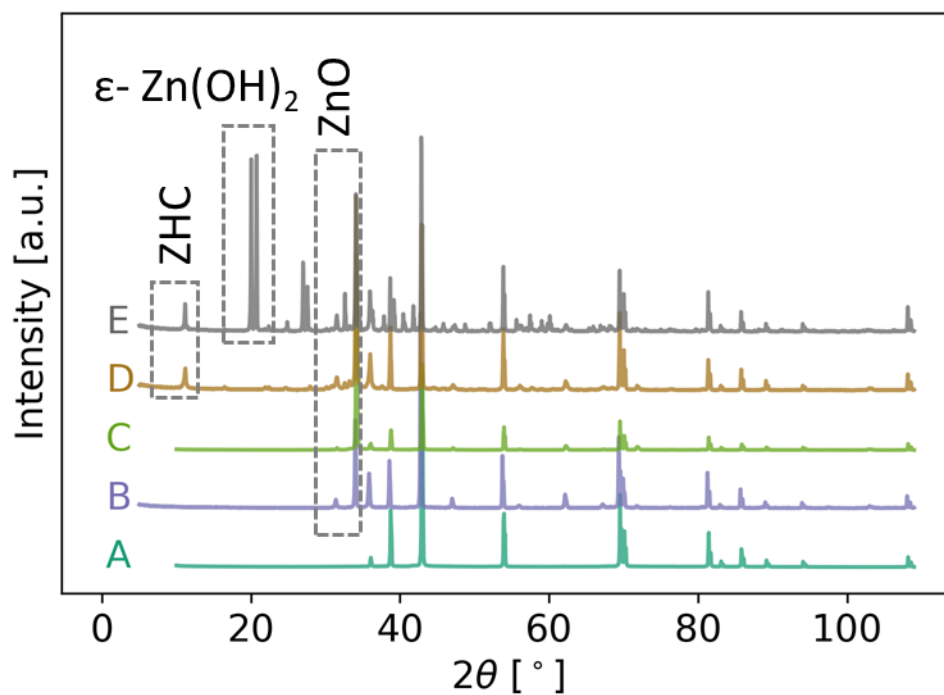


Figure 52. XRD pattern of zinc coupons (as prepared) exposed to [C₄C₁im]Cl solutions with a water content of 98 mol%. [A] unexposed metal. [B] 120 °C and 16 hours (IL-2). [C] 70 °C and 3.5 days (IL-1). [D] 20 °C and 18 days (IL-1). [E] 20 °C and 44 days (IL-1). Published by The Royal Society of Chemistry ¹⁶⁹.

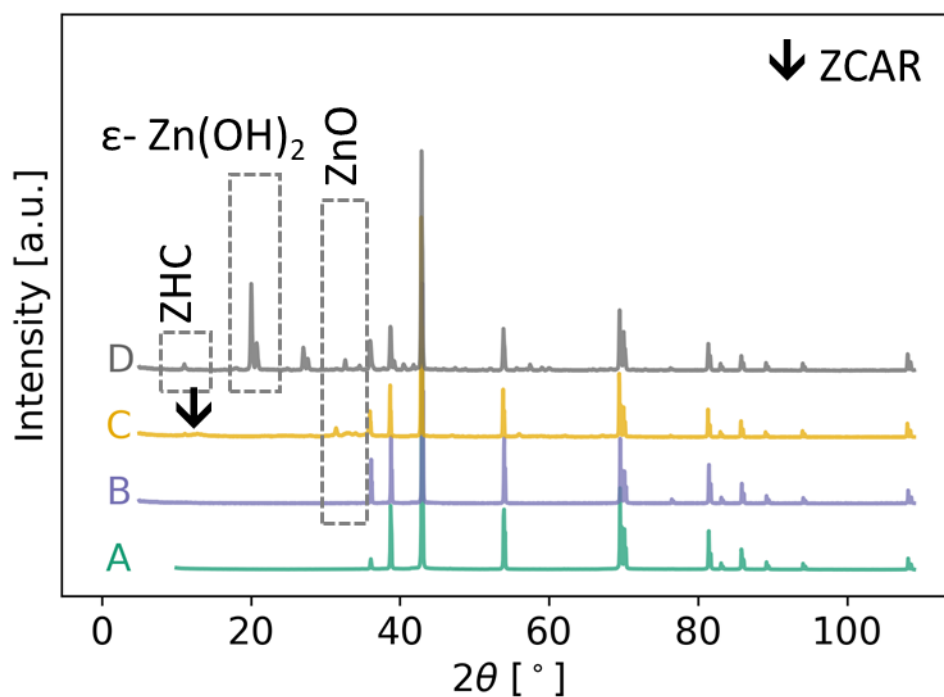


Figure 53. XRD pattern of zinc coupons (as prepared) exposed to [C₄C₁im]Cl (IL-2) at 20 °C and 98%mol. [A] unexposed metal. [B] 6 days. [C] 12 days. [D] 46 days. Published by The Royal Society of Chemistry ¹⁶⁹.

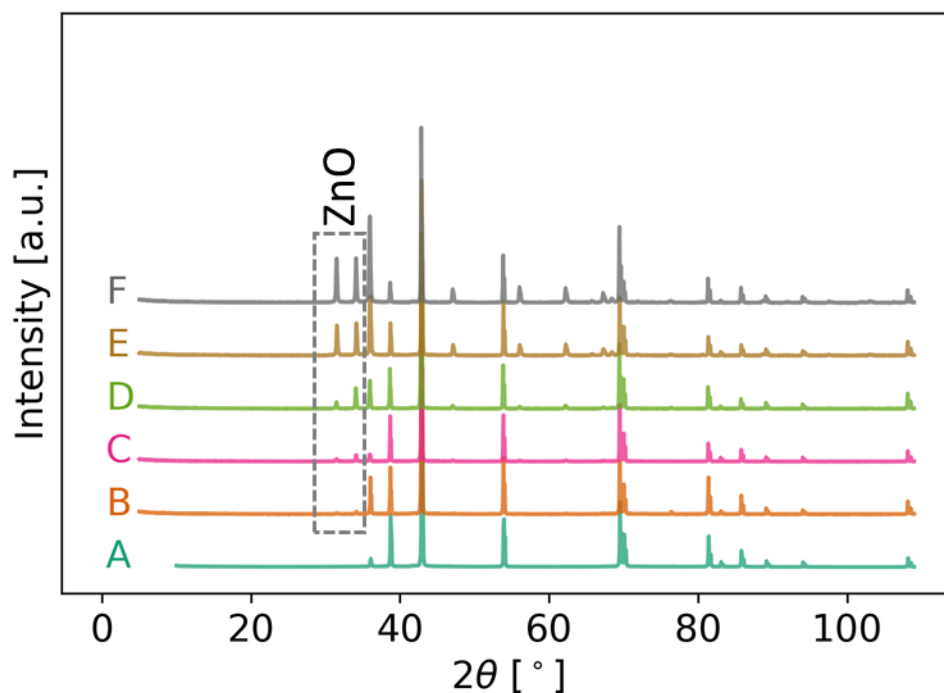


Figure 54. XRD pattern of zinc coupons (as prepared) exposed to [C4C1im]Cl solutions with a water content of 75 mol%. [A] unexposed metal. [B] 20 °C and 18 days (IL-1). [C] 20 °C and 26 days (IL-1). [D] 70 °C and 5 days (IL-1). [E] 70 °C and 6 days (IL-2). [F] 120 °C and 16 hours (IL-2). Published by The Royal Society of Chemistry ¹⁶⁹.

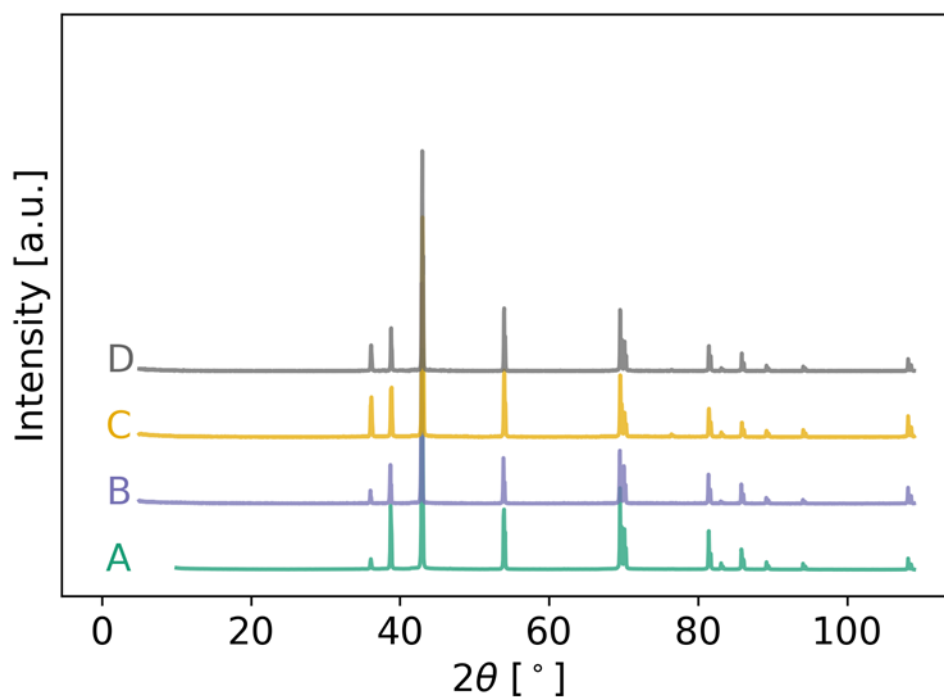


Figure 55. XRD pattern of zinc coupons (as prepared) exposed to dried [C4C1im]Cl. [A] unexposed metal. [B] 70 °C and 14 days. [C] 120 °C and 12 days. [D] 120 °C and 16 days. Published by The Royal Society of Chemistry ¹⁶⁹.

The occurrence of the different chemical species is as follows:

- Zinc oxide (ZnO) was detected in water and [C₄C₁im]Cl/water at all experimental conditions tested except in neat IL (residual water case).
- Zinc chloride hydroxide monohydrate (Zn₅(OH)₈Cl₂·H₂O) formation was only observed in [C₄C₁im]Cl at high water content (98 mol%) and at temperatures below 70°C.
- Zinc hydroxide (ε- Zn(OH)₂) was only observed in [C₄C₁im]Cl at high water content (98 mol%), room temperature and long exposure time.
- Zinc carbonate hydroxide (Zn₅(CO₃)₂(OH)₆Cl₂·H₂O): Traces of this compounds was observed only at room temperature in water and in aqueous [C₄C₁im]Cl (IL-2) at room temperature and high water content (98 mol%), most likely due to atmospheric CO₂^{188–191}.

3.5.4.2 SEM images

As shown in Figure 56 to Figure 58, a diversity of materials formed in [C₄C₁im]Cl solutions and water.

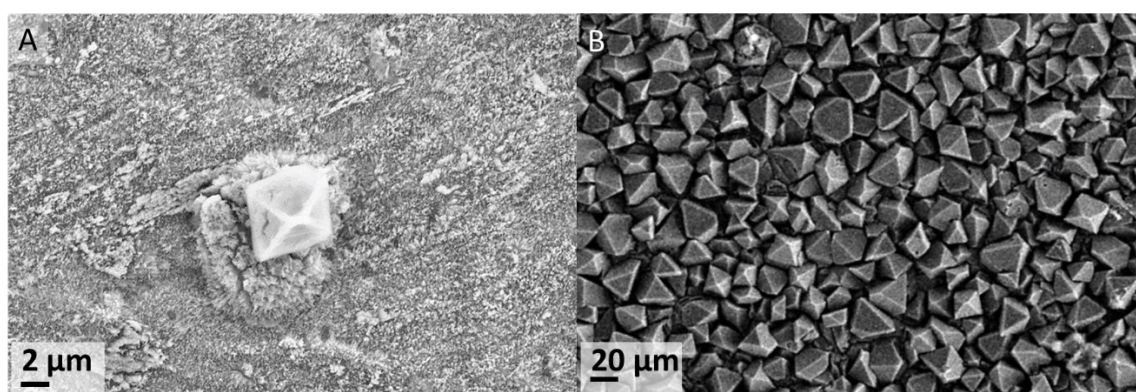


Figure 56. SEM imaging showing zinc surface exposed to [C₄C₁im]Cl (IL-1, X_{H₂O}=0.98 solution at 20 ± 1 °C). (A) Single octahedron Zn(OH)₂ particle after 18-d exposure (approximate length of 7.9 ± 0.6 μm). (B) Multiple Zn(OH)₂ crystals after 44-d exposure with a mean length of 21 ± 6 μm (n=84). Published by The Royal Society of Chemistry¹⁶⁹.

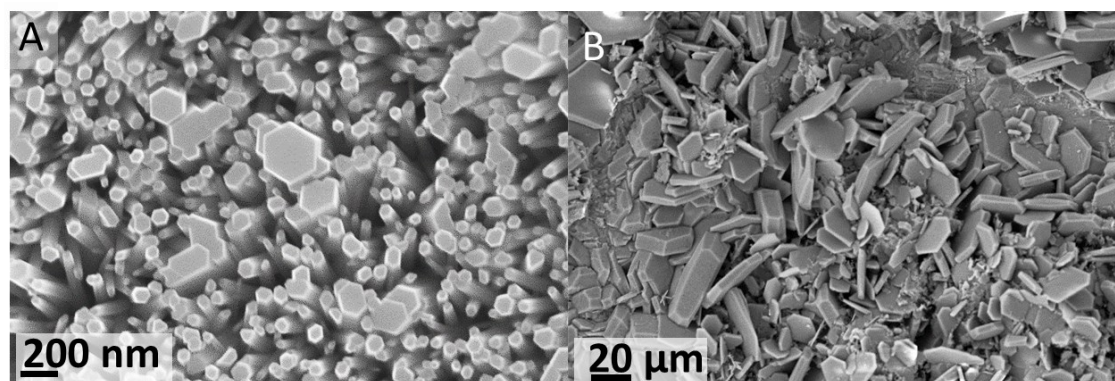


Figure 57. Magnified zinc surface exposed to [BMIM]Cl X_{H₂O}=0.98 solution at 70 ± 1 °C. (A) ZnO nanorods after 4-d exposure (magnification 134.17 kX) (average size 90 ± 40 nm, n=361). (B) ZHC plate-like crystals after 15-d exposure (magnification 1.44 kX). Estimated thickness 2.5 ± 1.5 μm (n=85), diameter 19 ± 8 μm (n=85). Published by The Royal Society of Chemistry¹⁶⁹.

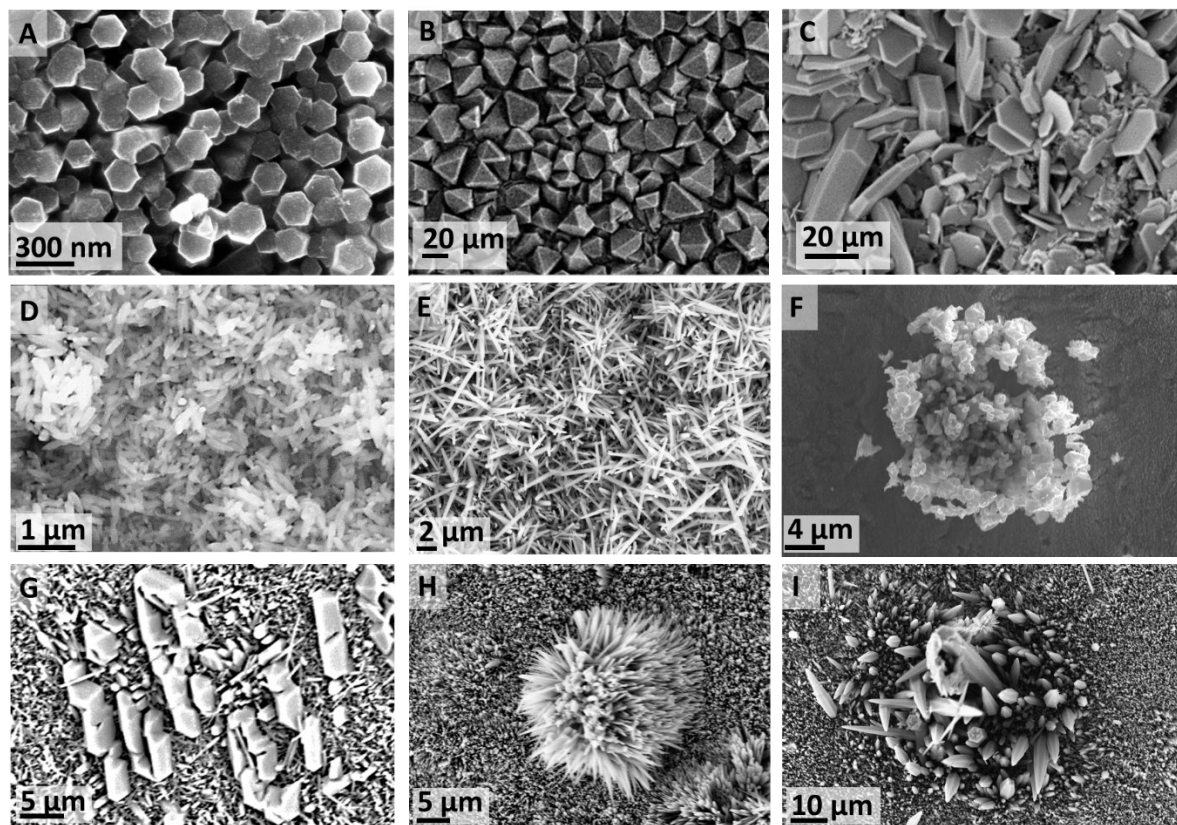


Figure 58. Summary of the most representative structures. [A] ZnO flat-topped hexagonal rods. [B] ϵ -Zn(OH)₂ octahedrons. [C] ZHC plates. [D] ZnO short rods (round and sharp ended). [E] ZnO needles. [F] ZnO polycrystalline structure. [G] ZnO thick crystals. [H] ZnO 3D needle flower. [I] ZnO 3D thick crystal flower. Published by The Royal Society of Chemistry ¹⁶⁹.

Table 17 summarises the main structures observed with SEM/EDX for Zn exposed to IL-solutions.

Table 17. Summary of the most representative structures. [A] ZnO flat-topped hexagonal rods. [B] ϵ -Zn(OH)₂ octahedrons. [C] ZHC plates. [D] ZnO short rods (round and sharp ended). [E] ZnO needles. [F] ZnO polycrystalline structure. [G] ZnO thick crystals. [H] ZnO 3D needle flower. [I] ZnO 3D thick crystal flower ¹⁶⁹. Refer to Figure 58.

Solvent	IL	Water Content [mol%]	Temp [°C]	Exposure Time [days]	[A]	[B]	[C]	[D]	[E]	[F]	[G]	[H]	[I]	Others
[C ₄ C ₁ im]Cl	1	Residual	70	14										
	2	Residual	120	12										
	2	Residual	120	16										
	2	70	120	5.8	X								X	
	1	75	20	18	X									
	1	75	20	26										
	1	75	70	5										
	2	75	120	1	X									(3)
	2	75	120	16h	X						X		X	
	2	98	20	6										(5,7)
	2	98	20	6		X								(1,5)
	2	98	20	14										(1,5)

Solvent	IL	Water Content [mol%]	Temp [°C]	Exposure Time [days]	[A]	[B]	[C]	[D]	[E]	[F]	[G]	[H]	[I]	Others	
	2	98	20	16		X								(1,5)	
	1	98	20	18	X										
	1	98	20	44		X	X	X					X	(1,2)	
	2	98	20	48			X							(1,5)	
	1	98	70	3.5	X						X	X			
	1	98	70	15			X	X	X		X	X	X		
	2	98	120	1	X						X		X	(4)	
	2	98	120	16h	X										
Water	-	-	20	2	X					X				(2)	
	-	-	20	2	X					X			X	(2)	
	-	-	70	6	X			X	X		X	X			
	-	-	70	6					X		X	X			
	-	-	120	2.6											(6)
	-	-	120	4.6	X							X		X	(3)

1. Amorphous.
2. Cotton Like.
3. Coarse material
4. Agglomerate of small crystals
5. Flakes
6. Small crystal without well-defined shape
7. Sample Agitated (650 rpm)

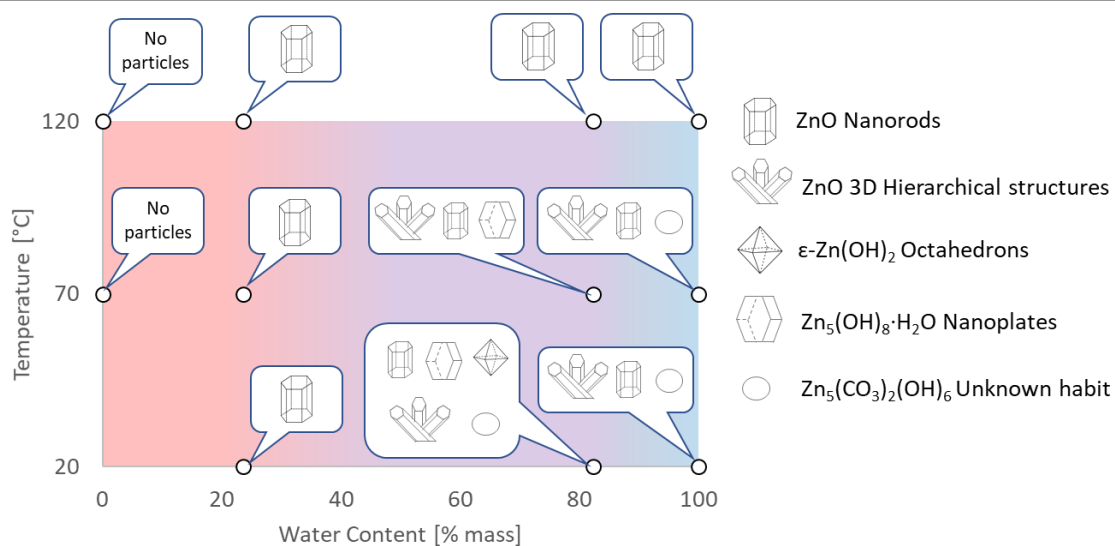


Figure 59. Summary of Zn-based materials, obtained by direct oxidation of metallic zinc in $[C_4C_{1im}]Cl$ solutions, as a function of experimental conditions. Published by The Royal Society of Chemistry ¹⁶⁹.

3.5.4.3 Water controls

In control experiments, Zn foils were exposed to demineralized water for a duration of three and six days at room temperature and 70 °C. At room temperature for both exposure times, the Zn foils were covered with flat-topped hexagonal nanorods along with the formation of

micrometre-scale clusters of a polycrystalline material distributed across the surface (Figure 171 in Appendix 5). At 6 d-exposure time, larger nanorods are observed (Figure 173 in Appendix 5). At 70 °C and 3-d exposure time, several structures were observed, flat-topped hexagonal nanorods, thicker structures ending with a point and rounded ends, and micro-meter scale polygonal plates (Figure 172 in Appendix 5). At 6-d exposure, the flat-topped hexagonal nanorods are no longer visible, and the entire surface of covered with the other structures, including the formation of well-defined needles (Figure 174 in Appendix 5). At 120 °C, ZnO flat-topped nanorods formed along with a thin coarse material (Figure 175 in Appendix 5), probably as a result of dissolution of ZnO to form Zn^{2+} ions, followed by their subsequent redeposition as ZnO. The structures were analysed by XRD spectra, where peak patterns indicate both the presence of Zn and ZnO at all temperatures and traces of zinc carbonate hydroxide (ZCAR) $\text{Zn}_5(\text{CO}_3)_2(\text{OH})_6$ (Figure 51).

The formation of ZnO nanoparticles by wet-oxidation of etched Zn foils in water had been reported^{192,193} without the formation of $\text{Zn}(\text{OH})_2$, which is in agreement with the experiments. Interestingly, the ZnO structures observed in each of those works and in this work are similar but not identical, suggesting that other factors are driving the crystal morphology of these materials in water. This also raises the issue that ZnO morphology is not fully controlled in water environment without the presence of other substances, such as ILs, stabilisers or surfactants.

3.5.4.4 Water-rich case (98 mol%)

When metallic Zn foils were exposed to a high-water content (98 mol%) $[\text{C}_4\text{C}_{1\text{im}}]\text{Cl}$ solutions, the predominant species was ZnO at all temperatures (IL-1). At a temperature equal or lower than 70 °C $\text{Zn}_5(\text{OH})_8\text{Cl}_2 \cdot \text{H}_2\text{O}$ (zinc hydroxychloride monohydrate (ZHC) or Simonkolleite^{38–40}) also formed. The occurrence of this compound is significant as it shows stable Zn-Cl complexes form at these conditions. Such compounds were not seen in our experiments at lower water content nor in a previous synthesis by Li *et al.*¹⁹⁴ using the same IL and zinc acetate precursor. At 20 °C, two additional crystalline compounds were detected by XRD, namely $\epsilon\text{-Zn}(\text{OH})_2$ and traces of $\text{Zn}_5(\text{CO}_3)_2(\text{OH})_6$ (Hydrozincite) most likely due to atmospheric CO_2 ^{188–191}.

In the water-rich case at 20 °C (IL-1), the main two species that formed after 18-d exposure were ZnO (Figure 161 in Appendix 5) and ZHC plates (Figure 162 in Appendix 5). Additionally, a few $\epsilon\text{-Zn}(\text{OH})_2$ octahedrons were also observed at short exposure times (Figure 56a). However, at an increased exposure time of 44 d, many more $\epsilon\text{-Zn}(\text{OH})_2$ micrometre-scale octahedrons (Figure 56b) were observed in addition to both ZnO and ZHC. The significant increase in the

quantity of ϵ -Zn(OH)₂ at longer exposure time was not expected as this compound is generally reported to be metastable¹⁹⁵ and would appear to be an intermediate species on the pathway to ZnO formation (Figure 64 in section 3.5.4.8), which is more stable thermodynamically at standard conditions (refer to section 3.5.4.8 for a detailed discussion). However, the driving force (standard free energy) for the dehydration of ϵ -Zn(OH)₂ to form ZnO at standard conditions is small in magnitude. It was noticed that ZHC was systematically detected for the cases where ϵ -Zn(OH)₂ significantly formed, with an increase in the pH of the medium (Table 18). This allows us to infer that as ZHC forms and chloride anions are incorporated into the ZHC crystal, hydroxide anions must remain in solution to achieve the electrical neutrality of the medium, increasing the pH of the solution. This increase in the concentration of hydroxide anions in the [C₄C₁im]Cl solutions with 98 mol% must be the cause of ϵ -Zn(OH)₂ formation, which allows us to infer that by adjusting the pH, the compounds formed can be further controlled.

Table 18. pH measurements for IL-1 solutions¹⁶⁹.

Solvent	Water Content [mol%]	Temp [°C]	Exposure Time [days]	pH
	Residual	70	14	-
	75	20	18	7.15
	75	20	26	7.49
[C ₁ C ₄ im]Cl	75	70	5	7.28
	98	20	18	7.98
	98	20	44	8.07
	98	70	4	7.57
	98	70	15	7.71
	-	20	3	6.7
Water	-	20	6	6.73
	-	70	3	6.91
	-	70	6	6.81

Halogens, such as chloride, and 1-methylimidazole are common impurities that are often present in ILs which originate from their synthesis route. There is a controversy in the scientific community regarding the effect of contaminants in the IL on the synthesis of nanoparticles¹⁹⁶. To verify this point, experiments were repeated using another batch of IL from another supplier (IL-2). The findings were reproducible, ϵ -Zn(OH)₂ was not detected at short exposure times while ϵ -Zn(OH)₂ octahedrons also formed in significant quantities at longer exposure times. These experiments show that the formation of the ϵ -Zn(OH)₂ crystalline phase is independent of the contaminants in the IL. However, amorphous Cl-containing structures were observed at long exposure times (44 d) in the samples exposed to the IL-1 (Figure 163 in Appendix 5) and

not seen in the sample exposed to the IL-2. Additionally, ZnO structures did not form to a great extent in the samples exposed to IL-2 batch (Appendix 5). This indicates that the formation of some species at these conditions (high-water content and low temperatures) is affected by the presence of contaminants in the IL.

After a 4-d exposure at 70 °C (IL-1), only flat-topped hexagonal nanorods were observed (Figure 4A). This kind of nanorod arrangement over a metallic conductor is ideal for many applications such as gas sensing, nano-generators, nano-lasers¹⁹⁷. By contrast, with an increased duration to 15 d, a variety of ZnO morphologies were observed, as well as trace evidence of ZHC plates (Figure 57B). At a further increased temperature (120 °C) (IL-2), the ZnO flat-topped nanorods were again observed, albeit at shorter durations of 16 and 24 h. However, thin wool-like structure (Figure 166 in Appendix 5), were also noted. At higher temperatures, the effects of the contaminants in the IL seem to not be significant.

The conversion pathway between Zn(OH)_2 and ZnO is complex and have been studied in literature. Demoisson *et al.* studied the effect of temperature and pressure on the size and morphology of hydrothermal ZnO particles from ambient to supercritical conditions prepared reacting $\text{Zn(NO}_3)_2$ with KOH solutions in the ranges of 1 – 300 bar and 30 – 400 °C¹⁹⁵. They found Zn(OH)_2 phases at temperatures lower than 52 °C and noticed that an increased temperature promotes the transformation of the wulffingite phase (Zn(OH)_2) into the oxide phase. This process which had been reported as favoured at higher temperatures, both from a free energy and kinetic perspective. Moreover, they found traces of $\beta\text{-Zn(OH)}_2$ in one of their experiments and proposed that this phase could be an intermediate of the transformation from $\epsilon\text{-Zn(OH)}_2$ to pure ZnO through a dissolution/precipitation mechanism (Eq. 84 in 3.5.4.8). Another study in the transformation of Zn(OH)_2 to ZnO had proposed 2 additional possible mechanisms, in situ crystallization and solid–solid phase transformations^{198,199}.

In summary, the formation of ZnO was the predominant species at temperatures equal to or higher than 70 °C. Depending on the experimental conditions, ZnO forms a diversity of habits ranging from 1D nanorods to high hierarchical arrangements, flower-like structures (similar to the ones formed in the water control). The favourability of ZnO at increased temperatures has been previously reported, where the formation of ZHC has only been observed at temperatures below 90 °C^{38–40} and the formation of $\epsilon\text{-Zn(OH)}_2$ is only achieved at temperatures lower than 70 °C^{37,41–43}. At temperatures lower than 70 °C all these species, with different habits, might co-exist. Therefore, if the goal is to synthesize ZnO, the formation of the other compounds could be avoided if the synthesis is performed at higher temperatures or through calcination of the species formed, which easily yield ZnO.

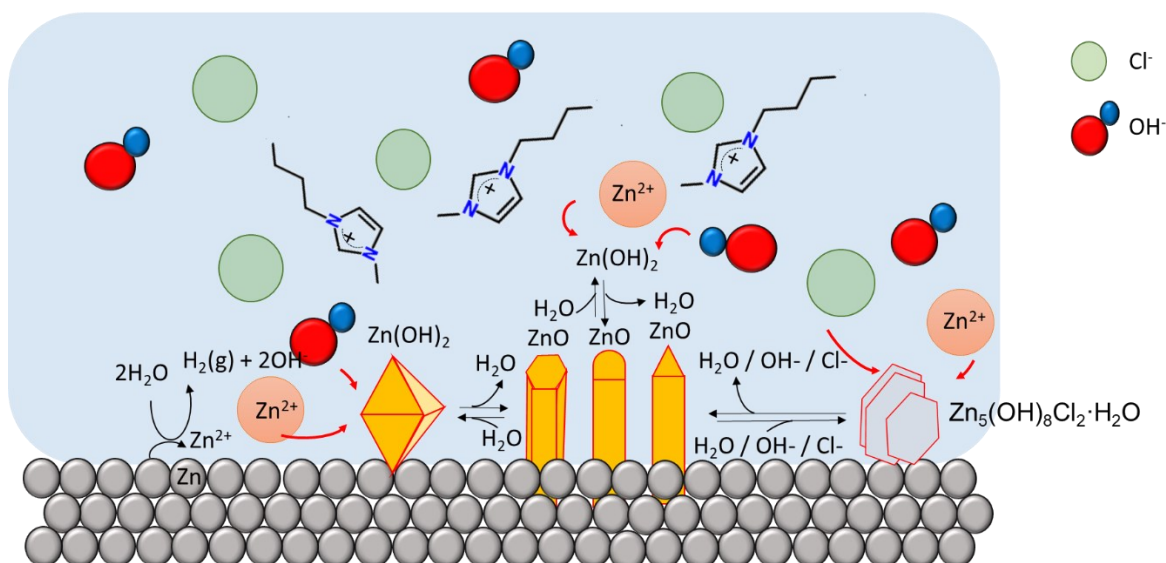


Figure 60. Cartoon of Zn-based micro/nano particles in $[C_4C_{1im}]Cl$ at high water content. At this water content, chloride anions can diffuse freely to react with Zn cations to form Zn-Cl compounds. Published by The Royal Society of Chemistry ¹⁶⁹.

3.5.4.5 Calcination

The products, mainly ϵ -Zn(OH)₂ and ZHC, on the coupon surface after 44-d exposure to $X_{H_2O}=0.98$ solution (IL-1) at 20 °C were recovered by scratching the surface of the metal and subsequently calcinated in a TGA instrument (section 3.3.3.4). The post-calcination products contained only ZnO (Figure 61F), generally conserved the overall crystal shape, and induced porosity. For example, the ϵ -Zn(OH)₂ octahedrons were converted to ZnO octahedrons (Figure 61A/D) and the ZHC plates were converted to ZnO plates (Figure 61B/E).

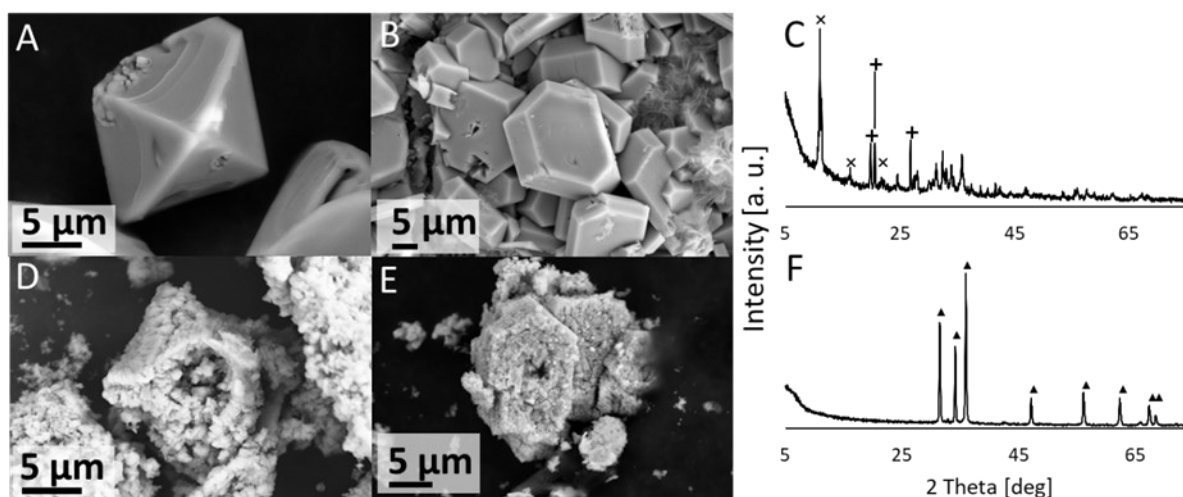


Figure 61. SEM Images of the ZnO precursors formed in the zinc surface exposed to $[C_4C_{1im}]Cl$ (IL-1, $X_{H_2O}=0.98$ solution, $20 \pm 1^\circ C$ and 44d) before and after calcination. ϵ -Zn(OH)₂ octahedrons before (A) and after calcination (D). ZHC particles before (C) and after (E) calcination. Both ϵ -Zn(OH)₂ and ZHC are transformed to ZnO with overall conservation of the morphology with increased porosity. XRD spectra of the ϵ -Zn(OH)₂ and ZHC powder before (C) and after calcination (F). Main peaks from diffraction patterns had been labelled: (x) ZHC, (+) ϵ -Zn(OH)₂ and (▲) ZnO. Published by The Royal Society of Chemistry ¹⁶⁹.

A series of thermal processes can be seen from the TGA thermogram (Figure 62), as a consequence of the superposition of the thermal decomposition of these substances. First, a small mass loss of 1.7% is seen between 80-100 °C attributed to the removal of the physically adsorbed water molecules onto the surface of the sample, followed by a thermal process attributed to the removal of the hydration water of ZHC²⁰⁰ simultaneously with the thermal decomposition of ϵ -Zn(OH)₂ (100-300 °C) (Eq. 79)²⁰¹. At high temperatures, a massive mass loss is observed in the range of 300-500 °C, which is in agreement with the TGA observed for the thermal decomposition of Zn₅(OH)₈Cl₂·H₂O given by Moezzi *et al*²⁰². They explained in detail the different paths for the thermal decomposition of ZHC and attributed this last mass loss to the decomposition of an amorphous Zn(OH)₂·ZnCl₂ phase, formed by the rearrangement of the crystalline ZHC phase (Eqs. 79-78).

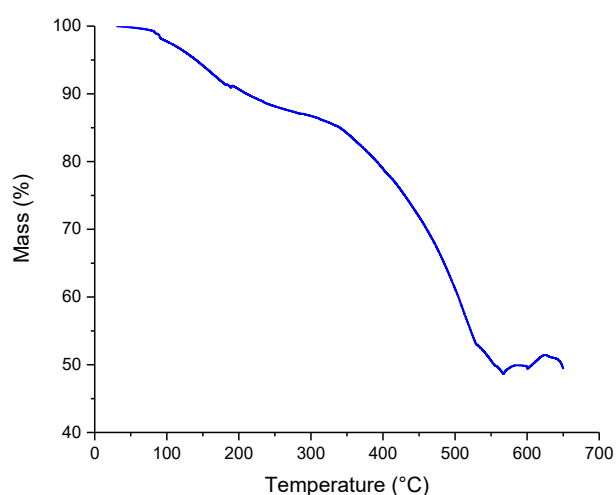
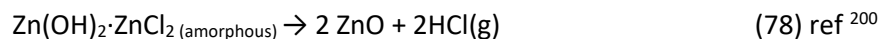
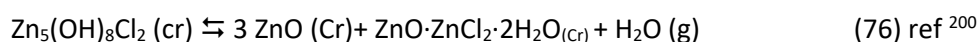
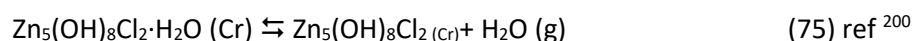


Figure 62. Thermogram for the calcination of ϵ -Zn(OH)₂ and ZHC into ZnO. Published by The Royal Society of Chemistry¹⁶⁹.

3.5.4.6 IL-rich case (75 mol%)

Regardless of the source of the IL used, the temperature and experimental duration, the metallic zinc substrate oxidised resulting in the formation of hexagonal ZnO (Wurtzite). At 20 °C, crystal growth with time is evident: 77 ± 24 nm ($n = 126$) diameter after 18-d exposure to 150 ± 30 nm ($n=278$) after 26-d exposure (Figure 160 in Appendix 5). This increase in particle size results in improved surface coverage of the substrate (Figure 167 in Appendix 5). At 26-d exposure time, a very small fraction of the surface showed a material containing Cl detected by EDX and XRF (1750 mg/kg) (Figure 169 in Appendix 5).

The formation of ZnO hexagonal nanorods in the IL-rich case are hypothesized to take place in a water environment (reverse micelle) formed between the metal surface and the polar regions of the IL (Figure 63). Water promotes the oxidation of the metallic zinc, producing an unstable $\text{Zn}(\text{OH})_2$ phase, which dehydrates to form ZnO. The $[\text{C}_4\text{C}_1\text{im}]\text{Cl}$ creates a barrier thereby controlling the intermicellar exchange rate¹⁹⁴, and thus limiting excessive growth and agglomeration of ZnO particles formed. This contrasts with the rich-water (and water control) case where agglomeration was observed (high hierarchical arrangements). However, as most of the studies that probe solvent structure at metal interfaces focused on polarized electrode surfaces²⁰³ the solvent nano-environment near the surface of unpolarized metallic zinc is unknown. Therefore, the existence of such water nano-environment near the zinc surface awaits experimental verification.

This phenomenon is similar to a previously suggested formation of micelles whereby the cation $[\text{C}_4\text{C}_1\text{im}]^+$ to capture the crystallization water from a zinc salt (e.g. $\text{Zn}(\text{CH}_3\text{COO})_2 \cdot 2\text{H}_2\text{O}$). This would then form reverse micelles where the water is found in the core (polar region) in which the zinc acetate precursor dissolves. Subsequently, $[\text{OH}]^-$ ions penetrate the micelles and react with Zn^{2+} to form ZnO. This synthetic route using Zn salt precursors yielded ZnO spherical nanoparticles with 15 - 20 nm diameters¹⁹⁴ whereas direct oxidation of zinc foils yields hexagonal nanorods.

These two routes show that despite the high chloride molality (from the $[\text{C}_4\text{C}_1\text{im}]\text{Cl}$), there is an absence of chloride-containing Zn compounds. In this mixture, as previously discussed, the chloride will preferentially remain close to the cation, $[\text{C}_4\text{C}_1\text{im}]^+$, and does not react with Zn. The lack of chloride-containing products suggests that the IL is not consumed in the ZnO formation process, which would allow its recovery and reuse leading to cost-effective and eco-friendly large-scale production processes.

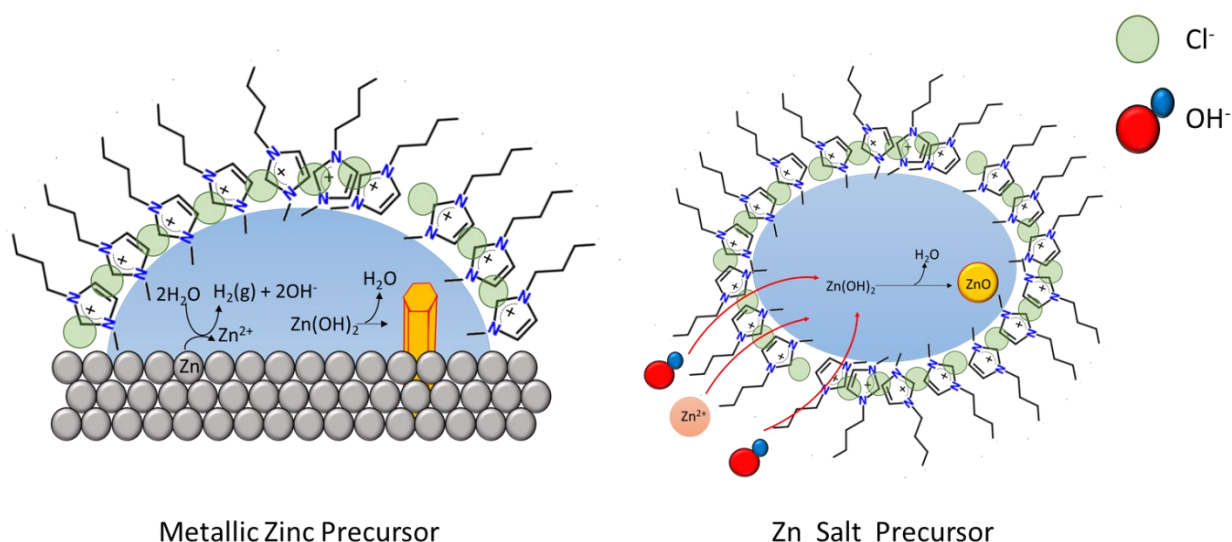


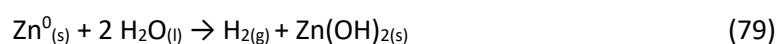
Figure 63. Schematic of ZnO formation in $[C_4C_1im]Cl$ at low water content. Left: Zn salts as precursors¹⁹⁴. Right: Metallic Zinc as precursor. Published by The Royal Society of Chemistry¹⁶⁹.

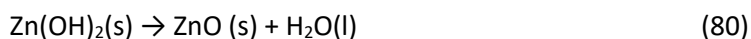
3.5.4.7 Residual water case

Due to the hygroscopic nature of $[C_4C_1im]Cl$, anhydrous conditions are extremely difficult to achieve^{67,204,205}. At 70 °C, when metallic zinc was exposed to $[C_4C_1im]Cl$ (IL-1) containing residual water, the surface was virtually unchanged, except a few irregular nanometre-size features suspected to be ZnO (Figure 170A in Appendix 5). Further, no significant amounts of Zn in the bulk solution were detected (Table S1). At 120 °C (IL-2), the surface contained spherical features (Figure 170B Appendix 5) for which EDX showed traces of oxygen, likely adsorbed to the surface from the atmosphere, and no chloride. At both temperatures, the XRD patterns showed only the presence of zinc. These results confirm that the presence of water is essential for the formation of ZnO, *via* the oxidation of Zn at the surface coupled with the cathodic reduction of water. We can infer that in fully dry IL, no reaction will occur at temperatures equal or less than 120 °C.

3.5.4.8 Overall considerations

The mechanisms for the ZnO formation in solution and over the metal surface can be supported from thermodynamic calculations. The change in the standard-state free energy for reaction Eq. 79 is negative ($\Delta G^0 = -79.3 \text{ kJ/mol} < 0$) and it is favoured by both enthalpy ($\Delta H^0 = -70.3 \text{ kJ/mol} < 0$) and entropy ($\Delta S^0 = 30.3 \text{ J/mol.K} > 0$) changes, thus metallic zinc will react with water to form $Zn(OH)_2$ spontaneously. Once formed, it can dehydrate to form ZnO (Eq. 80)





The change in the standard-state free energy for reaction Eq. 80 is small in magnitude and its value will strongly depend on the data set used for the thermodynamic calculations. When CRC data is used (Table 19), $\Delta G^0 = -4.1\text{kJ/mol}$ is obtained, which is consistent with the values found in literature ¹⁹⁵, however, other authors had reported a value of $\Delta G^0 = -1.13\text{kJ/mol}$ ¹⁹⁸. In any case, reaction 80 is not favoured by the change in enthalpy ($\Delta H^0 > 0$) but it is favoured by the change in entropy ($\Delta S^0 > 0$) due to an increase in the number of molecules, one being liquid. This indicates that Zn(OH)_2 does spontaneously convert to ZnO at room temperature and in pure water, and explains why this compound is not formed at high temperatures.

Table 19. Values of standard enthalpy (ΔH^0), standard free energy (ΔG^0) and standard entropy (ΔS^0) used for thermodynamic calculations ^{37,169}.

	ΔH^0 kJ/mol	ΔG^0 kJ/mol	ΔS^0 J/mol.K
Zn(OH)₂ (s)	-641.9	-553.5	81.2
ZnO (s)	-350.5	-320.5	43.7
Zn (s)	-	-	41.6
H₂O (l)	-285.8	-237.1	70.0
H₂ (g)	-	-	130.68

The variety of Zn-compounds particles observed as a function of conditions and the exposure time can be explained by changes in the nature of the IL-water system. The degree of interaction of the chloride in $[\text{C}_4\text{C}_1\text{im}]\text{Cl}$ with other species in the system can be tuned by weakening the interaction between cation and anion by the addition of a solvent, such as water. Therefore, by adjusting the water content of the mixture, the system transitions from an IL-like behaviour at low water content to a concentrated-aqueous-like behaviour at high water content. In the IL-rich case under the tested conditions, chloride does not seem to react with Zn to form Zn-chloride containing solids whereas, in the water-rich region, such materials formed. The nature of the solvent has a great influence in the nucleation and growth processes of the micro/nanomaterials particles obtained by Oxidative Ionothermal Synthesis (OIS), leading to a diversity of compounds with different chemical compositions, morphologies and sizes (Figure 64).

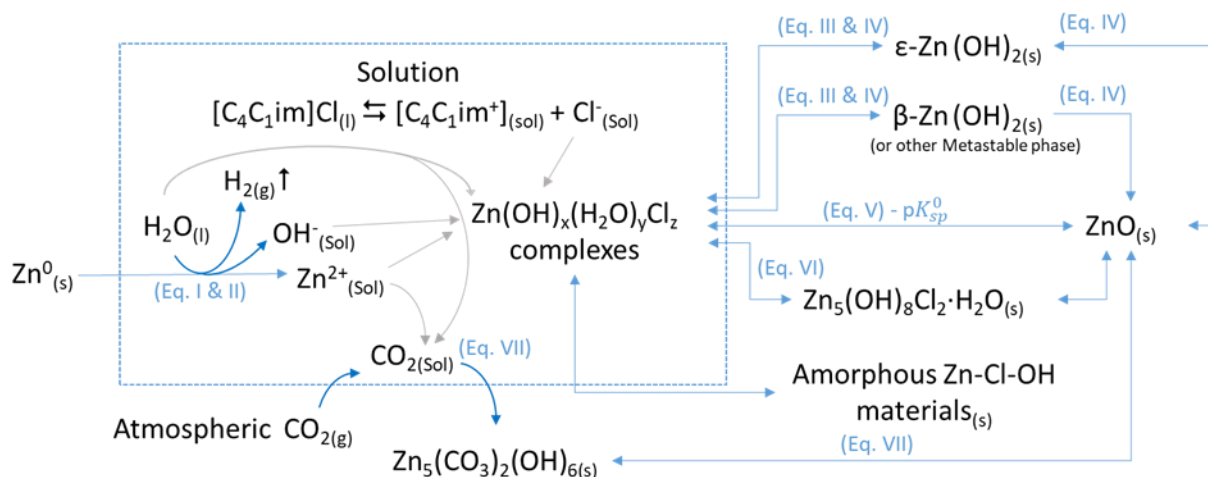
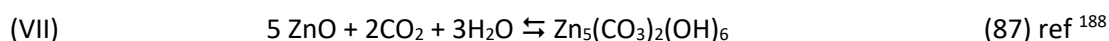
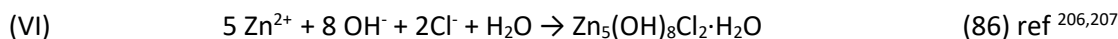
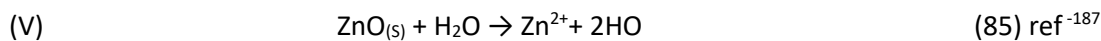
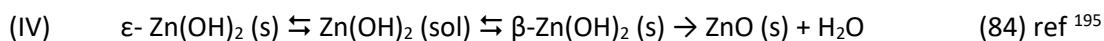
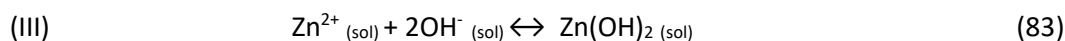
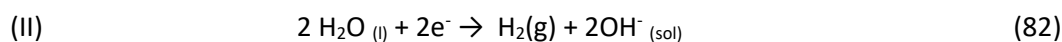
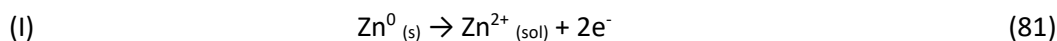


Figure 64. General conversion paths of metallic zinc into ZnO in $[C_4C_1im]Cl$ /water systems. Equations in the scheme are not balanced (*vide infra* Eqs. 81-87). The predominant path and species formed will depend on the temperature and water content. Published by The Royal Society of Chemistry ¹⁶⁹.



3.5.5 Anion effect on IL-induced corrosion: $Cl^-/[NTF_2]^-/[HSO_4]^-$

The mass change rate (MCR) of different metals exposed to dry ILs with different anions at 70 °C are shown in Figure 65.

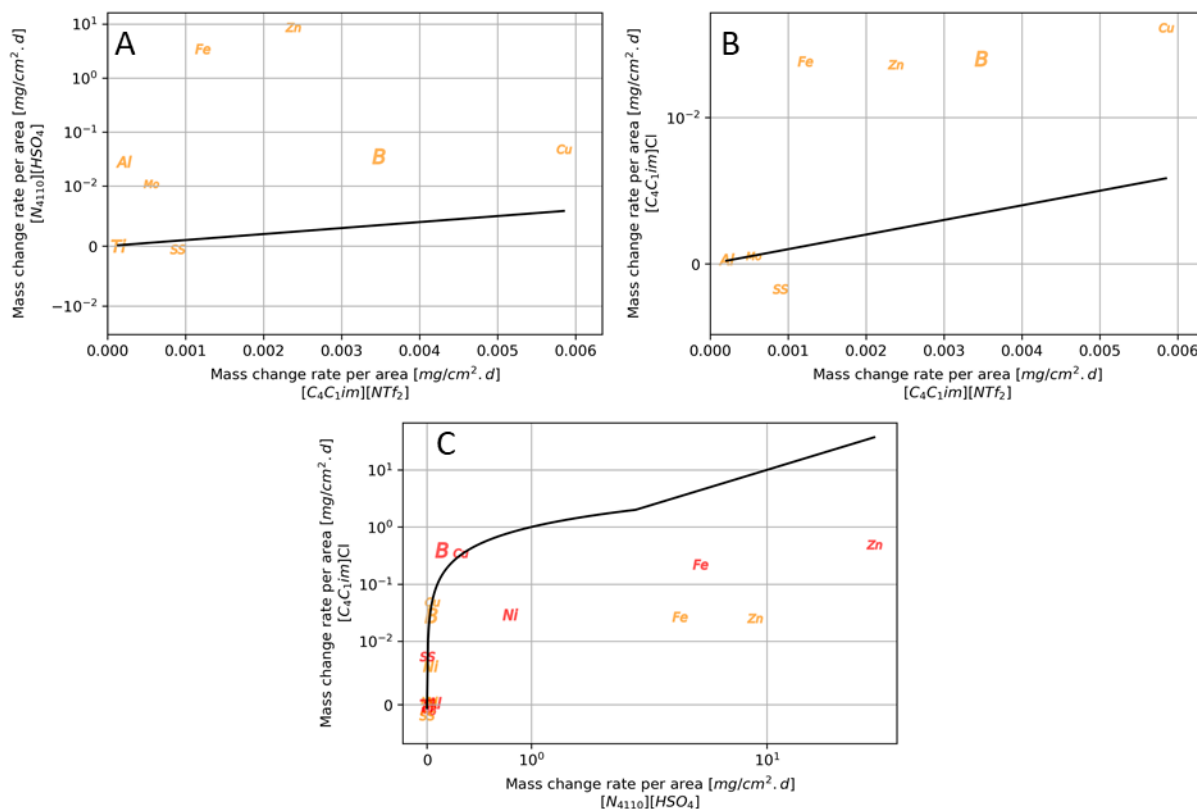


Figure 65. Effect of the anion on the corrosion rate of metals exposed to dry ILs. Orange = 70 °C and red = 120 °C. Metals are represented by their chemical symbols, while “B” and “SS” are used for brass and 304 SS respectively. The black line corresponds to iso-MCR.

As $[C_4C_1im][NTf_2]$ is a weakly coordinating IL, it would be expected that metals exposed to this IL will experience lower MCRs than when exposed to other ILs, such as $[N_{4110}][HSO_4]$ or $[C_4C_1im]Cl$. This was the observed result for all metals except for 304 SS, which had a higher MCR in $[C_4C_1im][NTf_2]$ compared to the MCR in the other ILs (Figure 65A/B).

The higher CR of 304 SS in $[C_4C_1im][NTf_2]$ is an unexpected result given that the pure metals in the alloy (Fe and Ni) are all more prone to corrode in $[N_{4110}][HSO_4]$. There are two possible explanations for this phenomenon. Whether corrosion products are forming and depositing in ILs other than $[C_4C_1im][NTf_2]$ or chromium is being leached selectively from 304 SS at a higher rate. However, no metals were found by XRF (detection limit 1 ppm) in the IL after the immersion test of 304 SS in $[C_4C_1im][NTf_2]$ (section 3.5.2.3). This result is consistent with observations on CS AISI 1018, that show higher CR in $[C_4C_1im][NTf_2]$ than $[C_4C_1im]Cl$ explained in section 3.5.2.5^{185,186}.

Cu, brass, Zn and Fe are systematically more prone to corrosion in other ILs than $[C_4C_1im][NTf_2]$ (Figure 65A/B).

Al and Mo have the same MCRs in the AIL but increases in $[N_{4110}][HSO_4]$ (Figure 65A/B). Finally, Ti has a negligible MCR in all these systems (Figure 65A/B).

When comparing the MCR in $[C_4C_1im]Cl$ and $[N_{4110}][HSO_4]$, most of the metals follow the iso-MCR curve (Figure 65C). Zn and Fe have higher MCR in $[N_{4110}][HSO_4]$ due to the acidic protons. At 120 °C, Ni has a higher MCR in $[N_{4110}][HSO_4]$ forming a greenish material. Brass at has a slightly higher MCR in $[C_4C_1im]Cl$ than in $[N_{4110}][HSO_4]$.

3.5.6 Cation effect on IL-induced corrosion: protic Vs. aprotic ILs

Figure 66 shows the results for the MCR metals exposed to $[HC_1im]Cl$ vs. $[C_4C_1im]Cl$. In general, the MCR in the PIL is higher than in the AIL, except for Al and Mo.

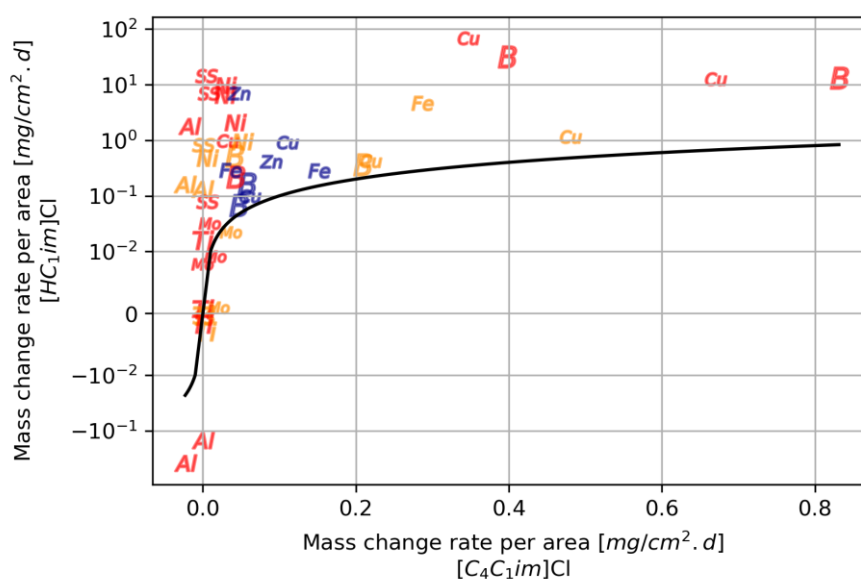


Figure 66. MCR of metals exposed to $[HC_1im]Cl$ vs. MCR of metals exposed to $[C_4C_1im]Cl$. Blue = 20 °C, orange = 70 °C and red = 120 °C. Metals are represented by their chemical symbols, while "B" and "SS" are used for brass and 304 SS respectively. The black line corresponds to iso-MCR.

Al is a type-2 metal as it gains mass in $[C_4C_1im]Cl$ /water mixtures at high temperatures. The MCR of Mo is only slightly higher in the PIL, behaving like a type-1 metal in these systems. The reason for this increase in the MCR of samples exposed to $[HC_1im]Cl$ can be explained by the presence of the acidic proton, which can act as an oxidizing agent. Also, $[HC_1im]Cl$ can decompose at high temperatures to form HCl, which is an oxidising agent. Additionally, as discussed in section 3.2.7, the longer the alkyl chain in the cation of an IL, the higher its corrosion inhibition efficiency, therefore one would expect higher MCR in $[HC_1im]Cl$ than $[C_4C_1im]Cl$.

3.5.7 Anion effect on IL-induced corrosion - protic ILs

The effect of the anion Cl^- vs. $[HSO_4]^-$ on the MCR of metals exposed to PIL is shown in Figure 67, where it can be seen that there is no systematic trend.

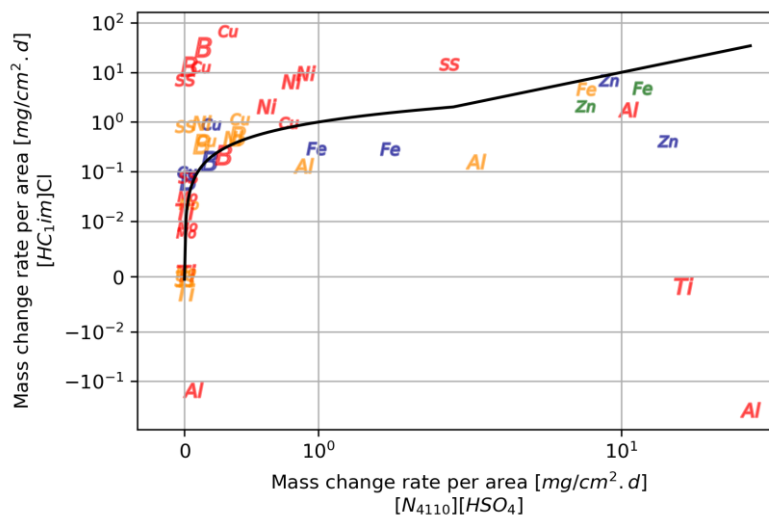


Figure 67. MCR of metals exposed to $[\text{HC}_1\text{im}]\text{Cl}$ vs. MCR of metals exposed to $[\text{N}_{4110}][\text{HSO}_4]$. Blue = 20 °C, green = 45 °C, orange = 70 °C and red = 120 °C. Metals are represented by their chemical symbols, while “B” and “SS” are used for brass and 304 SS respectively. The black line corresponds to iso-MCR.

The corrosion behaviour of Mo is similar in both ILs. For Al, Ti, Fe and Zn, the attack is more pronounced in $[\text{HSO}_4]^-$ than Cl^- . Fe and Zn are particularly sensitive to acidic media, which explains the high MCR of these metals in $[\text{N}_{4110}][\text{HSO}_4]$. In general, Ti has excellent corrosion resistance in all the systems except in solutions of $[\text{N}_{4110}][\text{HSO}_4]$ 98 mol% at 120 °C, which can completely dissolve the metal.

Cu, is the only metal, tested in the work, with a positive standard reduction potential, which explains its excellent corrosion resistance in $[\text{N}_{4110}][\text{HSO}_4]$. However, $[\text{HC}_1\text{im}]\text{Cl}$ can completely dissolve Cu, especially in anhydrous conditions. The presence of chloride drastically enhances the MCR for Cu. The MCRs for brass, 304 SS and Ni are also higher in $[\text{HC}_1\text{im}]\text{Cl}$ than in $[\text{N}_{4110}][\text{HSO}_4]$.

These results show that there is no general trend on the MCR for metals exposed to PIL with $[\text{HSO}_4]^-$ and Cl^- anions, and that this is rather a metal-dependent behaviour. It is noteworthy that the comparison of the anions is not completely fair as the cation moiety is not identical in both ILs. The anion present in an IL can have a dramatic effect in its properties, for example, $[\text{C}_4\text{C}_1\text{im}][\text{NTf}_2]$ is hydrophobic while $[\text{C}_4\text{C}_1\text{im}]\text{Cl}$ is hydrophilic. Therefore, it is expected that the cation will have a minor effect on the corrosion behaviour on these systems, and even if the values might not be the same for $[\text{HC}_1\text{im}]^+$ and $[\text{N}_{4110}]^+$, the trends observed should be the same. However, the effect on the cation (aromatic vs. aliphatic) on the corrosion behaviour of metals exposed to these PILs cannot be ruled out in the absence of experimental data. Therefore, performing the experiments with $[\text{HC}_1\text{im}][\text{HSO}_4]$ and/or $[\text{N}_{4110}]\text{Cl}$ is necessary to reach a definitive conclusion on the effect of the cation.

3.5.8 Temperature effect on IL-induced corrosion

The effect of temperature on the MCR for metals exposed to ILs is given in Figure 68. Despite the fact that it would be expected that the MCR will increase with temperature, this was not the case for all systems.

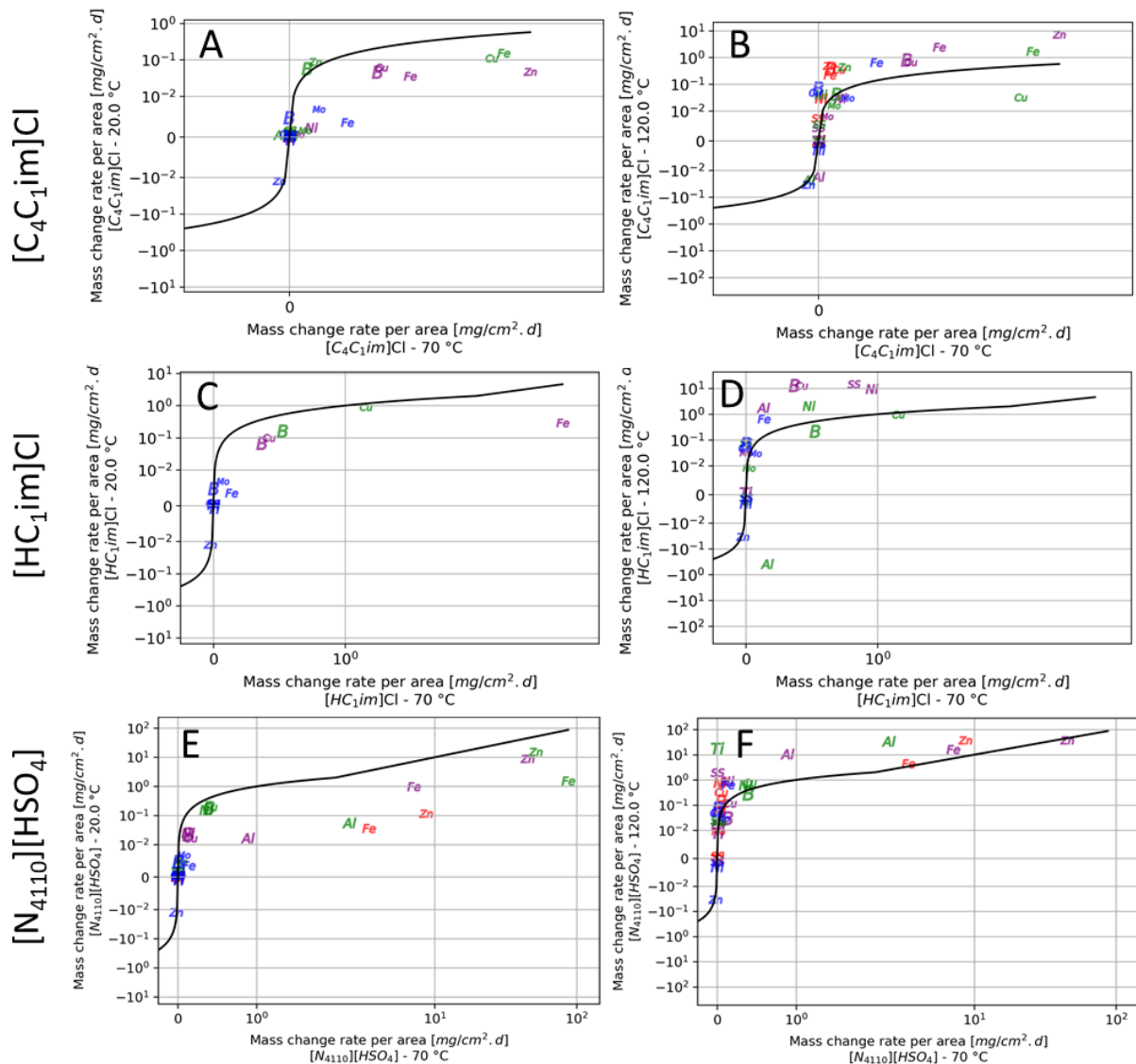


Figure 68. MCR of metals exposed to corrosive media. Left figures (A, C and E): MCR at 20 °C vs MCR at 70 °C. Right figures (B, D and F): MCR at 120 °C vs MCR at 70 °C. Red = dry IL, purple = 75 mol%, green = 98 mol% and blue = water. The black line corresponds to iso-MCR.

In $[C_4C_{1im}]Cl$, the MCR increases with temperature (or remains the same within the experimental error) for all systems except for Al (metal type-2) and Cu, which at 98 mol%, has a higher MCR higher at 70 °C than 120 °C (Figure 68A/B). A similar situation takes places in $[HC_{1im}]Cl$, were Al and brass samples exposed to 98 mol% solutions have a higher MCR at 70 °C than 120 °C (Figure 68C/D). A possible cause for the reduction of MCR with increasing temperature might be the fast formation of protective passive layers. Another possible explanation is a reduction of the solubility of oxygen and CO_2 in the ILs due to increasing

temperature. If these species are responsible for the corrosion process, then a temperature increase would lead to a reduction in the MCR.

For the $[N_{4110}][HSO_4]$, all systems had a higher corrosion rate at higher temperatures (Figure 68E/F).

3.5.9 Water effect on IL-induced corrosion

The effect of water on the corrosion rates of metals exposed to PIL and AIL is shown in Figure 69.

In $[C_4C_{1im}]Cl$, the addition of water to the IL increases the corrosion rate for all systems except for Cu and Brass at 120 °C (Figure 69C/F). In the presence of water, most metals are close to the iso-MRC except for Fe, Cu, Zn and brass. The maximum MCR for Fe happens at 98 mol% at 70 °C and at 75 mol% at 120 °C. Cu has similar behaviour. Brass and Zn showed a clear maximum MRC at 75 mol% (Figure 69I). These results can be misleading as Zn and brass are type-3 metals, meaning that deposition products might remain in the surface, underestimating the MCR. Al gains mass when exposed to water solutions of this IL (type-2 metal).

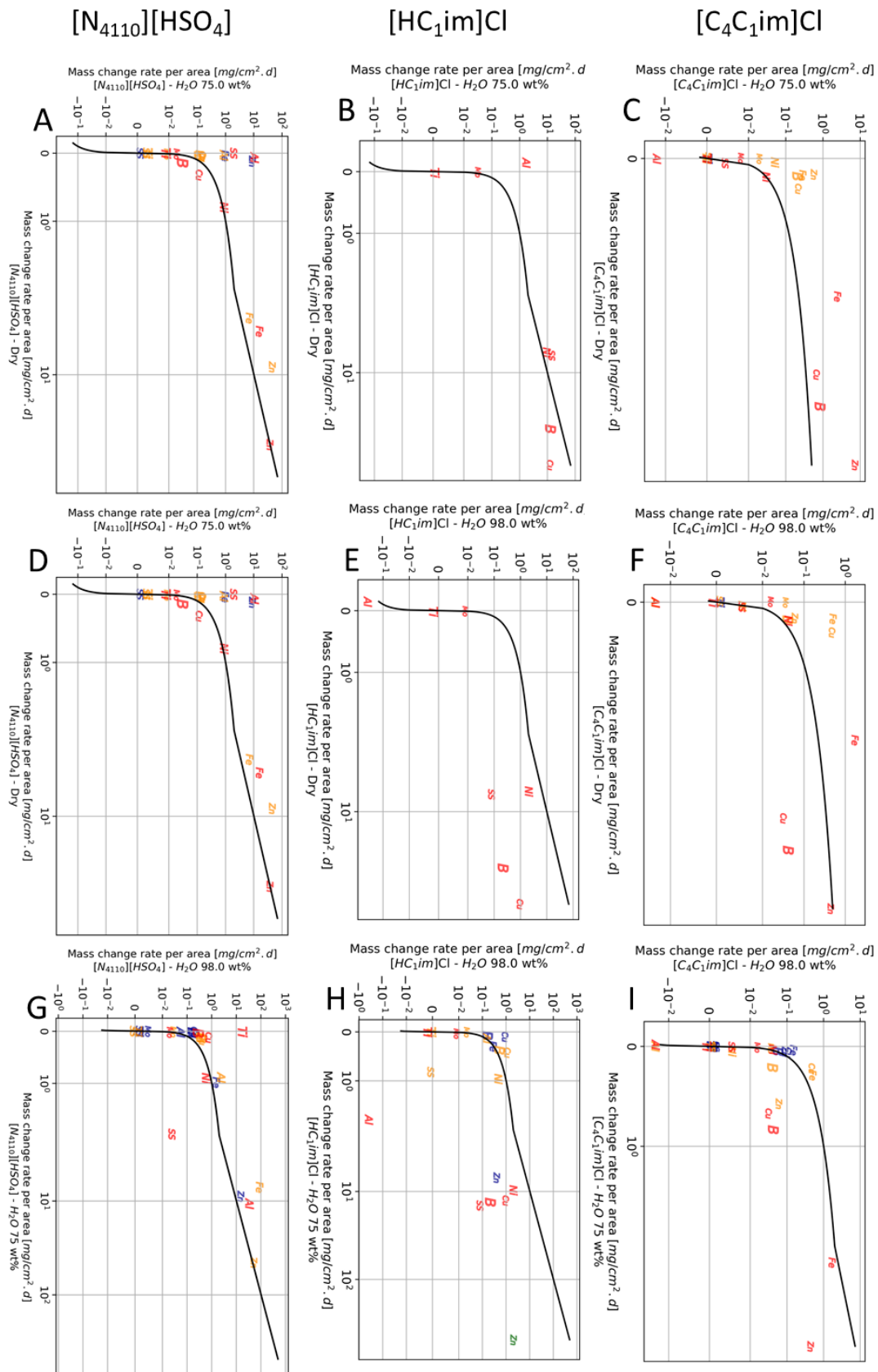


Figure 69. MCR of metals exposed to corrosive media. Left figures MCR at 75 mol% vs MCR at dry conditions. Centre figures MCR at 98 mol% vs MCR at dry conditions. Right figures MCR at 98 mol% vs MCR at 75 mol%. Blue = 20 °C, green = 45 °C, orange = 70 °C and red = 120 °C. The black line corresponds to iso-MCR.

The situation in $[\text{HC}_{1\text{im}}]\text{Cl}$ is completely different. For example, dry $[\text{HC}_{1\text{im}}]\text{Cl}$ is extremely corrosive to copper and brass at 120 °C (Figure 69B/E). Ni and 304 SS are more prone to corrosion in dry IL than at 98 mol% (Figure 69E). Generally speaking, water acts as a corrosion inhibitor in this ILs (Figure 69H).

For metals exposed to $[\text{N}_{4110}][\text{HSO}_4]$, water acts as a corrosion promoter for all the metals tested at all conditions (within the experimental errors) (Figure 69A/D/F). At 120 °C, 304 SS experience a higher MCR at 75 mol% than 98 mol%. However, it was observed deposition of material in this system, underestimating the true MCR (type-3 metal) (Figure 69F). Ti has negligible MCR for all systems tested except at 98 mol% and 120 °C, in which it can be dissolved completely (Figure 69F).

These results clearly show that water can be either a corrosion inhibitor or corrosion promoter depending on the metal, IL and temperature.

3.5.10 Semiquantitative-categorization method

The classification system for all the metals and ILs studied in this work is summarised in Table 20.

Table 20. Summary of the classification system by metals and ILs (section 3.4).

Metal	$[\text{C}_4\text{C}_1\text{im}]\text{Cl}$	$[\text{HC}_{1\text{im}}]\text{Cl}$	$[\text{N}_{4110}][\text{HSO}_4]$	$[\text{C}_4\text{C}_1\text{im}][\text{NTf}_2]$	Water
Aluminium	0 2	0 2 3	0 3	0	2
Copper	4	4	4	3	2 4
Iron	0 3 4	4	4	0	3
Molybdenum	1	1	1	1	1
Nickel	0	4	0	4	0
Titanium	0	0	0	4	0
Zinc	0 3	4	0	4	3
Brass	0 3 4	4	0	4	3 2 4
SS304	0	0	4	3 4	0

Type 0: Negligible mass change rate without visual changes. All the metals, except for Mo, experience this type of behaviour under certain conditions. Most of the metals exposed to $[\text{C}_4\text{C}_1\text{im}][\text{NTf}_2]$ fall under this category except for Mo, Cu and brass. $[\text{C}_4\text{C}_1\text{im}]\text{Cl}$ and $[\text{N}_{4110}][\text{HSO}_4]$ have the highest occurrence of type-0 behaviour while $[\text{HC}_{1\text{im}}]\text{Cl}$ and DI water present the lowest.

Type-1: Negligible mass change rate with visual changes. Mo is the only type-1 metal observed in this work, as it forms dark layers that could not be characterised by any of the analytical techniques used in this work. To properly study such layers, other methods such as SIMS or XPS are needed.

Type-2: Active corrosion with deposition of material with overall mass gain. Al was the metal that clearly experienced this type of behaviour in all water-soluble ILs except for $[N_{4110}][HSO_4]$, in which active dissolution takes place. Cu and brass samples also experienced a net mass gain when exposed to DI water. This group of metals can also be employed for particles and composite fabrication via the Oxidative Ionothermal Synthesis (OIS) (section 3.6).

Type-3: Active anodic dissolution with deposition of material with overall mass loss. Zn and brass exposed to $[C_4C_{1im}]Cl$ /water mixtures exhibit the formation of many structures which remain firmly attached to the surface. Aluminium is mainly a type-2 metal, but under certain conditions in PILs, the samples experienced a net weight loss and were classified as type-3. This is probably due to increased solubility of the corrosion products in the corrosion media. Fe exposed to $[C_4C_{1im}]Cl$ /water mixtures showed the formation of corrosion products firmly attached to the surface, under certain conditions. Cu and brass experienced this behaviour in $[C_4C_{1im}]Cl$. Finally, 304 SS, also experienced this behaviour in $[N_{4110}][HSO_4]$ under certain conditions. Metals of this type are excellent candidates for the synthesis of hybrid materials and composites through the OIS method described in detail in section 3.6.

Type-4: Active anodic dissolution without visual changes with overall mass loss. This behaviour was observed for all metals except Al and Mo. It is more common in PILs. The growth of corrosion products on the surface of the metal after exposure to corrosive media were observed for some metals, such as Fe. However, these particles were loosely attached, and were easily removed during the post washing step. Therefore, such systems were classified as type-4. These layers do not offer protection against corrosion. This group of metals might be used under some conditions to produce particles via the OIS. However, as particles do not remain firmly attached to the surface, the production of composite materials is unlikely.

The S-suffix: Active corrosion with passivation. Not observed in this work.

Regarding the different surface analysis techniques, it has been observed the following:

- SEM/EDX: This is a very effective technique to observe morphological changes on the surface of metals as well as chemical composition changes. It is efficient for all types except for type-0, as samples exposed to corrosive media cannot be distinguished from untreated samples.

- XRD: This is a powerful technique to identify crystalline corrosion products but can only be applied for metals type-2 and type-3, where corrosion products are deposited on the surface. Metals type-1 form a very thin layer that was not detectable by conventional XRD measurements; therefore, other experimental techniques are needed for this type of systems.

3.6 The Oxidative Ionothermal Synthesis (OIS)

It was observed that some metals and alloys, such as Zn, Cu, Fe and brass, can be oxidized in ILs and water solutions to yield layers of nano- and micro-sized particles with controlled morphology. It has been hypothesised that this principle could be applied for the synthesis of metal oxides, such as zinc oxide (ZnO), and other materials. As shown in section 3.5.4, Zn oxidises in aqueous [C₄C₁im]Cl to form a diversity of particles with different chemistries, shapes and sizes, all of which can be controlled by adjusting the process conditions, such as temperature, exposure time and water concentration.

A high-level assessment of the Oxidative Ionothermal Synthesis (OIS) concept for ZnO production had been performed. However, as this concept is at an early stage of development, and as such, many assumptions were made to evaluate a large-scale process based on this technology, it was decided not to include it in the main text of this thesis, rather it was kept in the appendices (Appendix 7). In the following section, a summary of the main findings is presented.

3.6.1 Zinc oxide (ZnO)

ZnO is a multifunctional material due to the breadth of physical and chemical properties, including high chemical stability, high electrochemical coupling coefficient, a broad range of radiation absorption and significant photostability²⁰⁸. These favourable properties, along with their low-cost, low toxicity, high biocompatibility and high biodegradability of ZnO based composites²⁰⁹, have encouraged the development of an ever-increasingly wide range of applications, *e.g.* catalysis, optoelectronics, sensors, transducers, energy conversion, solar cells, rubber, cosmetics, electronics, pharmaceuticals and for medical sciences^{169,210}. Although it occurs naturally as the mineral zincite, most zinc oxide is produced synthetically²¹¹.

3.6.2 Industrial ZnO production

Despite the fact that there are a great diversity of synthesis methods for ZnO nanomaterials reported in the scientific literature, the vast majority of them have no actual commercial interest, mainly for their production cost, product quality or due to their difficulty to be scaled-up ²¹¹. Some of these methods are discussed in detail in Appendix 7. At industrial scale, pyrometallurgical methods are the main production processes, namely the French (or Direct) process and the American (or Direct) process ²¹¹. There are also hydrometallurgical (wet chemistry) methods, which can be used to obtain nano ZnO ²¹¹. Each process produces grades of ZnO with different purities and properties and hence different applications ²¹¹. These processes are described in detail in Appendix 7. A brief description of them is given below:

French Process: This process employs metallic zinc as starting material, which is vaporized at high temperatures (>1000 °C) and oxidized with atmospheric air (zinc melts at 420 °C and boils at 907 °C) ²¹¹. In a typical plant, the ZnO powder formed by combustion enters a cooling duct before it is collected in a bag-house at a temperature below 100 °C. After collection, the powder is fractionated according to particle size using vibrating hopper sieves ²¹¹. The French process is widely considered to be the fastest and most productive industrial method to produce ZnO, however, the product from this process is not optimised for all applications. The quality of the ZnO depends on the precursors used ²¹¹. For instance, ZnO produced by the French process can have high purity (>99%) if high purity zinc is used as a feedstock. Other zinc-containing feed materials such as galvanizer's dross, die-casting alloys or zinc ash may also be used for less demanding applications and are becoming increasingly popular due to their lower cost ²¹¹. However, if metal residues are to be used then various liquid and/or vapour-phase separation techniques may be needed prior to zinc vaporization and oxidation to eliminate Cd, Pb, Fe, and Al ²¹¹.

American Process: This process makes use of a feedstock containing a mixture of oxidized zinc-containing (ore) materials, which is reacted with a carbonaceous reducing agent at elevated temperature to produce vaporized metallic zinc ²¹¹. The zinc vapour moves into a combustion chamber where it is re-oxidized in a similar manner to that used in the French process to produce ZnO. Finally, the oxide is collected in a bag-house ²¹¹. A variety of zinc-containing raw materials can be used, including zinc ores (oxidic or sulfidic), zinciferous materials and flue dusts, lead blast furnace slags, mill slimes, electrolytic-zinc leach residues, skimmings from casting furnaces, off-grade zinc oxides and zinc ash from hot dip galvanization ²¹¹. Lead and chloride can be present in zinc ash and must be removed prior to the manufacture of ZnO ²¹¹. Generally, the ZnO obtained *via* de American process has lower quality and purity compared

to that produced by the French process, and may contain traces of lead, cadmium and sulfur. The reason for this is the lower purity of the feed material and the carbonaceous reductant ²¹¹. In general, direct process ZnO is used in the paint and ceramic industries rather than for rubber ²¹¹.

Wet chemical methods: Zinc oxide produced *via* wet chemical processes can be categorized into three main groups ²¹¹:

1. ZnO produced as a by-product of the production of sodium dithionate ²¹¹.
2. ZnO made by the reaction of a zinc salt such as zinc sulfate and a base such as ammonium or sodium hydroxide, followed by calcination or drying of the Zn(OH)₂ or ZnO produced ²¹¹.
3. ZnO produced by a two-step reaction of zinc salts and carbon-containing bases such as sodium carbonate, ammonium bicarbonate or urea followed by calcination or alkaline treatment of the resultant basic zinc carbonate ²¹¹.

Other wet chemistry methods (discussed in Appendix 7) have been developed but have limited industrial applications ²¹¹.

The main characteristics of industrial processes for ZnO production are summarized in Table 21.

Table 21. Summary of main processes for ZnO production

Process	Precursor	Process conditions	Product	Remarks
American Process (Direct Process)	Zinc concentrates (ore) and oxidized zinc-containing materials.	High temperatures (>1000 °C) ²¹¹ .	Low purity than the French Process may contain traces of lead, cadmium and sulfur. The specific surface area of direct process ZnO is generally 1–3 m ² /g ²¹¹ .	Requires the use of a carbonaceous reducing agent ²¹¹ .
French Process (Indirect Process)	Metallic zinc and secondary zinc sources (purification required).	High temperatures (>1000 °C) ²¹¹ .	ZnO can have high purity (>99%). Particle morphology is not controlled; therefore, the product cannot be used on some applications. The particles are generally nodular in shape and the individual primary ZnO crystallites are 30–2000 nm in size. The surface area of French process ZnO is generally 3–5 m ² /g but can reach 12 m ² /g ²¹¹ .	Main production method for bulk ZnO ²¹¹ .
Wet Chemistry Methods	Zinc salts (<i>e.g.</i> ZnSO ₄ and Zn(NO ₃) ₂).	Synthesis temperature generally below 100 °C ²¹¹ .	Good control of particle morphology. specific surface area (>40 m ² /g) ²¹¹ .	Typically requires precipitation agents (bases) and calcination at temperatures between 350 - 600 °C ²¹¹ .

Process	Precursor	Process conditions	Product	Remarks
OIS Process	Metallic zinc and zinc-containing alloys (brass). Other secondary zinc sources need to be validated experimentally.	Synthesis temperature generally below 120 °C.	Different morphologies were observed (e.g. nanorods and 3D flowers Figure 58), ranging from nano- to micro-sized particles.	Water is consumed in the oxidation process with hydrogen production. Hydrogen produced could be used as fuel in a large-scale process. It is believed that the IL can be recovered and recycled, but this awaits experimental proof.

3.6.3 OIS process – Products

Emerging technologies are being developed rapidly as scientists and engineers continue to discover and use materials that exhibit novel or enhanced properties that improve performance over conventional products and processes ²¹². These innovative materials are often referred to as advanced materials ²¹³. Even though this term has become more commonly used in recent years as a descriptor for nano-based materials, it covers a wide range of materials with engineered properties created through the development of specialized processing and synthesis technology. Advanced materials include ceramics, high value-added metals and metal oxides, electronic materials, composites, polymers, and biomaterials ^{212,213}.

Because the diverse properties of zinc oxide, both chemical and physical, bulk ZnO (conventional grades) is widely used in a broad range of applications and products, including, tyres, ceramics, pharmaceuticals, agriculture, paints, electronics and cosmetics ^{210,211}. Advanced ZnO particles, such as nanomaterials, have properties that outperform the ones of conventional ZnO grades, leading to product improvement and may also allow the development of new technologies.

Examples of how advanced materials can improve existing products is the case of ZnO for tyre manufacturing, which is currently the sector consuming most of this material (~58% of global ZnO)²¹⁴. Przybyszewska *et al.* showed that rubbers produced with ZnO nanoparticles had better mechanical properties than those obtained by using commercial micro-sized ZnO grades ²¹⁵. This means that for the same rubber quality, the amount of ZnO could be reduced by almost 40% if advanced ZnO is used ²¹⁵. This is significant as it would not only reduce the cost of the final product (if advanced ZnO could be produced at bulk scale at low cost), but improve the sustainability of the tyre as less non-renewable materials (Zn) are being used (resource depletion mitigation, section 1.2.1).

Examples of emerging technologies based on advanced ZnO include biomedical and therapeutic applications, such as anticancer ^{216,217} and antibacterial ^{218,219}. There are also

several applications in catalysis, such as solar photocatalysts to remove Persistent Organic Pollutants (POPs) ²²⁰. ZnO nanoparticle arrays have been used in optical biosensors ²²¹, electrical biosensors (*e.g.* for cardiac biomarker detection ²²²) and for gas sensing applications ²²³. In electronic and optoelectronic devices, there are several studies on ZnO as an alternative to gallium nitride (GaN) based compounds for fabrication of UV/blue light emitting diodes (LEDs) ²²⁴. At the time of writing, there were no commercial ZnO LEDs due to some limitations on the development of p-type ZnO, but it has been speculated that in the coming years there may be a breakthrough in p-doping of ZnO which will make possible the replacement of GaN as the material of choice for making short-wavelength light emitters and detectors ^{224,225}. ZnO-based nanomaterials had also been used for lithium-ion, lithium–sulfur batteries and other energy storage devices, and despite the fact that ZnO-based technologies are not commercially available yet, it is believed that ZnO will play a major role in the next generation of batteries because of its reduced cost, reduced environmental impact compared to other metals, high availability and potential to improve battery performance ²²⁶.

It has been shown that particle morphology has an important effect on the performance of all of the above applications, which require particles with a high degree of homogeneity in terms of particle habit and size. Despite the fact that advanced ZnO can improve product quality and enable those new technologies (and possibly others), the methods to produce them are expensive or difficult to scale-up, and therefore, the market still dominated by bulk ZnO, produced *via* the pyrometallurgical processes (*i.e.* the French and American processes). In a quest to produce advanced ZnO, a diversity of synthetic routes are available in the scientific literature ^{210,211}. It was observed that ZnO with different morphologies formed over the surface of metallic zinc (and brass) exposed to [C₄C₁im]Cl solutions. This principle can be used to produce nano-ZnO arrays on metallic substrates which might have applications in sensing and electronic devices. Moreover, the particles grown over the metal could be removed by mechanical means to produce ZnO powders. As this morphological control cannot be achieved *via* the pyrometallurgical processes, it would be interesting to explore the properties of the particles formed *via* the OIS process (ZnO and other metal oxides and hydroxides) and their applications. However, the quality of the particles obtained through the OIS process compared to other methods for different applications still awaits experimental validation.

3.6.4 OIS process – Sustainability considerations

In this section, the OIS process will be compared to the main industrial methods for ZnO production in terms of sustainability. This assessment is performed according to the green

chemistry and engineering principles mentioned in section 1.2.3. The analysis for the OIS process is based on the extrapolation of the experimental results obtained in section 3.5.4 to industrial scale, and as such, it should be considered preliminary until the OIS process is demonstrated at a larger scale.

3.6.4.1 Feedstocks and waste generation

Considering the battery limits of each of the main industrial processes for ZnO described previously, their typical feedstocks are Zn-containing ores for the American process, metallic Zn for the French process, and Zn salts for the wet chemistry methods. The typical conversion paths towards ZnO are depicted in Figure 70.

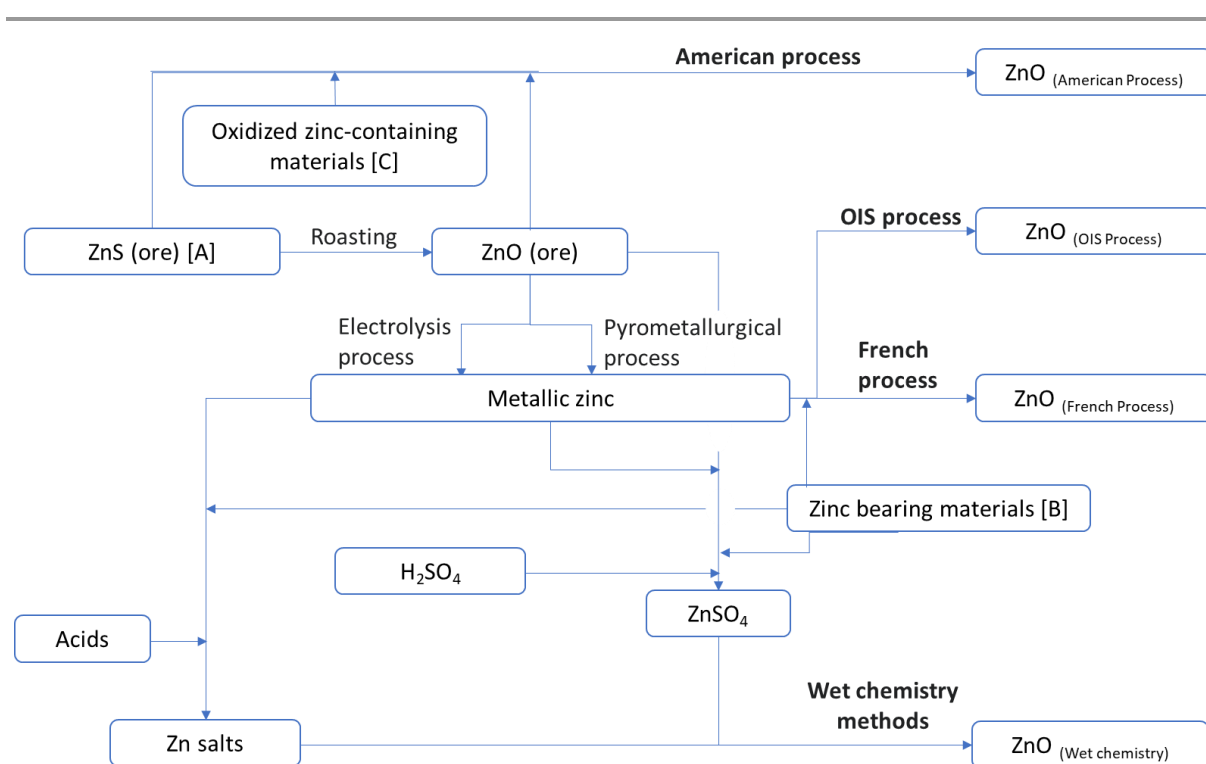


Figure 70. Schematic of the main industrial processes for ZnO production.[A] Zinc ore is typically zinc sulfide obtained by concentrating sphalerite. [B] Galvanizer's dross, die-casting alloys or zinc ash²¹¹. [C] Zinc ores (oxidic or sulfidic), zinciferous materials and flue dust, lead blast furnace slags, mill slimes, electrolytic-zinc leach residues, skimmings from casting furnaces, off-grade zinc oxides and zinc ash from hot dip galvanization²¹¹.

Processes using pure metallic zinc will be more sustainable in terms of atom economy, less hazardous chemical usage and waste generated, if the analysis excludes the processes to produce the zinc from the ores. With this regard, the French process and the OIS process would be better than the others if pure zinc is used. In the French process, the oxidizer is atmospheric oxygen, therefore this process has the best atom economy compared to the others and generates virtually no wastes if pure zinc is used²¹¹. In the OIS process, the oxidizer is water and hydrogen is produced as a by-product. It is noteworthy that it is technically possible to

recover this water in waste heat recovery units working in full condensing mode to minimize the water consumption of the process, and therefore increasing the environmental credentials²²⁷. If secondary zinc sources are used for these processes, the impurities present in the feedstock will become by-products and potential waste²¹¹.

The American process uses mainly zinc ores (and other materials containing oxidized forms of zinc), which can contain traces of hazardous metals (*e.g.* Cd and/or Pb) that would need to be dealt with²¹¹. Additionally, it uses carbon-based materials to obtain zinc vapour. The carbonaceous reducing agents are oxidized generating CO/CO₂, and therefore increasing the GHG emissions for this process²¹¹.

Typical wet chemical methods, including methods in ILs (Ionothermal methods), use zinc salts and a precipitator to produce zinc hydroxide, which is in turn calcinated at high temperature (350-600 °C) to obtain ZnO²¹¹. These processes will have the lowest carbon economy and will generate the maximum quantity of by-products which potentially will become waste. The anion of the zinc salt (*e.g.* Cl⁻, NO₃⁻, [CH₃COO]⁻, [SO₄]²⁻ or [CO₃]²⁻) and the cation of the precipitator (Na⁺ for NaOH, NH₄⁺ for NH₄OH) will form residual salts, that accumulate in the reaction medium or washed out with water. The possibility of valorising the residual salts form will depend on the market and the recovery cost, but most likely they will become a waste, with the environmental implications, and increasing waste management cost.

In light of the above, and the green chemistry principles of prevention, atom economy and less hazardous chemical syntheses (section 1.2.3), it appears that when pure zinc is used, the OIS process can have a similar environmental footprint in terms of waste generated compared to the French process if the IL can be recovered and reused. At this stage it is unclear what would happen if secondary zinc sources are used in the OIS process. Compared to the American process and other wet chemistry methods using zinc salt as metal precursors and bases, the OIS process has a clear advantage in terms of by-product/waste generation.

3.6.4.2 Energy consumption and CO₂ emissions

The pyrometallurgical processes, *i.e.* the French and American processes, consume a large amount of energy to melt, vaporize and overheat zinc vapours at temperatures higher than 1000 °C²¹¹. This energy is typically supplied by burning fossil fuels (natural gas) leading to a large amount of CO₂ being released to the atmosphere. This is obviously not a sustainable approach to produce ZnO, as it is not aligned with the global efforts to reduce the CO₂ emissions as mentioned in section 1.2.2. Moreover, according to the Green Chemistry principle

of “design for energy efficiency” and to the Green Engineering principles 1 “Inherent rather than circumstantial” and 4 “maximize mass, energy, space, and time efficiency”, energy should be minimized (section 1.2.3).

The energy consumption for the OIS process was estimated and compared with the energy consumption of the French process, which is the main industrial method for ZnO production. The electrical energy consumption for the OIS process has been estimated between 0.228-0.286 GJ/ton ZnO (63.2-79.4 kWh/ton ZnO) and no thermal energy consumed if the hydrogen produced in the process is used as fuel. The thermal energy consumption for the French Process ranges from 3.5 GJ/ton ZnO for a very performant system (BURNS 3-Crucible Vaporizer) to 13 GJ/ton ZnO for typical multi-crucible (200 L) vaporizers, as reported by a major ZnO production furnaces manufacturer BURNS ²²⁸. This thermal energy is supplied by burning natural gas. Electrical consumption for the French Process has been assumed negligible for the comparison. Based on these numbers, it can be seen the magnitude of the energy savings, which are at least 1 order of magnitude lower than the French process.

The CO₂ emissions per unit of energy will depend on the energy source. The Department for Business, Energy and Industry Strategy ²²⁹ recommends the following conversion rates: Natural Gas – 0.20428 kgCO₂e/kWh and UK Grid Electricity – 0.2556 kgCO₂e/kWh, other organisations may use other conversion factors. From the total energy consumption, the total equivalent CO₂ emissions per ton of ZnO was calculated. The results show an important reduction of the CO₂ emissions, which were estimated in the range of 199 - 738 kgCO₂e/ton ZnO for the French Process and in the range of 16-20 kgCO₂e/ton ZnO for the OIS Process, which could be further reduced once the process is optimized. This represents a significant improvement for sustainability purposes that would off-set the water consumption of the OIS process and the wastewater stream containing traces of IL (if any). A more detailed environmental assessment should be performed to quantify both effects. Moreover, it should be highlighted that the energy consumption for the OIS process is mostly electrical power, as such, if green electricity is used, the CO₂ emissions from this process would be quasi-eliminated.

Wet chemistry methods will often produce zinc hydroxide or zinc carbonates, which needs to be calcinated at temperatures between 350 - 600 °C to obtain the ZnO ²¹¹. This is an improvement from the pyrometallurgical processes, but the calcination step will still generate great quantities of CO₂ if fossil fuels are used.

A more sustainable approach will be to produce the synthesis at conditions that will yield directly ZnO without the formation of the hydroxide (or other chemical products) that would

require calcination at high temperatures. This can be achieved by some hydrothermal methods (method 2, 4 and 6 in section A7.4.2 – Appendix 7) and the OIS process.

In summary, in terms of energy consumption and CO₂ emissions, the OIS process, and hydrothermal methods leading to ZnO, would be the most sustainable. If calcination is required, the OIS process will be similar to other wet chemistry processes, but better than the pyrometallurgical process. Moreover, process safety is improved if the synthesis is carried out at low temperatures and without the need of dangerous chemicals such as bases or acids typically used in the wet chemistry methods (Green chemistry principle of “Inherently Safer Chemistry for Accident Prevention” section 1.2.3).

3.6.5 OIS process – Economic potential

A high-level techno-economic analysis was performed to establish the capital investment cost (CAPEX) and operating cost (OPEX) for the OIS process compared to the industry standard, the French Process. As the OIS concept is at early stage of development and many assumptions were made for the CAPEX and OPEX estimation, it was decided not to include this material in the main text of this thesis, but rather presented it in the appendices (Appendix 7).

According to a major ZnO production furnaces manufacturer (BURNS²²⁸) the CAPEX for a French Process plant of 20 kton/year is around 950 \$US/ton ZnO. The overall CAPEX per ton of ZnO for the OIS process had been estimated between 884 and 1590 \$US/ton ZnO. When compared to the total CAPEX for the French Process, the value ranges between -7% and +65%. This shows that the order of magnitude of an OIS plant is comparable to the French Process. It needs to be stressed that the CAPEX estimation for the OIS process had been performed on a high-level basis and with conservative assumptions. Therefore, there is room for process optimization to further reduce the investment cost. Further, no showstoppers were identified for the scale-up of the laboratory procedure to produce ZnO *via* OIS process. A detailed discussion on the CAPEX estimation model is given in Appendix 7.

The maximum OPEX contributor for the OIS process is IL losses, assumed as 1% of the recirculating loop. This figure should be verified experimentally but it is believed that is a conservative estimate. Lowering the IL to solid ratio or implementing systems to minimize IL losses, such as re-concentration with membranes, would significantly reduce the OPEX and improve the environmental footprint of the OIS process by decreasing the amount of waste. The minimum production cost (minimum CAPEX and OPEX) for the OIS process have been estimated at 100 \$US/ton of ZnO produced vs. 83.4 \$US/ton for the French Process (based in

a highly efficient ZnO production system by BURNS), which represents a 17% production cost increase when compared to the French Process. The more pessimistic scenario leads to a production cost of 188.8 \$US/ton (maximum CAPEX and OPEX), which is a 126% more expensive than the highly efficient ZnO production system by BURNS and 4.5% more expensive compared to the performance of typical (200 L) vaporizers. Further details of the OPEX estimation is given in Appendix 7.

The production costs of the OIS system are in the same order of magnitude of the French Process but there is a clear advantage in terms of energy savings. However, with the pessimistic assumption of 1% IL losses, the savings due to energy reduction are offset by the IL losses. Nonetheless, as mentioned previously, the OIS system allows control of the particle morphology, which can improve existing products and open the door to new applications. The market price of ZnO nanoparticles with controlled morphologies is extremely high compared to bulk zinc, which can range up to 60000 \$US/ton vs. 2000 \$US/ton²¹⁴, therefore, even if the processing costs are higher for the OIS process than the French process, the increase in the value of the produced material will likely make an OIS plant economically viable. Moreover, it is expected that the CAPEX/OPEX can be further reduced after process optimization.

3.6.6 OIS process – Overall considerations

It has been shown in this work that Zn-based nano/micro materials (and other metal-based materials such as Fe, Al and Cu) can be obtained by direct oxidation of the metal in $[C_4C_{1im}]Cl$ aqueous solutions. By adjusting the water content, temperature and exposure time, the particle chemistry and morphology can be controlled. For example, not only ZnO is obtained by contacting metallic Zn with aqueous ILs, but also different species such as ϵ -Zn(OH), $Zn_5(OH)_8Cl_2 \cdot H_2O$ and $Zn_5(CO_3)_2(OH)_6$ can be obtained. These materials can be used as intermediates for ZnO nano/micro materials by calcination. It has been hypothesised that this method can be used as a viable alternative to produce ZnO (and other metal-based compounds) at large scale. Another significant finding is the fact that ZnO can be produced also by oxidation of corrosion-resistant alloys (brass), which opens the door to the use of secondary metal sources and valorisation of metallic wastes into valuable nanomaterials (circular economy and zero waste). This methodology was compared with common processes for ZnO production in terms of product quality, sustainability and economic potential, and it appears that the IOS process has economic and environmental potential (summarized in Table 22) to replace pyrometallurgical processes, and therefore, further work should be carried out to

reach a definitive conclusion about the OIS concept as a variable large-scale production method.

Table 22. Preliminary comparison of OIS process against main industrial methods for ZnO production

Process	Product		Sustainability		
	Quality	Cost	Impact of Raw Materials	Waste Generation	CO ₂ eq emissions
OIS	High	Low	Low	None/Low	Low
French	Low	Low	Low	None	High
American	Low	Low	High	Medium	High
Wet chemistry	High	High	High	High	Medium

3.7 Conclusions and future work

3.7.1 Corrosion behaviour of metals exposed to ILs

The corrosion rates measured in this study were obtained by standard weight-loss measurements. As such, these tests do not provide detailed kinetic nor mechanistic data pertaining to the anodic and cathodic processes separately. Efforts were done to explain the experimental results with established mechanisms for analogous systems, *i.e.* acids, organic and inorganics salts (Appendix 5). However, detailed electrochemical experiments are still needed to formulate the detailed mechanisms of corrosion in ILs.

Even though they are yet to be fully understood, the results obtained from this work have highlighted some interesting trends, that can be used as a reference for further analysis of the corrosion behaviour of metals exposed to ILs.

The corrosion phenomenon is extremely complex in nature and it is strongly affected by the experimental conditions. Some of the factors affecting corrosion can be summarised as follow:

- **Metal:** Generally speaking, the corrosion tendency of metal is determined by its position in the electromotive series. However, this factor is usually of minor importance, being outweighed by other effects, *e.g.* whether protective or nonprotective (oxide or other) films are formed. Also, other factors known to affect the corrosion process include the physical condition of the surface (cuts, scratches, crevices), metal composition, atomic structure, microscopic and macroscopic heterogeneities, stress (tensile, compressive, cyclic), phases (single metal vs. alloys) and/or bimetallic contacts.
- **Corrosive Media:** Chemical nature of the IL (cation and anion), concentration of reactive species (water) and impurities, pressure, temperature, velocity, abrasive particles.

- Metal/corrosive media interphase: kinetics of metal oxidation and dissolution, kinetics of reduction of species in solution, nature and location of corrosion products, film growth and film dissolution.

Moreover, the corrosion behaviour of metals in IL is system dependent, which combined with the large number of possible ILs, makes it extremely hard to generalize the corrosion behaviours. Nonetheless, the corrosivity trend of ILs can be summarized as follows:

- MCR in PIL > AIL, due to the presence of protons which can be reduced to H₂ in the cathodic reaction.
- MCR in PILs containing [HSO₄]⁻ and Cl⁻ is metal-dependent: Al, Fe, Zn and Ti are more prone to corrosion in [HSO₄]⁻ containing PILs while Cu, Br, Ni, 304 SS are more prone to corrosion in Cl⁻ containing PILs. This is likely due to differences in the anodic dissolution mechanisms of those metals, which can be affected by the anions in different ways. Mo is resistant in both media, likely due to the formation of a passive layer which manifested with a change in the appearance of the metal (dark layer not characterised).
- MCR in dry AILs containing Cl⁻ is generally higher than [NTf₂]⁻, except for 304 SS.
- There is no apparent correlation between the CRs of metals exposed to IL-containing media (determined through immersion test) and their standard reduction potential (EMF series). All direct corrosion comparisons between IL and aqueous systems containing acids or inorganic salts fall short and are not meaningful at all.
- In general, the MCR is enhanced by increasing temperature.
- In general, water acts as a corrosion promotor in IL systems, except for [HC₁im]Cl containing Cu and Ni (and their alloys), for which the dry conditions are more severe.

Corrosion phenomena are also affected by many other variables not covered in this work, such as pH, motion, surface finishes, gas content, etc. More experiments are needed to understand the effect of these variables on the corrosion behaviour of metals in ILs. Electrochemical experiments should also be performed to obtain detailed mechanistic information of the reaction taking place in the cathode and the anode, their rates, and how different variables affects them.

Some variables affecting corrosion cannot be controlled, for example, inhomogeneities in the composition of the metals or the thermal history of the samples during fabrication, resulting in some stochastic effects. Therefore, for systems showing high degree of scatter in the data, more experiments should be performed to obtain statistically significant results. In many

studies, to avoid variations in the corrosion rate due to different surface finishes, it was reported that greater reproducibility can often be obtained if a common surface is used on all specimens. As the intention of this study is to evaluate potential candidates for practical applications, surfaces were used as “received” with their corresponding passive layers, without any surface treatment (such as wet grinding with 120 grit abrasive or pickling). Doing these treatments can improve the reproducibility of the results and provide a better estimate of the inherent corrosion resistance of a material, however, commercial metallic materials might behave differently due to the existence of such stable passive layers on their surfaces.

3.7.2 Material selection

There are no general rules governing the choice of a material for a particular application. The decision is driven mainly by the economics rather than the corrosion behaviour, and preferably the selected material should be the most inexpensive one with adequate properties to fulfil a given application, taking safety aspects into account. Other considerations when selecting metallic materials are availability and ease of construction of process equipment.

Ideally, the selected metal should be such that no corrosion occurs at all (type-0), but this is not always technologically or economically viable. It is therefore necessary, to tolerate certain levels of corrosion that will not be detrimental to the safety of a process equipment during its expected lifetime. It is a common practice in engineering applications to choose inexpensive construction materials and apply a design margin, *e.g.* extra metal thickness, for corrosion allowance. If this strategy is chosen for IL-based processes, it needs to be kept in mind that metals will be leached into the IL phase. IL-process stream contamination with metals might generate certain issues, such as IL degradation, catalyst poisoning, product contamination, and/or disposal problems.

The experiments performed in this work is the first step towards material selection, as other parameters need to be tested before industrial implementation, such as corrosion behaviour of welded parts, mechanical properties, stress corrosion cracking, etc. Materials should be tested at conditions which are similar to the real process conditions, including: temperature, pressure, flow conditions, chemical composition of the IL stream, and/or presence of solid (erosion-corrosion).

Even though more testing is required, based on the experimental results it can be suggested the following candidates:

- [C₄C₁im][NTf₂]: In general, this IL is not a very corrosive at temperatures lower than 150 °C for Al, Ti and 304 SS. However, XRF revealed the presence of Al in the neat IL. It is unclear if this metal contamination is due to the use of Al in the manufacturing facilities. If metals are not desired in the IL, Al should be avoided until the reasons for the presence of this metal in the IL are clarified. Cu and its alloys should be avoided when handling this IL.
- [C₄C₁im]Cl: Ti and 304 SS showed good corrosion resistance to this IL. However, the use of common steels in chloride-containing media should be confirmed, due to other forms of corrosion not explored in this work. A material commonly used in brine applications is 25 Cr duplex (not tested) ¹⁴⁵.
- [HC₁im]Cl: This is a very aggressive IL, the only metal that performed well under all tested conditions is Ti.
- [N₄₁₁₀][HSO₄]: Is a very aggressive medium. Cu and brass performed well, but the industrial use of these metals in high-temperature applications is limited. Ti showed excellent resistance, but it can be completely dissolved under some conditions, and therefore its use should be avoided. 304 steel can be severely attacked in this IL as well. It is noteworthy that a high-level test was performed using a tantalum coated washer (Tantaline®) that showed excellent corrosion resistance in this IL. Other alloys should be tested to identify potential candidates for applications using the hydrogen sulfate based ILs.

Fortunately, there are also non-metallic materials that can be used in industrial applications. For example, polymers (PTFE or PFA) or glass liners. The use of such liners would protect equipment from corrosion but will reduce the thermal transfer efficiency of heat exchangers. There are some non-metallic materials that have been used for heat transfer applications, such as SiC, graphite and ceramics. However, the performance of such materials needs validation before implementation in pilots and large-scale IL-based processes.

3.7.3 Semi-quantitative categorization method

A simple semi-quantitative categorisation system was used to classify the corrosion behaviour of materials (metals) exposed to corrosive environment. It is expected that as more systems are classified according to this categorization method corrosion trends will become evident. This would allow establishing analogies between different materials and corrosive media, which ultimately could lead to a better understanding of the corrosion mechanisms taking

place at their interfaces. This is essential for choosing the right material for a given application and for the development of novel corrosion mitigation strategies, such as new materials and alloys and/or corrosion inhibitors.

As mentioned before, the corrosion behaviour is strongly affected by the nature of both material and corrosive medium as well as the conditions at which the process takes place. Therefore, it is important to mention all relevant parameters when classifying a system. It can provide information to identify the best analytical technique to study a particular system.

A full description of the semiquantitative categorization method is presented in Appendix 4. It is noteworthy that this method does not intend to replace industrial standards, but to expand on them, to maximize the amount of information that can be extracted from laboratories or field immersion tests.

3.7.4 Oxidative Ionothermal Synthesis (OIS)

It has been shown in this work an Oxidative Ionothermal Synthesis (IOS) of Zn-based nano/micro materials (both crystalline and amorphous) by direct oxidation of metallic Zn in $[\text{C}_4\text{C}_{1\text{im}}]\text{Cl}$ and water mixtures. By adjusting the water content, temperature and exposure time, different species such as $\epsilon\text{-Zn}(\text{OH})_2$, $\text{Zn}_5(\text{OH})_8\text{Cl}_2\cdot\text{H}_2\text{O}$ and $\text{Zn}_5(\text{CO}_3)_2(\text{OH})_6$, that can be used as intermediates for ZnO nano/micro materials, are obtained.

The use of IL and water mixtures for making nanoparticles via direct oxidation of metals (OIS) might be used to synthesise materials-by-design (as hetero-structures, core-shell structures or metals with modified surfaces) with physicochemical properties tailored to meet industrial relevant needs. Additionally, the use of these solvents in combination with metals could lead to a more cost-effective and environmentally friendly processes for large-scale synthesis of a wide range of nano and micro materials. This approach might be used not only for Zn-based nano-micro materials, but also extended to other metals.

The use of IL and water mixtures for making nanoparticles via direct oxidation of metals (OIS) might be used to synthesize materials-by-design (as hetero-structures, core-shell structures or metals with modified surfaces) with physicochemical properties tailored to meet industrial relevant needs. A high-level techno-economic analysis on the use of ILs in combination with metals suggest that this production method could lead to more cost-effective and environmentally friendly processes for large-scale synthesis of a wide range of nano and micro materials. As a result, further work towards the development of the OIS process is justified not only for Zn-based nano-micro materials but also extended to other metals and alloys. However,

this concept is at an early stage of development and further work is required to reach a definitive conclusion about the technical and economic feasibility of this method.

3.7.5 Lessons learnt and recommendations for future work

For the first set of immersion experiments, a PTFE tape was rolled into a thread to hold the samples. Under magnification, some PTFE threads attached to the rim of the cavity used to support the metal coupons (Figure 71). As the MCR determination by weight loss method relies on the accurate measurement of the mass difference, the presence of such threads would induce a negative error. After this was observed, PVC filaments were used to support the samples, which do not leave any residual material on the metal coupons. There were successfully used in IL media to temperatures up to 150 °C. This is the recommended filament to hold the samples in these experiments.

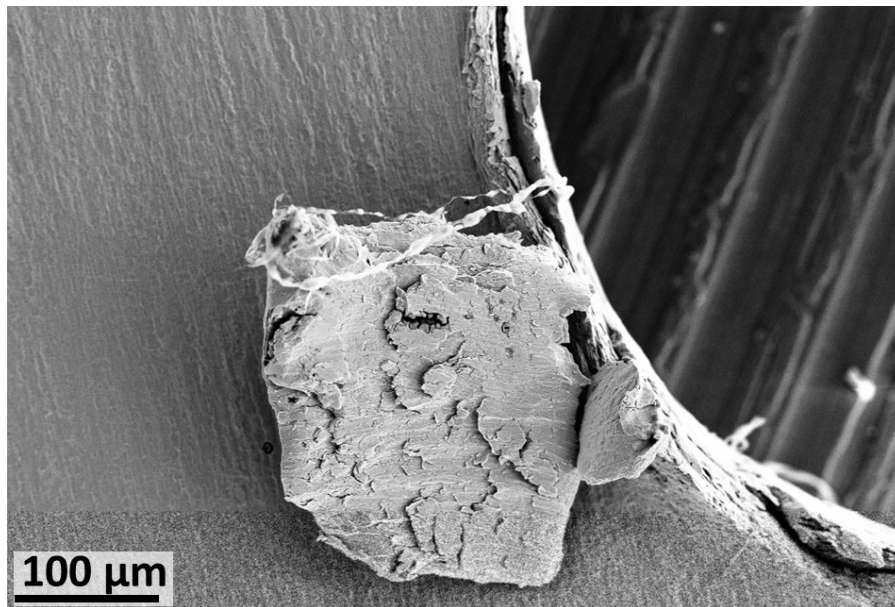


Figure 71. Detail of the rim of the cavity used to hold a molybdenum sample.

Another issue that can be seen in Figure 71 is the presence of metal debris from the drilling process, that might detach under the influence of corrosion leading to positive errors. Such defects were not observed systematically, but to minimize sources of random errors, a file should be used after the drilling process to remove any possible debris.

Finally, the samples had a thickness of 0.125 mm, which was fine for most of the metals. However, for light metals such as Al, the samples were not rigid but easily malleable foils. Thicker samples would be easier to manipulate reducing the chances of mechanical damage or bending during sample handling. Additionally, testing thicker samples would allow longer

testing time. This can be useful to verify if the corrosion layers formed (when application) are stable and provide surface passivation.

Due to the high cost of ILs or the difficulty to synthesise some of them at large scale in the laboratory, for metals type-0 and type-1, the quantity of solvent can be reduced from the quantity recommended in the standards, *i.e.* 0.2 ml/mm², or multiple samples could be tested in the same solution.

3.7.6 Future work

3.7.6.1 *Corrosion behaviour of metals in ILs*

The detailed mechanisms of metallic corrosion are highly complex and are affected by many variables. To achieve a complete understanding of the corrosion behaviour of metals exposed to ILs, many branches of pure sciences and engineering must be involved. Electrochemical methods to study these systems is needed to understand the detailed mechanisms of corrosion.

3.7.6.2 *Oxidative Ionothermal Synthesis (OIS)*

Regarding the fundamental science behind this novel synthesis approach, there is still room for investigation; *e.g.* test more ILs, metals and conditions. Ways to improve conversion yields and particle morphological control need to be explored.

It is also necessary to understand in detail the mechanisms of metal oxidation and crystal growth in the OIS so that particle morphology can be better controlled. Additionally, understanding how particle morphology affects the properties of a material is key to tailor materials for a given application.

Chapter 4 - Techno-economic analysis for an eucalyptus biorefinery using the IonoSolv Process

4.1 Motivation

4.1.1 Eucalyptus fractionation using [N₂₂₂₀][HSO₄]

Lignocellulosic biomass (LB) derived products are considered a promising sustainable alternative to petroleum-derived fuels and chemicals. However, to achieve the transformation of LB into useful chemicals, it is necessary to fractionate it into its constituent materials. For bioethanol production, an additional processing step, known as pretreatment (4.2.4), is required to enhance the enzymatic conversion of cellulose into glucose⁷. The pretreatment of different lignocellulosic feedstocks with ILs has been extensively studied using Aprotic Ionic Liquids (AILs)^{230–235}. It has been shown that AILs can successfully fractionate and pretreat LB but there are some limiting factors for their industrial application, such as IL cost, stability and the requirement for very low water contents for optimum performance¹⁴⁰, which are discussed in detailed in section 4.2.6. Previous work has shown that PIL-pretreatment based on the hydrogen sulfate ILs, such as [N₂₂₂₀][HSO₄], are able to remove more lignin than dilute acid pretreatment, reduce the total process time to produce high yields of sugar from the recovered product and produce less degradation products²³⁰.

Eucalyptus has been proposed as a promising raw material for biorefining as large quantities of residues are available from fast grown plantations. Eucalyptus has been used for fuel, charcoal, pulp and paper, and widely employed for sawn timber production²³⁶. The rapid growth of Eucalyptus and their ease to adapt to various environmental conditions makes this species a potentially abundant source of fermentable sugars²³⁶.

In this chapter, the use of a hydrogen sulfate based ionic liquid ([N₂₂₂₀][HSO₄]) for Eucalyptus fractionation is explored. Additionally, the effects of CO₂ (sub-critical and supercritical) and pressure on the pretreatment performance will be investigated as a means to improve the pretreatment performance. The rationale for this choice is explained in section 4.2.8. The experimental data obtained in the laboratory is used to perform a detailed techno-economic analysis for a biorefinery to produce bioethanol from Eucalyptus based on this technology and benchmarked against a biorefinery using the Acid Catalysed Steam Explosion (ACSE) pretreatment, which has been proposed as a viable pretreatment for large-scale biorefineries²³⁷.

4.1.2 Objectives

The main objective of this chapter is to assess the technical and economic feasibility of a 2G ethanol production plant from wood (*Eucalyptus*) via enzymatic hydrolysis and fermentation and to provide recommendations for further research and development.

The base-case plant was designed and costed to determine a realistic current price for wood-derived ethanol. The individual processing sections are largely based on laboratory data, which have been used to estimate the CAPEX and OPEX of an enzyme hydrolysis integrated process with a production capacity of 56.8 MM L/y (15 MM gal/y). Two technologies for the biomass fractionation step are considered, namely, IL pretreatment (ionoSolv process) and Acid Catalysed Steam Explosion (ACSE), which is one of the most popular pretreatment methods²³⁸. The IL-based technology was modelled in detailed and evaluated whereas the ACSE process had been taken from a technical report (feasibility study) prepared by Stone & Webster Engineering Corporation (SWEC), for an enzyme-based ethanol plant production, for the Solar Energy Research Institute (SERI).

The main objectives of this section are:

- Study the pretreatment performance of *Eucalyptus red grandis* with the inexpensive protic IL *N,N,N*-triethylammonium hydrogen sulfate ($[\text{N}_{2220}][\text{HSO}_4]$) and optimize the pretreatment conditions with minimum severity (time and temperature) to obtain high saccharification yields.
- Investigate the effect of pressurized CO_2 on the deconstruction of *Eucalyptus Red Grandis* during ionoSolv pretreatment as a means to improve pretreatment performance.
- Perform a process design, and capital cost (CAPEX) and operating cost (OPEX) estimates based on laboratory data for the ionoSolv process and compare it with the ACSE process.

4.2 Theoretical background

At the time of writing, fossil fuels (oil, coal and gas) were the main sources of energy and chemicals (Figure 72). As mentioned in section 1.2.2, the main issue about these fossil fuels is that their use raises the CO_2 concentration in the atmosphere, leading to an increase in the Earth's temperature, which can have catastrophic consequences. Therefore, to address the global climate change problem a lot of research is carried out to find sustainable sources of energy such as solar, wind and biomass, just to mention some examples.

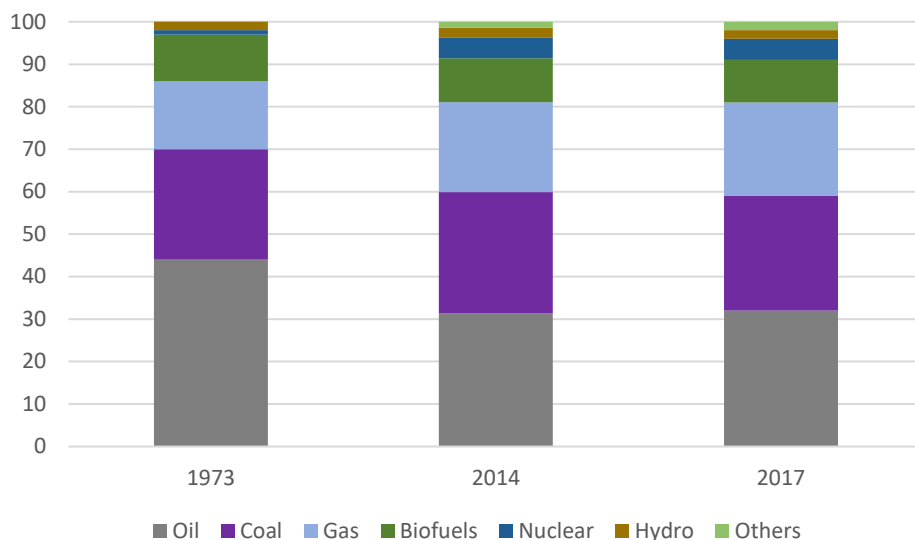


Figure 72. World Total Primary Energy Supply (TPES). 1973 and 2014 ²³⁹; 2017 ²⁴⁰. Others include geothermal, solar, wind, heat and others.

Lignocellulosic biomass (LB) is an abundant and geographically diverse natural resource, thus it is a good candidate as a renewable feedstock for the production of not only energy, but also (liquid) fuels, chemicals and materials ⁷. The cellulose contained in LB can be enzymatically hydrolysed to glucose, that can then be fermented into ethanol or transformed to other substances via chemical reactions, such as hydroxymethylfurfural (HMF) or levulinic acid ^{7,241}.

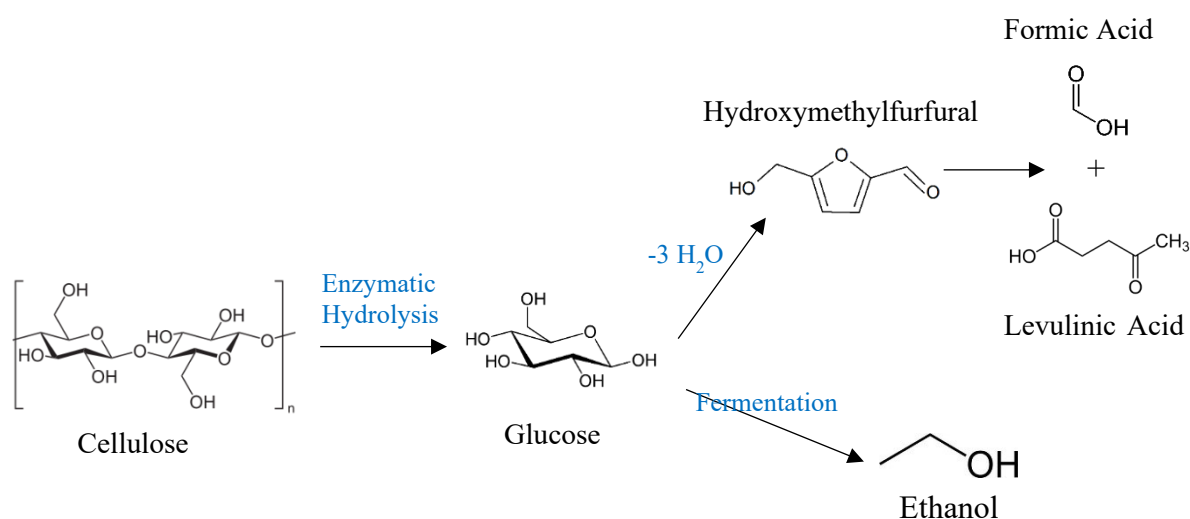


Figure 73. Potential uses of cellulose.

Cellulose fibres are contained in a complex lignin-hemicellulose structure, which hinders cellulose biodegradation by enzymes, thus, this protecting shield needs to be removed in order to be able to break down the cellulose into its monomers for further transformation. The process of separating the biomass components is called biomass deconstruction or fractionation. The process to make the cellulose more active towards enzymatic

saccharification is called pretreatment, which can be achieved in many different ways (refer to section 4.2.4) ^{7,241}.

4.2.1 Lignocellulosic biomass

Lignocellulosic biomass (LB) is a composite material, a stored source of solar energy collected by plants during the photosynthesis process in which CO₂ is captured and converted to plant materials. It is composed mainly of cellulose, hemi-cellulose and lignin ²⁴¹. It also contains smaller amounts of pectins, inorganic compounds, proteins, and extractives, such as waxes and lipids, which also have potential value. The exact composition of lignocellulose depends on the species, the plant tissue, and the growth conditions. Examples of LB sources include: agricultural crop residues (such as rice straw or corn stover), wood residues from the forestry and milling industries, Municipal Solid Waste (MSW) from urban areas, herbaceous energy crops (such as switchgrass, miscanthus) and woody crops.

Table 23. Example of LB Composition [% wt/wt].

Feedstock	Cellulose (%)		Hemicellulose (%)			Lignin		Extractives	Ash	Ref
						AIL	ASL			
	Glucan	Xylan	Arabinan	Galactoman	Mannan					
Switchgrass	45			31.4		12.0				242
Grasses	25–40			35–50		10–30				242
	40.7	19.6	2.2	1.0		23.8		1.8	3.9	243
<i>Miscanthus</i>	43.6	18.3	3.4	2.4	1.1	26.5		4.7	1.3	244
<i>x giganteus</i>	42			25		28		9		245
	42.5	24				27.5		5	4	246
	50.1	22.4				26.8			0.7	88
<i>Eucalyptus nitens</i>	42	22.3				22.9		4.7	0.25	247
<i>Eucalyptus globulus</i> [A]	39.9	14.9	0.3	1.3	0.4	23.6	4.8		0.32	248
Eucalyptus Chips	39.9	24.6				29.5				249
Eucalyptus Chips	42.6	15.4	1.9	2.3		28.3	2.4	3.3	0.9	250
<i>Eucalyptus red grandis</i>	44.9	11.4				26.2		3.5		251
	53.4	10.6				28.1	5.2	0.7	-	This work

[A] 0.1% rhamnan.

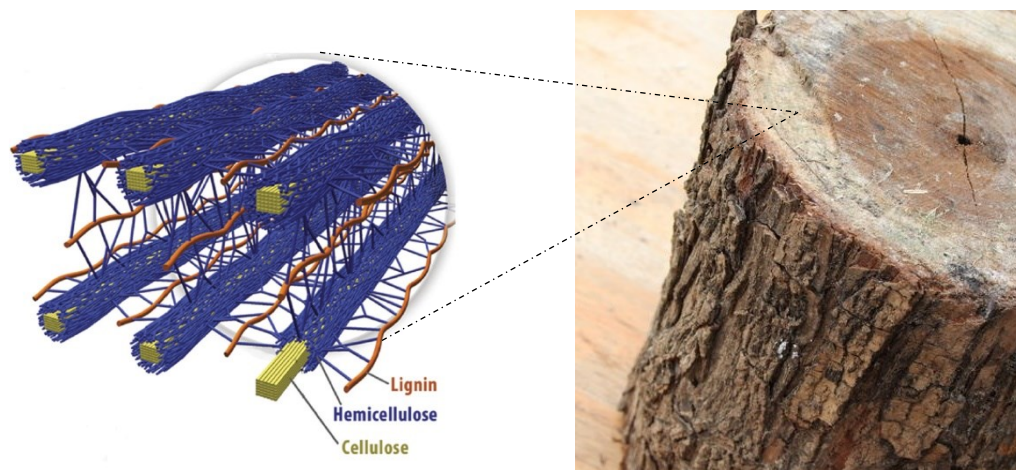


Figure 74. Spatial arrangement of cellulose hemicellulose and lignin in the cell walls of lignocellulosic biomass.

Estimates of how much energy could be produced from biomass worldwide are quite variable due to differences in the assumptions (for example, about land use) that enter into such calculations²⁵². As can be seen in Figure 72, biomass is the most important energy source after fossil energies (oil, gas and carbon) and it accounted for almost 10% of the energy of the world Total Primary Energy Supply (TPES) from 1974 to 2017. It is forecasted that the quantity of energy from biomass will increase in the coming years, especially if the policies to limit the global temperature increase by 2 °C are applied^{239,240}.

An analysis by a group of U.S. government scientists of how much biomass could be available for bioenergy production in the United States estimated that as much as 1.3 billion dry tons could be available annually by approximately 2030²⁵³. If 90% of the sugars derived from the biomass were utilized by a biological process for ethanol production (*i.e.* 90% conversion efficiency), that amount of biomass would produce approximately 130 billion gallons of cellulosic ethanol, equivalent on an energy basis to approximately 87 billion gallons of gasoline, which represented about 27% of world consumption in 2006²⁵³. To put this figure into perspective, in 2006 the United States used 138 billion gallons of gasoline, 44% of world consumption²⁵³.

4.2.1.1 Cellulose

Cellulose is the largest single component of lignocellulose and the most abundant organic molecule on Earth. It is found mainly as a structural component of plant and algal cell walls but is also produced by some animals, such as tunicates, and several bacteria²⁵⁴. Although the cellulose content of different LB feedstocks varies significantly, it is typically in the range of 35–50 wt% (Table 23).

Cellulose is a linear polymer of glucose units. The glucopyranosyl monomers are linked by 1-4- β glycosidic bonds. The β configuration at the anomeric carbons leads to a stretched chain conformation, with hydrogen bonds linking these chains into flat sheets. This is in contrast to starch, which has a helical shape due to the α configuration at the anomeric carbon (Figure 75).

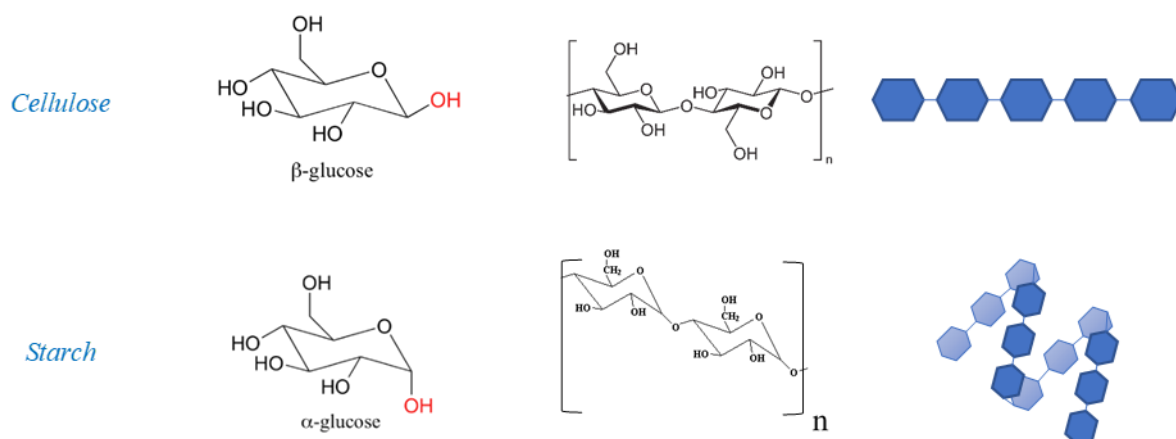


Figure 75. Cellulose and starch structure. From left to right: monomer, polymer form, superstructure.

The linear conformation enables the packing of numerous cellulose strands into crystalline fibrils²⁵⁵. The number of glucosyl units in one polymer strand can be 10^4 or higher²⁵⁶. Although the monomer (glucose) and short oligomers are soluble in water, cellulose is not, due to its high molecular weight (solubility is usually inversely related to polymer length). Native cellulose is recalcitrant toward dissolution because of its high crystallinity²⁵⁷. Its ordered structure is the result of a three-dimensional hydrogen-bond (H-bond) network between the hydroxyl groups present in each polymer chain. Effective cellulose solvents must compete for the existing intermolecular H-bond interactions, in order to separate the polymer chains from each other, resulting in the dissolution of the biopolymer²⁵⁸.

Most cellulosic materials consist of crystalline and amorphous domains, in varying proportions, depending on both source and history (Figure 76). The physical properties of cellulose, as well as their chemical behaviour and reactivity, are strongly influenced by the arrangement of the cellulose molecules with respect to each other and to the fibre axis, as well. Most of the reactants penetrate only the amorphous regions and it is only in these regions with a low level of order that the reactions can take place, leaving the intercrystalline regions unaffected. Starting from this, the behaviour of both regions has been extensively studied to elucidate the micro and macro responses of the cellulose material to thermal, hydrothermal and chemical treatments²⁵⁹. Glucan is the general term for a polysaccharide derived from D-glucose. Glucans

include diverse glucose polymers that differ in the position of glycosidic bonds, which can be short or long, branched or unbranched, alpha or beta isomers, and soluble or particulate ²⁶⁰.

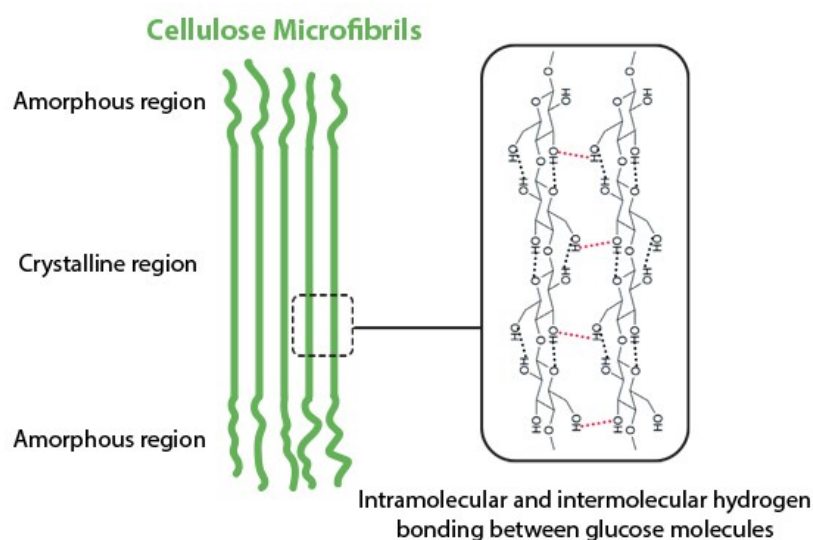


Figure 76. Cellulose microfibrils structure. Modified from ²⁶¹.

4.2.1.2 Hemicellulose

Hemicellulose is a group of polysaccharides and makes up around 25 wt% of the biomass (Table 23). These carbohydrate polymers are of lower molecular weight than cellulose (degree of polymerisation around 100–200) ²⁶². Hemicellulose may be composed of both hexose and pentose sugars; the C₆ sugars glucose, mannose, galactose and the C₅ sugars xylose and arabinose (Figure 77). Hemicellulose polymers can be branched and may be decorated with functionalities such as acetyl and methyl groups, cinnamic, glucuronic and galacturonic acids.

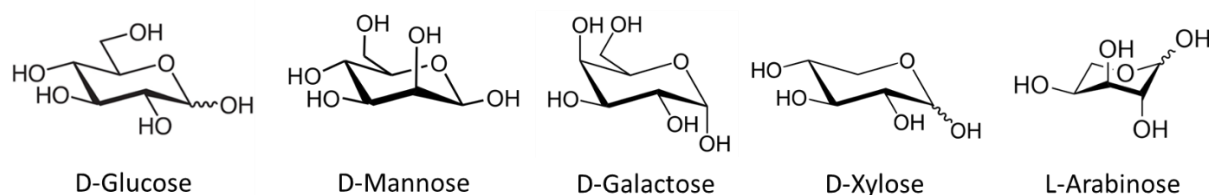


Figure 77. The hexoses and pentoses typically found in hemicellulose.

Hemicellulose is thought to bind non-covalently to the surface of cellulose fibrils. It acts as an amorphous matrix material, holding the cellulose fibrils in place (Figure 74). Softwood and hardwood hemicelluloses differ significantly. They have different sugars, such as hexoses and pentoses in the main chain and different amounts of decorated functionalities. The most common hemicellulose sugar in grasses and hardwood is xylose. In softwood, mannose is the major hemicellulose sugar ²⁶².

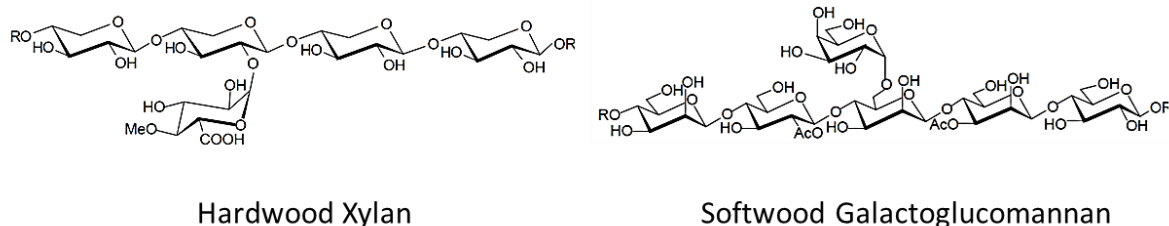


Figure 78. Example of hemicellulose structure for hardwood and softwood ²⁶³.

It has been suggested that the substitution with hydrophobic groups such as acetyl and methyl groups enhances the affinity of hemicellulose to lignin and thus aids the cohesion between the three major lignocellulosic polymers ²⁶². Due to its non-crystalline nature, hemicellulose is more susceptible to depolymerisation than cellulose (especially in acidic conditions), an aspect of its behaviour that is exploited by many deconstruction strategies, including the IL pretreatment with $[N_{2220}][HSO_4]$ ³. Hemicelluloses are quite easily hydrolysed under acidic conditions to monosaccharides ²⁶⁴.

4.2.1.3 Lignin

Lignin is the third most abundant biopolymer on earth, comprising up to 20–35 wt% of LB (Table 23) and about 40% of its energy content (lower and higher heating value basis) ^{265,266}. Lignin is an aromatic, water-insoluble polymer but can become water-soluble, as in the case for sulphite pulping which produces lignosulfonates. It provides waterproofing, structural reinforcement and resilience to biological and physical attack compared to the all-carbohydrate cell walls of immature plant tissues. It is biosynthesised mainly from three types of monomers: coniferyl, sinapyl and p-coumaryl alcohols ²⁶⁷. Once incorporated into the lignin polymer, the subunits are identified by their aromatic ring structure and therefore called guaiacyl, syringyl and p-hydroxyphenyl subunits, respectively.

The composition of lignin differs between softwood, hardwood, and grasses, with softwood consisting almost exclusively of guaiacyl units while hardwood also contains a large number of syringyl units. This difference in composition has a great effect on the delignification chemistry and therefore on biomass deconstruction ²⁶⁸. The most common linkages in Eucalyptus lignin are depicted in Figure 79.

The presence of lignin in LB generates a protective barrier that prevents plant cell destruction by fungi and bacteria for conversion to fuel ²⁶⁹. Therefore, lignin crust is one of the major obstacles for an energy-efficient biomass deconstruction process. Native lignin not only prevents access of polysaccharide hydrolases to their substrates but modified lignin adhering to the pulp after pre-treatment also causes unproductive binding of hydrolases ²⁵⁶. Lignin can

also form inhibitors for hydrolases and fermentative organisms, including syringyl aldehyde and vanillic acid ²⁷⁰.

Most chemical deconstruction methods modify lignin by hydrolysing its ether bonds, but only some remove it from the pulp (e.g. organosolv pulping, some base treatments, sulphite pre-treatment and pulping, Kraft pulping, acetic acid pre-treatment). The removal of lignin is usually a combination of chemical fragmentation and the ability of the liquor to solvate the modified lignin fragments³.

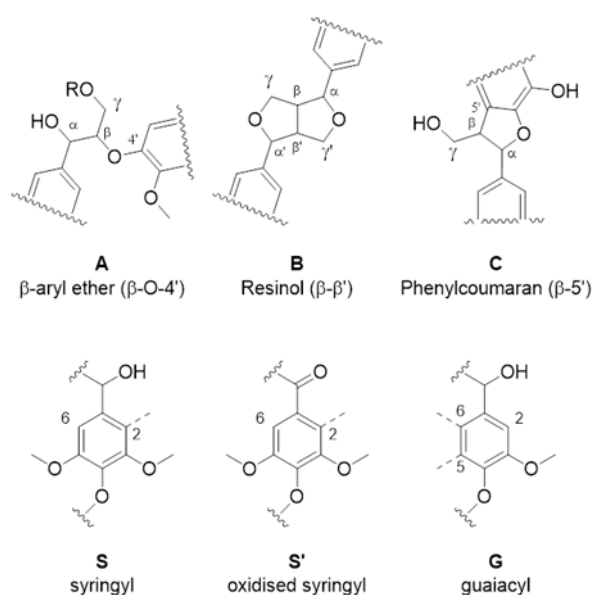


Figure 79. The most prominent ether bonds and lignin subunit in Eucalyptus lignin. Published by The Royal Society of Chemistry ³².

4.2.2 Hardwood

Willows, poplars and eucalyptus are examples of potential hardwood biorefinery crops. Hardwoods have more complex structures than softwoods, and their lignin is made up of guaiacyl and syringyl units (Figure 78).

Eucalyptus has been planted for energy, cellulose production and solid wood uses as it can supply the wood relative fast. These plantations of eucalyptus have presented, generally, high growth rate, but with the advance in genetics and the use of clones, nowadays in South America growth rates of 50 m³/ha.y are reached at commercial scale and higher 70 m³/ha.y in small research plots. In Brazil, Argentina and Uruguay it is not rare to find one-year-old trees surpassing 6 meters of height ²⁷¹.

Although the genus *Eucalyptus* has more than 600 species and varieties, those planted on commercial-scale do not surpass a dozen, among them *E. grandis*. The general belief is that fast grown wood presents lower density and poor quality, but it has been shown that for this

species, the wood does not vary among trees of the same seed, some growing fast and others slowly²⁷². For these reasons, *Eucalyptus grandis* had been chosen as the feedstock for this study.

4.2.3 Second generation bioethanol

One of the most studied methods for conversion of biomass involves the saccharification of cellulosic materials and fermentation to fuel-grade ethanol. Ethanol production by microbial fermentation of carbohydrates is a well-developed technology^{273–275}. Cellulose from wood is in abundant supply and is relatively inexpensive, whereas the market for other sources of sugar-containing crops traditionally used in ethanol production may be adversely affected as the world population grows and the demand for food supplies increases. Ethanol production from sugars by fermentation. First Generation (1G) ethanol is an easy process that has been known for millennia. It consists of 2 stages: fermentation and purification^{273–275}. Many advances have been made in those stages so that today many technically feasible alternatives for alcohol production exist. However, the hydrolysis of biomass to generate fermentable sugars Second Generation (2G) ethanol is still a difficult and expensive step due to the chemical stability of cellulose^{273–275}. Hydrolysis of cellulose consists of breaking down the complex cellulosic polysaccharide to its component sugars, which can be microbially fermented to alcohols^{273–275}. There are several biomass pretreatment technologies which will be discussed in section 4.2.4. The ones under evaluation in this Chapter are the IonoSolv and Acid Catalysed Steam Explosion (ACSE). During the biomass pretreatment via the IonoSolv process, hemicellulose and most of the lignin are dissolved in the IL solution while a cellulose-rich pulp is formed, which can be used for materials or for bioethanol production after enzymatic saccharification. In the ACSE process, cellulose is converted to glucose (hexoses); and hemicellulose, could be converted to xylose (pentoses); while lignin remains as a by-product.

Ethanol is a high-value liquid fuel which can be derived from renewable (non-petroleum) feedstocks. Ethanol, as a beverage, has been produced for centuries from starch and sugar-bearing fruits, vegetables, and grain products^{273–275}. Unfortunately, these feedstocks are primarily used for both human and animal consumption and are considered both economically and politically unattractive as feedstocks for fuel ethanol plants on a large-scale application (food vs. fuel dilemma). An alternative biomass feedstock which is not part of the basic food chain is wood²⁷⁶.

4.2.4 Biorefinery

A biorefinery, analogous to a petroleum refinery, produces fuel, heat, electricity and/or chemicals from biomass ⁸. LB fractionation is the conceptual basis of the “lignocellulose biorefinery”. The National Renewable Energy Laboratory (NREL) definition of a biorefinery is “a facility that integrates conversion processes and equipment to produce fuels, power and chemicals from biomass”. The IEA Bioenergy Task 42 broadened the biorefinery concept, proposing that biorefinery stands for “the sustainable processing of biomass into a spectrum of bio-based products (food, feed, chemicals and/or materials) and bioenergy (biofuels, power and/or heat)” ⁹. Integrated biorefineries can provide a sustainable approach by reducing the carbon footprint of the final products. They can also improve biomass processing economics as well as environmental issues ^{277,278}.

The predominant biomass-derived fuels are biodiesel, obtained from oily plants such as rapeseed and oil palm ²⁷⁹, and ethanol, which can be obtained from any kind of plant ^{273–275}. Ethanol is obtained directly by microbial fermentation from sucrose-containing plants, *e.g.* sugar cane, via enzymatic or chemical hydrolysis and subsequent fermentation from starch, *e.g.* corn, which is known as 1G bioethanol. 2G Ethanol is produced from lignocellulosic biomass, *i.e.* trees, grasses, but requires a pre-treatment step prior to hydrolysis and fermentation (Figure 80) ²⁸⁰.

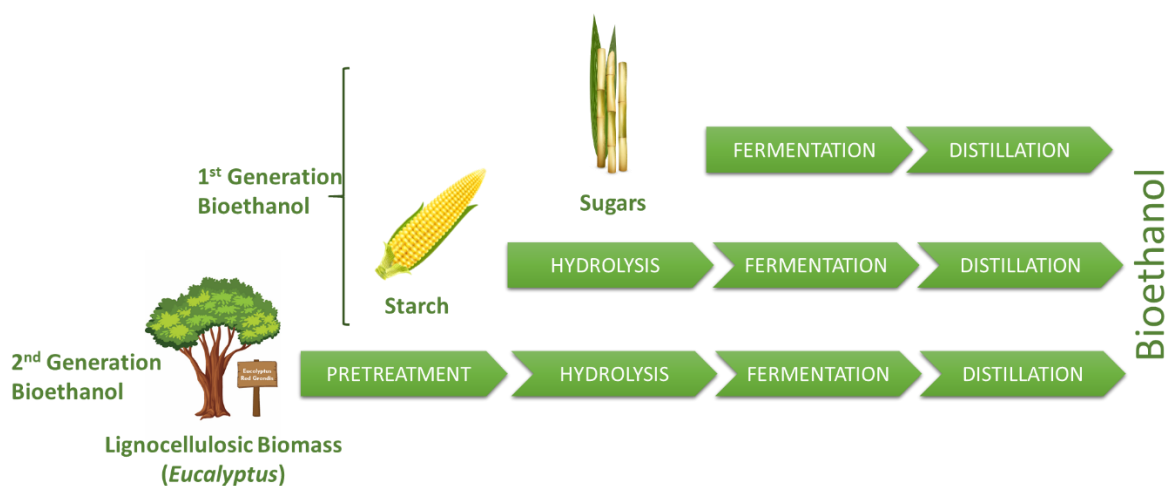


Figure 80. 1G and 2G bioethanol production. Adapted from ref ²⁸⁰. 1G bioethanol from sugary plants only requires fermentation and in the case of starchy plants a hydrolysis step while 2G generation bioethanol requires a pretreatment step.

Lignocellulosic biomass is more abundant, grown faster and easier, and less limited by the local climate than agricultural plants ²⁸¹. For these reasons, the use of lignocellulosic biomass as a biorefinery feedstock is therefore environmentally and socioeconomically preferential ²⁸².

However, as mentioned previously in section 4.2.3, the high recalcitrance of lignocellulose requires pretreatment.

Generally speaking, the energy requirements, as well as the nature and recyclability of chemicals and solvents involved in a chemical process are crucial parameters that will influence the overall environmental impact and economics of a biorefinery ^{283,284}. Other parameters which need to be considered for capital costs (CAPEX) and operating costs (OPEX) estimations include the solid to liquid ratio ²⁸⁵, the residence time ²⁸⁶, temperature and water usage ²⁴⁴.

4.2.5 Lignocellulosic biomass pretreatment

The plant cell walls found in LB are complex structures which are difficult to break down or deconstruct, into their constituent polymers and monomers. This recalcitrance makes it more expensive and energy-intensive to convert lignocellulose into fermentable pentoses and hexoses (*e.g.* xylose and glucose) than the starches in feedstocks such as corn or sucrose in sugarcane ²⁸⁷.

The goal of pre-treatment methods is to make the cellulose accessible for chemical or biological transformations. They work by affecting the structure of biomass by solubilizing or modifying the structure of its constituents (*e.g.* cellulose, hemicellulose and lignin), reducing cellulose crystallinity or increasing the available surface area and pore volume of the material, making it more accessible to the enzymes enhancing the hydrolysis kinetics.

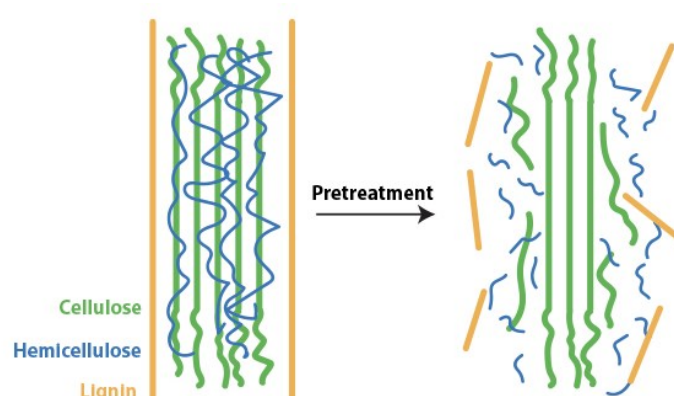


Figure 81. Pre-treatment scheme.

There are many biomass conversion pathways in various stages of development. Some of these methods include Steam Explosion (STEX) ²⁸⁸, Ammonia Fibre Expansion (AFEX) ²⁸⁹, concentrated acid ²⁹⁰, dilute acid ²⁹¹, hot water ²⁹², organosolv ^{293,294}, lime pretreatment ²⁹⁵ and ionic liquid (IL) pretreatments ^{281,285,296,297}, including the ionoSolv process ^{31,32,244,298,299}. Each pretreatment method will affect different LB types in different ways, which means that methods effective to

treat one type of biomass might not be as effective for others. Typically, acidic conditions result in hemicellulose hydrolysis, which also commonly results in the formation of degradation products, such as furfural, HMF and levulinic acid ^{297,300}. In contrast, at high pH, lignin is dissolved and cellulose and hemicelluloses constitute the solid fraction. Figure 82 summarises the typical composition of pretreated pulp with different methods where pH is the main cause for the outcome of the procedure ³⁰⁰.

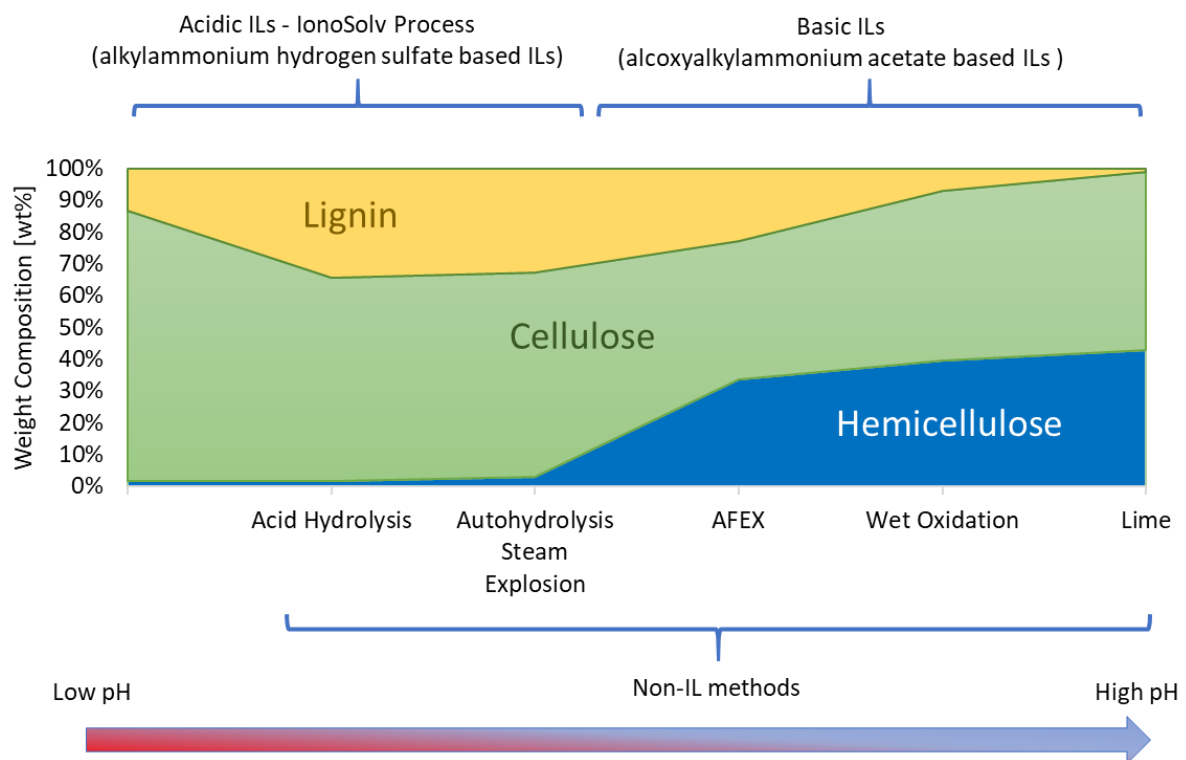


Figure 82. Typical pulp composition after biomass pretreatment as a function of reaction pH. Compositions are indicative and the exact values will depend on biomass type and pretreatment severity. Adapted from reference ³⁰⁰.

All of the pretreatment technologies mentioned above have advantages and disadvantages, and there is no biomass pre-treatment available today that can process a diverse range of LB feedstocks at high yields in a cost-effective way ^{287,301}. The production of bioethanol from LB is no longer limited by technology but for the economics of the process. For this reason, there are a diversity of pretreatment methods under development to improve the economic viability of a biorefinery ^{242,269,287,297,302-304}. Main pretreatment methods are discussed in the following section.

4.2.5.1 Lime pretreatment

Lime pretreatment has proven to be a useful method for selectively reducing the lignin content of lignocellulosic biomass without significant loss in carbohydrates, thus realizing an important increase in biodigestibility ²⁹⁵. However, the most effective lime pretreatment requires

pressurized oxygen to be delivered at 13.8 barg (1.4 MPa or 200 psig) ²⁸⁷. In this pretreatment, the biomass is pretreated with calcium hydroxide and water under different conditions of temperature and pressure. It can be accomplished in 3 ways: (1) short-term pretreatment that lasts up to 6 h, requires temperatures of 100–160 °C, and can be applied with or without oxygen (pressure ~1.4 MPa) ²⁹⁵; (2) long-term pretreatment taking up to 8 weeks, requiring only 55–65°C, and capable of running with or without air (atmospheric pressure) ²⁹⁵; and (3) simple pretreatment requiring 1 h in boiling water, without air or oxygen ²⁹⁵. Nonoxidative conditions are effective at low lignin contents (below ~18% lignin), whereas oxidative conditions are required for high lignin contents (above ~18% lignin) ²⁹⁵.

4.2.5.2 *Ammonia fibre expansion pretreatment*

Ammonia Fibre Expansion (AFEX) is an important pretreatment technology that combines physical (high temperature and pressure) and chemical (ammonia) processes to achieve effective LB pretreatment ³⁰⁵. The AFEX pretreatment increases the surface accessibility for hydrolysis, promotes cellulose decrystallization and partial hemicellulose depolymerization, and reduces the recalcitrance to enzymatic hydrolysis of the treated biomass ³⁰⁵. Theoretical glucose yield upon optimal enzymatic hydrolysis on AFEX-treated corn stover is approximately 98% ³⁰⁵. Furthermore, AFEX offers several unique advantages over other pretreatments, which include near complete recovery of the pretreatment chemical (ammonia), nutrient addition for microbial growth through the remaining ammonia on pretreated biomass, and not requiring a washing step during the process which facilitates high solid loading hydrolysis ³⁰⁵. The AFEX appears to be an effective pre-treatment for corn stover and other agricultural residues, but it requires ammonia recycling and does not effectively pretreat hardwoods and softwoods ²⁸⁷.

4.2.5.3 *Organic solvent (organosolv) pretreatment*

Organic solvent (organosolv) pretreatment is recognized as a promising LB fractionation technology for biofuels and biochemicals as it can produce cellulose, lignin, and hemicellulose with high purity, with easy solvent recovery and reuse ^{293,294,306}. Typical organic solvents used in the organosolv process include ethanol, methanol, ethylene glycol, glycerol, acetic acid, and formic acid ³⁰⁶. The organosolv process can remove lignin from LB in large amounts (similar to the alkaline pretreatments), which can be recovered with high purity ²⁹⁷. Some drawbacks of the organosolv process are that it typically requires the presence of additional catalysts (sulfuric acid), and the solvents must be completely removed after use due to their inhibitory

effect on downstream saccharification and fermentation ²⁸⁷. Moreover, it can lead to a higher Minimum Ethanol Selling Price (MESP) compared to the NREL diluted process ³⁰⁷

4.2.5.4 Dilute sulfuric acid and steam explosion pretreatments

Dilute sulfuric acid pretreatment effectively solubilizes the majority of the hemicellulose and small amounts of lignin, but at higher temperatures, this pretreatment also generates polysaccharide-degradation products that are known to be inhibitory to downstream fermentation organisms, which lowers the overall sugar yields obtained ²⁹⁷. Steam pretreatment can be applied to various types of materials, but the need of impregnating agents to improve yield results in some of the same shortcomings observed with dilute acid ²⁹⁷.

Steam explosion (STEX) (or steam pretreatment) is one of the most widely investigated methods for many purposes on a large range of lignocellulosic materials and in combination with other pretreatment procedures ²⁹⁷. The term “steam explosion” is originally based on the notion that steam, under high pressure inside the cell structure, is rapidly released and expanded by depressurising the reactor vessel. This causes disruption of the cell structure similar to that of an explosive action ²⁹⁷. The term “steam explosion” is somewhat misleading since an explosion in the physical sense does not take place ²⁹⁷. It has been proposed that the Acid Catalysed Steam Explosion method can be a viable alternative for 2G bioethanol production. The engineering aspects of this process are further discussed in section 1.1.1.

4.2.5.5 Carbon dioxide based pretreatments

Carbon dioxide (CO₂) explosion, without ILs, has been used in lignocellulose pretreatment in the form of CO₂ explosion pretreatment, typically requiring high pressure (between 200 and 276 bar) ³⁰¹. At least three different mechanisms are thought to contribute to the effectiveness of supercritical CO₂ explosion pretreatment ³⁰¹:

1. Similar to the STEX, CO₂ is able to penetrate the micropores in biomass under pressure. Upon pressure release, it ruptures the pores and exposes more cellulose surfaces to cellulase enzymes during hydrolysis step ³⁰¹.
2. For some biomass derivatives (Avicel), it was observed a reduction in cellulose crystallinity. However, this is not a systematic observation. For instance, corn stover did not find a significant change in crystallinity from X-ray diffraction (XRD) data. It was speculated that corn stover is a LB with cellulose microfibrils embedded in

hemicelluloses, lignin and glycoproteins, and therefore, its less prone to cellulose crystallinity changes that Avicel, that is pure cellulose ³⁰¹.

3. CO₂ dissolution in water present in the wet biomass increases the acidity considerably, enhancing the pretreatment. In fact, pretreatment was found ineffective for dry biomass ³⁰¹.

A comparison between supercritical CO₂ combined with different solvents (water and water:ethanol (2:1) mixtures) for the pretreatment of rice husk revealed that there is a significant influence of the solvent on the pretreatment performance. When water alone was used, the enzymatic digestibility of the pretreated pulp increased compared to the untreated biomass. In the water:ethanol mixtures, the performance increased by 74% compared to the conventional diluted acid pretreatments, which showed a 58% increase. Regarding the cellulose crystallinity, dilute acid pretreatment increased the CrI of the untreated biomass sample from 33% to 35% while the sample pretreated with supercritical CO₂ in water:ethanol mixtures experienced a reduction in the CrI from 33% to 31% ³⁰⁸. Therefore, it was concluded that supercritical pretreatment with water:ethanol mixture provided the best performance according to crystallinity modification and pulp enzymatic digestibility ³⁰⁸. This result seems counterintuitive due to the high pressures required in the supercritical CO₂. The argument presented is a decrease in the cost of the raw materials, as the acid cannot be recycled and it is consumed on a permanent basis, while the CO₂ and water:ethanol was recovered and recycled. However, there is not enough details provided in the original reference to verify this conclusion. It has also been shown that CO₂ atmospheres have an effect on biomass fractionation using the Aprotic Ionic Liquid (AIL) 1-ethyl-3-methylimidazolium chloride [C₂C₁im]Cl ³⁰⁹. IL-based pretreatments will be discussed in section 4.2.6.

4.2.5.6 *Summary of non-IL pretreatment methods*

As mentioned before, there is a vast variety of LB suitable to produce biofuels and chemicals summarized in Table 24. It is important to highlight that one technology that is efficient for a particular type of LB material might not work for another type, due to differences in their chemical composition.

Table 24. Summary of main pretreatment methods.

Category	Pretreatment Method		Remarks
Mechanical	Comminution	Milling and grinding	
	Ultrasonic		
Chemical & Physicochemical	Steam Explosion		Steam explosion is commonly used to pretreat lignocellulosic materials. Discussed in detail in section 1.1.1.
	Ionic Liquids	<ul style="list-style-type: none"> • AILs • Acidic PILs (hydrogen-sulfate based IL (Imperial College London)) • Basic PILs • Switchable IL 	Discussed in detail in section 4.2.6.
	Liquid hot water (HLW)		
	Ammonia Fibre Explosion (AFEX).		
	Ammonia recycle percolation (ARP)		
	Soaking in aqueous ammonia (SAA)		
	Carbon Dioxide Explosion		
	Hot Water	Other Terms: <ul style="list-style-type: none"> • Hydrothermally • Aqueous or steam/aqueous fractionation • Uncatalysed Solvolysis • Aqua Solv 	
	Acid Hydrolysis	<ul style="list-style-type: none"> • Concentrated • Diluted • Very Diluted 	Most commonly used acid is sulfuric acid. Nitric acid, hydrochloric acid and phosphoric acid have also been tested.
	Oxidative delignification	<ul style="list-style-type: none"> • Zoonosis • Hydrogen peroxide • Wet oxidation • Sodium hydroxide • Potassium hydroxide • Calcium hydroxides³¹⁰ • Ammonium hydroxide 	
Alkaline Hydrolysis			
Organosolv Process	The solvents commonly used in the process are methanol, ethanol, acetone, ethylene glycol, diethylene glycol, and tetrahydrofurfuryl alcohol.	Organic acids such as oxalic, acetylsalicylic, and salicylic acids can also be used as catalysts in the organosolv process.	
Thermal	<ul style="list-style-type: none"> • Combustion • Pyrolysis • Liquefaction • Gasification 		
Biological	Fungi		
Others	Pulsed-Electric-Field Pre-treatment (PEF) ³¹¹		
	Electron beam irradiation and NaOH ³¹²		
	Radio-frequency- (RF) based dielectric heating in the NaOH ³¹³		
	Microwave ^{314,315}		

4.2.6 Ionic liquids for biomass fractionation

For the production of value-added products from LB, the efficient pretreatment and fractionation methods not only need to be efficient, but they need to be cost-effective. It is also important that the products can be recovered at a high yield using common separation and recovery equipment ²⁹⁷. The potential technologies for commercialisation must be safe from health and environmental perspectives. A particularly interesting group of chemicals that have been explored for LB fractionation are ionic liquids (ILs). It has been found that LB biomass may be solubilised completely or partially in ILs ^{297,316}. Even though ILs have been known to dissolve LB for a long time (there is a 1934 patent for cellulose solubilisation process in IL “CELLULOSE SOLUTION” 1,943,176), up to date, their industrial applications at large scale for this purpose have not been accomplished, mainly due to their high cost as mentioned before.

As mentioned previously, there are several reviews on pretreatment methods. In old reviews dating from 2002 to 2009, ILs are not mentioned at all ^{242,303,317}. In more recent reviews dating from 2010-2017, ILs stated to be mentioned but just as an academic curiosity with no detailed discussion ^{302,304,318}. However, in the most recent reviews (2019) at the time of writing, ILs are discussed with greater details ²⁹⁷. This clearly shows that ILs are being considered as a viable option for LB pretreatment, as many studies have been conducted in the last decade to understand and to improve the utilisation of ILs for LB pretreatment ^{246,296,319–326}. It has been noticed that the term IL, in the context of LB pretreatment, has been generally used to describe AILs able to dissolve cellulose. In a review by Wang *et al.* (2012) ³¹⁶, this type of ILs were discussed ³¹⁶. In this review, there are 67 ILs mentioned with no reference to the acidic PILs, such as hydrogen sulfate ILs. Reddy, P. (2015) ³²⁷ reviewed AIL for pretreatment and their applications in other unit operations within a biorefinery. The most recent review consulted for this work (2020) on the advancements in ILs for LB pretreatment as a green alternative, several IL pretreatments were compared to other common methodologies and included a section of techno-economic viability of these substances for commercial-scale pretreatment plant ³²⁸.

As mentioned in section 2.2, there is an extremely large number of cations/anions combinations that will lead to ILs. Therefore, generalization about their interactions with LB should be avoided. Also, the biomass type will affect the nature of IL-LB interactions. For example, it has been noticed that hardwoods dissolve faster in IL than softwoods in imidazolium based IL ³²⁹. After reviewing the scientific literature on IL-based pretreatment, 4 types of ILs had been identified, namely aprotic ionic liquid pretreatment, acidic protic ionic liquid pretreatment, basic protic ionic liquid pretreatment and switchable ionic liquid

pretreatment. Figure 83 shows the chemical structures of different ILs within each group. Each of these pretreatment types is discussed in the following section:

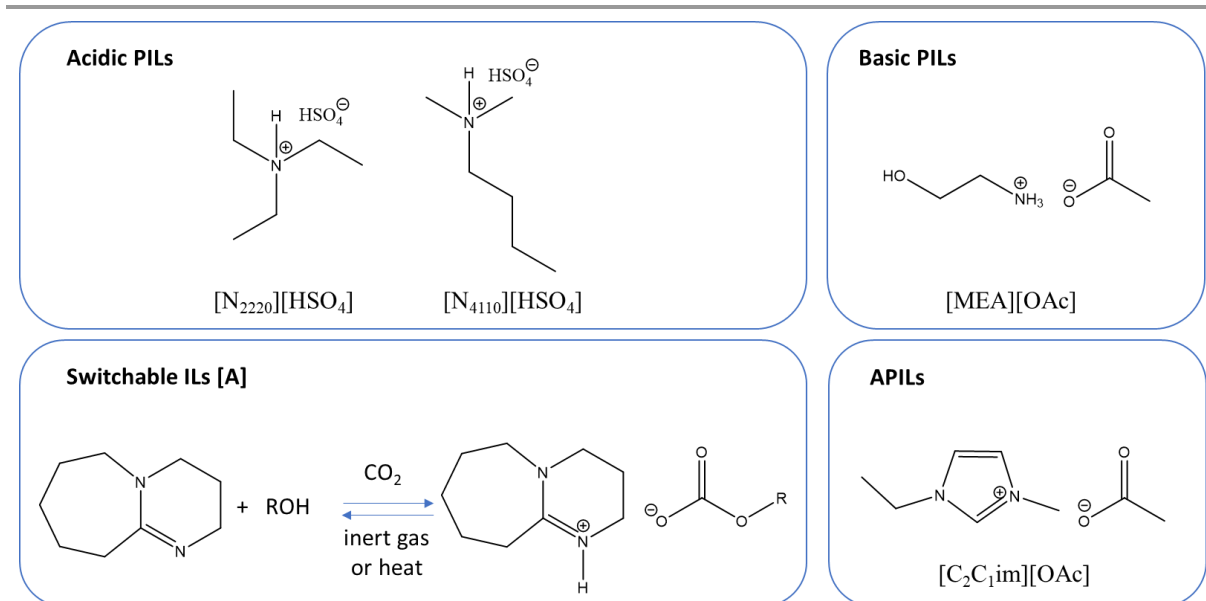


Figure 83. Different types of ILs used for LB pretreatment. [A] Example of a switchable ionic liquid formed from 1,8-diazabicyclo-[5.4.0]-undec-7-ene (DBU), an alcohol and CO_2 ^{330,331}.

4.2.6.1 Aprotic ionic liquid pretreatment

In recent years, there have been a plethora of studies on the selective and total dissolution of LB in ILs. Findings from these studies have stimulated interest in the use of these substances for LB pretreatment in a biorefinery. Aprotic imidazolium ILs have been the most popular ILs investigated for this purpose^{297,316,327}.

Swatloski and his group reported the pioneer study on the dissolving capability of a series of ILs containing 1-butyl-3-methylimidazolium ($[\text{C}_4\text{C}_1\text{im}]^+$) as cation for cellulose³³². Among the ILs tested, 1-butyl-3-methylimidazolium chloride ($[\text{C}_4\text{C}_1\text{im}]\text{Cl}$) could dissolve up to 25 wt% of cellulose in the pulp with microwave heating. The regeneration of the dissolved cellulose in an amorphous form was also demonstrated using anti-solvents (such as water) which were IL soluble. This work showcased the ability of ILs to not only dissolve cellulose but also to modify its crystalline structure³³². Also, it was noted the marked influence of water present in the ILs in amounts greater than 1% (wt/wt) to diminish the ability of these ILs to dissolve cellulose. In addition to cellulose, the solubilisation of other lignocellulosic biomass components (hemicellulose and lignin) was also demonstrated in this type of ILs³³².

One of the most studied ILs within this group are the 1,3-dialkylimidazolium acetates, especially 1-ethyl-3-methylimidazolium acetate $[\text{C}_2\text{C}_1\text{im}][\text{OAc}]$, which has been used with various feedstocks, e.g. switchgrass²³⁰, wood flour²³¹, corn stover²³², bagasse²³³, rice straw

²³⁴, cotton and eucalyptus ²³⁵. The enzymatic hydrolysis of three cellulose-containing materials: cotton, spruce and oak sawdust pretreated with this IL was studied ³³³. In short, the experimental procedure was as follow: 2% (wt/wt) substrate was added to 10 ml of [C₂C₁im][OAc] and incubated the suspension at 45 °C for 40 min. After incubation, the pretreated substrate was precipitated by addition of water (2:1 v/v water-to-IL) ³³³. The solid fraction was enzymatically hydrolysed and fermented to ethanol. The glucose yields after pretreatment were 70% for cotton, 60% for oak sawdust, while spruce sawdust resulted in a yield of only 50% ³³³. The ethanol yields were in all cases around 50% ³³³. This has to be considered a low yield if compared with commonly reported ethanol yields from other studies performed at higher temperatures ^{297,333}.

These ILs present low toxicity and viscosity, but despite the promising results, there are some limiting factors (further discussed in section 4.2.6.6) for its industrial application, such as IL cost and stability and the requirement for very low water contents for optimum performance ¹⁴⁰. Although some ILs are capable of dissolving or swelling cellulose, the presence of water in these protic IL systems retards the transformation of cellulose I to amorphous/cellulose II (Figure 76) while amorphous bits of the cellulose and virtually all of the hemicellulose are removed ³³⁴.

The effect of the composition of the atmosphere under which the pretreatment is carried out with this type of ILs was investigated ³⁰⁹. In that work, wood flour from Western red cedar (*Thuja plicata*) samples were treated with [C₂C₁im]Cl at 120 °C under various atmospheres such as oxygen (O₂), nitrogen (N₂), air, and carbon dioxide (CO₂), both dried and humidified ³⁰⁹. It was found that the percentage of residue after the treatment significantly changed with the chemical composition of the atmosphere, which proved that this parameter has a significant effect on the liquefaction and depolymerization of wood in this IL. However, the humidity hardly affected the liquefaction under any atmosphere ³⁰⁹. The amount of residue when the pretreatment was done under different atmospheres was as follows: vacuum 39 wt%, nitrogen 36 wt%, CO₂ 34 wt%, air 19 wt% and O₂ 6 wt%. This showed that O₂ had the most significant effect on the liquefaction of wood in [C₂C₁im]Cl ³⁰⁹.

The AIL pretreatment process is also referred to as “the dissolution process” ³. Perhaps the major challenge of this method for large-scale implementation is the water sensitivity as stated before. Cellulose has extremely low water solubility and the IL used for biomass dissolution are highly hygroscopic. Also, raw biomass is wet, typically containing 50 wt% (or more) water and even thoroughly air-dried biomass typically contains around 5–10 wt% residual moisture. This means that drying would be an important step in this kind of process, to avoid water build-up

in the IL which may reach levels that prevent cellulose dissolution. The energy costs of this drying have to be assessed and have the potential to be a process-limiting problem ³.

An advantage of the dissolution process over the [HSO₄]-based IL Process is the recovery of the majority of the hemicelluloses with the pulp, although along with some lignin, as the delignification in this process is not complete ³²⁹. The lignin remaining after saccharification could be further processed for chemicals production or burned, depending on the purity ³.

In summary, the general strategy to fractionate LB using APIs consist in the solubilization of each of the major components of LB followed by the regeneration of dissolved cellulosic materials from an IL medium with anti-solvents such as water or ethanol. Regarding the interactions of different types of LB with this type of ILs, it was been shown that in general, herbaceous biomass is more easily dissolved than woody biomass (in particular softwoods) under similar conditions ³²⁷.

4.2.6.2 Switchable ionic liquid pretreatment

There are some mentions in the literature about the potential of switchable ILs for the selective dissolution of hemicelluloses and lignin, resulting in enriched cellulose matrices ^{330,335}. This type of ILs are formed from the exothermic reaction of an acid gas (CO₂, SO₂ or other acid gases/gas mixtures) with a mixture of an organic superbases such as an amidine (*e.g.* 1,8-diazabicyclo-[5.4.0]-undec-7-ene, DBU) and alcohol (or other hydroxyl containing compounds) ³³¹. This class of ILs is capable of reversible compositional changes (polarity switch) upon the release of the acid gas facilitated by heating and/or passing an inert gas through the viscous ionic salt (Figure 83)(the base and alcohol mixture has a lower polarity than the IL). The change in properties significantly affects the chemical processes involved during the reaction and separation steps ³³⁰. In a typical lab procedure, a biomass sample is immersed in the IL and pretreated at 100 °C under normal atmospheric pressure for 1 – 5 days without any stirring. Thereafter, the IL/wood mixture is filtered and the undissolved material separated, washed several times with warm water (60 °C) and dried. The recovered IL could be recycled or anti-solvent (CH₃OH) can be added to induce precipitation of the dissolved compounds ³³⁵. The suitability of this principle was investigated to pretreat fresh nordic birch wood (*B. pendula*) for a time period of 1–5 days at 100 °C and under atmospheric pressure ³³⁵. It was shown at best, 57% of the hemicelluloses and 50% of lignins were dissolved from the native birch and the treated chips contained about 55% cellulose ³³⁵. It was also found that up to 76% of the recovered species removed from the spent IL liquor originated from hemicelluloses, mainly from xylan ³³⁵. The spent ILs were reused for fresh wood dissolution in four consecutive cycles and each time the wood dissolution

efficiency was similar³³⁵. Despite the fact that the change of solvent polarity in these systems might seem interesting for LB fractionation, it is not clear how this principle can be used to enhance the separations. Moreover, the long pretreatment times, and the fact the temperatures required for this method are close to the decomposition temperature of these ILs, would likely make this method not viable for a large scale biorefinery. In fact, the scientific publications on the use of these ILs for LB processing are scarce and no recent publications are available. This lack of interest appears to corroborate the assumption on the feasibility of this methodology. However, it seems that research about the use of this type of switchable solvents is now focussing on other topics, such as extraction methods for lipids from microalgae^{336,337}.

4.2.6.3 Basic protic ionic liquid pretreatment

It has been shown that an acetate based PIL monoethanolammonium acetate, [MEA][OAc], is effective for lignocellulose pretreatment³³⁸. This IL can dissolve lignin (up to 80 wt % at 160 °C for 0.5 h) from switchgrass (*Panicum virgatum*) while leaving the majority of the hemicellulose in the pulp. Considerable sugar yields upon saccharification were reported, above 80% for glucose, with good water tolerance of up to 20 wt%³³⁸. [MEA][OAc] synthesis is a simple acid-base neutralization using two bulk chemicals without the need for dilution in water, resulting in low solvent cost estimated around 1.8 \$US/kg³³⁹, which is more than an order of magnitude cheaper than the widely used AIL [C₂C₁im][OAc], which has an estimated solvent cost of 20–50 \$US/kg at bulk scale³. [MEA][OAc], was used for the pretreatment of sugar cane bagasse^{58,340}. In a study to address process scale-up of this method for sugar cane bagasse fractionation, it was found that using a 1:1 (wt/wt) mixture of [MEA][OAc] and monoethanolammonium hexanoate [MEA][Hex] increased delignification compared with pure ILs with 13% (wt/wt) solids loading, water present in the reaction medium and under mild temperature conditions (90 °C)³⁴⁰. Another study investigated the effects of the base:acid ratios (β) from 0.1 to 10 and recycling of the solvent on the pretreatment performance of sugar cane bagasse with [MEA][Ac]⁵⁸. It was found that lignin extraction and glucose release during enzymatic saccharification increased with base (amine) content, reaching up to 84% and 96%, respectively, after 72 h of saccharification for the $\beta = 10$. Up to 97% of the solvent was recovered for the $\beta = 1.0$ ⁵⁸. A higher acid content led to increased hemicellulose extraction into the liquid phase and IL recovery⁵⁸. Partial conversion of the PIL into N-(hydroxyethyl) acetamide was observed after pretreatment, with up to 86% of conversion after the sixth use for $\beta = 1.0$ ⁵⁸. Acetamide formation leads to a drop in pretreatment performance

(saccharification yield and accumulated lignin recovery) efficiency, which might be the major challenge for large scale implementation of this method, due to the difficulties of solvent purification and recyclability⁵⁸.

4.2.6.4 Acidic protic ionic liquid pretreatment – The *ionoSolv* process

Dr Agnieszka Brandt-Talbot et al.³³⁹ pioneered the use of acidic PILs, such as *N,N,N*-triethylammonium hydrogen sulfate $[N_{2220}][HSO_4]$, to pretreat LB³³⁹. Extensive work on this type of ILs had been produced by Dr Agnieszka Brandt-Talbot and Professor Dr Jason Hallett's group at Imperial College London^{3,88,341–346}. This process has been used at lab-scale to efficiently pretreat several feedstocks, such as grass *Miscanthus giganteus*,²⁹⁹ sugarcane bagasse³⁴⁷ and willow⁵⁷ using triethylammonium hydrogen sulfate, $[N_{2220}][HSO_4]$, while a similar IL, *N,N,N*-dimethylbutylammonium hydrogen sulfate $[N_{4110}][HSO_4]$, has been used to effectively pretreat softwood pine, a more recalcitrant feedstock for enzymatic hydrolysis as mentioned previously, with nearly full recovery of glucose³¹.

As an example, $[N_{2220}][HSO_4]$ solubilized up to 100% hemicellulose and 75% lignin of *Miscanthus giganteus* grass. Further enzymatic saccharification on miscanthus yielded around 77% glucose. This IL was also reused with 99% recovery for four times²⁹⁹. In a typical lab procedure, a mixture of $[N_{2220}][HSO_4]$ and water (20 wt%) is used to pretreat LB at temperatures between 120 - 180 °C. After the pretreatment, the solid fraction, a cellulose-rich pulp with high enzymatic digestibility, is recovered. The hemicellulosic and lignin fractions dissolved in the IL. The lignin can be recovered by the addition of an anti-solvent (water) to the IL-mixture. A detailed experimental procedure for this pretreatment is described in section 4.3.2.

A comparative study on cost-effective protic ILs suggests that ILs obtained through an improved design based on the hydrogen sulfate anion are (cost)-effective delignifiers³⁴⁸. Alkylammonium hydrogen sulfate ILs can be produced at much-reduced cost compared to alkylimidazolium ILs due to cheaper starting materials and ease of synthesis (section A1.1). Moreover, these PILs perform well in the presence of water, *e.g.* switchgrass pretreatment with $[N_{2220}][HSO_4]$ containing 20 wt% water resulted in a glucose yield of 45%. This represents a 75% efficiency compared to $[C_2C_1im][Ac]$ at a fraction of the cost³⁴⁸. The utilization of this type of IL-water mixtures to extract the lignin and hemicellulose while leaving behind a cellulose-rich pulp is known as *ionoSolv* process^{3,16}.

In summary, the goal in the IonoSolv process is to selectively remove lignin from the LB, by dissolving it in the IL phase while leaving behind a cellulose-rich solid, which can be separated from the liquid by filtration ^{3,16}. It has been noticed that [HSO₄]-based ILs remove both lignin and hemicellulose. The resulting pulp is then washed, and it can be used to obtain ethanol through enzymatic hydrolysis and fermentation or can be used for cellulose-based products. The filtrate will contain lignin, hemicelluloses, degradation products and other components of LB, such as oils, acetic acid, ferulic acid, vanillin, other small lignin fragments, furfurals and levulinic acid ³.

The recovery of volatiles generated as degradation products (such as furfural, HMF, acetic acid) could be performed by distillation/solvent extraction. Lignin can be precipitated from the IL by adding an antisolvent such as water. Excess water (and other impurities) are removed from the IL, before recycling ³.

4.2.6.5 Summary of IL-based pretreatment methods

4 types of ILs had been identified for LB pretreatment and their interactions with LB is summarized in Table 25.

Table 25. Interactions of LB with IL.

IL	Cellulose	Hemicellulose	Lignin
PIL Hydrogen-sulfate based ILs ³	Unaltered under mild conditions (less than 150 °C).	Dissolves. Breaks into its monomers.	Dissolves. At high temperatures and long times, solubilised lignin reacts to form cross-linked products that might precipitate back into the LB.
PIL Alcoxyalkylammonium acetate based ILs <small>58,340</small>	Does not dissolve.	Does not dissolve.	Dissolves.
AIL Imidazolium based ILs <small>324,329</small>	Dissolves cellulose rendering it amorphous and porous.	Dissolves hemicellulose.	Partially dissolve lignin. It leaves behind a lignin-rich solid.
Switchable IL ³³⁰	Unaltered.	Can be recovered from the solution. Some depolymerization occurs.	Dissolves.

4.2.6.6 Challenges of IL-based pretreatments

At the time of writing, there are still major technical, economic and environmental hurdles that block the industrial-scale implementation of IL-based pretreatment processes. It has been highlighted in the scientific literature that the key points blocking the path towards achieving commercialisation of IL-based biorefinery include: (1) IL recovery and recycling, (2) toxicity, biodegradability and renewability, (3) solids loading and size reduction, (4) water tolerance, (5) viscosity, and (6) IL cost ^{327,328}.

4.2.6.6.1 IL cost

Many ILs, especially the AILs, remain to date the most expensive research-grade solvents under investigation for the dissolution of biomass. The bulk cost for industrial organic solvents such as acetone is around 1.50 \$US/kg ³²⁷. The best-case bulk estimate cost of [C₂C₁im][OAc] is 20 \$US /kg as previously mentioned ^{3,16}. As mentioned in section 2.2, work has been performed targeting the production of low-cost ILs, such as the PILs. [MEA][OAc] is estimated around 1.8 \$US/kg ^{27,339} while the hydrogen sulfate ILs are estimated at a bulk cost as low as 0.78 \$/kg, making it one of the most economically viable candidates (in terms of solvent cost) for LB processing applications ^{28,30}.

4.2.6.6.2 Water tolerance

The investigation of ILs as pure solvents in many academic studies (including this work) has necessitated scrupulous drying of ILs to provide results with 'dry' ILs. This situation is not realistic in biomass processing at an industrial scale, as LB can contain high amounts of water. Drying of the biomass and ensuring a water-free processing environment will negatively impact the process economics. It has been shown that the presence of water in some ILs, such as in the case of the AILs discussed in section 4.2.6.1, can produce a significant impairment of their ability to dissolve cellulose. This will be a major challenge for the implementation of IL-based pretreatment methods sensitive to water at large scale. Many strategies such as distillation, extraction, adsorption and membrane separation (including pervaporation and membrane distillation), have been explored to remove water from these ILs ^{327,349}. It has been proposed that at large scale, distillation is the main unit operation to be used for recovery of the ILs. However, the energy cost associated with distillation is high, which may impair the overall feasibility of a large-scale process ^{327,349}. For these reasons, the use of ILs that do not require anhydrous conditions to be effective in biomass pretreatment, such as the hydrogen sulfate based ILs, would be easier to implement in large scale processes.

4.2.6.6.3 Toxicity, biodegradability and renewability

The toxicity, biodegradability and renewability of ILs are important aspects to consider for their industrial applications. For example, BASF utilised [C₂C₁im][OAc] over [C₂C₁im]Cl in their commercial CELLIONIC™ formulation of IL solutions of cellulose, due to the higher toxicities and corrosivity of chloride-containing ILs ¹⁶¹.

It has been speculated that in the future IL-based biorefineries will involve the use of biological agents (such as enzymes) that are exposed to ILs in fermentation or biocatalytic conversions, in which ILs could even serve as the media for the microbial processes ³²⁷. Therefore, the biocompatibility of ILs will be an important factor to offset process complexities and additional costs to purify IL-pretreated biomass for downstream microbiological processes ³²⁷. In addition, non-toxic ILs would have the potential to be used in the production of food-grade chemicals ³²⁷. There are also concerns on the effects on the environment and biomass processing of residual amounts of impurities from the synthesis of the ILs, such as 1-methylimidazole from the synthesis of imidazolium-based ILs. It is expected that more stringent IL purification methods would be needed increasing their cost ³²⁷.

Biodegradable ILs are desirable to minimise the environmental impact of these substances, especially with the ever-tightening grip of environmental regulations on the use of industrial solvents ³²⁷. For example, cholinium ILs are a class of ILs that have low toxicity and are readily biodegradable ³²⁷. In addition to biodegradability, the production of ILs from renewable materials is a very important consideration in a biorefinery and in this regard bio-based ILs have been prepared and tested for biomass pretreatment. For instance, cholinium amino acids, such as choline lysine, choline glycine and choline alanine, were tested for the pretreatment of sugarcane bagasse ^{327,350}.

4.2.6.6.4 Solids loading and size reduction

In the majority of studies involving IL pretreatment of biomass, solid loadings have typically been about 5% (wt/wt) ³⁵⁰. This value is low when compared to the solids loadings of other chemical pretreatment methods. The solids loading has important repercussions for the throughput and economics of the pretreatment process as there would be cost savings if less of the IL solvent can be used and more biomass processed per pretreatment ³⁵⁰. In addition to solids loading, comminution of biomass has frequently been applied in studies involving ILs with limited work performed on biomass that has not been reduced in size ³⁵⁰. The energetic requirements for the comminution of biomass can adversely affect the economics of biorefinery processes to a significant extent ³⁵⁰.

Several efforts, to explore the points mentioned above (e.g. using not milled biomass or higher solids loading), have been conducted to improve IL-based pretreatment methods. For example, work performed on the impact of high solids loading on the performance of AILs ([C₂C₁im][OAc]) to pretreat corn stover pretreatment with particles sizes ranging between 1 – 2 mm, at 125 °C for 1 h with biomass loadings of 4.8 – 50% (wt/wt) ²³². It was shown that over a wide range of biomass loadings from 4.8 – 33% (wt/wt), the yields of glucose and xylose from enzymatic hydrolysis remained similar at 80% and 50%, respectively ²³². For loadings above 33% (wt/wt), there was less lignin extracted and less disruption of cellulose crystallinity, resulting in a decrease in enzymatic hydrolysis efficiency ²³². In another study using the same IL to pretreat switchgrass at 160 °C for 3 h with biomass loadings in the IL varying between 3% and 50% (wt/wt) it was found that as the biomass loading increased, the relative glucan content of the recovered solid samples decreased with increasing levels of lignin and hemicellulose ³⁵¹. Maximum glucose recovery (nearly 100%) was obtained for the solid recovered after pretreatment with a biomass loading of 10% (wt/wt) but dropped significantly at higher biomass loadings ³⁵¹. However, an unexpected advantage of increasing the loading levels to 40 – 50% (wt/wt) was the decrease in the cellulose crystallinity which produced faster enzymatic hydrolysis kinetics and could potentially lower enzyme loading levels to improve the economic viability of IL pretreatment ³⁵¹.

The effect of biomass loading and particle size on pretreatment performance has been also investigated for the hydrogen sulfate based IL. Miscanthus samples were pretreated with [N₂₂₂₀][HSO₄] at 120 °C for 6 h, using solid loadings ranging from 2 to 50 wt% in unstirred 15 mL pretreatment tubes ³⁵². Pulp yields showed a steady increase from 51 to 63% upon increasing the biomass loading from 2 to 50 wt%. Lignin yields concomitantly decreased from quantitative recovery at 2 wt% loading to only half of the theoretical lignin recovery at 50 wt% loading ³⁵². Delignification similarly reached 86% at low loadings but decreased to 47% at 50 wt% loading ³⁵². Accordingly, the saccharification yield fell gradually with increasing solids loading, with the highest yields (77%) obtained at 2 wt% loading, from where it decreased to 23% at 50 wt% loading.

For experiments involving different particle sizes (coarse > 1 cm, medium 1–3 mm, and fines 18 – 0.85 mm), three different feedstock-solvent combinations were tested: Miscanthus (80 wt% [N₂₂₂₀][HSO₄], 120 °C, 6 h, 20 wt% loading) Brown treated pine (*Pinus sylvestris*) (80 wt% [N₂₂₂₀][HSO₄], 170 °C, 30 min, 20 wt% loading) and Miscanthus-dilute acid (3 wt% H₂SO₄, 120 °C, 1.5 h, 20 wt% loading) ³⁵². In general, it was shown that there are not significant differences in the glucan recovery values for coarse and medium particles while a slight

reduction was noted for fine particles. Hemicellulose extraction was more effective for finer particles due to greater sugar accessibility. The delignification showed an interesting trend in that it was maximum for medium (1 – 3 mm) particles. Coarse particles (10–12 mm) were less delignified due to poor lignin extraction associated with the lower surface area to volume ratio of larger particles; and fine particles (0.18 – 0.85 mm) had the lowest delignification and lower saccharification yields ³⁵².

These results show that there are no benefits of extensive grinding the wood to form fine particles for the IonoSolv process to be effective, which can lead not only to energy savings on the milling process (reduced OPEX), but also to CAPEX savings, as no stringent wood particle size reduction equipment would be needed. The results on biomass loading suggest that this parameter could be used to optimize the biorefinery. The impact of biomass loading on the IonoSolv process was investigated through sensitivity analysis (section 4.4.9.4).

4.2.7 Techno-economic analysis for biorefineries

An excellent techno-economic analysis (TEA) comparing six pretreatment technologies (AFEX, dilute acid, lime, liquid hot water, soaking in aqueous ammonia and SO₂-impregnated STEX) for 2G bioethanol production from switchgrass showed limited differentiation in the projected economic performances of the different pretreatment options, except for the soaking in aqueous ammonia processes, that exhibit significantly lower monomer sugar and ethanol yields ²⁸⁶. As previously stated, switchgrass is not very recalcitrant in contrast to softwood, which may lead to a larger variation of the estimated costs ²⁹⁷.

A TEA for the organosolv process revealed that the Minimum Ethanol Selling Price (MESp) of the current organosolv process was slightly higher than the NREL diluted process ³⁰⁷. Therefore, in order to improve the organosolv pretreatment for commercialization, several strategies have been proposed ^{306,307}:

- The pretreatment conditions (temperature, pretreatment time, solvent concentration, and catalysts) should be optimized to maximize product yield, product quality, and to minimize pretreatment cost ³⁰⁶.
- Develop a continuous pretreatment system suitable for flexible biomass feedstocks ³⁰⁶.
- Develop lignin-based products to improve overall biorefinery economic potential ³⁰⁶.

Those strategies will improve the economic performance, not only for the organosolv process but for other pretreatment technologies as well.

A preliminary TEA for biological production of ethanol using an IL-based pretreatment process showed that the MESP for this methodology is likely to be higher than dilute acid pretreatment³⁵³. That assessment revealed that the IL cost was the most important parameter, as previously stated, and that lowering the IL loading was more important than increasing the IL recycle rate. Another TEA of a 113 million L/year (30 million gal/year) biorefinery using [C₂C₁][OAc] to produce fermentable sugars from three different feedstocks, corn stover, switchgrass, and poplar estimated the sugar production costs of 2.7, 3.2, and 3.0 \$US/kg respectively. IL recovery was identified to be the most sensitive parameter followed by IL cost and heat recovery. It was highlighted that for AIL pretreatment to be economically competitive with sulfuric acid pretreatment, >97% IL recovery, ≤\$1/kg IL cost, and >90% waste heat recovery were necessary. Other challenges for the use of [C₂C₁][OAc] in biorefineries have also been highlighted, such as significant water-wash related to the high toxicity³³⁸. A preliminary TEA for a low cost (~\$1 per kg) and biocompatible PIL, [MEA][OAc], without pH adjustments, water-wash, and solid–liquid separations, and using simultaneous saccharification and fermentation (SSF) showed that this technology could potentially reduce the MESP by more than 40% compared to scenarios that require pH adjustment prior to SSF³³⁸.

4.2.7.1 *Techno-economic analysis for the ionoSolv process – Early models*

A preliminary TEA to evaluate the economic and environmental potential of different technologies for biorefineries, for the production of biofuels and chemicals, showed that they have the potential to deliver sustainable solutions for the substitution of crude-oil-derived products³⁵⁴. It was also shown that biorefineries cannot be considered as “green” or sustainable alternative only based on the fact that they are using renewable feedstocks, and it was concluded, that if they were not designed taking into account environmental criteria (*e.g.* energy consumption and waste generation), their environmental footprint could be higher than conventional crude-oil-based refineries³⁵⁴. Therefore, biorefineries should not be only optimized in economic terms, but also taking into account environmental considerations³⁵⁴. When pretreatment technologies, with different maturity levels, were compared in that assessment taking into account economic and environmental considerations, it was concluded that the acid-based methods (concentrated sulfuric acid) were the most viable technology³⁵⁴. AILs were too expensive without improving the environmental performance of the biorefinery, due to excessive energy consumption, water usage and waste generated³⁵⁴. A preliminary evaluation for the ionoSolv process revealed a significant improvement compared to the AIL-based biorefinery, but it was worse than the acid pretreatments³⁵⁴. However, it was

acknowledged that the ionoSolv process could be competitive, but that a more detailed evaluation was required ³⁵⁴.

There have been several preliminary techno-economic analyses of the ionoSolv process ¹⁷⁻¹⁹. The technical and economic feasibility of an ionoSolv biorefinery using miscanthus was confirmed by simulating the process with gProms. It was found that the energy requirements to dry the IL, through flash distillation, was the major contributor to the overall energy consumption and it was highlighted that the process could be heat integrated to make it energy sufficient ¹⁷. This model was further optimized to reduce the water consumption (by introducing a wastewater treatment facility) and the energy consumption by conducting heat integration and using pervaporation technology for water removal from the IL solution. The energy consumption of the optimized process was 9.5 MJ/kg-dry biomass (compared to 12.6 MJ/kg-dry biomass) and a water consumption of 17.13 kg-water/s (compared to 63.23 kg-water/s) ¹⁸. It has been noticed that none of these works benchmarked this process against other viable pretreatment alternatives, such as the acid catalysed pretreatment.

4.2.8 Knowledge gaps

It has been noticed that despite the large number of scientific articles and reports about the conversion of biomass to liquid fuels and chemicals that are available in the scientific literature, bio-derived chemicals represent only a small fraction of the overall chemical and fuel market. The limiting factor for large scale biorefineries is no longer technical but economic related. For them to become an industrial reality, it is therefore extremely important to reduce the cost of these processes.

There is an increasing interest in the use of ILs for biomass processing, as these solvents are considered green, due to their low volatilities, and have adjustable properties ¹. However, despite these advantages, common ILs currently suffer from clear and significant challenges that stand in the way of commercialization of IL-based pretreatments. These include their relatively high cost, the requirement of significant IL recovery and recycling, and the water sensitivity of the biomass pretreatment process ^{327,328}. There has been extensive work on a particular type of acidic PILs based on the hydrogen sulfate anion, which tackles all of the problems highlighted for other IL-based methods. *i.e.* they can be produced at low cost, can be recovered and recycled, and are very efficient for the fractionation of different LB types (grass, hardwoods and softwoods) into cellulose-rich pulps (with high enzymatic digestibility) and lignin, even in the presence of water, for large particle size and high biomass loadings. For these

reasons, it has been suggested that they are excellent candidates for the pretreatment step within a biorefinery^{3,88,341–346,352,355}.

However, at the time this thesis started, the focus of the work done on the ionoSolv process had been centred about understanding (at lab scale) how several parameters of the ionoSolv process (*e.g.* IL type, temperature, time, water concentration, particle size, base:acid ratio, solid loading and scale) affected the pretreatment performance (*e.g.* pulp yields, glucose yields after enzymatic hydrolysis, hemicellulose removal, lignin removal and recovery) for different biomass types without detailed techno-economic analysis to verify the feasibility of this process for a large scale biorefinery. Some early TEAs were too preliminary to reach a definite conclusion about the industrial feasibility of the ionoSolv process and were not compared to other technologies which are considered as viable alternatives (*e.g.* acid catalysed pretreatments). Therefore, the main objective of this study is to evaluate the technical feasibility of the biorefinery to produce 2G ethanol for Eucalyptus using the ionoSolv process. The performance of the IL-based biorefinery will be compared to a popular pretreatment process, *i.e.* the Acid Catalysed Steam Explosion (ACSE) pretreatment.

As mentioned in sections 4.2.5.5 and 4.2.6.1, CO₂ atmospheres have an effect on biomass fractionation using both non-IL and AIL ([C₂C₁im]Cl) methods³⁰⁹. Ways in which CO₂ can influence the pretreatment performance includes a decrease of the solution viscosity (improving mass transfer between the LB and the IL medium)^{356–359}, reaction with the IL to form carbamates⁵⁸, reaction with the water in the system to form carbonic acid and/or perturbation of the LB structure by diffusion into the pores and braking the LB matrix by expansion upon depressurisation³⁰¹. The effect of CO₂ atmospheres and pressure on LB pretreatment using PILs, and in particular the hydrogen sulfate based ILs, have not been studied. Therefore, in this work, these effects in the pretreatment performance of hardwoods (Eucalyptus) with a PIL ([N₂₂₂₀][HSO₄]) is investigated in collaboration with Dr Joana M. Lopes as a potential route to improve the ionoSolv process performance.

4.3 Experimental methods

4.3.1 Materials

4.3.1.1 Synthesis of triethylammonium hydrogen sulfate [N₂₂₂₀][HSO₄]

The ionic liquid selected for this study was triethylammonium hydrogen sulfate [N₂₂₂₀][HSO₄], synthesized using the reactor described in section 2.3.2. The water content of 20 wt% was confirmed by Karl-Fischer titration (section 2.3.3.1) in triplicate. For consistency, this same

batch of IL solution was used for all pretreatment experiments. The base:acid ratio was not controlled.

4.3.1.2 CO₂ experiments

The pretreatments under CO₂ atmospheres were conducted in a Parr reactor (Series Compact Reactor - PARR 5500 and a reactor controller Parr 4848). Alkylammonium hydrogen sulfates ILs can interact with stainless steels (Chapter 3). To avoid any interference of the presence of metal in the pretreatment or reactor corrosion problems, a glass liner was used to hold the IL and biomass and all the wetted parts were protected with PTFE coatings and liners (Figure 84). CO₂ from a 5 kg CP grade CO₂ DIP Tube cylinder from BOC was used (Purity 99.995% pressure 50 bar).

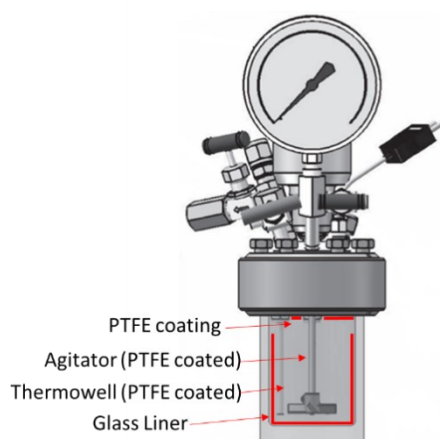


Figure 84. Schematic representation of the reactor used for the CO₂ atmosphere experiments. Published by The Royal Society of Chemistry ³².

4.3.1.3 Feedstock

A Plank of *Eucalyptus Red red grandis* was obtained from a local lumber supplier (origin and age of the specimen unknown). It was air-dried, chopped and sieved (180-850 μm, 20 + 80 US mesh scale) prior to use and stored in plastic bags at room temperature in the dark. The pulp was characterized using FTIR (appendix 12).

4.3.2 Biomass fractionation and characterisation

The experimental procedures and formulae to calculate the moisture content, biomass fraction, compositional analysis, delignification, and hemicellulose removal, saccharification assay and biomass fractionation are described in this section ³².

4.3.2.1 Moisture content

For both raw and pretreated biomass, the moisture content was determined according to the protocol by the National Renewable Energy Laboratory (NREL) “Determination of Total Solids in Biomass and Total Dissolved Solids in Liquid Process Samples”³⁶⁰ by weighing out approximately 100 mg of biomass/pulp onto a preweighed piece of aluminium foil and recording the weight using the analytical balance. The foil with the biomass/pulp was folded and oven dried (T = 105 °C) overnight. The hot packets were placed in a desiccator to allow cooling to room temperature. The weight was recorded immediately, and the moisture content calculated.

$$\%Total\ Solids = \left(\frac{Weight_{Foil+oven\ dried\ biomass} - Weight_{foil}}{Weight_{air-dried\ biomass}} \right) \cdot 100\% \quad (88)$$

$$\%Moisture = 100 - \left(\frac{Weight_{Foil+oven\ dried\ biomass} - Weight_{foil}}{Weight_{air-dried\ biomass}} \right) \cdot 100\% \quad (89)$$

The moisture content of all *Eucalyptus red grandis* samples (raw and pretreated) ranged from 7% - 9%.

4.3.2.2 Biomass fractionation

The ionic liquid/water mixture was prepared by adding 20 wt% of water to the hydrogen sulfate ionic liquid triethylammonium hydrogen sulfate [N₂₂₂₀][HSO₄] and mixing until a homogenous solution was obtained. The water content was confirmed by Karl-Fischer titration in triplicate (section 2.3.3.1). The required amount of IL/water mixture was weighed into a 15 ml glass pressure tube with silicone front seal (Ace Glass) and the exact weight recorded. The air-dried biomass (*Eucalyptus red grandis*) was added to obtain a solvent ratio of 1:10 g/g. The containers were capped, and the content mixed with a vortex shaker. The samples were then placed into a preheated convection oven (OMH60 Heratherm Advanced Protocol Oven). After the pretreatment period, they were taken out and left to cool at room temperature. After the pretreatment, 40 mL of ethanol was added to the pretreatment mixture and the suspension transferred into a 50 mL centrifuge tube. The tube was shaken for one minute and the mixture then left at room temperature for at least 1 hour. The tube was mixed again for 30 seconds and then centrifuged at 3500 rpm for 1 hour. The supernatant was decanted carefully into a round bottom flask. The washing step was repeated three more times. The remaining pulp was then transferred into a cellulose thimble and further washed by Soxhlet extraction with refluxing ethanol (150 mL) for 24 hours. The thimbles were then left on the bench overnight to dry. The ethanol used for the Soxhlet extraction was combined with the previous washes and evaporated under reduced pressure at 40 °C, leaving the dried ionic liquid/lignin mixture. To

the dried ionic liquid/lignin mixture, 30 mL of water was added to precipitate the lignin. The suspension was then transferred into a 50 mL falcon tube, shaken for one minute and then left at room temperature for at least 1 hour. The tube was centrifuged and the supernatant decanted and collected in a round bottom flask. This washing step was repeated twice more. The air-dried pulp yield was determined by weighing the recovered biomass from the cellulose thimbles. The oven-dried yield was determined as described in section 4.3.2.1.

$$Yield_{pulp} = \left(\frac{Weight_{air-dried\ biomass\ after\ pretreatment}}{Weight_{air-dried\ biomass\ before\ pretreatment}} \right) \cdot \left(\frac{\%Moisture_{air-dried\ biomass\ after\ pretreatment}}{\%Moisture_{air-dried\ biomass\ before\ pretreatment}} \right) \cdot 100\% \quad (90)$$

The lid of the Falcon tube containing the lignin was removed. The tube was covered with a cellulose-paper, to avoid lignin contamination or losses and put into a vacuum oven overnight to dry at 40 °C under vacuum. The dried lignin was weighed the next day and lignin yields, and delignification calculated.

$$Lignin_{untreated} = Weight_{air-dried\ untreated\ biomass} \cdot \left(\frac{100 - \%Moisture}{100} \right) \cdot \%Lignin_{untreated\ dry\ basis} \quad (91)$$

$$Yield_{lignin} = \frac{Weight_{dried\ lignin\ after\ pretreatment}}{Weight_{air-dried\ untreated\ biomass} \cdot \left(\frac{100 - \%Moisture}{100} \right)} \cdot 100\% \quad (92)$$

$$Recovery_{lignin} = \left(\frac{Weight_{dried\ lignin\ after\ pretreatment}}{Lignin_{untreated}} \right) \cdot 100\% \quad (93)$$

$$Delignification = \left(\frac{Lignin_{untreated} - (Lignin_{pulp} \cdot Yield_{pulp})}{Lignin_{untreated}} \right) \cdot 100\% \quad (94)$$

Where $Lignin_{untreated}$ is the lignin content in untreated Eucalyptus, $Lignin_{pulp}$ is the lignin content in the pulp and $Yield_{pulp}$ is the oven-dried yield of pulp.

The experiments under CO₂ atmosphere were carried in a similar way. The biomass and IL were weighted in a glass liner, which was placed into the Parr reactor described in the experimental section of the main manuscript. The reactor was sealed according to the manufacturer instructions. The agitator of the reactor was used to mix the biomass and the IL, then it was switched off. The reactor was then pressurized with CO₂ to the required pressure. After the experiments, the reactor was let to cooled down to 50 °C and depressurised slowly by opening the depressuring valve. Once the reactor reached ambient temperature and pressure, it was

opened, the glass liner removed and the pretreated biomass washed as described previously. A video describing the experimental protocol is available for consultation ³⁶¹.

4.3.2.3 Extractive determination

Ethanol extractives determination was carried out according to a published procedure by NREL “Determination of Extractives in Biomass” ³⁶² in triplicates. Around 2.5 g were weighted and transferred into a cellulose thimble, which was placed into a Soxhlet extraction apparatus with refluxing ethanol (190 + 5 mL) for 24 hours. After this period, the system was allowed to cool down and the thimbles were washed with fresh ethanol and then left overnight to dry at room temperature. The solids were dried and the extractive content calculated:

$$\%Extractives = 100 - \left(\frac{Weight_{air-dryed\ extracted\ biomass}}{Weight_{air-dryed\ untreated\ biomass}} \right) \cdot 100\% \quad (95)$$

4.3.2.4 Compositional analysis

Compositional analysis was carried out according to a published procedure by NREL “Determination of Structural Carbohydrates and Lignin in Biomass” ³⁶³. 300 mg (on oven-dry basis) of air-dry biomass after pretreatment and raw biomass without the extractive was weighed into a 100 mL pressure tube and the weight recorded. 3 mL of 72% sulfuric acid was added, the samples stirred with a Teflon stir rod and the pressure tubes placed into a preheated water bath at 30 °C. The samples were stirred again every 15 min for one hour, they were then diluted with 84 mL distilled water and sealed. The samples were autoclaved (Sanyo Labo Autoclave ML5 3020 U) for one hour at 121 °C and left to cool. The samples were then filtered through filtering ceramic crucibles of a known weight. The filtrate was stored in two plastic tubes and the remaining residue washed with distilled water. The crucibles were placed into a convection oven (VWR Venti-Line 115) at 105 °C for 24±2 hours. They were placed in a desiccator for 15 min and the weight recorded. The crucibles were then placed into a muffle oven (Nabertherm + controller P 330) and ashed to constant weight at 575 °C. The crucible weight after ashing was recorded. The content of Acid Insoluble Lignin (AInL) was determined according to Eq. 96.

$$\%AInL = \frac{Weight_{crucible+ AIR} - Weight_{crucible+ ash}}{Weight_{oven-dry\ sample}} \cdot 100 \quad (96)$$

where $Weight_{crucibles + AIR}$ is the weight of the oven-dried crucibles plus the acid insoluble residue, $Weight_{crucibles + ash}$ is the weight of the crucibles after ashing to constant temperature at 575 °C.

The supernatant was used for the determination of Acid Soluble Lignin content (ASL) by UV analysis at 240 nm (Eq. 97) using a Perkin Elmer Lambda 650 UV/Vis spectrometer.

$$\%ASL = \frac{A}{l \cdot \varepsilon \cdot c} \cdot 100\% = \frac{A \cdot V_{\text{filtrate}}}{l \cdot \varepsilon \cdot \text{Weight}_{\text{oven-dry sample}}} \cdot 100\% \quad (97)$$

Where A is the absorbance at 240 nm, l is the path length of the cuvette in cm (1 cm in this case), ε is the extinction coefficient (25 L/g cm), c is the concentration in mg/mL, the oven-dried weight of the sample in mg and V_{filtrate} is the volume of the filtrate in mL and equal to 86.73 mL.

Calcium carbonate was added to the second liquid fraction until pH 5 was reached. The liquid was passed through a 0.2 μm PTFE syringe filter and subsequently submitted to HPLC analysis (Shimadzu, Aminex HPX-97P from Bio-Rad, 300 x 7.8 mm, purified water as mobile phase at 0.6 ml/min, column temperature 85 °C, de-ashing columns were used as pre-filters) for the determination of total sugar content. Calibration standards with concentrations of 0.1, 1, 2 and 4 mg/mL of glucose, xylose, mannose, arabinose and galactose were used. Sugar recovery standards were prepared as 10 mL aqueous solutions close to the expected sugar concentration of the samples and transferred to pressure tubes. 278 μL 72% sulfuric acid was added, the pressure tube closed and autoclaved and 3 the sugar content determined as described above. The sugar recovery coefficient (SRC) was determined according to Eq. 98 and the sugar content of the analysed sample using Eq. 99.

$$SRC = \frac{C_{\text{HPLC}} \cdot V}{\text{initial weight}} \quad (98)$$

$$\%Sugar = \frac{C_{\text{HPLC}} \cdot V \cdot \text{corr}_{\text{anhydro}}}{SRC \cdot \text{Weight}_{\text{oven-dry sample}}} \cdot 100\% \quad (99)$$

where C_{HPLC} is the sugar concentration detected by HPLC, V is the initial volume of the solution in mL (10.00 mL for the sugar recovery standards and 86.73 mL for the samples), initial weight is the mass of the sugars weighed in, $\text{Corr}_{\text{anhydro}}$ is the correction for the mass increase during hydrolysis of polymeric sugars (0.90 for the C₆ sugars glucose, galactose and mannose and 0.88 for the C₅ sugars xylose and arabinose) and the oven-dried weight of the sample in mg.

4.3.2.5 Saccharification assay

Saccharification assays were carried out according to a protocol published by the NREL “Low Solids Enzymatic Saccharification of Lignocellulosic Biomass”³⁶⁴ in triplicate with blanks (also in triplicate). All reagents were purchased from Sigma Aldrich. The detailed procedure is as follows:

100±10 mg (ODW basis) of air-dried was placed into a Sterilin tube and the weight recorded. Three enzyme-only blanks were run with 100 µL of purified water instead of biomass to correct for sugar residues present in the enzyme solutions. 9.9 mL solution made from 5 mL 100mM sodium citrate buffer at pH 4.8, 40 µL tetracycline solution (10 mg/mL in 70% ethanol), 30 µL cycloheximide solution (10 mg/mL in purified water), 4.71 mL purified water and 50 µL of Novozymes experimental enzyme mixture NS-22201 was added, the tubes closed and placed into an Stuart Orbital Incubator (S1500) at 50 °C and 250 rpm for 7 days at 50 °C and 250 rpm. End point samples were obtained by filtering 1 mL of the saccharification mixture through a PTFE syringe filter. Samples were analysed on Shimadzu HPLC system with RI detector and an Aminex HPX87P column (BioRad, 300 x 7.8 mm) with purified water as mobile phase (0.6 mL/min). The column temperature was 85 °C and acquisition time was 40 min. Calibration standards with concentrations of 0.1, 1, 2 and 4 mg/mL of glucose, xylose, mannose, arabinose and galactose and 8 mg/mL of glucose were used.

4.3.3 Biorefinery - Base case definition

The IonoSolv process units have been modelled in HYSYS V8.8 to obtain the Heat and Materials Balances (HMB) for process equipment sizing and costing. The conditions leading to the best saccharification yields, determined experimentally, will be used for the base case. Details on the assumptions of the simulations are given in Appendix 13.

To evaluate the IonoSolv process, all units have been considered the same as per the reference project except for the Pretreatment” and “Steam Explosion/Wash” units, which have been replaced for the different units within the IonoSolv process, namely “Pretreatment Unit”, “Lignin Recovery” and “IL Conditioning”. A block flow diagram for the integrated biorefinery is shown in Figure 85.

Several preliminary process schemes were tested to determine the best level of thermal integration and water usage (not shown in this work). A simplified Process Flow Diagram (PFD) of the concept retained for the IonoSolv process is given in Figure 86 (detailed PFDs and process description are given in Appendix 13). The IonoSolv concept has been designed taking into consideration Green Chemistry and Engineering practices (section 1.2.3). For example, heat integration was performed to minimize the energy demand of the process.

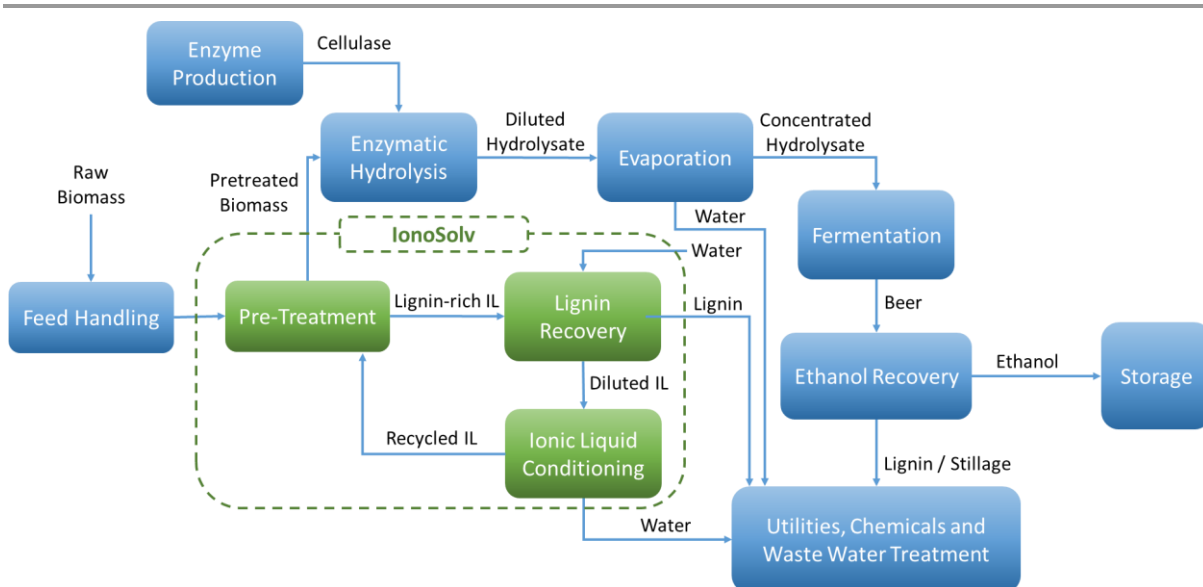


Figure 85. Potential process block flow diagram for the IonoSolv-based biorefinery.

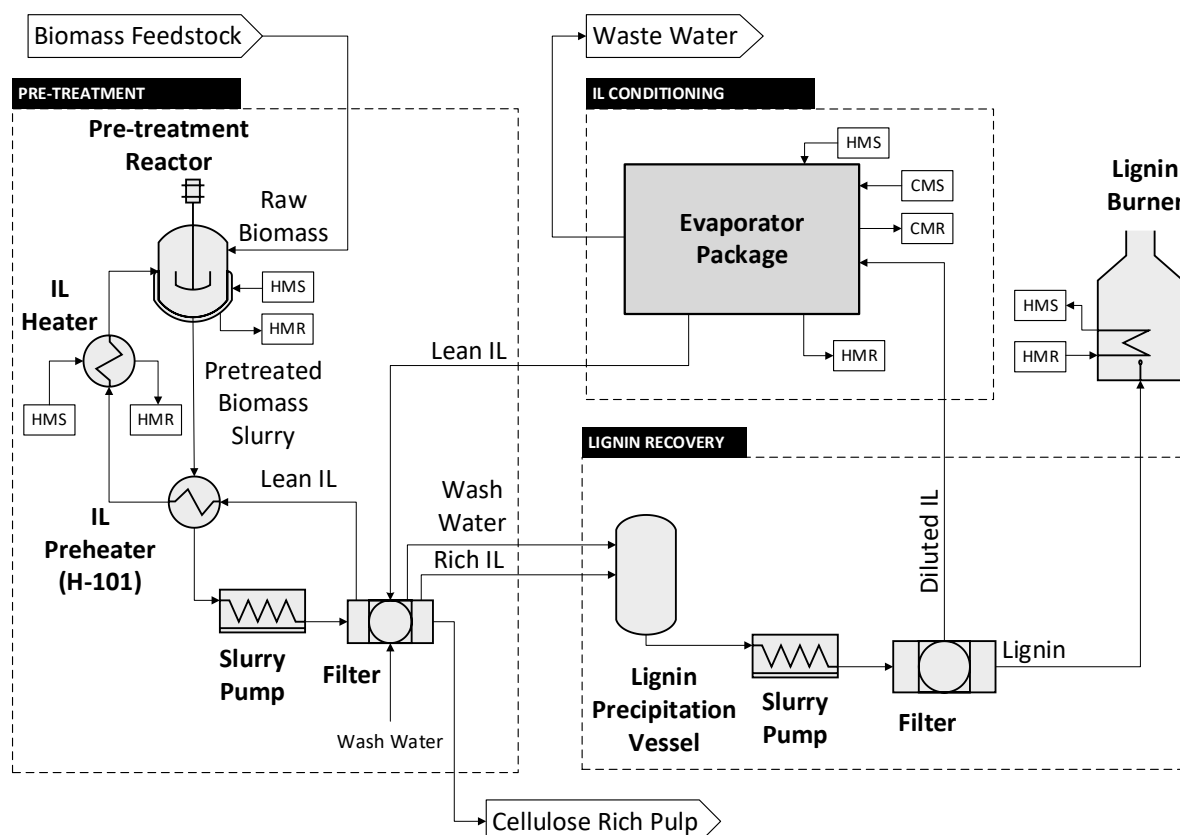


Figure 86. Simplified PFD for the IonoSolv Process. HMS: heating medium supply, HMR: heating medium return, CMS: cooling medium supply and CMR: cooling medium return. Detailed PFDs are given in appendix 13.

The SERI project is processing 210 238 metric tonnes of dry wood (*Eucalyptus globulus*) a year, of which 94% is used to produce ethanol. The rest 6% represents small chips, wood dust and debris not suitable for ethanol production and are sent to the boiler to generate heat²³⁷. The same basis is used to model the IonoSolv based biorefinery.

The compositional analysis of *Eucalyptus red grandis* determined experimentally in this work, and the composition of the *Eucalyptus globulus* (blue gum) from the reference project are given in Table 26. For a fair comparison of the 2 processes, the same composition as per the reference project have been assumed for the IonoSolv process, with the best process performance determined experimentally (details in Appendix 13). For simulations purposes, the glucomannan fraction has been combined with the cellulose fraction and the “other polysaccharides” have been combined with the glucuronoxytan and modelled as xylan.

Table 26. Eucalyptus composition for process evaluation.

Components	<i>Eucalyptus red grandis</i>	<i>Eucalyptus globulus</i> (blue gum)	
		IonoSolv Process	Reference Project ²³⁷
Extractives	0.7	1.3	1.3
Lignin	33.3	21.9	21.9
Cellulose	53.4	52.7	51.3
Glucomannan (C ₆)	-	-	1.4
Glucuronoxytan	10.6	23.8	19.9
Other Polysaccharides	-	-	3.9
Residual Constituents	-	0.3	0.3

The base case development has been done based on the following material balance. Material streams from the reference project have been taken as reported while for the IonoSolv project they have been determined by applying the process performance on *Eucalyptus red grandis* to the composition of the reference project. Other assumptions from the reference project have been kept the same: 8% glucose used for enzyme production, 95% fermentation efficiency (2% for yeast production and 3% side reactions of sugar degradation). The results are summarised in Table 27.

The energy that could be obtained from burning fuels, organic residues, lignin and/or methane was calculated assuming 100% efficiency in the boiler. The HHV for the combusted materials used are 24.6 ± 0.9 MJ/kg for lignin (average HHV value for IonoSolv *Miscanthus* lignins ⁸⁸), 17.1 ± 0.4 MJ/kg for cellulose and all other organic compounds (average value from different cellulose sources ³⁶⁵) and 55.1 MJ/kg for methane ¹⁴¹.

Table 27. Overall mass balance.

Stream	Units	SERI Project	IonoSolv
Raw biomass total	kg/h	26 280	26 280
Raw biomass to pre-treatment	kg/h	24 704	24 704
Total Pre-treated Pulp (dry basis)	kg/h	17 263	11 499
Cellulose after pre-treatment	kg/h	12 673	11 066
Glucose to fermentation (after enzymatic hydrolysis)	kg/h	11 026	11 312
Available heat from combusted materials (boiler)	MW	76.6	100
Ethanol after fermentation (dry basis)	kg/h	5 385	5 541

Stream	Units	SERI Project	IonoSolv
Total ethanol production [A]	ton/year	43 077	44 328
	MML/year	54.6	56.2

A. Including 0.8 wt% water.

4.3.4 Biorefinery - Reference project description

The reference project used to benchmark the IonoSolv process is a feasibility study prepared by Stone & Webster Engineering Corporation (SWEC), for an enzyme-based ethanol plant production, for the Solar Energy Research Institute (SERI) ²³⁷. This project was selected for several reasons: C₅ sugars as the C₅ is not recovered as a by-product in the current models. In the reference project, C₅ sugars are sent to an anaerobic digester to produce a methane-rich gas, which is burned, along with the lignin and unconverted cellulose, in a boiler to produce high-pressure steam for process use. In the IonoSolv process, it is assumed that C₅ sugars are converted to pseudo-lignins that co-precipitate with the lignin and are also burnt for energy production.

The site for the plant of the reference project was located on the island of Hawaii, near the city of Hilo. The full-scale plant is capable of producing 56.8 MM L/y (15 MM gallons/year) of fuel-grade ethanol from eucalyptus wood chips (463 500 tons/year of feedstock wet basis). The main pretreatment technology is Acid Catalysed Steam Explosion (ACSE) using diluted sulfuric acid. A detailed description of the different process units in the reference project is given in Appendix 13 and the original reference ²³⁷.

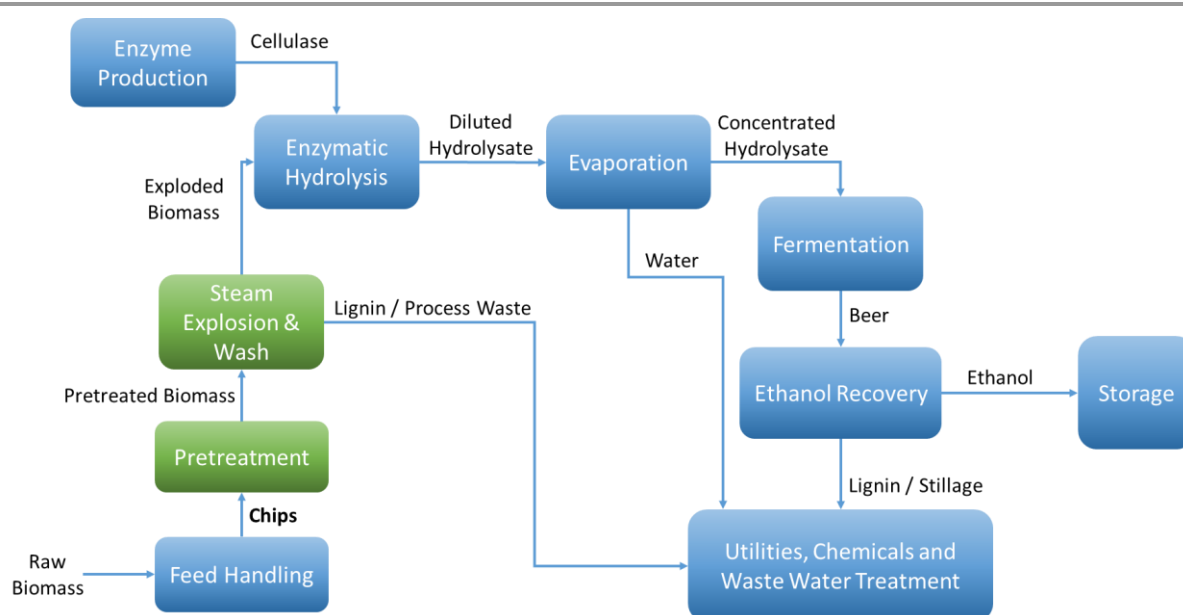


Figure 87. Simplified block flow diagram of the reference project. More details are given in Appendix 13.

The saccharification yield in the reference project was assumed to 84% by the engineering contractor, based on data produced for cellulose conversion from a steam-exploded corn stover (University of California, Berkeley), since information on steam-exploded eucalyptus was not available at the time that work was produced ²³⁷. In a study using a similar pretreatment (*i.e.* ACSE) to pretreat *Eucalyptus grandis* under various pretreatment conditions (200–210 °C, 2–5 min) after impregnation of the wood chips with 0.087 and 0.175 wt% H₂SO₄ ³⁶⁶, it was found that temperatures of 200 °C were enough to yield pulps which led to 90% glucose recovery ³⁶⁶. This study confirms that the assumption of 84% sugar yield, made to develop the reference case, is achievable for eucalyptus. The performance of the reference project was not updated as the experimental results were obtained at laboratory scale and not in a pilot plant. Moreover, the enzymatic hydrolysis efficiency depends on the nature of the enzymes used, which are not the same as per the reference project. Updating the reference project with these results would require detailed modelling of the entire biorefinery, which will require an enormous amount of work. For these reasons, it was decided not to change the reference project for the first benchmarking of the IonoSolv process.

4.3.5 Biorefinery - Capital cost (CAPEX) estimation

According to the engineering contractor for the reference project, the CAPEX estimate for the ethanol plant was generated using budgetary cost estimates from vendors (vendor quotes) and their in-house cost estimates based on equipment specifications. The total CAPEX estimation for the reference project was reported in 1984 \$US and was corrected to 2019 \$US using Eq. 1 in Appendix 14 and the respective Chemical Engineering Plant Cost Index (CEPCI) 322.6 (1984) and 607.5 (2019) ³⁶⁷.

For the IL-based biorefinery, only the process units related to the pretreatment were evaluated in detail. For the other process units, the process scheme and design assumptions were assumed the same as the reference project. The total installed equipment cost (TIEC) for such units was corrected according to capacity using Eq. 2 in Appendix 14 and a scaling exponent equal to 0.6. For the IonoSolv-based biorefinery, it has been assumed a full spare for rotating equipment (pumps).

The anaerobic digester unit (Unit 800) was removed from the IonoSolv biorefinery as it is assumed that organics in the IL phase will react to form pseudo-lignins that will co-precipitate with the lignin and sent to the burner as a solid. Therefore, the amount of organic molecules in the wastewater streams is too low to justify the installation of the digester for methane production. This point would need to be confirmed during the detailed engineering phase.

The purchased equipment cost for the ionoSolv evaluation is either based on correlations found in the literature (Couper *et al.*)³⁶⁸ or on quotations from vendors. Details on the specific assumptions for equipment sizing and costing are given in Appendix 13. The installed equipment cost is obtained by multiplying the purchased cost by an installation factor. The factors used are given in appendix 14.

Regarding the material selection for the ionoSolv equipment, it has been assumed the use of stainless steel 316. As mentioned in Chapter 3, [HSO₄]-based ILs can attack 304 SS but not molybdenum. For this assessment, it has been assumed that SS 316 will have better corrosion performance than SS 304, as it contains 2 - 3 wt% Mo, when exposed to the IL-water mixtures. However, the corrosion rate of this material needs to be validated at process conditions. In the absence of detailed corrosion data, there are other cost-effective alternatives to expensive corrosion resistance alloys and metals for corrosive media, such as the use of low-cost carbon steel protected with glass or polymer (PTFE, PEEK) liners. The use of these liners typically results in less expensive pipes and process equipment than SS 316, therefore, the assumption that SS 316 can be used is considered conservative, in terms of cost estimation, for most equipment. One exception could be the heat exchangers, that might require a more expensive metallurgy. Suitable construction materials need to be validated to establish a more accurate CAPEX estimation.

4.3.6 Biorefinery – OPEX estimation

4.3.6.1 Variable costs

The variable operating costs comprise raw materials, chemicals, utility costs and waste treatment fees. These costs are only incurred when a chemical plant is in operation and depend on the production capacity. The operating time considered for the evaluation is 8000 hours per year. More information about variable cost is given in Appendix 14.

The *Eucalyptus globulus* (also known as Blue Gum) feedstock is purchased as chipped wood from a local eucalyptus-tree farm. Electricity needed to power all electrical equipment, instrumentation and facilities is purchased from the local grid. Process water is supplied from a well. Wastewater and disposal fees for solid residues to local treatment centres are included in the model as per the reference project²³⁷.

The main chemicals needed for the ACSE process are sulfuric acid and sodium hydroxide while IL is required for the ionoSolv process. Chemical cost depends on the location of the plant, and it is therefore assumed the same as the reference project. The 1984 costs were compared with

most recent values (Appendix 14) and despite the time difference, the chemical costs are within an order of magnitude. For this reason, no corrections due to time difference were performed on the OPEX. For the purpose of the model, the IL cost has been considered at 1000 \$US/ton based on an estimated production cost of 780 \$US/ton plus shipping³⁰.

The utility consumption for the IonoSolv process was simulated with HYSYS according to the model assumptions (Appendix 13). The utility consumption for the other units of the plant are based on the reference project and scaled up/down according to their relative size.

4.3.6.2 Fixed cost

The fixed operating costs are always incurred independently of the production capacity. As processing capacities and unit operations are similar for the two concepts under consideration, it is assumed that the fixed costs for both biorefineries are identical as defined in the reference project²³⁷. More information about variable costs is given in Appendix 14.

Both biorefineries will require the same workforce, with the same salaries, labour burden and overheads which include mainly maintenance and insurance. In the reference project, the plant was assumed to be constructed by contractors using union labour, for which the labour wage rates were taken from a labour survey generated for the Hilo area at the time the project was developed (1984). The workforce costs include a margin for overhead expenses based on 100% of salaries. It is mentioned in the report that this assumption was based on a general criterion used for synfuel plants (Gas Research Institute). The plant personnel are composed of 57 plant operators, 6 control room staff and 10 laboratory staff²³⁷. Impact on working capital was neglected at this stage as the cost of the hydrogen sulfate ILs is one order of magnitude less than AILs³⁵³.

Other fixed costs, such as maintenance and insurance, are taken as per the reference project²³⁷. The insurance and local taxes represent 1.5% of the plant total installed cost²³⁷.

4.4 Results and discussion

4.4.1 Pretreatment experiment setup, temperature profiles and severity factors

The bench-scale pretreatment experiments were carried out according to a published procedure³⁶¹ in unstirred 15ml glass pressure tubes from ACEglass. They were loaded with ground biomass (air-dried) and solvent ($[\text{N}_{2220}][\text{HSO}_4]$ containing 20wt% water) in a 1:10 g/g biomass (on an oven-dried basis) to solvent ratio at room temperature. The samples were then placed inside a fan-assisted oven preheated to a fixed temperature for the duration of the

pretreatment and finally taken out of the oven and allowed to cool down by natural convection.

The temperature profiles of the reaction medium were measured with the help of a Fluorinated Ethylene Propylene (FEP) coated K thermocouple (TC Direct) placed in a glass pressure tube containing ionic liquid solution. Typical temperature profiles for the experiments are shown in Figure 88 (additional data are given in Figure 230 in Appendix 10). The reaction takes place in a non-isothermal regime, and the system reaches ~99% of the target temperature after 30 minutes (independent of the reaction temperature). The cooling time from reaction temperature to room temperature is also ~30 minutes.

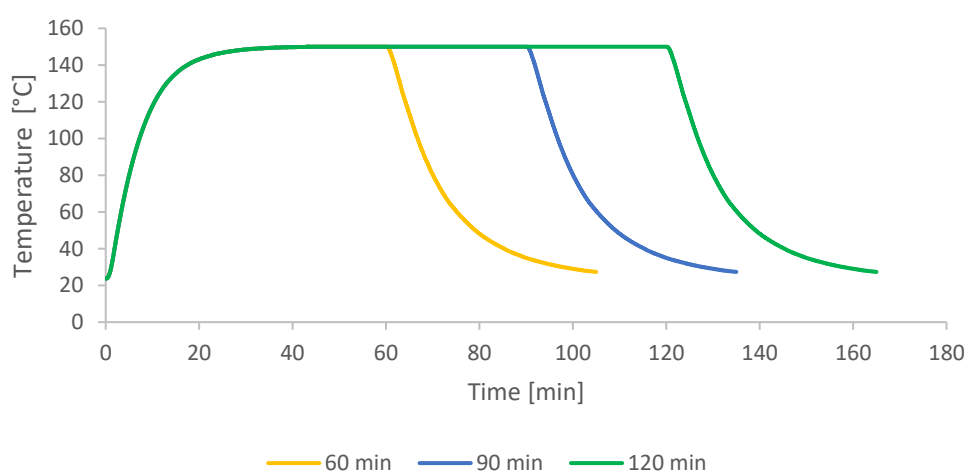


Figure 88. Typical reaction medium temperature inside an unstirred reaction tube (15 ml) at an oven temperature of 150°C for different pretreatment times. Published by The Royal Society of Chemistry ³².

A set of larger-scale experiments was conducted in 120ml glass pressure tubes from ACEglass and 180 °C in a 1:10 g/g biomass to solvent ratio (on an oven dried basis) at room temperature. The heating profile of the pressure tubes was significantly impacted (increased mass and reduced contact of the medium with the wall of the container) leading to a very poor performance. The results are given in Figure 231 in Appendix 10 to make researchers aware of how experimental modifications can have a significant impact on the outcome of pretreatment and to illustrate the complexities of process scale-up. This case will not be further discussed in this work.

The severity factor relationship has been calculated according to the method developed by Chornet and Overend, which takes into account the pretreatment temperature and time to predict conditions that result in similar yields from the breakdown of hemicellulose to its component sugars according to the following relationship ³⁶⁹:

$$R_0 = t \cdot e^{\frac{T-100}{14.75}} \quad (100)$$

Where R_0 is the severity factor, T is the temperature of the reaction medium in °C and t is the time in minutes. As the temperature profiles are not isothermal (Figure 88), the severity factors have been calculated by integration of the temperature profiles over time, according to:

$$R_0 = \int_0^{time} e^{\frac{T(t)-100}{14.75}} dt \quad (101)$$

The exponential term is consistent with the heuristic that the reaction rate will double for every 10 °C increase in temperature. Eq. 100 predicts that the value of R_0 remains the same if the time t is divided in half for every 10 °C increase in temperature. The integral form of the equation has some similarities to the H-factor equation that was developed by Rydholm to relate time and temperature for delignification in Kraft pulping, another example of variables to quantify the severity of a pretreatment ³⁶⁹:

$$H = \int_0^{time} e^{43.2 - \frac{16115}{T[K]}} dt \quad (102)$$

4.4.2 Effect of intensified $[N_{2220}][HSO_4]$ on pretreatment

Process intensification affects pulp composition in different ways. Pulp yield and composition as a function of pretreatment conditions are given in Figure 89. As expected, the pulp yields decrease with increasing severity (temperature and/or pretreatment time). Figure 90 shows the amount of material remaining in the pulp after pretreatment relative to the initial amount as a function of time for each main biomass component (mass fraction of hemicellulose $[Hr/H_0]$, cellulose $[Cr/C_0]$, and lignin $[Lr/L_0]$).

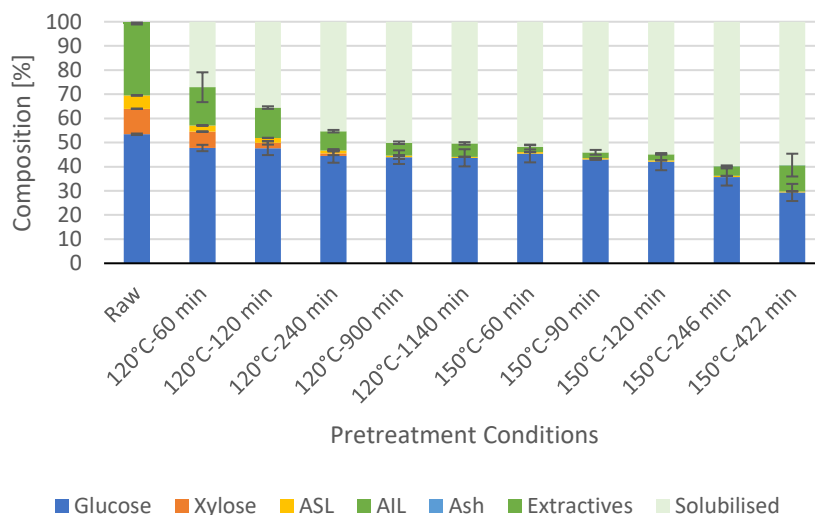


Figure 89. Eucalyptus pulp composition at different pretreatment conditions using $[N_{2220}][HSO_4]$ with 20wt% water as pretreatment solvent. Published by The Royal Society of Chemistry ³².

As can be seen in Figure 90A, the hemicellulosic fraction $[H_r/H_0]$ is easily removed from the pulp and complete removal can be achieved at high severity factors. Compared with previous work, it appears that the hemicellulosic fraction from Eucalyptus can be removed easier than the one from willow ⁵⁷ or Miscanthus ²⁹⁹. Complete hemicellulose removal was achieved at 120 °C and pretreatment times equals or higher than 240 min, and for 150 °C and pretreatment times higher than 60 min.

Pretreatment of *Eucalyptus nitens* using a combination of autohydrolysis (water at 195 °C removed 80.7% xylan) and hydrogen sulfate ILs (*i.e.* $[C_4C_{1im}][HSO_4]$ and $[N_{2220}][HSO_4]$) resulted in pulps with a residual xylan content ranging from 3.3-3.8% and lignin content ranging from 18.2-13.2% depending on the severity ²⁴⁷. Compared to the *Eucalyptus red grandis* results, a xylan fraction was present in the pulps for all experimental conditions. Even though it seems that the hemicellulosic fraction in *Eucalyptus red grandis* is easier to remove than in *Eucalyptus nitens*, more experiments are required to conclude this point. The reason for this is that the pretreatments were not carried out under the same conditions and different samples should be tested.

Regarding the combination of autohydrolysis with ionoSolv pretreatment, it has been reported that during autohydrolysis, polysaccharide hydrolysis evolves uniformly due to the presence of an acetic acid catalyst which is formed due to the cleavage of acetyl groups present in the hemicellulosic fraction of some lignocellulosic biomass ²⁴⁷. It has been shown in this work that the hydrogen based ILs perform extremely well without the need of the autohydrolysis step. However, the autohydrolysis step, or equivalent method, might be used in large scale processes to remove and valorise the hemicellulosic fraction, that otherwise will solubilise in

the IL, and degrade during the pretreatment conditions, yielding pseudo lignins and other degradation products ⁸⁸.

As explained in section 4.2.5, it is expected that acidic pretreatments will promote hemicellulose depolymerisation. Acid Catalysed Steam Explosion (ACSE) of *Eucalyptus grandis* was carried out under various pretreatment conditions (200 – 210 °C, 2 – 5 min) after impregnation of the wood chips with 0.087 and 0.175 wt% H₂SO₄ ³⁶⁶. Pretreatment at 0.175 wt% acid, 210 °C for 2 min was the best condition for hemicellulose recovery (mostly as xylose) in the water-soluble fraction, reaching almost 70% of the corresponding xylose theoretical yield ³⁶⁶. High hemicellulose removal has also been achieved with other pretreatment methods. For example, 96.6% of the xylan present in *Eucalyptus globulus* was solubilized when using the organosolv process at 200 °C for 69 min using 56% glycerol-water and a liquid to solid ratio of 10:1 (wt/wt) in dry basis ³⁷⁰. Interestingly, *Eucalyptus globulus* Labill pretreated with AILs ([C₂C₁im][OAc]) at 150 °C for 30 min and using a biomass-to-IL loading of 1:3 (wt/wt) showed no substantial hydrolysis of the hemicellulosic fraction ³⁷¹. The same trend was observed when eucalyptus was pretreated with other AILs (*i.e.* 1-allyl-3-methylimidazolium chloride ([amim]Cl) and 1-butyl-3-methylimidazolium acetate ([C₄C₁im][OAc]) ³⁷². These results suggest that AILs are not suitable to produce cellulose-rich pulps from eucalyptus.

The IL can also further degrade the cellulose fraction (lower Cr/C₀, Figure 90B), which is more evident at higher temperatures (150 °C). This is consistent with findings for other hardwoods, such as willow, in which the cellulose fraction was also degraded upon IL pretreatment ⁵⁷. It has been noticed that the cellulose fraction in these hardwoods decreases faster when compared to *Miscanthus* ²⁹⁹. There are several reasons that might explain this, for example, differences in the cellulose nature (crystallinity) between those biomasses type ^{257,259}. The analytical method does not discriminate between glucose monomers coming from cellulose or hemicelluloses, therefore, the hardwoods might contain glucose in the hemicellulosic fraction. Another reason might be that the IL was slightly acidic ($\beta < 1$) due to the synthesis method. In previous work, it was shown that the acid/base ratio of the IL affects the saccharification yields and the amount of glucan remaining in the pretreated solids, where an excess of acid leads to a more significant degradation of the cellulose fraction ⁵⁷.

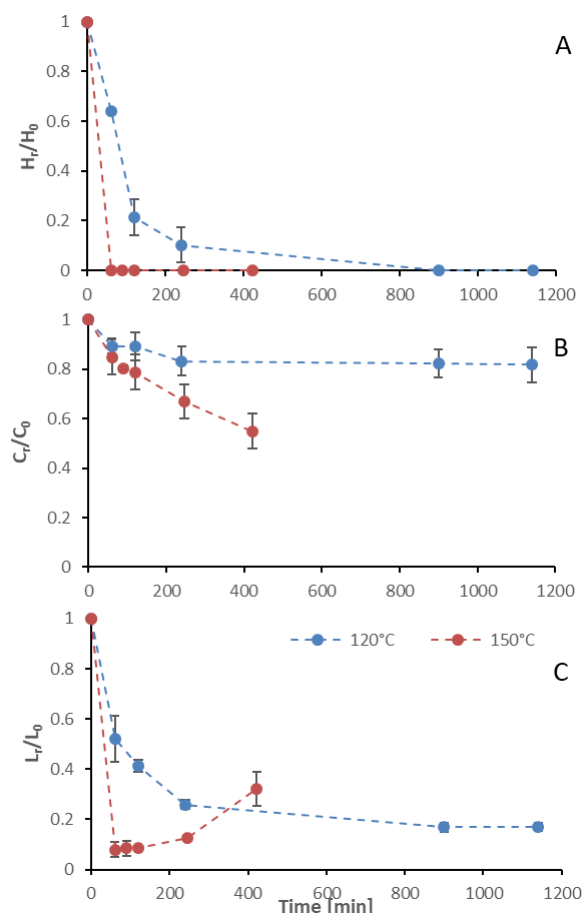


Figure 90. The mass fraction of [A] hemicellulose [H_r/H_0], [B] cellulose [C_r/C_0], and [C] lignin [L_r/L_0] remaining in the pulp after pretreatment as a function of time at two temperatures (blue line 120 °C, red line 150 °C). Dotted lines were added to guide the reader's eye and are not a kinetic fit. Eucalyptus was pretreated at a 1 : 10 g/g biomass to solvent ratio in 80% $[N_{2220}][HSO_4]$ with 20% water. Published by The Royal Society of Chemistry ³².

Residual lignin in the pulp (L_r/L_0 , Figure 90C) decreases with the severity and then increases at high severities which is consistent with previous work with *Miscanthus* ²⁹⁹, bagasse ³⁴⁷, pine ³¹ and willow ⁵⁷. High severities will promote pseudo-lignin formation and lignin condensation with a lower solubility in the IL media, which causes their back onto the pulp surface ^{31,57,299,347}.

At 120 °C the lignin content decreased monotonically, and it did not show an increase even after long pretreatment times (1140 min or 19 h). At 150 °C, the lignin content rapidly decreases at short pretreatment times and then gradually increases, reaching a minimum lignin content of ~3% in the pulps at short pretreatments (~8% of residual lignin [L_r/L_0]).

The recovered pulps and lignins were also investigated with FTIR to determine their composition on a qualitative basis. The results followed the same trends as the composition determined by wet chemistry methods (section 4.3.2.4) and therefore were not included in the main text (Appendix 12).

The saccharification yields of the pretreated pulps are depicted in Figure 91. They peaked at the minimum lignin content and reached a value of 83% (150 °C for 60 min), which is

comparable to other pretreatment methods, for example, $84 \pm 2\%$ glucose yield after enzymatic saccharification of dilute acid pretreated eucalyptus chips ²⁵⁰, *Eucalyptus globulus* pretreatment with $[C_2C_1im][Ac]$ ³⁷³ (3% wt/wt suspensions of wood chips in IL at 150 °C for 3 h) yielded to 85-95% glucose yield recovery depending on the eucalyptus mutant used, and the use of $[C_2C_1im]Cl$ *Eucalyptus globulus labill* (150 °C for 30 min and using a biomass-to-IL loading of 1:3 (wt/wt)) resulted in a maximum glucose yield of 82.2 wt% ³⁷¹.

Regarding non-IL methods, dilute sulfuric acid was used to pretreat eucalyptus chips prior to enzymatic hydrolysis with a maximum total sugars yield of 82% (combined xylose and glucose) and 76% for glucose, obtained at 160 °C, 0.75 wt% H₂SO₄ and 10 min residence time ²⁵⁰. These yields can be improved by steam explosions as shown in a study using Acid Catalysed Steam Explosion (ACSE) to pretreat *Eucalyptus grandis* under various pretreatment conditions (200 – 210 °C, 2 – 5 min) after impregnation of the wood chips with 0.087 and 0.175 wt% H₂SO₄ ³⁶⁶. It was found that temperatures of 200 °C were enough to yield steam-treated substrates from which a 90% cellulose conversion was obtained in 48 h, using low enzyme loadings of a Celluclast 1.5 I plus Novozym 188 mixture (Novo Nordisk) ³⁶⁶. This pretreatment method will be used to benchmark the techno-economic analysis of the iSolv process (section 4.3.4).

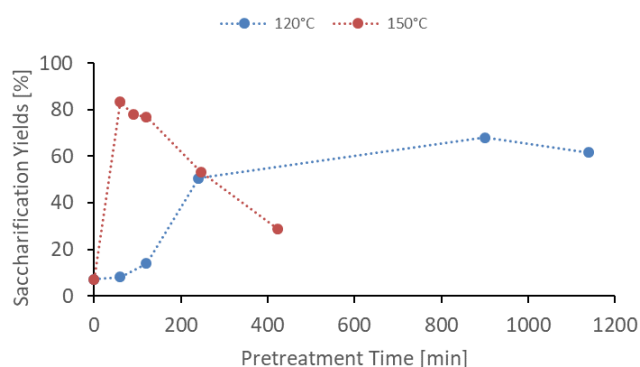


Figure 91. Glucose yield of pretreated Eucalyptus after enzymatic saccharification ³². Published by The Royal Society of Chemistry ³².

The saccharification yield follows a similar trend that the delignification calculated with Eq. 94 (numeric results shown in Table 81 in Appendix 10); it increases with increased severity, reaching a maximum, then decreasing at very high severities (Figure 91). A plot of saccharification yields vs delignification (Figure 92) shows some degree of correlation as previously shown for softwoods ³¹.

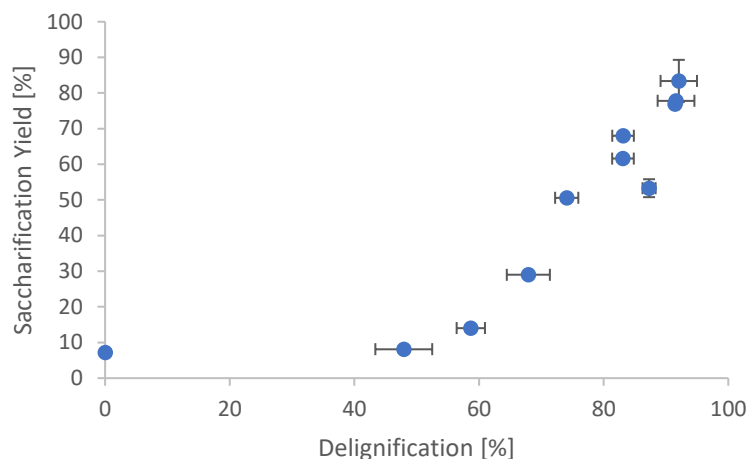


Figure 92. Correlation of enzymatic glucose release and delignification of *Eucalyptus* after pretreatment with $[N_{2220}][HSO_4]$ with a water content of 20 wt% and a solid to solvent ratio of 1 : 10 (wt/wt) at different temperatures and times. Percentage of the theoretical maximum according to compositional analysis is shown. Published by The Royal Society of Chemistry ³².

From the studies combining autohydrolysis with hydrogen sulfate ILs ²⁴⁷ to pretreat *Eucalyptus nitens*, it is hard to conclude which *Eucalyptus* species will be more suitable for biofuel production as enzymatic digestibility of *Eucalyptus nitens* pulps were not reported ²⁴⁷. However, in terms of pulp composition, both species led to high-cellulose content pulps.

It has been noticed that most scientific publications report cellulose recovery as a percentage of the maximum theoretical. This relative metric is useful for comparing trends during biomass fractionation but of little utility to evaluate the potential of a given feedstock for biomass production, due to differences in biomass composition. Therefore, we report the results as well in kg of glucan per 100 kg of biomass. Figure 93 shows a comparison of the absolute glucan content for *Eucalyptus Red Grandis* (this work) and *Eucalyptus nitens*.

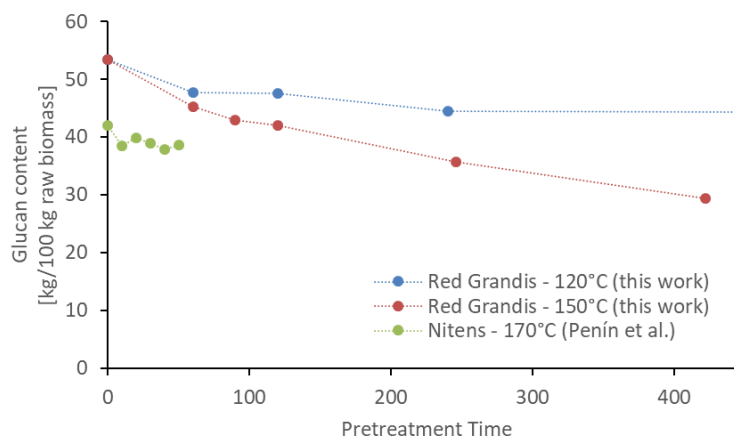


Figure 93. Glucan content of pulps obtained through fractionation of *Eucalyptus* with $[N_{2220}][HSO_4]$ ILs. Published by The Royal Society of Chemistry ³².

The trends are as expected, the glucan fraction decreases with increasing pretreatment times. The sample of *Eucalyptus red grandis* used in this study had a high initial glucan content when compared to literature values (Table 23). To draw a conclusion about the best Eucalyptus species to use as feedstock for a given purpose, several samples should be analysed in order to have an statistical significant amount that will allow assessing the variability between trees of different ages, grown in different locations, etc. Another source of error would be during the grinding and sieving of the biomass. In this study, it has been assumed that the chemical composition of the sieved samples (180 - 850 μm , 20 + 80 US mesh scale) is the same between the different fractions recovered and the chemical composition of the plank used is representative of all the zones of the tree.

In summary, the compositional analysis and saccharification data show that increasing the temperature from 120 °C to 150 °C can lead to pulps with a high cellulose content, no hemicelluloses and small quantities of lignin with high enzymatic digestibility; all of these with a reduction in the pretreatment time, which may lead to significant savings in the capital cost of the pretreatment reactor.

4.4.3 Predictive models

For accurate pretreatment performance predictions, detailed kinetic models need to be developed for each biomass component. Determining the kinetic parameters of heterogeneous reactions of biomass solubilization for non-isothermal systems is complex and therefore has been excluded from the scope of this work ²⁹⁹. However, it will be presented in a dedicated future paper, not only for eucalyptus but for other feedstocks that have been pretreated with hydrogen sulfate ionic liquids.

The severity factors can be used as a simplified approach to predict the simultaneous effect of temperature and time on the pretreatment performance, as no reaction mechanistic details nor parametric fittings are required. To account for the non-isothermal nature of the experiments, the severity factors have been calculated with Eqs. 101 and 102. Figure 94 shows the results of glucan and hemicellulose removal from the pulp as a function of the calculated severity factors according to Eq. 101. From Figure 94A it can be seen that glucan solubilization follows a linear trend within the range of severity factors spanned. This line does not go through the origin, suggesting that there must be a glucan fraction within the biomass that is easier to hydrolyse, and may be contained within the hemicellulose, as previously mentioned. Regarding the hemicellulose removal, it increases at low severity and it is complete at severities of ~ 1300 (Figure 94B). The lignin removal as a function of the severity factor (Eq. 101) and H-

factors (Eq. 102), are shown in Figure 95. Delignification shows maximum values in the range of R_0 1300-6900 or H 6900 – 16900 (Figure 95). Below this range, the lignin removal is not sufficient and above, the condensation reaction and pseudo-lignin formation lead to a decrease in the delignification as previously stated. It seems that the pretreatment performance can be correlated with the severity factors and H-factors, which shows promise as a prediction tool for process design.

The changes in lignin structure were analysed and reported in a scientific publication³². Eucalyptus lignin appears to undergo similar structural changes as other lignins during ionoSolv treatment, however with a lower degree of condensation occurring even after high severity treatments³². This is potentially a benefit for further downstream processing as it will allow for a more consistent lignin output. For the techno-economic analysis of the ionoSolv-based biorefinery, lignin is used as a fuel (section 4.3.3). Therefore, details on lignin chemistry will not be discussed in this work but can be found in ref³².

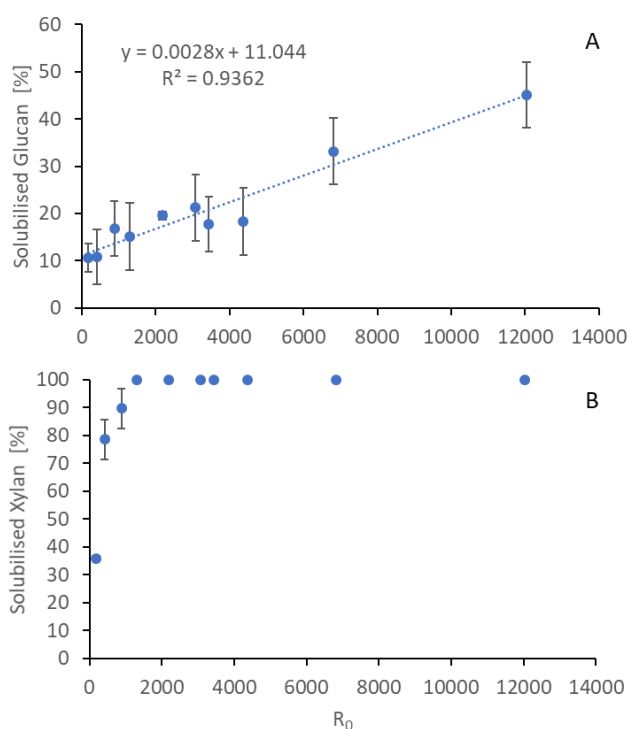


Figure 94. Polysaccharide dissolution as a function of the severity factors R_0 (Eq. 101). [A] Glucan. [B] Xylan. Eucalyptus was pretreated at a 1:10 g/g biomass to solvent ratio in 80 wt% $[N_{2220}][HSO_4]$ with 20 wt% water. Published by The Royal Society of Chemistry³².

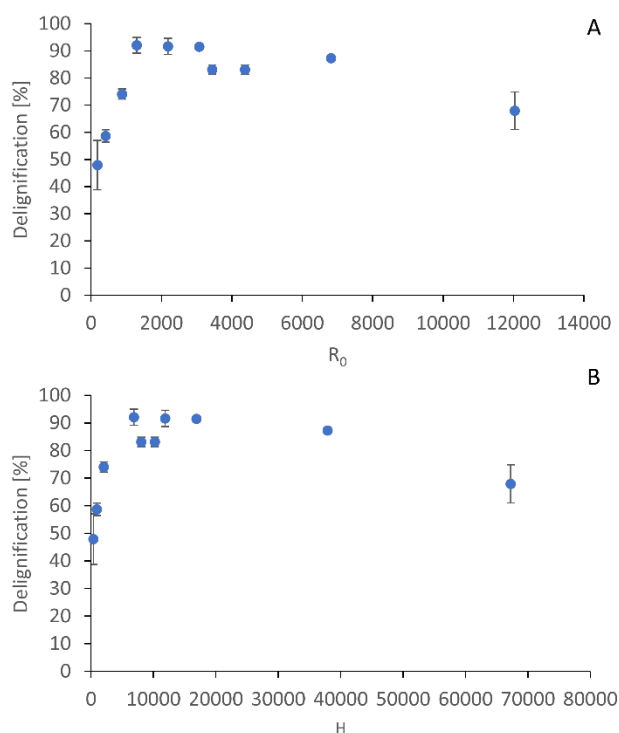


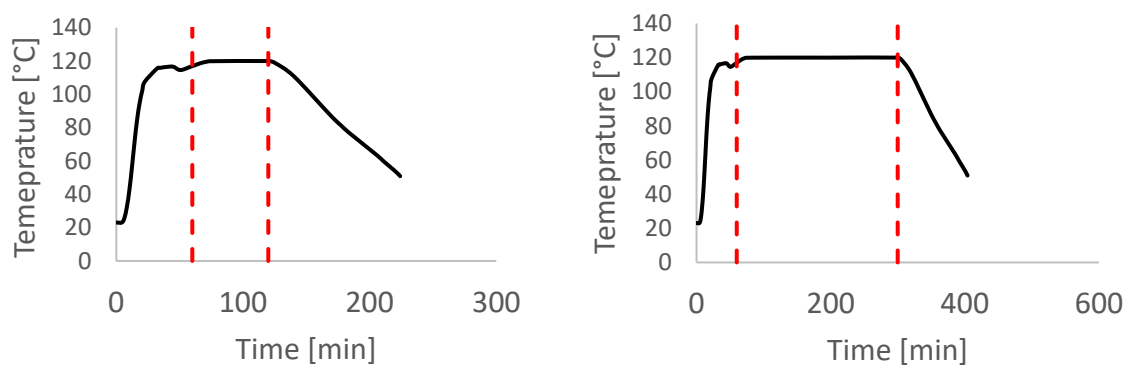
Figure 95. Predictive models for lignin removal. [A] Lignin removal as a function of severity factor R_0 (Eq. 101). [B] Lignin removal as a function of H-factors (Eq. 102). Published by The Royal Society of Chemistry ³².

4.4.4 Influence of pressure and CO₂ atmosphere on pretreatment

It has been shown that there is a significant influence of the atmosphere composition on the liquefaction and depolymerization of wood in the IL 1-ethyl-3-methylimidazolium chloride [C₂C₁im]Cl ³⁰⁹. To address the influence of CO₂ atmospheres on the performance of the pretreatment, a pressurised Parr reactor with a temperature controller was used. It has been noted that [N₂₂₂₀][HSO₄] can leach metals from steels, thus, to prevent sample contamination, the Parr reactor internals (thermocouple well) was coated with PTFE and the pretreatment was carried out in a glass liner fitted to the reactor. The same solvent and solid loading were used for the bench-scale experiments under normal atmosphere. CO₂ was loaded into the reactor at room temperature without purging the air inside. Two sets of experiments were performed: low severity (xL), with a final pressure of 20±2 barg, and high severity (xH) (82 ±2 barg) and a control without CO₂ (x0). For each pressure, two pretreatment times were tested: short time (30 min), i.e. low severity (Lx), and long pretreatment time (4 hours), i.e. high severity (Hx). The experimental conditions are summarised in Table 28 and the temperature profiles are depicted in Figure 96.

Table 28. CO₂ experimental matrix.

		Pretreatment Time	
		Low [30 min]	High [240 min]
Pressure	Low [2.1±0.2 MPa (20±2 barg)]	LL	HL
	High [8.3±0.2 MPa (82±2 barg)]	LH	HH

Figure 96. Temperature profile inside the high-pressure reactor. Right: 30 min pre-treatment (low). Left: 4h pre-treatment (high). Published by The Royal Society of Chemistry ³².

The experimental results of the pretreatment performed under CO₂ atmosphere are shown in Figure 97. Overall, there are no significant changes between performing the IL pretreatment under CO₂ atmosphere regardless of whether the internal CO₂ pressure is below or above the critical point (304.25 K or 31.10 °C and 73.84 bar ^{301,374}), as can be seen in Figure 97. The saccharification yields of the experiments show that there are no significant changes in the pretreatment performance with the addition of CO₂. Any effect on viscosity, due to CO₂ dissolution on the IL, has an insignificant effect on the pretreatment performance, suggesting that the overall pretreatment process in this type of IL is not mass controlled. There is a slight increase (<2%) in the saccharification yields at 20 barg of CO₂ and no significant changes at 82 barg. An ANOVA: Single Factor analysis performed in Excel (Appendix 11) shows that the differences between each experimental set are not statistically significant ($F < F_{crit}$) with 95% certainty ($\alpha=0.05$). In any case, as in absolute values, the changes in glucose recovery yields are not significant, this was not further investigated, as the industrial complexity of carrying out the pretreatment under CO₂ atmospheres will not justify its implementation, for such a marginal effect. Therefore, it can be concluded that the pretreatment performance is unaffected by CO₂ pressure and likely unaffected by other inert gases such as N₂. It remains unclear if O₂ will have a significant effect on pretreatment performance, as this gas showed an important influence in the biomass fractionation with the IL [C₂C₁im]Cl ³⁰⁹. However, the use of O₂ may create additional safety issues, and will not be explored. Better options to boost sugar recovery would be to optimize the severity factors (pretreatment temperature and time), IL base:acid ratio and water content ³².

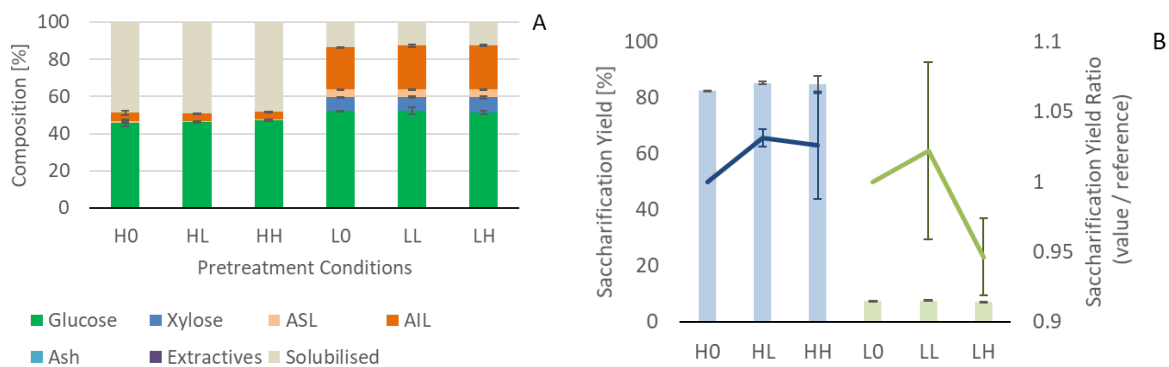


Figure 97. Effect of CO₂ atmospheres on Eucalyptus pretreatment. [A] Pretreated pulp compositions. [B] Saccharification yield of pretreated pulps (bars – left axis) and normalized saccharification yields relative to the control experiments (lines – right axis). H0 (no CO₂, 240 min), HL (20±2 barg CO₂, 240 min), HH (82±2 barg CO₂, 240 min), LO (no CO₂, 30 min), LL (20±2 barg CO₂, 30 min) and LH (82±2 barg CO₂, 30 min). Published by The Royal Society of Chemistry ³².

4.4.5 General CAPEX assessment for biorefineries

The general structure of a biorefinery producing biofuels (2G bioethanol) is similar to the process schemes shown in Figure 85 and Figure 87. A comparison of the cost contribution per process unit for two different biorefineries using different technologies and assumptions (the reference project SERI ²³⁷ used in this study and the NREL design 2011 ³⁷⁵) is given in Figure 98.

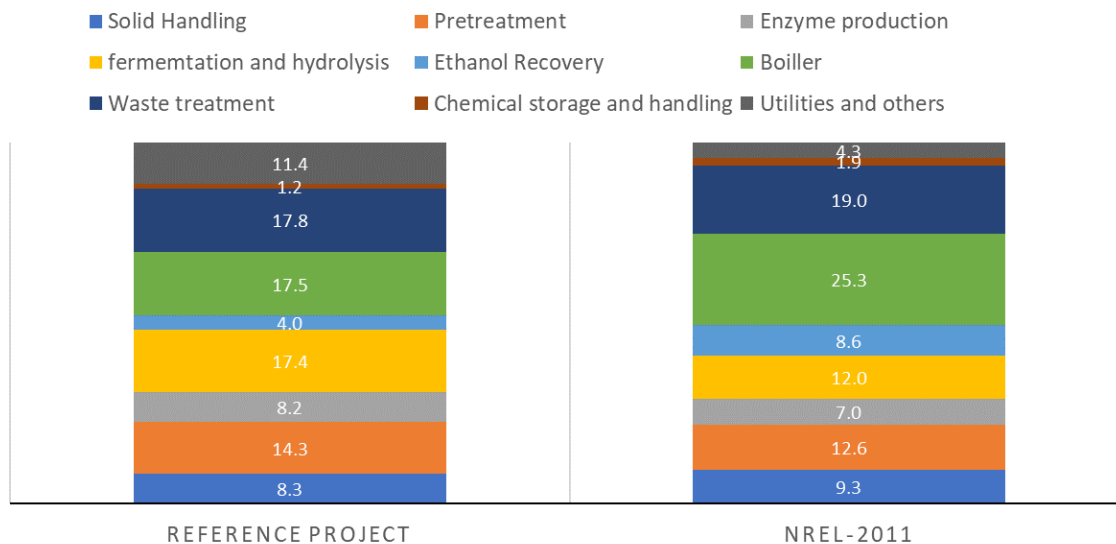


Figure 98. Relative contribution of process units to total installed equipment cost for 2 projects (the reference project ²³⁷ used in this study and the NREL design 2011 ³⁷⁵).

Despite the fact that the technologies used in each biorefinery project are different, it can be seen from Figure 98, that the relative contribution of different process units to the Total Installed Equipment Cost (TIEC) is similar for 2 projects. The major contributor to the TIEC is the lignin burner unit, which can significantly increase if electricity co-generation is implemented. However, the electricity contribution to the OPEX in the SERI project is ~15%

(section 4.4.6), therefore, installation of an electric generator would not only reduce the OPEX of the plant but opens the possibility to generate additional revenue from electricity export by burning by-products without commercial value. The economic benefits of installing a generator in a biorefinery would need to be evaluated on a case-by-case basis.

The waste treatment plant also represents an important fraction of the TIEC, thus reducing the waste stream would be beneficial not only for an environmental point of view but from a CAPEX perspective. The total contribution of the pretreatment step (excluding the enzymatic hydrolysis) in these projects only represents between 12.6 and 14.3%. From these figures, it might appear that optimization of the pretreatment step is not essential to improve the overall economics of a biorefinery. However, the pretreatment technology will impact the performance of the other process units and the overall ethanol production, leading to important savings, for example, a more active pretreated biomass for enzymatic hydrolysis, would lead to shorter residence times and less enzymes usage. Additionally, reducing the waste streams from the pretreatment step would reduce the cost of the waste treatment plant.

Besides ethanol, other chemical products could be produced, for example, organic molecules, such as furfural, HMF, sugars or CO₂ from the fermentation process or combustion could be recovered and monetized. These process alternates are not evaluated nor further discussed in this work.

4.4.6 CAPEX ionoSolv vs. ACSE pretreatments

4.4.6.1 Pretreatment units

The TEIC for the pretreatment units of the SERI project (2019) is 23.6 MM\$US (units 100 and 200) and 22.27 MM\$US (units 100, 2000 and 3000) for the ionoSolv biorefinery, which represent a 5.8% reduction on CAPEX. For a more accurate evaluation of the CAPEX variation between the two pretreatment options, it would be necessary to size and cost all the equipment of the SERI project with the same method as per the ionoSolv process. However, this detailed evaluation could not be performed since details on the sizing and the cost of the individual pieces of equipment from the SERI project are not provided. Moreover, the pretreatment unit in the SERI project contains non-conventional equipment which is not found in common costing correlations such as the steam guns. Any attempt to cost the equipment under the same assumptions will have great uncertainty due to the cost of miscellaneous pieces of equipment.

Figure 99 shows the equipment breakdown contribution of the IonoSolv process compared to the NREL design 2011³⁷⁵, which utilizes a dilute acid pretreatment (more information on Appendix 14).

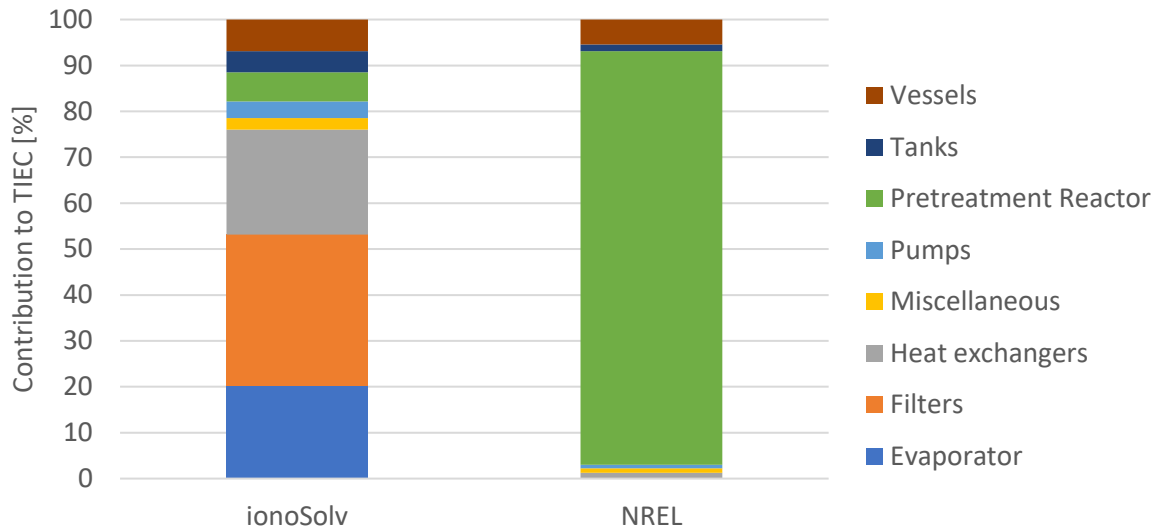


Figure 99. Equipment cost breakdown for the pretreatment unit, for the IonoSolv process and the NREL design 2011³⁷⁵.

The major contributor to the TEIC for the IonoSolv process is the 2 set of filters (pulp and lignin), which account for ~33% of the TEIC. There is a significant variation on the cost of the filtering technologies which depend on the level of automation, materials and particle size. Filter vendors were consulted to confirm the technical feasibility, the type of filter and the order of magnitude of the cost. More details are provided in Appendix 13. There are other technologies that could be explored to reduce the cost of the solid-liquid separation units, such as centrifugation, hydro-cyclones, and dewatering units.

The second contributor for the CAPEX is the heat exchanger used to recover heat (H-101). As shown in the following sections, the OPEX is the main contributor to the Minimum Ethanol Selling Price (MESPP), therefore OPEX reduction is essential to produce ethanol at market price. If the biorefinery is integrated into a system with excess heat without electricity cogeneration, H-101 could be eliminated to reduce the CAPEX. However, if the plant is generating electricity for export, it would be economically reasonable to minimize the heat composition of the process to maximize revenues from electricity export. The reason the high cost for this individual item is the low overall heat transfer coefficient (U) used for the sizing, which resulted in a large exchange area. The pessimistic assumption on the U value arises from the fact that the hot fluid is a slurry with solid particles and that there is no detailed data on the thermal behaviour of the IL-water and IL-slurry system. It is extremely important to measure

experimentally the transport properties of such fluid to perform a better design of this heat exchanger. More details on the cost of this item are given in the sensitivity analysis section 4.4.9.

Finally, the reactor cost for the IonoSolv process only contributes ~6% to the total cost, as oppose to the NREL design with the reactor accounts for almost 90% of the total TIEC ³⁷⁵. The reason for this is that for the IonoSolv process, it has been assumed that the reaction can be carried out in simple lined vessels, as no high pressures are required. It is critical to validate at pilot scale if the slurries can be easily loaded/unloaded into “batch reactors” working in parallel to achieve a pseudo-continuous operation. The NREL reactor system consists of a series of screw conveyors designed to handle steam. By analogy, it is likely that the 3.8% CAPEX reduction for the IonoSolv process when compared to the SERI is due mainly to a reduction of the reactor cost.

It is noteworthy to mention that both pretreatments lead to pulps of different compositions, as shown in Table 29. The composition of the IonoSolv pulps can be tailored by modifications of the pretreatment conditions as shown in section 4.4.2, and pulps with a very high cellulose content can be produced. Additionally, lignin can be easily recovered and isolated from the IonoSolv process. The IonoSolv pretreatment seems an interesting option for bioderived material production.

Table 29. Pretreated pulp composition. [A] Pulp prior to hydrolysis step (SERI project- stream 211) ²³⁷. [B] Steam exploded pulp prior to NaOH wash (SERI project- stream 212) ²³⁷. [C] IonoSolv pulp (*Eucalyptus red grandis*) pretreated with [N₂₂₂₀][H₂SO₄] 20 wt% water 150 °C and 60 min (Appendix 10)³².

	SERI Project		IonoSolv [C]
	Steam-exploded pulp [A]	NaOH washed pulp [B]	
Cellulose	51.6	73.4	94.2
Pentose	17.2	6.7	
Lignin	22.0	10.4	5.8
Others	9.3	9.5	

4.4.6.2 Entire biorefinery

The results for the CAPEX estimation for the entire biorefinery are given in Table 30.

Table 30. CAPEX estimation per unit for the reference project and the IonoSolv process.

	Unit	Component	Flowrate [kg/h]		Installed cost in 2019 [MM \$US]		
			SERI	IonoSolv	SERI	IonoSolv	
100	Pretreatment	Dry wood	24704	24704	5.39	9.85	(1)
200	Steam Explosion / Wash	n.a.	n.a.	n.a.	18.25	n.a	

	Unit	Component	Flowrate [kg/h]		Installed cost in 2019 [MM \$US]		
			SERI	IonoSolv	SERI	IonoSolv	
2000	Lignin Recovery	n.a.	n.a.	n.a.	n.a	6.0	
3000	Ionic Liquid Conditioning	n.a	n.a	n.a	n.a	6.4	
300	Enzyme Production	Cellulose	12673	11066	13.64	12.57	(2)
400	Hydrolysis	Cellulose	12673	11066	15.42	14.21	(2)
500	Evaporation	Water evaporated	105021	91704	5.29	4.87	(3)
600	Fermentation	Glucose	11026	11312	8.05	8.17	(4)
700	Distillation	Ethanol	5385	5541	6.53	6.64	(5)
800	Anaerobic Digestion	Dry matter	6611	0	13.73	0	(6)
900	Boiler	Heating (MW)	76.6	100.0	28.9	33.9	(7)
1000	Feedstock Handling	Dry wood	24704	24704	13.73	13.73	(1)
1100	Cooling Water	Water (m ³ /h)	2841	3157	2.14	2.28	
1200	Waste Treatment / Vent Scrubbing				15.62	15.62	
1300	Chemical Handling				0.37	0.37	
1400	Product Storage and Unloading	Same for both projects			1.61	1.61	
1500	Instrument Air / Fire Protection / Miscellaneous				16.69	16.69	
TIEC					165.33	157.81	
TOTAL Facilities investment					283.25	274.15	(8)

1. Same as the reference project.
2. Based on the total cellulose in the pulp after pretreatment and pulp yields.
3. Based on evaporated water. Inlet sugar content is 7 wt% and outlet content is 15 wt%.
4. Glucose calculated from glucose yields. Ref project 84% and 86% for IonoSolv process (section 4.4.1).
5. Based on ethanol produced. 95% glucose conversion to ethanol. Final product contains 0.8 wt% water.
6. Removed for the IonoSolv process as C₅ fraction is recovered as solid pseudo-lignins.
7. The boiler is scaled according to the total available heat HHV basis of combusted materials. For the IonoSolv process, it includes the fraction of the pretreated pulp containing combustible material that is not converted into ethanol.
8. Includes land, all direct and indirect cost and working capital. For the IonoSolv process, it included the initial IL inventory estimated at 337 ton.

When the entire biorefinery is considered, an overall reduction of 7.5% in the CAPEX is achieved when implementing the IonoSolv pretreatment. This result is promising and would suggest that more detailed studies to develop an IonoSolv biorefinery are justified. However, it is important to mention that the relative difference in the CAPEX evaluation of these projects is not completely accurate due to several uncertainties in the estimation. On the SERI project side, there are also several assumptions made for their estimation. Additionally, the project was developed in 1987 and costed in 1984, and therefore, correcting the cost to present value over such a long period will result in high uncertainties. Regarding the IonoSolv process, there

are still uncertainties in the material selection, reactor technology, solid separation units and the evaporator unit.

Regarding the absolute value, the level of detail of the estimate is consistent with a CAPEX Class 4 estimation with a typical accuracy of -30%/+50% (Appendix 14). It needs to be highlighted that the technologies have evolved since the development of the SERI project, therefore, in absolute values, it would be expected that the overall CAPEX for the biorefinery concept would decrease regardless of the pretreatment technology, if designed with more recent state-of-the-art processes, for example, one-pot hydrolysis and fermentation.

4.4.7 OPEX IonoSolv vs. ACSE pretreatments

The utility consumption for the two pretreatment options is given in Table 31, where it can be seen an increase in the utility load for the IonoSolv process.

Table 31. Utility consumption. [A] Including the increase in the electrical consumption due to cooling water system and water systems.

	Pretreatment Unit		Biorefinery	
	SERI	IonoSolv	SERI	IonoSolv
Water [m ³ / h]	54.2	115.0	193.3	236.4
Electricity [MW] [A]	0.51	0.6	8.29	7.4
Heating duty [MW]	16.0	20.1	47.9	52.8
Cooling duty [MW]	5.4	15.7	45.7	55.9

The increase in the water consumption is due to the assumptions on the water needed to wash the pulp for the IonoSolv process. A pessimistic value has been selected as there is not detailed data of the performance of the pulp washing step. The water consumption can be reduced by proper equipment selection for the filter or solid washing unit, and by process integration, *i. e.* the use of other wastewater streams to pre-wash the pulp with a final wash of fresh process water to remove the final traces of IL and other contaminants. This variable is further analysis in the sensitivity analysis.

The increase in the heating duty requirement is due mainly to the IL drying step, which accounts for 65% of the heating duty (13 MW). The reaction step consumes 7 MW, as energy is recovered by the IL Preheater (H-101). The evaporator load has been estimated assuming a 5-effect evaporator. However, the heating duty requirement will be strongly affected by the type of equipment selected (for example, mechanical recompression or a different number of effects). Adding more effects to the evaporator would reduce the heating requirement but will increase the CAPEX. Additionally, the amount of water needed to be removed will depend on

the water specification for the pretreatment unit, the moisture content of the feedstock and the amount of water needed to remove the lignin. A process optimization should be carried out to determine the best evaporator design and process scheme to minimize the MESP. These variables are addressed in the sensitivity analysis.

It has been noticed that the amount of heat available from combustible material is larger for the IonoSolv process than the SERI project (Table 27). The reason for this mainly due to the anaerobic digester efficiency, in which the C₅ fraction is transformed into methane and CO₂ in the SERI project, while the C₅ fraction is converted to solids in the IonoSolv process, with no losses due to CO₂ formation. The greater amount of potential recoverable heat from the IonoSolv process could justify the installation of an electrical power generator to reduce the OPEX and generate extra revenues from electricity export.

The increase in the electrical power consumption in the IonoSolv pretreatment unit is due to the increased number of rotating equipment (pumps and conveyors) and the agitators for the reactor. Interestingly, the overall electrical consumption of the biorefinery is reduced due to a small decrease in the downstream processing streams and the deletion of unit 800 (Anaerobic digestion), which includes a methane compressor. The increase in the cooling medium requirements is mainly due to the evaporator.

Figure 100 shows the contribution of the different utilities and raw materials to the OPEX.

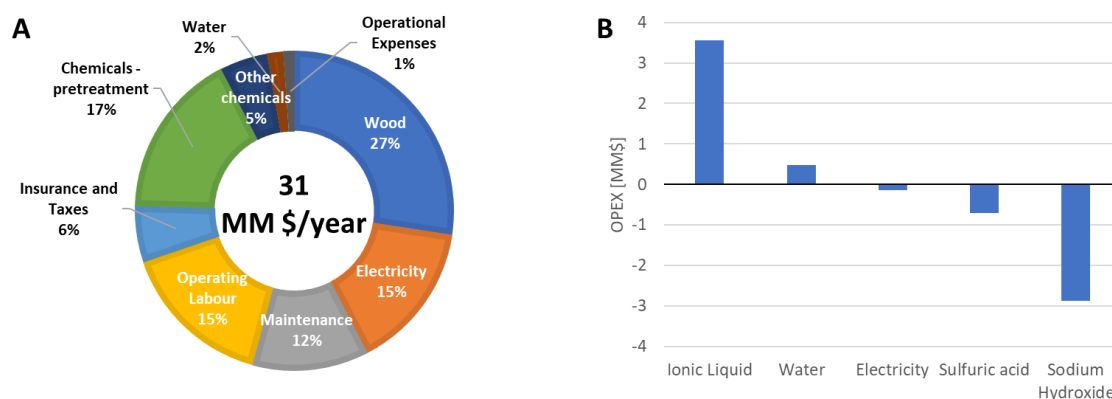


Figure 100. OPEX. [A] breakdown of the total OPEX for the SERI project. [B]. OPEX variations between the IonoSolv and the ACSE processes.

The total OPEX for the entire biorefinery for the SERI project is 31 MM\$US and 31.4 MM\$US for the IonoSolv case (details in Appendix Y). Overall, the OPEX is only 1.2% higher for the IonoSolv process, with the assumptions of the base case. The chemical consumption is very similar for both processes. It should be noticed that for the economic assessment, it has been assumed that the IL losses are 1% of the recirculating flow. During normal operation, some IL will be lost in the pulp, lignin and during their washing steps. IL might also degrade or react

with components of the biomass or metallic materials. Other non-process causes, such as inventory loss due to drainage for equipment maintenance and repairs, might contribute to the total IL losses. It is likely that the IL losses could be reduced in the commercial plant, however, this will need to be validated through pilot testing, and the conservative value of 1% will be kept for the economic assessment.

It seems that the acid-base neutralization products (sodium sulfate) for the SERI project contribute to the ash and sludge disposal costs, however, from the data provided in the reference project, it is not clear to which extent. As these waste streams are not present in the ionoSolv case, the sludge/ash disposal cost will be reduced for the ionoSolv process, however, no corrections were done at this stage.

In summary, it can be said the OPEX for the two processes is quite similar. It is likely that the OPEX for the ionoSolv process can be further reduced after detailed process optimizations at a later stage. The effects of some variables on the OPEX are explored in the sensitivity analysis section 4.4.9.

4.4.8 MESP ionoSolv vs. ACSE pretreatments

The optimistic MESP has been calculated using Eq. 70 in Appendix 14 for both the reference project (0.827 \$US/L) and the ionoSolv project (0.802 \$US/L). Despite the fact the OPEX is slightly high for the ionoSolv process, under the base case assumptions, the MESP for the ionoSolv based biorefinery is 3.2% lower than the SERI project. This result suggests that the ionoSolv process is a better alternative than ACSE to produce 2G ethanol. In the sensitivity analysis section, it is shown that there is still room to optimize the CAPEX/OPEX of the process that might lead to even lower MESP for the ionoSolv process.

A detailed cash flow analysis was not performed to determine the true MESP, as it depends more on financial and economic parameters rather than the process itself and will affect both options in similar manners. The MESP reported in the reference project taking into account their economic assumptions is 3.5 \$US/gal (0.925 \$US/L) in 1984, which is 30% higher than the optimistic MESP calculated with Eq. 70 at the same year (1984). Assuming that this difference will be equal for the ionoSolv process, the expected MESP is 1.074 \$US/L for SERI project and 0.925 \$US/L for the ionoSolv project. Ethanol is a commodity, and as such, its price changes in time. For reference, it was indicated in the SERI report that the ethanol selling price ranged between 1.47-1.67 \$US/gal (0.388-0.441 4 \$US/L) depending on the location. The average price in 2019 was 1.40 \$US/gal (0.371 \$US/L)³⁷⁶. Both projects with their underlying assumptions lead to a MESP ~2.8 times higher than the current market price. This does not mean that a

eucalyptus bioethanol plant is not viable, just that further process optimizations are required to lower the MESP. For example, in the SERI project, they performed a series of sensitivity analysis, including the valorisation of lignin and the C₅ fraction, whether as ethanol or furfural, and showed that the MESP can be reduced from 3.5 \$US/gal to 1.42 \$US/gal, ~60% reduction. Co-valorisation of other products such as CO₂ for the fermentation and boiler units, could further improve the overall biorefinery economics. Additionally, electricity cogeneration could be an interesting option to reduce the OPEX of the plant and to generate additional revenues from electricity exports to the grid.

It has been noticed that the major contributor to the OPEX is the cost of the eucalyptus, using cheaper sources, such as waste wood, will definitely improve the economics of the IonoSolv process, which has been successfully applied to this type of feedstocks³⁵⁵. Another competitive advantage of the IonoSolv process is the fact that it has been discovered that [N₄₁₁₀][HSO₄] is extremely efficient in pretreating softwood, such as pine, as opposed to the diluted acid pretreatment, which has a lower performance^{89,355}.

It needs to be emphasized that the main objective of this study is to evaluate the performance of the IonoSolv process in the context of a biorefinery compared to other technologies rather than minimizing the MESP. As mentioned earlier, the technologies have evolved since the SERI project development, so it is likely that if a biorefinery is sized using more recent technologies for the different processing steps, the overall MESP will be lower than the one calculated in this work.

4.4.9 Sensitivity analysis

The following section describes a series of sensitivity analyses performed on the IonoSolv process. Parameters that have been investigated include plant capacity, biomass moisture content, water content in the reactor, solid loading, water equivalent for lignin precipitation and water wash for pulp. It is noteworthy to mention that water content on the IL will impact the pretreatment performance. The results shown in this section does not take into consideration any variations on pretreatment performance due to water changes in the reaction section. Also, the sensitivity analysis only considers the pretreatment unit and not the entire biorefinery.

The data presented in this section have been normalized with respect to the base case. The reason for this is that the actual CAPEX and OPEX of the plant will depend upon many factors, e.g. final process scheme, design basis, sizing criteria, project-specific requirements, vendor

selection, etc. Therefore, the CAPEX and OPEX values are expected to change during the detailed engineering phase. However, the trends in terms of relative changes are expected to hold true.

The OPEX includes only the cost of electricity and process water as per the reference project. Heating duty is shown for reference as it will impact the size of the boiler and steam supply system (not evaluated) and chemicals for water make-up conditioning. Cooling duty is shown as well for reference but its impact on the CAPEX/OPEX in the utility system is not evaluated at this stage.

4.4.9.1 Plant capacity

Figure 101 shows the variations in CAPEX and OPEX with respect to the base case. As expected, the CAPEX varies following a power law due to economies of scale whereas the utility consumption varies linearly with capacity. This means that the CAPEX value normalized with the raw biomass should increase for plants smaller than the capacity of the base.

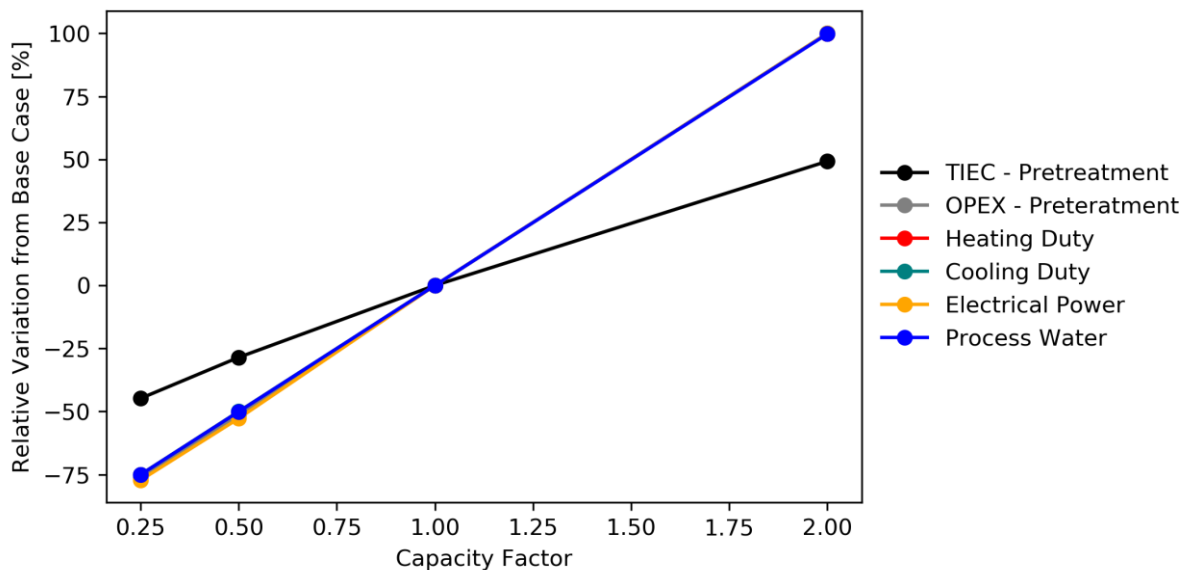


Figure 101. CAPEX and OPEX variations with plant capacity.

4.4.9.2 Biomass moisture content

The assumed moisture content on the raw biomass for the base is considered as 50% and the IL water content exiting the evaporator has been fixed to 20 wt%. It has been shown that the ionoSolv pretreatment is viable even at high water content, up to 40 wt%, depending on the biomass type²⁴⁴. For this reason, even though the water content in the reactor is not constant

and a small impact is expected on the pretreatment performance, it has been assumed that it remains unaffected. When the moisture content decreases, it is expected that the utility consumption will be reduced, as there is less material (water), circulating in the process and due to the fact that less water needs to be removed from the process. Figure 102 shows the impact of the moisture content in the raw biomass. As expected, the OPEX decreases with decreasing moisture content. Surprisingly, the overall CAPEX increases as the moisture content decreases. To better understand this behaviour, the breakdown per equipment as a function of moisture content is presented in Figure 103. From this figure, all process equipment whether remains constant or decreases except the heat exchangers, which have the opposite trend and their total contribution to the overall CAPEX outweighs the savings in the other equipment.

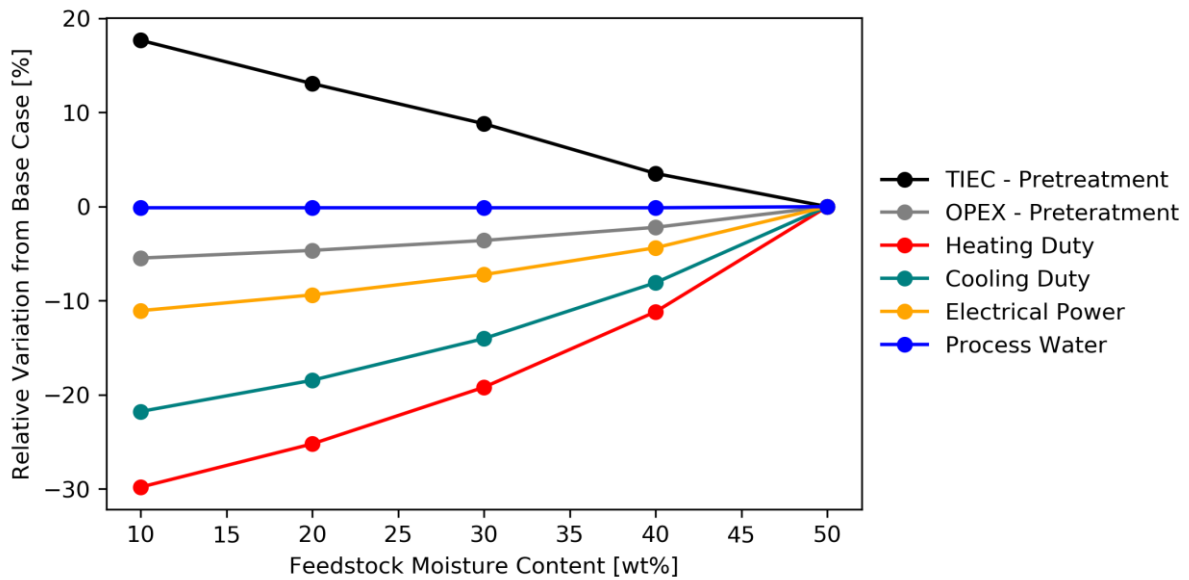


Figure 102. CAPEX and OPEX variations as a function of moisture content in the raw biomass.

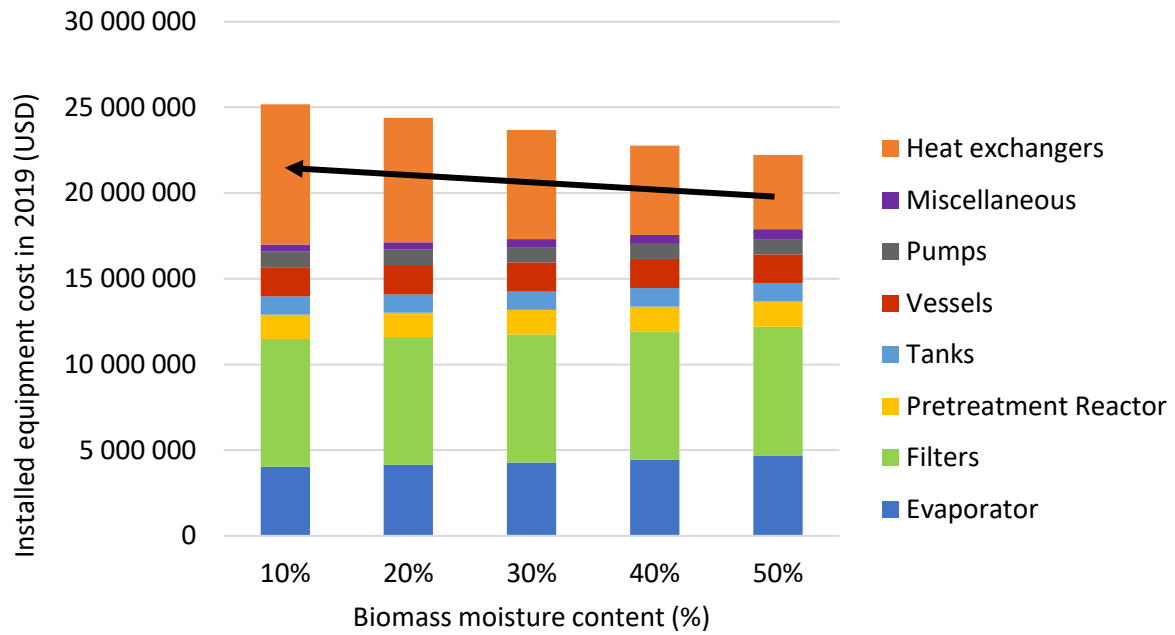


Figure 103. Breakdown per equipment for the CAPEX variations as a function of the moisture content in the raw biomass.

From Figure 104 it can be seen that the evaporator and the heat exchanger used to recover heat, follow different trends with regards to the moisture content in the raw biomass. In terms of cost, the evaporator cost will be reduced whereas the heat exchanger cost will be increased. The reason the surface increase of the IL preheater with decreasing moisture content is due to changes in the heat capacities and flowrates, which lead to a higher AU when the heat exchanger is specified to have a minimum overall approach of 5 °C. In this case, the flow rate of IL solution is adjusted to meet the liquid to solid ratio specification for the process. More details about this behaviour are given in Appendix 13. If this design spec is relaxed, for example 10 °C, the surface area of H-101 will decrease, however, the surface area of H-102 will increase as well as the heating duty.

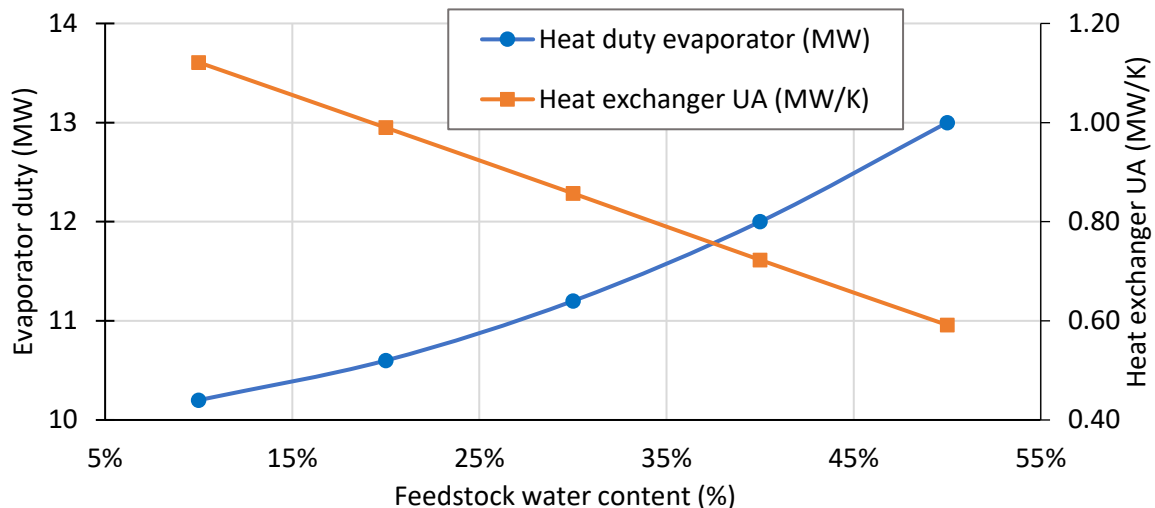


Figure 104. Evaporator Duty and Heat Exchanger UA variations as a function of moisture content in the raw biomass.

At this stage, due to the lack of detailed information regarding the thermal behaviour of the ionic liquid and the slurry, pessimistic assumptions have been considered for the Overall Heat Exchange Coefficient (U) to size this heat exchanger. Such assumptions lead to a high cost for this heat exchanger. It is extremely important to consult with vendors for the Evaporator and the IL Preheater Heat Exchanger to establish a more detailed cost estimation and determine which equipment is driving the overall CAPEX. When more detailed data is available, further studies could be carried out to further optimize the process:

- Design basis relaxation: heat exchanger type capable of handling slurries to minimize surface area or impact on the process of changing the design basis, minimum heat exchanger approach.
- No heat integration: an extreme case without heat integration between the IL entering the reactor and the slurry exiting the reactor. In this case, the IL preheater would be replaced for a cooler, as it has been assumed that the filtration needs to be carried out at lower temperatures. It is expected that the OPEX will significantly increase due to higher heating and cooling requirements. For the CAPEX, the cost of the IL heater will be reduced, as steam heat exchangers have a higher U value leading to smaller transfer areas, but the additional cost of the slurry cooler needs to be established to confirm if there are significant CAPEX savings. It needs to be investigated if units downstream the reactor can be operated at high temperatures ($< 150\text{ }^{\circ}\text{C}$), in order to confirm if a slurry cooler is needed and what would be its outlet temperature.

- Biomass drying: the installation of a solid drying unit, to reduce the moisture content of the biomass, could be foreseen. The CAPEX and OPEX impact of such schemes should be addressed once detailed data is available.

With the current assumptions for the sizing and cost estimations for the evaporator and the heat exchangers (given in Appendix 13), it is not possible to conclude the effect of moisture content in the biomass in the CAPEX. Depending on the real cost of the heat exchanger and the evaporator, the CAPEX can either increase or decrease with decreasing moisture content. It needs to be reminded that according to the Green Chemistry and Engineering principles, energy inputs should be minimized (section 1.2.3).

4.4.9.3 Water content in the reactor

The water content in the reactor is an important variable for the ionoSolv process. It is known that some water is needed for the fractionation of the biomass, however, the solubility of the lignin decreases with water content, therefore at high water contents, typically above 40%, a rapid decrease in the pretreatment performance is observed ²⁴⁴.

It is expected that the lower the water content in the reactor, the more the OPEX will increase, as more water will need to be removed from the process. The CAPEX and OPEX variations of the pretreatment unit as a function of the water content in the reactor are depicted in Figure 105.

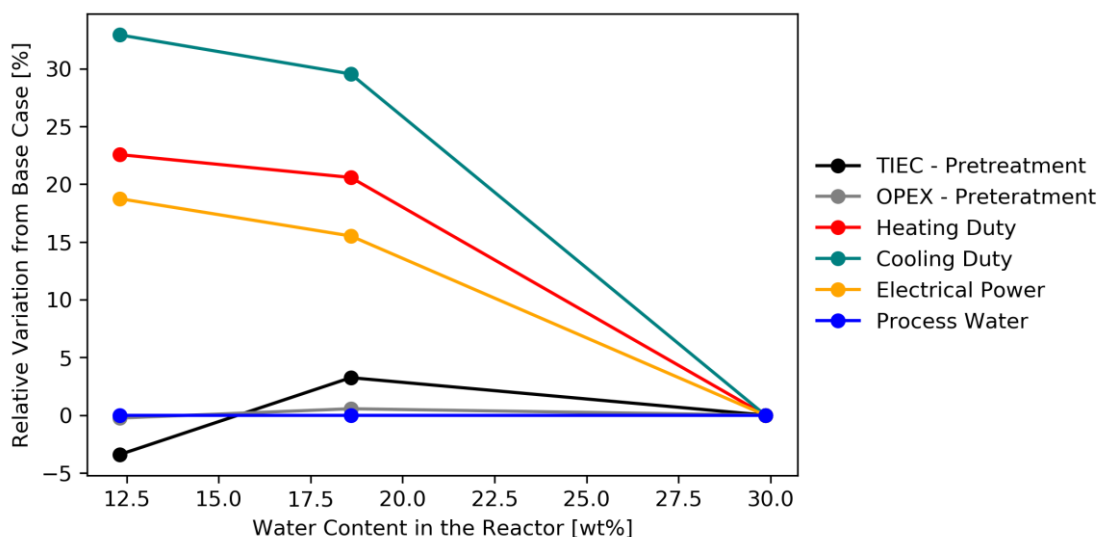


Figure 105. CAPEX and OPEX as a function of the water content inside the reactor. For these cases, the moisture content in the feedstock is 30 wt%.

As expected, the OPEX cost is increasing with decreasing moisture content in the reactor. Surprisingly, similarly to the moisture content case, the CAPEX follows a reverse trend of what

would be expected, as higher IL drying requirements would lead to an increased CAPEX due to the evaporator unit. The intensive drying of the IL is actually one of the main problems of the water sensitive [C₂C₁im][OAc]-based pretreatment ¹⁶. Despite an increase in the evaporator cost, an overall CAPEX reduction is observed due to savings in the IL preheater (H-101), which is driving the overall TIEC.

With the current assumptions for the sizing and cost estimations for the evaporator and the heat exchangers (given in in Appendix 13), it is not possible to conclude the effect of moisture content in the biomass on the CAPEX. Depending on the real cost of the heat exchanger and the evaporator, the CAPEX can either increase or decrease with decreasing moisture content.

4.4.9.4 Solid loading

The solid loading is one important variable for the pre-treatment process. Figure 106 shows the CAPEX and OPEX variations as a function of solid loading. As expected, both CAPEX and OPEX decrease with increasing solid loadings. The reason for this is less IL-solution needed, reducing the equipment size and the utility consumption. Increasing the solid loading from 14% to 25%, leads to a reduction of the CAPEX and OPEX of ~25%. However, the following estimations have been performed assuming that the pretreatment performance is not impacted by the solid loading. Despite the fact that the CAPEX and OPEX are improved by increasing the solid loading, experimental results show that the pretreatment performance is negatively impacted ³¹. Further studies should take this into account to find the optimum.

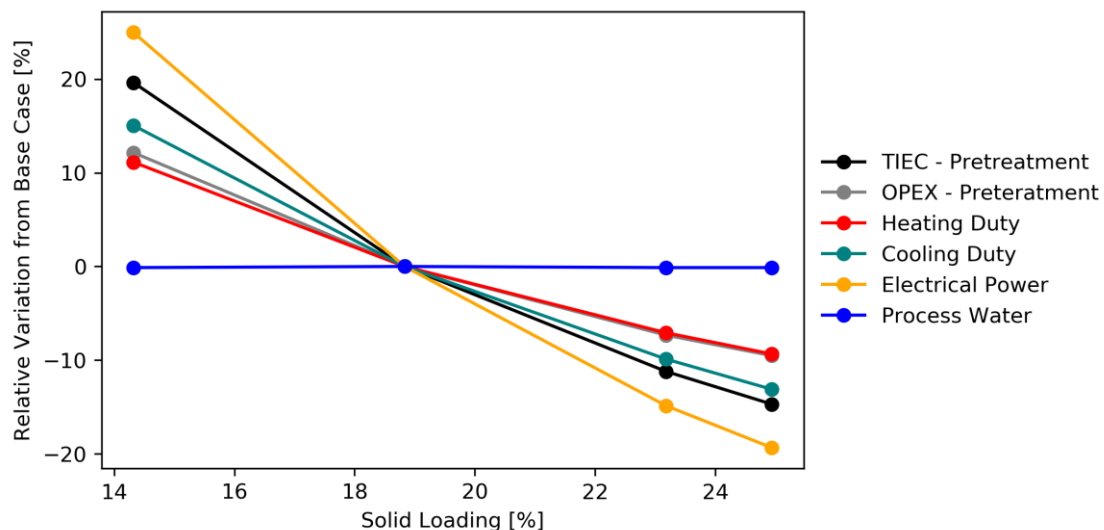


Figure 106. CAPEX and OPEX variations as a function of solid loading.

In conclusion, the solid loading should be maximized from a CAPEX and OPEX perspective taking into account a decrease in the pretreatment performance.

4.4.9.5 Water equivalent for lignin precipitation

Figure 107 shows the CAPEX and OPEX variations as a function of the water equivalents needed to precipitate the lignin. As expected, both CAPEX and OPEX increases with increasing water equivalents needed for lignin precipitation. The reason for this is that more water needs to be removed from the diluted IL solution to reach the specification for the biomass fractionation reactions, increasing the evaporator size and the utility consumption. The impact is bigger on OPEX than CAPEX, from 0.65 to 3 equivalents, CAPEX increases by 18% while the OPEX increases by 77%.

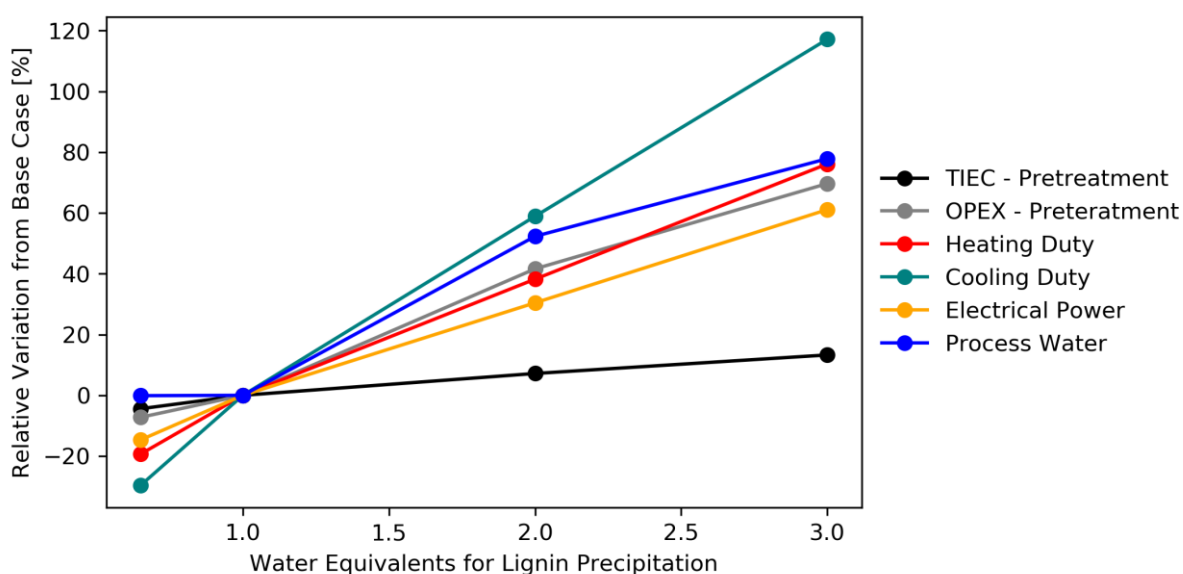


Figure 107. CAPEX and OPEX as a function of the water equivalents needed for lignin precipitation.

In conclusion, water usage for lignin precipitation should be minimized from a CAPEX and OPEX perspective. However, reducing the amount of water needed to precipitate the lignin, leads to high residual lignin content in the IL, which might have a detrimental effect on the pretreatment performance. For example, lignin precipitation during the water washing step would reduce the enzymatic activity of the pulp, as the deposited lignin may act as a protective layer⁸⁸. Additionally, circulating a lignin-rich IL solution may lead to fouling of pipes and process equipment such as heat exchangers.

4.4.9.6 Water wash for pulp

The IL losses need to be minimized from an environmental and economic point of view. There are many reasons for solvent losses in industrial applications. In the IonoSolv process, the pulp needs to be washed after the pretreatment steps, as mentioned before, to recover the maximum amount of IL. Additionally, it is necessary to generate an IL-free pulp that meets the specifications to be used as a material or for further chemical transformations. As there is no

detailed data to model the washing step, it has been assumed for the base case a quantity of 10 kg H₂O/kg dry pulp, of which 2 kg H₂O/kg dry pulp is used for IL recovery. For the remaining washing water, it has been assumed that the IL is diluted, and the energy requirements to recover the IL would be extremely high. Therefore, this waste stream is used for other unit operations, such as lignin wash, but ultimately IL in this diluted fraction is not recovered and ends in the drain system. It has been assumed that the waste treatment plant at the end front of the plant will reduce the IL levels in the water to an acceptable level for discharge to the environment. Increasing the overall water usage for pulp wash has a negligible impact on CAPEX and a minor impact on OPEX (from 10 to 20 kg H₂O/kg dry pulp, less than 1%) if the equivalents used to recover most of the IL is kept at 2 kg H₂O/kg dry pulp. The reason for this is that water would still be needed for lignin precipitation, therefore, if there is not an increase in the water content of the streams sent to lignin precipitation, the changes on CAPEX and OPEX will be minor. On the other hand, if more water is needed to recover the IL, a significant effect on both CAPEX and OPEX is expected. From Figure 108, it can be seen that increasing the water equivalents necessary for IL recovery from 2 to 16, CAPEX increases by 14% and OPEX by 29%.

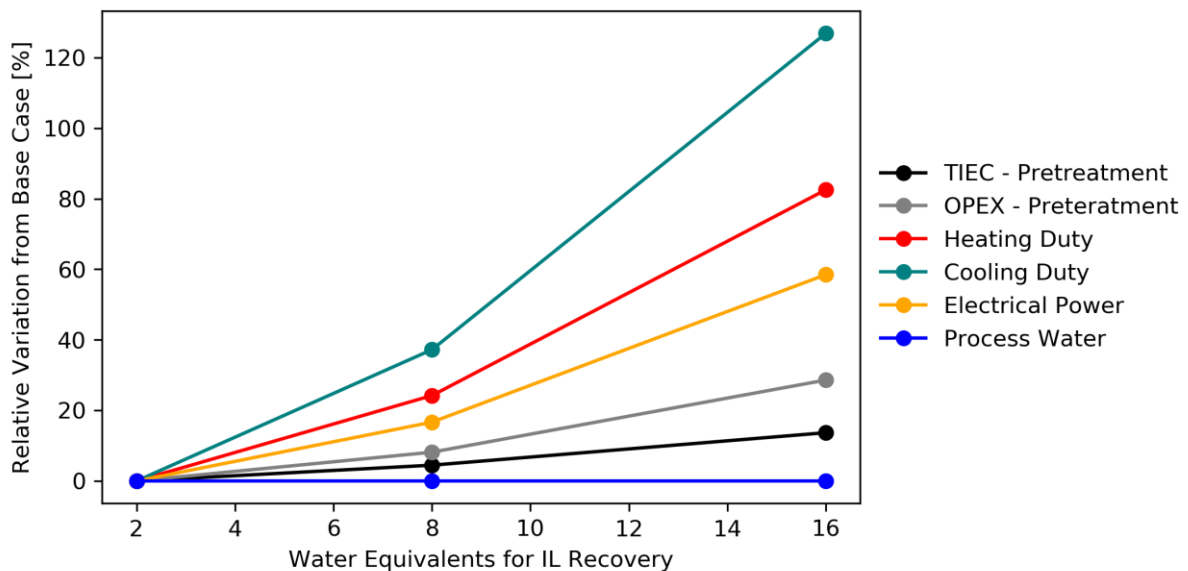


Figure 108. Equivalent of water needed to recover the IL. For these cases, a total of 20 kg of water per kg of pulp have been used.

In conclusion, the water usage for IL recovery needs to be minimized. When sufficient data is available, the washing step could be modelled, *e.g.* a counter-flow washing, to optimize the water usage for the IL recovery. The energy cost of recovering the IL needs to be compared to

the IL price, to determine what are the maximum IL quantities which are going to be recovered from this unit operation.

4.4.9.7 Sensitivity analysis key findings

It was found that the water specifications (moisture content in the raw biomass, water specification in the recycled IL, water needed for lignin precipitation) in the process have a complex effect on the CAPEX and OPEX. Interestingly, the size of the evaporator and the heat exchanger used to recover heat (H-101) are affected in opposite ways, *i.e.*, specifications that will decrease the load of the evaporator will increase the UA of H-101, and vice versa. The overall impact on the CAPEX cannot be determined conclusively without detail sizing and costing of these pieces of equipment. However, from an OPEX perspective, the overall water to be removed from the process should be minimized, for example, by minimizing the water needed for lignin precipitation. This will in turn minimize the energy demand of the ionoSolv process, increasing its environmental credentials.

4.5 Conclusions

It has been demonstrated that the ionic liquid [N₂₂₂₀][HSO₄] can be successfully applied for the pretreatment of *Eucalyptus red grandis* to obtain cellulose-rich pulps with no hemicelluloses and low lignin contents. Additionally, these pretreated pulps have excellent enzymatic digestibility. This shows that Eucalyptus can be used as feedstock for cellulose-based materials, as well as biochemicals and biofuel production.

Even though the IL recyclability was not tested for Eucalyptus pretreatment, it is expected that pretreatment performance will not be significantly impacted. This, combined with the low cost of [HSO₄]-based ILs, and the fact that no extensive drying is required, show promise for implementation in large scale bio-refineries. Additionally, different parameters affecting the pretreatment outcome *e.g.* pretreatment temperature and time, water content, agitation, base:acid ratio, can be optimised to meet the specifications for a given application (materials, biochemical or biofuels).

CO₂-enriched atmospheres did not have a significant effect on pretreatment performance, nor in the properties of the pulp and lignin. This shows that the ionoSolv process is pressure insensitive in inert gases and CO₂ up to 82 barg.

The TEA revealed that the ionoSolv process shows promise to improve the economics and environmental performance of a biorefinery for 2G ethanol production when compared to acid

catalysed steam explosion, and further research work and pilot plant developments are therefore justified.

Despite the fact that there are many uncertainties associated with the plant design at this stage of development which makes any definitive economic evaluations unreliable, the analysis performed in this section suggest that Eucalyptus pretreatment with IL looks promising for 2G ethanol production, as the CAPEX is likely to be equal or less than an ACSE process while the OPEX will likely be less after process optimization. Additionally, the ionoSolv process could also be used to produce cellulose-rich and lignin materials, which would not be possible with the alternate method, which does not remove lignin to a significant extent from the biomass feedstock.

Through the different sensitivity analyses, it has been shown that there is room for further optimization of the process. There are many variables affecting the pretreatment performance, which in turn, will affect the economics of the process. For advanced optimization, it is required to explore the effect of such variables (base:acid ratio, water content in the IL, recycled ILs, solid loading) on pulp composition and saccharification performance, and evaluate again the process model taking those results into account. Due to the multidimensional nature of the ionoSolv process, this exploration can be done through a Design of Experiments (DoE) approach.

Further, a more detailed design for the construction of a large scale process and a definitive cost estimate will require specific information for the properties of the pretreated wood, hydrolysate and waste streams, and also, detailed equipment performance evaluated through a pilot plant. Parameters to be investigated in junction with process equipment vendors are reactor technology (batch vs. continuous), solid separation efficiencies, pulp and lignin washes, and IL regeneration. The effective selection of materials for construction requires testing of alloys at process conditions.

The scaling-up of the ionoSolv process should follow normal engineering workflow, and in light of the results found here, the construction of a pilot plant to address the above points, and reduce the uncertainties prior to large scale implementation, is justified. Further, the process economics will be positively impacted if by-product credits are considered. This clearly justifies continued research and development to find uses for lignin and ways to valorise the hemicellulose fraction, for chemical productions such as furfural. Furthermore, process optimizations, and better process integration, should be extended beyond the pretreatment unit to include other processing units within the biorefinery both to reduce CAPEX/OPEX and therefore, the MESP.

4.5.1 Further work

Further work on the pretreatment process should address the effects of base:acid ratios and water content in the IL during pretreatment, the effect of water needed for lignin precipitation, IL recyclability, assessment of the fate and effects of the hemicellulosic fraction and sugar degradation products on the pretreatment, and how they accumulate in the solvent.

Despite severities (R_0) and H-factors appearing to be promising tools for predicting process performance for the ionoSolv process, it is necessary to develop generalised severity factors and detailed kinetic models, which include water content and base:acid ratio, in order to perform process optimisations. Determining the kinetic parameters of heterogeneous reactions of biomass solubilization for non-isothermal systems is complex and therefore has been excluded from the scope of this work. Additionally, kinetic models for chemical reactions taking place in the IL media, such as sugar degradation and conversion to HMF, furfural and levulinic acid, should be determined.

Regarding the analytical methods used to establish the pulp composition, it must be mentioned that they were developed for biomass characterisation instead of cellulose-rich pulps. For consistency, all the work performed in Professor Dr Jason Hallett's group is done following the same protocols, which allows comparison of the trends between different feedstocks, ILs and conditions. However, for accurate determinations, other analytical techniques should be used for detailed characterisation of the chemical components of the biomass and pulps. It would be important at some point understanding the accuracy of these methods applied to pulps. Even though the absolute values might change, it is expected that all the trends will hold true, even if more sophisticated chemical analysis are formed.

The ionoSolv process is currently at the laboratory-scale of development. The design of the biorefinery for the SERI project and the ionoSolv process developed in this work both assume that laboratory data can be scaled to commercial size. It has been shown that moisture content and water content specifications have a complex effect on the pretreatment unit that needs to be addressed in detail, *i.e.* impact of water content on pretreatment performance. As shown in Chapter 3, hydrogen sulfates based IL interact with metals, therefore, the choice of materials will play a major role in the technical and economic feasibility of the pretreatment unit based on this technology.

To summarize the main findings that need to be addressed to provide better economic evaluations and to provide detail data for pilot plant and commercial-scale plant design are:

- Assess detailed process performance taking into account the impact of solid loading and water content in the IL on pulp yields, composition and digestibility as well as for lignin. IL recyclability, including IL regeneration, degradation, build-up of impurities and impact on pulp and lignin.
- Validation of material of construction. The ILs used in the ionoSolv process can be aggressive for conventional steel used in construction materials. Non-metallic materials, such as PTFE or glass liners can be easily applied to pipes and some equipment (vessels, tanks) to protect them from corrosion. However, as shown in this study, the heat exchangers have a significant contribution to the CAPEX of the plant. Adding a coating to heat exchangers will reduce their efficiency, increasing the required transfer area, which in turn will increase the CAPEX. There are also non-metallic materials for heat transfer operations, such as SiC or graphite, that could be explored for the ionoSolv process.
- Validate with vendors the main equipment technologies and incorporate vendor feedback in the design. Other options can be foreseen for the reactions (batch vs. continuous), replace filters by centrifuges and dewatering units and the evaporator technology.
- Effluents from the plant: the impact of the presence of IL in the wastewater treatment plant needs to be addressed. Also, environmental norms and regulations regarding the IL, and other effluents of the plant, need to be understood.
- In order to improve the process economics and thus make it more competitive with traditional fossil-fuel based refineries, full valorisation of all biomass components is required, such as the lignin fraction ³⁷⁷, which is mainly used as a fuel in current biorefineries. Additionally, valorisation of the hemicellulosic fraction dissolved in the IL needs to be addressed to further improve the economics of this process. For example, recovery of monomeric sugars by adsorption with zeolites, or promote the oxidation of C₅ sugars to valuable products, such as furfural, and separating this component in the distillation step. Another option would be to add a first pretreatment step to remove the hemicellulosic fraction, such as auto-hydrolysis of biomass in water at high temperature or alkali-pretreatment.
- By-product credits: Besides ethanol, other chemical products could be produced, for example, organic molecules, such as furfural, HMF, sugars or CO₂ from the

fermentation process or combustion could be recovered and monetized. These process alternates are not discussed in this work.

Chapter 5 - Overall conclusions

This study contributed to expanding the knowledge on the use of ionic liquids for the development of large-scale sustainable processes for advanced materials production. It focused on the use of hydrogen sulfate based ILs for lignocellulosic biomass fraction to produce bio-derived materials, such as bioethanol, lignin and cellulose-rich pulps *via* the ionoSolv process. *Eucalyptus red grandis* was fractionated using the IL [N₂₂₂₀][HSO₄]. The experimental data obtained in the laboratory was used to evaluate the technical and economic feasibility of the ionoSolv-based biorefinery using Eucalyptus as feedstock for bioethanol production, which was compared to a biorefinery using an alternative fractionation technology, the Acid Catalysed Steam Explosion (ACSE) process, considered as a viable alternative for bioethanol production.

A systematic corrosion study of metals exposed to ILs was carried out to identify possible construction materials for the ionoSolv process for a more accurate techno-economic analysis of a biorefinery based on this process. It was observed that some metal/IL/water systems yielded the formation of metal oxides (and other metal-based materials) with well-defined particle morphologies. This method was termed the Oxidative Ionothermal Synthesis (OIS) and it was hypothesized that this process could be used for metal oxide (and other metal-based materials) production at large scale.

The great number of ILs that exist combined with the fact that their properties can be tuned, will open the door not only for the applications explored in this thesis but likely to many others in different areas.

5.1 Bioderived materials *via* the ionoSolv process

The use of hydrogen-sulfate-based ILs have been investigated to generate bioderived materials from Eucalyptus (Chapter 4) and a techno-economic analysis of this technology was performed for large scale 2G ethanol production and benchmarked against one of the most popular pretreatments, the ACSE process, to activate the pretreated lignocellulosic biomass towards enzymatic saccharification. The results from the analysis showed that the ionoSolv process, when compared to the ACSE process, could be competitive in terms of capital cost (CAPEX) and operating costs (OPEX) for a large scale implementation of a biorefinery using Eucalyptus as feedstock. The biorefinery CAPEX and OPEX were similar for both pretreatment technologies. However, the ionoSolv process showed some environmental advantages such as reduced waste and the possibility to reduce the energy consumption through process integration. It

needs to be highlighted that in general hardwoods (*e.g.* Eucalyptus) are less recalcitrant to pretreatment than softwoods, which will require more stringent conditions. Therefore, it is believed that for a softwood biorefinery, the CAPEX and OPEN differences between the ionoSolv process and other methods will be amplified in favour of the ionoSolv process.

When compared to other IL pretreatments, the ionoSolv process also shows some advantages. For example, ILs used to dissolve cellulose, such as [C₂C₁im][OAc] are water sensitives, more expensive than [HSO₄]-based IL and there is a loss of pretreatment performance when recycled. Due to all these effects combined, it is likely that a large-scale process based on cellulose-dissolving ILs will not be economically viable. Basic ILs, such as alkoxyammonium acetates, able to dissolve lignin but leaving behind the cellulosic and hemicellulosic fractions, face a major problem as the cation (the amine) and the anion (acetate) react each other to form an imide, with low pretreatment performance. This will negatively affect the economics of the process due to frequent IL inventory replenishment. This effect can be enhanced with feedstock containing acetate groups.

Lab-scale results and the TEA suggest that the ionoSolv process could be successfully used for the production of 2G ethanol, and other bioderived materials, such as lignin and cellulose-rich pulps. Additionally, it has been shown that the process is efficient to pretreat waste wood, which might enable a circular economy approach by the valorisation of waste. Further research towards the development of such processes is justified.

5.2 Corrosion of metals exposed to ILs

A systematic study on the corrosion behaviour of metals exposed to IL/water mixtures was conducted (Chapter 3), as finding suitable construction materials for IL-based processes is extremely important, both the technical and economic feasibility of a process. This study highlighted some interesting trends on the corrosion behaviour of metallic materials exposed to these substances, but overall, it is a system-dependent phenomenon. As expected, the corrosion phenomena were more extreme with increasing temperatures for most of the systems studied. The effects of water on the corrosion of metals exposed to ILs has a non-systematic and complex behaviour. For an aprotic ionic liquid (AIL) containing chloride ([C₄C₁im]Cl) and a protic ionic liquid (PIL) containing the hydrogen sulfate anion ([N₄₁₁₀][HSO₄]), in general, water acts as a corrosion promotor, whereas in a protic and chloride containing IL ([HC₁im]Cl) it acted as a corrosion inhibitor. More corrosion testing is required to validate the materials of construction for IL-based processes.

5.3 Oxidative Ionothermal Synthesis (OIS) for advanced materials production?

At first, it was quite frustrating observing extreme corrosion in some metal-IL systems, as the main goal of the corrosion study presented in Chapter 3 was to find suitable construction materials for IL-based processes. In the case of Zn, it was remarkable the number of different chemistries, morphologies/habits and sizes that would be obtained by exposing this metal to IL/water mixtures. Investigating more about the applications and synthesis methods for zinc oxide (ZnO), which was the main corrosion by-product, the concept of direct oxidation of metals in IL/water mixtures [Oxidative Ionothermal Synthesis (OIS)] to produce metal oxides (and other metal-based materials) became extremely attractive. An initial high-level techno-economic analysis of this one-pot synthetic method for metal-based compound production at large scale showed that it offers environmental, economic and synthetic (morphological control) advantages when compared to the main industrial methods.

This synthetic route offers enormous opportunities for exploration in a virtually unknown area of research. That is, understanding at a fundamental level how the IL/water mixtures impact the formation of different particles, including the chemistry, and in turn, how these relate to the inherent properties of the material. This might open the door to much interesting research in the field of materials science. As there is a huge number of possible ionic liquids that can be used, it is expected that new materials can be prepared through this method which will allow new exciting applications. For instance, there are some examples of hexagonal ZnO nanorod arrays grown by other methods, which have been used for nano-lasers, sensing and piezoelectric.

Despite the fact the preliminary techno-economic analysis was performed for a popular material (ZnO), the analysis of the corrosion products for other metals exposed to IL/water mixtures (*e.g.* iron, copper and aluminium) suggest that this methodology can be applied across a wider range of metals. Additionally, the fact that replacing Zn by brass (Cu₆₃/Zn₃₇) also resulted in ZnO hexagonal rods, is significant as it shows that the method works, even in alloys with low Zn content, which can enable the use of secondary metal sources and the valorisation of metallic wastes for a circular economy approach.

To develop the Oxidative Ionothermal Synthesis (OIS) and the inoSolv process, and other IL-based applications, detailed thermophysical data, information on the long term stability of the IL at process conditions, IL recyclability and corrosion data for metals exposed to IL systems are still missing. A detailed discussion on the future work is given in each section of this thesis.

5.4 Challenges and future work

The corrosion behaviour of metals exposed to ILs is system dependent, *i.e.* the nature of the metal and IL, and also it is affected by many variables such as concentration and nature of cosolvents, temperature and exposure time, and therefore, in some cases, the corrosion behaviour may be unpredictable. The relatively high cost of some ILs, coupled with process uncertainties and the risk of employing metallic materials in IL-based processes, make the use of these substances in large-scale processes unattractive. This is why overcoming these challenges is crucial for the development of IL based processes.

Filling in these gaps can be done by measuring IL properties, collecting more experimental data and by doing more corrosion testing. Doing this will result in the reduction of the risk of implementing these substances in large scale processes.

IL-based methods might contribute to the development of sustainable and cost-effective processes for advanced material production both for biomass processing and metal oxide production, opening the door to circular economy approaches if waste woods or metallic wastes are used. IL-based processes may also enable the discovery of new materials.

The development of pilot plants to evaluate the process performance and corrosion behaviour in these systems is a requirement *sine qua non* towards the construction and operation of safe and sustainable IL-based processes.

The knowledge of the underlying science of ILs, combined with their interesting properties and the great number of these substances, will certainly lead to sustainable and cost-effective exciting new applications so that the use of ILs will be more than just a “laboratory or academic curiosity” and become a reality in large scale processes.

*** The End ***

References

1. Clarke, C. J., Tu, W. C., Levers, O., Bröhl, A. & Hallett, J. P. Green and Sustainable Solvents in Chemical Processes. *Chem. Rev.* **118**, 747–800 (2018).
2. Kalb, R. S. Toward Industrialization of Ionic Liquids. in 261–282 (2020). doi:10.1007/978-3-030-35245-5_11
3. Brandt, A., Gräsvik, J., Hallett, J. P. & Welton, T. Deconstruction of lignocellulosic biomass with ionic liquids. *Green Chem.* **15**, 550–583 (2013).
4. G.H., B. Report of the World Commission on Environment and Development: Our Common Future (The Brundtland Report). *United Nations* (1987).
5. Vijayavenkataraman, S., Iniyan, S. & Goic, R. A review of climate change, mitigation and adaptation. *Renewable and Sustainable Energy Reviews* (2012). doi:10.1016/j.rser.2011.09.009
6. Anderson, T. R., Hawkins, E. & Jones, P. D. CO₂, the greenhouse effect and global warming: from the pioneering work of Arrhenius and Callendar to today's Earth System Models. *Endeavour* **40**, 178–187 (2016).
7. Zhao, X., Zhang, L. & Liu, D. Biomass recalcitrance. Part I: the chemical compositions and physical structures affecting the enzymatic hydrolysis of lignocellulose. *Biofuels, Bioprod. Biorefining* **6**, 465–482 (2012).
8. Stöcker, M. Biofuels and biomass-to-liquid fuels in the biorefinery: catalytic conversion of lignocellulosic biomass using porous materials. *Angew. Chem. Int. Ed. Engl.* **47**, 9200–11 (2008).
9. Lindorfer, J. et al. *Technical, Economic and Environmental Assessment of Biorefinery Concepts*. IEA Bioenergy task 42 (2019).
10. Vert, M. et al. Terminology for biorelated polymers and applications (IUPAC Recommendations 2012). *Pure Appl. Chem.* **84**, 377–410 (2012).
11. ACS. Green Chemistry. Available at: <https://www.acs.org/content/acs/en/greenchemistry.html>. (Accessed: 11th November 2020)
12. Anastas, P. T. & Warner, J. C. Green Chemistry: Theory and Practice. *Green Chem. Theory Pract. Oxford Univ. Press. New York* (1998).
13. Abraham, M. A. & Nguyen, N. "Green engineering: Defining the principles" - resdts from the sandestin conference. *Environ. Prog.* **22**, 233–236 (2003).
14. Anastas, P. T. & Zimmerman, J. B. Peer Reviewed: Design Through the 12 Principles of Green Engineering. *Environ. Sci. Technol.* **37**, 94A-101A (2003).
15. Hallett, J. P. & Welton, T. Room-temperature ionic liquids: Solvents for synthesis and catalysis. 2. *Chemical Reviews* **111**, 3508–3576 (2011).
16. Abouelela, A. R., Gschwend, F. V., Malaret, F. & Hallett, J. P. Commercial Aspects of Biomass Deconstruction with Ionic Liquids. in 87–127 (2020). doi:10.1007/978-3-030-35245-5_5
17. Outón Gil, R. Conceptual design, simulation and economic evaluation of the IonoSolv process. (2017).
18. Sukma, S. Designing an IonoSolv Pretreatment Process in The Biorefinery Plant. (Imperial College London, 2017).
19. Varnava, D. SYSTEM ANALYSIS FOR THE PRODUCTION OF RENEWABLE CARBOHYDRATES FROM WASTE WOOD. (Imperial College London, 2018).
20. Welton, T. Ionic liquids: a brief history. *Biophys. Rev.* **10**, 691–706 (2018).
21. Plechkova, N. V & Seddon, K. R. Applications of ionic liquids in the chemical industry. *Chem. Soc. Rev.* **37**, 123–150 (2008).
22. Dean, P. M., Pringle, J. M. & MacFarlane, D. R. Structural analysis of low melting organic salts: Perspectives on ionic liquids. *Phys. Chem. Chem. Phys.* **12**, 9144–9153 (2010).
23. Saihara, K., Yoshimura, Y., Ohta, S. & Shimizu, A. Properties of water confined in ionic liquids. *Sci. Rep.* **5**, 1–10 (2015).
24. Cha, S. et al. Structures of ionic liquid–water mixtures investigated by IR and NMR spectroscopy. *Phys. Chem. Chem. Phys.* **16**, 9591–9601 (2014).
25. Welton, T. Room-Temperature Ionic Liquids . Solvents for Synthesis and Catalysis Room-Temperature Ionic Liquids . Solvents for Synthesis and Catalysis. *Synthesis (Stuttg)*. **99**, 2071–2084 (1999).
26. Seddon, K. R. The International George Papatheodorou Symposium. in *Proceedings, S. Boghosian et al., Eds. (Institute of Chemical Engineering and High Temperature Chemical Processes)* 131–135 (1999).
27. Chen, L. et al. Inexpensive ionic liquids: [HSO₄]⁻-based solvent production at bulk scale. *Green Chem.* **16**, 3098–3106 (2014).
28. Chen, L. et al. Inexpensive ionic liquids: [HSO₄]⁻-based solvent production at bulk scale. *Green Chem.*

- 16, 3098–3106 (2014).
29. Greaves, T. L. & Drummond, C. J. Protic ionic liquids: Properties and applications. *Chemical Reviews* **108**, 206–237 (2008).
 30. Baaqel, H. *et al.* protic ionic liquids – a case study in biomass. *Green Chem.* (2020). doi:10.1039/d0gc00058b
 31. Gschwend, F. J. V. *et al.* Quantitative glucose release from softwood after pretreatment with low-cost ionic liquids. *Green Chem.* (2019). doi:10.1039/c8gc02155d
 32. Malaret, F., Gschwend, F. J. V., Lopes, J. M., Tu, W.-C. & Hallett, J. P. Eucalyptus red grandis pretreatment with protic ionic liquids: effect of severity and influence of sub/super-critical CO₂ atmosphere on pretreatment performance. *RSC Adv.* **10**, 16050–16060 (2020).
 33. Belieres, J.-P. & Angell, C. A. Protic Ionic Liquids: Preparation, Characterization, and Proton Free Energy Level Representation †. *J. Phys. Chem. B* **111**, 4926–4937 (2007).
 34. Shmukler, L. E., Fedorova, I. V., Gruzdev, M. S. & Safonova, L. P. Triethylamine-Based Salts: Protic Ionic Liquids or Molecular Complexes? *J. Phys. Chem. B* **123**, 10794–10806 (2019).
 35. Yoshizawa, M., Xu, W. & Angell, C. A. Ionic Liquids by Proton Transfer: Vapor Pressure, Conductivity, and the Relevance of ΔpK_a from Aqueous Solutions. *J. Am. Chem. Soc.* **125**, 15411–15419 (2003).
 36. Stoimenovski, J., Izgorodina, E. I. & MacFarlane, D. R. Ionicity and proton transfer in protic ionic liquids. *Phys. Chem. Chem. Phys.* **12**, 10341 (2010).
 37. *CRC Handbook of Chemistry and Physics, 99th Edition.* (CRC Press, 2018).
 38. Lenarcik, B. & Ojczenasz, P. The influence of the size and position of the alkyl groups in alkylimidazole molecules on their acid-base properties. *J. Heterocycl. Chem.* **39**, 287–290 (2002).
 39. Trummal, A., Lipping, L., Kaljurand, I., Koppel, I. A. & Leito, I. Acidity of Strong Acids in Water and Dimethyl Sulfoxide. *J. Phys. Chem. A* **120**, 3663–3669 (2016).
 40. Levanov, A. V., Isaikina, O. Y. & Lunin, V. V. Dissociation constant of nitric acid. *Russ. J. Phys. Chem. A* **91**, 1221–1228 (2017).
 41. Yoshizawa, M., Xu, W. & Angell, C. A. Ionic Liquids by Proton Transfer: Vapor Pressure, Conductivity, and the Relevance of ΔpK_a from Aqueous Solutions. *J. Am. Chem. Soc.* **125**, 15411–15419 (2003).
 42. Fedorova, I. V. & Safonova, L. P. The Nature of the Interactions in Triethanolammonium-Based Ionic Liquids. A Quantum Chemical Study. *J. Phys. Chem. A* **122**, 4562–4570 (2018).
 43. Chatterjee, P., Ghosh, A. K., Samanta, M. & Chakraborty, T. Barrierless Proton Transfer in the Weak C–H···O Hydrogen Bonded Methacrolein Dimer upon Nonresonant Multiphoton Ionization in the Gas Phase. *J. Phys. Chem. A* **122**, 5563–5573 (2018).
 44. Fedorova, I. V. & Safonova, L. P. Quantum Chemical Modeling of the Structure and H Bonding in Triethanolammonium-Based Protic Ionic Liquids with Sulfonic Acids. *J. Phys. Chem. A* **123**, 3735–3742 (2019).
 45. Fedorova, I. V. & Safonova, L. P. Ion Pair Structures and Hydrogen Bonding in R_nNH₄⁺–n Alkylammonium Ionic Liquids with Hydrogen Sulfate and Mesylate Anions by DFT Computations. *J. Phys. Chem. A* **124**, 3170–3179 (2020).
 46. Shmukler, L. E., Fedorova, I. V., Gruzdev, M. S., Fadeeva, Y. A. & Safonova, L. P. Diethylamine-based ionic liquids: quantum chemical calculations and experiment. *Russ. Chem. Bull.* **68**, 2009–2019 (2019).
 47. Glasser, L. & Jenkins, H. D. B. Predictive thermodynamics for ionic solids and liquids. *Phys. Chem. Chem. Phys.* **18**, 21226–21240 (2016).
 48. Preiss, U., Verevkin, S. P., Koslowski, T. & Krossing, I. Going Full Circle: Phase-Transition Thermodynamics of Ionic Liquids. *Chem. – A Eur. J.* **17**, 6508–6517 (2011).
 49. Verevkin, S. P. Predicting Enthalpy of Vaporization of Ionic Liquids: A Simple Rule for a Complex Property. *Angew. Chemie Int. Ed.* **47**, 5071–5074 (2008).
 50. Kabo, G. J., Paulechka, Y. U., Kabo, A. G. & Blokhin, A. V. Experimental determination of enthalpy of 1-butyl-3-methylimidazolium iodide synthesis and prediction of enthalpies of formation for imidazolium ionic liquids. *J. Chem. Thermodyn.* **42**, 1292–1297 (2010).
 51. Kanzaki, R. *et al.* Acid–Base Property of N-Methylimidazolium-Based Protic Ionic Liquids Depending on Anion. *J. Phys. Chem. B* **116**, 14146–14152 (2012).
 52. Umaphathi, R., Attri, P. & Venkatesu, P. Thermophysical Properties of Aqueous Solution of Ammonium-Based Ionic Liquids. *J. Phys. Chem. B* **118**, 5971–5982 (2014).
 53. Kaupmees, K., Trummal, A. & Leito, I. Basicities of Strong Bases in Water: A Computational Study. *Croat. Chem. Acta* **87**, 385–395 (2014).
 54. Matuszek, K. *et al.* Protic Ionic Liquids Based on Oligomeric Anions [(HSO₄)(H₂SO₄)_x][–] (x = 0, 1, or 2) for a Clean ϵ -Caprolactam Synthesis. *Aust. J. Chem.* **72**, 130 (2019).

55. Wu, T.-Y. *et al.* Thermophysical properties of room temperature ionic liquids with oligomeric formate and hydrogen sulfate. *J. Taiwan Inst. Chem. Eng.* **43**, 58–66 (2012).
56. Matuszek, K., Chrobok, A., Coleman, F., Seddon, K. R. & Swadźba-Kwaśny, M. Tailoring ionic liquid catalysts: structure, acidity and catalytic activity of protonic ionic liquids based on anionic clusters, $[(\text{HSO}_4)(\text{H}_2\text{SO}_4)_x]^-$ ($x = 0, 1, \text{ or } 2$). *Green Chem.* **16**, 3463–3471 (2014).
57. Weigand, L., Mostame, S., Brandt-Talbot, A., Welton, T. & Hallett, J. P. Effect of pretreatment severity on the cellulose and lignin isolated from: *Salix* using IonoSolv pretreatment. *Faraday Discuss.* (2017). doi:10.1039/c7fd00059f
58. Nakasu, P. Y. S. *et al.* Interplay of acid-base ratio and recycling on the pretreatment performance of the protic ionic liquid monoethanolammonium acetate. *ACS Sustain. Chem. Eng.* acssuschemeng.0c01311 (2020). doi:10.1021/acssuschemeng.0c01311
59. Mazeau, K. & Heux, L. Molecular dynamics simulations of bulk native crystalline and amorphous structures of cellulose. *J. Phys. Chem. B* **107**, 2394–2403 (2003).
60. Abe, H. *et al.* Peculiar Concentration Dependence of H/D Exchange Reaction in 1-Butyl-3-methylimidazolium Tetrafluoroborate-D₂O Mixtures. *Open J. Phys. Chem.* **01**, 70–76 (2011).
61. Canongia Lopes, J. N. A. & Pádua, A. A. H. Nanostructural organization in ionic liquids. *J. Phys. Chem. B* **110**, 3330–3335 (2006).
62. Jiang, W., Wang, Y. & Voth, G. A. Molecular dynamics simulation of nanostructural organization in ionic liquid/water mixtures. *J. Phys. Chem. B* **111**, 4812–4818 (2007).
63. Miki, K., Westh, P., Nishikawa, K. & Koga, Y. Effect of an ‘ionic liquid’ cation, 1-butyl-3-methylimidazolium, on the molecular organization of H₂O. *J. Phys. Chem. B* **109**, 9014–9019 (2005).
64. Elaiwi, A. *et al.* Hydrogen bonding in imidazolium salts and its implications for ambient-temperature halogenoaluminate(III) ionic liquids. *J. Chem. Soc. Dalt. Trans.* 3467 (1995). doi:10.1039/dt9950003467
65. Katoh, R., Hara, M. & Tsuzuki, S. Ion Pair Formation in [bmim]I Ionic Liquids. *J. Phys. Chem. B* **112**, 15426–15430 (2008).
66. Stange, P., Fumino, K. & Ludwig, R. Ion Speciation of Protic Ionic Liquids in Water: Transition from Contact to Solvent-Separated Ion Pairs. *Angew. Chemie Int. Ed.* **52**, 2990–2994 (2013).
67. Reid, J. E. S. J., Walker, A. J. & Shimizu, S. Residual water in ionic liquids: Clustered or dissociated? *Phys. Chem. Chem. Phys.* **17**, 14710–14718 (2015).
68. Marcus, Y. & Hefter, G. Ion Pairing. *Chem. Rev.* **106**, 4585–4621 (2006).
69. Köddermann, T. *et al.* The Effect of Neutral Ion Aggregate Formation on the Electrical Conductivity of an Ionic Liquid and its Mixtures with Chloroform. *ChemPhysChem* **13**, 1748–1752 (2012).
70. Chaplin, M. F. Structure and Properties of Water in its Various States. in *Encyclopedia of Water* 1–19 (Wiley, 2019). doi:10.1002/9781119300762.wsts0002
71. Sharpe, A. G. The solvation of halide ions and its chemical significance. *J. Chem. Educ.* **67**, 309 (1990).
72. Wang, X.-B. Bulk-Like Features in the Photoemission Spectra of Hydrated Doubly Charged Anion Clusters. *Science (80-.)*. **294**, 1322–1325 (2001).
73. Vchirawongkwin, V., Rode, B. M. & Persson, I. Structure and Dynamics of Sulfate Ion in Aqueous Solution An ab initio QMCF MD Simulation and Large Angle X-ray Scattering Study. *J. Phys. Chem. B* **111**, 4150–4155 (2007).
74. Wang, Y. *et al.* Ratiometric detection of Raman hydration shell spectra. *J. Raman Spectrosc.* **47**, 1231–1238 (2016).
75. Yacovitch, T. I. *et al.* Infrared Spectroscopy of Hydrated Bisulfate Anion Clusters: $\text{HSO}_4^-(\text{H}_2\text{O})_{1-16}$. *J. Phys. Chem. Lett.* **2**, 2135–2140 (2011).
76. O’Brien, J. T., Prell, J. S., Bush, M. F. & Williams, E. R. Sulfate Ion Patterns Water at Long Distance. *J. Am. Chem. Soc.* **132**, 8248–8249 (2010).
77. Leenson, I. A. Sulfuric Acid and Water: Paradoxes of Dilution. *J. Chem. Educ.* **81**, 991 (2004).
78. Fedotova, M. V., Kruchinin, S. E. & Chuev, G. N. Local ion hydration structure in aqueous imidazolium-based ionic liquids: The effects of concentration and anion nature. *J. Mol. Liq.* **247**, 100–108 (2017).
79. Pluhařová, E., Fischer, H. E., Mason, P. E. & Jungwirth, P. Hydration of the chloride ion in concentrated aqueous solutions using neutron scattering and molecular dynamics. *Mol. Phys.* **112**, 1230–1240 (2014).
80. Pálinkás, G., Radnai, T., Szász, G. I. & Heinzinger, K. The structure of an aqueous ammonium chloride solution. *J. Chem. Phys.* **74**, 3522–3526 (1981).
81. Hewish, N. A. & Neilson, G. W. Ammonium ion coordination in concentrated aqueous ammonium chloride. *Chem. Phys. Lett.* **84**, 425–427 (1981).
82. Noto, R., Martorana, V., Migliore, M. & Fornili, S. L. Hydration of the Ammonium Ion: Monte Carlo

- Simulation. *Zeitschrift für Naturforsch. A* **46**, (1991).
83. Shinohara, H., Nagashima, U., Tanaka, H. & Nishi, N. Magic numbers for water–ammonia binary clusters: Enhanced stability of ion clathrate structures. *J. Chem. Phys.* **83**, 4183–4192 (1985).
 84. Nguyen, V. Q., Chen, X. G. & Yergey, A. L. Observations of magic numbers in gas phase hydrates of alkylammonium ions. *J. Am. Soc. Mass Spectrom.* **8**, 1175–1179 (1997).
 85. Hawlicka, E. & Dlugoborski, T. Molecular dynamics simulations of the aqueous solution of tetramethylammonium chloride. *Chem. Phys. Lett.* **268**, 325–330 (1997).
 86. Shishido, R. *et al.* An infrared spectroscopic and theoretical study on $(\text{CH}_3)_3\text{N-H} + -(\text{H}_2\text{O})_n$, $n = 1-22$: highly polarized hydrogen bond networks of hydrated clusters. *Phys. Chem. Chem. Phys.* **17**, 25863–25876 (2015).
 87. Ullah, Z., Azmi Bustam, M., Muhammad, N., Man, Z. & Khan, A. S. Synthesis and Thermophysical Properties of Hydrogensulfate Based Acidic Ionic Liquids. *J. Solution Chem.* **44**, 875–889 (2015).
 88. Gschwend, F. J. V., Malaret, F., Shinde, S. & Hallett, J. P. Rapid pretreatment of Miscanthus using the low-cost ionic liquid triethylammonium hydrogen sulfate at elevated temperatures. 3486–3498 (2018). doi:10.1039/c8gc00837j
 89. Gschwend, F. J. V. *et al.* Quantitative Glucose Release from Softwood after Pretreatment with Low-cost Ionic Liquids. *Green Chem.* **21**, 692–703 (2019).
 90. Cariglia, A. Design, construction and operation of a lab-scale pilot plant for the continuous production of a protic ionic liquid. (Imperial College London, 2015).
 91. METTLER TOLEDO. *Good Titration Practice™ in Karl Fischer Titration.* (2011).
 92. Iglesias-Otero, M. A., Troncoso, J., Carballo, E. & Romani, L. Density and refractive index in mixtures of ionic liquids and organic solvents: Correlations and predictions. *J. Chem. Thermodyn.* **40**, 949–956 (2008).
 93. Troncoso, J., Cerdeiriña, C. A., Sanmamed, Y. A., Romani, L. & Rebelo, L. P. N. Thermodynamic Properties of Imidazolium-Based Ionic Liquids: Densities, Heat Capacities, and Enthalpies of Fusion of [bmim][PF₆] and [bmim][NTf₂]. *J. Chem. Eng. Data* **51**, 1856–1859 (2006).
 94. Harris, K. R., Kanakubo, M. & Woolf, L. A. Temperature and Pressure Dependence of the Viscosity of the Ionic Liquids 1-Methyl-3-octylimidazolium Hexafluorophosphate and 1-Methyl-3-octylimidazolium Tetrafluoroborate. *J. Chem. Eng. Data* **51**, 1161–1167 (2006).
 95. Guggenheim, E. A. & Turgeon, J. C. Specific interaction of ions. *Trans. Faraday Soc.* **51**, 747 (1955).
 96. Castellan, G. W. *Physical Chemistry.* (1983).
 97. Hammett, L. P. & Deyrup, A. J. A SERIES OF SIMPLE BASIC INDICATORS. I. THE ACIDITY FUNCTIONS OF MIXTURES OF SULFURIC AND PERCHLORIC ACIDS WITH WATER 1. *J. Am. Chem. Soc.* **54**, 2721–2739 (1932).
 98. Gräsvik, J., Hallett, J. P., To, T. Q. & Welton, T. A quick, simple, robust method to measure the acidity of ionic liquids. *Chem. Commun.* **50**, 7258–7261 (2014).
 99. Thomazeau, C., Olivier-Bourbigou, H., Magna, L., Luts, S. & Gilbert, B. Determination of an Acidic Scale in Room Temperature Ionic Liquids. *J. Am. Chem. Soc.* **125**, 5264–5265 (2003).
 100. Umaphathi, R., Attri, P. & Venkatesu, P. Thermophysical Properties of Aqueous Solution of Ammonium-Based Ionic Liquids. *J. Phys. Chem. B* **118**, 5971–5982 (2014).
 101. Jacquemin, J., Anouti, M. & Lemordant, D. Physico-Chemical Properties of Non-Newtonian Shear Thickening Diisopropyl-ethylammonium-Based Protic Ionic Liquids and Their Mixtures with Water and Acetonitrile. *J. Chem. Eng. Data* **56**, 556–564 (2011).
 102. Xu, Y. Volumetric, viscosity, and electrical conductivity properties of aqueous solutions of two n-butylammonium-based protic ionic liquids at several temperatures. *J. Chem. Thermodyn.* **64**, 126–133 (2013).
 103. Hou, M. *et al.* Thermodynamic properties of aqueous solutions of two ammonium-based protic ionic liquids at 298.15K. *J. Mol. Liq.* **178**, 149–155 (2013).
 104. Glasser, L. Lattice and phase transition thermodynamics of ionic liquids. *Thermochim. Acta* **421**, 87–93 (2004).
 105. Gutowski, K. E., Holbrey, J. D., Rogers, R. D. & Dixon, D. A. Prediction of the Formation and Stabilities of Energetic Salts and Ionic Liquids Based on ab Initio Electronic Structure Calculations. *J. Phys. Chem. B* **109**, 23196–23208 (2005).
 106. Gutowski, K. E., Rogers, R. D. & Dixon, D. A. Accurate Thermochemical Properties for Energetic Materials Applications. II. Heats of Formation of Imidazolium-, 1,2,4-Triazolium-, and Tetrazolium-Based Energetic Salts from Isodesmic and Lattice Energy Calculations †. *J. Phys. Chem. B* **111**, 4788–4800 (2007).

107. Greaves, T. L., Weerawardena, A., Fong, C., Krodkiewska, I. & Drummond, C. J. Protic Ionic Liquids: Solvents with Tunable Phase Behavior and Physicochemical Properties. *J. Phys. Chem. B* **110**, 22479–22487 (2006).
108. Jacquemin, J. *et al.* Prediction of Ionic Liquid Properties. II. Volumetric Properties as a Function of Temperature and Pressure. *J. Chem. Eng. Data* **53**, 2133–2143 (2008).
109. Hepler, L. G. Thermal expansion and structure in water and aqueous solutions. *Can. J. Chem.* **47**, 4613–4617 (1969).
110. Shekaari, H., Zafarani-Moattar, M. T., Kazempour, A. & Ghasedi-Khajeh, Z. Volumetric Properties of Aqueous Ionic-Liquid Solutions at Different Temperatures. *J. Chem. Eng. Data* **60**, 1750–1755 (2015).
111. Sharma, G., Singh, V. & Gardas, R. L. Apparent molar properties of aqueous protic ionic liquid solutions at T = (293.15 to 328.15) K. *Ionics (Kiel)*. **21**, 1959–1965 (2015).
112. Ananthaswamy, J. & Atkinson, G. Thermodynamics of concentrated electrolyte mixtures. 4. Pitzer-Debye-Hueckel limiting slopes for water from 0 to 100.degree.C and from 1 atm to 1 kbar. *J. Chem. Eng. Data* **29**, 81–87 (1984).
113. Gardas, R. L., Dagade, D. H., Terdale, S. S., Coutinho, J. A. P. & Patil, K. J. Acoustic and volumetric properties of aqueous solutions of imidazolium based ionic liquids at 298.15 K. *J. Chem. Thermodyn.* **40**, 695–701 (2008).
114. Jacquemin, J. *et al.* Prediction of Ionic Liquid Properties. I. Volumetric Properties as a Function of Temperature at 0.1 MPa. *J. Chem. Eng. Data* **53**, 716–726 (2008).
115. Niedermeyer, H., Hallett, J. P., Villar-Garcia, I. J., Hunt, P. A. & Welton, T. Mixtures of ionic liquids. *Chem. Soc. Rev.* **41**, 7780 (2012).
116. Paulechka, Y. U., Kabo, A. G., Blokhin, A. V., Kabo, G. J. & Shevelyova, M. P. Heat Capacity of Ionic Liquids: Experimental Determination and Correlations with Molar Volume. *J. Chem. Eng. Data* **55**, 2719–2724 (2010).
117. Montalbán, M. G., Collado-González, M., Díaz-Baños, F. G. & Villora, G. Predicting Density and Refractive Index of Ionic Liquids. in *Progress and Developments in Ionic Liquids* (InTech, 2017). doi:10.5772/65790
118. Jennings, M. S. Y. New Characterization Techniques for Acidic Ionic Liquids. (Imperial College London, 2014).
119. Diederichsen, K. M., Buss, H. G. & McCloskey, B. D. The Compensation Effect in the Vogel–Tammann–Fulcher (VTF) Equation for Polymer-Based Electrolytes. *Macromolecules* **50**, 3831–3840 (2017).
120. Korson, L., Drost-Hansen, W. & Millero, F. J. Viscosity of water at various temperatures. *J. Phys. Chem.* **73**, 34–39 (1969).
121. Rodríguez, H. & Brennecke, J. F. Temperature and composition dependence of the density and viscosity of binary mixtures of water + ionic liquid. *J. Chem. Eng. Data* **51**, 2145–2155 (2006).
122. Grunberg, L. & Nissan, A. Mixture law for viscosity. *Nature* **164**, 799–800 (1949).
123. Kendall, J. & Monroe, K. P. THE VISCOSITY OF LIQUIDS. II. THE VISCOSITY-COMPOSITION CURVE FOR IDEAL LIQUID MIXTURES. 1. *J. Am. Chem. Soc.* **39**, 1787–1802 (1917).
124. Adam, O. E.-A. A. & Awwad, A. M. Estimation of excess molar volumes and theoretical viscosities of binary mixtures of benzene + n-alkanes at 298.15 K. *Int. J. Ind. Chem.* **7**, 391–400 (2016).
125. Mazan, V. & Boltoeva, M. Insight into the ionic interactions in neat ionic liquids by Diffusion Ordered Spectroscopy Nuclear Magnetic Resonance. *J. Mol. Liq.* **240**, 74–79 (2017).
126. Li, W., Kagan, G., Hopson, R. & Williard, P. G. Measurement of Solution Viscosity via Diffusion-Ordered NMR Spectroscopy (DOSY). *J. Chem. Educ.* **88**, 1331–1335 (2011).
127. Álvarez, V. H., Mattedi, S., Martin-Pastor, M., Aznar, M. & Iglesias, M. Synthesis and thermophysical properties of two new protic long-chain ionic liquids with the oleate anion. *Fluid Phase Equilib.* **299**, 42–50 (2010).
128. Greenwood, N. N. & Thompson, A. 700. Comparison of some properties of anhydrous sulphuric acid and dideuteriosulphuric acid over a range of temperature. *J. Chem. Soc.* 3474 (1959). doi:10.1039/jr9590003474
129. Keil, P., Kick, M. & König, A. Long-Term Stability, Regeneration and Recycling of Imidazolium-based Ionic Liquids. *Chemie Ing. Tech.* **84**, 859–866 (2012).
130. Ngo, H. L., LeCompte, K., Hargens, L. & McEwen, A. B. Thermal properties of imidazolium ionic liquids. *Thermochim. Acta* **357–358**, 97–102 (2000).
131. Del Sesto, R. E. *et al.* Limited thermal stability of imidazolium and pyrrolidinium ionic liquids. *Thermochim. Acta* **491**, 118–120 (2009).
132. Cao, Y. & Mu, T. Comprehensive Investigation on the Thermal Stability of 66 Ionic Liquids by

- Thermogravimetric Analysis. *Ind. Eng. Chem. Res.* **53**, 8651–8664 (2014).
133. Götz, M. *et al.* Long-term thermal stability of selected ionic liquids in nitrogen and hydrogen atmosphere. *Thermochim. Acta* **600**, 82–88 (2015).
 134. Liu, H., Maginn, E., Visser, A. E., Bridges, N. J. & Fox, E. B. Thermal and Transport Properties of Six Ionic Liquids: An Experimental and Molecular Dynamics Study. *Ind. Eng. Chem. Res.* **51**, 7242–7254 (2012).
 135. Liu, P., Wang, M. & Cheng, Z.-M. Thermal Stability and Vapor–Liquid Equilibrium for Imidazolium Ionic Liquids as Alternative Reaction Media. *J. Chem. Eng. Data* **60**, 836–844 (2015).
 136. Huddleston, J. G. *et al.* Characterization and comparison of hydrophilic and hydrophobic room temperature ionic liquids incorporating the imidazolium cation. *Green Chem.* **3**, 156–164 (2001).
 137. Lorenzo, M. *et al.* Long-term thermal stabilities of ammonium ionic liquids designed as potential absorbents of ammonia. *RSC Adv.* **5**, 41278–41284 (2015).
 138. Ohtani, H., Ishimura, S. & Kumai, M. Thermal Decomposition Behaviors of Imidazolium-type Ionic Liquids Studied by Pyrolysis-Gas Chromatography. *Anal. Sci.* **24**, 1335–1340 (2008).
 139. Maton, C., De Vos, N. & Stevens, C. V. Ionic liquid thermal stabilities: decomposition mechanisms and analysis tools. *Chem. Soc. Rev.* **42**, 5963–5977 (2013).
 140. Clough, M. T., Geyer, K., Hunt, P. A., Mertes, J. & Welton, T. Thermal decomposition of carboxylate ionic liquids: trends and mechanisms. *Phys. Chem. Chem. Phys.* **15**, 20480 (2013).
 141. Haynes W. M. *CRC Handbook of Chemistry and Physics, 97th Edition. CRC Handbook of Chemistry and Physics* (2017). doi:10.1136/oem.53.7.504
 142. Schwartz, D., Gadiou, R., Brillhac, J.-F., Prado, G. & Martinez, G. A kinetic study of the decomposition of spent sulfuric acids at high temperature. *Ind. Eng. Chem. Res.* **39**, 2183–2189 (2000).
 143. ASTM. Standard guide for laboratory immersion corrosion testing of metals. *ASTM Int.* **G31-12a**, 1–10 (2012).
 144. British Standards Institution. ISO 11845 : 2020 Corrosion of metals and alloys — General principles for corrosion testing. (2020).
 145. Gerhard Kreysa, M. S. *Corrosion Handbook, Corrosive Agents and Their Interaction with Materials, Volume 7, Sodium Chloride,*. (2007).
 146. Gerhardus H. Koch, Michiel P.H. Brongers, and Neil G. Thompson, Y. Paul Virmani, J. H. P. Costs of corrosion and Preventitive strategies. *NACE Int.* (2002).
 147. Baboian, R. *Corrosion Tests and Standards: Application and Interpretation-Second Edition. Corrosion Tests and Standards: Application and Interpretation-Second Edition* (2005). doi:10.1520/mnl20-2nd-eb
 148. Fontana, M. G., Greene, N. D. & Klerer, J. Corrosion Engineering. *J. Electrochem. Soc.* **115**, 142C (1968).
 149. Revie, R. W. & Uhlig, H. H. *Corrosion and Corrosion Control.* (John Wiley & Sons, Inc., 2008). doi:10.1002/9780470277270
 150. Schweitzer, P. A. *Corrosion resistance tables : metals, nonmetals, coatings, mortars, plastics, elastomers and linings, and fabrics / Philip A. Schweitzer.* (1995).
 151. Uerdingen, M., Treber, C., Balsler, M., Schmitt, G. & Werner, C. Corrosion behaviour of ionic liquids. *Green Chem.* **7**, 321–325 (2005).
 152. Fajardo, S., R. García-Galvan, F., Barranco, V., C. Galvan, J. & Feliu Batlle, S. A Critical Review of the Application of Electrochemical Techniques for Studying Corrosion of Mg and Mg Alloys: Opportunities and Challenges. in *Magnesium Alloys - Selected Issue* (IntechOpen, 2018). doi:10.5772/intechopen.79497
 153. Shi, Z., Liu, M. & Atrens, A. Measurement of the corrosion rate of magnesium alloys using Tafel extrapolation. *Corros. Sci.* **52**, 579–588 (2010).
 154. Hsieh, M. K., Dzombak, D. A. & Vidic, R. D. Bridging gravimetric and electrochemical approaches to determine the corrosion rate of metals and metal alloys in cooling systems: Bench scale evaluation method. *Ind. Eng. Chem. Res.* (2010). doi:10.1021/ie100217k
 155. Dwivedi, D., Lepková, K. & Becker, T. Carbon steel corrosion: a review of key surface properties and characterization methods. *RSC Adv.* **7**, 4580–4610 (2017).
 156. Dwivedi, D., Lepkova, K. & Becker, T. Emerging surface characterization techniques for carbon steel corrosion: A critical brief review. *Proc. R. Soc. A Math. Phys. Eng. Sci.* **473**, (2017).
 157. Verma, C., Ebenso, E. E. & Quraishi, M. A. Ionic liquids as green and sustainable corrosion inhibitors for metals and alloys: An overview. *Journal of Molecular Liquids* (2017). doi:10.1016/j.molliq.2017.02.111
 158. Likhanova, N. V. *et al.* The effect of ionic liquids with imidazolium and pyridinium cations on the corrosion inhibition of mild steel in acidic environment. *Corros. Sci.* **52**, 2088–2097 (2010).
 159. BHARDWAJ, M. & BALASUBRAMANIAM, R. Uncoupled non-linear equations method for determining kinetic parameters in case of hydrogen evolution reaction following Volmer–Heyrovsky–Tafel

- mechanism and Volmer–Heyrovsky mechanism. *Int. J. Hydrogen Energy* **33**, 2178–2188 (2008).
160. Karbaschi, M., Nasr-Esfahani, M. & Zendejdel, M. Inhibition of mild steel corrosion in hydrochloric acid solution by Fe and Cr Schiff base complexes. *Prot. Met. Phys. Chem. Surfaces* **51**, 918–927 (2015).
161. Sun, N., Rodríguez, H., Rahman, M. & Rogers, R. D. Where are ionic liquid strategies most suited in the pursuit of chemicals and energy from lignocellulosic biomass? *Chem. Commun.* **47**, 1405–1421 (2011).
162. Espinosa, T., Sanes, J., Jiménez, A. E. & Bermúdez, M. D. Surface interactions, corrosion processes and lubricating performance of protic and aprotic ionic liquids with OFHC copper. *Appl. Surf. Sci.* **273**, 578–597 (2013).
163. Jiménez, A. E., Bermúdez, M. D., Carrión, F. J. & Martínez-Nicolás, G. Room temperature ionic liquids as lubricant additives in steel-aluminium contacts: Influence of sliding velocity, normal load and temperature. *Wear* (2006). doi:10.1016/j.wear.2005.11.004
164. Qu, J., Truhan, J. J., Dai, S., Luo, H. & Blau, P. J. Ionic liquids with ammonium cations as lubricants or additives. *Tribol. Lett.* (2006). doi:10.1007/s11249-006-9081-0
165. Pisarova, L., Gabler, C., Dörr, N., Pittenauer, E. & Allmaier, G. Thermo-oxidative stability and corrosion properties of ammonium based ionic liquids. *Tribol. Int.* **46**, 73–83 (2012).
166. Sowmiah, S., Srinivasadesikan, V., Tseng, M.-C. & Chu, Y.-H. On the Chemical Stabilities of Ionic Liquids. *Molecules* **14**, 3780–3813 (2009).
167. Rodrigues, A. S. M. C. *et al.* Effect of the Methylation and N-H Acidic Group on the Physicochemical Properties of Imidazolium-Based Ionic Liquids. *J. Phys. Chem. B* (2015). doi:10.1021/acs.jpcc.5b05354
168. Niazi, A. A., Rabideau, B. D. & Ismail, A. E. Effects of water concentration on the structural and diffusion properties of imidazolium-based ionic liquid-water mixtures. *J. Phys. Chem. B* **117**, 1378–1388 (2013).
169. Malaret, F., Hallett, J. & Campbell, K. S. Oxidative ionothermal synthesis for micro and macro Zn-based materials. *Mater. Adv.* **1**, 3597–3604 (2020).
170. ASTM International. Standard Practice for Preparing , Cleaning , and Evaluating Corrosion Test. *Significance* **90**, 1–9 (1999).
171. British Standards Institution. ISO 8047: Corrosion of metals and alloys - Removal of corrosion products from corrosion test specimens. *Bs En Iso 8047* (2009).
172. Heusler, K. E., Landolt, D. & Trasatti, S. Electrochemical corrosion nomenclature. *J. Electroanal. Chem. Interfacial Electrochem.* **274**, 345–348 (1989).
173. Burrell, G. L., Bugar, I. M., Separovic, F. & Dunlop, N. F. Preparation of protic ionic liquids with minimal water content and 15N NMR study of proton transfer. *Phys. Chem. Chem. Phys.* **12**, 1571 (2010).
174. Wallace, W. E. NIST Chemistry webBook, NIST Standard Reference Database Number 69. in *NIST Chemistry WebBook, NIST Standard Reference Database Number 69* (2019). doi:citeulike-article-id:3211271
175. Liu, T., Vilar, R., Eugénio, S., Grondin, J. & Danten, Y. Electrodeposition of copper thin films from 1-ethyl-3-methylimidazolium bis(trifluoromethylsulfonyl)imide. *J. Appl. Electrochem.* **45**, 87–93 (2015).
176. Weisser, T. S. THE DE-ALLOYING OF COPPER ALLOYS. *Stud. Conserv.* **20**, 207–214 (1975).
177. Papadopoulou, O., Vassiliou, P., Grassini, S., Angelini, E. & Gouda, V. Soil-induced corrosion of ancient Roman brass - A case study. *Mater. Corros.* **67**, 160–169 (2016).
178. Singh, R. N., Bahadur, L. & Singh, P. Electrochemical behaviour of brass (Cu/Zn, 63/37) in binary mixtures of acetonitrile and water. *Electrochim. Acta* **32**, 895–899 (1987).
179. Santos, C. I. S., Mendonça, M. H. & Fonseca, I. T. E. Corrosion of brass in natural and artificial seawater. *J. Appl. Electrochem.* **36**, 1353–1359 (2006).
180. Desai, M. N. Corrosion Inhibitors for Brasses. *Mater. Corros. und Korrosion* **24**, 707–716 (1973).
181. Kazansky, L. P., Pronin, Y. E. & Arkhipushkin, I. A. XPS study of adsorption of 2-mercaptobenzothiazole on a brass surface. *Corros. Sci.* **89**, 21–29 (2014).
182. Perissi, I., Bardi, U., Caporali, S. & Lavacchi, A. High temperature corrosion properties of ionic liquids. *Corrosion Science* **48**, 2349–2362 (2006).
183. Tolstoguzov, A. B., Bardi, U. & Chenakin, S. P. Study of the corrosion of metal alloys interacting with an ionic liquid. *Bull. Russ. Acad. Sci. Phys.* **72**, 605–608 (2008).
184. Perissi, I., Bardi, U., Caporali, S., Fossati, A. & Lavacchi, A. Ionic liquids as diathermic fluids for solar trough collectors' technology: A corrosion study. *Sol. Energy Mater. Sol. Cells* **92**, 510–517 (2008).
185. Arenas, M. F., Reddy, R. G., Associate, R. & Professor, A. Corrosion of Steel in Ionic Liquids. *J. Min. Metall. J. Min. Met* **39**, 81–91 (2003).
186. Reddy, R. G., Zhang, Z., Arenas, M. F. & Blake, D. M. Thermal Stability and Corrosivity Evaluations of Ionic Liquids as Thermal Energy Storage Media. *High Temp. Mater. Process.* (2003). doi:10.1515/HTMP.2003.22.2.87

187. Li, Y., Zou, Y. & Hou, Y. Synthesis and characterization of simonkolleite nanodisks and their conversion into ZnO nanostructures. *Cryst. Res. Technol.* **46**, 305–308 (2011).
188. Kowalik, P. *et al.* Structure and morphology transformation of ZnO by carbonation and thermal treatment. *Mater. Res. Bull.* **65**, 149–156 (2015).
189. Bitenc, M. *et al.* The growth mechanism of zinc oxide and hydrozincite: A study using electron microscopies and in situ SAXS. *CrystEngComm* **14**, 3080–3088 (2012).
190. Nassar, M. Y., Moustafa, M. M. & Taha, M. M. Hydrothermal tuning of the morphology and particle size of hydrozincite nanoparticles using different counterions to produce nanosized ZnO as an efficient adsorbent for textile dye removal. *RSC Adv.* **6**, 42180–42195 (2016).
191. Wang, M. *et al.* Synthesis of hierarchically structured ZnO nanomaterials via a supercritical assisted solvothermal process. *Chem. Commun.* **50**, 930–932 (2014).
192. Tan, W. K. *et al.* Formation of highly crystallized ZnO nanostructures by hot-water treatment of etched Zn foils. *Mater. Lett.* **91**, 111–114 (2013).
193. Balela, M. D. L., Pelicano, C. M. O. & Lockman, Z. In situ mixed potential study of the growth of zinc oxide hierarchical nanostructures by wet oxidation of zinc foil. *J. Mater. Sci.* **52**, 2319–2328 (2017).
194. Li, K., Luo, H. & Ying, T. One-step, solid-state reaction to ZnO nanoparticles in the presence of ionic liquid. *Mater. Sci. Semicond. Process.* **14**, 184–187 (2011).
195. Demoisson, F., Piolet, R. & Bernard, F. Hydrothermal synthesis of ZnO crystals from Zn(OH)₂ metastable phases at room to supercritical conditions. *Cryst. Growth Des.* **14**, 5388–5396 (2014).
196. Łuczak, J., Paszkiewicz, M., Krukowska, A., Malankowska, A. & Zaleska-Medynska, A. Ionic liquids for nano- and microstructures preparation. Part 1: Properties and multifunctional role. *Adv. Colloid Interface Sci.* **230**, 13–28 (2016).
197. Ozgur, Ü., Hofstetter, D. & Morkoç, H. ZnO devices and applications: A review of current status and future prospects. in *Proceedings of the IEEE* (2010). doi:10.1109/JPROC.2010.2044550
198. Nicholas, N. J., Franks, G. V. & Ducker, W. A. The mechanism for hydrothermal growth of zinc oxide. *CrystEngComm* **14**, 1232–1240 (2012).
199. Wang, M., Zhou, Y., Zhang, Y., Hahn, S. H. & Kim, E. J. From Zn(OH)₂ to ZnO: a study on the mechanism of phase transformation. *CrystEngComm* **13**, 6024 (2011).
200. Moezzi, A., Cortie, M. & McDonagh, A. Transformation of zinc hydroxide chloride monohydrate to crystalline zinc oxide. *Dalt. Trans.* **45**, 7385–7390 (2016).
201. Ghotbi, M. Y. Synthesis and characterization of nano-sized ε-Zn(OH)₂ and its decomposed product, nano-zinc oxide. *J. Alloys Compd.* **491**, 420–422 (2010).
202. Moezzi, A., Cortie, M. & McDonagh, A. Transformation of zinc hydroxide chloride monohydrate to crystalline zinc oxide. *Dalt. Trans.* **45**, 7385–7390 (2016).
203. Hayes, R., Warr, G. G. & Atkin, R. Structure and Nanostructure in Ionic Liquids. *Chem. Rev.* **115**, 6357–6426 (2015).
204. O'Mahony, A. M., Silvester, D. S., Aldous, L., Hardacre, C. & Compton, R. G. Effect of water on the electrochemical window and potential limits of room-temperature ionic liquids. *J. Chem. Eng. Data* **53**, 2884–2891 (2008).
205. Maiti, A., Kumar, A. & Rogers, R. D. Water-clustering in hygroscopic ionic liquids - An implicit solvent analysis. *Phys. Chem. Chem. Phys.* **14**, 5139–5146 (2012).
206. Tanaka, H., Fujioka, A., Futoyu, A., Kandori, K. & Ishikawa, T. Synthesis and characterization of layered zinc hydroxychlorides. *J. Solid State Chem.* **180**, 2061–2066 (2007).
207. Cousy, S., Gorodylova, N., Svoboda, L. & Zelenka, J. Influence of synthesis conditions over simonkolleite/ZnO precipitation. *Chem. Pap.* **71**, 2325–2334 (2017).
208. Kumar, S. S., Venkateswarlu, P., Rao, V. R. & Rao, G. N. Synthesis, characterization and optical properties of zinc oxide nanoparticles. *Int. Nano Lett.* **3**, 30 (2013).
209. Zhao, L.-H., Zhang, R., Zhang, J. & Sun, S.-Q. Synthesis and characterization of biocompatible ZnO nanoparticles. *CrystEngComm* **14**, 945–950 (2012).
210. Özgür, Ü. *et al.* A comprehensive review of ZnO materials and devices. *Journal of Applied Physics* **98**, 1–103 (2005).
211. Moezzi, A., McDonagh, A. M. & Cortie, M. B. Zinc oxide particles: Synthesis, properties and applications. *Chemical Engineering Journal* (2012). doi:10.1016/j.cej.2012.01.076
212. Kennedy, A. *et al.* A Definition and Categorization System for Advanced Materials: The Foundation for Risk-Informed Environmental Health and Safety Testing. *Risk Anal.* **39**, 1783–1795 (2019).
213. Advanced Materials. Available at: <https://onlinelibrary.wiley.com/page/journal/15214095/homepage/productinformation.html>.

214. IHS Markit. Available at: <https://ihsmarkit.com/index.html>.
215. Przybyszewska, M. & Zaborski, M. The effect of zinc oxide nanoparticle morphology on activity in crosslinking of carboxylated nitrile elastomer. *Express Polym. Lett.* **3**, 542–552 (2009).
216. Wiesmann, N., Tremel, W. & Brieger, J. Zinc oxide nanoparticles for therapeutic purposes in cancer medicine. *J. Mater. Chem. B* **8**, 4973–4989 (2020).
217. Pantic, S., Skodric, S. R., Loncar, Z. & Pantic, I. Zinc oxide nanoparticles: potential novel applications in cellular physiology, pathology, neurosciences and cancer research. *Rev. Adv. Mater. Sci.* **58**, 17–21 (2019).
218. Allafchian, A. & Hosseini, S. S. Antibacterial magnetic nanoparticles for therapeutics: a review. *IET Nanobiotechnology* **13**, 786–799 (2019).
219. Jiang, J., Pi, J. & Cai, J. The Advancing of Zinc Oxide Nanoparticles for Biomedical Applications. *Bioinorg. Chem. Appl.* **2018**, 1–18 (2018).
220. Ong, C. B., Ng, L. Y. & Mohammad, A. W. A review of ZnO nanoparticles as solar photocatalysts: Synthesis, mechanisms and applications. *Renew. Sustain. Energy Rev.* **81**, 536–551 (2018).
221. Tereshchenko, A. *et al.* Optical biosensors based on ZnO nanostructures: advantages and perspectives. A review. *Sensors Actuators B Chem.* **229**, 664–677 (2016).
222. Shanmugam, N. R., Muthukumar, S. & Prasad, S. A review on ZnO-based electrical biosensors for cardiac biomarker detection. *Future Science OA* (2017). doi:10.4155/fsoa-2017-0006
223. Zhu, L. & Zeng, W. Room-temperature gas sensing of ZnO-based gas sensor: A review. *Sensors Actuators A Phys.* **267**, 242–261 (2017).
224. Pearton, S. J. & Ren, F. Advances in ZnO-based materials for light emitting diodes. *Curr. Opin. Chem. Eng.* **3**, 51–55 (2014).
225. Rahman, F. Zinc oxide light-emitting diodes: a review. *Opt. Eng.* **58**, 1 (2019).
226. Zhang, J., Gu, P., Xu, J., Xue, H. & Pang, H. High performance of electrochemical lithium storage batteries: ZnO-based nanomaterials for lithium-ion and lithium–sulfur batteries. *Nanoscale* **8**, 18578–18595 (2016).
227. Summerfield, I. & Crowther, M. Report for : DECC Desk study on the development of a hydrogen-fired appliance supply chain. (2016).
228. BURNS ENERGY SYSTEMS LTD. Ultra High Efficiency ZnO Furnaces. Available at: <https://www.burnsenergy.ca/>.
229. Department for Business, E. & I. S. Greenhouse gas reporting: conversion factors 2019. Available at: <https://www.gov.uk/government/publications/greenhouse-gas-reporting-conversion-factors-2019>.
230. Li, C. *et al.* Comparison of dilute acid and ionic liquid pretreatment of switchgrass: Biomass recalcitrance, delignification and enzymatic saccharification. *Bioresour. Technol.* (2010). doi:10.1016/j.biortech.2009.10.066
231. Lee, S. H., Doherty, T. V., Linhardt, R. J. & Dordick, J. S. Ionic liquid-mediated selective extraction of lignin from wood leading to enhanced enzymatic cellulose hydrolysis. *Biotechnol. Bioeng.* **102**, 1368–76 (2009).
232. Wu, H. *et al.* Facile pretreatment of lignocellulosic biomass at high loadings in room temperature ionic liquids. *Biotechnol. Bioeng.* **108**, 2865–2875 (2011).
233. Sant’Ana da Silva, A., Lee, S. H., Endo, T. & P.S. Bon, E. Major improvement in the rate and yield of enzymatic saccharification of sugarcane bagasse via pretreatment with the ionic liquid 1-ethyl-3-methylimidazolium acetate ([Emim] [Ac]). *Bioresour. Technol.* (2011). doi:10.1016/j.biortech.2011.08.085
234. Nguyen, T. A. D. *et al.* Pretreatment of rice straw with ammonia and ionic liquid for lignocellulose conversion to fermentable sugars. *Bioresour. Technol.* (2010). doi:10.1016/j.biortech.2010.04.053
235. Ebner, G. *et al.* The effect of 1-ethyl-3-methylimidazolium acetate on the enzymatic degradation of cellulose. *J. Mol. Catal. B Enzym.* (2014). doi:10.1016/j.molcatb.2013.11.001
236. Rockwood, D. L., Rudie, A. W., Ralph, S. A., Zhu, J. Y. & Winandy, J. E. Energy product options for Eucalyptus species grown as short rotation woody crops. *Int. J. Mol. Sci.* (2008). doi:10.3390/ijms9081361
237. Chem Systems, I. *Economic Feasibility Study of an Enzymatic Hydrolysisbased Ethanol Plant with Prehydrolysis Pretreatment. Subcontract Report SERISTR-231-3135, Prepared under Subcontract XX-3-03097-1.* (1987).
238. Kretschmer, W. *et al.* *Integrated sustainability assessment of BIOLYFE second generation bioethanol (Deliverable 12.3: Final report).* (2013).
239. (IEA), I. E. A. *Key World Energy Statistics.* (2016).

240. International Energy Agency. World Energy Balances 2019. *World Energy Balanc. Overv.* (2019).
241. International Energy Agency (IEA). *Good Practice Guidelines: Bioenergy Project Development and Biomass Supply.* (2007).
242. Sun, Y. & Cheng, J. Hydrolysis of lignocellulosic materials for ethanol production : a review q. *Bioresour. Technol.* **83**, 1–11 (2002).
243. Dussan, K., Girisuta, B., Haverty, D., Leahy, J. J. & Hayes, M. H. B. Kinetics of levulinic acid and furfural production from *Miscanthus×giganteus*. *Bioresour. Technol.* **149**, 216–224 (2013).
244. Brandt, A. *et al.* Ionic liquid pretreatment of lignocellulosic biomass with ionic liquid–water mixtures. *Green Chem.* **13**, 2489 (2011).
245. Dee, S. & Bell, A. T. Effects of reaction conditions on the acid-catalyzed hydrolysis of miscanthus dissolved in an ionic liquid. *Green Chem.* **13**, 1467–1475 (2011).
246. Padmanabhan, S., Kim, M., Blanch, H. W. & Prausnitz, J. M. Solubility and rate of dissolution for *Miscanthus* in hydrophilic ionic liquids. *Fluid Phase Equilib.* **309**, 89–96 (2011).
247. Penín, Lange, Santos, Crestini & Parajó. Characterization of Eucalyptus nitens Lignins Obtained by Biorefinery Methods Based on Ionic Liquids. *Molecules* **25**, 425 (2020).
248. Gütsch, J. S., Nousiainen, T. & Sixta, H. Comparative evaluation of autohydrolysis and acid-catalyzed hydrolysis of Eucalyptus globulus wood. *Bioresour. Technol.* **109**, 77–85 (2012).
249. Wei, W., Zhang, H. & Jin, Y. Comparison of microwave-assisted zinc chloride hydrate and alkali pretreatments for enhancing eucalyptus enzymatic saccharification. *Energy Convers. Manag.* (2019). doi:10.1016/j.enconman.2019.02.054
250. Wei, W., Wu, S. & Liu, L. Enzymatic saccharification of dilute acid pretreated eucalyptus chips for fermentable sugar production. *Bioresour. Technol.* (2012). doi:10.1016/j.biortech.2012.01.003
251. Yu, Q. *et al.* Two-step liquid hot water pretreatment of Eucalyptus grandis to enhance sugar recovery and enzymatic digestibility of cellulose. *Bioresour. Technol.* **101**, 4895–4899 (2010).
252. Carroll, A. & Somerville, C. Cellulosic biofuels. *Annu Rev Plant Biol* **60**, 165–182 (2009).
253. Perlack, R. D., Stokes, B. J., Eaton, L. M. & Turnhollow, A. F. US Billion-ton update. Biomass Supply for a Bioenergy and Bioproducts Industry. *Renew. Energy* 1–229 (2005). doi:10.1089/ind.2011.7.375
254. Lee R. Lynd, Paul J. Weimer, Willem H. van Zyl, I. S. P. Microbial Cellulose Utilization: Fundamentals and Biotechnology. *Microbiol. Mol. Biol. Rev.* **66**, 506–577 (2002).
255. OSullivan, A. C. Cellulose: the structure slowly unravels. *Cellulose* **4**, 173–207 (1997).
256. Jørgensen, H., Kristensen, J. B. & Felby, C. Enzymatic conversion of lignocellulose into fermentable sugars: Challenges and opportunities. *Biofuels, Bioproducts and Biorefining* **1**, 119–134 (2007).
257. Pinkert, A., Marsh, K. N., Pang, S. & Staiger, M. P. Ionic liquids and their interaction with cellulose. *Chem. Rev.* **109**, 6712–6728 (2009).
258. Feng, L. & Chen, Z. lan. Research progress on dissolution and functional modification of cellulose in ionic liquids. *Journal of Molecular Liquids* **142**, 1–5 (2008).
259. Ciolacu, D., Ciolacu, F. & Popa, V. I. Amorphous Cellulose – Structure and Characterization. *Cellul. Chem. Technol.* **45**, 13–21 (2011).
260. Goodridge, H. S., Wolf, A. J. & Underhill, D. M. β -glucan recognition by the innate immune system. *Immunol. Rev.* **230**, 38–50 (2009).
261. Zhou, C. & Wu, Q. Recent Development in Applications of Cellulose Nanocrystals for Advanced Polymer-Based Nanocomposites by Novel Fabrication Strategies. in Ch. 0 (InTech, 2012). doi:10.5772/48727
262. Timell, T. E. Recent progress in the chemistry of wood hemicelluloses. *Wood Sci. Technol.* **1**, 45–70 (1967).
263. Kilpeläinen, P. Pressurized hot water flow-through extraction of birch wood. (Åbo Akademi University, 2015).
264. Sjöström, E. *Wood chemistry, fundamentals and applications. Carbohydrate Research* **252**, (1993).
265. Ragauskas, A. J. *et al.* Lignin valorization: improving lignin processing in the biorefinery. *Science* **344**, 1246843 (2014).
266. Kärkäs, M. D., Matsuura, B. S., Monos, T. M., Magallanes, G. & Stephenson, C. R. J. Transition-metal catalyzed valorization of lignin: the key to a sustainable carbon-neutral future. *Org. Biomol. Chem.* **14**, 1853–1914 (2016).
267. Ralph, J. *et al.* Lignins: Natural polymers from oxidative coupling of 4-hydroxyphenyl- propanoids. *Phytochemistry Reviews* **3**, 29–60 (2004).
268. Hage, R. El *et al.* Characterization of milled wood lignin and ethanol organosolv lignin from miscanthus. *Polym. Degrad. Stab.* **94**, 1632–1638 (2009).

269. Kumar, P., Barrett, D. M., Delwiche, M. J. & Stroeve, P. Methods for pretreatment of lignocellulosic biomass for efficient hydrolysis and biofuel production. *Ind. Eng. Chem. Res.* **48**, 3713–3729 (2009).
270. Berlin, A. *et al.* Inhibition of cellulase, xylanase and beta-glucosidase activities by softwood lignin preparations. *J. Biotechnol.* **125**, 198–209 (2006).
271. Sánchez Acosta, M. Mastrandrea, C. Tarcisio Lima, J. Wood Technologies And Uses Of Eucalyptus Wood From Fast Grown Plantations For Solid Products. in *51st International Convention of Society of Wood Science and Technology* 12 (2008).
272. Tinto, J. C. Comparacion de crecimientos en Eucalyptus grandis com bajo y alto crecimiento. in *Jornadas Forestales de Entre Ríos* (1995).
273. Kim, T. H., Taylor, F. & Hicks, K. B. Bioethanol production from barley hull using SAA (soaking in aqueous ammonia) pretreatment. *Bioresour. Technol.* **99**, 5694–5702 (2008).
274. Kaparaju, P., Serrano, M., Thomsen, A. B., Kongjan, P. & Angelidaki, I. Bioethanol, biohydrogen and biogas production from wheat straw in a biorefinery concept. *Bioresour. Technol.* **100**, 2562–8 (2009).
275. Zhuang, X. *et al.* Liquid hot water pretreatment of lignocellulosic biomass for bioethanol production accompanying with high valuable products. *Bioresour. Technol.* **199**, 68–75 (2016).
276. Searchinger, T. *et al.* Use of U.S. Croplands for Biofuels Increases Greenhouse Gases Through Emissions from Land-Use Change. *Science (80-.)*. **319**, 1238–1240 (2008).
277. Yan, L., Greenwood, A. a., Hossain, A. & Yang, B. A comprehensive mechanistic kinetic model for dilute acid hydrolysis of switchgrass cellulose to glucose, 5-HMF and levulinic acid. *RSC Adv.* **4**, 23492 (2014).
278. Clark, J. H., Luque, R. & Matharu, A. S. Green Chemistry, Biofuels, and Biorefinery. *Annu. Rev. Chem. Biomol. Eng.* **3**, 183–207 (2012).
279. Hennecke, A. M. *et al.* Biofuel greenhouse gas calculations under the European Renewable Energy Directive - A comparison of the BioGrace tool vs. the tool of the Roundtable on Sustainable Biofuels. *Appl. Energy* **102**, 55–62 (2013).
280. Brandt, A., Gräsvik, J., Hallett, J. P. & Welton., T. Deconstruction of lignocellulosic biomass with ionic liquids. *Green Chem.* **15**, 550 (2013).
281. Shi, J. *et al.* One-pot ionic liquid pretreatment and saccharification of switchgrass. *Green Chem.* **15**, 2579 (2013).
282. Sathitsuksanoh, N., George, A. & Zhang, Y.-H. P. New lignocellulose pretreatments using cellulose solvents: a review. *J. Chem. Technol. Biotechnol.* **88**, 169–180 (2013).
283. Macrelli, S., Mogensen, J. & Zacchi, G. Techno-economic evaluation of 2 nd generation bioethanol production from sugar cane bagasse and leaves integrated with the sugar-based ethanol process. 1–18 (2012).
284. Baral, N. R. & Shah, A. Techno-economic analysis of cellulose dissolving ionic liquid pretreatment of lignocellulosic biomass for fermentable sugars production. *Biofuels, Bioprod. Biorefining* **10**, 70–88 (2016).
285. Xu, F. *et al.* Transforming biomass conversion with ionic liquids: process intensification and the development of a high-gravity, one-pot process for the production of cellulosic ethanol. *Energy Environ. Sci.* (2015). doi:10.1039/C5EE02940F
286. Tao, L. *et al.* Process and technoeconomic analysis of leading pretreatment technologies for lignocellulosic ethanol production using switchgrass. *Bioresour. Technol.* **102**, 11105–11114 (2011).
287. Klein-Marcuschamer, D., Simmons, B. A. & Blanch, H. W. Techno-economic analysis of a lignocellulosic ethanol biorefinery with ionic liquid pre-treatment. *Biofuels, Bioprod. Biorefining* (2011). doi:10.1002/bbb.303
288. Cotana, F. *et al.* Production of bioethanol in a second generation prototype from pine wood chips. *Energy Procedia* **45**, 42–51 (2014).
289. Alizadeh, H., Teymouri, F., Gilbert, T. I. & Dale, B. E. Pretreatment of switchgrass by ammonia fiber explosion (AFEX). *Appl. Biochem. Biotechnol.* **121–124**, 1133–1141 (2005).
290. Wijaya, Y. P. *et al.* Comparative study on two-step concentrated acid hydrolysis for the extraction of sugars from lignocellulosic biomass. *Bioresour. Technol.* **164**, 221–231 (2014).
291. Hu, F. & Ragauskas, A. Suppression of pseudo-lignin formation under dilute acid pretreatment conditions. *RSC Adv.* **4**, 4317 (2014).
292. Pielhop, T., Larrazábal, G. O. & Rudolf von Rohr, P. Autohydrolysis pretreatment of softwood – enhancement by phenolic additives and the effects of other compounds. *Green Chem.* **18**, 5239–5247 (2016).
293. Xu, Y., Li, K. & Zhang, M. Lignin precipitation on the pulp fibers in the ethanol-based organosolv pulping. *Colloids Surfaces A Physicochem. Eng. Asp.* **301**, 255–263 (2007).

294. Li, M., Tu, M., Cao, D., Bass, P. & Adhikari, S. Distinct roles of residual xylan and lignin in limiting enzymatic hydrolysis of organosolv pretreated loblolly pine and sweetgum. *J. Agric. Food Chem.* **61**, 646–54 (2013).
295. Sierra, R., Granda, C. B. & Holtzapple, M. T. Lime Pretreatment. in 115–124 (2009). doi:10.1007/978-1-60761-214-8_9
296. Socha, A. M., Parthasarathi, R., Shi, J., Pattathil, S. & Whyte, D. Efficient biomass pretreatment using ionic liquids derived from lignin and hemicellulose. 1–9 (2014). doi:10.1073/pnas.1405685111
297. Galbe, M. & Wallberg, O. Pretreatment for biorefineries: a review of common methods for efficient utilisation of lignocellulosic materials. *Biotechnol. Biofuels* **12**, 294 (2019).
298. Cox, B. J. & Ekerdt, J. G. Pretreatment of yellow pine in an acidic ionic liquid: extraction of hemicellulose and lignin to facilitate enzymatic digestion. *Bioresour. Technol.* **134**, 59–65 (2013).
299. Gschwend, F. J. V., Malaret, F., Shinde, S., Brandt-Talbot, A. & Hallett, J. P. Rapid pretreatment of: *Miscanthus* using the low-cost ionic liquid triethylammonium hydrogen sulfate at elevated temperatures. *Green Chem.* **20**, 3486–3498 (2018).
300. Carvalheiro, F., Duarte, L. C. & Gírio, F. M. Hemicellulose biorefineries: A review on biomass pretreatments. *Journal of Scientific and Industrial Research* (2008).
301. Gu, T., Held, M. A. & Faik, A. Supercritical CO₂ and ionic liquids for the pretreatment of lignocellulosic biomass in bioethanol production. *Environ. Technol. (United Kingdom)* (2013). doi:10.1080/09593330.2013.809777
302. Harmsen, P., Huijgen, W., López, L. & Bakker, R. Literature Review of Physical and Chemical Pretreatment Processes for Lignocellulosic Biomass. *Food Biobased Res.* 1–49 (2010).
303. Mosier, N. *et al.* Features of promising technologies for pretreatment of lignocellulosic biomass. *Bioresource Technology* **96**, 673–686 (2005).
304. Zhu, J. Y., Pan, X. & Zalesny, R. S. Pretreatment of woody biomass for biofuel production: Energy efficiency, technologies, and recalcitrance. *Applied Microbiology and Biotechnology* **87**, 847–857 (2010).
305. Balan, V., Bals, B., Chundawat, S. P. S., Marshall, D. & Dale, B. E. Lignocellulosic Biomass Pretreatment Using AFEX. in 61–77 (2009). doi:10.1007/978-1-60761-214-8_5
306. Zhang, K., Pei, Z. & Wang, D. Organic solvent pretreatment of lignocellulosic biomass for biofuels and biochemicals: A review. *Bioresour. Technol.* **199**, 21–33 (2016).
307. Kautto, J., Realff, M. J., Ragauskas, A. J. & Kässi, T. Economic analysis of an organosolv process for bioethanol production. *BioResources* (2014). doi:10.15376/biores.9.4.6041-6072
308. Daza Serna, L. V., Orrego Alzate, C. E. & Cardona Alzate, C. A. Supercritical fluids as a green technology for the pretreatment of lignocellulosic biomass. *Bioresour. Technol.* (2016). doi:10.1016/j.biortech.2015.09.078
309. Nakamura, A., Miyafuji, H. & Saka, S. Influence of reaction atmosphere on the liquefaction and depolymerization of wood in an ionic liquid, 1-ethyl-3-methylimidazolium chloride. *J. Wood Sci.* (2010). doi:10.1007/s10086-009-1081-x
310. Kim, S. & Holtzapple, M. T. Delignification kinetics of corn stover in lime pretreatment. *Bioresour. Technol.* **97**, 778–785 (2006).
311. Kumar, P., Barrett, D. M., Delwiche, M. J. & Stroeve, P. Pulsed electric field pretreatment of switchgrass and wood chip species for biofuel production. *Ind. Eng. Chem. Res.* **50**, 10996–11001 (2011).
312. Chosdu, R., Hilmy, N., Erizal, Erlinda, T. B. & Abbas, B. Radiation and chemical pretreatment of cellulosic waste. *Radiat. Phys. Chem.* **42**, 695–698 (1993).
313. Hu, Z., Wang, Y. & Wen, Z. Alkali (NaOH) pretreatment of switchgrass by radio frequency-based dielectric heating. *Appl. Biochem. Biotechnol.* **148**, 71–81 (2008).
314. Wang, H., Maxim, M. L., Gurau, G. & Rogers, R. D. Microwave-assisted dissolution and delignification of wood in 1-ethyl-3-methylimidazolium acetate. *Bioresour. Technol.* **136**, 739–42 (2013).
315. Keshwani, D. R. & Cheng, J. J. Microwave-based alkali pretreatment of switchgrass and coastal bermudagrass for bioethanol production. *Biotechnol. Prog.* **26**, 644–652 (2010).
316. Wang, H., Gurau, G. & Rogers, R. D. Ionic liquid processing of cellulose. *Chem. Soc. Rev.* **41**, 1519–1537 (2012).
317. Kumar, P., Barrett, D. M., Delwiche, M. J. & Stroeve, P. Methods for pretreatment of lignocellulosic biomass for efficient hydrolysis and biofuel production. *Industrial and Engineering Chemistry Research* **48**, 3713–3729 (2009).
318. Chen, H. *et al.* A review on the pretreatment of lignocellulose for high-value chemicals. *Fuel Process. Technol.* **160**, 196–206 (2017).

319. Hyvörynen, S. *et al.* Sugars and sugar derivatives in ionic liquid media obtained from lignocellulosic biomass: Comparison of capillary electrophoresis and chromatographic analysis. *Catal. Today* **223**, 18–24 (2014).
320. da Costa Lopes, A. M., João, K. G., Morais, A. R. C., Bogel-Lukasik, E. & Bogel-Lukasik, R. Ionic liquids as a tool for lignocellulosic biomass fractionation. *Sustain. Chem. Process.* **1**, 3 (2013).
321. Prado, R., Erdocia, X. & Labidi, J. Study of the influence of reutilization ionic liquid on lignin extraction. *J. Clean. Prod.* **111**, 125–132 (2016).
322. Cheng, G. *et al.* Impact of ionic liquid pretreatment conditions on cellulose crystalline structure using 1-ethyl-3-methylimidazolium acetate. *J. Phys. Chem. B* **116**, 10049–10054 (2012).
323. An, Y. X., Zong, M. H., Wu, H. & Li, N. Pretreatment of lignocellulosic biomass with renewable cholinium ionic liquids: Biomass fractionation, enzymatic digestion and ionic liquid reuse. *Bioresour. Technol.* **192**, 165–171 (2015).
324. Kilpeläinen, I. *et al.* Dissolution of wood in ionic liquids. *J. Agric. Food Chem.* **55**, 9142–9148 (2007).
325. Magalhães da Silva, S. P., da Costa Lopes, A. M., Roseiro, L. B. & Bogel-Lukasik, R. Novel pre-treatment and fractionation method for lignocellulosic biomass using ionic liquids. *RSC Adv.* **3**, 16040 (2013).
326. Rieland, J. M. & Love, B. J. Ionic liquids: A milestone on the pathway to greener recycling of cellulose from biomass. *Resour. Conserv. Recycl.* **155**, 104678 (2020).
327. Reddy, P. A critical review of ionic liquids for the pretreatment of lignocellulosic biomass. *S. Afr. J. Sci.* **Volume 111**, (2015).
328. Usmani, Z. *et al.* Ionic liquid based pretreatment of lignocellulosic biomass for enhanced bioconversion. *Bioresour. Technol.* **304**, 123003 (2020).
329. Sun, N. *et al.* Complete dissolution and partial delignification of wood in the ionic liquid 1-ethyl-3-methylimidazolium acetate. *Green Chem.* **11**, 646 (2009).
330. Eta, V. *et al.* Loop vs. batch reactor setups in the fractionation of birch chips using switchable ionic liquids. *Chem. Eng. J.* **238**, 242–248 (2014).
331. Jessop, P. G., Heldebrant, D. J., Li, X., Eckert, C. A. & Liotta, C. L. Reversible nonpolar-to-polar solvent. *Nature* **436**, 1102–1102 (2005).
332. Swatloski, R. P., Spear, S. K., Holbrey, J. D. & Rogers, R. D. Dissolution of Cellulose with Ionic Liquids. *J. Am. Chem. Soc.* **124**, 4974–4975 (2002).
333. Alayoubi, R. *et al.* Low temperature ionic liquid pretreatment of lignocellulosic biomass to enhance bioethanol yield. *Renew. Energy* **145**, 1808–1816 (2020).
334. Shi, J. *et al.* Understanding the role of water during ionic liquid pretreatment of lignocellulose: Co-solvent or anti-solvent? *Green Chem.* (2014). doi:10.1039/c4gc00373j
335. Anugwom, I. *et al.* Treating birch wood with a switchable 1,8-diazabicyclo-[5.4.0]-undec-7-ene-glycerol carbonate ionic liquid. *Holzforschung* **66**, 809–815 (2012).
336. Imbimbo, P., D’Elia, L., Liberti, D., Olivieri, G. & Monti, D. M. Towards green extraction methods from microalgae learning from the classics. *Appl. Microbiol. Biotechnol.* **104**, 9067–9077 (2020).
337. Harris, J., Viner, K., Champagne, P. & Jessop, P. G. Advances in microalgal lipid extraction for biofuel production: a review. *Biofuels, Bioprod. Biorefining* **12**, 1118–1135 (2018).
338. Sun, J. *et al.* One-pot integrated biofuel production using low-cost biocompatible protic ionic liquids. *Green Chem.* **19**, 3152–3163 (2017).
339. Brandt-Talbot, A. *et al.* An economically viable ionic liquid for the fractionation of lignocellulosic biomass. *Green Chem.* **19**, 3078–3102 (2017).
340. Ferrari, F. A., Pereira, J. F. B., Witkamp, G.-J. & Forte, M. B. S. Which Variables Matter for Process Design and Scale-Up? A Study of Sugar Cane Straw Pretreatment Using Low-Cost and Easily Synthesizable Ionic Liquids. *ACS Sustain. Chem. Eng.* **7**, 12779–12788 (2019).
341. Verdía, P., Brandt, A., Hallett, J. P., Ray, M. J. & Welton, T. Fractionation of lignocellulosic biomass with the ionic liquid 1-butylimidazolium hydrogen sulfate. *Green Chem.* **16**, 1617 (2014).
342. Brandt, A. *et al.* Ionic liquid pretreatment of lignocellulosic biomass with ionic liquid-water mixtures. *Green Chem.* **13**, 2489–2499 (2011).
343. Brandt, A. *et al.* Soaking of pine wood chips with ionic liquids for reduced energy input during grinding. *Green Chem.* **14**, 1079 (2012).
344. Brandt, A., Hallett, J. P., Leak, D. J., Murphy, R. J. & Welton, T. The effect of the ionic liquid anion in the pretreatment of pine wood chips. *Green Chem.* **12**, 672 (2010).
345. Schrems, M. *et al.* Ionic liquids as media for biomass processing: Opportunities and restrictions. in *Holzforschung* **65**, 527–533 (2011).
346. Chen, M. *et al.* Design of a combined ionosolv-organosolv biomass fractionation process for biofuel

- production and high value-added lignin valorisation. *Green Chem.* (2020). doi:10.1039/D0GC01143F
347. Chambon, C. L. *et al.* Pretreatment of South African sugarcane bagasse using a low-cost protic ionic liquid: a comparison of whole, depithed, fibrous and pith bagasse fractions. *Biotechnol. Biofuels* (2018). doi:10.1186/s13068-018-1247-0
348. George, A. *et al.* Design of low-cost ionic liquids for lignocellulosic biomass pretreatment. *Green Chem.* **17**, 1728–1734 (2015).
349. Zhou, J. *et al.* Recovery and purification of ionic liquids from solutions: a review. *RSC Adv.* **8**, 32832–32864 (2018).
350. Hou, X.-D., Li, N. & Zong, M.-H. Facile and Simple Pretreatment of Sugar Cane Bagasse without Size Reduction Using Renewable Ionic Liquids–Water Mixtures. *ACS Sustain. Chem. Eng.* **1**, 519–526 (2013).
351. Cruz, A. G. *et al.* Impact of high biomass loading on ionic liquid pretreatment. *Biotechnol. Biofuels* **6**, 52 (2013).
352. Chambon, C. P. L. C. Towards an economically viable ionic liquids based biorefinery: lignocellulose fractionation and value-added products from lignin. (Imperial College London, 2017). doi:https://doi.org/10.25560/68042
353. Klein-Marcuschamer, D. B. A. S. & Blanch, H. W. Techno-economic analysis of a lignocellulosic ethanol biorefinery with ionic liquid pre-treatment. *Biofuels, Bioprod. Biorefining* **5**, 562–569 (2011).
354. Morales, M. Process Design and Sustainability Assessment for Biorefinery Technologies. (ETH Zurich, 2016). doi:https://doi.org/10.3929/ethz-a-010797794
355. Gschwend, F. J. V. Towards an economical ionic liquid based biorefinery. (Imperial College London, 2017). doi:https://doi.org/10.25560/72875
356. Seddon, K. R., Stark, A. & Torres, M. J. Influence of chloride, water, and organic solvents on the physical properties of ionic liquids. in *Pure and Applied Chemistry* (2000). doi:10.1351/pac200072122275
357. Scurto, A. M. *et al.* Melting point depression of ionic liquids with CO₂: Phase equilibria. *Ind. Eng. Chem. Res.* (2008). doi:10.1021/ie070312b
358. Lopes, J. M. *et al.* Melting point depression effect with CO₂ in high melting temperature cellulose dissolving ionic liquids. Modeling with group contribution equation of state. *J. Supercrit. Fluids* (2016). doi:10.1016/j.supflu.2015.07.021
359. Machida, H., Takesue, M. & Smith, R. L. Green chemical processes with supercritical fluids: Properties, materials, separations and energy. in *Journal of Supercritical Fluids* (2011). doi:10.1016/j.supflu.2011.04.016
360. Sluiter, A. *et al.* Determination of total solids in biomass and total dissolved solids in liquid process samples. *Natl. Renew. Energy Lab.* **9** (2008). doi:NREL/TP-510-42621
361. Gschwend, F. J. V. *et al.* Pretreatment of Lignocellulosic Biomass with Low-cost Ionic Liquids. *J. Vis. Exp.* (2016). doi:10.3791/54246
362. Sluiter, A. *et al.* Determination of Extractives in Biomass. *Biomass Anal. Technol. Team Lab. Anal. Proced.* 1–8 (2004). doi:2008
363. Sluiter, A. *et al.* NREL/TP-510-42618 analytical procedure - Determination of structural carbohydrates and lignin in Biomass. *NREL/TP-510-42618* **17** (2012). doi:NREL/TP-510-42618
364. Resch, M. G., Baker, J. O. & Decker, S. R. *Low Solids Enzymatic Saccharification of Lignocellulosic Biomass Laboratory Analytical Procedure (LAP)*. (2015).
365. Blokhin, A. V. *et al.* Thermodynamic Properties of Plant Biomass Components. Heat Capacity, Combustion Energy, and Gasification Equilibria of Cellulose. *J. Chem. Eng. Data* **56**, 3523–3531 (2011).
366. Emmel, A., Mathias, A. L., Wypych, F. & Ramos, L. P. Fractionation of Eucalyptus grandis chips by dilute acid-catalysed steam explosion. *Bioresour. Technol.* **86**, 105–115 (2003).
367. Chemical Engineering Magazine. Chemical Engineering Magazine Plant Cost Index. Available at: <http://www.che.com/pci/>.
368. James R. Couper W. Roy Penney James R. Fair W. Roy Penney Stanley M. Walas James R. Fair Stanley M. Walas. *Chemical Process Equipment*. (Elsevier, 2005). doi:10.1016/B978-0-7506-7510-9.X5000-1
369. Wyman, C. E. & Yang, B. Combined severity factor for predicting sugar recovery in acid-catalyzed pretreatment followed by enzymatic hydrolysis. in *Hydrothermal Processing in Biorefineries: Production of Bioethanol and High Added-Value Compounds of Second and Third Generation Biomass* (2017). doi:10.1007/978-3-319-56457-9_6
370. Romani, A., Ruiz, H. A., Teixeira, J. A. & Domingues, L. Valorization of Eucalyptus wood by glycerol-organosolv pretreatment within the biorefinery concept: An integrated and intensified approach. *Renew. Energy* **95**, 1–9 (2016).
371. Lienqueo, M. E. *et al.* Second generation bioethanol from *Eucalyptus globulus* Labill and *Nothofagus*

- pumilio*: Ionic liquid pretreatment boosts the yields. *Ind. Crops Prod.* **80**, 148–155 (2016).
372. Xu, J., Liu, B., Hou, H. & Hu, J. Pretreatment of eucalyptus with recycled ionic liquids for low-cost biorefinery. *Bioresour. Technol.* (2017). doi:10.1016/j.biortech.2017.03.081
373. Papa, G. *et al.* Exploring the effect of different plant lignin content and composition on ionic liquid pretreatment efficiency and enzymatic saccharification of *Eucalyptus globulus* L. mutants. *Bioresour. Technol.* **117**, 352–359 (2012).
374. NIST. NIST Standard Reference Database Number 69. *NIST Chemistry WebBook* (2016). doi:10.18434/T4D303
375. Humbird, D. *et al.* Process Design and Economics for Biochemical Conversion of Lignocellulosic Biomass to Ethanol. *Renew. Energy* **303**, 147 (2011).
376. Markets Insider. Ethanol Price. Available at: <https://markets.businessinsider.com/commodities/ethanol-price>. (Accessed: 4th July 2020)
377. Labbé, N. *et al.* Activation of lignocellulosic biomass by ionic liquid for biorefinery fractionation. *Bioresour. Technol.* **104**, 701–707 (2012).
378. Cvjetko Bubalo, M., Radošević, K., Radojčić Redovniković, I., Halambek, J. & Gaurina Srček, V. A brief overview of the potential environmental hazards of ionic liquids. *Ecotoxicol. Environ. Saf.* **99**, 1–12 (2014).
379. Thuy Pham, T. P., Cho, C. W. & Yun, Y. S. Environmental fate and toxicity of ionic liquids: A review. *Water Res.* **44**, 352–372 (2010).
380. Govinda, V. *et al.* Effect of anion variation on the thermophysical properties of triethylammonium based protic ionic liquids with polar solvent. *Thermochim. Acta* **556**, 75–88 (2013).
381. Kavitha, T., Attri, P., Venkatesu, P., Rama Devi, R. S. & Hofman, T. Temperature dependence measurements and molecular interactions for ammonium ionic liquid with N-methyl-2-pyrrolidone. *J. Chem. Thermodyn.* **54**, 223–237 (2012).
382. Govinda, V., Attri, P., Venkatesu, P. & Venkateswarlu, P. Thermophysical properties of dimethylsulfoxide with ionic liquids at various temperatures. *Fluid Phase Equilib.* **304**, 35–43 (2011).
383. Govinda, V., Reddy, P. M., Attri, P., Venkatesu, P. & Venkateswarlu, P. Influence of anion on thermophysical properties of ionic liquids with polar solvent. *J. Chem. Thermodyn.* **58**, 269–278 (2013).
384. Bowers, J., Butts, C. P., Martin, P. J., Vergara-Gutierrez, M. C. & Heenan, R. K. Aggregation Behavior of Aqueous Solutions of Ionic Liquids. *Langmuir* **20**, 2191–2198 (2004).
385. Hanibah, H., Hashim, N. Z. N. & Shamsudin, I. J. Molar conductivity behavior of ionic liquid compare to inorganic salt in electrolyte solution at ambient temperature. *AIP Conf. Proc.* **1877**, (2017).
386. Liu, W., Cheng, L., Zhang, Y., Wang, H. & Yu, M. The physical properties of aqueous solution of room-temperature ionic liquids based on imidazolium: Database and evaluation. *J. Mol. Liq.* **140**, 68–72 (2008).
387. Shekaari, H. & Mousavi, S. S. Conductometric studies of aqueous ionic liquids, 1-alkyl-3-methylimidazolium halide, solutions at T = 298.15–328.15 K. *Fluid Phase Equilib.* **286**, 120–126 (2009).
388. Yang, Q. *et al.* The effect of molecular solvents on the viscosity, conductivity and ionicity of mixtures containing chloride anion-based ionic liquid. *J. Ind. Eng. Chem.* **19**, 1708–1714 (2013).
389. Chen, Y. J., Xuan, X. P., Zhang, H. H. & Zhuo, K. L. Conductivities of 1-alkyl-3-methylimidazolium chloride ionic liquids in monosaccharide+water solutions at 298.15K. *Fluid Phase Equilib.* **316**, 164–171 (2012).
390. Yang, Q. *et al.* The effect of molecular solvents on the viscosity, conductivity and ionicity of mixtures containing chloride anion-based ionic liquid. *J. Ind. Eng. Chem.* **19**, 1708–1714 (2013).
391. Chen, Y. J., Xuan, X. P., Zhang, H. H. & Zhuo, K. L. Conductivities of 1-alkyl-3-methylimidazolium chloride ionic liquids in monosaccharide+water solutions at 298.15K. *Fluid Phase Equilib.* **316**, 164–171 (2012).
392. Institution, B. S. BS EN ISO 8044 : 2015 BSI Standards Publication Corrosion of metals and alloys — Basic terms and definitions. (2015).
393. Ghali, E. Aluminum and Aluminum Alloys. in *Uhlig's Corrosion Handbook* 715–745 (John Wiley & Sons, Inc., 2011). doi:10.1002/9780470872864.ch54
394. Wang, H. Z., Leung, D. Y. C., Leung, M. K. H. & Ni, M. A review on hydrogen production using aluminum and aluminum alloys. *Renewable and Sustainable Energy Reviews* (2009). doi:10.1016/j.rser.2008.02.009
395. Owoeye, F. T., Adetunji, O. R., Omotosho, A., Azodo, A. P. & Aiyedun, P. O. Investigation of corrosion performance of aluminum and zinc alloys in three acidic media. *Eng. Reports* **2**, (2020).
396. Nie, H., Schoenitz, M. & Dreizin, E. L. Calorimetric investigation of the aluminum-water reaction. *Int. J. Hydrogen Energy* (2012). doi:10.1016/j.ijhydene.2012.05.012
397. Irankhah, A., Seyed Fattahi, S. M. & Salem, M. Hydrogen generation using activated aluminum/water

- reaction. *Int. J. Hydrogen Energy* **43**, 15739–15748 (2018).
398. Al'myasheva, O. V., Korytkova, E. N., Maslov, A. V. & Gusarov, V. V. Preparation of nanocrystalline alumina under hydrothermal conditions. *Inorg. Mater.* (2005). doi:10.1007/s10789-005-0152-7
399. Digne, M., Sautet, P., Raybaud, P., Toulhoat, H. & Artacho, E. Structure and stability of aluminum hydroxides: A theoretical study. *J. Phys. Chem. B* (2002). doi:10.1021/jp014182a
400. Vargel, C. Freshwater. in *Corrosion of Aluminium* 299–327 (Elsevier, 2004). doi:10.1016/B978-008044495-6/50023-9
401. Shen, C., Li, X., Lu, Y. & Li, C. Effect of ionic liquid 1-methylimidazolium chloride on the vapour liquid equilibrium of water, methanol, ethanol, and {water+ethanol} mixture. *J. Chem. Thermodyn.* **43**, 1748–1753 (2011).
402. Kreysa Gerhard, S. M. *Corrosion Handbook: Corrosive Agents and Their Interaction with Materials Hydrochloric Acid, Nitric Acid*. (Wiley VCH, 2005).
403. Zhang, Q. B. & Hua, Y. X. Corrosion inhibition of aluminum in hydrochloric acid solution by alkylimidazolium ionic liquids. *Mater. Chem. Phys.* (2010). doi:10.1016/j.matchemphys.2009.07.035
404. Li, X., Deng, S. & Fu, H. Inhibition by tetradecylpyridinium bromide of the corrosion of aluminium in hydrochloric acid solution. *Corros. Sci.* (2011). doi:10.1016/j.corsci.2011.01.032
405. Vostrikov, A. A., Fedyaeva, O. N., Fadeeva, I. I. & Sokol, M. Y. The formation of Al₂O₃ nanoparticles in the oxidation of aluminum by water under sub- and supercritical conditions. *Russ. J. Phys. Chem. B* (2010). doi:10.1134/S199079311007002X
406. Bermúdez, M. D., Jiménez, A. E. & Martínez-Nicolás, G. Study of surface interactions of ionic liquids with aluminium alloys in corrosion and erosion-corrosion processes. *Appl. Surf. Sci.* (2007). doi:10.1016/j.apsusc.2007.03.008
407. Toumiat, K., Guibadj, A. & Taouti, M. Copper Corrosion Inhibition using BTAH Inhibitor in Sodium Chloride Medium: Experimental and Theoretical Studies. *Eurasian J. Anal. Chem.* **12**, 275–294 (2016).
408. Arjmand, F. & Adriaens, A. Influence of pH and Chloride Concentration on the Corrosion Behavior of Unalloyed Copper in NaCl Solution: A Comparative Study Between the Micro and Macro Scales. *Materials (Basel)*. **5**, 2439–2464 (2012).
409. TrabANELLI, G., Zucchi, F., Brunoro, G. & Carassiti, V. Inhibition of copper corrosion in chloride solutions by heterocyclic compounds. *Mater. Corros. und Korrosion* **24**, 602–606 (1973).
410. Fan, W. *et al.* Differential Oxidative Stress of Octahedral and Cubic Cu₂O Micro/Nanocrystals to *Daphnia magna*. *Environ. Sci. Technol.* **46**, 10255–10262 (2012).
411. Haq, I. U., Akhtar, K. & Malook, K. Synthesis and characterization of monodispersed copper oxide and their precursor powder. *Mater. Res. Bull.* **57**, 121–126 (2014).
412. Fateh, A., Aliofkhaezraei, M. & Rezvanian, A. R. Review of corrosive environments for copper and its corrosion inhibitors. *Arab. J. Chem.* **13**, 481–544 (2020).
413. Sherif, E. S. M. Corrosion behavior of copper in 0.50 M hydrochloric acid pickling solutions and its inhibition by 3-amino-1,2,4-triazole and 3-amino-5-mercapto-1,2,4-triazole. *Int. J. Electrochem. Sci.* (2012).
414. Rengstorff, G. W. P. Sulfuric Acid Friction and Wear Sulfuric Acid. (2018).
415. Sherif, E. S. M. Corrosion and corrosion inhibition of pure iron in neutral chloride solutions by 1,1'-thiocarbonyldiimidazole. *Int. J. Electrochem. Sci.* (2011).
416. Groysman, A. *Corrosion for Everybody*. (Springer Netherlands, 2010). doi:10.1007/978-90-481-3477-9
417. Linnenbom, V. J. The Reaction between Iron and Water in the Absence of Oxygen. *J. Electrochem. Soc.* **105**, 322 (1958).
418. Darwish, N. A., Hilbert, F., Lorenz, W. J. & Rosswag, H. The influence of chloride ions on the kinetics of iron dissolution. *Electrochim. Acta* **18**, 421–425 (1973).
419. Whitman, W. G., Russell, R. P., Welling, C. M. & Cochrane, J. D. The Effect of Velocity on the Corrosion of Steel in Sulfuric Acid. *Ind. Eng. Chem.* **15**, 672–677 (1923).
420. Gatos, H. C. Acceleration of the Dissolution of Iron in Sulfuric Acid by Ferric Ions. *J. Electrochem. Soc.* **103**, 286 (1956).
421. Damon, G. H. Acid Corrosion of Steel. *Ind. Eng. Chem.* **33**, 67–69 (1941).
422. Conroy, J. T. The rate of dissolution of iron in hydrochloric acid. *J. Soc. Chem. Ind.* **20**, 316 (1901).
423. Taneja, J. N. Dissolution of iron in hydrochloric acid. (1967).
424. Bessone, J., Karakaya, L., Lorbeer, P. & Lorenz, W. J. The Kinetics of iron dissolution and passivation. *Electrochim. Acta* (1977). doi:10.1016/0013-4686(77)80054-6
425. Ma, Y., Han, F., Li, Z. & Xia, C. Corrosion Behavior of Metallic Materials in Acidic-Functionalized Ionic Liquids. *ACS Sustain. Chem. Eng.* **4**, 633–639 (2016).

426. Lyon, S. B. Corrosion of Molybdenum and its Alloys. in *Shreir's Corrosion* 2157–2167 (Elsevier, 2010). doi:10.1016/B978-044452787-5.00106-2
427. JONES, E. S., MOSHER, C. J. F., SPEISER, R. & SPRETNAK, J. W. The Oxidation of Molybdenum. *CORROSION* **14**, 20–26 (1958).
428. de Castro, I. A. *et al.* Molybdenum Oxides – From Fundamentals to Functionality. *Advanced Materials* (2017). doi:10.1002/adma.201701619
429. Abdallah, M. & El-Etre, A. Y. Corrosion Inhibition of Nickel in Sulfuric Acid Using Tween Surfactants. *Port. Electrochim. Acta* **21**, 315–326 (2003).
430. Abd El Aal, E. E., Zakria, W., Diab, A. & Abd El Haleem, S. M. Anodic dissolution of nickel in acidic chloride solutions. *J. Mater. Eng. Perform.* (2003). doi:10.1361/105994903770343312
431. Parshutin, V. V., Bogdashkina, N. L. & Chernova, G. P. The effect of medium on the corrosion and electrochemical behavior of nickel. *Prot. Met.* **43**, 59–65 (2007).
432. Ohtsuka, T. & Heusler, K. E. Potential-dependent properties of the passivating film on nickel in sulphuric acid solution from multiple-angle-of-incidence reflectivity measurements. *J. Electroanal. Chem. Interfacial Electrochem.* **102**, 175–187 (1979).
433. Kish, J. R., Ives, M. B. & Rodda, J. R. Corrosion Mechanism of Nickel in Hot, Concentrated H₂SO₄. *J. Electrochem. Soc.* **147**, 3637 (2000).
434. Prando, D. *et al.* Corrosion of titanium: Part 1: aggressive environments and main forms of degradation. *J. Appl. Biomater. Funct. Mater.* **15**, 0–0 (2017).
435. Abkhoshk, E., Jorjani, E., Al-Harshsheh, M. S., Rashchi, F. & Naazeri, M. Review of the hydrometallurgical processing of non-sulfide zinc ores. *Hydrometallurgy* **149**, 153–167 (2014).
436. Stanojevic, D., Toskovic, D. & Rajkovic, M. B. Intensification of zinc dissolution process in sulphuric acid. *J. Min. Metall. Sect. B Metall.* (2005). doi:10.2298/jmmb0501047s
437. Hurlen, T. *et al.* Corrosion of Zinc. Effect of pH. *Acta Chem. Scand.* (1962). doi:10.3891/acta.chem.scand.16-1346
438. Thomas, S., Birbilis, N., Venkatraman, M. S. & Cole, I. S. Corrosion of zinc as a function of pH. *Corrosion* (2012). doi:10.5006/1.3676630
439. Gerischer, H. & Sorg, N. Chemical dissolution of zinc oxide crystals in aqueous electrolytes-An analysis of the kinetics. *Electrochim. Acta* (1992). doi:10.1016/0013-4686(92)85035-J
440. Dilasari, B., Jung, Y. & Kwon, K. Comparative study of corrosion behavior of metals in protic and aprotic ionic liquids. *Electrochem. commun.* **73**, 20–23 (2016).
441. Bakkar, A. & Neubert, V. Electrodeposition onto magnesium in air and water stable ionic liquids: From corrosion to successful plating. *Electrochem. commun.* **9**, 2428–2435 (2007).
442. Saadawy, M. Kinetics of Pitting Dissolution of Austenitic Stainless Steel 304 in Sodium Chloride Solution. *ISRN Corros.* (2012). doi:10.5402/2012/916367
443. CHIBA, A., SAKAKURA, S., KOBAYASHI, K. & KUSAYANAGI, K. Dissolution amounts of nickel, chromium and iron from SUS 304, 316 and 444 stainless steels in sodium chloride solutions. *J. Mater. Sci.* **32**, 1995–2000 (1997).
444. Abdallah, M. Corrosion behaviour of 304 stainless steel in sulphuric acid solutions and its inhibition by some substituted pyrazolones. *Mater. Chem. Phys.* **82**, 786–792 (2003).
445. Okamoto, G. & Shibata, T. Stability of passive stainless steel in relation to the potential of passivation treatment. *Corros. Sci.* **10**, 371–378 (1970).
446. Herler, R., Shetty, P., Shetty, S. D. & Kini, U. A. Corrosion Inhibition of 304 SS in Hydrochloric Acid Solution by N – Furfuryl N' – Phenyl Thiourea. *Port. Electrochim. Acta* **29**, 69–78 (2011).
447. Liu, B. Y., Xue, Y. J., Yang, Z. H. & Fang, X. X. Corrosion Behavior of Austenitic Stainless Steel in Hydrochloric Acid Solution and Flow. *Mater. Sci. Forum* **850**, 78–85 (2016).
448. PHELPS, E. H. & VREELAND, D. C. Corrosion of Austenitic Stainless Steels in Sulfuric Acid. *CORROSION* **13**, 21–26 (1957).
449. Kritzer, P., Boukis, N. & Dinjus, E. Review of the Corrosion of Nickel-Based Alloys and Stainless Steels in Strongly Oxidizing Pressurized High-Temperature Solutions at Subcritical and Supercritical Temperatures. *CORROSION* **56**, 1093–1104 (2000).
450. Perissi, I. *et al.* Ionic liquids: Electrochemical investigation on corrosion activity of ethyl-dimethyl-propylammonium bis(trifluoromethylsulfonyl)imide at high temperature. *Russ. J. Electrochem.* **48**, 434–441 (2012).
451. Tseng, C. H. *et al.* Corrosion behaviors of materials in aluminum chloride-1-ethyl-3- methylimidazolium chloride ionic liquid. *Electrochem. commun.* **12**, 1091–1094 (2010).
452. *THE GLOBAL MARKET FOR ZINC OXIDE NANOPARTICLES.* (2014).

453. Kolodziejczak-Radzimska, A. & Jesionowski, T. Zinc oxide—from synthesis to application: A review. *Materials (Basel)*. **7**, 2833–2881 (2014).
454. ECHA. Substance information - Zinc Oxide. Available at: <https://echa.europa.eu/substance-information/-/substanceinfo/100.013.839>.
455. Mortimer, M., Kasemets, K. & Kahru, A. Toxicity of ZnO and CuO nanoparticles to ciliated protozoa *Tetrahymena thermophila*. *Toxicology* (2010). doi:10.1016/j.tox.2009.07.007
456. Nohynek, G. J., Lademann, J., Ribaud, C. & Roberts, M. S. Grey Goo on the Skin? Nanotechnology, Cosmetic and Sunscreen Safety. *Crit. Rev. Toxicol.* **37**, 251–277 (2007).
457. Goods Administration. Literature Review on the safety of titanium dioxide and zinc oxide nanoparticles in sunscreens Scientific review report Therapeutic Goods Administration Literature Review on the safety of titanium dioxide and zinc oxide nanoparticles in sunscreens. (2016).
458. Burnett, M. E. & Wang, S. Q. Current sunscreen controversies: A critical review. *Photodermatology Photoimmunology and Photomedicine* (2011). doi:10.1111/j.1600-0781.2011.00557.x
459. ASME. *D4295 – 89 Standard Classification for Rubber Compounding Materials—Zinc Oxide*. (2017).
460. Publication, B. S. I. S. PD CEN ISO / TS 80004-8 : 2015 BSI Standards Publication Nanotechnologies — Vocabulary. (2015).
461. BS ISO 9298:2017 Rubber compounding ingredients — Zinc oxide — Test methods. (2017).
462. ASTM. D79 – 86 Standard Specification for Zinc Oxide Pigments. **73**, 1–2 (2014).
463. Mahmud, S., Abdullah, M. J., Putrus, G. A., Chong, J. & Mohamad, A. K. Nanostructure of ZnO fabricated via French process and its correlation to electrical properties of semiconducting varistors. *Synth. React. Inorganic, Met. Nano-Metal Chem.* **36**, 155–159 (2006).
464. Charinpanitkul, T. *et al.* Facile synthesis of tetrapodal ZnO nanoparticles by modified French process and its photoluminescence. *J. Ind. Eng. Chem.* (2012). doi:10.1016/j.jiec.2011.11.028
465. Antonietti, M., Kuang, D., Smarsly, B. & Zhou, Y. Ionic liquids for the convenient synthesis of functional nanoparticles and other inorganic nanostructures. *Angew. Chemie - Int. Ed.* **43**, 4988–4992 (2004).
466. Łuczak, J., Paszkiewicz, M., Krukowska, A., Malankowska, A. & Zaleska-Medynska, A. Ionic liquids for nano- and microstructures preparation. Part 2: Application in synthesis. *Adv. Colloid Interface Sci.* **227**, 1–52 (2016).
467. Kang, X., Sun, X. & Han, B. Synthesis of Functional Nanomaterials in Ionic Liquids. *Adv. Mater.* **28**, 1011–1030 (2016).
468. Zhu, H., Huang, J. F., Pan, Z. & Dai, S. Ionothermal synthesis of hierarchical ZnO nanostructures from ionic-liquid precursors. *Chem. Mater.* **18**, 4473–4477 (2006).
469. Movahedi, M., Kowsari, E., Mahjoub, A. R. & Yavari, I. A task specific basic ionic liquid for synthesis of flower-like ZnO by hydrothermal method. *Mater. Lett.* **62**, 3856–3858 (2008).
470. Zhou, X. *et al.* Formation of ZnO hexagonal micro-pyramids: a successful control of the exposed polar surfaces with the assistance of an ionic liquid. *Chem. Commun.* **1**, 5572–5574 (2005).
471. Liu, D. P., Li, G. D., Su, Y. & Chen, J. S. Highly luminescent ZnO nanocrystals stabilized by ionic-liquid components. *Angew. Chemie - Int. Ed.* **45**, 7370–7373 (2006).
472. Greene, L. E., Yuhas, B. D., Law, M., Zitoun, D. & Yang, P. Solution-grown zinc oxide nanowires. *Inorganic Chemistry* **45**, 7535–7543 (2006).
473. Ji, Y. One-step method for growing of large scale ZnO nanowires on zinc foil. *Mater. Lett.* **138**, 92–95 (2015).
474. Kumar, V., Kim, J. H., Pendyala, C., Chernomordik, B. & Sunkara, M. K. Gas-Phase, Bulk Production of Metal Oxide Nanowires and Nanoparticles Using a Microwave Plasma Jet Reactor. *J. Phys. Chem. C* **112**, 17750–17754 (2008).
475. Petzold, F. G. *et al.* Nickel supported on zinc oxide nanowires as advanced hydrodesulfurization catalysts. *Catal. Today* **198**, 219–227 (2012).
476. Vostrikov, A. A., Shishkin, A. V & Timoshenko, N. I. Synthesis of Zinc Oxide Nanostructures during Zinc Oxidation by Sub- and Supercritical Water. *Tech. Phys.* **33**, 30–34 (2007).
477. H.Y. Dang, J. W. and S. S. F. The synthesis of metal oxide nanowires by directly heating metal sample in appropriate oxygen atmosphere. *Nanotechnology* **6**, 738–741 (2003).
478. Yu, T. *et al.* Substrate-Friendly Synthesis of Metal Oxide Nanostructures Using a Hotplate. *Small* **2**, 80–84 (2006).
479. Cho, S. *et al.* Large-scale fabrication of sub-20-nm-diameter ZnO nanorod arrays at room temperature and their photocatalytic activity. *J. Phys. Chem. C* **113**, 10452–10458 (2009).
480. Wang, L. *et al.* Systematic Investigation on Morphologies, Forming Mechanism, Photocatalytic and Photoluminescent Properties of ZnO Nanostructures Constructed in Ionic Liquids. *Inorg. Chem.* **47**,

- 1443–1452 (2008).
481. Bettini, S. *et al.* Promising Piezoelectric Properties of New ZnO@Octadecylamine Adduct. *J. Phys. Chem. C* **119**, 20143–20149 (2015).
482. Bisht, G. *et al.* Synthesis, Characterization, and Study of In Vitro Cytotoxicity of ZnO-Fe₃O₄ Magnetic Composite Nanoparticles in Human Breast Cancer Cell Line (MDA-MB-231) and Mouse Fibroblast (NIH 3T3). *Nanoscale Res. Lett.* (2016). doi:10.1186/s11671-016-1734-9
483. Lanje, A. S., Sharma, S. J., Ningthoujam, R. S., Ahn, J.-S. & Pode, R. B. Low temperature dielectric studies of zinc oxide (ZnO) nanoparticles prepared by precipitation method. *Adv. Powder Technol.* **24**, 331–335 (2013).
484. Souza, J. D., Souza, V. S. & Scholten, J. D. Synthesis of Hybrid Zinc-Based Materials from Ionic Liquids: A Novel Route to Prepare Active Zn Catalysts for the Photoactivation of Water and Methane. *ACS Sustain. Chem. Eng.* (2019). doi:10.1021/acssuschemeng.8b04809
485. Rabieh, S., Bagheri, M., Heydari, M. & Badii, E. Microwave assisted synthesis of ZnO nanoparticles in ionic liquid [Bmim]Cl and their photocatalytic investigation. *Mater. Sci. Semicond. Process.* **26**, 244–250 (2014).
486. Benhebal, H. *et al.* Photocatalytic degradation of phenol and benzoic acid using zinc oxide powders prepared by the sol–gel process. *Alexandria Eng. J.* **52**, 517–523 (2013).
487. Edition, F. Guidelines for Drinking-water Quality. *World Health* (2011). doi:10.1016/S1462-0758(00)00006-6
488. WHO, W. H. organisation. *A compendium of standards for wastewater reuse in the eastern Mediterranean region. WHO-EM/CEH/142/E* (2006).
489. Coleman, D. & Gathergood, N. Biodegradation studies of ionic liquids. *Chemical Society Reviews* (2010). doi:10.1039/b817717c
490. Zhang, C. *et al.* Acute toxicity, biochemical toxicity and genotoxicity caused by 1-butyl-3-methylimidazolium chloride and 1-butyl-3-methylimidazolium tetrafluoroborate in zebrafish (*Danio rerio*) livers. *Environ. Toxicol. Pharmacol.* (2017). doi:10.1016/j.etap.2017.02.018
491. Matches. Process Equipment Cost Estimates. (2014). Available at: <https://www.matche.com/equipcost/Default.html>.
492. Ukpower. energy/tariffs-per-unit-kwh. Available at: https://www.ukpower.co.uk/home_energy/tariffs-per-unit-kwh.
493. Publication, B. S. I. S. PD ISO/TR 15916:2015 Basic considerations for the safety of hydrogen systems. (2015).
494. Astbury, G. R. Venting of low pressure hydrogen gas a critique of the literature. *Process Saf. Environ. Prot.* (2007). doi:10.1205/psep06054
495. The Engineering ToolBox. Available at: <https://www.engineeringtoolbox.com/>.
496. EPA. EPA/815/R-99/010 Guidance manual for compliance with the interim enhanced water treatment rule: Turbidity provisions. (1999).
497. Kim, I. Transport and retention of silver nanoparticles in granular media filtration.
498. Latham, A. H., Freitas, R. S., Schiffer, P. & Williams, M. E. Capillary magnetic field flow fractionation and analysis of magnetic nanoparticles. *Anal. Chem.* (2005). doi:10.1021/ac050611f
499. Duesberg, G. S. Separation of carbon nanotubes by size exclusion chromatography. *Chem. Commun.* (1998). doi:10.1039/a707465d
500. Lee, J. S., Stoeva, S. I. & Mirkin, C. A. DNA-induced size-selective separation of mixtures of gold nanoparticles. *J. Am. Chem. Soc.* (2006). doi:10.1021/ja061651j
501. Sun, X. *et al.* Separation of nanoparticles in a density gradient: FeCo@C and gold nanocrystals. *Angew. Chemie - Int. Ed.* (2009). doi:10.1002/anie.200805047
502. Akthakul, A., Hochbaum, A. I., Stellacci, F. & Mayes, A. M. Size fractionation of metal nanoparticles by membrane filtration. *Adv. Mater.* (2005). doi:10.1002/adma.200400636
503. Kang, P. K. & Shah, D. O. Filtration of nanoparticles with dimethyldioctadecylammonium bromide treated microporous polypropylene filters. *Langmuir* (1997). doi:10.1021/la961010+
504. Krieg, E., Weissman, H., Shirman, E., Shimoni, E. & Rybtchinski, B. A recyclable supramolecular membrane for size-selective separation of nanoparticles. *Nat. Nanotechnol.* (2011). doi:10.1038/nnano.2010.274
505. Sweeney, S. F., Woehle, G. H. & Hutchison, J. E. Rapid purification and size separation of gold nanoparticles via diafiltration. *J. Am. Chem. Soc.* (2006). doi:10.1021/ja0558241
506. Sharma, V., Park, K. & Srinivasarao, M. Shape separation of gold nanorods using centrifugation. *Proc. Natl. Acad. Sci. U. S. A.* (2009). doi:10.1073/pnas.0800599106

507. Hanauer, M., Pierrat, S., Zins, I., Lotz, A. & Sönnichsen, C. Separation of nanoparticles by gel electrophoresis according to size and shape. *Nano Lett.* (2007). doi:10.1021/nl071615y
508. Xiong, B. *et al.* Separation of nanorods by density gradient centrifugation. *J. Chromatogr. A* (2011). doi:10.1016/j.chroma.2011.04.038
509. Robertson, J. D. *et al.* Purification of Nanoparticles by Size and Shape. *Sci. Rep.* (2016). doi:10.1038/srep27494
510. Lee, H. *et al.* Liquid filtration of nanoparticles through track-etched membrane filters under unfavorable and different ionic strength conditions: Experiments and modeling. *J. Memb. Sci.* (2017). doi:10.1016/j.memsci.2016.11.023
511. Trzaskus, K. W. Filtration of engineered nanoparticles using porous membranes. (University of Twente, 2016). doi:10.3990/1.9789036540452
512. Bell, G. R. A. Analysis and Development of a Decanter Centrifuge - Power consumption analysis, development of a composite bowl, and feed accelerator analysis. (University of Canterbury, 2013).
513. Szepessy, S. & Thorwid, P. Low Energy Consumption of High-Speed Centrifuges. *Chem. Eng. Technol.* **41**, 2375–2384 (2018).
514. Gsell, George V.; Nunez, Chet; Klein, Kim; Essary, B. WFI : A Cost Review - A Cost Evaluation of Alternative Systems for WFI Production Absent Distillation. (2019).
515. KTH. INNOVATION READINESS LEVEL.
516. Yamamuro, O., Minamimoto, Y., Inamura, Y., Hayashi, S. & Hamaguchi, H. Heat capacity and glass transition of an ionic liquid 1-butyl-3-methylimidazolium chloride. *Chem. Phys. Lett.* **423**, 371–375 (2006).
517. Hu, H.-C., Soriano, A. N., Leron, R. B. & Li, M.-H. Molar heat capacity of four aqueous ionic liquid mixtures. *Thermochim. Acta* **519**, 44–49 (2011).
518. CHECAL. AGITATOR POWER. Available at: <https://www.checalc.com/solved/agitator.html>.
519. CHECAL. INSULATION HEAT LOSS CALCULATION. Available at: <https://checalc.com/calc/inshoriz.html>.
520. Popescu, C. M. *et al.* Spectral characterization of eucalyptus wood. *Appl. Spectrosc.* (2007). doi:10.1366/000370207782597076
521. Boeriu, C. G., Bravo, D., Gosselink, R. J. A. & Van Dam, J. E. G. Characterisation of structure-dependent functional properties of lignin with infrared spectroscopy. in *Industrial Crops and Products* (2004). doi:10.1016/j.indcrop.2004.04.022
522. Pandey, K. K. A study of chemical structure of soft and hardwood and wood polymers by FTIR spectrscopy. *J. Appl. Polym. Sci.* **71**, 1969–1975 (1999).
523. Harrington, K. J., Higgins, H. G. & Michell, A. J. Infrared spectra of Eucalyptus regnans F. Muell. and Pinus radiata D. Don. *Holzforschung-International J. Biol. Chem. Phys. Technol. Wood* **18**, 108–113 (1964).
524. Sugiyama, J., Vuong, R. & Chanzy, H. Electron Diffraction Study on the Two Crystalline Phases Occurring in Native Cellulose from an Algal Cell Wall. *Macromolecules* **24**, 4168–4175 (1991).
525. Chen, W., Lickfield, G. C. & Yang, C. Q. Molecular modeling of cellulose in amorphous state. Part I: Model building and plastic deformation study. *Polymer (Guildf)*. **45**, 1063–1071 (2004).
526. Ribeiro da Silva, M. A. V. *et al.* Thermochemistry of α -D-xylose(cr). *J. Chem. Thermodyn.* **58**, 20–28 (2013).

Appendix 1 - Supplementary information on ILs

A1.1. IL cost

Figure 109 shows the cost per kilogram of selected ILs taken from chemical suppliers. It is noteworthy to mention that the cost shown here should be interpreted as a relative guideline rather than the absolute price, as it will vary depending on the quantities and the purity required. In order to have an idea of the relative cost of ILs, several suppliers were consulted that the cost of the IL normalized.

Sigma-Aldrich (MERCK) supplies small quantities for research (typically in the gr scale), therefore, when normalizing the cost per kilogram, some ILs are excessively high. BASF works in co-operation with Sigma-Aldrich to supply quantities for pilot-scale trials (100 kg scale) and supply contracts on ton-scale.

Iolitec is another IL supplier, for both lab and pilot plant capacities, who include in their catalogue larger quantities of IL (up to 1 - 5 kg), and therefore the IL price per kg is less than Sigma-Aldrich. This comparison is not quite fair, for the reasons mentioned above, Sigma-Aldrich can also supply larger quantities (in the kg scale at a lower cost) but this is not part of their standard products and needs to be done through their quotation service. Again, the exercise is to compare the cost trend rather than their absolute value.

Lastly, Alibaba, the major platform for Chinese e-commerce, was consulted [April 2019] to verify the bulk cost of ILs by Chinese manufactures. The cost in this platform is given as a range, depending on the quantities, the minima and maxima for each IL had been reported also.

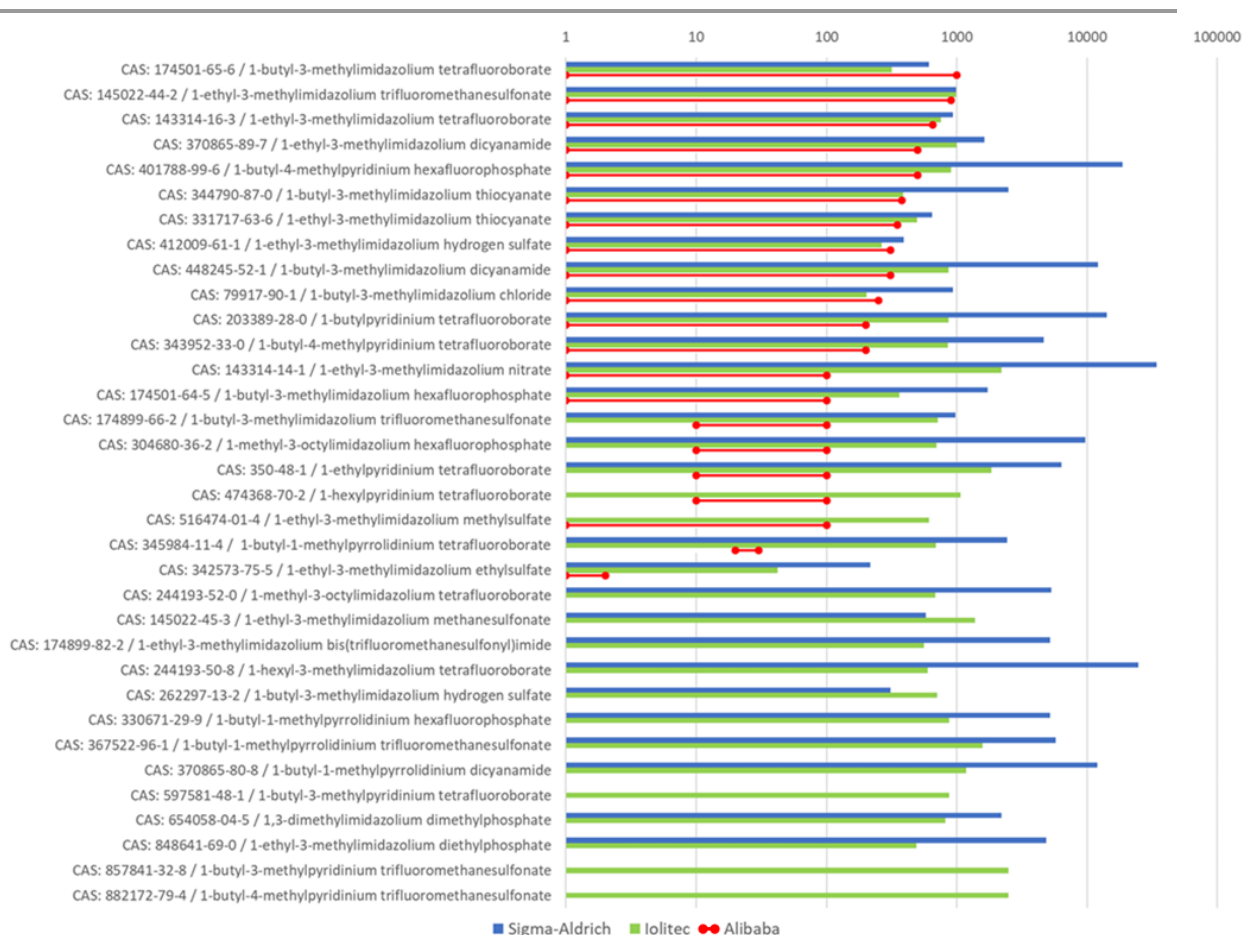


Figure 109. Cost of ILs [GBP / kg] from 3 different suppliers. Red line represents the cost range by Chinese suppliers (Alibaba).

From the assessment (Figure 109) it can be seen that 1-ethyl-3-methylimidazolium ethylsulfate [C₄C₁im][C₂H₅SO₄] (CAS 342573-75-5) is systematically the least expensive IL. This is consistent with the expectation that the protic version containing hydrogen-sulfate ILs should be even less expensive.

Fluorinated ILs, such as bis(trifluoromethylsulfonyl)imide-based ILs, are typically used in research as hydrophobic ILs but their price is too high even at bulk scale, and therefore it is very unlikely that this kind of ILs can be used as a solvent in large scale processes. However, they are extremely popular in the scientific literature, and therefore, the corrosion behaviour of 1-butyl-3-methylimidazolium bis(trifluoromethylsulfonyl)imide [C₄C₁im][NTf₂] is also studied in Chapter 3.

A1.2. Toxicity of ILs and impact on the environment

The toxicological and environmental impact of ILs are becoming of increasing interest as ILs are becoming very popular and are being used in larger quantities. So far, the properties of ILs

which gained them the “environmentally friendly” label are low volatility (reduced losses, air pollution and lower exposure risk to humans as they cannot be ingested by inhalation), non-flammability (process safety) and excellent stability (recycling and reusing potential). These properties of ILs meet the demands of the waste hierarchy developed by European Union Directive 2008/98/EC (European Union, 2008) and make them good candidates for environmentally benign and sustainable processes. However, as mentioned before, due to the great number of ILs, these properties are general trends and need to be assessed on a case-by-case basis.

A complete life cycle analysis of ILs should be considered when determining if they can be considered as green solvents. Key considerations are raw materials, waste treatment of chemicals and energy consumption for production. In IL synthesis, the selection of cation, anion and solvents used has a significant effect on toxicity and economics. An area of increasing interest to avoid potential toxicity is by using ions of known toxicity. Moreover, biodegradation is another significant issue that should be considered in the future use of IL in industry^{378,379}. Table 32 summarizes some general guidelines regarding the toxicity and biodegradability of ILs.

Table 32. General guidelines regarding the toxicity and biodegradability of ILs. Adapted from ref³⁷⁸.

		CATION-CHAINS	CATION-CORE	ANIONS
TOXICITY	Recommended	Short polar side-chains	Morpholinium- and Pyridinium-based IL	Alkyl sulfates, alkyl sulphonates and salts or organic acids
	Not Recommended	Long hydrophobic alkyl chains	Imidazolium-based IL	Fluorine-contained ions
BIODEGRADABILITY	Recommended	Long hydrophobic alkyl chains	Pyridinium-based IL	Alkyl sulfates, alkyl sulphonates and salts or organic acids
	Not Recommended	Introduction of polar functional groups into side-chain	Imidazolium-based IL	Fluorine-contained ions

A1.3. Thermodynamic properties of [HSO₄]-based ILs

Table 33. Thermodynamic parameters for some species of relevance for PIL formation taken from the literature

36

	$\Delta_{\text{hyd}}G$ [kJ/mol]
<i>N,N,N</i> -Dimethylbutylammonium	-228.4
<i>N</i> -Methylpyrrolidinium	-234.7
<i>N</i> -Heptylammonium	-304.1
<i>N</i> -Butylammonium	-307.5
Acetate	-357.2

Table 34. Density of reference alkylamines/sulfuric acid-based ILs (1:1) as reported in the literature.

	Density [g/cm ³]				Reference
	298.15	303.15	308.15	313.15	
[N ₄₁₁₀][HSO ₄] ($\beta=1$)	1.1934	1.1903	1.1876	1.1845	This work
<i>N</i> -Ethylammonium hydrogen sulfate	1.4380 (27 °C)				Ref ¹⁰⁷
[N ₂₀₀₀][HSO ₄] <i>N,N,N</i> -Triethylammonium hydrogen sulfate	1.14289	1.14183	1.14072	1.14002	Ref ^{52,380,381}
[N ₂₂₂₀][HSO ₄] <i>N,N</i> -Diethylammonium hydrogen sulfate	1.02839	1.02397	1.02054	1.01656	Ref ^{52,381,382}
[N ₂₂₀₀][HSO ₄] <i>N,N,N</i> -Trimethylammonium hydrogen sulfate	1.46758	1.46357	1.46350	1.45563	Ref ^{52,381,383}
[N ₁₁₁₀][HSO ₄]					

As expected, the density of [N₄₁₁₀][HSO₄] showed a linear decrease with increasing temperature for all of the tested base:acid (β) ratios. The data were fitted to a linear equation (Eq. 103) where ρ [g/cm³] is the density, T is the temperature [K], and A_0 , A_1 refer to the correlation coefficients. The respective values of the correlation coefficients are listed in Table 3, together with the R^2 and the standard error of the estimate σ_{est} , indicating the high accuracy of predictions.

$$\rho = A_0 T + A_1 \quad (103)$$

Table 35. Correlation coefficients; Density as a function of temperature for different base/acid molar ratios of $[N_{4110}][HSO_4]$

β	A_0	A_1	R^2	σ_{est}
1.10	-5.7135E-04	1.3519	0.99993	0.0001
1.05	-5.7354E-04	1.3573	0.99997	0.0001
1.00	-5.7596E-04	1.3651	0.99983	0.0002
0.95	-5.8016E-04	1.3735	0.99981	0.0003
0.90	-5.8112E-04	1.3833	0.99998	0.0003
0 $[H_2SO_4]^{128}$	-9.9398E-04	1.8514	0.99978	0.0003

Table 36. Experimental viscosity determination as a function of temperature for $[N_{4110}][HSO_4]$ ($\beta = 1$) determined by the falling ball method, section 2.3.3.5.

Temperature	η (cP)	σ
15	3142.99	8.69
	3159.53	
	3155.93	
17	2737.85	62.83
	2619.70	
	2715.84	
19	2496.63	-
	1687.62	
26.5	1710.36	29.11
	1745.41	
	424.87	
50.5	459.59	23.33
	469.22	
	164.44	
70	160.44	2.16
	163.86	
	55.50	
102	55.21	1.14
	53.39	
	45.41	
109	45.62	0.99
	47.23	
	31.18	
132	30.83	0.55
	30.9	

Table 37. Self-diffusion coefficients for $[N_{4110}][HSO_4]$ calculated with DOSY ($\Delta = 1.9999$ s, $\delta = 0.01$ s, $\gamma = 26752$ rad/s.Gauss).

Beta (β) → Temperature [°C]↓	Self-diffusion coefficient [m ² /s]				
	0.9	0.95	1	1.05	1.1
25	6.20×10^{-13}	7.37×10^{-13}	1.03×10^{-12}	1.33×10^{-12}	1.61×10^{-12}
50	2.43×10^{-12}	3.10×10^{-12}	4.11×10^{-12}	6.88×10^{-12}	8.11×10^{-12}
90	1.15×10^{-11}	1.65×10^{-11}	2.57×10^{-11}	3.92×10^{-11}	4.81×10^{-11}
130	-	-	6.23×10^{-11}	-	-

Appendix 2 - [C₄C₁im]Cl-water system structures

At low water content, water molecules forms pockets (or inverse micelles) confined in the nano-domain environment formed by the cation-anion networks. It has been shown that in some cases, for example 1-butyl-3-methylimidazolium tetrafluoroborate [C₄C₁im][BF₄], the IL ions are able to adjust their relative position/orientation when water is added into the IL structure, with little disruption of the IL network, as proven by the small change in the chemical shifts of the ¹H signals generated by the [C₄C₁im]⁺ cation up to a water concentration of 90 mol%⁶⁰. Contrarily, the properties of the water located in the core of these reverse micelles can exhibit drastic changes in its behaviour, as proven by the split of the water signal in H-NMR²³. In contrast, [C₄C₁im]-halide ILs, such as [C₄C₁im]Cl, is more prone to changes in its structure when water is added²⁴.

Experimental values of the specific conductivity κ as a function of IL concentration are shown in Figure 110. Two data sets from literature have been taken for diluted and one data set for concentrated [C₄C₁im]Cl¹⁶⁹.

The electrical conductivities κ have been converted to molar conductivities (Λ) (κ/c) and plotted according to Kohlraush's empirical law (Figure 111) (Eq. 104)¹⁶⁹.

$$\Lambda = \Lambda_0 - KC^{\frac{1}{2}} \quad (104)$$

In Eq. 104, Λ_0 is the molar conductivity at infinite dilution, K is an empirical constant that depends on the type of the electrolyte and C is the solute concentration in mol/L. The linear portions in represent regimes of approximately constant association. The break points between these portions occur when the nature of the charge carriers changes^{384,385}.

From Figure 110, it can be seen that the specific conductivity deviate from linearity at concentrations higher than 0.29 mmol/L. However, due to the number of data points, it is not possible to accurately determine the Critical Aggregation Concentration (CAC) from these conductivity data sets¹⁶⁹.

From Figure 111, it can be seen that at high IL concentrations, the values of molar conductivity follow a linear trend, that doesn't extrapolate to the molar conductivity at infinite dilution. At concentrations lower than 1 mol/L, the molar conductivity values start to diverge from this line and approaches the Kohlraush's empirical law. The two experimental conditions selected for this study. *i.e.* water-rich case and IL-rich case, lie within the extremes of a linear portion of the

Kohlraush's plot, suggesting that the nature of the charge carriers is the same for both cases

169.

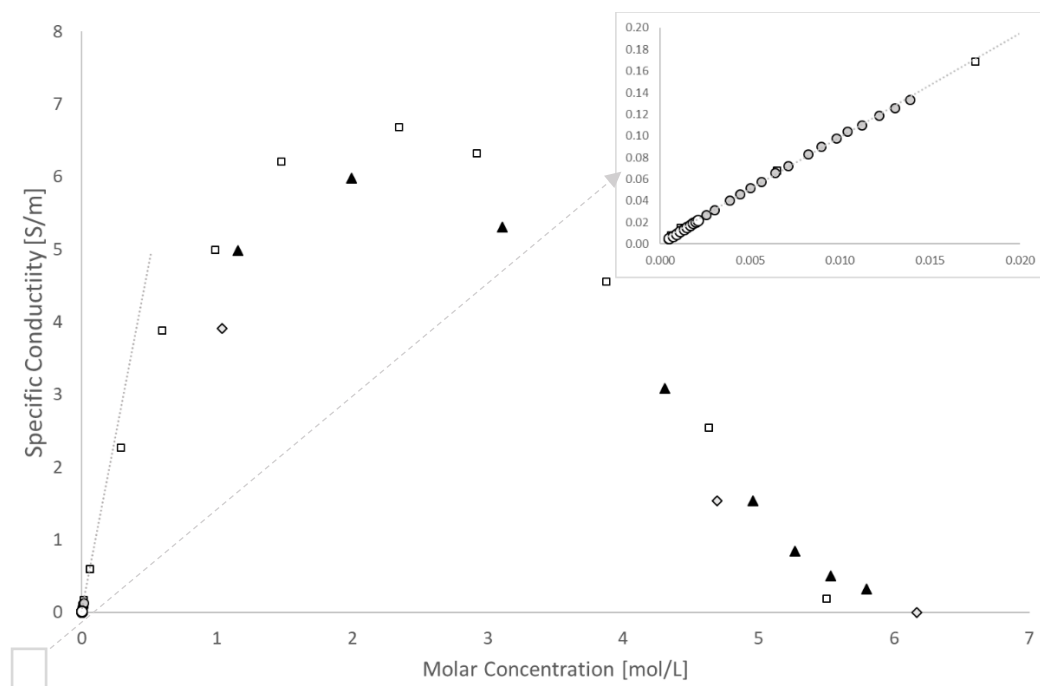


Figure 110. Specific conductivity (κ) over IL molar concentration. Experiment data: (\diamond) This work (water-rich case 1.02 mol/L^{1/2}, IL-rich case 2.17 mol/L^{1/2}, residual water Case 2.48 mol/L^{1/2}). Data from literature included (error bars not shown): (\square) 30 °C³⁸⁶ (\circ) 25 °C³⁸⁷ (\blacktriangle) 25 °C³⁸⁸ (\circ) 25 °C³⁸⁹. Line represent the linear regression of the data for diluted solutions. Insert shows a detail in the diluted region. Published by The Royal Society of Chemistry ¹⁶⁹.

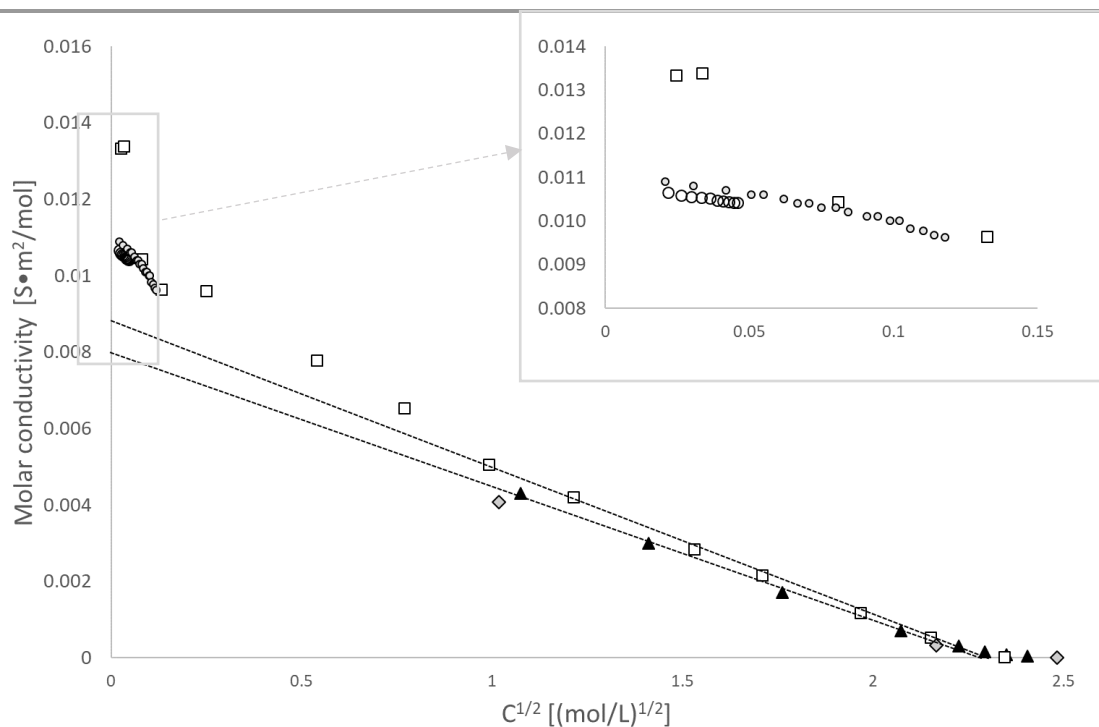


Figure 111. Molar electrical conductivity (Λ_m) over the square root of the IL molar concentration. Experiment data: (\diamond) This work (water-rich case 1.02 mol/L^{1/2}, IL-rich case 2.17 mol/L^{1/2}, residual water Case 2.48 mol/L^{1/2}). Data from literature included (error bars not shown): (\square) 30 °C³⁸⁶ (\circ) 25 °C³⁸⁷ (\blacktriangle) 25 °C³⁹⁰ (\circ) 25 °C³⁹¹. Lines represent the linear regression of the data for concentrated solutions. Insert shows a detail in the diluted region. Published by The Royal Society of Chemistry ¹⁶⁹.

Appendix 3 – Definition of terms

Some terms used in this work are define in the standard “Corrosion of metals and alloys - Basic terms and definitions” (ISO 8044:2020) ³⁹² as follows:

Anode: *Electrode* at which *anodic reaction* predominates.

Anodic reaction: *Electrode reaction*, equivalent to a transfer of positive charge from the electronic conductor to the *electrolyte*. Current enters the *electrolyte* from the electronic conductor. An anodic reaction is an *oxidation* process. An example common in *corrosion* is: $M \rightarrow M^{n+} + ne^{-}$.

Cathode: *Electrode* at which *cathodic reaction* predominates.

Cathodic reaction: *Electrode reaction* equivalent to a transfer of negative charge from the electronic conductor to the

Corrosion product: Substance formed as a result of *corrosion*.

Corrosion rate: *Corrosion effect* on a metal per time. The unit used to express the corrosion rate depends on the technical system and on the type of corrosion effect. Thus corrosion rate may be expressed as an increase in *corrosion depth* per time, or the mass of metal turned into *corrosion products* per area of surface and per time, etc. The corrosion effect may vary with time and may not be the same at all points of the corroding surface. Therefore, reports of corrosion rates should be accompanied by information on the type, time dependency and location of the corrosion effect.

Corrosion test: Test carried out to assess the *corrosion resistance* of a metal, the environmental contamination by *corrosion products*, the effectiveness of *corrosion protection*, or the *corrosivity* of an environment.

Corrosion: Physicochemical interaction between a metal and its environment that results in changes in the properties of the metal, and which may lead to significant impairment of the function of the metal, the environment, or the technical system, of which these form a part. This interaction is often of an electrochemical nature.

Corrosive agent: Substance which when in contact with a given metal will cause *corrosion*.

Corrosive environment: Environment that contains one or more *corrosive agents*.

Crevice corrosion: *Localized corrosion* associated with, and taking place in, or immediately around, a narrow aperture or clearance formed between the metal surface and another surface (metallic or non-metallic).

De-aeration: Removal of air from environment. If only oxygen is removed the term “de-oxygenation” is more appropriate.

Dealloying: *Selective corrosion*.

Deposit corrosion: *Localized corrosion* associated with, and taking place under, or immediately around, a deposit of *corrosion products* or other substance.

Dezincification of brass: *Selective corrosion* of brass resulting in preferential removal of zinc.

Electrode reaction: Interfacial reaction equivalent to a transfer of charge between an electronic conductor and an *electrolyte*.

Electrode: Electronic conductor in contact with an *electrolyte*. In the electrochemical sense the electrode is in fact restricted to narrow regions on both sides of the interface of this system.

Electrolyte. Current enters the electronic conductor from the *electrolyte*. A cathodic reaction is a *reduction* process, e.g. $\frac{1}{2} \text{O}_2 + \text{H}_2\text{O} + 2\text{e}^- \rightarrow 2\text{OH}^-$.

Electrolyte: Medium in which electric current is transported by ions.

General corrosion: *Corrosion* proceeding over the whole surface of the metal exposed to the *corrosive environment*.

Hydrogen embrittlement: Process resulting in a decrease of the toughness or ductility of a metal due to absorption of hydrogen: Hydrogen embrittlement often accompanies hydrogen formation, for example by *corrosion* or electrolysis, and can lead to cracking.

Intergranular corrosion: *Corrosion* in or adjacent to the grain boundaries of a metal.

Layer corrosion: *Corrosion* of internal layers of wrought metal, occasionally resulting in exfoliation, i.e. detachment of unattacked layers. Exfoliation is generally oriented in the direction of rolling, extrusion or principal deformation.

Localized corrosion: *Corrosion* preferentially concentrated on discrete sites of the metal surface exposed to the *corrosive environment*. Localized corrosion can result in, for example, pits, cracks, or grooves. During *reduction*, the reducing agent is oxidized.

Oxidation: Process in which a reactant loses one or more electrons.

Oxidizing agent: Substance causing *oxidation* by accepting electrons. During oxidation, the oxidizing agent is reduced.

Passivation: Decrease of *corrosion rate* by a *passivation layer*.

Pickling: Removal of oxides or other compounds from a metal surface by chemical or electrochemical action.

Pitting corrosion: *Localized corrosion* resulting in pits, i.e. cavities extending from the surface into the metal.

Protective layer: Layer of a substance on a metal surface that decreases the *corrosion rate*. Such layers may be applied or arise spontaneously, for example by *corrosion*.

Reducing agent: Substance causing *reduction* by donating electrons.

Reduction: Process in which a reactant accepts one or more electrons.

Selective corrosion: *corrosion* an alloy whereby the components react in proportions that differ from their proportions in the alloy.

Tribo-corrosion: Any form of corrosion that involves constant removal of the passive layer due to fluid or particles impact on the corroding surface or the friction between the corroding surface and another surface. Tribo-corrosion includes but is not restricted to: *wear corrosion*, *fretting corrosion* and *erosion corrosion*. process may result in an increase in friction of bearing surfaces in addition to causing material loss.

Uniform corrosion: *General corrosion* proceeding at almost the same rate over the whole surface.

Appendix 4 – Surface analytical techniques for corrosion studies

It has been established that surface features of materials, such as texture and surface energy, along with defects dislocation related to their mechanical processing, impact the corrosion behaviour, and therefore it is helpful to characterise the surface of materials in order to gain a better understanding of the corrosion processes ¹⁴⁷. Some surface analysis methods to study corrosion (in-situ and ex-situ post exposure) and techniques had been reviewed in literature ^{147,155,156}. These techniques include atomic force microscopy (AFM), X-ray diffraction spectroscopy (XRD) or high-temperature XRD, X-ray photoelectron spectroscopy (XPS), Raman spectroscopy, Fourier transform infrared spectroscopy (FTIR). Some emerging future techniques for surface characterization which are also reviewed in literature ^{155,156} include: Kelvin probe force microscopy (KPFM), Scanning tunnelling microscopy (STM) Scanning electrochemical microscopy (SECM), Secondary ion mass spectrometry (SIMS), X-ray absorption spectroscopy, Rutherford backscattering spectroscopy, Auger electron spectroscopy, Particle-induced X-ray emission, Electron probe microanalysis (EPMA), Near-edge X-ray absorption fine structure spectroscopy, X-ray photoemission electron microscopy, Low-energy electron diffraction, Small-angle neutron scattering and neutron reflectometry and Conversion electron Moessbauer spectroscopy (CEMS).

Some of the above techniques are non-destructive and can be used after the MCR has been determined, to identify corrosion products on the surface, for example, XRD can be used to identify crystalline phases while XPS can be used to identify oxidation states. Other non-destructive techniques, such as XRF, can be used to identify the bulk chemical composition of the samples, this can be particularly useful to study the selective demetallation of alloys or presence of the corrosive media in the corrosion products or inclusion in the material.

It is expected that as more materials are studied and categorised, the best analytical methods, from the ones mentioned above or emerging surface analysis techniques, can be identified for each type of system.

The ASTM G 31 ¹⁴³ standard mentions 3 post-exposure tests that can be carried out after the immersion test. Mechanical property comparison (tensile strength) ASTM Test Methods E8, cross-section microscopically examination to assess dealloying or intergranular attacks and embrittlement attack checked by bending test.

Appendix 5 – Details on the interaction of metals exposed to ILs

A5.1. Aluminium

Aluminium (Al) is a chemical element with an atomic number of 13. It is the most widely used non-ferrous metal. It is also the third most abundant metal in the crust of the Earth, almost twice as plentiful as iron, the fourth most abundant metal. Al is the lightest commonly used metals; and together with its alloys, possess a number of valuable mechanical, electrical, and thermal properties, making it a popular choice ³⁹³.

As Al is a widely used material, there is a large interest in studying its corrosion behaviour. In water, Al corrosion generates hydrogen gas. There is interest in harvesting this for energy applications ³⁹⁴.

A5.1.1. Corrosion rates

The results for the mass change of aluminium samples exposed to different corrosion media (water-soluble ILs) are given in Figure 112. For [C₄C₁im][NTf₂], results are given in section 3.5.2.

When Al is exposed to [C₄C₁im]Cl the mass change rate (MCR) is negligible, even at long exposure times, for the dry and 75 mol% cases. However, in the 98 mol% case, the MCR significantly increased (negative value), indicating corrosion products are depositing on the surface of the metal. This effect is amplified with temperature (Figure 112A/B).

Aluminium exposed to [HC₁im]Cl under dry conditions experiences a small MCR, which significantly increases with the presence of water. The maximum MCR is experienced at 75 mol% and decreases at higher water contents (Figure 112C/D). The reason for this is the deposition of corrosion products on the surface of the metal. In the water control cases, aluminium samples gain mass after the immersion experiments, further confirming deposition of material. This increase in mass was extreme in the water control at 120 °C. When exposed to the IL-water systems, for all conditions tested, the mass change per area increases with time, except for 98 mol% at 120 °C, for which it decreases. This confirms that anodic dissolution is the predominant mechanism in the PIL at 75 mol% without the deposition of corrosion products while deposition of corrosion products takes place at high water content. As temperature increases from 70 °C to 120 °C, the MCRs are more significant in either direction (positive or negative). The MCR in the dry case was negligible and independent of time and was extreme in pure water. The large error bar of the water case at 120 °C is probably due to detachment of material during the washing process.

When aluminium samples are exposed to $[N_{4110}][HSO_4]$. The MCR increases with water content and with temperature (Figure 112E/F). The corrosivity of the dry IL is very low, even at 120 °C, and dramatically increases with water. No material deposition is observed for this system, suggesting that the corrosion products are soluble in acidic media.

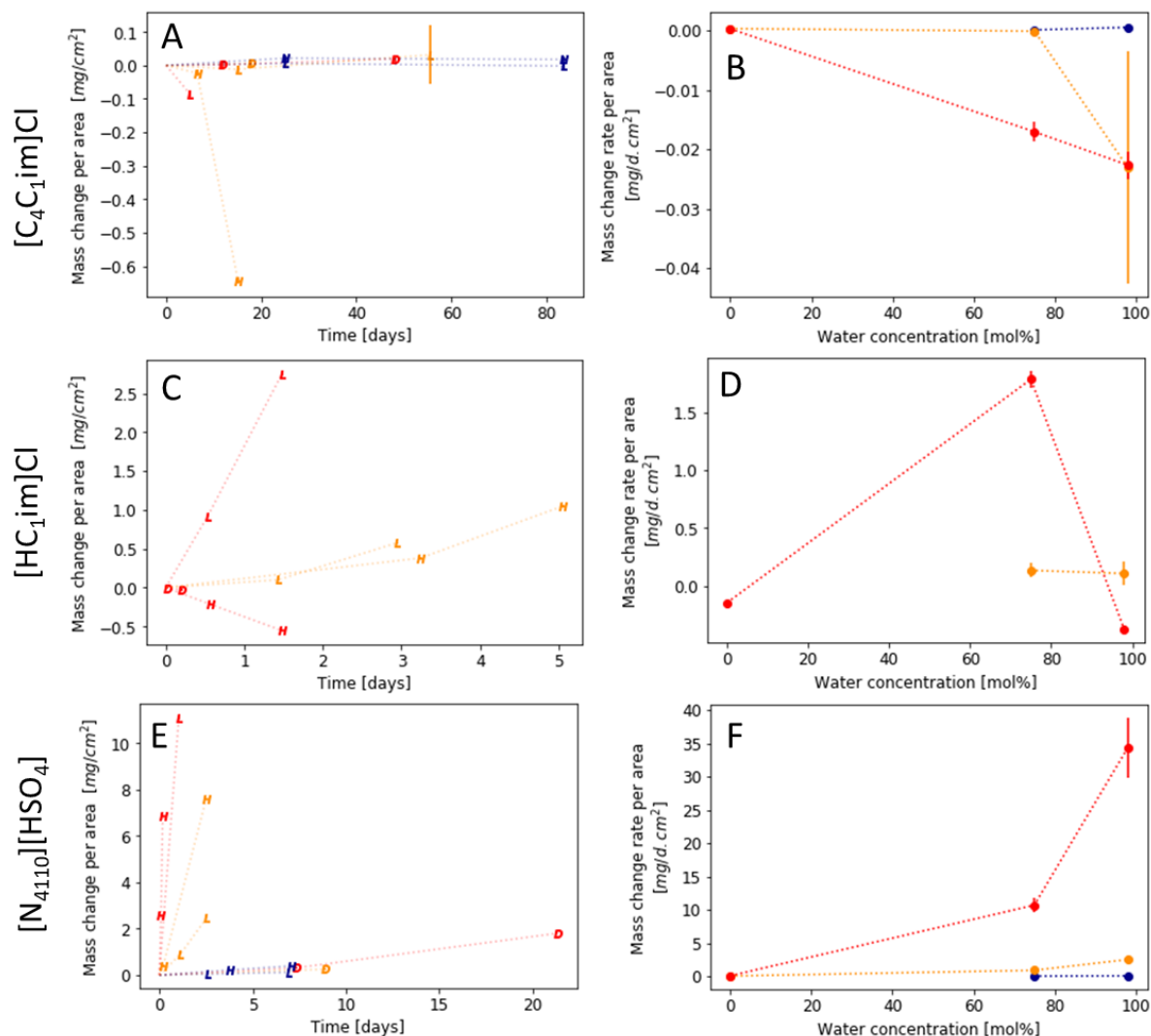


Figure 112. Mass change rates for aluminium exposed to corrosive media. Left figures (A, C and E): Mass change per area as a function of time. Right figures (B, D and F): Mass change rates as a function of water content calculated from the average of the MCRs. Legend, D: dry, L: low water case, H: high water case, W: water. Colours: Blue 20 °C, orange 70 °C and red 120 °C. Lines have been added to guide the eye.

A5.1.2. XRD

XRD was performed on selected samples. The pattern of the aluminium sample pre-exposure is shown in Figure 113A. Only four peaks can be observed in the diffraction pattern corresponding to the following signals: 200 (44.5°), 220 (65.2°), 311 (78.3°) and 400 (99.4) (reference code: 00-001-1180). No changes in the diffraction pattern were observed to

samples exposed to different corrosive media except for the samples exposed to water at 120 °C which showed a white powder identified as Al(OH)₃ (reference code: 00-012-0460) (Figure 113F).

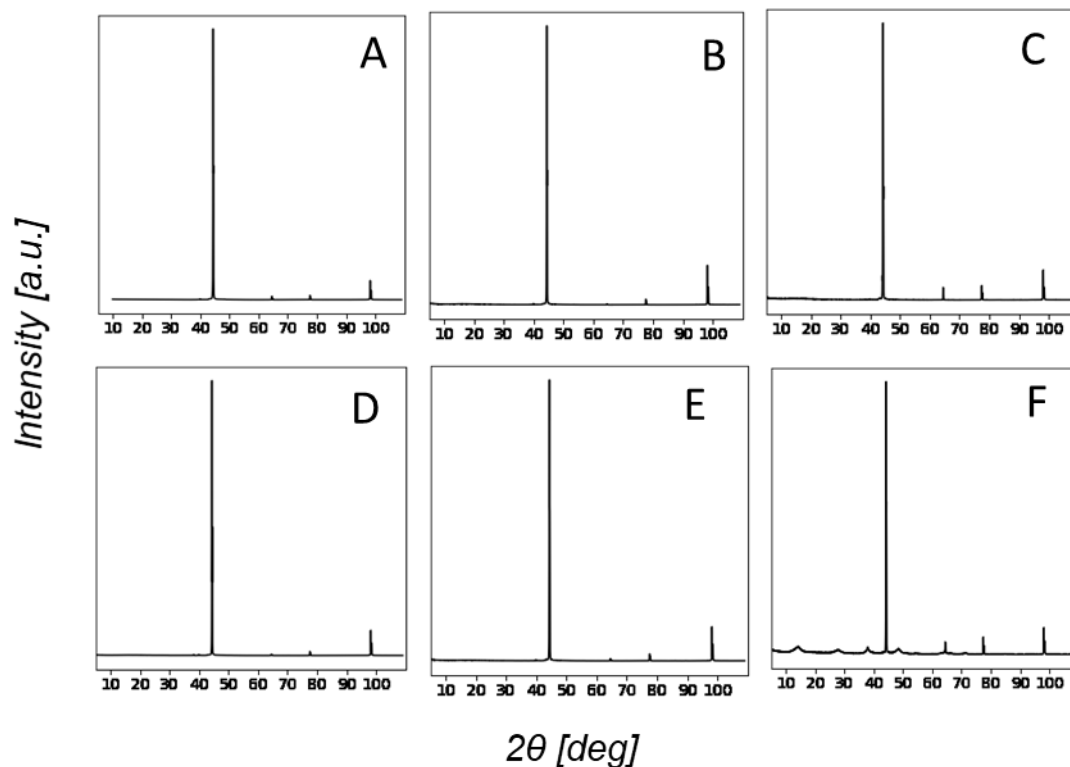


Figure 113. XRD patterns from aluminium samples exposed to corrosive media. [A] Unexposed metal sample. [B] [N₄₁₁₀][HSO₄], 120 °C, dry, 7.34 d. [C] [C₄C₁im]Cl, 120 °C, 75 mol% 5.05 d. [D] [C₄C₁im]Cl, 120 °C, 75 mol%, 3.25 d [E] [HC₁im]Cl, 70 °C, 98 mol% 5.05 d. [F] H₂O, 120 °C, 0.6 h.

A5.1.3. XRF

XRD measurements performed on Al samples are summarized in Table 38. Chlorine content was found in samples exposed to [C₄C₁im]Cl and [HC₁im]Cl, suggesting the deposition of chloride-containing species, consistent with the negative MCR. Sulphur was not detected in samples exposed to [N₄₁₁₀][HSO₄], further confirming the anodic dissolution and suggesting no product formation on the surface of the metal.

Table 38. XRF results summary for aluminium.

Solvent	Observations
-	Al : 99.961% (Traces: La, Ti, P, Ca)
H ₂ O	Samples showed traces of S, due to contamination. Cl found in the samples. The traces of S and P increased except for sample (70 °C, dry, 18 d).
[C ₄ C ₁ im]Cl	Samples (120 °C, 75 mol%, 5.05 d), (120 °C, 98 mol% 19.9 d) and (70 °C 98 mol% 15.1 d) showed significant amounts (>1%). Dry Samples (120°C, dry, 18 d) and (70°C, dry, 18 d) did not show significant amounts detected.

Solvent	Observations
[HC _{1im}]Cl	Significant Amount of Cl in samples with high water content 98 mol% at 70 °C and 120 °C.
[N ₄₁₁₀][HSO ₄]	No significant changes. Sulphur content did not increase.

A5.1.4. SEM

SEM and SEM/EDX results for selected aluminium samples exposed to corrosive media are given in Figure 114 to Figure 118. SEM images for Al exposed to [N₄₁₁₀][HSO₄] were not studied as the MCR for these systems were positive, which means that material was dissolving into the media with no material deposition, confirmed by XRF and XRD.

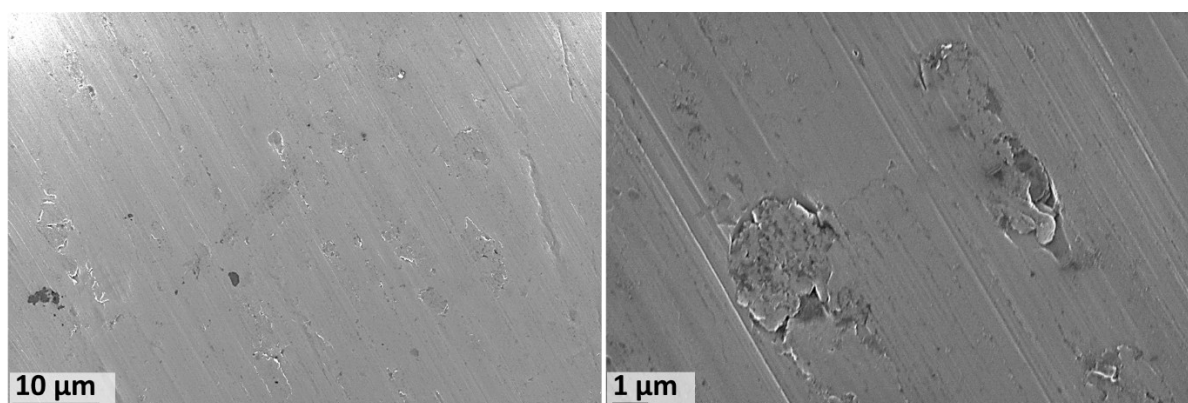


Figure 114. SEM Images obtained for a cleaned but untreated Al sample.

Whilst samples exposed to [HC_{1im}]Cl with high water content showed the presence of Cl (XRF); SEM/EDX (Figure 117) shows no evidence of crystalline structures, nor suggestions from the XRD diffraction patterns. The presence of Cl could originate from traces of IL remaining in the samples, or from very few crystals (thin layer) with an undetectable XRD pattern due to either insufficient material, a similar diffraction pattern to Al or amorphous material with no diffraction patterns. However, SEM images revealed that there are morphological changes of the Al surface exposed to [HC_{1im}]Cl SEM images, including zones with cracks and heavily attacked zones forming sponge-like structures.

The surface of the aluminium samples exposed to chloride-containing ILs exhibit cracks that cover the entire surface (Figure 115 to Figure 117). This is consistent with reports of Al exposed to HCl or NHO₃ aqueous solutions³⁹⁵. This is not observed when Al is exposed to H₂SO₄ aqueous solutions³⁹⁵.

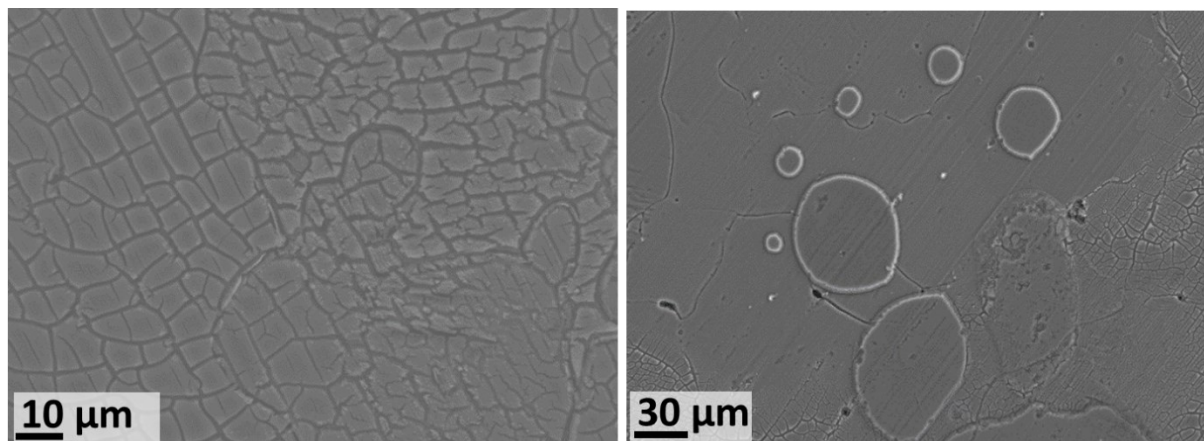


Figure 115. SEM images of Al exposed to [HC₁im]Cl (70 °C, 98 mol% and 1 d).

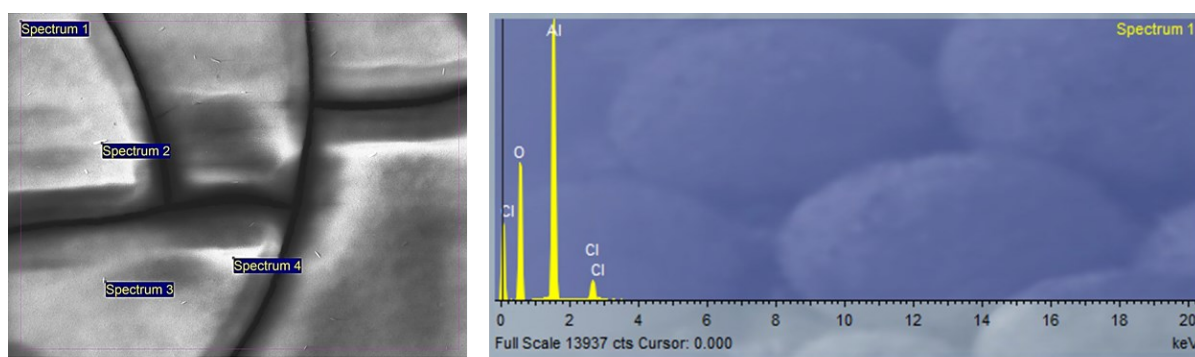


Figure 116. SEM/EDX images of Al exposed to [C₄C₁im]Cl (70 °C, 98 mol% and 15.10 d). EDX atomic ratio O:Al:Cl (30.9:11.4:1.0) and O:Zn = 2.7.

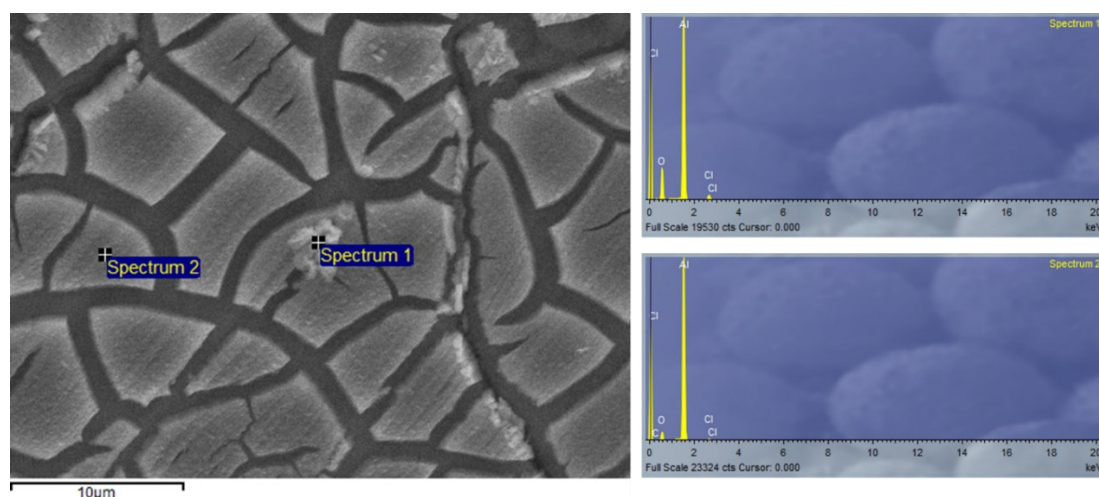


Figure 117. SEM/EDX image 1 of Al exposed to [HC₁im]Cl (70 °C, 98 mol% and 1 d). EDX atomic ratio O:Al:Cl (35.1:27.6:1.0) and O:Zn = 1.3 for spectrum 1 and (47.8:95.1:1.0) and O:Zn = 0.5 for spectrum 2.

The samples exposed to DI water clearly showed the formation of a white powder over the surface, suspected to be Al(OH)₃ from the XRD diffraction patterns. Figure 118 shows clear micrometre-sized crystals.

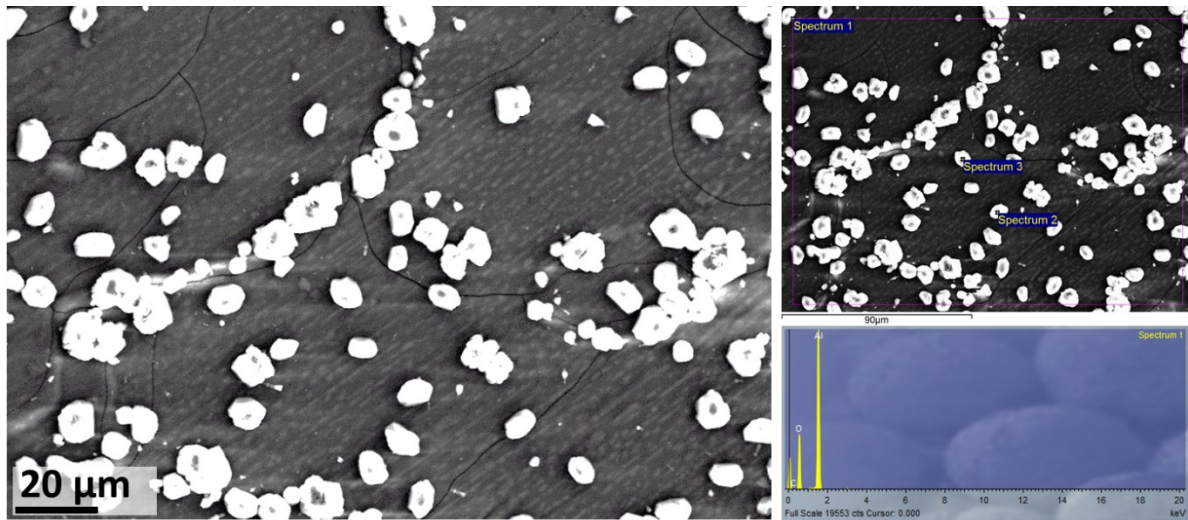


Figure 118. SEM/EDX image 2 of aluminium exposed to H₂O (70 °C and 4.50 d). EDX atomic ratio is O:Al = 2.03.

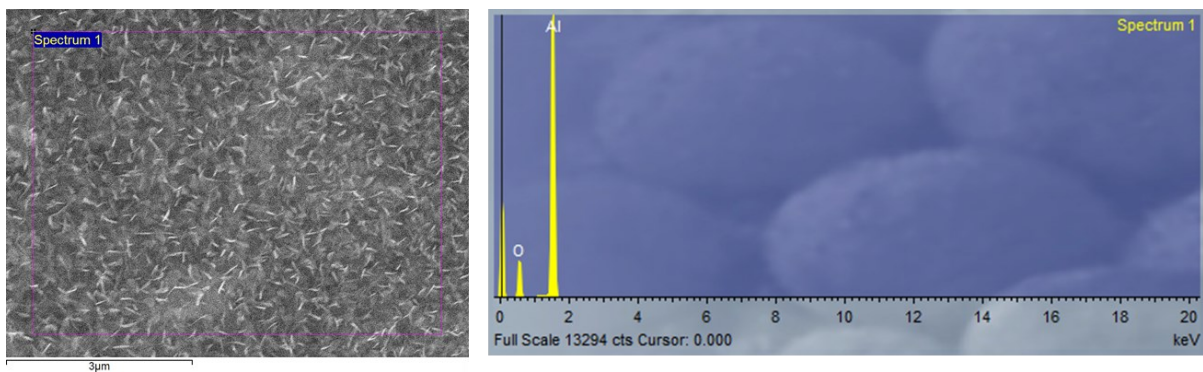


Figure 119. SEM/EDX image 2 of aluminium exposed to H₂O (70 °C and 4.50 d). EDX atomic ratio O:Al = 1.

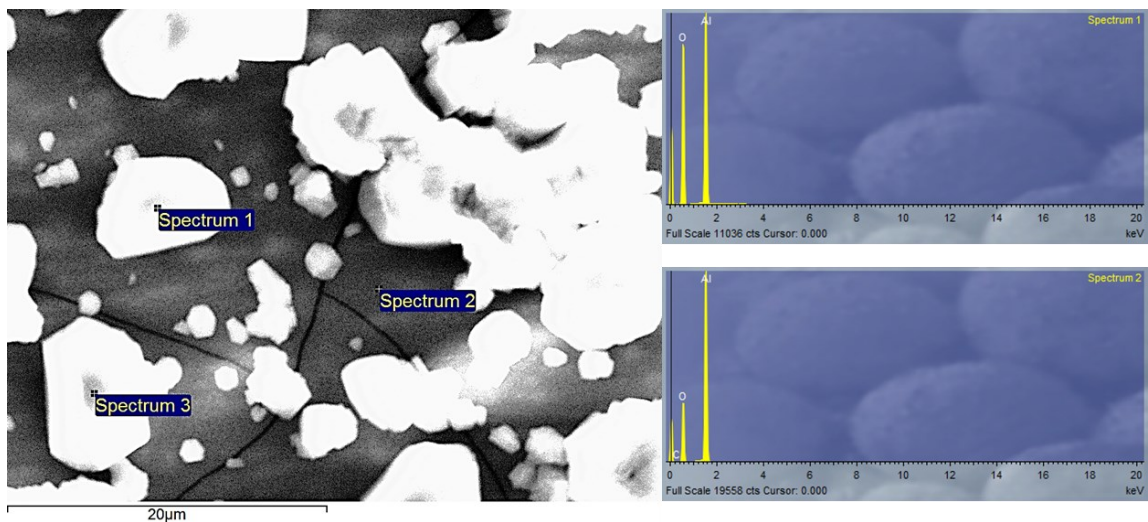


Figure 120. SEM/EDX images of Al exposed to H₂O (70 °C and 4.50 d). EDX atomic ratio is O:Al for spectra 1 and 3 is 3.2 ± 0.5 and for spectrum 2 is 1.9.

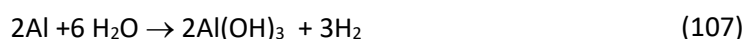
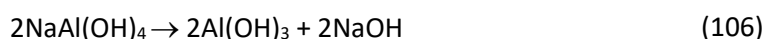
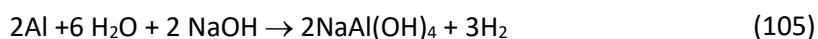
The mol ratio of O:Al is 1.5 in Al₂O₃ and 3 in Al(OH)₃. In the EDX spectrum of the micrometre-scale crystal shown in Figure 120 has O:Zn ratio of 3.2 ± 0.5 , suggesting that the large crystals are composed of Al(OH)₃. The regions without apparent crystals (Figure 118 to Figure 120),

showed a reduced O:Al ratio (1.9), which could mean whether the formation of the oxide form or less surface coverage by Al(OH)₃ leading to stronger Al signals.

A1.1.1. Overall considerations

Since pure aluminium is a highly electronegative metal, it is susceptible to corrosion. However, Al and its alloys are usually well protected by a dense oxide layer formed on their surface. When a fresh surface of aluminium is exposed to air or water, a surface film of aluminium oxide immediately begins to form and grow rapidly to form a stable film, with a thickness of about 5 nm (50Å) (when oxidized in air)¹⁴⁷. Thus, aluminium-based materials are normally recognized to have good resistance to corrosion³⁹³. Such resistance can be a great advantage for its use as construction materials.

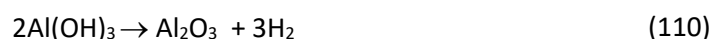
As shown previously, the corrosion processes of Al in water generates Al(OH)₃ which is consistent with data available in literature³⁹⁴. The most common reactions between Al and water have been investigated in alkaline media and neutral media. Hydroxide ions (OH⁻), in strongly alkaline solutions, are able to destroy the protective oxide layer on the aluminium surface forming Al(OH)₃. Therefore, aluminium and its alloys readily dissolved in the alkaline environment even at room temperature, resulting in hydrogen production. Among different alkalis, sodium hydroxide (NaOH) is the most commonly encountered alkali with the following series of reactions:



The two steps shown in the above (Eqs 105 and 106), were suggested to be involved in the hydrogen generation process *via* Al corrosion in alkaline media. NaOH depleted for the hydrogen evolution in the first step (Eq. 105) will be regenerated through the NaAl(OH)₄ decomposition in the second step (Eq. 106). Therefore, only water is consumed during the whole process if the reaction is properly controlled. Adding the steps shown in Eqs. 105 and 106 together yield the overall reaction as expressed given in Eq. 107, which also correspond to the direct reaction of Al and water in neutral conditions without the help of alkalis^{394,396,397}. Calculated from (Eq. 107), the theoretical hydrogen yield of this reaction in stoichiometric ratios is only 3.7 wt%, which is higher than other metals, such as Mg and Zn (3.3 wt% and 2.4 wt%, respectively)³⁹⁴. Another reaction between Al and water at low temperature reported in

the literature is given in Eq. 108 ³⁹⁷ whereas it has been reported that the reaction of Al with water, or steam, at high temperatures yields alumina (Eq. 109) ³⁹⁴.

It is known that surface passivation in neutral water occurs much more easily and the metal activity with water is extremely low.



Visual inspection of the corroded Al samples exposed to water revealed localised corrosion rather than uniform corrosion. This can be explained by the Pourbaix diagrams, where thermodynamics show that aluminium oxide films are stable in a pH range of 4 to 9 ¹⁴⁷. Outside this range, the aluminium oxide film dissolved rapidly in strong acids and bases and Al is then attacked uniformly ¹⁴⁷.

Alumina (Al_2O_3) exists in a wide variety of polymorphs, being the most stable the α - Al_2O_3 (corundum) ³⁹⁸. Aluminium hydroxides are the precursors of metastable aluminas which are used in many applications in industrial catalysis, such as γ - Al_2O_3 . Aluminium hydroxides exhibit the generic formula ($\text{Al}_2\text{O}_3 \cdot x\text{H}_2\text{O}$) where x stands for the degree of hydration. The extreme value, $x=0$, corresponds to the alumina's' stoichiometry. Depending on the degree of hydration x, different types of hydroxides are distinguished. Experimentally, at least six different aluminium hydroxides are well-identified:

- Aluminum trihydroxides $\text{Al}(\text{OH})_3$, for which $x=3$, are gibbsite (γ - $\text{Al}(\text{OH})_3$), bayerite (α - $\text{Al}(\text{OH})_3$), and nordstrandite.
- Aluminum monohydroxides AlOOH , for which $x=1$, are boehmite (γ - AlOOH) and diaspore (α - AlOOH).
- A more dehydrated species is tohdite ($5\text{Al}_2\text{O}_3 \cdot \text{H}_2\text{O}$), corresponding to $x=0.2$.

Gibbsite, bayerite, diaspore and boehmite (the major constituent of many bauxite minerals) are natural solids ³⁹⁹. The transformation of aluminium hydroxides to alumina according to Eq. 110 have been reported in literature ^{398,399}. It has been shown that the variations of the Gibbs free energy are negative for all hydroxides, which is consistent with the fact that, at the earth's surface, Al is found in the form of hydroxides or oxyhydroxides. The dehydrated species

become stable only at high temperatures. Furthermore, the higher the degree of hydration, the more stable is the polymorph³⁹⁹.

A5.1.4.1 Al corrosion in chloride media

It is generally accepted that chloride ions have the highest power of penetration into natural oxide films, because they are small and very mobile and because its dimension is close to that of oxygen. Chlorides (Cl^-), as well as other halogens, can enhance corrosion of aluminium in water, while sulfates ($[\text{SO}_4]^-$) might or might not enhance Al corrosion in water¹⁴⁷. Chlorides may substitute oxygen atoms in the alumina network. This leads to a decrease in the film's resistivity, which facilitates the release of aluminium atoms that diffuse into the solution⁴⁰⁰.

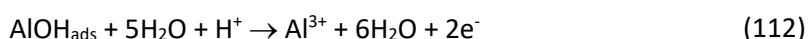
For aqueous systems, the aggressivity of a medium with respect to metals in general, and aluminium in particular, depends to a large extent on its chloride and sulfate concentration. It has been reported that the penetration power of a natural oxide film by anions, in particular chlorides, the density and depth of pitting generally increases with increasing chloride concentration⁴⁰⁰. In ionic liquid media, as shown in Figure 26, the mobility of the anions decreases with increasing ionic liquid concentration, and may explain why strong negative mass changes were observed in the high water content cases.

Some work claims that the action of chlorides on aluminium corrosion is independent of the action of the associated cation (or cations, if several are present). At a given chloride concentration, there is no perceptible difference between the action of a solution of potassium chloride (KCl), sodium chloride (NaCl) or ammonium chloride (NH_4Cl)⁴⁰⁰. It needs to be tested if this holds true for IL containing chlorides in dilute environments. Another study investigated the effects of sodium chloride (NaCl), potassium chloride (KCl) and barium chloride (BaCl_2) on the Al-water reaction. It was shown that the kinetics of hydrogen production from Al was increased in presence of BaCl_2 in comparison with KCl and NaCl, but cumulative hydrogen production was the highest for NaCl. In this process, the Al was milled in the presence of the salts. Al foils or powders without milling yielded low kinetic rates but was increased with ball milling and salt addition³⁹⁷. These results must be linked to the physical modification of the Al sample rather than the chemical action of chlorides.

In general, aeration and oxygenated conditions will accelerate Al corrosion. Conversely, deaeration will retard the corrosion¹⁴⁷. However, it has been reported that oxygen dissolved in water has less influence on aluminium corrosion than on steel corrosion⁴⁰⁰

[HC₁im]Cl is obtained by the reaction of HCl with methylimidazole. The thermal decomposition temperature of [HC₁im]Cl determined by TGA was reported as 157.2 °C, likely forming the imidazole and hydrochloric acid (HCl) ⁴⁰¹. Mass loss of Al in pure HCl depends on the acid concentration and it has been quantified for concentrations ranging from 1.5 to 5 M ⁴⁰². Even at the lowest concentration, for a test duration of 160 min, Al has an extraordinarily high corrosion rate of 487 g/m²h (1580 mm/y), which shows that this material cannot be used with HCl. It is known that amines can inhibit aluminium corrosion in HCl, so therefore it is expected that corrosion in [HC₁im]Cl will be less than in the pure acid. In a study with 6 amines, it was established that the inhibition capacity depends on the concentrations of the inhibitor and the acid, with an efficiency reported as: Methylamine < ethylamine < propylamine < butylamine < allylamine < benzylamine ⁴⁰². From these trends, it can be seen that the protective effect increases with the size of amine. Similar trends have been observed for alkyimidazolium chlorides [C₈C₁im]Cl > [C₆C₁im]Cl > [C₄C₁im]Cl ⁴⁰³. If this behaviour holds true for ionic liquids exposed to Al it would be expected that larger alkyl chains in the cation moiety of the ionic liquid, the lower the corrosion rates. Further, other ionic liquids have been proposed to act as corrosion inhibitors for the corrosion of Al in HCl, such as tetradecylpyridinium bromide ⁴⁰⁴

In aqueous media, it has been reported that the corrosion of aluminium depends on the concentration of anions in solution. A general mechanism for the dissolution of Al reported in literature ⁴⁰³ is as follows:



It has been reported that the controlling step in the aluminium dissolution is the complexation reaction between the hydrated cation and the anion chloride (Eq. 114). The methylimidazolium contains a nitrogen atom in the heteroaromatic ring that is protonated from the neutralization reaction with HCl. As discussed in section 3.2.7, protonated imidazolium ring, such as [HC₁im]Cl, and positively charged imidazolium rings, such as in [C₄C₁im]Cl, can adsorb in metallic surfaces via a diversity of interactions to inhibit corrosion. The adsorption of imidazolium rings on the aluminium surface would protect the surface against the water molecules, blocking the formation of AlOH_{ads} (Eq. 111). Thus both the oxidation reaction of

AlOH_{ads} to Al^{3+} as shown by step (Eq. 112) and the complexation reaction between the hydrated cation $[\text{AlOH}]^{2+}$ species which are formed in step (Eq. 113) and chloride ions can be prevented (Eq. 114) ⁴⁰³.

A5.1.4.2 Al corrosion in sulfate media

The corrosion rates of Al in H_2SO_4 in various concentrations of sulfuric acid at various temperatures under oxygen flow have been reported in the literature ⁴⁰². At 50 °C and for acid concentrations of 6 wt%, 50 wt% and 96.5 wt% is 4.67, 22.40, 44.60 mm/y respectively ⁴⁰². In another study comparing Al (99.32%) exposed to different acids, it has been shown that the corrosion rates depends on acid concentration and exposure time, and there is not a clear trend on which acid is more severe towards aluminium, however, the order of magnitude of HCl and H_2SO_4 are similar ³⁹⁵. The corrosion of Al in sulfuric acid exhibits comparable or lower rates than in hydrochloric acid probably due to the coordinating nature of chlorides, as explained above (Eq. 114). Based on the results from mineral acids, one would expect that the corrosion rate for Al exposed to protic ILs to be higher (or similar) in $[\text{HC}_{1\text{im}}]\text{Cl}$ than $[\text{N}_{4110}][\text{HSO}_4]$, however, this is not the case. $[\text{HC}_{1\text{im}}]\text{Cl}$ is only slightly acidic, and its solutions in water have a pH ~ 5 at 1 wt%, whereas the same concentration of $[\text{N}_{4110}][\text{HSO}_4]$ yields to very acidic solutions of pH ~ 1.5 (section 2.2.4). Acidic protons are required for the oxidation reaction of AlOH_{ads} to Al^{3+} as shown by step (Eq. 112). Here, the coordinating effect of Cl^- (Eq. 114) is outweighed by the acidity of the hydrogen sulfate based ILs. Exposure to aqueous $[\text{N}_{4110}][\text{HSO}_4]$ results in positive mass change even at low temperatures, showing that these solutions are able to destroy the protective AlO_2 layer on the aluminium surface, yielding to active dissolution of Al. This layer is stable in dry ionic liquid and the attack proceeds at very low rates, even at high temperatures.

A5.1.4.3 Al categorization system

Regarding the classification system, Al and water will be classified as type-2. Other examples of Al oxidation in water includes a study in which massive aluminium samples were oxidized by sub and supercritical water with the formation of $(\text{AlOOH})_n$ and $(\text{Al}_2\text{O}_3)_n$ nanoparticles. Predominantly large (300 – 400 nm) $\alpha\text{-Al}_2\text{O}_3$ particles were formed when supercritical water was injected into a reactor with aluminium. Smaller (20–50 nm) $\gamma\text{-Al}_2\text{O}_3$ particles were also observed in samples oxidized by water vapour. The attack proceeded without the formation of protective oxide films ⁴⁰⁵. For this reason, the Al samples exposed to water will be classified

as type-2. The H₂SO₄ in aqueous media will be classified as type-3 metals, whereas in dry ionic liquids will be classified at type-0.

No significant colour change was appreciable in the solutions and neat ILS after the immersion tests, which is in accordance with other studies ⁴⁰⁶. The general aspect of the coupons is summarised in

Table 39, as well as their classification system and corrosion types.

Table 39. Summary of the classification system and corrosion type for aluminium exposed to corrosive media. Corrosion types: NC: no corrosion, PC: pitting corrosion, USC: uniform surface corrosion and NUSC: non-uniform corrosion. Section 3.4.

	Solvent →	[C ₄ C ₁ im]Cl			[HC ₁ im]Cl			[N ₄₁₁₀][HSO ₄]			[C ₄ C ₁ im][NTf ₂]	Water
	Water Content [mol fraction] →	Dry	0.75	0.98	Dry	0.75	0.98	Dry	0.75	0.98	Dry	1
	Temperature [°C] ↓											
Classification System (Section 3.4)	20	0	0	0					3	3		2
	70	0	0	2		3	3	0	3	3	0	2
	120	0	2	2	0	3	2	0	3	3		2
	150										0	
Corrosion Type	20	NC	NC	NC					USC	USC		NUSC
	70	NC	NC	NUSC		NUSC	NUSC	NC	USC	USC	NC	NUSC
	120	NC	NUSC	NUSC	NC	NUSC	NUSC	NC	USC	USC		NUSC
	150										NC	

A5.1.4.4 Al corrosion in other ILS

IL corrosion of Al alloys by other ILS studied by immersion corrosion tests have been reported in the literature ^{163,406}, addressing the corrosion of aluminium alloy (ASTM 2011) in [C₂C₁im][BF₄], [C₆C₁im][BF₄], [C₈C₁im][BF₄], [C₂C₁im][CF₃SO₃], [C₂C₁im][TOS], [C₆C₁im][PF₆] and [C₄C₁py][NTf₂]. Even though corrosion rates were not quantified, from the information provided in the publication, Al in [C₂C₁im][BF₄], [C₆C₁im][BF₄], [C₈C₁im][BF₄], [C₂C₁im][TOS], [C₆C₁im][PF₆] and [C₄C₁py][NTf₂] can be classified as type-0, at room temperature and dry, as the mass loss is very small. Under these conditions, it was reported that [C₂C₁im][CF₃SO₃] formed aluminium oxide. Also, fluorine and sulphur, present in the anion, were also detected, possible types are type-1, type-2 or type-2S, however, from the information provided this study is not possible to assign a category. Al experienced positive weight loss when exposed [C₂C₁im][BF₄] and water, therefore it a type-3 at room temperature ⁴⁰⁶. In another study with the same ILS, it was reported that there was no weight loss or corrosive attack when steel balls or aluminium disks are immersed for 100 h in a base oil containing 1 wt% IL additives ¹⁶³. In this study, it was reported that corrosion on the aluminium surface (ASTM 2011) only took place after 100 h immersion at room temperature in [C₂C₁im][BF₄] 1 wt% solution in water, with the formation of a white precipitate containing oxygen and fluorine. Addition of water to [C₂C₁im][BF₄] increases corrosion due to hydrolysis of the tetrafluoroborate anion, which

causes hydrogen evolution and formation of aluminium fluoride (black layer). IL corrosion in IL have been also studied through electrochemical methods, but will not be discussed here.

A5.2. Copper

Copper (Cu) is a chemical element with an atomic number of 29. It is a soft, malleable, and ductile metal with very high thermal and electrical conductivity. A freshly exposed surface of pure Cu has a pinkish-orange colour. Cu is used as a conductor of heat and electricity, as a construction material, and as a constituent of various metal alloys, such as sterling silver used in jewellery, cupronickel used to make marine hardware and coins, and constantan used in strain gauges and thermocouples for temperature measurement. Cu is one of the few metals that can occur in nature in a directly usable metallic form (native metals) ⁴⁰⁷.

A5.2.1. Corrosion rates

The results for the mass change of Cu samples exposed to different corrosion media (water-soluble ILs) are given in Figure 121. Corrosion results in [C₄C₁im][NTf₂] are given in section 3.5.2.

When Cu is exposed to [C₄C₁im]Cl solutions, the corrosion rates are very small in the residual water case and increase with water content. The maximum MCR was observed at 98 mol% for samples exposed at 20 and 70 °C whereas the samples exposed at 120 °C showed a minimum MCR at high water content and a maximum at 75 mol% (Figure 121A/B).

The attack was extreme when copper was exposed to [HC₁im]Cl, with a maximum attack in dry conditions. In this IL the MCR decreases with increasing water content (Figure 121C/D).

The MCR of copper exposed to [N₄₁₁₀][HSO₄], is in the same order of magnitude that in [C₄C₁im]Cl, following similar trends. In this IL, the attack in dry conditions was small and increased with water content, however at 120 °C and 75 mol%, there was a drop in the MCR (Figure 121E/F).

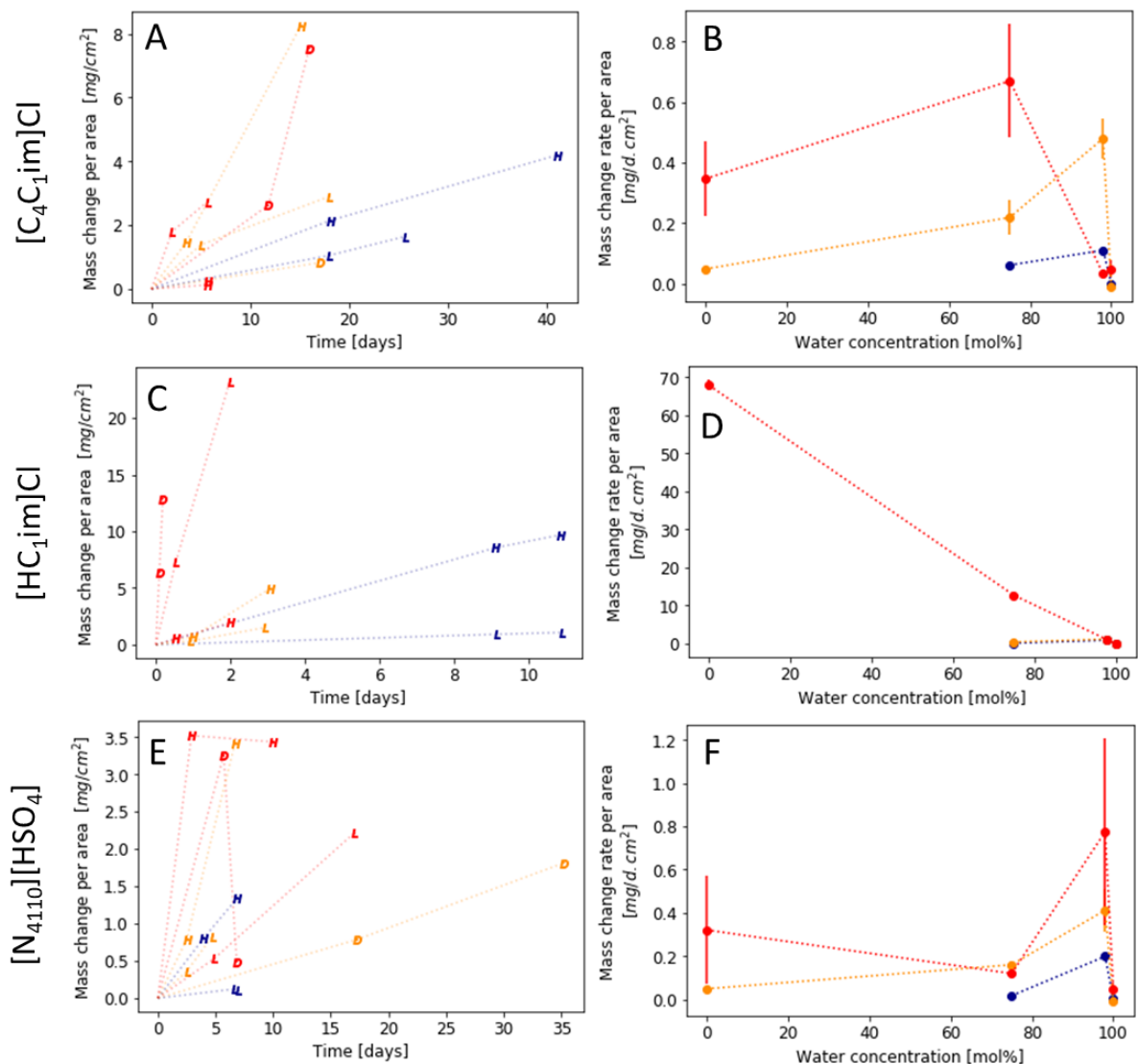


Figure 121. Mass change rates for Cu exposed to corrosive media. Left figures (A, C and E): Mass change per area as a function of time. Right figures (B, D and F): Mass change rates as a function of water content calculated from the average of the MCRs. Legend, D: dry, L: low water case, H: high water case, W: water. Colours: Blue 20 °C, orange 70 °C and red 120 °C. Lines have been added to guide the eye

A1.1.2. XRD

XRD was performed on selected samples. The pattern of the copper sample pre-exposure is shown in Figure 122A. Only four peaks can be observed in copper corresponding to the following signals: 111 (43.3°), 200 (50.5°), 220 (74.1°) and 311 (89.9°) (reference code: 00-002-1225). No changes in the diffraction pattern were observed to all samples except for the samples exposed to water at 70 °C which showed the formation of a black layer identified as CuO (Figure 122D). 2 signal characteristics to CuO (tenorite, reference code: 00-002-1040), 002 (35.6°) and 111 (38.8°) can be seen in Figure 122D, an unidentified signal was seen at 32°.

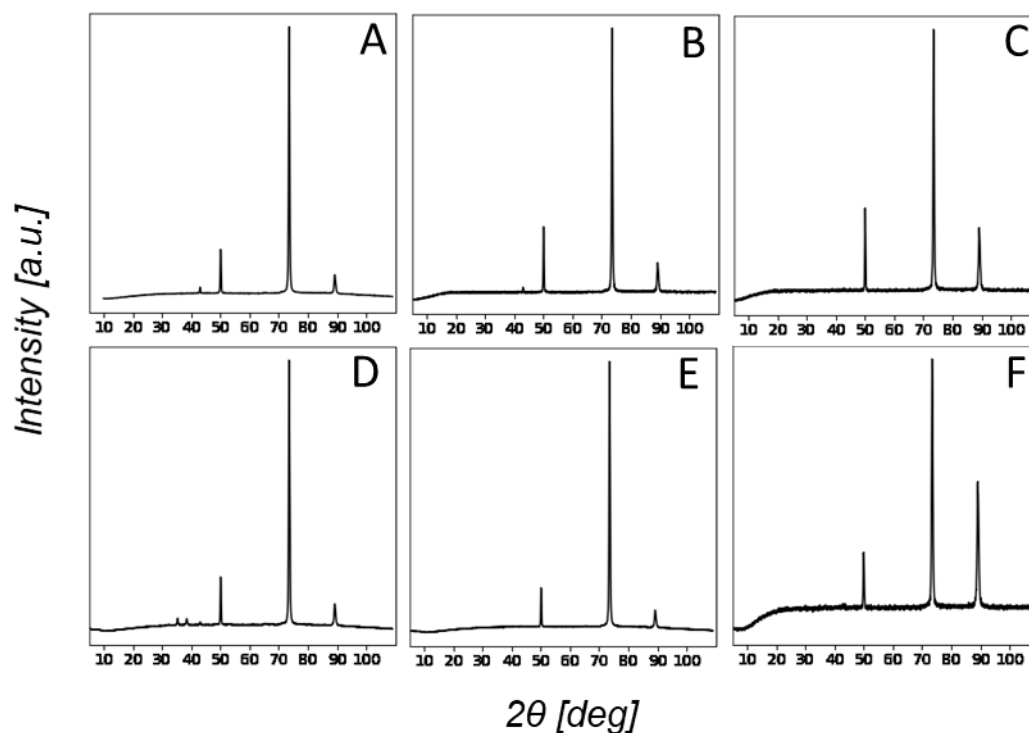


Figure 122. XRD patterns from copper samples exposed to corrosive media. [A] Unexposed metal sample. [B] $[C_4C_{1im}]Cl$, 70 °C, 75 mol% and 18 d. [C] $[N_{4110}][HSO_4]$, 120 °C, 75 mol% and 17 d. [D] Water, 70 °C and 4.5 d. [E] $[C_4C_{1im}]Cl$, 70 °C, 75 mol% and 5.0 d. [F] $[HC_{1im}]Cl$, 75 °C and 13 h.

A1.1.3. XRF

Table 40 shows the XRF results summary for copper. Chloride was detected in samples exposed to $[C_4C_{1im}]Cl$, suggesting that Cl-containing species are present in the surface of the metal. When exposed to $[HC_{1im}]Cl$, only 1 sample showed an increase in the chloride content. No changes were observed in the chemical composition of the metal when exposed to $[N_{4110}][HSO_4]$, which suggest that S-containing species attached to the surface are present.

Table 40. XRF results summary for Cu.

Solvent	Observations
-	Cu: 99.85% (Traces of Al, Si, Tb)
H ₂ O	Samples showed traces of S, due to contamination.
$[C_4C_{1im}]Cl$	Increased in the Cl content: Significant change when exposed at 20 °C, 98 mol% and 18.10 d (6.2%). Slight increase: when exposed at 70 °C, 98 mol% and 15.10 d and at 120 °C, 75 mol% and 2.10 d and 98 mol% and 5.67 d. Not detected in samples exposed to 20 °C, 75 mol% and 25.71 d and at 120 °C, dry and 12 and 16 d.
$[HC_{1im}]Cl$	No significant changes. 1.8% detected in the sample exposed at 120 °C, 98 mol% and 2.00 d.
$[N_{4110}][HSO_4]$	No significant changes

A1.1.4. SEM

The SEM images of the unexposed copper are given in Figure 123. When copper is exposed to $[C_4C_{1im}]Cl$ medium, it can be seen a clear attack on the surface leading to a sponge-like structure with sharp ends and cavities, with the formation of bipyramidal crystals (Figure 125 to Figure 127). It can be seen from Figure 126, that this attack does not occur uniformly across the surface, and that there are some zones unaffected. Figure 128 shows the magnified surface of copper exposed to $[N_{4110}][HSO_4]$ solutions, it can be seen that the attack is severe at 70 °C and 98% mol, leading to the same patterns observed in $[C_4C_{1im}]Cl$, while at lower temperature and water content (75 mol%), the surface is attacked but it does not show the same morphological modifications. When exposed to $[HC_{1im}]Cl$, the sponge-like pattern can be seen even at low temperatures (20 °C), which is consistent with the fact that the attack is more severe in this ILs (Figure 129). In the water controls, when copper was exposed at 70 °C, the surface was covered with a flower-like structure identified as CuO (Figure 124).

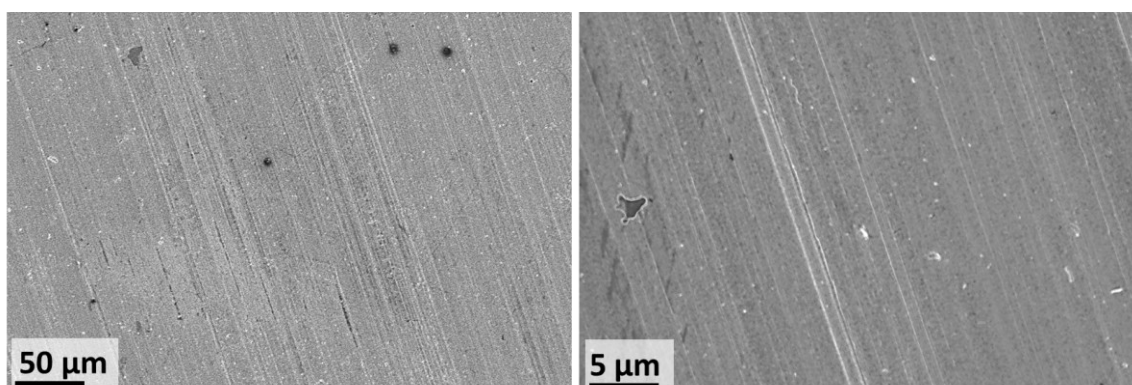


Figure 123. SEM images obtained for a cleaned but untreated Cu sample.

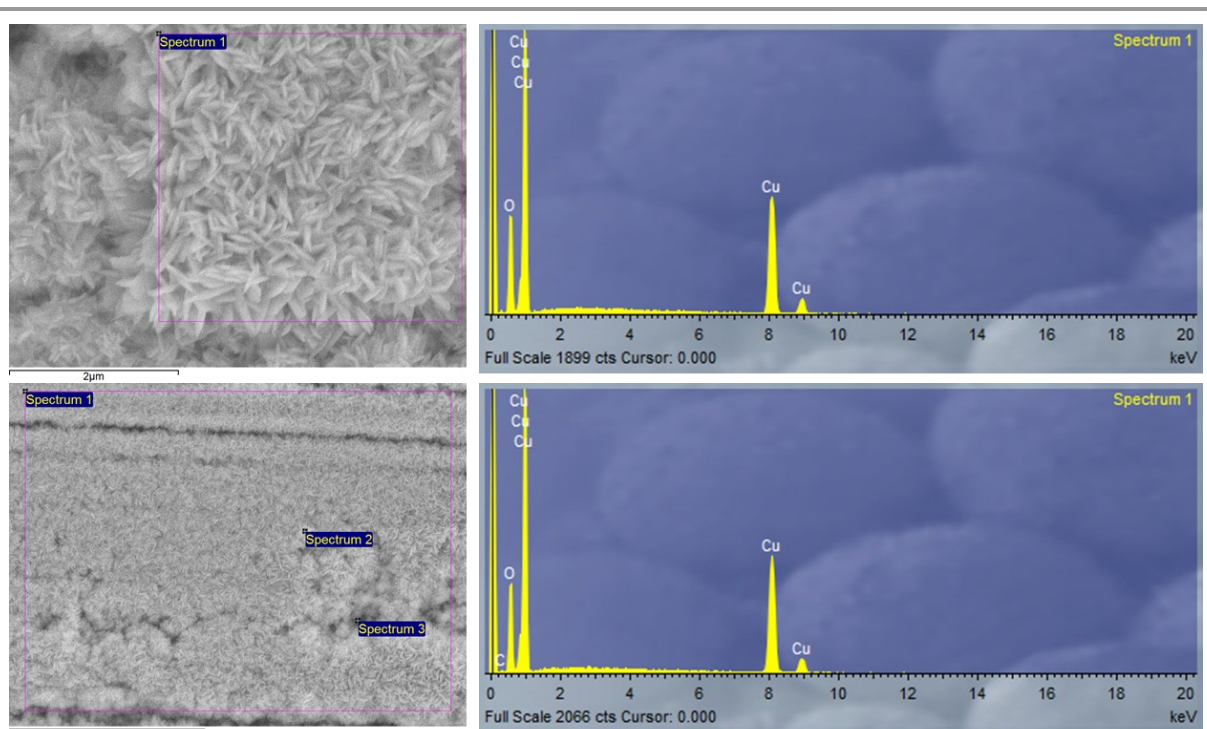


Figure 124. SEM/EDX images of copper exposed to water, 70 °C and 4.5 d. EDX atomic ratio Cu:O 1:0.83 (spectrum 1 – top figure), 1:83 (spectrum 1 and 2 – bottom figure) and 11.2:1 (spectrum 3 – bottom figure).

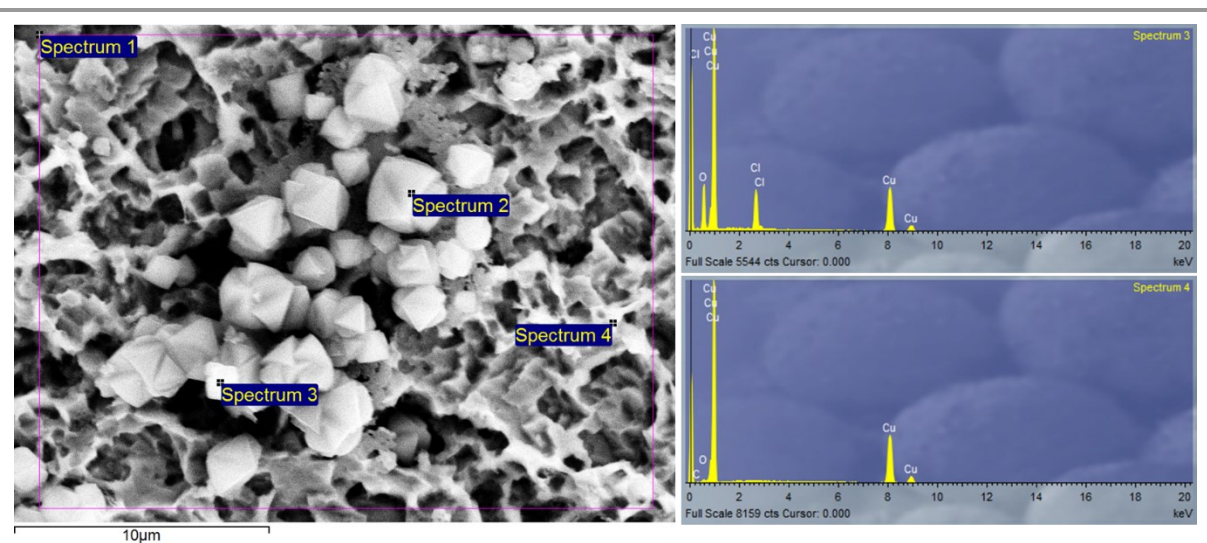


Figure 125. SEM/EDX images of copper exposed to $[C_4C_{1im}]Cl$ 20 °C, 98 mol% and 18 d. EDX atomic ratio Cu:O:Cl 14.9:5.8:1 (spectrum 1), 11.3:4.8:1 (spectrum 2), 3.2:5.7:1 (spectrum 3) and Cu:O 13:1 (spectrum 4, chloride not detected).

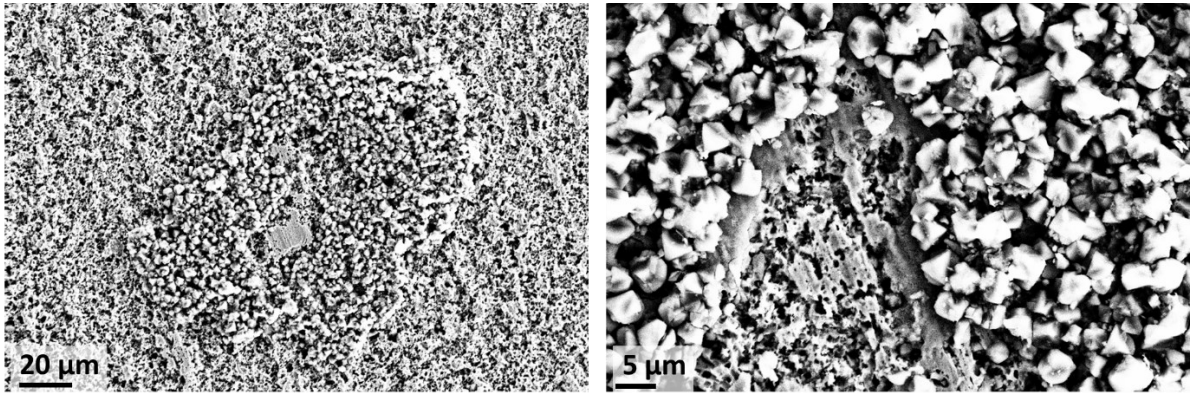


Figure 126. SEM images of copper exposed to $[C_4C_{1im}]Cl$ at 20 °C, 98 mol% and 41 d.

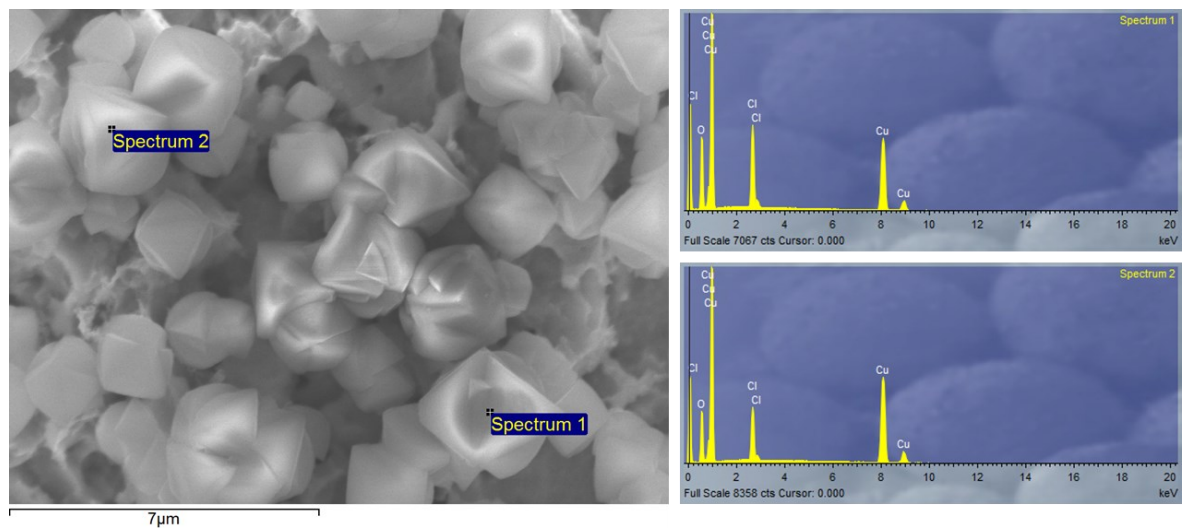


Figure 127. SEM/EDX images of copper exposed to $[C_4C_{1im}]Cl$ at 70 °C, 98 mol% and 15 d. EDX atomic ration Cu:O:Cl 2.7:4.8:1 (spectrum 1) and 4.7:5.0:1 (spectrum 2).

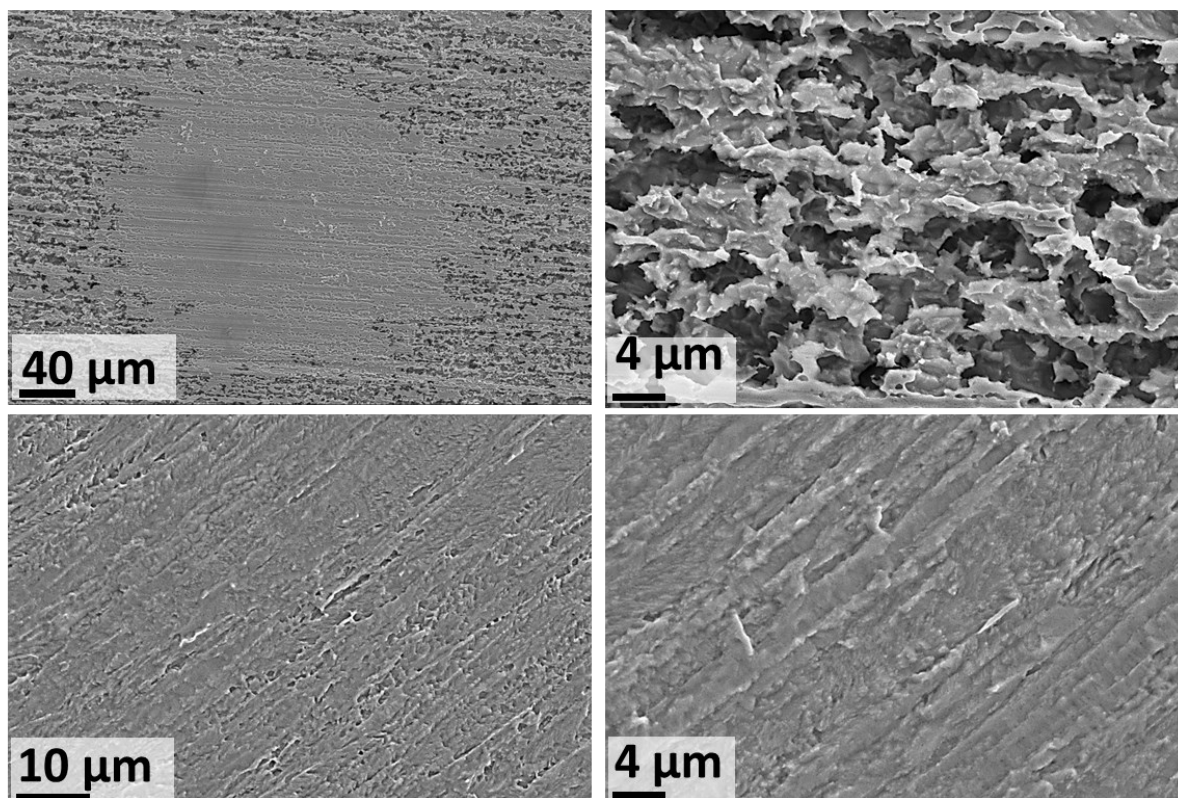


Figure 128. Top figures: SEM images of copper exposed to $[N_{4110}][HSO_4]$ at 70 °C, 98 mol% and 6.7 d. Bottom figures: SEM images of copper exposed to $[N_{4110}][HSO_4]$ at 20 °C, 75 mol% and 18 d.

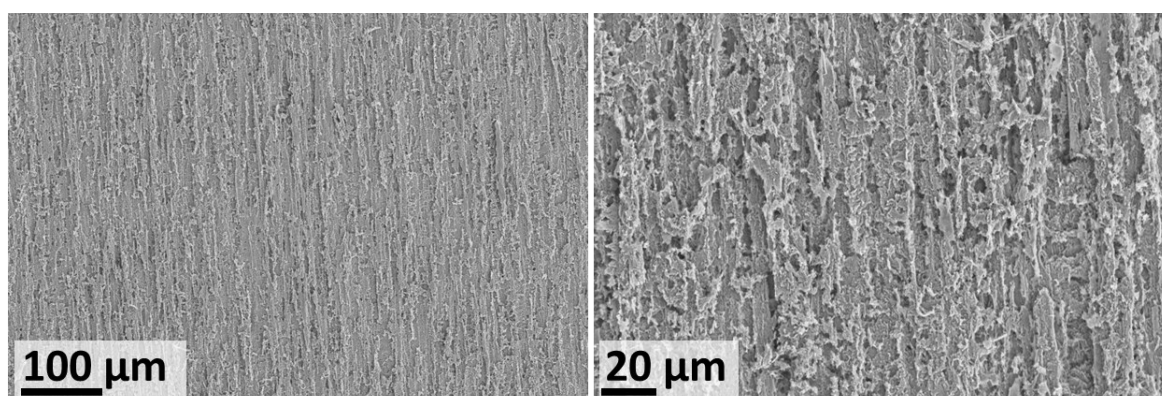


Figure 129. SEM images of copper exposed to $[HC_{1im}]Cl$ at 20 °C, 98 mol% and 11 d.

A5.2.2. Overall considerations

A5.2.2.1 Cu corrosion in chloride media

It is known that the corrosion mechanism of Cu is strongly dependent on the presence of chloride anions. Several corrosion mechanisms of this metal in different chloride containing environments have been reported in the scientific literature ⁴⁰⁸. The main differences among the available models are the descriptions of the initial electro-dissolution reactions of the bare Cu. Three reversible mechanisms have been considered ⁴⁰⁸.



In the reactions (Eqs. 115-116) and (Eq. 117) the cupric chloride forms directly from Cu, while the third set of reactions (Eqs. 118-119) represents the dissolution of Cu to cuprous chloride in the first step. It has been proposed that Cu corrodes in neutral NaCl solutions to form the complex $[\text{CuCl}_2]^-$ according to Eqs. 118. and 119⁴⁰⁷. It is also mentioned in the literature the ability of Cu^+ to undergo disproportionation according to Eq. 120.



Several values for the corrosion rate of Cu in NaCl have been reported in literature calculated by gravimetric methods. The reported corrosion rate of copper exposed to an aerated solution of NaCl 0.5M is 3.4×10^{-5} mm/y⁴⁰⁷. This value was obtained by fitting a straight line to the reported data forced through the origin (8.37×10^{-5} mg/cm².d) and converted to penetration rate. When exposed to $[\text{C}_4\text{C}_1\text{im}]\text{Cl}$ solutions, the attack rates were 0.0250 ± 0.001 mm/y at 20 °C and 75 mol% (~4.4 mol Cl/L) and 0.045 ± 0.001 mm/y at 20 °C and 98 mol% (~1.1 mol Cl/L). The corrosion data in NaCl and $[\text{C}_4\text{C}_1\text{im}]\text{Cl}$ solutions are summarized in Figure 130.

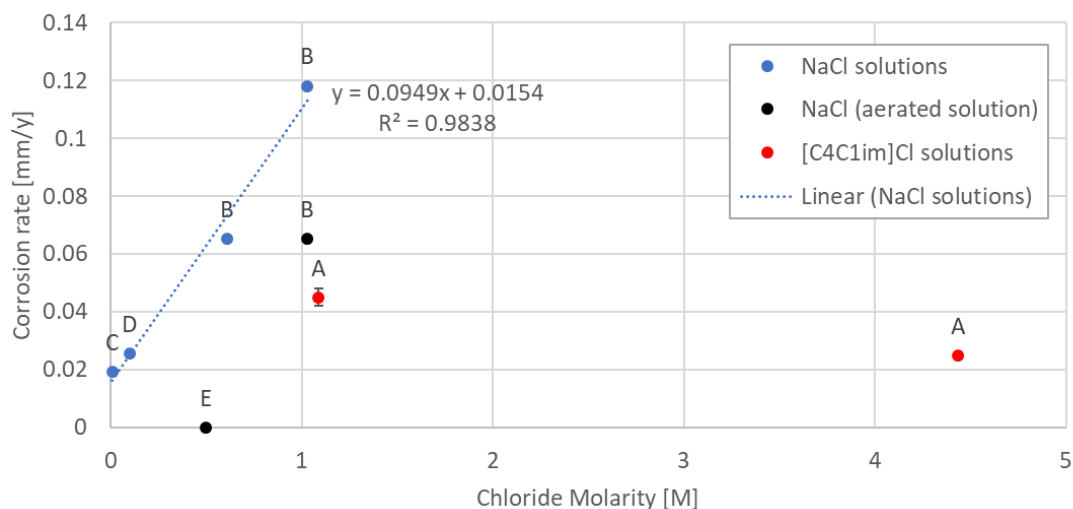


Figure 130. [A] This work (20 °C). [B] Taken from the Corrosion handbook⁴⁰², original references (170-173) not checked. [C] Taken from the Corrosion handbook⁴⁰², original reference (176) not checked. [D] 25 °C⁴⁰⁹. [E] Room temperature⁴⁰⁷.

The attack in non-aerated NaCl solutions on Cu (taken from different sources) follows a linear trend with the chloride molarity for concentrations below 1M (Figure 130). This is consistent with several studies that had shown that the concentration of chloride increases the corrosion rates for Cu⁴⁰⁸. It can also be seen in Figure 130 that there is a significant decrease in the corrosion rates when the solutions are aerated at room temperature. Regarding the corrosion rates in [C₄C₁im]Cl solutions, it can be seen that they are lower than the NaCl solutions. These results suggest that the corrosion rates of Cu exposed to this IL will be lower than NaCl, at the same chloride molarity and temperature. However, corrosion data calculated by gravimetric methods of Cu exposed to NaCl at high temperatures, could not be found to confirm if this is valid at higher temperatures.

No characteristic signals could be seen in the XRD diffraction patterns that would allow a conclusive characterisation of the particles formed over the surface of the Cu samples exposed to [C₄C₁im]Cl solutions. Regarding the crystalline bipyramidal structures seen over the Cu surface. Several Cu oxidation products with similar geometries have been reported in the literature, such as Cu₂O octahedral crystals⁴¹⁰ or Cu₂(OH)₃Cl bipyramidal particles⁴¹¹. The atomic ratio measured determined via EDX for the crystalline structures formed are not consistent, probably due to interferences with the metallic layer underneath the crystals. However, both oxygen and chloride were detected, oxygen being present in larger quantities. This allows to hypothesize that the particles observed are dicopper chloride trihydroxide Cu₂(OH)₃Cl. Additionally, the SEM images of this compound synthesized in copper chloride - urea systems are shown in that work⁴¹¹ are similar to the ones obtained when solid Cu is exposed to [C₁C₄im]Cl solutions. In that work, it was shown that Cu₂(OH)₃Cl could be calcinated at 700 °C, leading to the formation of CuO particles, in which the overall morphology was generally conserved with increased porosity and crystallite size⁴¹¹. The reaction proposed for the formation of Cu₂(OH)₃Cl is⁴¹¹:



A similar reaction could occur in the [C₁C₄im]Cl solutions, where the cupric anion could be formed by disproportionation of the cuprous anion (Eq. 120) and the OH⁻ species could be originated from autohydrolysis of water or by the cathodic reaction involving oxygen or water. However, more experiments are needed to conclude if the species formed is Cu₂(OH)₃Cl.

It would be expected that the corrosion rates will be higher at higher temperatures. This was observed in all conditions except for the samples exposed at 120 °C and 98 mol%, in which a significant drop in the corrosion rate was observed. In fact, the corrosion rates were lower

than the samples exposed to 20 °C. This low corrosion rate under these conditions was observed for 2 independent experiments, which suggest that it should be a physical reality rather than due to experimental errors. One possible explanation is the formation of protective layers during the pre-heating time of the Cu samples at high temperature, as they were pre-heated inside the vessel containing oxygen and water vapour. Those layers could be unstable in high chloride containing medium, but stable in the 98 mol%, which can explain the experimental results observed. However, more experiments are needed to conclusively establish if this behaviour is a physical reality or due to experimental errors.

Cu has a slightly more noble potential than a standard hydrogen electrode [E_0 (Cu/Cu²⁺) = 0.33V] (Table 7) and should therefore be resistant in non-oxidising acids. The absence of depolarizing agents (such as oxygen) in non-oxidizing acids decreases the corrosion rate of Cu. In contrast to high-alloy steels, for example, the chromium-nickel steels, Cu and Cu-based materials do not form passive layers in acid solutions. Cu corrosion is therefore largely determined by transport processes and by the diffusion of dissolved oxygen into the acid as well as the removal of the soluble corrosion products. The latter leads to erosion-corrosion under extreme flow conditions ⁴⁰². It has been reported that a chemical equilibrium exists on a Cu surface immersed in an acidic aqueous solution, which is practically lying completely to the left because of the position of Cu in the electromotive series (Eq. 122) ⁴⁰²:

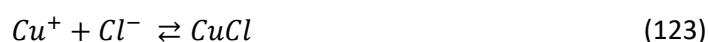


It has been reported in the literature that the corrosion rate of Cu in HCl (particularly in moderate concentration) is higher than H₂SO₄, due to the formation of soluble compounds such as [CuCl₂]⁻ ⁴¹². The reaction in Eq. 122 can be forced to proceed to the right by the presence of oxidizing agents, water being formed, or by complexing substances which bind the Cu(I) ion ⁴⁰². This would explain why the corrosion rates are higher in HCl than in H₂SO₄, a trend that was also observed when copper was exposed to the protic ionic liquids, in which Cu experienced an extreme attack in [HC₁im]Cl, and low corrosion rates in [N₄₁₁₀][HSO₄] with similar order of magnitude than in [C₄C₁im]Cl. These results show that Cu is more prone to corrosion in a coordinating environment than acidic environments.

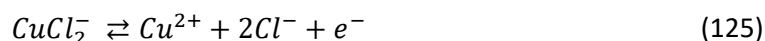
It has been reported that Cu is insoluble in non-oxidizing acids without the action of oxidizing agents, as is the case for sulfuric acid in a wide range of temperatures and concentrations. In contrast, Cu and its alloys dissolve in oxidizing acids, such as, for example, in concentrated hot sulfuric acid (Section 3.2.6.1) ⁴⁰². Similar to H₂SO₄, the attack on Cu by hydrochloric acid is not

only dependent on the concentration and the temperature but, in particular, on the presence of oxidising agents. Cu is strongly attacked by aerated hydrochloric acid ⁴⁰².

According to the literature, anodic dissolution reaction of copper in HCl rapidly occurs through oxidation of metallic Cu to cuprous ion (Eqs. 115). Then cuprous ion reacts with chloride ion from solution to precipitate insoluble CuCl on the surface (Eq. 123), which does not give enough protection to the Cu surface due to poor cohesion, so by combining with another chloride ion, transforms to soluble cuprous chloride complex (Eq. 124) ⁴¹³:



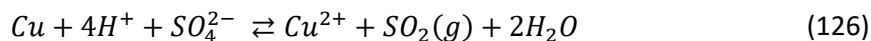
It has been reported that the $[\text{CuCl}_2^-]$ complex may oxidize to cupric ions (Eq. 125) ⁴¹³:



The cathodic reaction in aerated acidic chloride solution is the reduction of oxygen (Table 7). Surprisingly, the corrosion rates of copper in $[\text{HC}_{1\text{im}}]\text{Cl}$ were extreme when dry, when the presence of oxidising species was minor. In this environment, the only species that could be reduced is the of H^+ ions to hydrogen gas. The chloride molarity at 20 °C of the $[\text{HC}_{1\text{im}}]\text{Cl}$ solutions is 6.7 M (75 mol%) and 1.1 M (98 mol%) and in dried conditions at 120 °C is 9.8 M. Reported data for Cu corrosion in HCl solutions by weight loss is scarce and not consistent. The corrosion rate reported for 1 M HCl solution at 25 °C is 8.4 mm/y (0.865 mg/cm².h) while the measured CR in $[\text{HC}_{1\text{im}}]\text{Cl}$, 20 °C and 98 mol% is 0.37 ± 0.01 mm/y. Unfortunately, data was not found at higher chloride concentrations or higher temperatures to establish a comparison of all experimental conditions. However, based on the results at high water content, it would be expected that Cu will be less prone to corrosion in $[\text{HC}_{1\text{im}}]\text{Cl}$ than in HCl, due to the inhibition effect of the cation. It has been reported that some organic protonated heterocyclic molecules, such as triazole, may adsorb through electrostatic interaction between positively charged molecules and negatively charged metal surface caused by chloride ions from the solution, and that such adsorbed film protects the surface by blocking mainly the active sites on the copper surface (section 3.2.7) ^{412,413}.

A5.2.2.2 Cu corrosion in sulfate media

The corrosion reaction of Cu in sulfuric acid is as follows:



Corrosion rate values taken from literature for copper exposed to sulfuric acid, static conditions and air access are shown in Figure 131⁴⁰², where it can be seen that it strongly depends on the concentration and temperature of the system. The corrosion rates without the presence of air are extremely small (<0.11 mm/y) for all concentrations at 20 °C⁴⁰². The corrosion rates of copper exposed to [N₄₁₁₀][HSO₄] are lower than aerated solutions but in the same order of magnitude of deaerated solutions. Interestingly, the corrosion behaviour of Cu in this IL is similar to sulfuric acid, showing that this metal is very resistant to H⁺ in the absence of coordinating species such as chlorides.

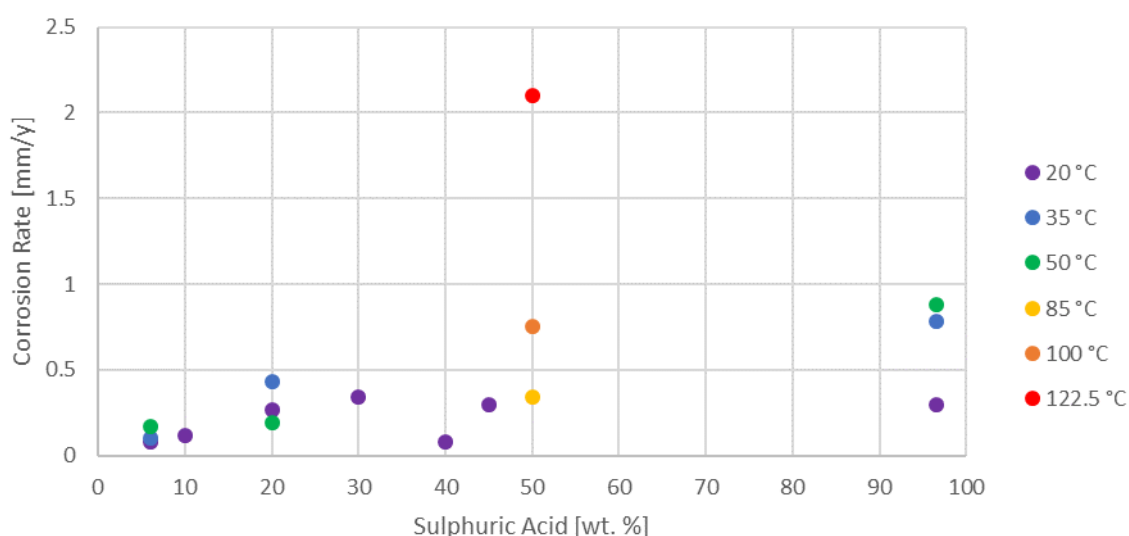


Figure 131. Corrosion rates of copper exposed to H₂SO₄. Static conditions and air access⁴⁰².

Cu exposed to DI water showed a strange behaviour. Samples at temperatures lower than 70 °C can gain mass when exposed to water but lose mass at high temperature. The XRD spectra for a sample exposed to water at 70 °C revealed the formation of CuO (Figure 122 [D]), which was also observed in the SEM images (Figure 124).

A5.2.2.3 Cu categorization system

Table 41 summarizes the classification system and corrosion behaviour of copper exposed to corrosive media. Copper showed good resistance to [C₄C_{1im}]Cl and [N₄₁₁₀][HSO₄] but showed extreme corrosion in [HC_{1im}]Cl when dried.

Table 41. Summary of the classification system and corrosion type for copper exposed to corrosive media. Corrosion types: NC: no corrosion, PC: pitting corrosion, USC: uniform surface corrosion and NUSC: non-uniform corrosion. Section 3.4.

	Solvent →	[C ₄ C ₁ im]Cl			[HC ₁ im]Cl			[N ₄₁₁₀][HSO ₄]			[C ₄ C ₁ im][NTf ₂]	Water
	Water Content [mol fraction] →	Dry	0.75	0.98	Dry	0.75	0.98	Dry	0.75	0.98	Dry	1
	Temperature [°C] ↓											
Classification System (Section 3.4)	20	4	4	4				0	4			2
	70	4	4	4	4	4	4	4	4	4	3	2
	120	4	4	4	4	4	4	4	4	4	3	4
	150										3	
Corrosion Type	20	NC	NC	NC				NC	USC			NUSC
	70	NC	NUSC	NUSC	USC	USC	USC	USC	USC	USC	NUSC	NUSC
	120	NUSC	NUSC	NUSC	USC	USC	USC	USC	USC	USC		NUSC
	150										NUSC	

A5.2.2.4 Cu corrosion in other ILs

The corrosion behaviour of copper in IL had been investigated in the literature. In a study comparing several metals (carbon steel, austenitic stainless steel, nickel-based alloy C22, copper, brass and aluminium (AlMg₃)) it was concluded that copper and brass had the worst corrosion resistance to IL media. It was shown that the addition of water to increased aprotic ILs increased the corrosion rates and that corrosion inhibitors could be used to protect Cu¹⁵¹. The corrosion behaviour of Cu in fluorinated ILs is discussed in section 3.5.2.

A5.3. Iron

Iron (Fe) is a chemical element with symbol Fe and atomic number 26. It is by mass the most common element on Earth, forming much of Earth's outer and inner core. Iron alloys, such as steel, inox, cast iron and special steels are by far the most common industrial metals, because of their high mechanical properties and low cost¹⁴⁵.

A5.3.1. Corrosion rates

The results for the mass change of Fe samples exposed to different corrosion media (water-soluble ILs) are given in Figure 132. Corrosion results in [C₄C₁im][NTf₂] are given in section 3.5.2.

When Fe is exposed to [C₄C₁im]Cl solutions, the corrosion rates are very small in the residual water case and increase with water content. The maximum MCR was observed at 98 mol% for samples exposed at 20 and 70 °C whereas the samples exposed at 120 °C experienced a maximum MCR at 75 mol% (Figure 132A/B).

The attack was extreme when Fe was exposed to $[\text{HC}_1\text{im}]\text{Cl}$, therefore, the maximum temperature tested was 70 °C at 75 mol% and 45 °C at 98 mol%. From the data obtained, it seems that the attack is more severe at high water contents in the IL (Figure 132C/D).

The MCRs of Fe exposed to $[\text{N}_{4110}][\text{HSO}_4]$ were very small in the residual water case and increased with increasing water concentration. The maximum attack was observed in the high water content region (98 mol%) and was not tested at 120 °C (Figure 132E/F).

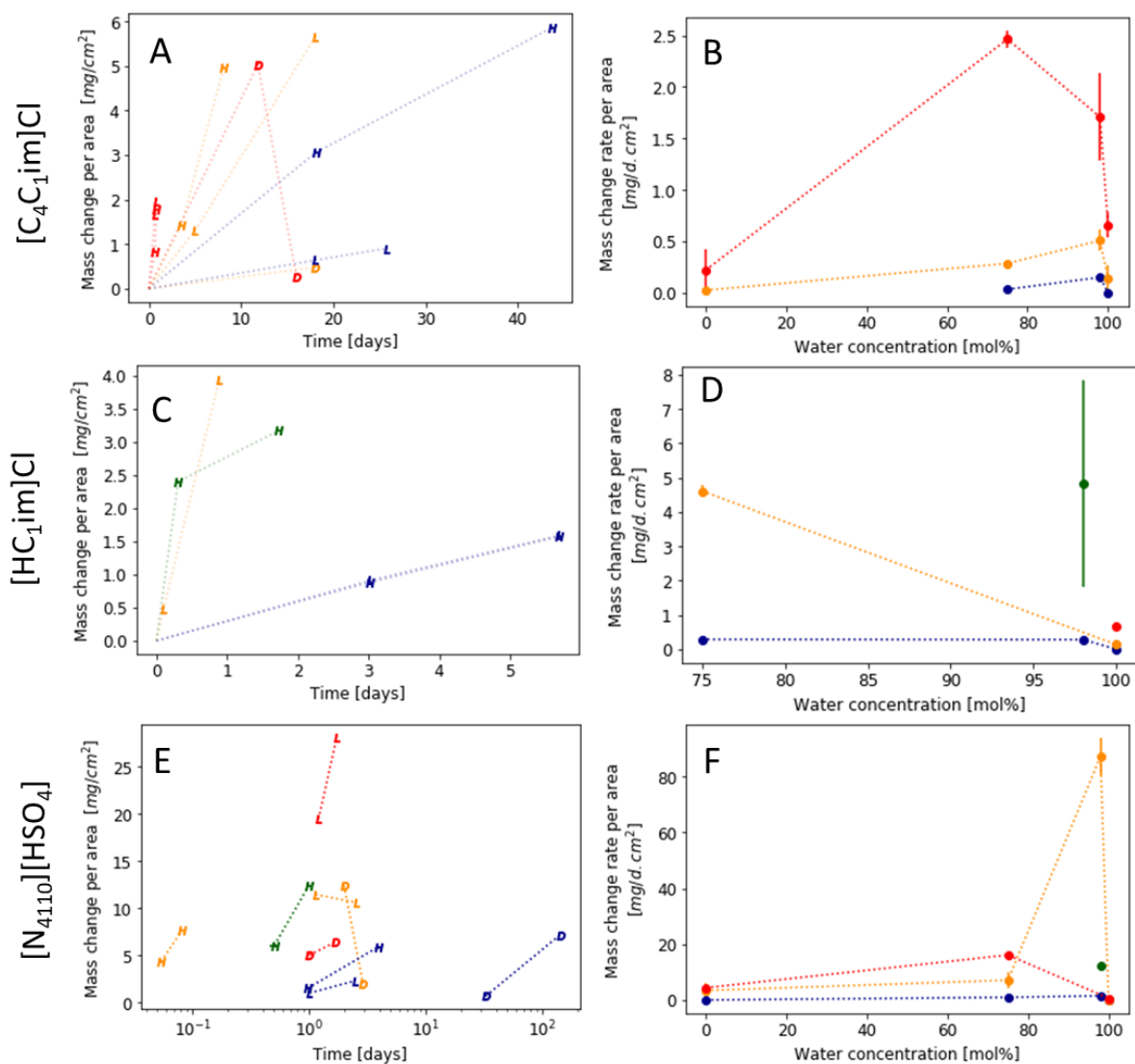


Figure 132. Mass change rates for Fe exposed to corrosive media. Left figures (A, C and E): Mass change per area as a function of time. Right figures (B, D and F): Mass change rates as a function of water content calculated from the average of the MCRs. Legend, D: dry, L: low water case, H: high water case, W: water. Colours: Blue 20 °C, green 45 °C, orange 70 °C and red 120 °C. Lines have been added to guide the eye.

A5.3.2. XRD

XRD was performed on selected samples. The pattern of the Fe sample pre-exposure is shown in Figure 133A. Only four peaks can be observed in the diffraction pattern of Fe corresponding to the following signals: 110 (44.6°), 200 (64.7°), 211 (82.4°) and 220 (99.4°) (reference code:

00-001-1262). XRD diffraction patterns of Fe are shown in Figure 133 and Figure 134 exposed to $[N_{4110}][HSO_4]$ and Cl containing-ILs respectively. No new signals were observed, only changes in the relative intensities. The only exception was an Fe sample of lesser purity (99.5% instead of 99.9%) exposed to water at 70 °C, which showed a brown corrosion product identified as Fe_2O_3 (Figure 133D). This shows that Fe of lesser purity is easier to oxidize, and the amount of corrosion products were detectable *via* XRD. However, all the experiments were performed with high purity iron and the effect of the purity was not further explored.

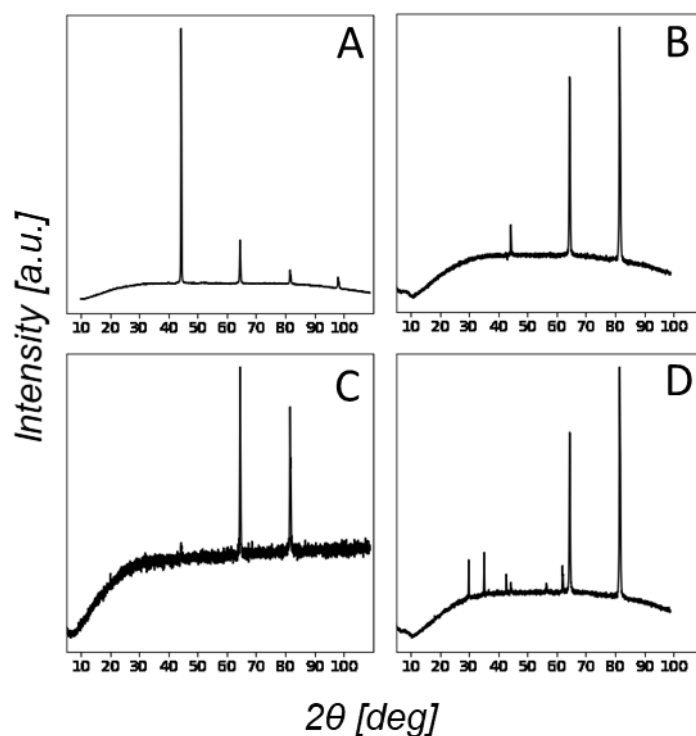


Figure 133. XRD patterns from iron samples exposed to corrosive media. [A] Unexposed metal sample. [B] Water, 70 °C and 3d. [C] $[N_{4110}][HSO_4]$ 120 °C and 1.7d. [D] Water, 70 °C and 3d, sample purity 99.5%.

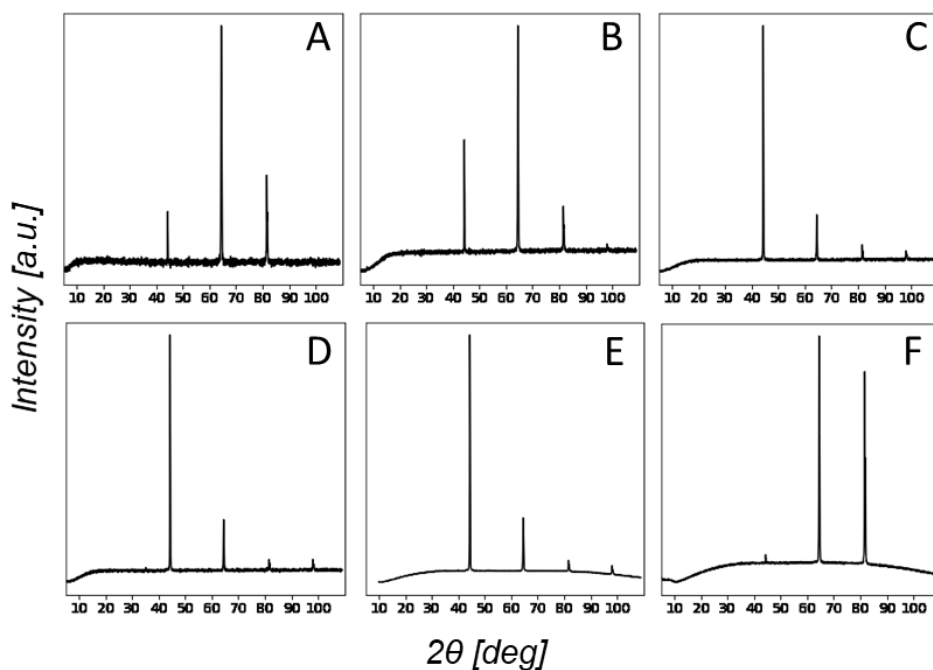


Figure 134. XRD patterns from iron samples exposed to $[C_4C_{1im}]Cl$ solutions. [A] 20 °C, 75 mol% and 25.72 d. [B] 70 °C, 75 mol% and 17.99 d. [C] 120 °C, 75 mol% and 50 min. [D] 120 °C, 98 mol% and 50 min. [E] 70 °C, 98 mol% and 3.52 d. [F] 120 °C, 75 mol% and 50 min.

A5.3.3. XRF

The XRF results for Fe samples are summarised in Table 42. Only the samples exposed to $[N_{4110}][HSO_4]$ at 70 °C and 75 mol% experienced a significant change in the chemical composition.

Table 42. XRF results summary for Fe.

Solvent	Observations
-	Fe: 99.723% (Traces of Al, Si)
H ₂ O	Samples showed traces of S, due to contamination.
$[C_4C_{1im}]Cl$	No significant changes.
$[HC_{1im}]Cl$	No significant changes.
$[N_{4110}][HSO_4]$	Significant amount of sulphur in samples exposed at 70 °C and 75 mol% for 1.1 and 2.5 d (circa 18%)

A5.3.4. SEM

The SEM images of untreated Fe foils are given in Figure 135. Oxygen was not detected via XRD in the untreated samples. The SEM/EDX images from iron exposed to $[C_4C_{1im}]Cl$ solutions are shown in Figure 136 and Figure 137. From those figures, it can be seen that Fe forms oxides in those systems with different morphologies. Figure 136 shows the formation of 500 ± 100 nm Fe₂O₃ cubes and 4 ± 1 μm cuboctahedra structures. Figure 137 shows the formation of 115 ± 5 nm diameter hexagonal iron oxide plates.

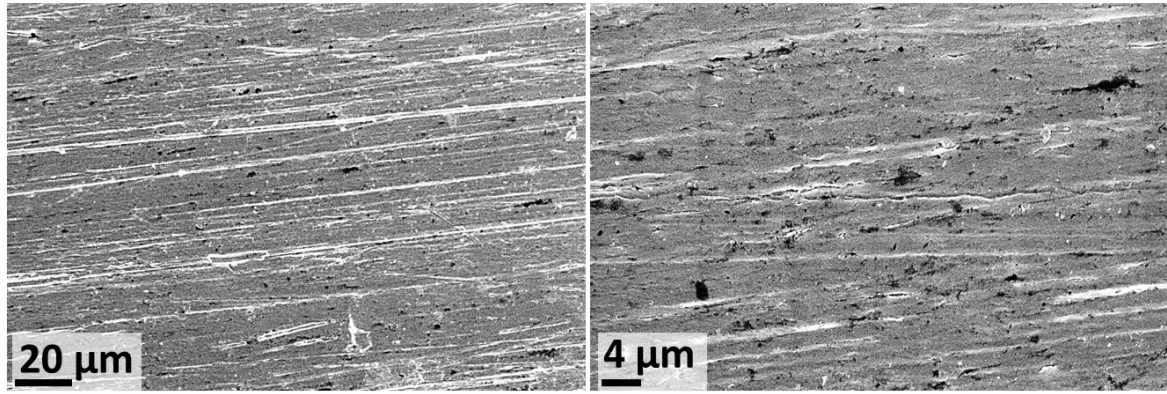


Figure 135. SEM images obtained for a cleaned but untreated Fe sample.

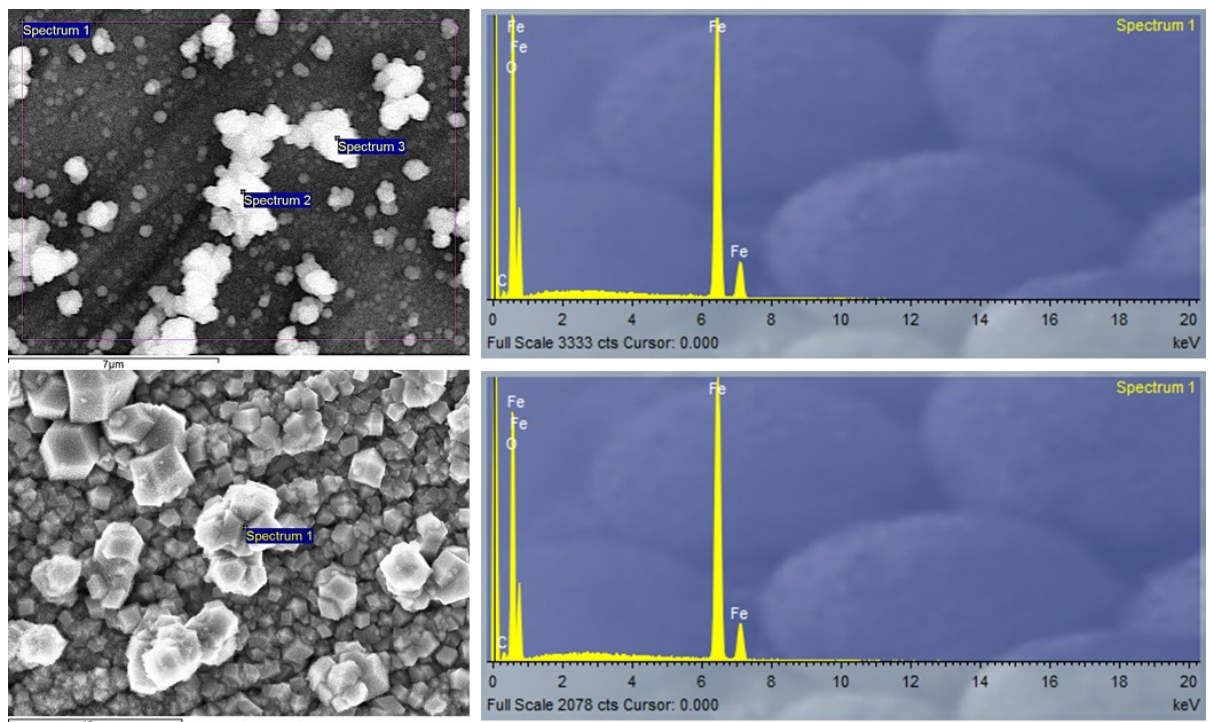


Figure 136. SEM/EDX images of Fe exposed to $[C_4C_{1im}]Cl$. Top figure: 70 °C, 75 mol% and 5.00 d. Bottom figure: 70 °C, 98 mol% and 8.09 d shows the formation of 500 ± 100 nm Fe_2O_3 cubes and 4 ± 1 μm cuboctahedra structures. Top figure EDX O:Fe average atomic ratio 1:1.68 (± 0.08). Bottom figure. EDX O:Fe ratio 1:1.6.

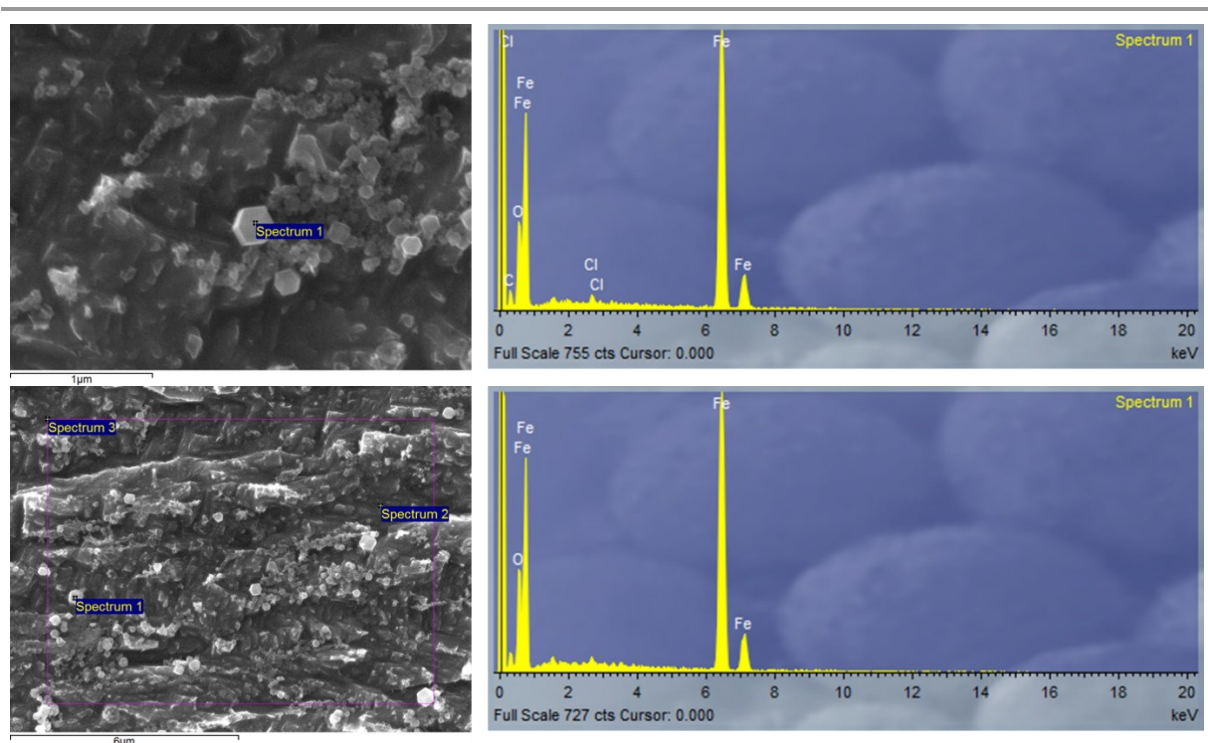


Figure 137. SEM/EDX images of Fe exposed to $[C_4C_{1im}]Cl$ (70 °C , 8 mol% and 3.5 d). Top figure EDX O:Fe atomic ratio 2:8. Traces of Cl detected Cl:Fe 1:100. Details of 115 ± 5 nm diameter hexagonal Iron oxide plates. Bottom figure. EDX O:Fe ratio 2:3. No oxygen detected in other zones.

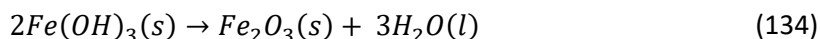
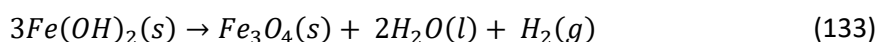
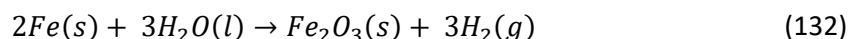
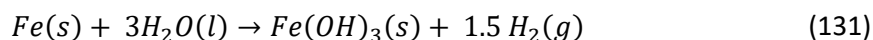
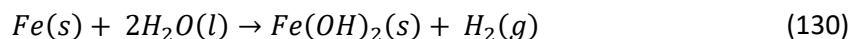
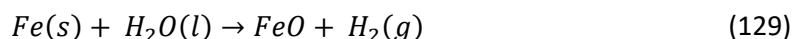
A5.3.5. Overall considerations

The corrosion of Fe with the accompanying formation of oxidation products on the surface is a complex process, which depends upon many factors, such as pH, presence of oxygen and coordinating species^{414,415}.

The iron corrosion process starts with a simple, and almost universally accepted, anodic reaction, shown in Eq. 127. It has been reported that trivalent iron ions do not form directly in measurable quantities in the anodic reaction, and complex ions only form directly in special solutions^{414,415}. The Fe^{2+} ions dissolved in the solution can take part in several parallel reactions, for example, they can form $Fe(OH)_2$ that might deposit on the surface (Eq. 130), where a series of other reactions can occur⁴¹⁴.



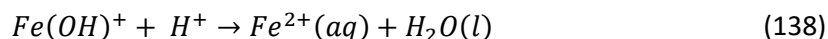
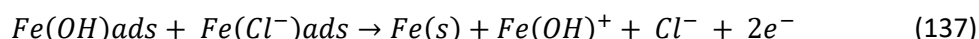
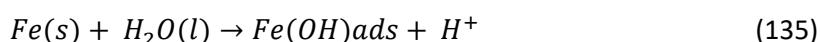
The cathodic reaction in the absence of oxygen is the reduction of protons into hydrogen gas, whereas the reduction of oxygen will take place in aerated neutral solutions (Table 7). When there is no dissolved oxygen in water, iron reacts with water according to the following reactions⁴¹⁶:



Details on the thermodynamic aspects of reactions given in Eqs. 129-134 are discussed in the scientific literature ^{416,417}. It has been shown that the most stable form for iron oxide is Fe₂O₃. For reaction (Eq. 131), ΔG° 298 > 0; this means that this reaction is not spontaneous at 25°C. Ferric hydroxide (III) (Fe(OH)₃) is not thermodynamically stable and, on transforming to Fe₂O₃, gives intermediate products characterized by partial dehydration and the polymeric structure of ferric hydroxides ⁴¹⁶.

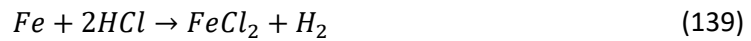
A5.3.5.1 Fe corrosion in chloride media

The dissolution mechanism of Fe in concentrated NaCl solutions into ferrous proposed by Darwish *et al.* is as follows ⁴¹⁸:



By analogy, the corrosion process of Fe in [C₄C₁im]Cl should follow a similar path, in which the presence of chloride anions catalyses the oxidation process, and explains why the MCR in [C₄C₁im]Cl solutions are higher than in water. The corrosion of iron in a 3.5 wt% NaCl solution at room temperature calculated through electrochemical methods was 0.175 mm/y ⁴¹⁵. The penetration rate calculated from the MCR data for Fe exposed to [C₄C₁im]Cl at room temperature were 0.01638 ± 0.00007 mm/y and 0.070 ± 0.008 mm/y at 75 and 98 mol% respectively. It is noticed that the corrosion rates are lower than in NaCl, probably due to adsorption of the [C₄C₁im]⁺ cation on the surface of the metal inhibiting reactions Eq. 135 and 136.

Fe reacts with HCl and H₂SO₄ to form the corresponding salts and hydrogen evolution according to:



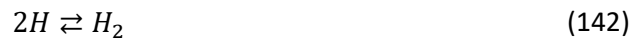
The rate of dissolution of pure Fe in these minerals acids was not found in the scientific literature, however, some data is available for mild steels. The rate of dissolution of unannealed mild steel (C:0.12%, Mn .38%, P:0.053%, S, 0.034%, Si traces) in sulfuric acid solutions (0 .0043 to 5 N) was studied by Whitman *et al.* ⁴¹⁹ at 23 °C. The main purpose of this study was to find the effect of rotational speed on the corrosion rate. The corrosion process in the presence of acids was explained with Eq. 141:



The rate at which this reaction progresses is dependent on the following factors:

- a. Metal: The corrosion tendency of metal is determined by its position in the electromotive series. This factor is usually of minor importance, being obscured by such effects as protective or nonprotective oxide or other films, overvoltage to the evolution of hydrogen gas, and the physical condition of the surface. In commercial steels and irons, the presence of elements other than iron or of products of corrosion on the surface of the metal may materially change the overvoltage and the consequent ease of liberating gaseous hydrogen ⁴¹⁹.
- b. Acidity: Acidity is a measure of hydrogen ion concentration of the acid. Increasing acidity increases the tendency to corrode by increasing the electromotive force for hydrogen gas evolution. The passifying action exhibited by various strong oxidizing acids is generally accredited to a rapidly formed film of adherent oxide on the metal surface and has no direct relation to the acidity of the solution ⁴¹⁹.
- c. Ferrous Ion Concentration: According to the law of mass action the increase in ferrous ions should decrease the rate of corrosion but this factor seems to play a minor role ⁴¹⁹. However, Gatos reported that the dissolution of iron in sulfuric acid was increased by ferric ions ⁴²⁰.
- d. Removal of Hydrogen: This is the most important factor for the progress of corrosion. Hydrogen can be removed in two ways: by the evolution of gaseous hydrogen (Eq. 142)

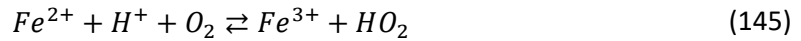
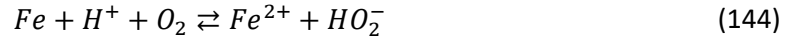
or by depolarization through oxidation either by dissolved oxygen or by some other oxidizing agent (Eq. 143):



Hydrogen gas evolved by an electrode reaction is dependent upon the hydrogen-ion concentration (acidity), the overvoltage, and the potential of the metal. The overvoltage is a variable factor dependent upon the specific experimental conditions including the composition of the metal surface, the rate of gas evolution, and the work done against surface tension in forming the bubbles of hydrogen ⁴¹⁹. A number of investigators have shown that the rate at which iron corrodes under natural waters is largely determined by the rate at which dissolved oxygen can diffuse into the metal surface to remove the polarizing film of hydrogen ⁴¹⁹.

Damon reported the dissolution rates of hot rolled and annealed mild steel and carbon steel (containing 0.8 wt% carbon) in sulfuric acid solutions (1 to 35.5 N) at 25 °C. The main objective of this study was to find the effect of carbon content and of the acid concentration on the rate of corrosion of 5 different types of steel in sulfuric acid. For all the steels tested, the maximum corrosion rate decreased between 11 N and 14 N sulfuric acid. Higher carbon steels were much more susceptible to corrosion than the lower carbon steels. It was found that steel containing between 0.06 and 0.37 wt% carbon had the lowest corrosion rate for all concentrations of acid. The steel specimens became passive in acids more concentrated than 17 N. The passivating film was shown to be ferrous sulfate ⁴²¹. As shown in section A5.9.5, this compound also formed in 304 SS when exposed to $[N_{4110}][HSO_4]$.

The first study on the dissolution of Fe in hydrochloric acid was made by Conroy more than a century ago ⁴²². In these experiments, the effects of acid concentration and temperature on the dissolution rates were investigated. The loss of weight was determined at one-hour intervals, but the rate of corrosion was evaluated from hydrogen gas evolution and expressed as cm³ of hydrogen evolved per hour. It was concluded that the rate of dissolution was doubled for each addition of 30 grams hydrochloric acid per litre of the solution or for each rise of 10°C in the temperature. Other studies on the dissolution of iron in HCl concluded that the activation energy for this process is 9400 kcal per gram mole ⁴²³. In that work, it was also shown that the iron oxidation starts with the process described in (Eq. 141) and that in the presence of oxygen, the rate increases due to the following reactions:

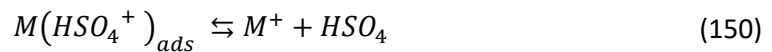
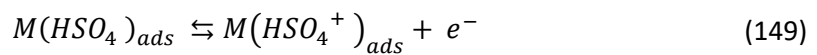
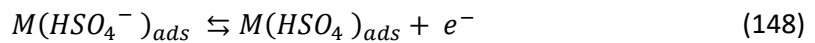
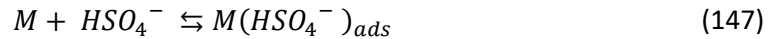


By analogy with the above mechanisms, the corrosion process of iron in protic ILs should follow the same mechanisms. [HC₁im]Cl leads to slightly acidic solutions (pH = ~5), those the chloride and the protons can participate in Eq. 136 and 138.

A5.3.5.2 Fe corrosion in sulfate media

The anodic behaviour of pure, recrystallized Fe in acid sulfate and perchlorate solutions free of oxygen was investigated using an iron rotating disk electrode by cyclic. The determined kinetic data confirmed mainly the previously proposed dissolution mechanism and it was shown that the iron dissolution kinetics was independent of the anion concentration in the overall potential range ⁴²⁴.

The corrosion behaviour of metallic materials (Fe, Ni and SS 304) in acidic-functionalized ILs, containing the [HSO₄]⁻ anion was studied through electrochemical methods, and the following anodic mechanisms were proposed ⁴²⁵:



A5.3.5.3 Fe categorization system

The corrosion behaviour of Fe exposed to ILs according to the classification method is summarized in Table 43.

Table 43. Summary of the classification system and corrosion type for iron exposed to corrosive media. Corrosion types: NC: no corrosion, PC: pitting corrosion, USC: uniform surface corrosion and NUSC: non-uniform corrosion. Section 3.4.

	Solvent →	[C ₄ C ₁ im]Cl			[HC ₁ im]Cl			[N ₄₁₁₀][HSO ₄]			[C ₄ C ₁ im][NTf ₂]	Water
	Water Content [mol fraction] →	Dry	0.75	0.98	Dry	0.75	0.98	Dry	0.75	0.98	Dry	1
	Temperature [°C] ↓											
Classification System (Section 3.4)	20		3	3		4	4	0	4	4		3
	45					4	4					
	70	0	3	3				0	4	4	0	3
	120	0	4	4				0	4	4		3
	150										0	
Corrosion Type	20		NUSC	NUSC		USC	USC	NC	USC	USC		NUSC
	45					USC	USC					
	70	NC	NUSC	NUSC				NC	USC	USC	NC	NUSC
	120	NC	NUSC	NUSC				NC	USC	USC		NUSC
	150										NC	

A5.3.5.4 Fe corrosion in other ILs

As mentioned before, the corrosion of pure iron in ionic liquids have only been assessed through electrochemical methods in 2 acidic-functionalized ILs, one containing the [HSO₄]⁻ ⁴²⁵.

A5.4. Molybdenum

Molybdenum (Mo) is a chemical element with atomic number 42. It does not occur naturally as a free metal on Earth and it is found only in various oxidation states in minerals. The free element, a silvery metal with a grey cast, has the sixth-highest melting point among all elements. It readily forms hard, stable carbides in alloys, and for this reason, most of the world production of the element (about 80%) is used in steel alloys, including high-strength alloys and superalloys ⁴²⁶.

A5.4.1. Corrosion rates

The results for the mass change of Mo samples exposed to different corrosion media (water-soluble ILs) are given in Figure 138. Corrosion results in [C₄C₁im][NTf₂] are given in section 3.5.2.

Mo samples exposed to corrosive media experience in all cases the formation of a dark layer over the metal. The mass changes were small, even at long exposure times, and were positive in all instances. This metal behaves similarity in all corrosive media. Generally, the maximum mass change was observed for DI water and decreased with increasing IL concentration, except in [HC₁im]Cl, which shows higher corrosion at 75 mol% at 120 °C (Figure 138D).

The MCR were higher at 70 °C than at 120 °C for all experiments, except for the PILs at 75 mol% (Figure 138D/F).

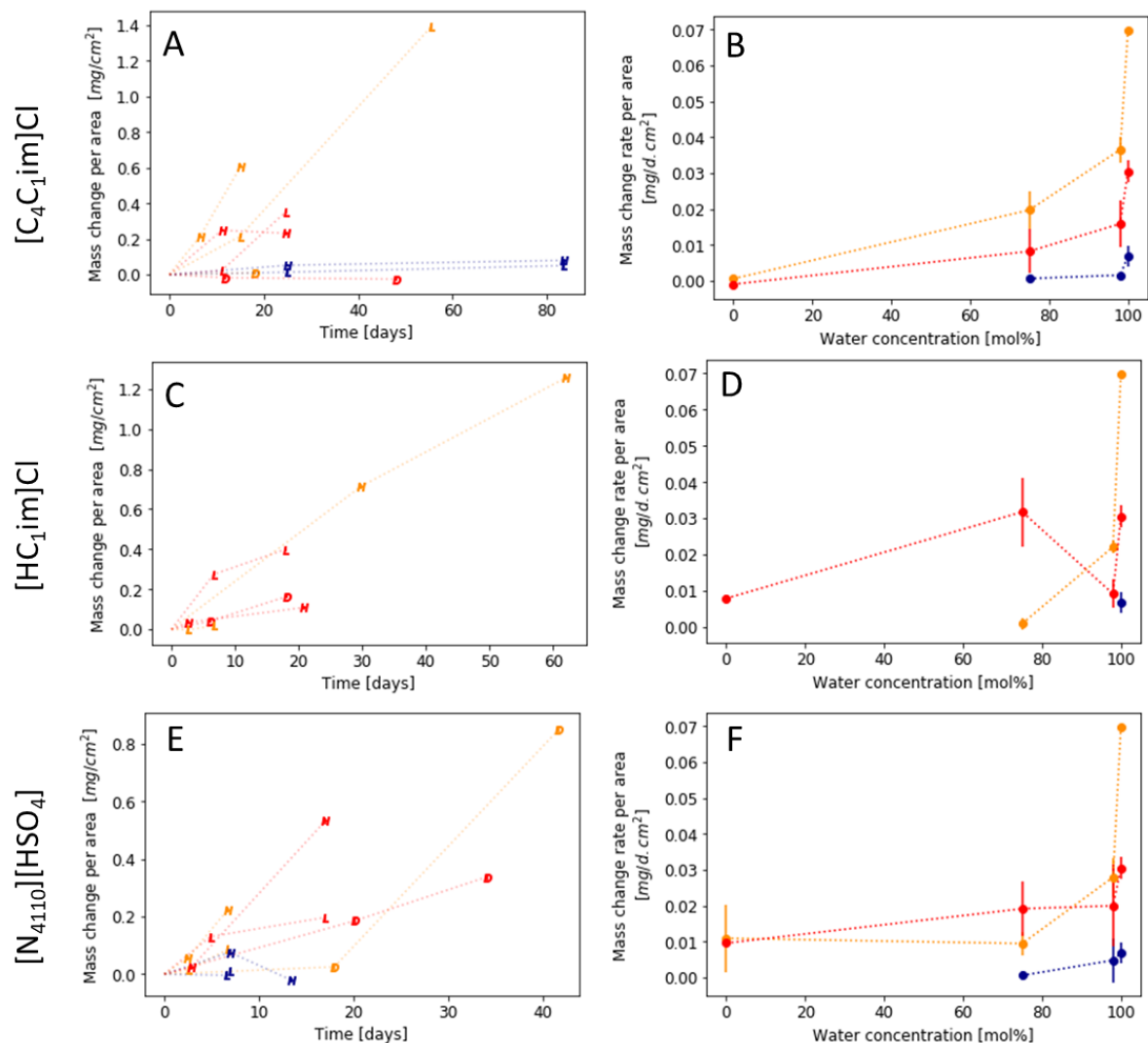


Figure 138. Mass change rates for Mo exposed to corrosive media. Left figures (A, C and E): Mass change per area as a function of time. Right figures (B, D and F): Mass change rates as a function of water content calculated from the average of the MCRs. Legend, D: dry, L: low water case, H: high water case, W: water. Colours: Blue 20 °C, orange 70 °C and red 120 °C. Lines have been added to guide the eye.

A5.4.2. XRD

XRD was performed on selected samples. The pattern of the Mo sample pre-exposure is shown in Figure 139A. Only 2 strong signals can be observed in Mo samples corresponding to 200 (58.8°) and 211 (74.0°) (reference code: 00-001-1207). No new signals in the diffraction pattern were observed in all tested samples, only relative intensities changes.

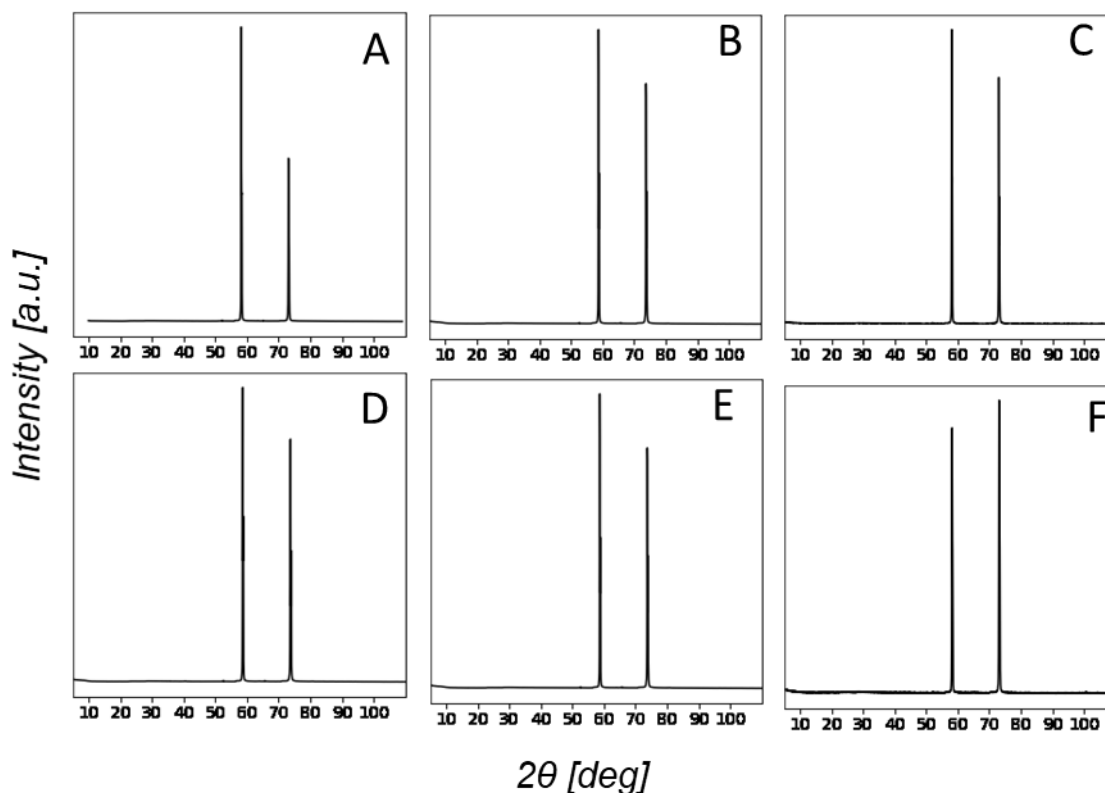


Figure 139. XRD patterns from Mo samples exposed to corrosive media. [A] Unexposed metal sample. [B] [C₄C₁im]Cl (70 °C, 98 mol% and 6.53 d). [C] [HC₁im]Cl (120 °C, 75 mol% and 6.66 d). [D] Water (70 °C, 100 mol% and 4.50 d). [E] [C₄C₁im]Cl (120 °C, 98 mol% and 11.15 d). [F] [HC₁im]Cl (120 °C, 98 mol% and 20.85 d).

A5.4.3. XRF

XRD results for Mo samples are summarised in Table 44. No significant changes in the elemental composition of Mo samples were observed.

Table 44. XRF results summary for Mo.

Solvent	Observations
-	Mo: 99.559% (Traces of Al, Si, La). Several samples showed traces of Zr.
H ₂ O	No significant changes.
[C ₄ C ₁ im]Cl	No significant changes.
[HC ₁ im]Cl	No significant changes.
[N ₄₁₁₀][HSO ₄]	No significant changes.

A5.4.4. SEM

The SEM/EDX images for Mo are shown in Figure 140 to Figure 142. Overall, no corrosion products were observed deposited on the samples analysed. Samples exposed to water did not show any significant morphological changes. A sample exposed to [C₄C₁im]Cl showed cracks throughout the surface.

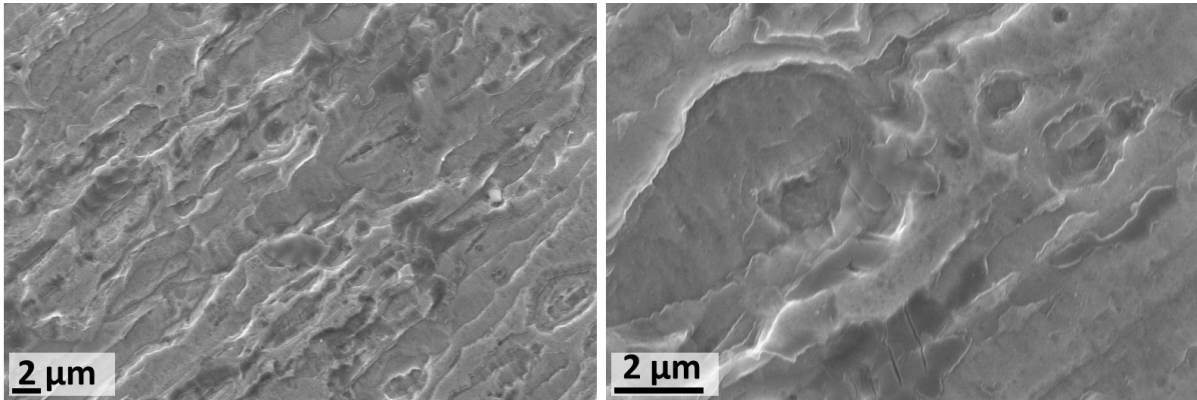


Figure 140. SEM Images obtained for a cleaned but untreated Mo sample.

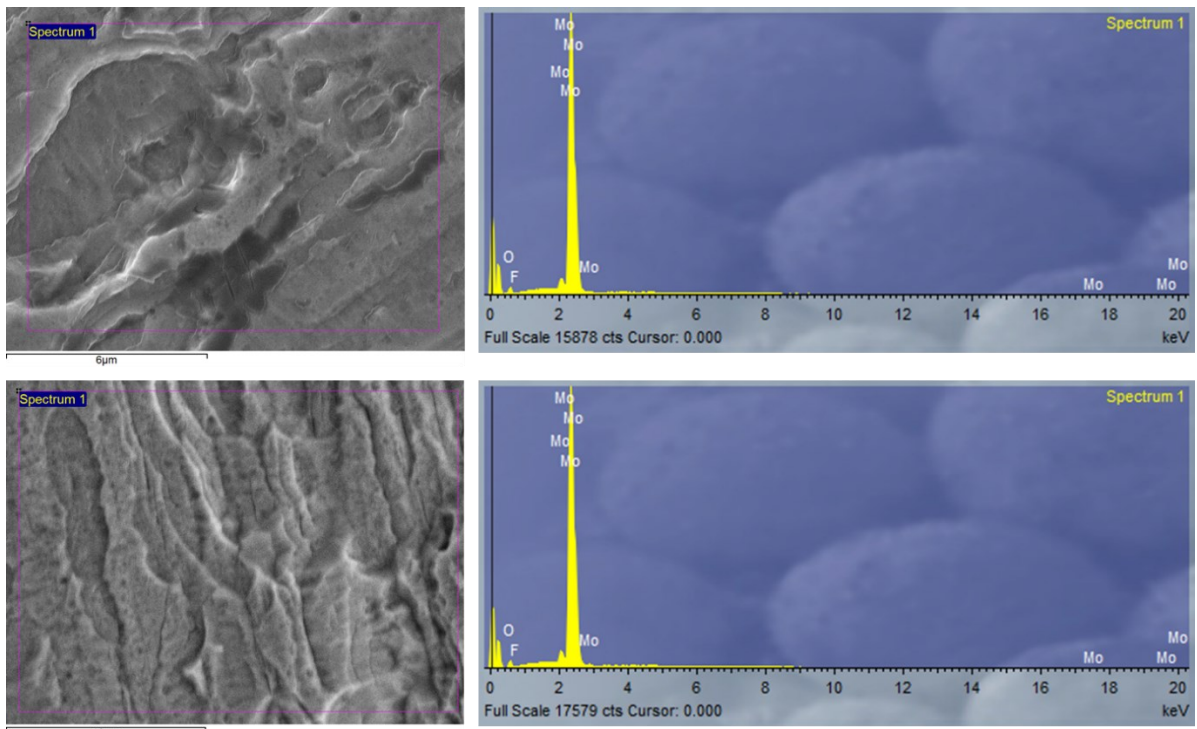


Figure 141. SEM/EDX for Mo samples. Top figure: Untreated molybdenum. Bottom figure: Molybdenum exposed to water (70 °C and 4.50 d). EDX atomic ratio (F:O:Mo) for an untreated sample is 1:5.6:11.3 and for the sample exposed to water 1:9.7:18.2.

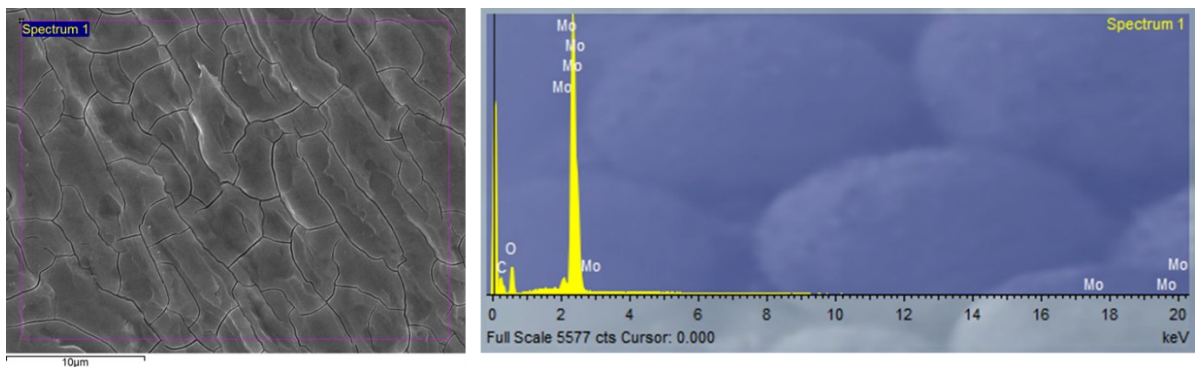


Figure 142. SEM/EDX for Mo samples exposed to $[C_4C_{1im}]Cl$ (70 °C, 98 mol% and 4.50 d). EDX atomic ratio (C:O:Mo) is 1.8:2.2:1.

A5.4.5. Overall considerations

Overall, the corrosion resistance of Mo in the IL under the explored conditions is excellent.

It has been reported that contrary to most other passive metals, Mo is relatively unaffected by the presence of halide ions and is consequently relatively resistant to most localized corrosion processes. Molybdenum thus has generally excellent performance in nonoxidizing acids to near-neutral environments (containing halides or otherwise) and particularly in hydrohalide acids (e.g., HCl). However, in neutral-to-alkaline conditions, where molybdenum oxyanions become more stable, dissolution of molybdenum increases. The reported corrosion rate of Mo in different mineral acids after 6 days exposure at temperatures between 25-35 °C (aerated) was 0.03 – 0.06 mm/year for HCl 1% and 35% respectively, and 0.5-10 mm/year for H₂SO₄ at 1 wt% and 30 wt%⁴²⁶. The maximum CR of Mo exposed to [HC₁im]Cl solution observed in the experimental conditions covered, was at 120 °C and 75 mol% with a value of 0.011 ± 0.003 mm/year. This shows that the CR in [HC₁im]Cl is less than HCl. The maximum CR of Mo exposed to [N₄₁₁₀][HSO₄] solution, observed in the experimental conditions covered, was at 120 °C and 98 mol% with a value of 0.007 ± 0.004 mm/year. The order of magnitude of the CR of [N₄₁₁₀][HSO₄] is several orders of magnitude lower than for H₂SO₄, and is within the order of magnitude of [HC₁im]Cl, showing that the Mo corrosion process is not significantly impacted by the acidic conditions of hydrogen sulfate anion nor the coordinating capabilities of chloride anions.

The corrosion rate after 6 days immersion test in Cl-containing salts is lower than in HCl. For NaCl (3%) was 0.01 mm/y and NH₄Cl was 0.005 mm/y in aerated solution and was 0 for both salts when deaerated⁴²⁶. Both Cl- containing ionic liquids had similar CR. The maximum CR of Mo exposed to [C₄C₁im]Cl solution observed in the experimental conditions covered, was at 70°C and 98 mol% with a value of 0.013 ± 0.001 mm/year and at 20 °C and 98 mol% was only 0.0005 ± 0.0002 mm/year, which is lower than NaCl and NH₄Cl, most likely due to the corrosion inhibition effect of ILs as previously mentioned (section 3.2.7).

Generally speaking, the CR of Mo were higher in DI water and in the IL solution. It has been reported that in aqueous conditions, molybdenum and its alloys are effectively passive and show low corrosion rates. Under flow, high temperature water containing 400 ppb dissolved oxygen at pH 6–7, molybdenum and its alloys were found to have significantly better corrosion resistance than tungsten and its alloys. Up to 260 °C, neither material is corroded significantly, where Mo showed a corrosion rate ~0.25 mm/year and ~0.50 mm/year at 320 °C⁴²⁶. In our experiments under static conditions, the calculated attack was for 20, 70 and 120 °C was 0.002 ± 0.001, 0.02484 ± 0.00004 and 0.011 ± 0.001 mm / year respectively.

It would have been expected the CR to increase with increasing temperatures. However, the CR at 70 °C were higher than at 120 °C. There are several explanations for this behaviour.

1. Dissolved oxygen. As mentioned earlier, it has been shown that dissolved oxygen might have an effect on Mo dissolution. As the solution were not deaerated, changes in temperature will lead to differences in oxygen solubilities. Indeed, oxygen solubility is expected to decrease with temperature, therefore, at 120 °C, there will be less dissolved oxygen slowing down the corrosion process.
2. Formation of passive layers in corrosive media. It would be expected an increase in the reaction rates with increasing temperature. In the high-temperature experiments, the formation of a passive layer could form faster, protecting the material against further corrosion.
3. Formation of passive layers during preheating time. In the experiments conducted at high temperatures, the sample was preheated in a sealed container containing the solution before immersion. This means that during the pre-heating time (2h), the sample was exposed to water vapour and oxygen. It is possible that during the preheating step, the protective layer is formed, reducing the CR once immersed.

No particles were observed on the surfaces of the samples tested. EDX results showed the presence of F in some samples. It is noteworthy to mention that this element was not be detected by XRF as the instrument used for the XRF measurements can only detect elements with a higher atomic number than F (Section 3.3.3.3). Mo forms a diversity of oxides (crystalline and amorphous), such as the stoichiometric ones: MoO₂, MoO₃, the non-stoichiometric such as Mo₁₈O₅₂, Mo₁₇O₄₇, Mo₈O₂₃, MoO₃, Mo₄O₁₁, Mo₉O₂₆ and MoO_{3-2γ} (0<γ<1) ^{427,428}. The samples exposed to corrosive media turned dark. Molybdenum trioxide (MoO₃) is the end product of the complete oxidation of molybdenum and have been reported to be a stable white solid that might have a blue or green tinge due to the presence of traces amount of metal ions in lower valence state. Molybdenum dioxide (MoO₂) have been described in the literature as a brownish-black, violet powder or as a substance that forms dark bluish-violet prisms ⁴²⁷. The EDX showed that the presence of oxygen over the surface of the sample was significant, however, the stoichiometric ratio O:Mo for the samples exposed to water and untreated was ~1:2, which doesn't correspond to any molybdenum oxides. The reason might be interferences for the metal beneath the oxide layer. Indeed, if the layer is very thin, the signals from the metal underneath will increase the Mo ratio. Another explanation would be the layer is not uniform throughout the surface. In the sample exposed to [C₄C₁im]Cl, the ratio of oxygen to

Mo increase to 2.2:1, which is not conclusive to established if the passive layer is composed of MoO₂ or MoO₃.

A5.4.5.1 Mo categorization system

Regarding the classification system, Mo has been classified as type-1, due to the small corrosion rates and the fact that the surface changes colour. The corrosion is classified as general surface corrosion. The results are summarised in Table 45.

Table 45. Summary of the classification system and corrosion type for Mo exposed to corrosive media. Corrosion types: NC: no corrosion, PC: pitting corrosion, USC: uniform surface corrosion and NUSC: non-uniform corrosion. Section 3.4.

	Solvent →	[C ₄ C ₁ im]Cl			[HC ₁ im]Cl			[N ₄₁₁₀][HSO ₄]			[C ₄ C ₁ im][NTf ₂]	Water
	Water Content [mol fraction] →	Dry	0.75	0.98	Dry	0.75	0.98	Dry	0.75	0.98	Dry	1
	Temperature [°C] ↓											
Classification System (Section 3.4)	20		1	1					1	1		1
	70	1	1	1		1	1	1	1	1	1	1
	120	1	1	1	1	1	1	1	1	1		1
	150										1	
Corrosion Type	20		UC	UC					UC	UC		UC
	70	UC	UC	UC		UC	UC	UC	UC	UC	UC	UC
	120	UC	UC	UC	UC	UC	UC	UC	UC	UC		UC
	150										UC	

A5.4.5.2 Mo corrosion in other ILs

The corrosion behaviour of Mo in IL has not been studied so far. Other techniques need to be used in this system to study the nature of the layer formed over the samples.

A5.5. Nickel

Nickel (Ni) is a chemical element with the symbol Ni and atomic number 28. It is a silvery-white lustrous metal with a slight golden tinge. Nickel belongs to the transition metals and is hard and ductile. Pure native nickel is found in Earth's crust only in tiny amounts. Ni is a very important metal and is used in many applications. Pure Ni has good corrosion resistance and is frequently used as a protective coat for other metals and alloys or as alloying element in combination with other metals. Ni-based alloys show considerable resistance against different types of corrosion. Even the addition of a small quantity of nickel to an alloy improves its corrosion resistance character. Other uses of Ni includes catalyst for hydrogenation, cathodes for batteries and pigments ⁴²⁹.

A5.5.1. Corrosion rates

The results for the mass change of Ni samples exposed to different corrosion media (water-soluble ILs) are given in Figure 143. Corrosion results in $[\text{C}_4\text{C}_1\text{im}][\text{NTf}_2]$ are given in section 3.5.2.

Ni exposed to $[\text{C}_4\text{C}_1\text{im}]\text{Cl}$, at 20 °C for both water contents, shows no appreciable increase in the corrosion rate, even after long exposure times. (Figure 143A). At 120 °C, the same behaviour is observed at 75 mol% water content (Figure 143A). These results suggest passivation of the surface under those conditions. However, an experiment conducted for long exposure time (~2 months) at 70 °C and 75 mol% showed an increase in the mass loss without signs of passivation. MRC increases with temperature except at 75 mol%

Ni experienced the highest MCR when exposed to $[\text{HC}_1\text{im}]\text{Cl}$. Maximum MCR values took place at 75 mol% and decreased with increasing water content. Ni corrosion in neat $[\text{HC}_1\text{im}]\text{Cl}$ was significant. MRC increases with temperature (Figure 143C/D).

When Ni is exposed to $[\text{N}_{4111}][\text{HSO}_4]$ at 120 °C, similar trends to $[\text{HC}_1\text{im}]\text{Cl}$ are observed. *i.e.* significant MCR in neat conditions with a maximum at 75 mol%. At 70 °C, this trend inverts, the lowest corrosion rate was observed at dry conditions and increased with water content. (Figure 143F).

Overall, $[\text{C}_4\text{C}_1\text{im}]\text{Cl}$ is less corrosive than the protic ILs. $[\text{HC}_1\text{im}]\text{Cl}$ has the highest corrosion rates, an order of magnitude higher than $[\text{N}_{4111}][\text{HSO}_4]$. The corrosion rates in pure water were extremely small at all temperatures to be quantified through weight loss methods.

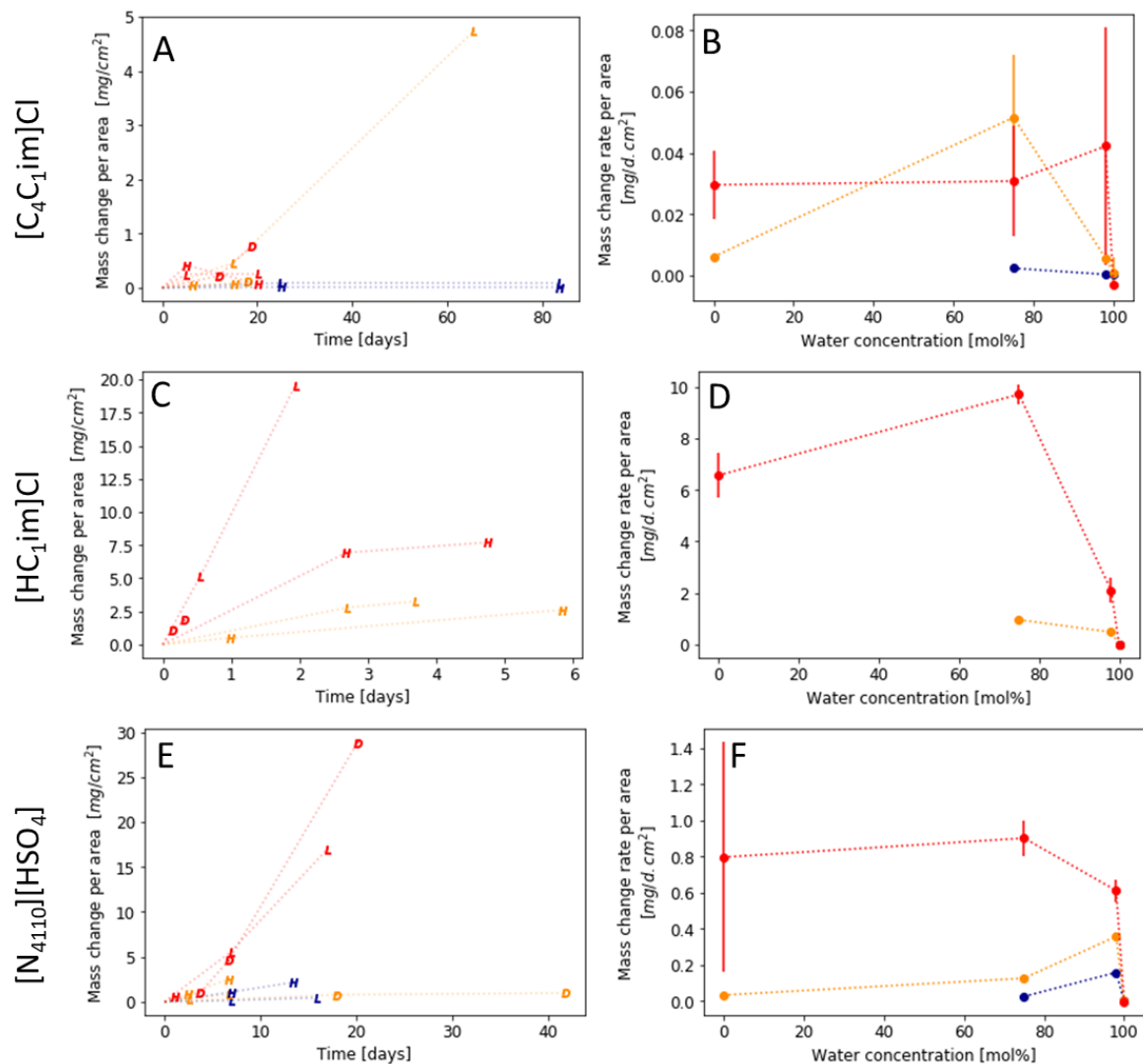


Figure 143. Mass change rates for nickel exposed to corrosive media. Left figures (A, C and E): Mass change per area as a function of time. Right figures (B, D and F): Mass change rates as a function of water content calculated from the average of the MCRs. Legend, D: dry, L: low water case, H: high water case, W: water. Colours: Blue 20 °C, orange 70 °C and red 120 °C. The lines have been added to guide the reader's eye.

A5.5.2. XRD

XRD results are shown in Figure 144. In general, nickel samples did not show significant corrosion changes under visual inspection and XRD technique was not appropriate to detect the chemical composition of thin films. For this reason, only samples exposed to $[N_{4110}][HSO_4]$ were tested, as XRF results showed a significant increase in the amount of sulphur (Table 46). The diffraction patterns showed five peaks, corresponding to 111 (44.5°), 200 (51.8°), 220 (76.4°), 311 (92.9°) and 222 (98.4°) (reference code: 00-004-0850). No significant changes were observed. The sample exposed to $[N_{4110}][HSO_4]$ (120 °C, dry and 3.71 d) showed an unidentified weak signal at around $2\theta \sim 30$.

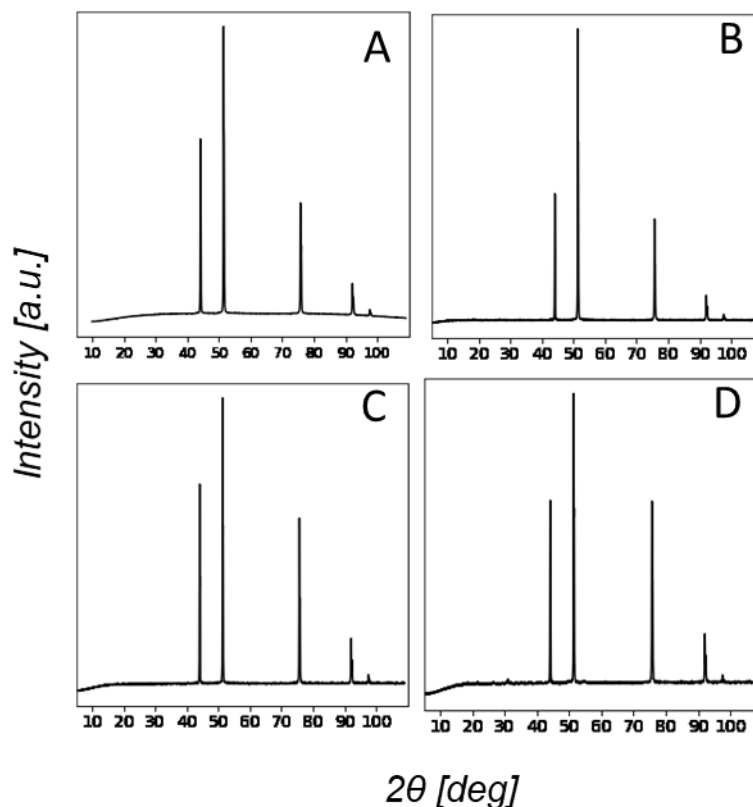


Figure 144. XRD patterns from nickel samples exposed to corrosive media. [A] Unexposed metal sample. [B] $[N_{4110}][HSO_4]$ (70 °C, dry and 17.96 d). [C] $[N_{4110}][HSO_4]$ (120 °C, dry and 20.12 d). [D] $[N_{4110}][HSO_4]$ (120 °C, dry and 3.71 d).

A5.5.3. XRF

XRF results summary for Ni is given in Table 46. A significant amount of sulphur was observed under some conditions for samples exposed to $[N_{4110}][HSO_4]$, suggesting the formation of sulphur containing products.

Table 46. XRF results summary for Ni.

Solvent	Observations
-	Ni: 99.675% (Traces of Dy, Si, Al, S)
H ₂ O	No significant changes.
$[C_4C_{1im}]Cl$	No significant changes. A slight increase in Cl content in samples (120 °C, 75 mol% and 5.11 d) and (120 °C, 98 mol% and 5.12 d).
$[HC_{1im}]Cl$	No significant changes. A slight increase in Cl content in samples: (70 °C, 75 mol% and 2.70 d), (120 °C, dry and 4.44 h), (120 °C, 98 mol% and 2.68 d) and (120 °C, 75 mol% and 4.90 d).
$[N_{4110}][HSO_4]$	Slight increase in S content. Significant increase in (70 °C, dry and 17.96 d), (120 °C, dry and 6.69 d) (~15%) and (120 °C, dry and 20.12 d) (~4%)

A5.5.4. SEM

The SEM/EDX images for selected samples are shown in Figure 145 to Figure 147. Overall, no significant morphological changes were observed. Some sections showed traces of yttrium (Y),

consistent with the XRF results. A sample exposed to water showed some white features that contained trace amounts of oxygen.

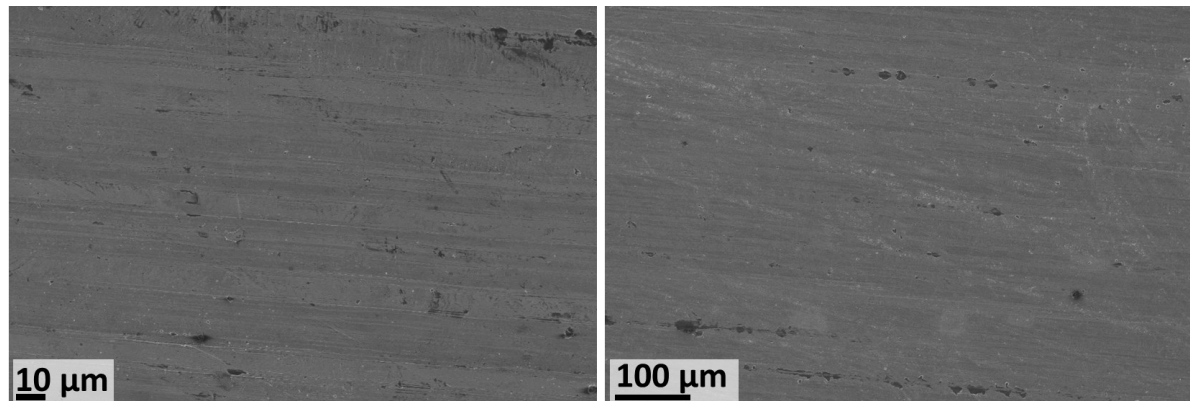


Figure 145. SEM Images obtained for a cleaned but untreated Ni sample.

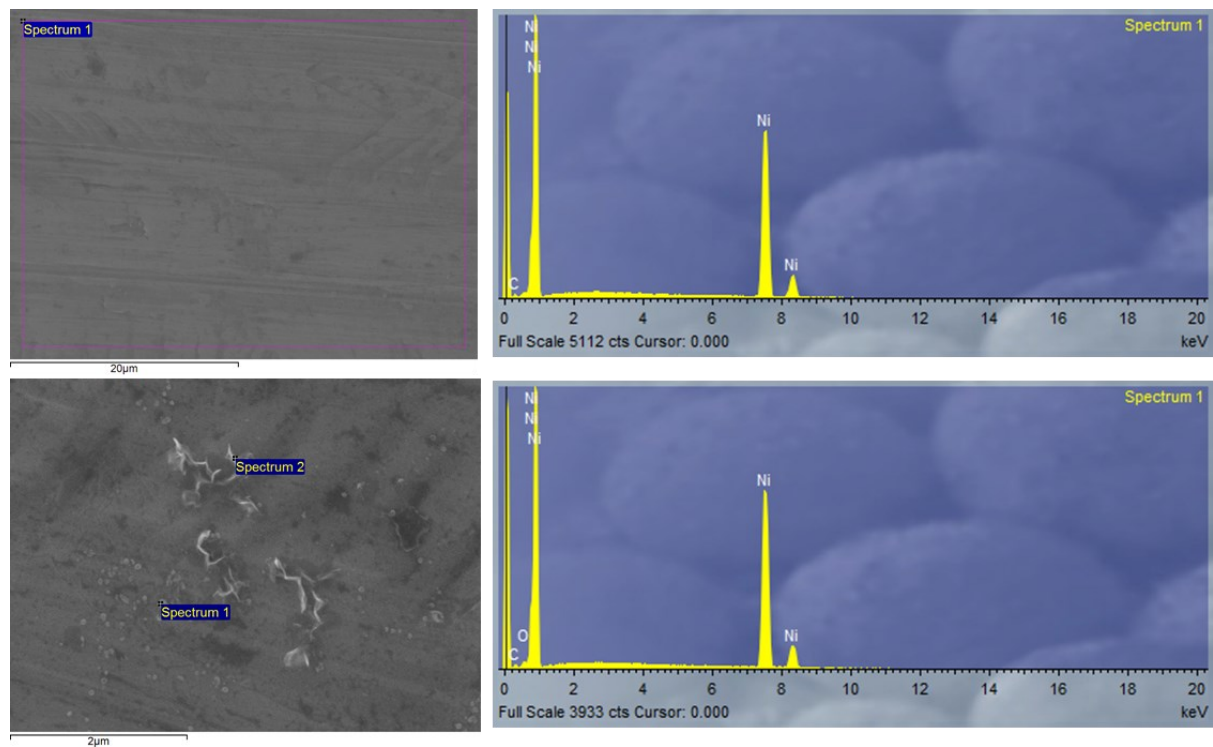


Figure 146. SEM/EDX for molybdenum samples. Top figure: Untreated molybdenum. Bottom figure: Molybdenum exposed to water (70 °C and 16 d). EDX atomic ratio (O:Ni) for sample exposed to water 1:24.4.

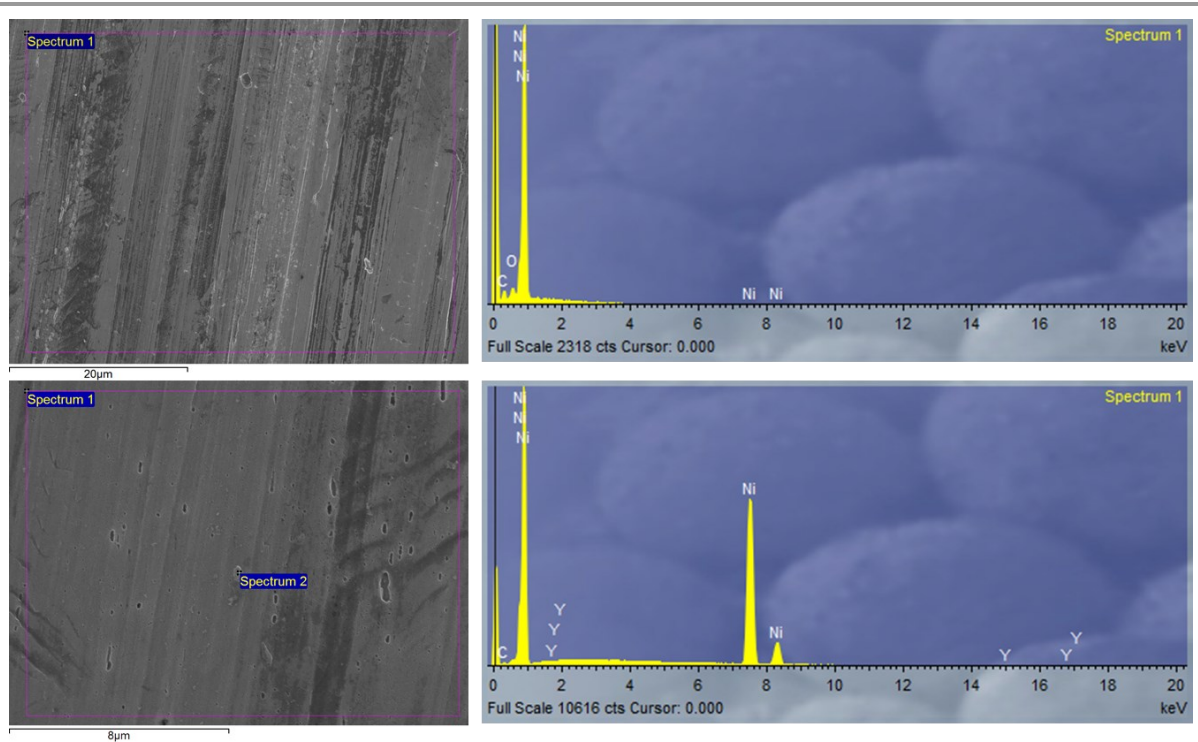
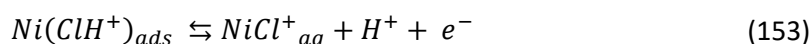
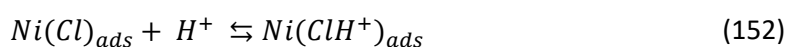
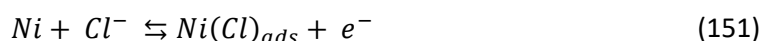


Figure 147. SEM/EDX for nickel samples exposed to $[C_4C_1im]Cl$ (70 °C, 98 mol% and 15.11 d). EDX atomic ratio O:Ni is 2:98 and Y:Ni is 0.1:99.9.

A5.5.5. Overall considerations

A5.5.5.1 Ni corrosion in chloride media

The corrosion resistance of nickel is due to the formation of a passive film on its surface upon exposure to the corrosive media ⁴²⁹. It has been noticed that the study of corrosion on pure Ni is limited to a few studies while the work on nickel alloys is vast. While it has been reported the use of pure nickel in very alkaline medium, it only exhibits a certain resistance in dilute hydrochloric acid at room temperature. This attack is enhanced by aeration and the presence of oxidising agents in the acid ⁴⁰². The anodic dissolution of Ni was studied by electrochemical methods and it was shown that it increases with acid concentration and stirring, but in this study, the presence of oxygen showed an increased tendency to passivation. Additionally, it was shown that amines inhibited Ni dissolution in HCl by adsorption mechanisms ⁴³⁰. The following mechanism was proposed for the dissolution of the Ni anode in acidic chloride solution ⁴³⁰:



The same mechanism was also proposed for the dissolution of iron in acidic chloride solutions⁴¹⁸. In the above mechanism, the rate-determining step (Eq. 152) is not an electrochemical process but is a chemical adsorption step that forms a kind of ion-pair at the electrode surface⁴¹⁸. This mechanism is consistent with the experimental determinations. The low MCR observed in [C₄C₁im]Cl, which forms neutral solutions upon dilution, leading to a small concentration of protons. In dry IL, there are no chemical species that can experience reduction; therefore, the oxidation is inhibited. In the presence of water, the C2 carbon in the imidazole ring might play a role in the increased corrosion rate compared to water. The MCR of [C₄C₁im]Cl at 20 °C 98 mol% (~80 wt% water content) was 0.0005 ± 0.0003 mg/d.cm², whereas in NaCl solution (20 wt% Na, 20°C and 15 d), was 0.014 mg/d.cm²⁴³¹, this shows that the corrosion in IL media is less than in inorganic salts, probably due to inhibitory effects of the cation moiety, which adsorbs in the surface of the metal inhibiting the corrosion process (section 3.2.7).

The presence of acidic protons in [HC₁im]Cl, clearly enhances the CR of Ni in this medium. Acidic protons can be reduced to hydrogen gas, and higher corrosion rates were observed in the low water content region. In the high-water region, there is a drop in the CRs. A corrosion study performed at room temperature (20 °C) and 1 hour showed that Ni dissolved in concentrated HCl with a rate of 22.68 mg/d.cm² and no corrosion on 48% sulfuric acid under the same conditions⁴³¹. The MRC of Ni exposed to protic ILs follows the same trends, *i.e.* it is more corrosive in [HC₁im]Cl than [N₄₁₁₀][HSO₄].

According to thermodynamic considerations and to the position of Ni in the electrochemical series (Table 7), the metal would be expected to dissolve as Ni²⁺ ions, with the evolution of H₂. In practice, the corrosion resistance of Ni in acid solutions is better than that indicated from the potential pH equilibrium diagrams attributed to the formation of a protective film of oxide or hydrated oxide. Furthermore, the position of Ni in the electrochemical series, which is only moderately active with respect to the H⁺/H₂ equilibrium, renders its corrosion rate in nonoxidizing acids slow in the absence of oxidants. It has been shown that the corrosion inhibition efficiencies non-ionic surfactant compounds, such as tween 80, 60, 40 and 20, in the corrosion of Ni in HCl solutions increase with increasing the hydrocarbon chain length, the presence of a double bond in the chemical structure of the surfactant and with increasing the surfactant concentration⁴²⁹. Similar trends have been observed for ILs used in inhibitors for other metals, which allow us to infer that the CR of ILs with longer chains than the ones studied here will be less corrosive.

A5.5.5.2 Ni corrosion in sulfate media

A corrosion study performed at room temperature (20 °C) and 1 hour showed that Ni does not corrode in 48 wt% sulfuric acid, due to the presence of a passive film consisting predominantly of Ni oxide formed on the metal surface. In the dilute solutions, nickel corrodes vigorously (due to the dissolution of oxide passive film) forming nickel sulfate⁴³¹. The rate of nickel dissolution in 5 wt% sulfuric acid solution was reported as 4.44 mg/d.cm² when exposed for 24h and decreased to 3.19 mg/d.cm² after 96-hour exposure⁴³¹. The experimental results of the corrosion of Ni exposed to [N₄₁₁₀][HSO₄] follow this trend for room temperature and 70 °C, *i.e.* the corrosion rates increase upon dilution. However, at 120 °C, the trend is reversed, and high corrosion rates were observed in dry condition (1.433 ±0.003 mg/d.cm²). The corrosion rates of Ni in this IL are less than in H₂SO₄. It was reported that the passive film formed on Ni surface in low concentrations of sulfuric acid is NiOOH⁴³² or NiO and Ni₂O₃⁴²⁹. On the other hand, β-NiSO₄·6H₂O was suggested as the passive compound formed in very high concentrations of sulfuric acid^{429,433}. The corrosion mechanism of Ni in hot sulfuric acids are discussed in the scientific literature⁴³³.

The corrosion behaviour of metallic materials in acidic-functionalized ILs, containing the [HSO₄]⁻ anion discussed for iron in section A5.3.5 also applied to Ni.

A5.5.5.3 Ni categorization system

Table 47 summarises the corrosion behaviour of Ni exposed to IL/solutions according to the categorization method. Ni is whether not affected by the corrosion medium (type-0) or actively dissolves without the deposition of products (type-4). It should be mentioned than in some high-level testing of Ni in [N₄₁₁₀][HSO₄] at 150 °C and 75 mol% water, a green solid deposited over the surface of the Ni (type-3).

Table 47. Summary of the classification system and corrosion type for nickel exposed to corrosive media. Corrosion types: NC: no corrosion, PC: pitting corrosion, USC: uniform surface corrosion and NUSC: non-uniform corrosion. Section 3.4.

	Solvent →	[C ₄ C ₁ im]Cl			[HC ₁ im]Cl			[N ₄₁₁₀][HSO ₄]			[C ₄ C ₁ im][NTf ₂]	Water	
	Water Content [mol fraction] →	Dry	0.75	0.98	Dry	0.75	0.98	Dry	0.75	0.98	Dry	1	
	Temperature [°C] ↓												
Classification System (Section 3.4)	20		0	0					0	4			0
	70	0	0	0		4	4	0	4	4		0	0
	120	0	0	0	4	4	4	4	4	4		0	0
	150											0	
Corrosion Type	20		NC	NC					NC	UC			NC
	70	NC	NC	NC		UC	UC	NC	UC	UC		NC	NC
	120	NC	NC	NC	UC	UC	UC	UC	UC	UC			NC
	150											NC	

A5.5.5.4 Ni corrosion in other ILs

Corrosion of pure nickel in ionic liquids has only been assessed through electrochemical methods in acidic-functionalized ILs, containing the $[\text{HSO}_4]^-$ anion⁴²⁵ and in Lewis neutral chloroaluminate ionic liquid, which will not be discussed here.

A5.6. Titanium

Titanium (Ti) is a chemical element with atomic number 22. It has mechanical properties comparable to mild steel, which has a very high strength to weight ratio, the highest of any metallic element. For these reasons, it has become an important material in the aerospace industry. Thanks to its corrosion resistance, its use has expanded to other applications, such as power plants, the food industry, petrochemical plants, refineries, heat exchangers, marine structures and medical prostheses⁴³⁴.

A5.6.1. Corrosion rates

The results for the mass change of titanium samples exposed to different corrosion media (water-soluble ILs) are given in Figure 148. Corrosion results in $[\text{C}_4\text{C}_{1\text{im}}][\text{NTf}_2]$ are given in section 3.5.2.

In general, the corrosion rates for Ti are extremely small, and that the order of magnitude of the measured rates is comparable to the order of magnitude of the experimental errors. The only exception was Ti exposed to $[\text{N}_{4110}][\text{HSO}_4]$ at high water contents (98 mol%) and 120 °C, which presented extremely high corrosion rates. Indeed, in this medium, Ti can be completely solubilised to yield a purple solution. During the experiments performed in this IL at those conditions, it was noticed that samples were not affected a very short times, but were completely dissolved at longer times (23 hours, 27 hours and 3 days) (Figure 149). Various attempts were performed to adjust the time to find samples with a reasonable mass loss to quantify the corrosion rates and perform surface analysis. However, this was not possible, as to whether the sample did not present significant mass losses or was completely dissolved, the region in which this happens is highlighted in blue in Figure 149, and is between 6 hours and 23 hours. The corrosion rate was calculated using the data points at 23 and 27 hours, assuming linear corrosion between time 0 and 100% dissolution at the time the samples were taken out of the oven. This approach underestimates the true corrosion rates, representing only a minimum value. It is expected that the actual corrosion rates once the protective layer is removed to be much higher.

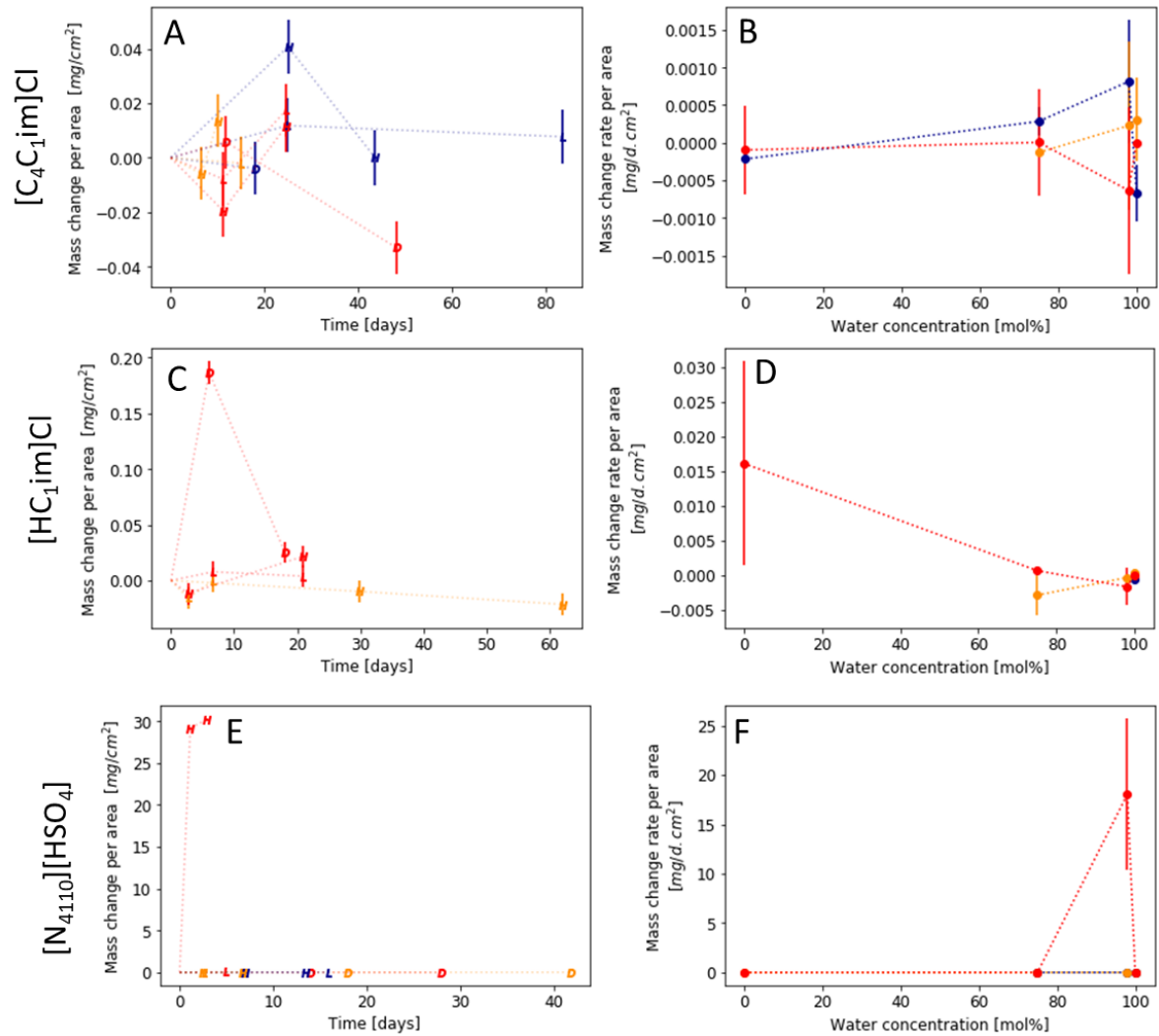


Figure 148. Mass change rates for Ti exposed to corrosive media. Left figures (A, C and E): Mass change per area as a function of time. Right figures (B, D and F): Mass change rates as a function of water content calculated from the average of the MCRs. Legend, D: dry, L: low water case, W: water. Colours: Blue 20 °C, orange 70 °C and red 120 °C. Lines have been added to guide the eye.

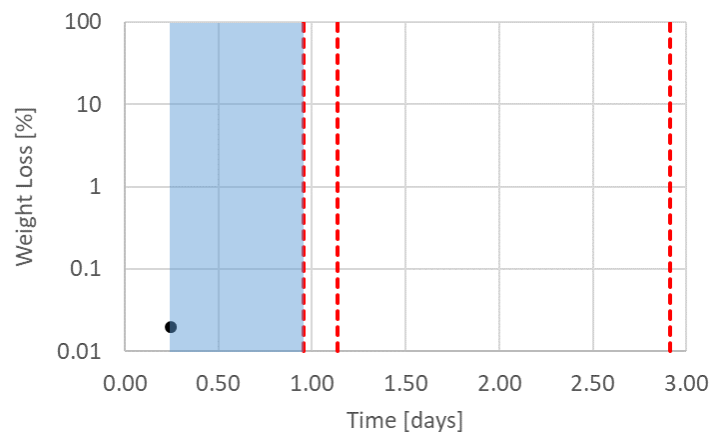


Figure 149. Corrosion behaviour of Ti samples exposed to $[N_{4110}][HSO_4]$, high water content (98 mol%) at 120 °C. Vertical lines correspond to specimens that completely dissolved. The blue region is the zone where the destructive attack starts.

A5.6.2. XRD

XRD was performed on selected samples. The pattern of the Ti sample pre-exposure is shown in Figure 150A. No significant changes were observed in the samples exposed to different corrosive media. $[N_{4110}][HSO_4]$ at 120 °C with high water content is capable of dissolving the Ti. The XRD spectra of a Ti sample exposed to those conditions showed no changes (Figure 150B), indicating that corrosion products are soluble in these solutions.

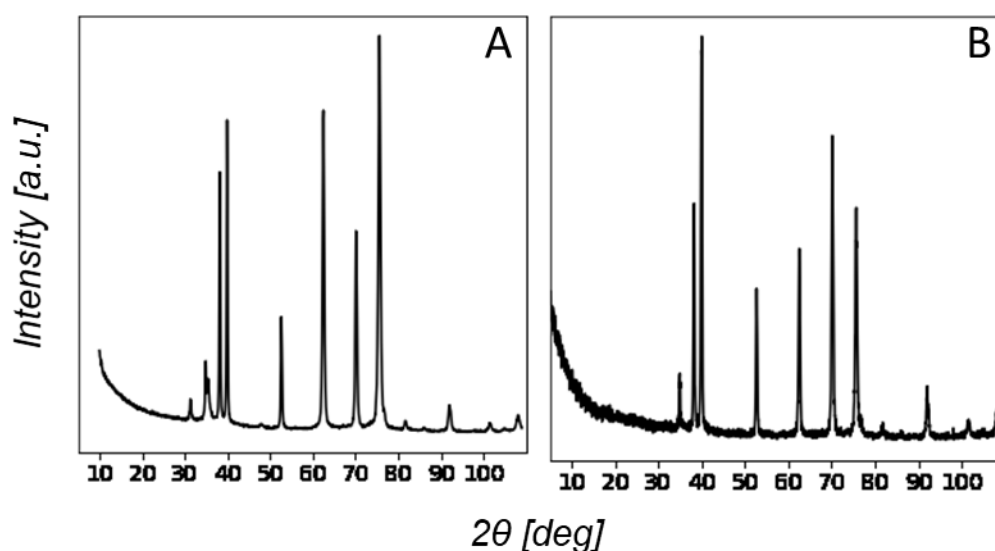


Figure 150. XRD patterns from Ti samples exposed to corrosive media. [A] Unexposed metal sample. [B] $[N_{4110}][HSO_4]$, (120 °C, 98 mol% and 2 d).

A5.6.3. XRF

XRF results summary for Ti is given in Table 48. No significant changes were observed at any experimental conditions.

Table 48. XRF results summary for titanium.

Solvent	Observations
-	Ti: 99.879% (Traces of W, Lu, Tb, P, Rb).
H ₂ O	No significant changes.
$[C_4C_{1im}]Cl$	No significant changes.
$[HC_{1im}]Cl$	No significant changes.
$[N_{4110}][HSO_4]$	No significant changes.

A5.6.4. SEM

SEM and SEM/EDX results for selected Ti samples exposed to corrosive media are given in Figure 151 and Figure 152. The untreated metal was delivered with a polished look. Under SEM, white features can be seen in the surface Figure 151. These zones are tungsten rich (W), which is consistent with the XRF results (Table 48), that shows traces of this element. In general, no apparent changes were observed from visual inspection of the titanium samples

exposed to all corrosive media tested in the work, with the exception of the sample exposed to $[N_{4110}][HSO_4]$ 98 mol% at 120 °C, which showed extreme corrosion and was able to completely dissolve the titanium coupons, forming a violet solution. Figure 152 shows 2 details of a sample exposed to $[C_4C_1im]Cl$ and water. No significant changes in the chemical composition are detected through EDX. The sample exposed to water showed white figures dispersed throughout the surface, however, any analytical technique tested shows any changes in chemical composition.

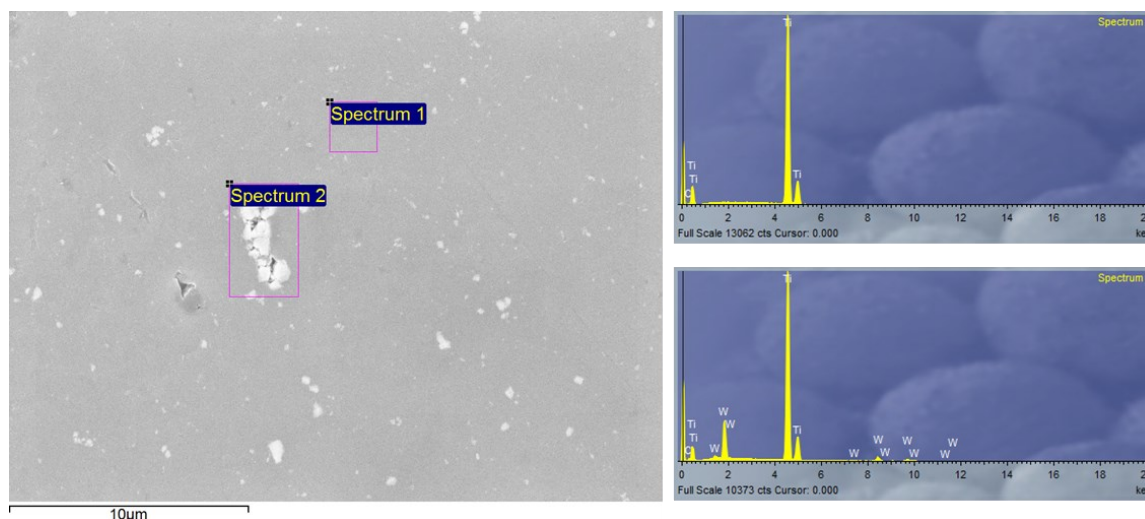


Figure 151. SEM/EDX images obtained for a cleaned but untreated Ti sample. EDX: Spectrum 1 only shows the presence of titanium. Spectrum 2 shows an atomic ratio of Ti:W of 14.6:1.

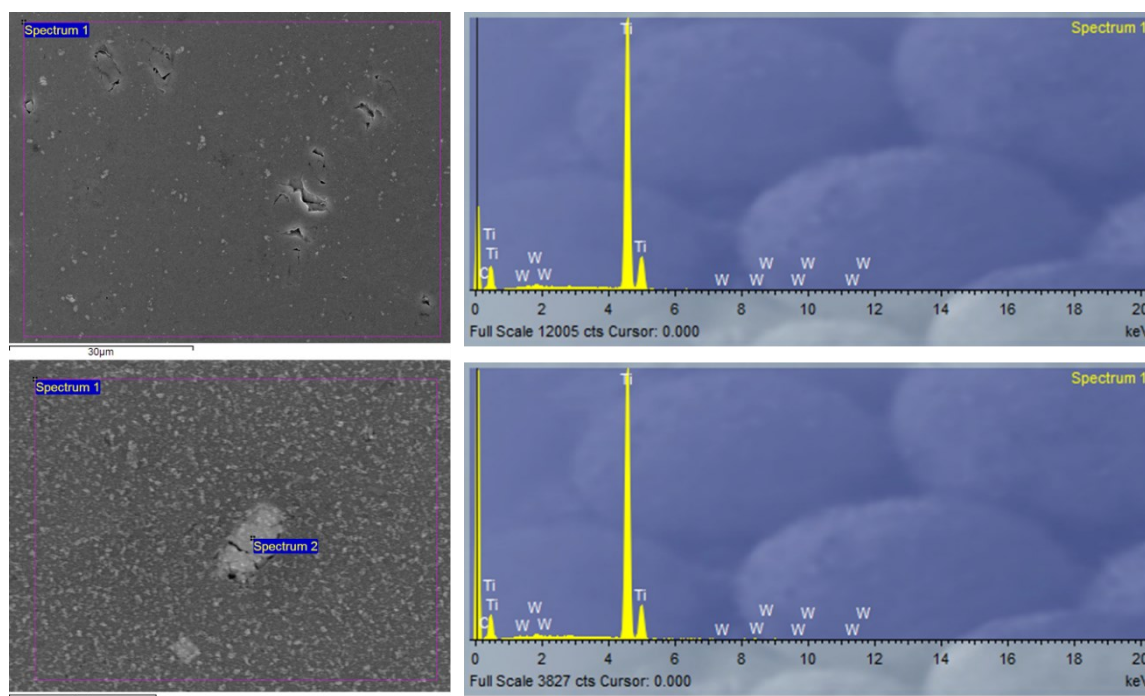


Figure 152. SEM/EDX for titanium exposed to corrosive media. Top: titanium exposed to $[C_4C_1im]Cl$ (70 °C, 98 mol% and 10.09 d). Bottom: titanium exposed to water (70 °C, 100 mol% and 16.00 d). EDX shows that the atomic ratio of Ti:W is 278.5:1 and 304.8:1 for the sample exposed to $[C_4C_1im]Cl$ and water respectively.

A5.6.5. Overall considerations

Titanium is a very reactive metal and forms a thin titanium dioxide film, approximately 1.5–10 nm in thickness when exposed to an aerated environment. This oxide is usually compact, adherent to the substrate and chemically stable in a variety of environments, and it is responsible for the excellent corrosion resistance of titanium⁴³⁴. Despite its excellent corrosion resistance, it has been reported that titanium suffers corrosion in aggressive environments. It may experience both uniform corrosion and localized corrosion, crevice and pitting, hydrogen embrittlement, stress-corrosion cracking, fretting corrosion and erosion⁴³⁴. To overcome these potential issues, specific alloys containing palladium, nickel and molybdenum were introduced. These elements promote cathodic reactions, helping the system to reach a passive condition. However, their inclusion is expensive⁴³⁴. Another option to improve the corrosion resistance of Ti is to increase the natural thickness of TiO₂ by surface treatments, such as oxidation treatments, specifically anodization, which can increase the TiO₂ thickness, to obtain a mostly amorphous phase. Thermal oxidation, chemical oxidation and ion implantation are other possible techniques⁴³⁴. Such strategies could be implemented to improve the corrosion resistance of this material in ionic liquids.

The nature and composition of the protective oxide covering the surface of titanium depends on the environmental condition in which it is formed. In aqueous environments, the oxide formed is mainly amorphous TiO₂ with some contributions of other oxidation states, such as Ti₂O₃ and TiO. At high temperatures, rutile, a crystalline and more chemically resistant form of TiO₂, grows, while intermediate temperatures usually generate less protective oxide, in the crystal form of anatase⁴³⁴.

A5.6.5.1 Ti corrosion in chloride media

According to the Pourbaix diagram (pH-potential) of Ti in water, Ti is in passive conditions over a wide range of potentials and becomes vulnerable only in strongly oxidizing conditions, where oxide is dissolved, and under strongly reducing conditions, where hydrides are formed. The passivity range is relatively insensitive to chlorides, and for this reason, Ti has an innate resistance in aqueous chloride-containing environments. For this reason, the corrosion rates of Ti in water and [C₄C₁im]Cl and were extremely low, up to a temperature of 120 °C. It has been reported that titanium experiences different types of corrosion at 120 °C in hydrochloric acid and chloride-containing solutions acidify with hydrochloric acid, such pitting corrosion as well as uniform and non-uniform surface corrosion⁴⁰². In this reference, it is shown that titanium offers good corrosion resistance in high chloride containing environments without

the presence of hydrochloric acid. For example: in KCl 25 wt% or NiCl₂ 30 wt% solutions, no corrosion was observed up to 160 °C. In NH₄Cl 25 wt% solution, an analogous form of the ionic liquids, pitting corrosion was observed 160 °C and no corrosion at 140 °C and below. For Ba₂Cl 30 wt% solutions, pitting corrosion was observed 140 °C and 160 °C, with no apparent corrosion at 120 °C and below ⁴⁰². Other chloride-containing solutions become dangerous for titanium only at high temperature. NH₄Cl, for example, causes just 0.004 and <0.001 mm/year of corrosion on titanium at concentrations of 20 wt% and 40 wt% at boiling temperature, but as the temperature is raised to 200 °C, corrosion speeds up to 3.9 mm/year at 40 wt% of NH₄Cl ⁴⁰². Due to the corrosion inhibition effect of [C₄C₁im]Cl discussed previously, it is probably safe to use Ti for high-temperature applications. However, experimental testing is required, not only for the corrosion of the metal but also for the stability of the ionic liquid in contact with Ti. [HC₁im]Cl can decompose at high temperatures, leading to HCl. At 100 °C, Ti can only be used safely with HCl up to a concentration of 0.5% ⁴⁰². Therefore, for high-temperature applications, more testing is required to establish if Ti can be safely used with [HC₁im]Cl. Hydrochloric acid is a non-oxidizing acid, and therefore, titanium is only moderately resistant to attack in its solutions. The main mechanism of corrosion in HCl is generalized corrosion. The corrosion rate increases uniformly with temperature and concentration. Deaerated solutions increase corrosion at lower acid concentrations, but reduce corrosion in concentrations above 10% ⁴³⁴.

A5.6.5.2 Ti corrosion in sulfate media

Ti corrosion resistance is strongly dependent on the resistance of its protective oxide, which can vary as a function of the surrounding environment. The existence of this layer can be the origin of the excellent corrosion resistance observed for in ionic liquid and water solutions, except in high-water content [N₄₁₁₀][HSO₄], which completely dissolved the metallic samples yielding a purple solution. This allows concluding that the presence of the protective layer is not stable in [N₄₁₁₀][HSO₄] with high water contents at high temperatures (120 °C), and that this layer dissolves at a considerable lower rate than the metal in its reduced form. Once the layer is consumed, the attack proceeds with at high rates, and therefore it is not possible to quantify accurately using thin coupons. This shows that there is no passivation in the dissolution of titanium in this media, and will be classified as type-4. For all other media, it will be classified as type-0.

Although titanium and zirconium have the same number of valence electrons and are in the same group in the periodic table, they differ in many chemical and physical properties. For

example, zirconium can be used in hot H₂SO₄ solutions while titanium use in H₂SO₄ containing environments is more limited. At room temperature, Ti is resistant up to concentrations of 10 wt%, but this value decreases rapidly as temperature increases: at boiling point, a corrosion rate as high as 9 mm/year is reported in solutions of H₂SO₄ 1 wt%. From room temperature up to 60 °C, the material is attacked with a linearly growing rate up to about 10 wt% concentration, then the corrosion rate grows more slowly with increasing concentration up to 40 wt%, after this value, the corrosion rate decreases, reaching a local minimum at 60 wt%, then restarts to grow rapidly up to a maximum at 80 wt%. At room temperature, purging the solution with nitrogen only slightly affects the corrosion rate, but at higher temperatures, the rate increases catastrophically in deaerated solutions. The presence in the solution of small amounts of oxidizing agents or heavy metal ions significantly increases corrosion resistance. As an example, the presence of 0.25% of copper sulfate in 30% H₂SO₄ reduces the corrosion rate to less than 0.1 mm/year^{402,434}. As expected, the corrosion rate of Ti is less in [N₄₁₁₀][HSO₄] than H₂SO₄. It has been reported that uniform corrosion occurs in reducing environments, particularly in acidic conditions at high temperature. In strong hot reducing acids, the oxide film is dissolved, and the bare metal is oxidized to soluble trivalent ions (Ti → Ti³⁺ + 3e⁻). In the presence of dissolved oxygen in the hot acid, the Ti³⁺ ions are oxidized to Ti⁴⁺ ions, and the latter subsequently hydrolyses to form insoluble titanium dioxide. This film may reduce corrosion propagation. In the absence of oxygen, when severe corrosion attack has occurred in a reducing hot acid solution, a matt silver-grey surface is observed, due to the formation of titanium hydrides in the film⁴⁰².

A5.6.5.3 Ti categorization system

It has been reported that Ti oxide film growth may manifest itself as a coloured surface and very slight weight gain by test coupons. The colour acquired from the oxide is due to interference between light rays reflected from the oxide and light rays reflected by the oxide and then reflected from the metal underneath, and for this reason, the resulting colour is strongly dependent on film thickness⁴³⁴. In the experiments, no apparent changes were observable in the coupons under any experimental conditions, therefore the systems are classified as type-0.

No significant colour change was appreciable in the solutions and neat ILs after the immersion except when immersed in [N₄₁₁₀][HSO₄] at high water content and 120 °C, which dissolved the material forming a violet solution. As per the coupons, no significant changes were observed at all.

Table 49 summarises the classification system as well as corrosion types for Ti and ILs systems. Titanium behaves at type-0 in all media at all conditions except in $[N_{4110}][HSO_4]$ 98%mol and 120 °C, in which actively dissolves without passivation (type-4).

Table 49. Summary of the classification system and corrosion type for titanium exposed to corrosive media. Corrosion types: NC: no corrosion, PC: pitting corrosion, USC: uniform surface corrosion and NUSC: non-uniform corrosion. Section 3.4.

	Solvent →	$[C_4C_1im]Cl$			$[HC_1im]Cl$			$[N_{4110}][HSO_4]$			$[C_4C_1im][NTf_2]$	Water	
	Water Content [mol fraction] →	Dry	0.75	0.98	Dry	0.75	0.98	Dry	0.75	0.98	Dry	1	
	Temperature [°C] ↓												
Classification System (Section 3.4)	20	0	0	0							0	0	
	70	0	0	0				0	0	0	0	0	
	120	0	0	0	0	0	0	0	0	4	0	0	
	150										0		
Corrosion Type	20	NC	NC	NC							CN	NC	NC
	70	NC	NC	NC				NC	NC	CN	CN	NC	NC
	120	NC	NC	NC	NC	NC	NC	CN	CN	USC			NC
	150										NC		

A5.6.5.4 Ti corrosion in other ILs

The corrosion behaviour of titanium has not been studied in common ionic liquids. Only 2 references were found in the literature for chloroaluminate-based ionic liquids with electrochemical measurements and will not be discussed here.

A5.7. Zinc

Zinc (Zn) is an element with atomic number 30. Zinc is a slightly brittle metal at room temperature and has a blue-silvery appearance when oxidation layers are removed. Corrosion-resistant zinc plating of iron (hot-dip galvanizing) is the major application for zinc ⁴³⁵.

A5.7.1. Corrosion rates

The results for the mass change of zinc samples exposed to different corrosion media (water-soluble ILs) are given in Figure 153. Corrosion results in $[C_4C_1im][NTf_2]$ are given in section 3.5.2.

The weight loss in all samples was positive. For the $[C_4C_1im]Cl$ system, the maximum MCR was observed at a water content of 75 mol% with a significant decreased at 98 mol%. From this data, one would think that a solution of this IL containing 75 mol% would be more aggressive towards Zn than at high water content. It was actually noticed that at high water content, some samples got severely attacked showing cracks and holes on the surface. As it will be shown

later, there was a diversity of materials deposited on the surface, reducing the apparent MCR. In dry $[\text{C}_4\text{C}_1\text{im}]\text{Cl}$ the attack was very small. The attack of protic ILs on zinc was extreme, and the experimental matrix was modified. Indeed, the maximum temperature tested for $[\text{HC}_1\text{im}]\text{Cl}$ was 45 °C. In this ILs at 75 mol%, the attack was more severe than at 98 mol%. At 45 °C, one sample experience extreme mass loss, probably due to the dissolution of an oxide protective layer, followed by rapid dissolution of the metallic zinc. In $[\text{N}_{4110}][\text{HSO}_4]$ the MCR could be measured at 120 °C for water contents below 75 mol%. However, at high water, it was tested only at 45 °C. This point showed a lower MCR than at room temperature. More experiments need to be carried out to determine if this behaviour is due to experimental errors or due to the formation of passive layers which are stable at this temperature. In dry $[\text{N}_{4110}][\text{HSO}_4]$ the attack was lower compared to the systems with water. At 120 °C, the attack was similar for dry IL and 75 mol%. However, in dry IL, the mass change per area for 2 determinations at different times was the same, which could be an indication that the Zn is in a passive state, *e.g.* if it reacted with residual water present in the IL to form thin protective layers not detectable with the analytical tools used in this work. To prove this point, more experimental work needs to be carried out.

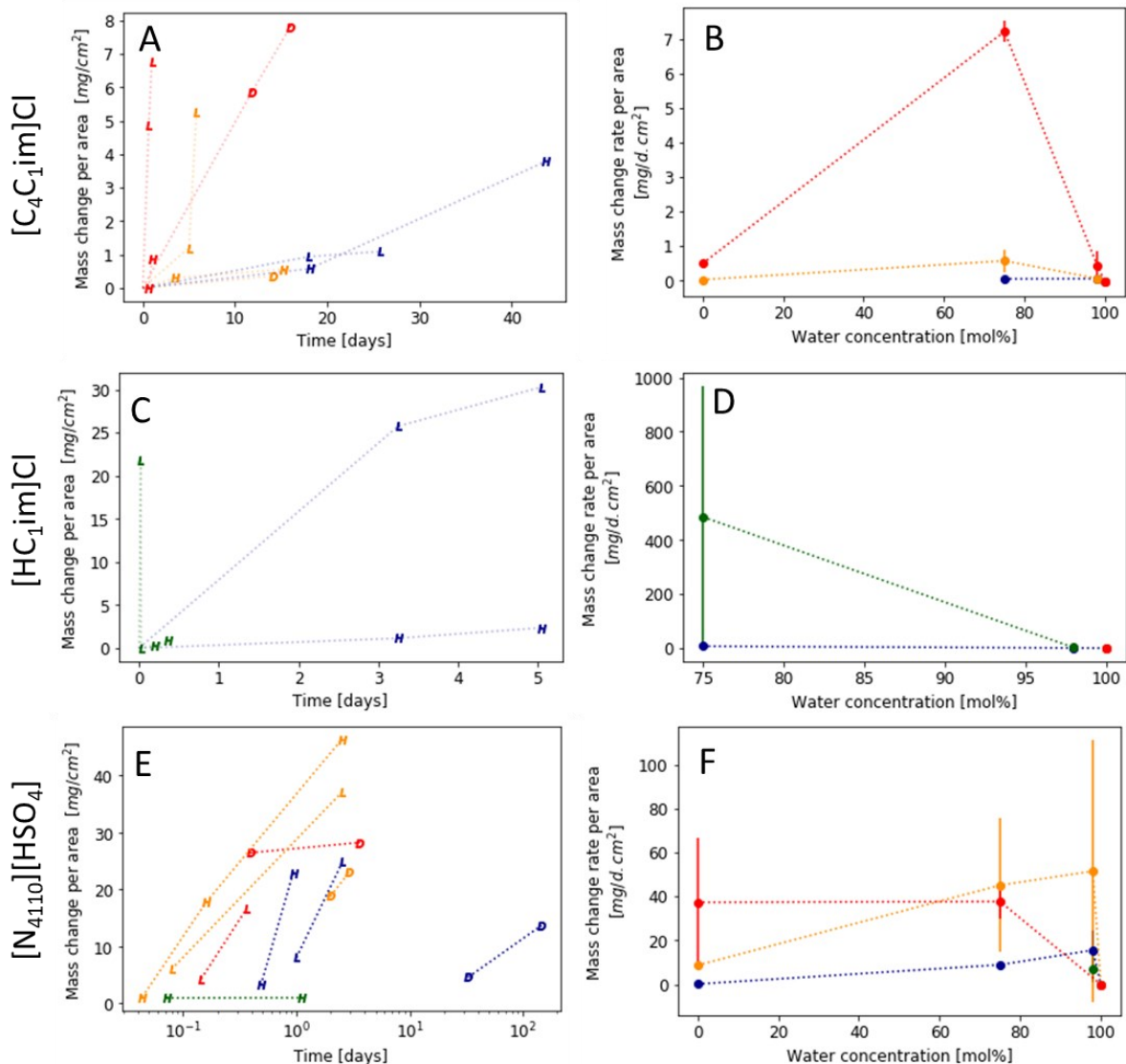


Figure 153. Mass change rates for Zn exposed to corrosive media. Left figures (A,C and E): Mass change per area as a function of time. Right figures (B, D and F): Mass change rates as a function of water content calculated from the average of the MCRs. Legend, D: dry, L: low water case, H: high water case, W: water. Colours: Blue 20 °C, green 45 °C, orange 70 °C and red 120 °C. Lines have been added to guide the eye.

As it will be explained later in the following sections, many chemical species were detected in [C₄C₁im]Cl at 20 °C and 98 mol%. To address the effect of contaminants in the IL on the formation of particles, the experiments were repeated with another batch of IL (IL-2) from another supplier, as explained in Section 3.3.1.1. Another set of experiments were performed under agitation with a magnetic stirrer and 650 rpm. Halogens, such as chloride, and 1-methylimidazole are common impurities that are often present in ILs which originate from their synthesis route. IL-1 formed transparent solutions while IL-2 formed orange solutions, which is consistent with the presence of 1-methylimidazole. The MCR at 20 °C and 98 mol% in IL-1 was 0.06 ± 0.03 mg/d.cm², in IL-2 0.09 ± 0.09 mg/d.cm² without agitation and 0.13 ± 0.07 mg/d.cm² with agitation. These results show that impurities and agitation have an impact on the MCR for zinc in [C₄C₁im]Cl at 20 °C and high water content. However, MRC measurement

for this system is misleading as a material is being deposited in the surface, as it will be shown in the next sessions.

A5.7.2. XRD

XRD proved to be a powerful technique to detect crystalline phases formed from zinc exposed to corrosive media. A diversity of compounds were seen when exposed to neutral media, *e.g.* water and $[C_4C_{1im}]Cl$, therefore, these systems were explored in detail (section 3.5.4.1). No significant changes were observed in the diffraction patterns when exposed to protic ILs ($[HC_{1im}]Cl$ and $[N_{4110}][HSO_4]$), thus only a few samples were tested. Selected XRD spectra are shown in Figure 154.

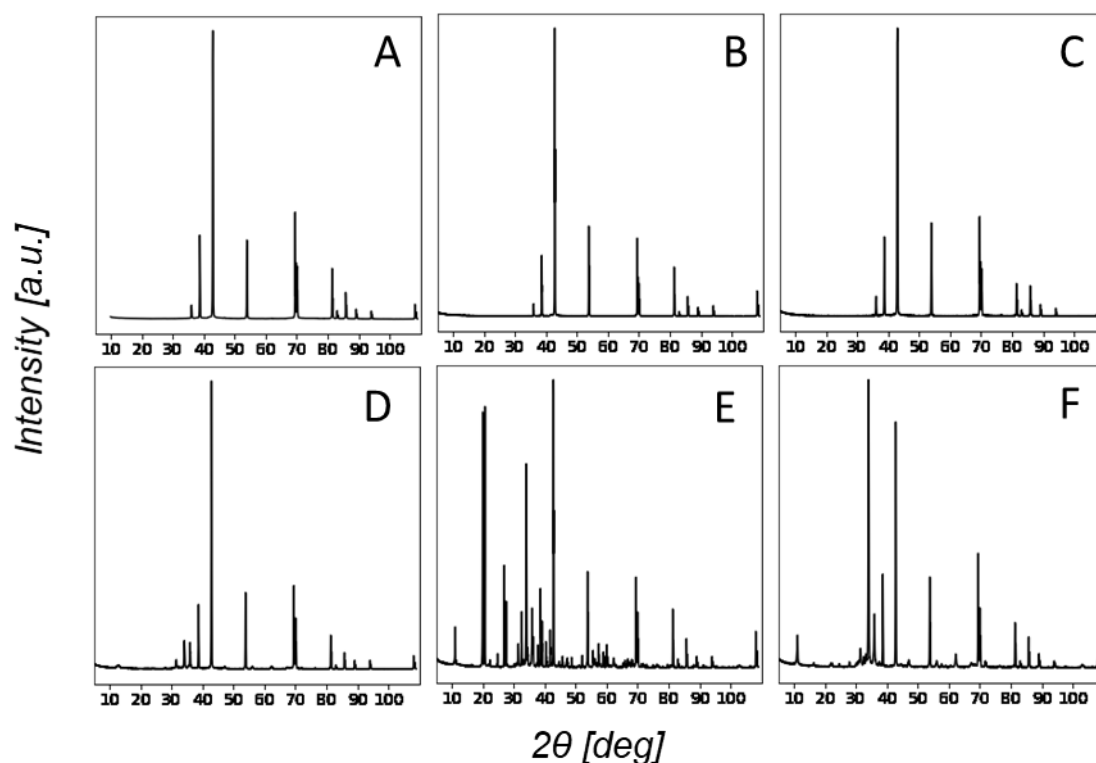


Figure 154. XRD patterns from Zn samples exposed to corrosive media. [A] Unexposed metal sample showing Zn signals. [B] $[N_{4110}][HSO_4]$ (70 °C, dry and 2.00 d) showing only Zn signals. [C] $[HC_{4im}]Cl$ (20 °C, 98 mol% and 5.05 d) showing only Zn signals. [D] Water (20 °C and 5.05 d) showing Zn, ZnO and ZCAR signals. [E] $[C_1C_{4im}]Cl$, (20 °C, 98 mol% and 25.72 d) showing Z, ZnO, ZHC and ϵ -Zn(OH)₂ signals. [F] $[C_1C_{4im}]Cl$, (20 °C, 98 mol% and 25.72 d) showing Z, ZnO, ZHC signals.

A5.7.3. XRF

XRF results summary for Zn is given in Table 50. Samples exposed to $[C_4C_{1im}]Cl$ showed a significant increase in the amount of Cl, consistent with the formation of ZHC. Samples exposed to $[HC_{1im}]Cl$ did not show any significant changes except for the detection of sodium, due to

sample contamination during handling. Slight amount of sulfur was observed under some conditions for samples exposed to $[N_{4110}][HSO_4]$. The origin of this signals is not clear, it might be from contamination during sample handling, insufficient sample cleaning or formation of sulphur containing products, undetected by the other techniques. Some samples showed the presence of sodium, due to contamination during sample handling.

Table 50. XRF results summary for Zn.

Solvent	Observations
-	Zn: 99.909% (Traces of Si, Co, S)
H ₂ O	No significant changes. Increased in the Cl content: Significant change (1.2%) when exposed at 20 °C and 98 mol% during 6.03 d and 14.31 d.
$[C_4C_{1im}]Cl$	Slight change when exposed to at 70 °C and 98 mol% during 3.53 d and 15.11 d, at 75 mol% for 5.83 d and at 20 °C and 98 mol% during 15.72 d and 47.90 d.
$[HC_{1im}]Cl$	No significant changes. Sodium detected (3%)
$[N_{4110}][HSO_4]$	Slight increase in the S content.

A5.7.4. SEM

For the zinc and neutral media, water and $[C_4C_{1im}]Cl$, corrosion products formed to a significant extent over the surface of the metals. Therefore, this section has been divided into PILs and AIL media.

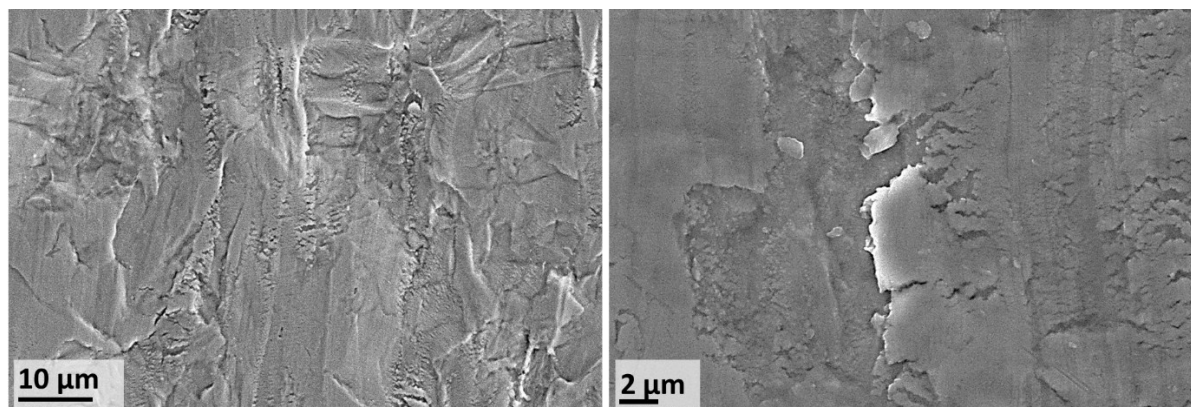


Figure 155. SEM Images obtained for a cleaned but untreated Zn sample.

A5.7.4.1 SEM images of Zn in PILs

The SEM/EDX images for Zn exposed to $[N_{4110}][HSO_4]$ are given in Figure 156 and Figure 157. In this system, Zn experiences a general surface attack with the formation of sponge-like patterns. The upper part of the sponge-like structures showed the presence of oxygen. It is not clear if this is due to adsorbed oxygen or due to the corrosion process itself in the IL medium

or reaction with atmospheric oxygen upon exposure for surface analysis. No particles were detected but pitting corrosion was also observed.

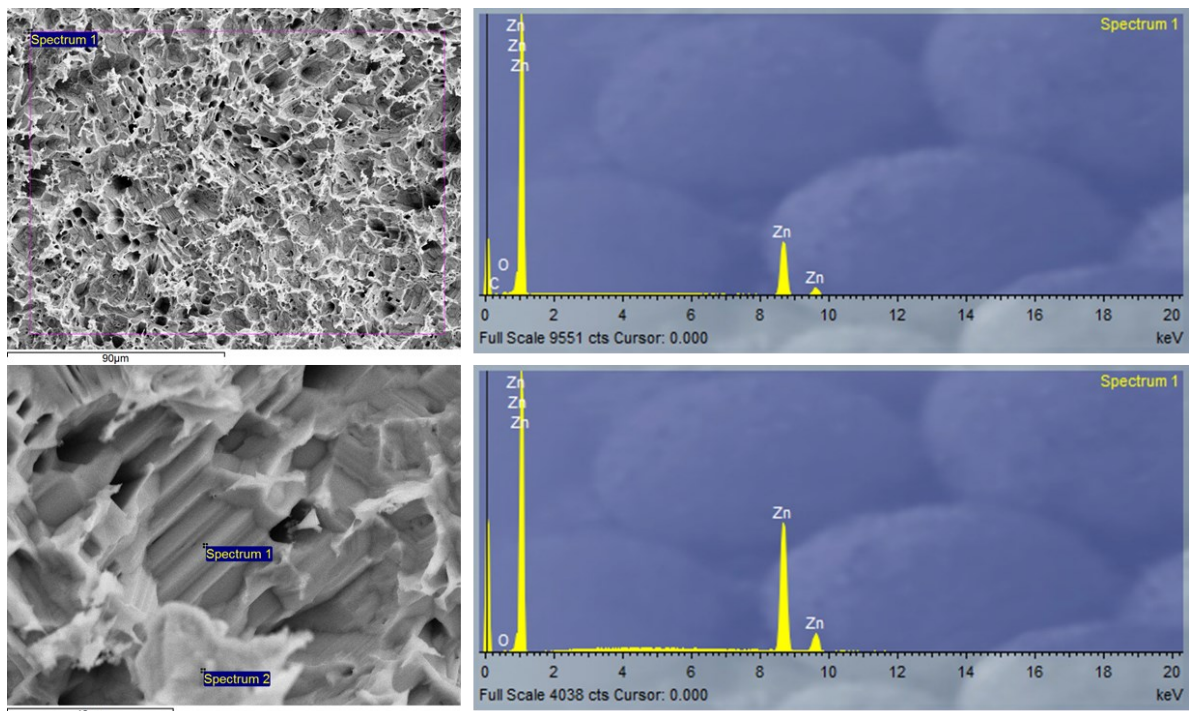


Figure 156. SEM/EDX of zinc exposed to $[N_{4110}][HSO_4]$ (75 mol%, 20 °C and 2.5 d). EDX Top figure. O:Zn atomic ratio 1:18 for spectrum 1. Bottom Figure. O:Zn atomic ratio 1:68 and 1:7 for spectrum 1 and 2 respectively.

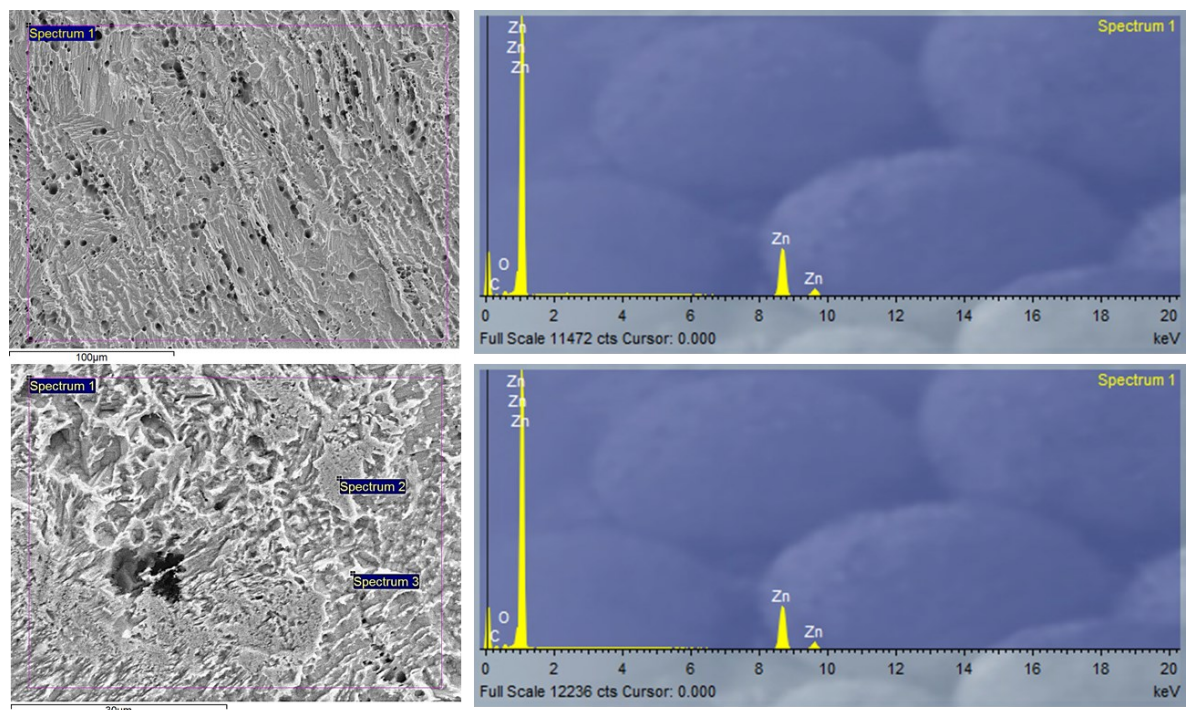


Figure 157. SEM/EDX of zinc exposed to $[N_{4110}][HSO_4]$ (98 mol%, 20 °C and 11.7 h). EDX Top figure. O:Zn atomic ratio 1:7.5 for spectrum 1. Bottom Figure. O:Zn atomic ratio 1:6 and 1:7 for spectrum 1 and 3 respectively and oxygen was not detected in zone 2.

The SEM/EDX images for Zn exposed to are given in Figure 158 and Figure 159. The samples exposed to low water content showed the formation of a sponge-like structure over the surface (Figure 158). The samples exposed to high water content showed extreme pitting corrosion but no particles nor oxygen was detected on the surface (Figure 159).

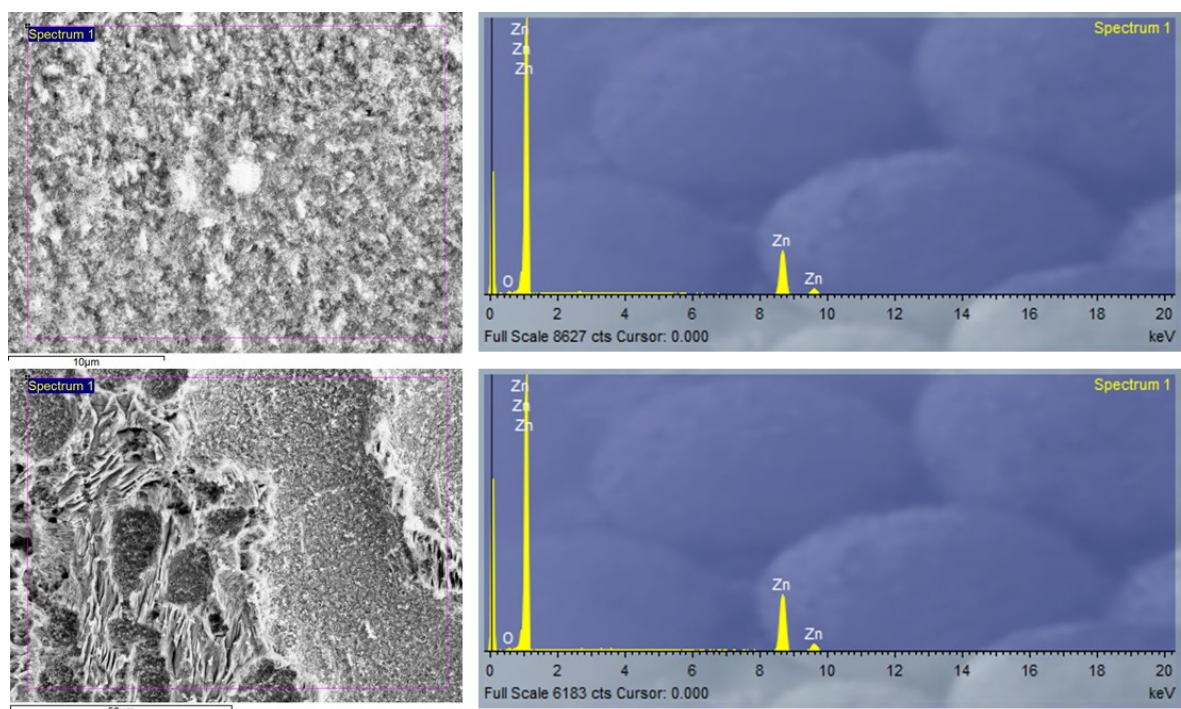


Figure 158. SEM/EDX of zinc exposed to $[\text{HC}_1\text{im}]\text{Cl}$ (75 mol%, 20 °C and 3.25 d). EDX Top figure. O:Zn atomic ratio 1:11.6 for spectrum 1. Bottom Figure. O:Zn atomic ratio 1:10.7 for spectrum 1.

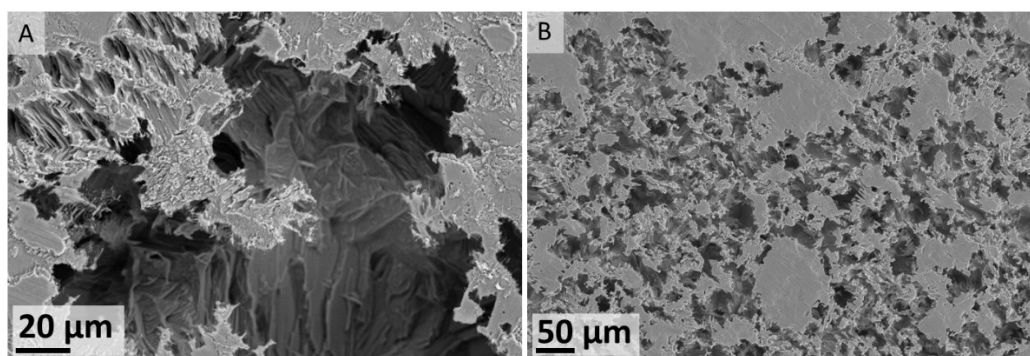


Figure 159. SEM of zinc exposed to $[\text{HC}_1\text{im}]\text{Cl}$ 98 mol% and 20 °C. [A] 3.25 d. [B] 5.05 d.

A5.7.4.2 SEM images of Zn in aprotic IL solutions and water

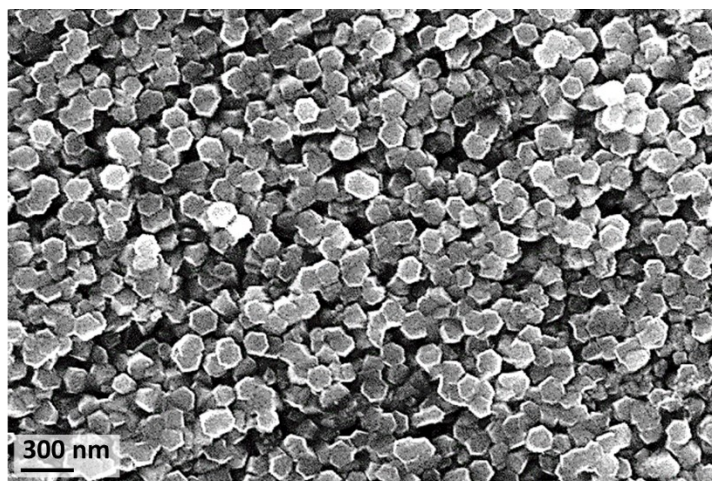


Figure 160. SEM image of zinc substrate after exposure to $[C_4C_1im]Cl$ (Sigma-Aldrich, $X_{H_2O}=0.75$ solution, 20 ± 1 °C) for 26 d, showing the top of hexagonal nanorods (average size 150 ± 30 nm, $n=278$). Published by The Royal Society of Chemistry ¹⁶⁹.

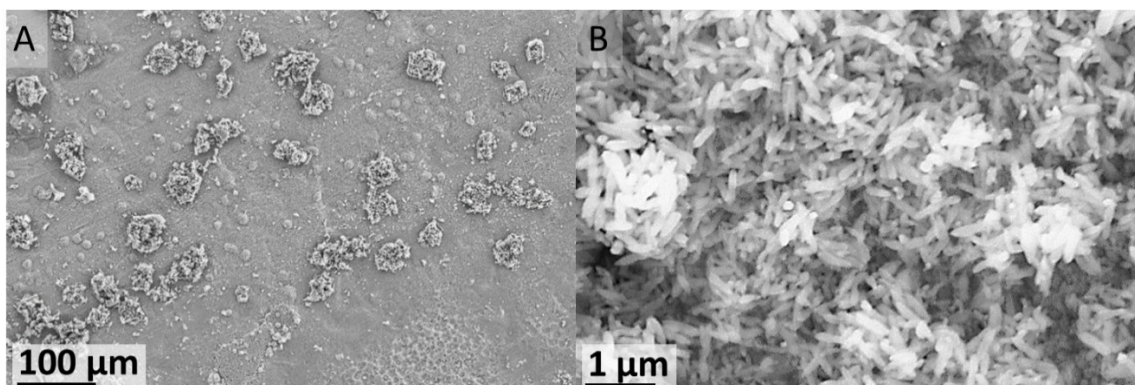


Figure 161. Magnified zinc surface exposed to $[C_4C_1im]Cl$ solution (IL-1, $X_{H_2O}=0.98$ and 20 ± 1 °C) for 18 d showing a ZnO structure. Published by The Royal Society of Chemistry ¹⁶⁹.

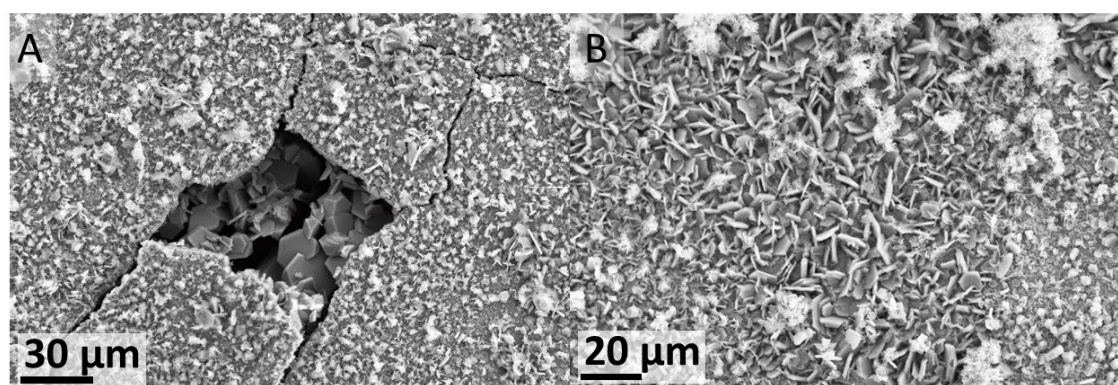


Figure 162. Magnified zinc surfaces exposed to $[C_4C_1im]Cl$ solution (IL-1, $X_{H_2O}=0.98$ at 20 ± 1 °C) for 18 d showing ZHC. Published by The Royal Society of Chemistry ¹⁶⁹.

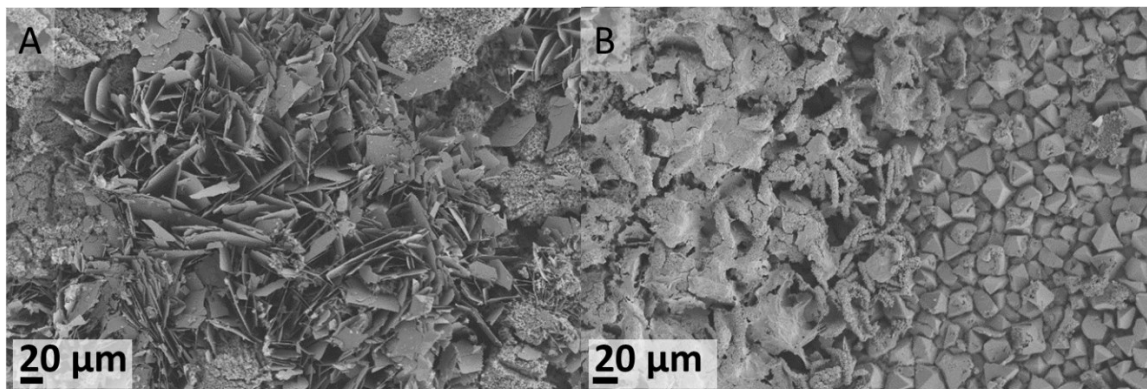


Figure 163. Magnified zinc surface exposed to $[C_4C_1im]Cl$ solution (IL-1, $X_{H_2O}=0.98$ and 20 ± 1 °C) for 44 d. [A] ZHC tablets. [B] ϵ - $Zn(OH)_2$ octahedrons and amorphous solid containing chlorides. Published by The Royal Society of Chemistry ¹⁶⁹.

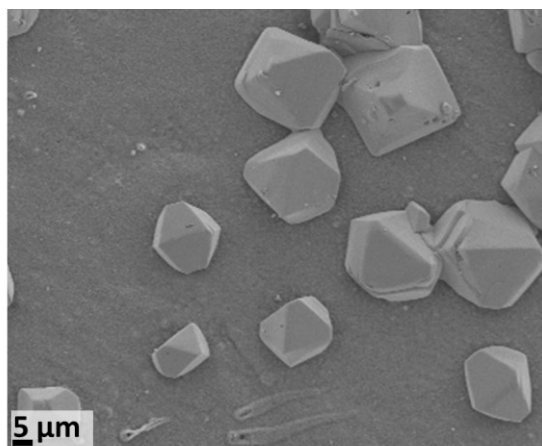


Figure 164. Magnified zinc surface exposed to $[C_4C_1im]Cl$ solution (IL-2, $X_{H_2O}=0.98$ and 20 ± 1 °C) for 46 d. ϵ - $Zn(OH)_2$ octahedrons. Published by The Royal Society of Chemistry ¹⁶⁹.

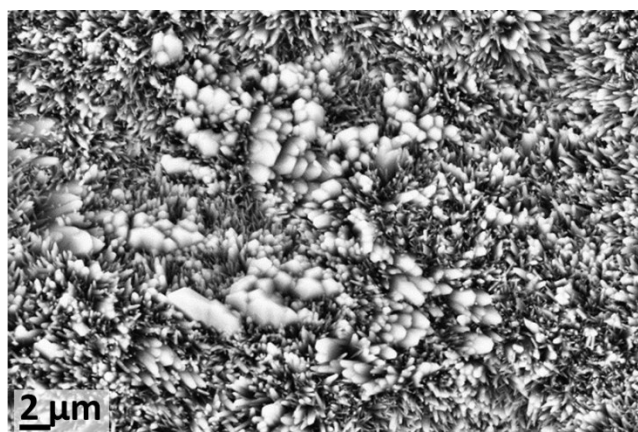


Figure 165. Magnified zinc surface exposed to $[C_4C_1im]Cl$ solution (IL-1, $X_{H_2O}=0.98$ solution and 70 ± 1 °C) for 15 d showing ZnO structures. Published by The Royal Society of Chemistry ¹⁶⁹.

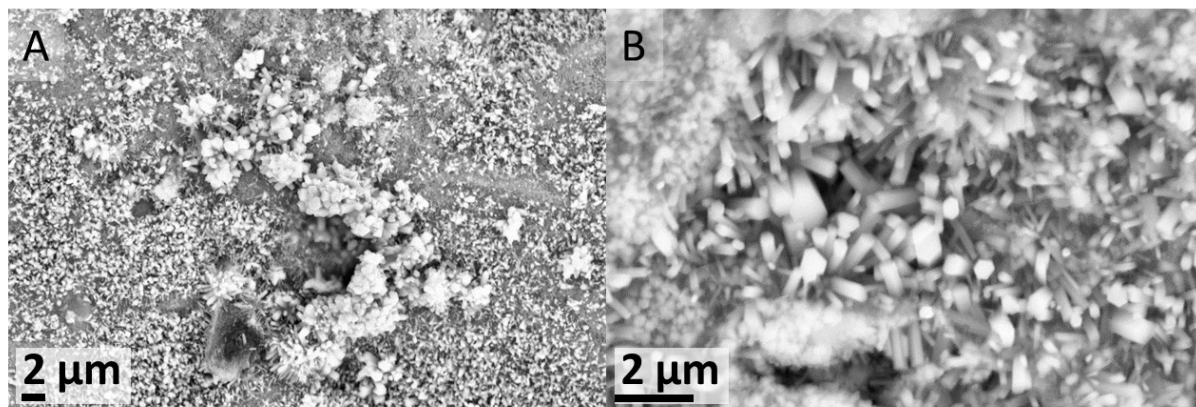


Figure 166. Magnified zinc surface exposed to $[C_4C_{1im}]Cl$ solution (IL-2, $X_{H_2O}=0.98$ at 120 ± 1 °C) for 1 d. [A] ZnO structures. [B] Detail of ZnO hexagonal nanorods. Published by The Royal Society of Chemistry ¹⁶⁹.

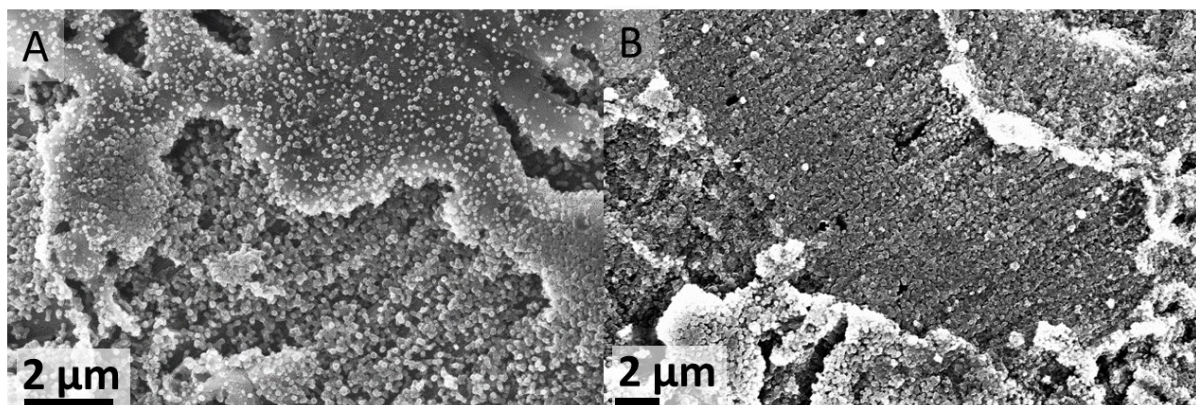


Figure 167. Magnified zinc surface exposed to $[C_4C_{1im}]Cl$ solution (IL-1, $X_{H_2O}=0.75$ at 20 ± 1 °C). [A] 18-d exposure showing ZnO hexagonal flat-topped nanorods. [B] 26-d exposure showing ZnO hexagonal flat-topped nanorods. Published by The Royal Society of Chemistry ¹⁶⁹.

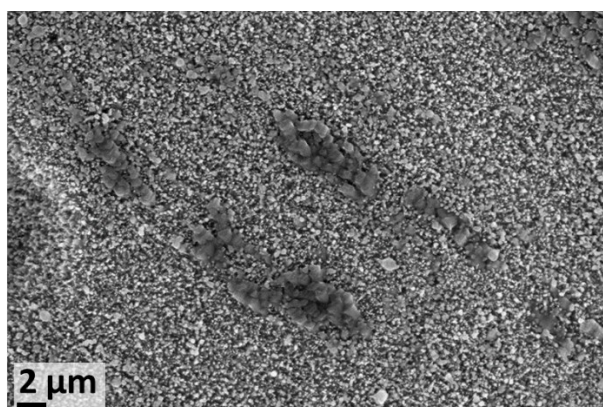


Figure 168. Magnified zinc surface exposed to $[C_4C_{1im}]Cl$ solution (IL-1, $X_{H_2O}=0.75$ at 120 ± 1 °C) for 16 h. The surface is covered with ZnO nanorods with micrometre-scale ZnO crystals. Published by The Royal Society of Chemistry ¹⁶⁹.

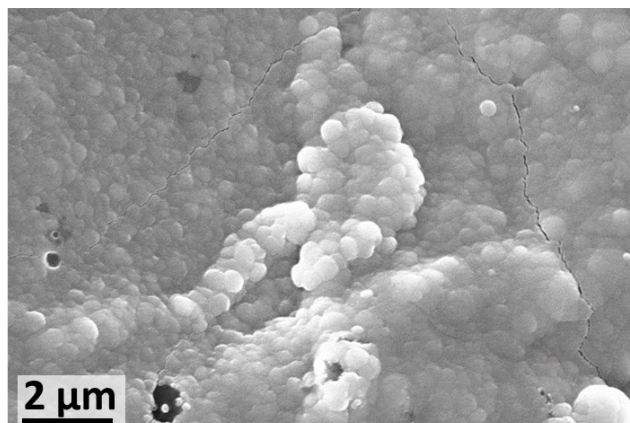


Figure 169. Magnified zinc surface exposed to $[C_4C_1im]Cl$ solution (IL-1, $X_{H_2O}=0.75$ and 20 ± 1 °C) for 26 d. Detail of the Cl containing material. Published by The Royal Society of Chemistry ¹⁶⁹.

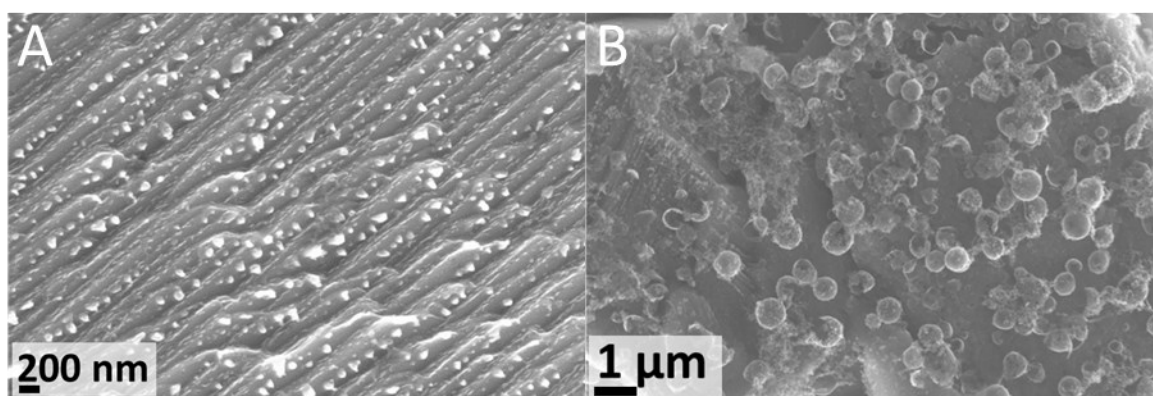


Figure 170. Magnified zinc surface exposed to dry $[C_4C_1im]Cl$. [A] IL-1, $X_{H_2O}=0.04$ at 70 ± 1 °C for 14 d. [B] IL-2, $X_{H_2O}=0.04$ at 120 ± 1 °C for 12 d. Published by The Royal Society of Chemistry ¹⁶⁹.

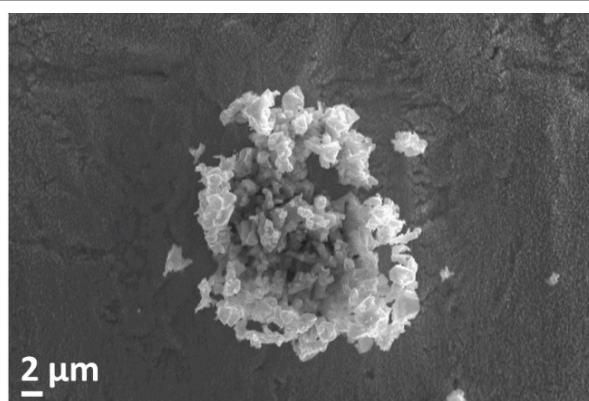


Figure 171. Micrometre-scale ZnO polycrystalline material. Zinc exposed to demineralized water for 3 days at 20 °C. Published by The Royal Society of Chemistry ¹⁶⁹.

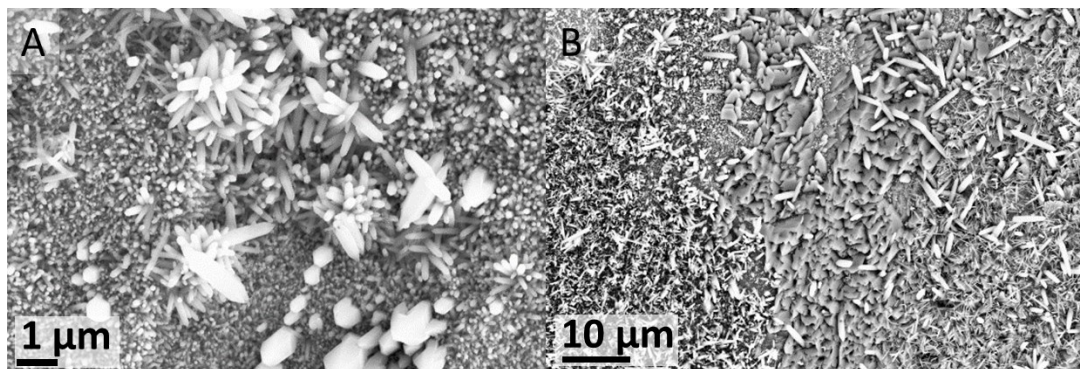


Figure 172. Zinc exposed to demineralized water for 3 days at 70 °C. [A] Flat-topped hexagonal nanorods and flowers ending with a point and rounded end. [B] Example of micrometre scale polygonal plates and other ZnO rods. Published by The Royal Society of Chemistry ¹⁶⁹.

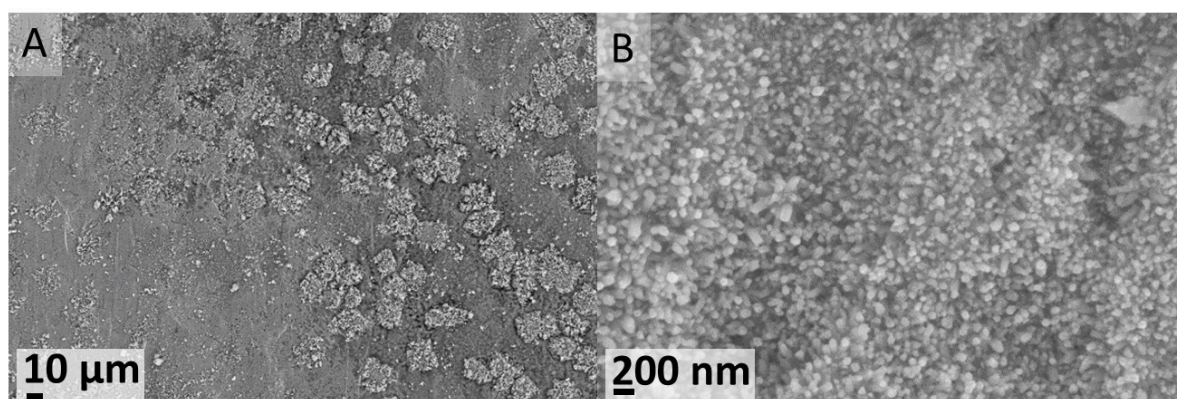


Figure 173. Example of polycrystalline material. Zinc exposed to demineralized water for 6 days at 20 °C. [A] Overall surface. [B] Detail of flat-topped hexagonal nanorods. Published by The Royal Society of Chemistry ¹⁶⁹.

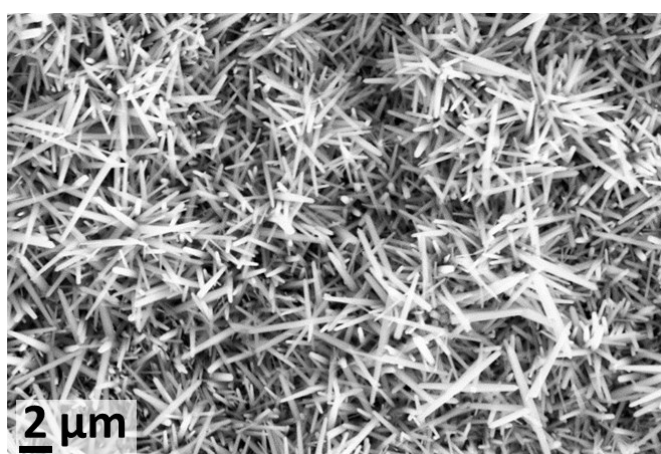


Figure 174. ZnO Nanorods formed in demineralized water after 6-d exposure at 70 °C. Published by The Royal Society of Chemistry ¹⁶⁹.

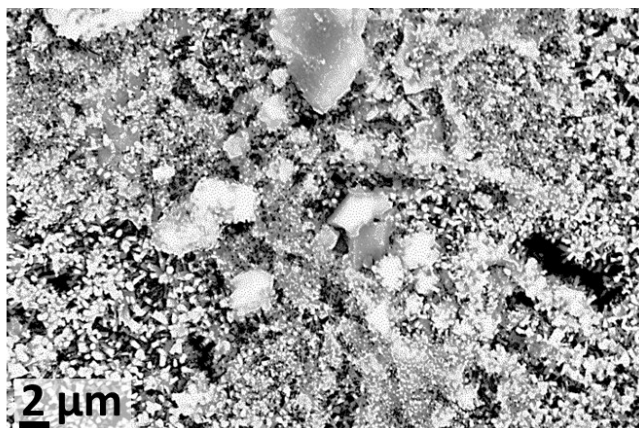


Figure 175. ZnO structures formed in demineralized water after 4.6-d exposure at 120 °C. Published by The Royal Society of Chemistry ¹⁶⁹.

A5.7.5. Overall considerations

A5.7.5.1 Zn exposed to PILs

Dissolution of zinc in sulfuric acid is a known process used for the industrial production of zinc sulfate. Interestingly, it has been noticed that if clean zinc is used for this purpose, the dissolution kinetics are relatively slow, which limits the production capacities. In a study it has been shown that the problem of slow dissolution of metals in non-oxidizing acid solutions is substantially connected with the process of hydrogen evolution that follows. In fact, because of the nature of zinc, the process of hydrogen evolution goes with great overpotential, which results in slow kinetics ⁴³⁶.

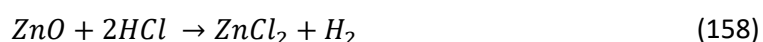
The overall chemical reaction between Zn and sulfuric acid is given in Eqs. 154-157. This process takes place as a sequence of electrochemical processes, and it has been noticed that the limiting step is the cathodic reaction. *i.e.* the reduction of H⁺ ions to form hydrogen ⁴³⁶. For this series of reactions, it has been found that the hydrogen evolution reaction is first order in hydrogen ion dependence and that the anodic dissolution reaction is pH-independent. Moreover, it was found that either no interaction (except for the electron balancing) exist between the two different electrode reactions when occurring simultaneously and at equivalent rates on the same metal surface, or an interaction exist which affect the corrosion by the same rate factor and the same potential difference at all pH-values ⁴³⁷.





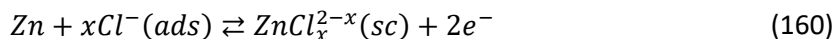
Solutions of $[\text{N}_{4110}][\text{HSO}_4]$ have a lower pH than $[\text{HC}_{1\text{im}}]\text{Cl}$, but the effects of chlorides on the anodic dissolution of zinc have a greater effect. Indeed, in chloride containing environments, it has been shown that the chloride concentration has an influence on the anodic dissolution of Zn⁴³⁷. This might be the reason why the MRC were so extreme in $[\text{HC}_{1\text{im}}]\text{Cl}$ compared to the other ILs. The corrosion of zinc across the pH range has been investigated previously by many researchers⁴³⁸. It has been reported that the corrosion rate vs. pH curve of zinc resembled the letter “U” with the corrosion rate being minimum in the pH range from 8.5 to 12.5⁴³⁸. That work is in agreement with the predictions by the Pourbaix diagram for Zn, which calculates the domain of zinc passivity to be in this pH range⁴³⁸. This agrees with our experimental observation, and explains why the MCR is higher in the protic ILs than in $[\text{C}_4\text{C}_{1\text{im}}]\text{Cl}$.

The SEM/EDX showed the presence of oxygen rich zones in the surface of the corroded Zn samples exposed to $[\text{N}_{4110}][\text{HSO}_4]$ at 75 and 98 mol% and only for the 75 mol%, which showed a sponge-like deposited over the surface. As mentioned earlier, traces of oxygen were found on some areas on the surface. It is not clear if this is just atmospheric oxygen adsorbing onto the surface, or the result of a corrosion process in the solutions or due ex-situ expose to atmospheric oxygen after the corrosion experiments. If this is actually due to a corrosion process in solution, it might be explained by a competing reaction between metallic zinc and water to form the oxide, which will then dissolve in the acidic medium at a slower rate. A study showed that the ZnO dissolution rate is controlled by the hydrolytic breaking of Zn-O bonds at kink sites which is catalysed by acids and by ligands which can form complexes with Zn^{2+} ions⁴³⁹. The $[\text{HSO}_4]^-$ anions are weakly coordinating, which might explain why traces of ZnO appeared and partially accumulated some regions of the surface at both water contents. ZnO its known to dissolved in acids such as HCl according to Eq. 158⁴³⁹. in the high water content, the ionic liquid is expected to be fully hydrated, and the interaction of the cation and anion weaken by the high water content as explained in section 3.3.1.1.2. In the high-water content environment, chloride anions can help the dissolution process of ZnO, which can explain why this was not observed in the 98 mol% region but was detected in the 75 mol%.



Extreme pitting was observed in $[\text{HC}_{1\text{im}}]\text{Cl}$ systems, specially at 98 mol%. Pitting has been described as a process in which the passive film breaks down at local sites and where the

exposed metal reacts with the chlorides in solution to form soluble chlorides. The pitting reaction in chloride media has been reported as follows ⁴³⁸:



where X refers to chlorides (x = 1,2,3,4), (ads) refers to adsorbed species and (sc) refers to surface-confined species. The above mechanism of pitting has no correlation with the solution pH, while localized acidity at the metal-metal oxide-solution interface plays a role in passivity breakdown ⁴³⁸.

A5.7.5.2 Summary of classification method from Zn exposed to corrosive media

Table 51 summarizes the corrosion behaviour of zinc exposed to corrosive media. Despite the oxygen rich zones in samples exposed to PILs detected via EDX, zinc has been classified as type-4 in these systems, as no changes in the XRD diffraction patterns were observed and visually the samples did not show any sign of corrosion product deposit.

Table 51. Summary of the classification system and corrosion type for zinc exposed to corrosive media. Corrosion types: NC: no corrosion, PC: pitting corrosion, USC: uniform surface corrosion and NUSC: non-uniform corrosion. Section 3.4.

Solvent →	[C ₄ C ₁ im]Cl			[HC ₁ im]Cl			[N ₄₁₁₀][HSO ₄]			[C ₄ C ₁ im][NTf ₂]	Water
Water Content [mol fraction] →	Dry	0.75	0.98	Dry	0.75	0.98	Dry	0.75	0.98	Dry	1
Temperature [°C] ↓											
20		3	3		4	4	0	4	4		3
45					4	4					
70	0	3	3				1	4	4	0	3
120	0	3	3				1	4	4		3
150										0	
20		NUSC	NUSC		PC	PC	NC	PC	PC		NUSC
45					PC	PC					
70	NC	NUSC	NUSC				USC	PC	PC	NC	NUSC
120	NC	NUSC	NUSC				USC	PC	PC		NUSC
150										NC	

A5.7.5.3 Zn corrosion in other ILs

The corrosion of metallic zinc in ILs have only been studies though electrochemical methods ^{440,441}. In those works, no mechanistic details are provided, but It was shown that zinc was more

prone to corrosion in protic ILs than aprotic ILs, which is consistent with the experimental observations in this work.

A5.8. Brass (Cu63/Zn37)

Brass is an alloy of Cu and Zn, in proportions which can be varied to achieve varying mechanical and electrical properties. It is a substitutional alloy, which means that atoms of the two constituents may replace each other within the same crystal structure. Brass can be alloyed with other elements, typically tin and lead, to improve its mechanical and corrosion resistance. Brass is still commonly used in applications where low friction and corrosion resistance is required, such as locks, gears, ammunition casings, zippers, plumbing, valves, and electrical plugs and sockets. Dezincification-resistant (DZR or DR) brasses, sometimes referred to as CR (corrosion resistant) brasses, are used where there is a large corrosion risk and where normal brasses do not meet the standards ¹⁴⁵.

A5.8.1. Corrosion rates

The results for the mass change of brass samples exposed to different corrosion media (water-soluble ILs) are given in Figure 121. Corrosion results in [C₄C₁im][NTf₂] are given in section 3.5.2.

It can be seen that when brass is exposed to [C₄C₁im]Cl solution, the corrosion rates are small in the residual water case and increase with water content (Figure 121A/B). The maximum MCR was observed at 98 mol% for samples exposed at 20 °C while the maximum shifted to 75 mol% for samples exposed at higher temperatures (70 °C and 120 °C). At these higher temperatures and 98 mol%, there was a significant drop in the MCR and the value was similar regardless of the temperature (Figure 121B).

The attack was extreme when brass was exposed to [HC₁im]Cl, with a maximum attack in dry conditions. In this IL the MCR decreases with increasing water content (Figure 121C/D).

The MCR of copper exposed to [N₄₁₁₀][HSO₄] is in the same order of magnitude but lower than in [C₄C₁im]Cl. In this IL, the attack in dry conditions was small and increased with water content, however at 120 °C and 75 mol%, there was a drop in the MCR, similar to the one observed for the copper system (Figure 121E/F).

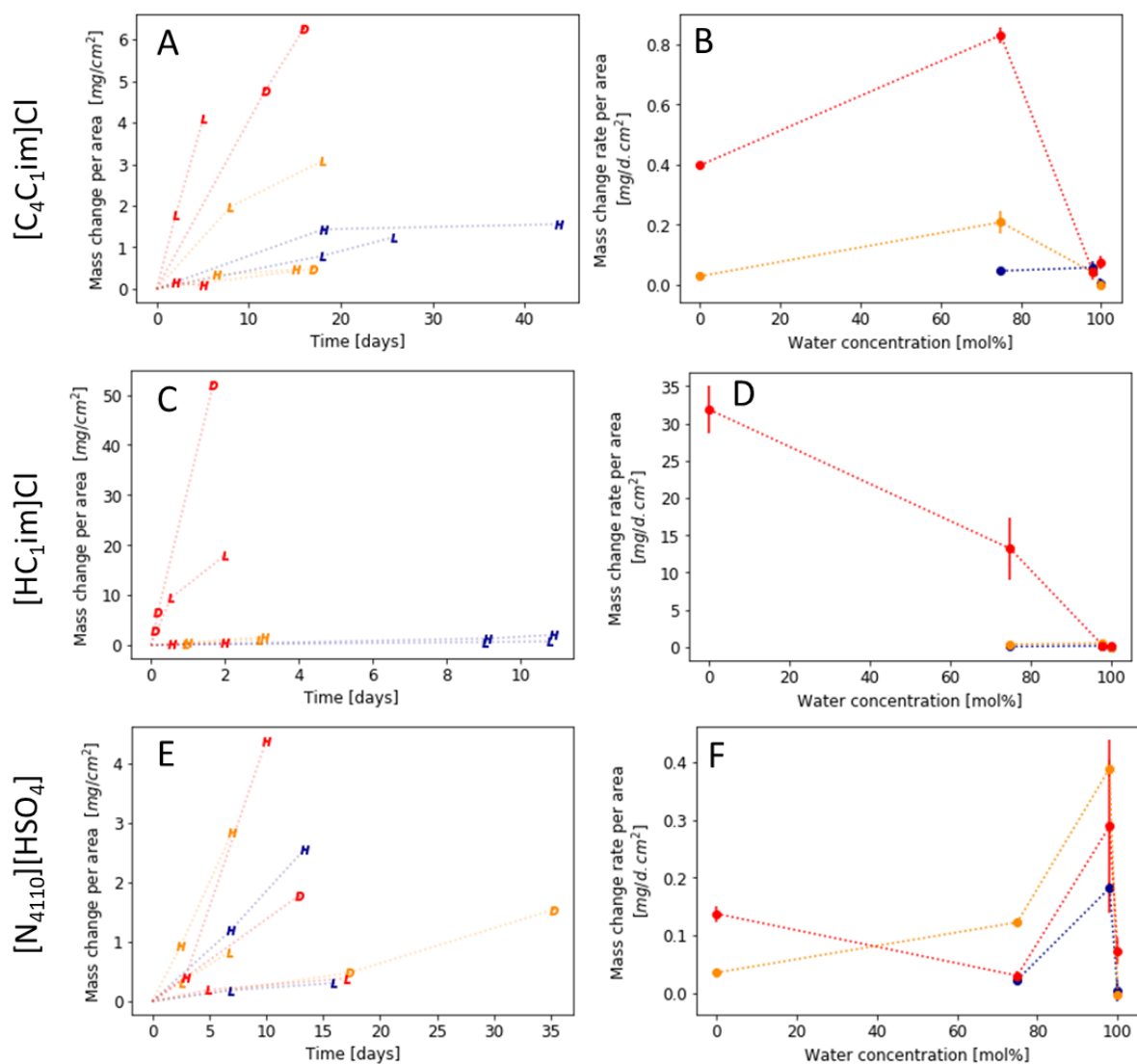


Figure 176. Mass change rates for brass exposed to corrosive media. Left figures: Mass change per area as a function of time. Right figures: Mass change rates as a function of water content calculated from the average of the MCRs. Legend, D: dry, L: low water case, H: high water case, W: water. Colours: Blue 20 °C, orange 70 °C and red 120 °C. Lines have been added to guide the eye.

A5.8.2. XRD

The XRD patterns for brass exposed to corrosive media are given in Figure 177. The spectrum of the untreated brass is shown in Figure 177A, where it can be seen four signals similar to Cu, but shifted to higher 2θ . When brass is exposed to $[C_4C_1im]Cl$, several substances can be detected in the XRD spectra, such as ZnO (Figure 177D/E/H) and ZHC (Figure 177H). When exposed to $[N_{4110}][HSO_4]$, in some samples a set of new signals appears forming a “duplet” from the original ones, as shown in (Figure 177C). Another sample exposed to this IL not only showed the duplet signals but a new set of signals not identified so far (Figure 177F). When exposed to $[HC_1im]Cl$, duplet signals were observed for some systems, but no additional signals were detected (Figure 177I). Finally, when exposed to water, a mixture of ZnO and CuO was

detected (Figure 177G). The XRD spectrum of brass samples was matched with the reference compound code: 00-050-1333 using HighScore suite, PANalytical's commercial powder diffraction analysis software.

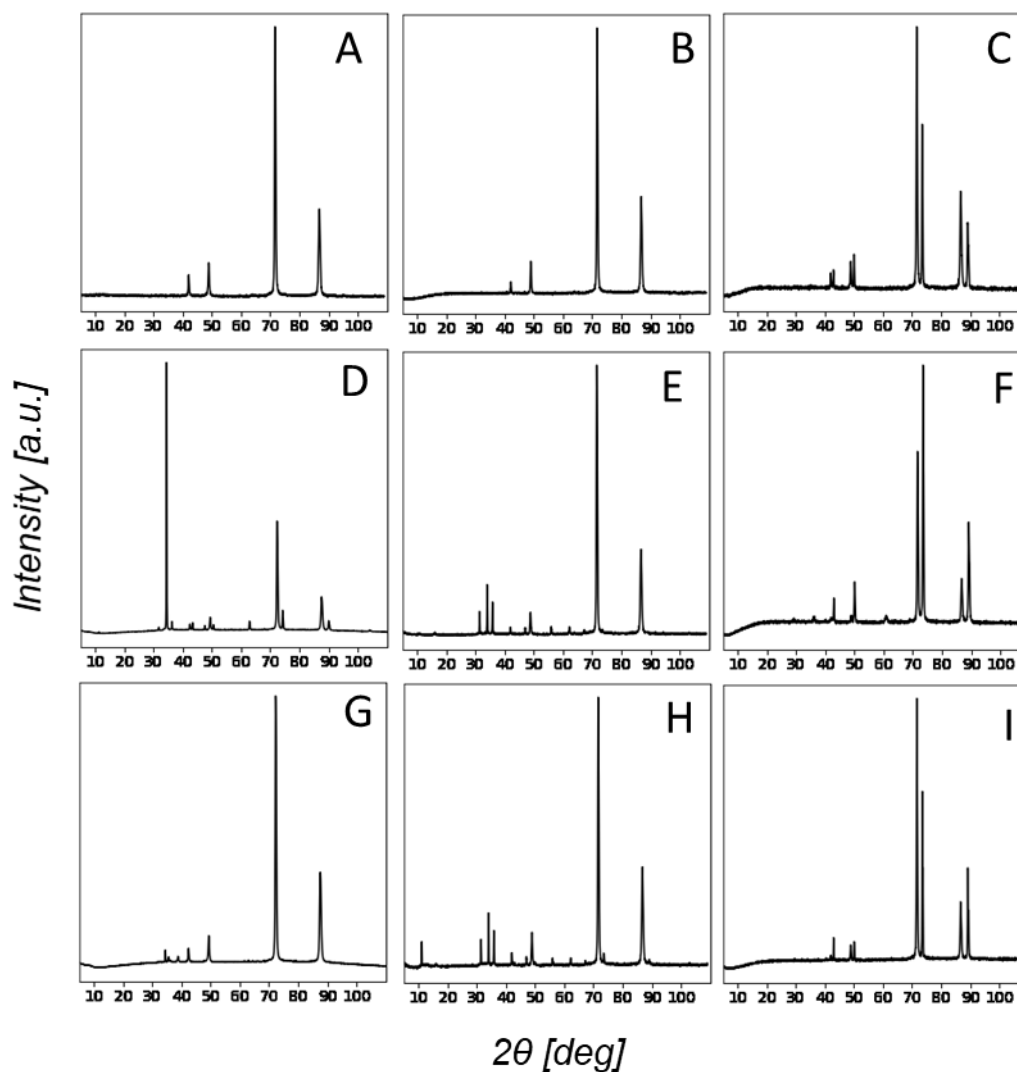


Figure 177. XRD patterns from brass samples exposed to corrosive media. [A] Unexposed metal sample. [B] $[C_1C_4im]Cl$, 70 °C, 75 mol% and 18 d. [C] $[N_{4110}][HSO_4]$, 120 °C, 98 mol% and 2.5 d. [D] $[C_1C_4im]Cl$, 70 °C, 98 mol% and 6.5 d. [E] $[C_1C_4im]Cl$, 20 °C, 98 mol% and 18 d. [F] $[N_{4110}][HSO_4]$ 120 °C, 98 mol% and 10 d. [G] Water, 70 °C and 4.5 d. [H] $[C_1C_4im]Cl$, 70 °C, 75 mol% and 18 d. [I] $[HC_4im]Cl$, 70 °C, 98 mol% and 6.5 d.

A5.8.2.1 XRF

The XRF data summary is given in Table 52. The results are consistent with what observed in the XRD patterns and SEM/EDX images. Samples exposed to $[C_4C_1im]Cl$, in which chloride-containing crystals were observed, showed an increase in the chlorine content. There was a slight increase in the sulphur content of the samples exposed to $[N_{4110}][HSO_4]$ suggesting the formation of S-containing compounds.

Table 52. XRF results summary for brass.

Solvent	Observations
-	Cu: 65.34 ± 0.05 / Zn: 34.46 ± 0.03 % (Cu/Zn = 1.896 ± 0.003) (Traces of Si, Cl, S)
H ₂ O	No significant changes.
[C ₄ C ₁ im]Cl	Increased in the Cl content: Significant change (1.2%) in samples exposed to 98 mol% solutions at 20 °C for 44d and 70 °C for 2.5 d. Sodium detected in the above samples and in samples exposed to 98 mol% solutions at 70 °C for 6.5 d and 75 mol%, 20 °C for 16 d.
[HC ₁ im]Cl	No significant changes.
[N ₄₁₁₀][HSO ₄]	Slight increase in the S content.

XRF data was used to track changes in the composition of the alloy exposed to corrosive media (Figure 177). From the data, it can be seen that the metal composition did not change when exposed to water. When exposed to [C₁C₄im]Cl the results show slight dezincification of the samples. When exposed to the PILs, [HC₄im]Cl and [N₄₁₁₀][HSO₄], the dezincification is extreme. Decuprification of brass when exposed to [C₁C₄im][NTf₂] was observed and is discussed in detail in section 3.5.2.

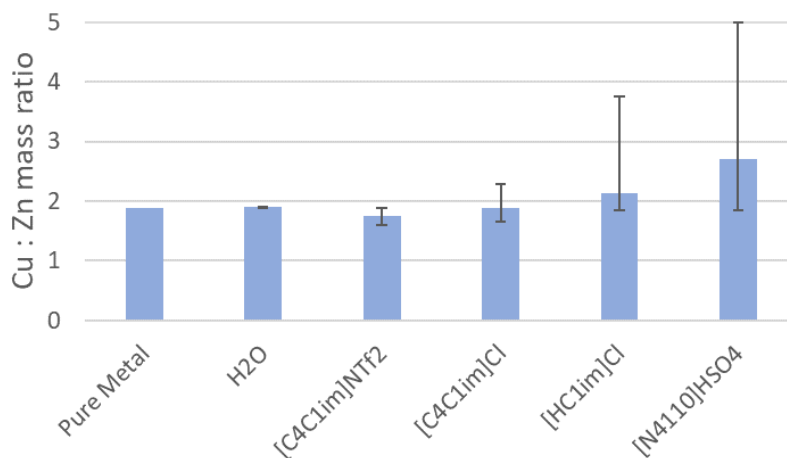


Figure 178. XRF composition for brass exposed to corrosive media.

A5.8.3. SEM

SEM/EDX images for selected brass samples exposed to different corrosive media are shown in Figure 179 to Figure 185. It can be seen from Figure 179 that the surface of the alloys (as received) showed defects. Diversity of structures formed when brass was exposed to [C₄C₁im]Cl systems. Figure 180 shows the detail of cotton-like structures which are rich in Cu and oxygen and some traces of chlorine. Figure 181 shows the detail of ZnO hexagonal rods while Figure 182 showed the details of ZnO needles. No crystals were observed in samples

exposed to $[N_{4110}][HSO_4]$. The surface experienced pitting corrosion, forming a sponge-like material with smooth edges. EDX analysis showed the surface is enriched in Cu, which confirms the dezincification process in this ILs (Figure 183 and Figure 184A). Brass experience extreme corrosion when exposed to dry $[HC_{1im}]Cl$, the SEM image of a sample exposed to this medium is shown in Figure 184B, where it can be seen an extreme pitting process. When brass was exposed to DI water, several structures were observed such as flower-like structures, similar to the ones observed in copper, and ZnO needles Figure 185.

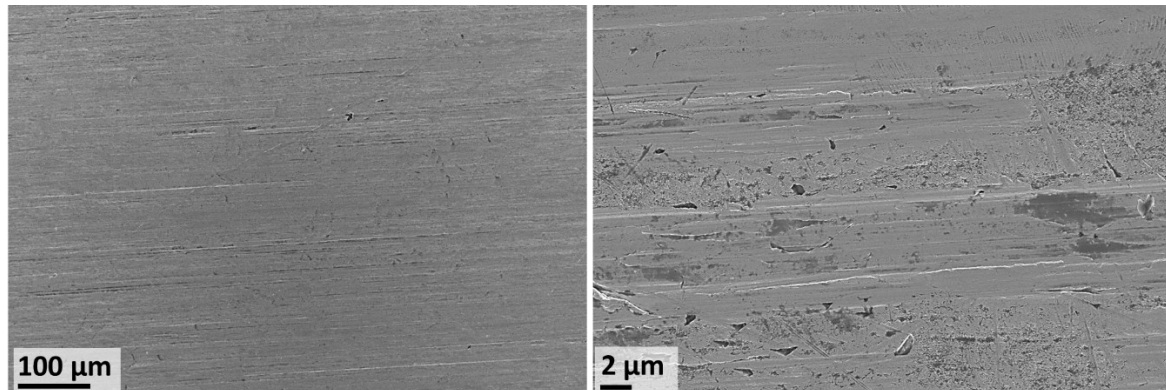


Figure 179. SEM/EDX of unexposed Brass.

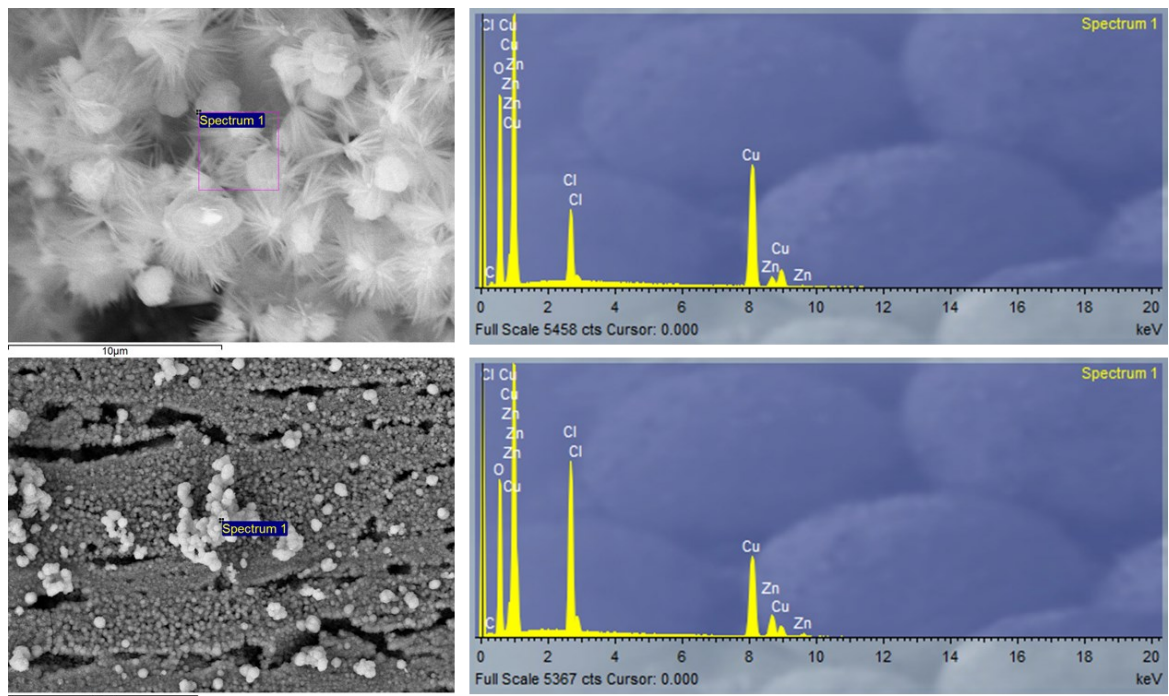


Figure 180. SEM/EDX of brass exposed to $[C_4C_{1im}]Cl$, 20 °C, 98 mol% and 18 d. EDX Cu:Zn:O:Cl atomic ratio 11:1:25.1:2 and 3.2:1:10.8:2.1 for the top and bottom figures respectively.

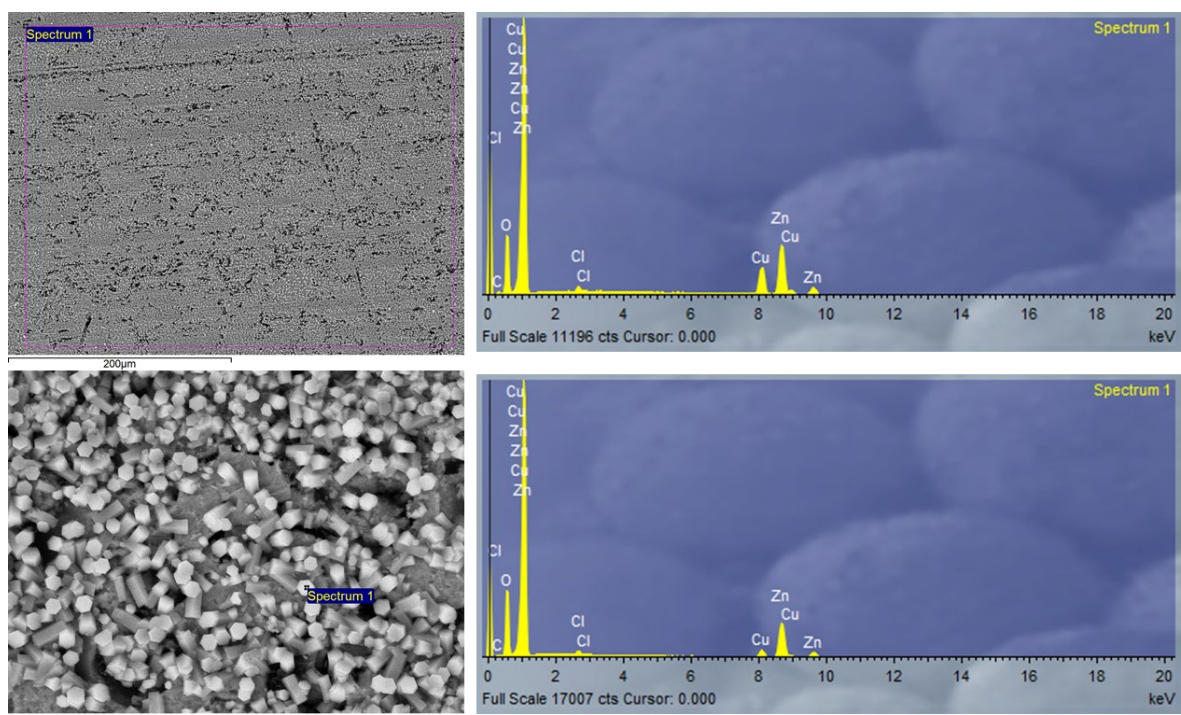


Figure 181. SEM/EDX of brass exposed to $[C_4C_{1im}]Cl$, 20 °C, 98 mol% and 18 d. EDX Cu:Zn:O:Cl atomic ratio 15.4:35.6:55:1 and 4.9:29.6:69:1 for the top and bottom figures respectively.

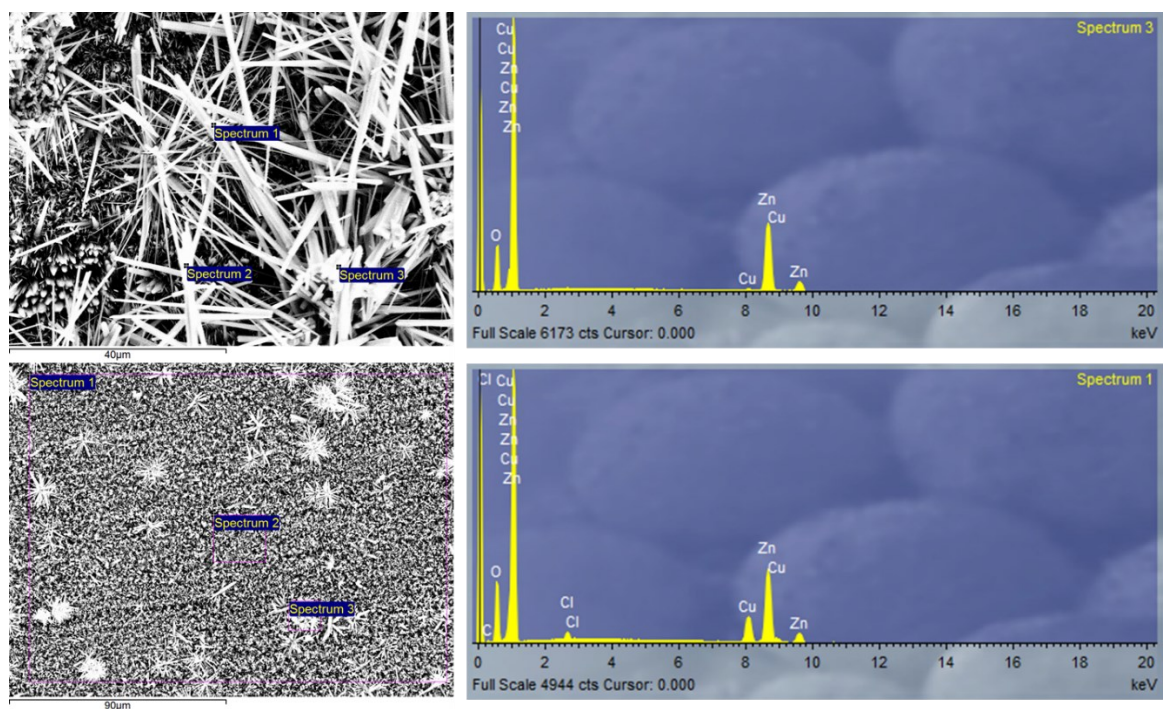


Figure 182. SEM/EDX of brass exposed to $[C_4C_{1im}]Cl$, 20 °C, 98 mol% and 18 d. EDX Cu:Zn:O:Cl atomic ratio 1:47.6:48.2:n.d. (top figure) and 10.9:37.8:44.3:1 and 8.4:28.3:37.5:1 for spectrum 1 and 2 of the bottom figure.

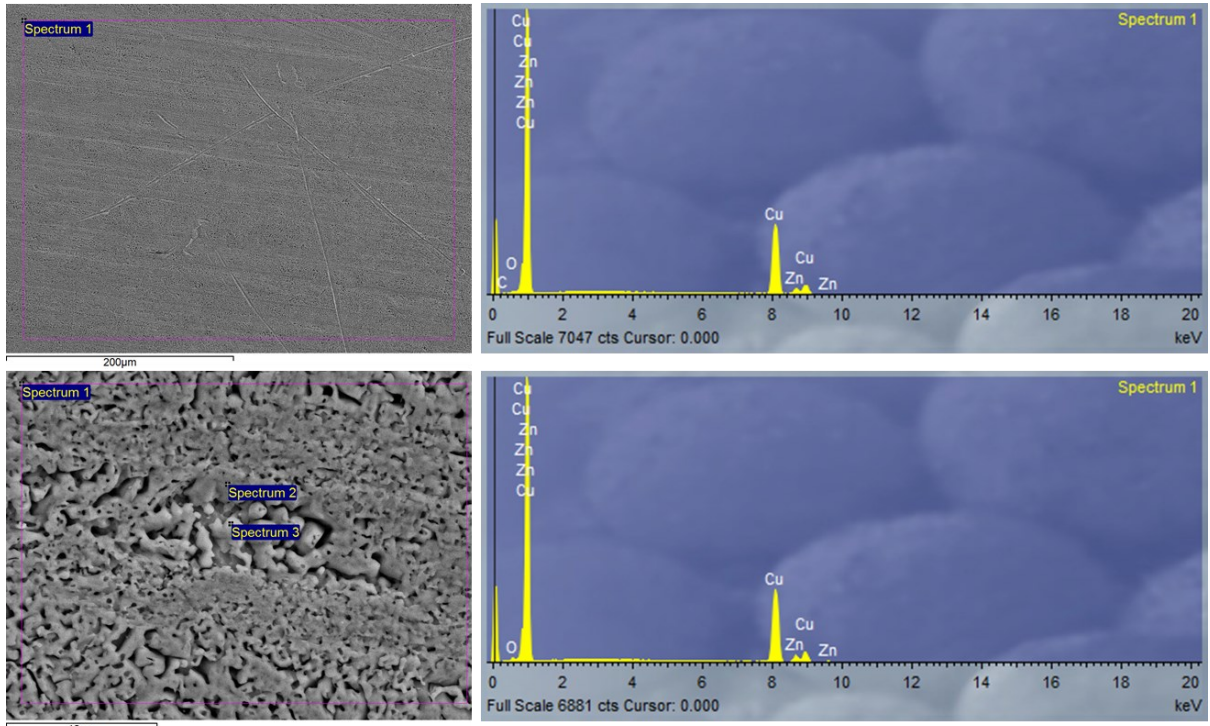


Figure 183. SEM/EDX of brass exposed to $[N_{4110}][HSO_4]$, 70 °C, 75 mol% and 6.7 d. EDX Cu:Zn:O atomic ratio 21.1:2:1 (top figure) and 16.8:1.8:1, 12:1:n.d. and 5:1:n.d. in spectrum 1, 2 and 3 respectively (bottom figure).

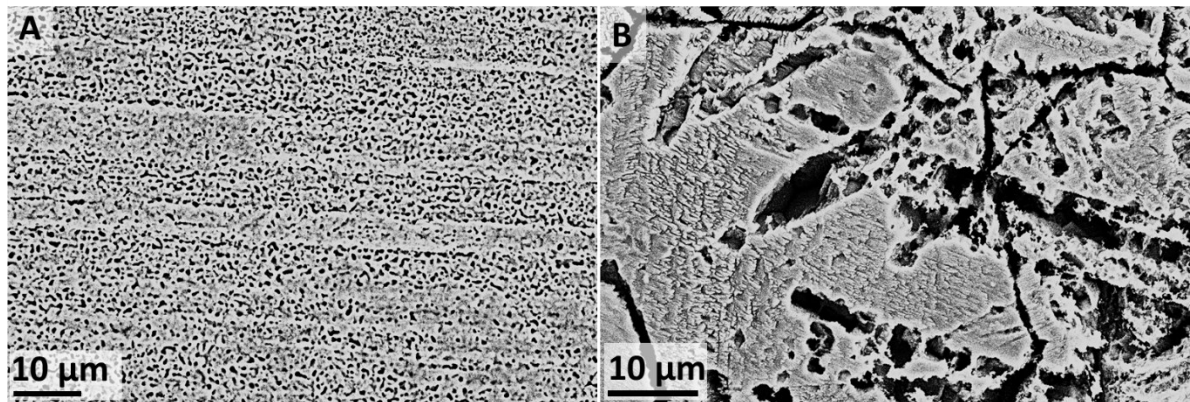


Figure 184. SEM/EDX of brass exposed to protic ILs. [A] $[N_{4110}][HSO_4]$, 120 °C, 98 mol% and 10 d. [B] $[HC_{1im}]Cl$, 120 °C, dry and 2.3 h.

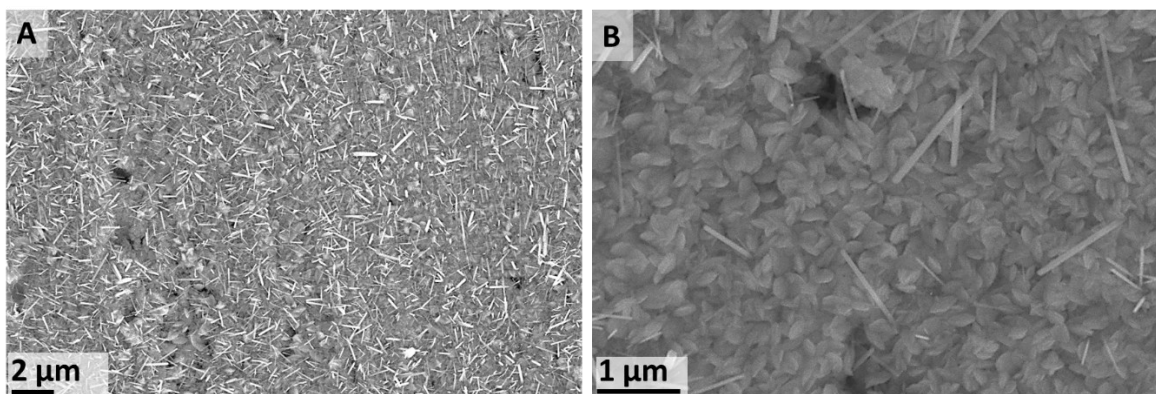


Figure 185. SEM images of brass exposed to water, 70 °C, 100 mol% and 6 d.

A5.8.4. Overall considerations

As expected, the corrosion behaviour of brass is a combination of the corrosion behaviour of its constituent metals, Cu and Zn. The corrosion rates are in the same order of magnitude of Cu, with improved resistance as expected. It has been reported in the literature that brass alloys containing 10 to 30 % zinc are close to pure copper in their chemical corrosion properties, which is consistent with the experimental results⁴⁰². However, when exposed to [C₄C₁im]Cl medium, similar structures as per the zinc system were observed. Details on chemical reactions of Cu and Zn exposed to different corrosion media are discussed in sections A5.2.2 and A5.7.5 respectively.

It has been reported degradation of the mechanical properties of brass exposed to corrosive environments. The reason for the impairment of the mechanical properties has been attributed to the formation of compounds that contain oxygen, hydrogen or sulphur. For example, the formation of Cu₂O is known to form a galvanic element with copper, in which the Cu₂O acts as a cathode, leading to the destruction of the material. Cu₂O also reacts with hydrogen, which is formed by acid corrosion and penetrates into the material, according to the Eq. 162, which can also cause the destruction of the material⁴⁰².



It has been reported that even though HCl has higher corrosion rates, it should be preferred over other acids, such as sulphamic acid, for acid washing of brass components, as it does not favour the reaction shown in Eq. 162⁴⁰². Additionally, it has been reported that brass alloys with high zinc contents are selectively corroded by hydrochloric acid with dezincing⁴⁰², which is consistent with the results when brass was exposed to the protic IL [HC₁im]Cl.

A5.8.4.1 Brass categorization system

Table 53 summarizes the corrosion behaviour of brass exposed to corrosive media

Table 53. Summary of the classification system and corrosion type for brass exposed to corrosive media. Corrosion types: NC: no corrosion, PC: pitting corrosion, USC: uniform surface corrosion and NUSC: non-uniform corrosion. Section 3.4.

Solvent →	[C ₄ C ₁ im]Cl			[HC ₁ im]Cl			[N ₄₁₁₀][HSO ₄]			[C ₄ C ₁ im][NTf ₂]	Water	
Water Content [mol fraction] →	Dry	0.75	0.98	Dry	0.75	0.98	Dry	0.75	0.98	Dry	1	
Temperature [°C] ↓												
20	0	3	3				0	4			2	
70	0	3	3	4	4	4	4	4	4	3	2	
120	4	4	4	4	4	4	4	0	4			4
150										3		
20	NC	NUSC	NUSC				NC	USC			NUSC	
70	NC	NUSC	NUSC	USC	USC	USC	USC	USC	USC	NUSC	NUSC	
120	NUSC	NUSC	NUSC	USC	USC	USC	USC	USC	USC			NUSC
150										NUSC		

A5.8.4.2 Brass corrosion in other ILs

The corrosion behaviour of brass in ILs had been reported only in a few systems. As mentioned in section A5.2.2, a study comparing several metals (carbon steel, austenitic stainless steel, nickel-based alloy C22, Cu, brass (CuZn40) and aluminium (AlMg₃)) concluded that Cu and brass had the worst corrosion resistance to IL media. It was shown that the addition of water to increased aprotic ILs increased the corrosion rates and that corrosion inhibitors could be used to protect Cu¹⁵¹. The corrosion behaviour of brass in fluorinated ILs is discussed in section 3.5.2.

A5.9. Stainless Steel 304

Stainless Steel 304 (European norm 1.4301) is one of the most common stainless steel used in the industry. It is an austenitic stainless steel that contains both chromium (between 18% and 20%) and nickel (between 8% and 10.5%) metals as the main non-iron constituents. It is less electrically and thermally conductive than carbon steel and is essentially non-magnetic. It has a higher corrosion resistance than regular steel and is widely used because of the ease in which it is formed into various shapes. For more severe corrosion conditions, when 304 stainless steel is too sensitive to pitting or crevice corrosion by chlorides or general corrosion in acidic applications, it is commonly replaced by stainless steel 316⁴⁴².

A5.9.1. Corrosion rates

The results for the mass change of stainless steel 304 samples exposed to different corrosion media (water-soluble ILs) are given in Figure 132. Corrosion results in $[C_4C_{1im}][NTf_2]$ are given in section 3.5.2.

When 304 SS is exposed to $[C_4C_{1im}][Cl]$ solution, the corrosion rates are very small over the range of conditions tested. Something interesting is that systematically, the second measurement at longer exposure times, experienced a decreased in the MC, being negative in some instances at temperatures below 70 °C, suggesting that corrosion products are being deposited on the surface. For temperatures equal as less than 70 °C, the MCR has a minimum value in the residual water region and increased with water content. The maximum MCR was observed at 98 mol% however at 20 °C it was higher than at 70 °C, it is unclear if this is due to experimental errors or deposition of materials in the samples. As expected, the MCR were higher at 120 °C, however, the maximum value was observed in the residual water case region. At increasing water content, the relative error increased compared to the other cases due to a lower MC at longer exposure times. It was noticed that the samples exposed to 98 mol% at 120 °C showed signals of corrosion.

The attack on 304 SS was maximum when exposed to $[HC_{1im}][Cl]$. In this IL, there is a significant attack in the residual water case, with a maximum MCR at 120 °C and 75 mol% and dropping at 98 mol%. A similar behaviour was observed when 304 SS was exposed to $[N_{4110}][HSO_4]$, where the attacks were relatively slow but showed a maximum at 120 °C and 75 mol%

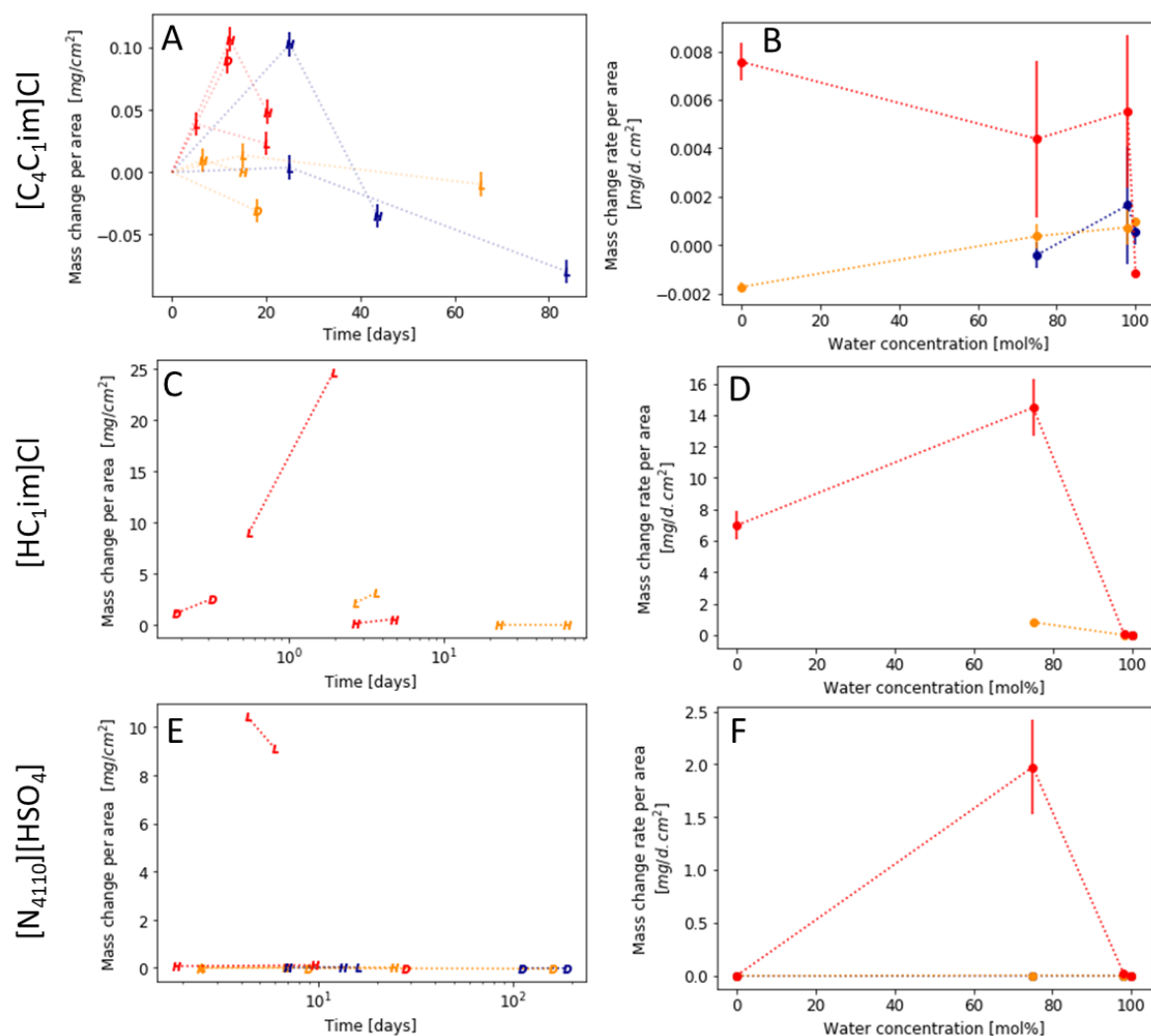


Figure 186. Mass change rates for SS304 exposed to corrosive media. Left figures: Mass change per area as a function of time. Right figures: Mass change rates as a function of water content calculated from the average of the MCRs. Legend, D: dry, L: low water case, H: high water case, W: water. Colours: Blue 20 °C, orange 70 °C and red 120 °C. Lines have been added to guide the eye.

A5.9.2. XRD

The XRD patterns from selected samples are shown in Figure 187. The XRD pattern for untreated 304 SS is shown in Figure 187A. Changes could be observed in the XRD patterns, clearly showing the formation of corrosion products over the surface of the metal for samples exposed to $[N_{4110}][HSO_4]$ at 120 °C and 75mol% (Figure 187B) and 98 mol% (Figure 187D), the substance was identified as iron sulfate hydrate ($FeSO_4 \cdot H_2O$). Small signals can be seen at $2\theta < 40^\circ$ for a sample exposed to $[C_4C_1im]Cl$ (Figure 187C), (compound not identified).

The diffraction patterns of the detected species were matched to the following references compounds using HighScore suite, PANalytical's commercial powder diffraction analysis software.

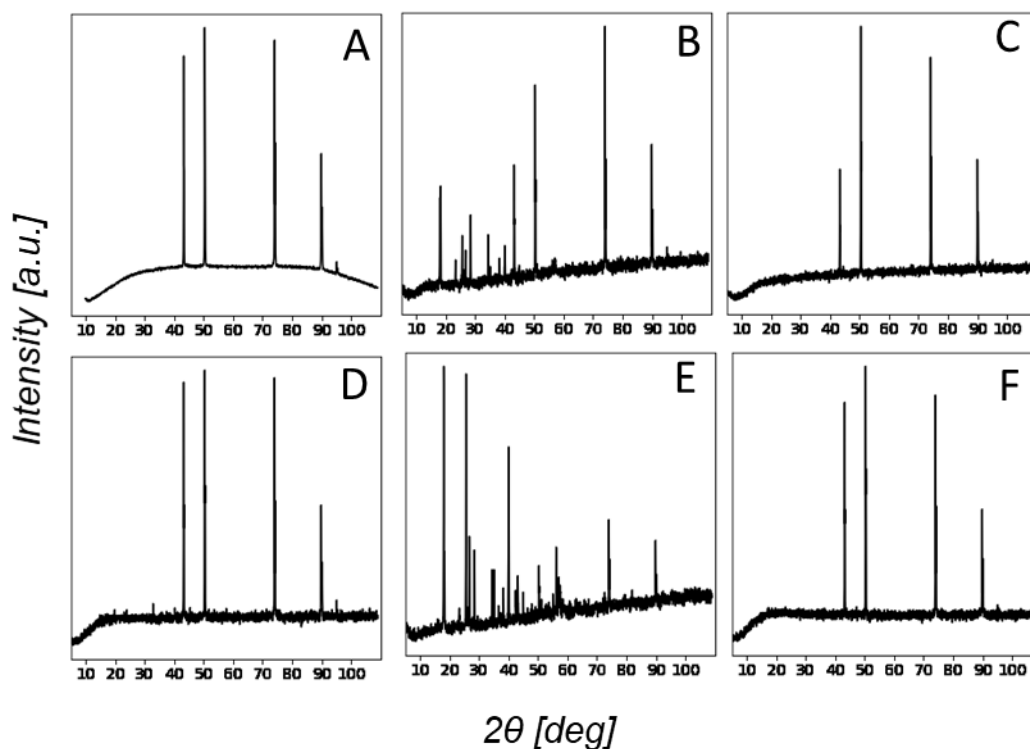


Figure 187. XRD patterns from 304 SS samples exposed to corrosive media. [A] Unexposed metal sample. [B] $[N_{4110}]HSO_4$ (120 °C, 75 mol% and 4.3 d. [C] $[N_{4110}][HSO_4]$ (120 °C, 98 mol% and 1.6 d. [D] $[C_1C_4im]Cl$, (120 °C, 98 mol% and 12.2 d. [E] $[N_{4110}][HSO_4]$ (120 °C, 75 mol% and 6 d. [F] $[N_{4110}][HSO_4]$ (20 °C, dry and 110 d).

A5.9.3. XRF

The XRF data summary is given in Table 54. The results are consistent with what observed in the XRD patterns and MCR. Samples exposed to $[N_{4110}][HSO_4]$ at 120 °C and 75 mol%, showed high MCR, new signals in the XRD patterns and significant amounts of sulphur in XRF.

Table 54. XRF results summary for 304 SS.

Solvent	Comments
-	Fe: 70.121%, Cr: 18.774, Ni: 8.738%, Mn 1.789%, Si 0.332% (Traces of S, Mo, P, V, La, Al, Ca, Cl, Rb, Sn, Se).
H ₂ O	No significant changes.
$[C_1C_4im]Cl$	No significant changes.
$[HC_4im]Cl$	No significant changes.
	Slight Increase in the S content.
$[N_{4110}][HSO_4]$	Significant increase when exposed at 120 °C and 75 mol% for 4.3 and 6 d; and at 120 °C and 98 mol% for 1.6d.

XRD data was used to track changes in the composition of the alloy exposed to corrosive media (Table 55). From the data, it can be seen that the metal composition did not change when exposed to water. When exposed to $[C_1C_4im][NTf_2]$ it can be seen a change in the ratios, suggesting a diminution of the Ni content in the samples. When exposed to $[C_1C_4im]Cl$ the results shows that the Fe:Ni ratio remains unchanged within the experimental error,

suggesting that those metals are being removed at the same rate, with an overall diminution of the Ni content. When exposed to [HC₄im]Cl, the Cr:Ni remains relatively constant, and the rations of those metals with iron are reduced, suggesting that in this IL, iron is being preferentially removed. Lastly, when 304 SS is exposed to [N₄₁₁₀][HSO₄] a significant change in the Fe:Ni suggest selective Ni dissolution. This results should be confirmed with ICP measurements.

Table 55. 304 SS composition changes via XRF.

System	Cr:Ni ratio	Fe:Cr ratio	Fe:Ni ratio
Untreated	2.15	3.74	8.02
H ₂ O	2.15	3.74	8.03
[C ₁ C ₄ im]NTf ₂	2.23 ± 0.07	3.72 ± 0.04	8.3 ± 0.2
[C ₁ C ₄ im]Cl	2.18 ± 0.05	3.68 ± 0.06	8.0 ± 0.2
[HC ₄ im]Cl	2.1 ± 0.1	3.66 ± 0.06	7.8 ± 0.6
[N ₄₁₁₀][HSO ₄]	2.2 ± 0.1	3.7 ± 0.3	8.2 ± 0.8

The solubility of the main metals contained in 304 SS in sodium chloride medium was studied and it was found that the normalized concentration of Fe, Cr and Ni in solution was 8.5%, 2.6% and 88.9% respectively ⁴⁴³. This ratio does not match the initial alloy composition, showing that Ni is leached at a higher rate than the other metals, in NaCl medium. This is consistent with the results observed for [C₄C₁im]Cl according to the XRF analysis shown in Table 55). However, due to the sensitivity of the XRF technique, this should be further confirmed by ICP measurements.

A5.9.4. SEM

SEM images for selected samples are shown in Figure 188 and Figure 189. It can be seen from Figure 188 that the surface of the alloys (as received) showed defects.

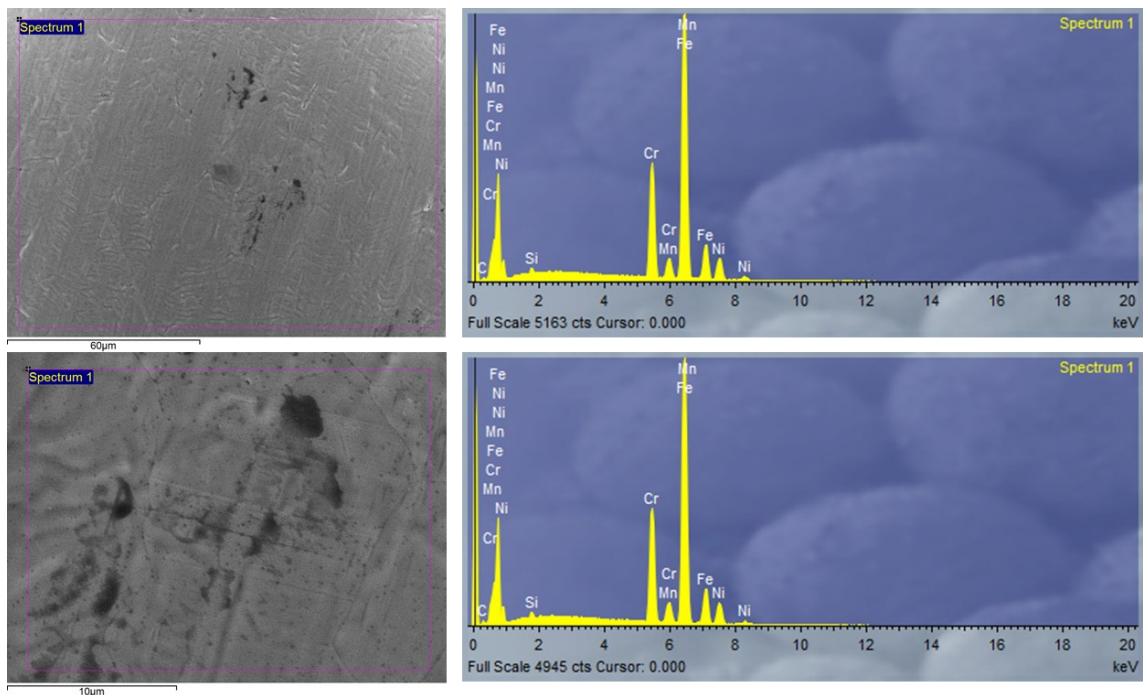


Figure 188. SEM/EDX of unexposed 304 SS. EDX Fe:Cr:Ni atomic ratio 8:50:2.46:1 and 8.22:2.32:for the top and bottom figures respectively.

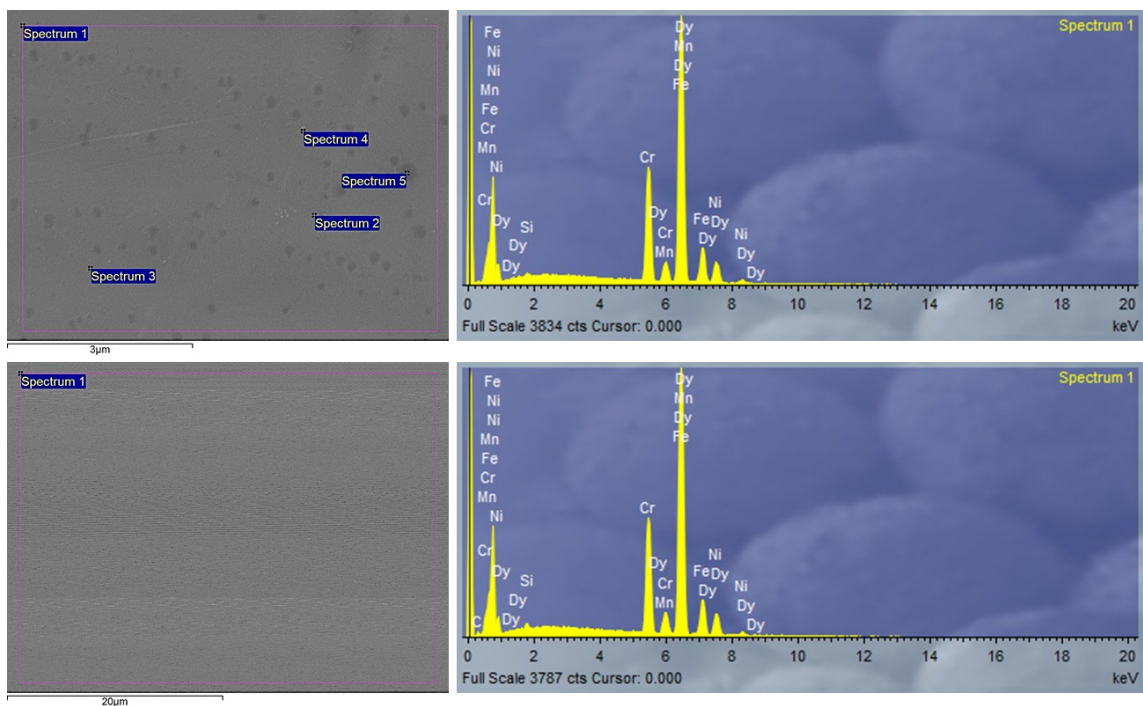
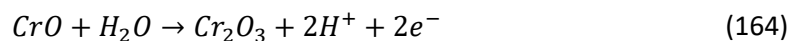
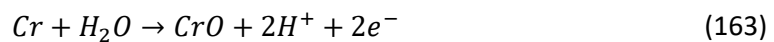


Figure 189. SEM/EDX of 304 SS exposed to $[N_{4110}]Cl$ (75 mol%, 20 °C and 2.5 d). EDX Top figure. Fe:Cr:Ni 7.04:2.07:1 average atomic ratio. Bottom Figure. Fe:Cr:Ni atomic ratio 7:22:2.10:1. Dy detected in both zones, atomic ratio Fe:Dy 27.0:1 and 27.5:1 for the top and bottom figures respectively.

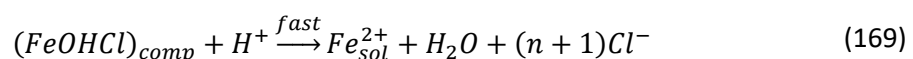
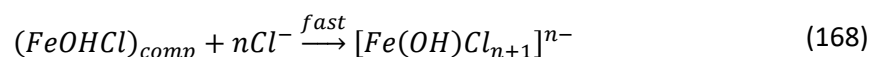
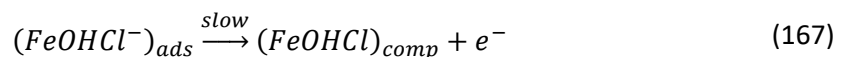
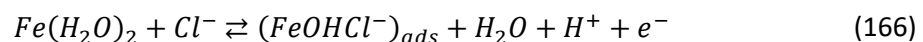
A5.9.5. Overall considerations

The corrosion behaviour of 304 SS is a combination of the trends observed for Fe and Ni, and as expected, the corrosion resistance of the alloy was improved compared to pure Fe. This improvement is mainly due to the presence of chromium oxide (Cr_2O_3), which is considered the main passive component, in the formed passive film⁴⁴⁴. The corrosion mechanisms of iron and nickel in different corrosion media have been discussed in sections A5.3.5 and A5.5.5 respectively. Even though chromium (Cr) is a major constituent of 304 SS, this metal was not included in the experimental matrix. The corrosion mechanisms of 304 SS was studied by electrochemical methods to elucidate the corrosion mechanisms. Similar to Fe and Ni the corrosion process starts with the oxidation of the metal in water, followed by a further oxidation step to form the stable oxide Cr_2O_3 ⁴⁴⁴. The oxidation steps of Cr in 304 SS in acidic media have been reported as follows:



A5.9.5.1 304 SS corrosion in chloride media

In [C4C1im]Cl media, 304 SS had the lowest MCR compared to Fe and Ni. It has been shown that the passive on stainless steel 304 exists mainly in the form $\text{H}_2\text{O}-\text{Fe}-\text{H}_2\text{O}$ and that chloride ions adsorb at certain points on the surface forming an intermediate complex⁴⁴⁵, which causes rapid dissolution of the passive film at these points leading to pitting corrosion. In most areas in which no chloride is adsorbed, passivation still takes place. The pitting kinetics of 304 SS had been studied in NaCl and the following mechanism was proposed, assuming the formation of the same intermediate complex previously described⁴⁴²:



The above mechanisms are similar to the mechanisms proposed for Fe dissolution in chloride-containing media discussed in section A5.3.5. Surprisingly, corrosion parameters have been extensively studied for 304 SS though electrochemical techniques (pitting corrosion, stress

corrosion cracking), in NaCl containing different substances, but no data was found on the corrosion rate of 304 in NaCl solutions alone, studied by weight loss methods. Therefore, the MCR obtained in $[C_4C_1im]Cl$ cannot be compared against NaCl. However, due to the inhibitory effects of ILs, produced by the adsorption of the cation in the surface inhibiting Eq. 165 and 166, it would be expected that the corrosion rates would be lower in the aprotic ionic liquid than in inorganic chloride salts, such as NaCl, at the same chloride concentration. As no significant corrosion was observed in the 304 SS samples exposed to $[C_4C_1im]Cl$ solutions, it will be classified as type-0.

When 304 SS is exposed to $[HC_1im]Cl$, the MCR was higher than for Ni, but within the order of magnitude and less than in Fe, which experienced extreme corrosion in this IL. XRF data of the 304 SS samples exposed to this IL showed the iron content was reduced, which is consistent with the increased MCR and the fact the iron is very sensitive to that media. When exposed to $[N_{4110}][HSO_4]$ media, the MCR were lower than Nickel at all conditions tested except at 120 °C and 75 mol% which showed extreme corrosion, with a 2-fold value compared to Ni.

A5.9.5.2 304 SS corrosion in sulfate media

It has been noticed that the corrosion rate data for 304 SS exposed to HCl and H_2SO_4 reported in the scientific literature, determined by weight loss, is scarce and difficult to compare as the experiments were not conducted in similar manners. Also, it has been noticed some inconsistencies in the trends, probably due to the many variables affecting the rates in corrosion phenomena. In a corrosion handbook, it has been reported that the corrosion rates of 304 SS in boiling 1% HCl and 10% H_2SO_4 are 81 mm/y and 400 mm/y respectively ¹⁴⁵. In another reference in the same handbook, there are some inconsistencies in the data presented and could not be checked against the original reference as it was in German and not available for consultation (ref 127 in ¹⁴⁵). It is indicated that at 2.5 M H_2SO_4 the corrosion rate is 45 mm/y with a maximum of ~70 mm/y at 8M at room temperature. The corrosion rate reported for 304 SS exposed to HCl 2N at 30°C is 1.8-1.9 mm/y (70.2 – 76.5 mpy) obtained through linear polarization and Tafel extrapolation at room temperature ⁴⁴⁶. To be able to determine in which acid the attack on 304 is more severe, the experiments need to be compared with the same concentration of acid and the same conditions. In an attempt to do so, corrosion rate data from the literature, calculated by weight loss method in different acidic media have been normalized to the same acid concentration and corrosion rate unit and shown in Figure 190.

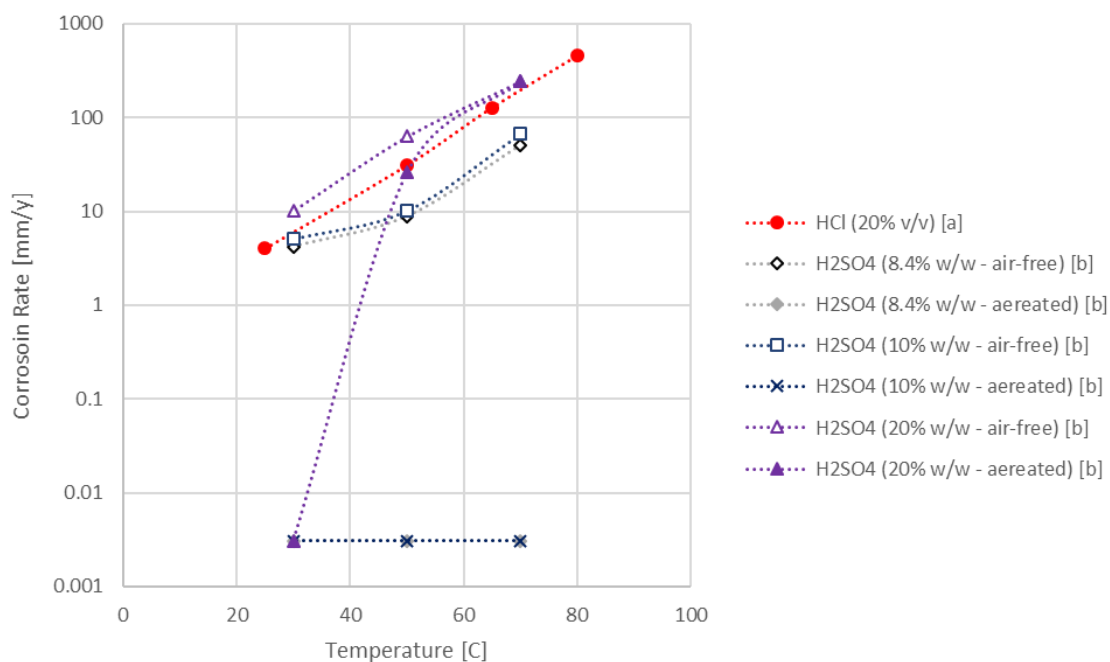


Figure 190. Corrosion rates for 304 SS exposed to acidic media taken from literature. [a] ref ⁴⁴⁷. [b] ref ⁴⁴⁸. Lines have been added to guide the eye.

It has been noticed that the corrosion phenomena of 304 SS depends upon many factors, such as surface treatment, acid concentration, temperature and the presence of air in the solution. The corrosion behaviour in H_2SO_4 is severally affected by saturating the solution with air or nitrogen ⁴⁴⁸. It was shown that the corrosion rates are lower (and for some concentrations negligible) when saturated with air and increased in air-free solutions. For H_2SO_4 concentrations below 10 wt%, the weight loss was negligible for the temperature range tested (30 to 70 °C), showing that oxygen forms stable passive layers that protect the metal. At 20 wt%, the corrosion rate of the aerated solution is negligible at 30 °C, increases with temperature and at 70 °C is similar to the air-free solution. Moreover, they showed that surface treatment of the steel specimens have ⁴⁴⁸. Data for corrosion in HCl was taken from literature, in which a solution of HCl 20% v/v (8.4 wt%) non-deaerated and under static condition was used for the comparison ⁴⁴⁷. From all the data presented, it would appear that 304 SS is attacked at higher rates in H_2SO_4 than in HCl at the same molarity. However, H_2SO_4 is a diprotic acid, at the same H^+ concentration, the corrosion rates in HCl would be higher. In the protic ILs, $[N_{4110}][HSO_4]$ leads to strong acidic solutions contrary to $[HC_{110}]Cl$, which leads to only slightly acidic solutions as explained in section 2.2.4.

From the above discussion, based only in the acidity o the solutions, it would be expected that 304 SS to be more attacked in $[N_{4110}][HSO_4]$ than in $[HC_{110}]Cl$, however, the opposite is observed. 304 SS showed small MCR when exposed to $[N_{4110}][HSO_4]$ expect at 120 °C, in which

extreme corrosion occurred with the deposition of material. However, under the same conditions in [HC_{1im}]Cl, the attack was maximum with a 6-fold value. As mentioned earlier, the corrosion resistance of 304 SS is due to the formation of a passive layer on its surface. This layer can also develop under oxidizing conditions in sulfuric acid and consists of iron oxide and chromium oxide with incorporated sulfates, which improve its stability ¹⁴⁵. The solutions used in the corrosion experiments were not de-aerated, and therefore, it would be expected to contain traces of oxygen that might lead to the formation of these passive layers. However, as mentioned before, at higher acid concentrations and/or higher temperatures, the protective layer is destroyed, or its formation inhibited. Also, it is known that 304 SS is also at risk of depassivation by chlorides, which might explain the high MCR observed in [HC_{1im}]Cl. Corrosion of 304 SS in acidic-functionalized ionic liquids containing the [HSO₄]⁻ have only been assessed through electrochemical methods ⁴²⁵ and is discussed in section A5.3.5.

It has been reported that the presence of chloride ions has a remarkable effect on the corrosion process of stainless steel, which is subjected to pitting and crevice corrosion in warm chloride environments and to stress corrosion cracking above about 60 °C. This can be explained by their strong adsorbing and penetrating power due to their small ion radius, chloride ions can damage the passive film to cause the local corrosion ⁴⁴⁷. As the temperature increases, the activity of chloride ions increases and the corrosion will be promoted ⁴⁴⁷.

A5.9.5.3 304 SS categorization system

The result in the protic ILs shows the same trends that in mineral acids and shows that the passive layers are more soluble and unstable in chloride-containing protic ILs than in protic [HSO₄]⁻ containing ILs. 304 SS and [HC_{1im}]Cl systems will be classified as type-4 for all experimental conditions tested except for 98 mol% at 20°C, for which no signs of corrosion were observed and will be classified as type-0. 304 SS and [N₄₁₁₀][HSO₄] will be classified as type-0 for all experimental conditions tested, except for 75 mol% at 70 °C, which will be classified as type-4 due to high corrosion rates and type-3 at 120 °C due to the high rates and material deposition on the surface.

Research work on the corrosion of stainless steels alloys in oxidizing high-temperature water is extensive for temperatures up to ~300 °C and concentrations of oxygen in the range of a few ppm, in the presence of different ions ⁴⁴⁹. It has been shown a good corrosion resistance in O₂/water solutions without other inorganic compounds, which is consistent with the results obtained in the water. 304 SS in the water system is classified as type-0.

Table 56 summarizes the corrosion behaviour of 304 SS exposed to corrosive media.

Table 56. Summary of the classification system and corrosion type for 304 stainless steel exposed to corrosive media. Corrosion types: NC: no corrosion, PC: pitting corrosion, USC: uniform surface corrosion and NUSC: non-uniform corrosion. Section 3.4.

Solvent →	[C ₄ C ₁ im]Cl			[HC ₁ im]Cl			[N ₄₁₁₀][HSO ₄]			[C ₄ C ₁ im][NTf ₂]	Water
Water Content [mol fraction] →	Dry	0.75	0.98	Dry	0.75	0.98	Dry	0.75	0.98	Dry	1
Temperature [°C] ↓											
20	0	0	0				0	0	0		
70	0	0	0	4		0	0	4	0	0	
120	0	0	0	4	4	4	0	3	0		
150										0	
20	NC	NC	NC				NC	CN	NC		
70	NC	NC	NC	USC		NC	CN	USC	NC	NC	
120	NC	NC	NC	USC	USC	USC	CN	NUSC	USC	NC	
150										NC	

A5.9.5.4 304 SS corrosion in other ILs

Corrosion of 304 SS in ionic liquids have only been assessed through electrochemical methods in acidic-functionalized ILs, containing the [HSO₄]⁻ anion as mentioned earlier ⁴²⁵.

The corrosion of several metals in aprotic ILs was studied using the “rotating cage” method, at a temperature of 90 °C in aerated solutions and 4-d exposure time ¹⁵¹. In this study, 304 SS showed excellent resistant in several aprotic IL medium, water-free or as an aqueous solution (estimated at less than 0.1 mm/y). However, it was mentioned that even though localised attack (*e.g.* pitting, intergranular corrosion) could not be observed in any of the experiments, these forms of corrosion should be studied in detail when this austenitic steel is exposed to corrosive media ¹⁵¹. It has also been studied In fluorinated ILs ^{184,450}, which will be addressed in section 3.5.2. Also, it has been studied in chloroaluminate ILs and will not be discussed here

⁴⁵¹.

Appendix 6 - Corrosion rates

The calculated mass change rates (MCR) by different methods are presented in Table 57. RAVE: Average value. RMAX: The maximum value. RO: The slope of a line forced through the origin. The CR were calculated from the MCR and density values (Eq. 70).

Table 57. Numeric values for the MCR by different methods.

Metal	Solvent	Temp. [°C]	Water conc. [mol%]	MCR [RAVE]	MCR_error [RAVE]	MCR [RMAX]	MCR_error [RMAX]	MCR [RO]	MCR_error [RO]	CR [RAVE]	CR_error [RAVE]
Al	H ₂ O	20	100	-0.69112	0.091582	-0.7827	0.048696	-0.77208	0.042806	-0.93429	0.123806
Al	H ₂ O	70	100	-6.20484	2.445459	-8.65029	0.411617	-3.78287	0.338169	-8.38802	3.305899
Al	H ₂ O	120	100	-156.543	146.8399	-303.383	1.513608	-34.6437	30.61549	-211.623	198.5058
Al	[C ₄ C ₁ im]Cl	20	75	0.000105	0.000129	0.000234	0.000391	-2.23E-06	7.06E-05	0.000143	0.000174
Al	[C ₄ C ₁ im]Cl	20	98	0.000532	0.000323	0.000855	0.00039	0.000263	0.000177	0.00072	0.000436
Al	[C ₄ C ₁ im]Cl	70	0	0.000324	3.24E-05	0.000324	0.00054	0.000324	inf	0.000437	4.37E-05
Al	[C ₄ C ₁ im]Cl	70	75	-0.00011	0.000671	-0.00078	0.000647	0.000472	0.000338	-0.00015	0.000906
Al	[C ₄ C ₁ im]Cl	70	98	-0.02308	0.019506	-0.04259	0.000575	-0.03645	0.01421	-0.03121	0.02637
Al	[C ₄ C ₁ im]Cl	120	0	0.000284	0.000119	0.000403	0.000202	0.000389	5.50E-05	0.000384	0.000161
Al	[C ₄ C ₁ im]Cl	120	75	-0.01705	0.001705	-0.01705	0.001909	-0.01705		-0.02305	0.002305
Al	[C ₄ C ₁ im]Cl	120	98	-0.02266	0.002266	-0.02266	0.001234	-0.02266		-0.03063	0.003063
Al	[C ₄ C ₁ im][NTf ₂]	70	0	0.00021	2.10E-05	0.00021	0.000351	0.00021	inf	0.000284	2.84E-05
Al	[C ₄ C ₁ im][NTf ₂]	150	0	2.87E-05	2.87E-06	2.87E-05	0.000143	2.87E-05		3.87E-05	3.87E-06
Al	[HC ₁ im]Cl	70	75	0.132873	0.062459	0.195332	0.003716	0.171198	0.049319	0.179625	0.084435
Al	[HC ₁ im]Cl	70	98	0.162485	0.044985	0.20747	0.002278	0.181181	0.040917	0.219656	0.060814
Al	[HC ₁ im]Cl	120	0	-0.14732	0.008425	-0.15575	0.389831	-0.13917	0.00212	-0.19916	0.01139
Al	[HC ₁ im]Cl	120	75	1.788829	0.069522	1.85835	0.009819	1.84219	0.044562	2.418231	0.093983
Al	[HC ₁ im]Cl	120	98	-0.37534	0.001773	-0.37711	0.017275	-0.37403	0.001192	-0.5074	0.002397
Al	[N ₄₁₁₀][HSO ₄]	20	75	0.017092	0.000298	0.01739	0.00381	0.016866	0.000194	0.023106	0.000403
Al	[N ₄₁₁₀][HSO ₄]	20	98	0.056956	0.001132	0.058088	0.002692	0.056328	0.000943	0.076996	0.001531
Al	[N ₄₁₁₀][HSO ₄]	70	0	0.02828	0.002828	0.02828	0.001144	0.02828		0.03823	0.003823
Al	[N ₄₁₁₀][HSO ₄]	70	75	0.888084	0.088137	0.976221	0.005462	0.946616	0.065895	1.200557	0.119149

Metal	Solvent	Temp. [°C]	Water conc. [mol%]	MCR [RAVE]	MCR_error [RAVE]	MCR [RMAX]	MCR_error [RMAX]	MCR [RO]	MCR_error [RO]	CR [RAVE]	CR_error [RAVE]
Al	[N ₄₁₁₀][HSO ₄]	70	98	2.498928	0.531808	3.030736	0.009067	3.023381	0.088143	3.378181	0.718926
Al	[N ₄₁₁₀][HSO ₄]	120	0	0.063397	0.021046	0.084443	0.000597	0.079984	0.012954	0.085703	0.028451
Al	[N ₄₁₁₀][HSO ₄]	120	75	10.67968	1.067968	10.67968	0.454918	10.67968	inf	14.43735	1.443735
Al	[N ₄₁₁₀][HSO ₄]	120	98	34.27945	4.516771	38.79622	0.145604	37.03496	3.578879	46.34073	6.106005
Brass	H ₂ O	20	100	0.004776	0.018523	0.0233	0.001981	0.001253	0.004062	0.002058	0.007982
Brass	H ₂ O	70	100	-0.00162	0.000646	-0.00226	0.001614	-0.00183	0.000341	-0.0007	0.000279
Brass	H ₂ O	120	100	0.072731	0.021984	0.094715	0.00389	0.06137	0.01882	0.031342	0.009474
Brass	[C ₄ C _{1im}]Cl	20	75	0.046123	0.002108	0.048231	0.000458	0.046844	0.001981	0.019876	0.000909
Brass	[C ₄ C _{1im}]Cl	20	98	0.05737	0.02178	0.07915	0.00067	0.041968	0.0154	0.024723	0.009386
Brass	[C ₄ C _{1im}]Cl	70	0	0.028181	0.002818	0.028181	0.000615	0.028181		0.012144	0.001214
Brass	[C ₄ C _{1im}]Cl	70	75	0.208404	0.037596	0.246	0.001626	0.183231	0.027924	0.089808	0.016201
Brass	[C ₄ C _{1im}]Cl	70	98	0.040926	0.010082	0.051008	0.001568	0.034016	0.007342	0.017636	0.004345
Brass	[C ₄ C _{1im}]Cl	120	0	0.397565	0.006225	0.40379	0.001494	0.395736	0.00595	0.171324	0.002683
Brass	[C ₄ C _{1im}]Cl	120	75	0.831436	0.024997	0.856432	0.00612	0.813642	0.017556	0.358293	0.010772
Brass	[C ₄ C _{1im}]Cl	120	98	0.042468	0.026312	0.068781	0.004765	0.023725	0.018467	0.018301	0.011339
Brass	[C ₄ C _{1im}][NTf ₂]	70	0	0.003475	0.002603	0.006079	0.000618	0.000921	0.000501	0.001498	0.001122
Brass	[C ₄ C _{1im}][NTf ₂]	150	0	0.093983	0.009398	0.093983	0.000356	0.093983		0.0405	0.00405
Brass	[HC _{1im}]Cl	20	75	0.067336	3.52E-06	0.06734	0.001192	0.067335	3.47E-06	0.029017	1.52E-06
Brass	[HC _{1im}]Cl	20	98	0.16411	0.022288	0.186398	0.001204	0.167992	0.021948	0.07072	0.009605
Brass	[HC _{1im}]Cl	70	75	0.364426	0.010106	0.374532	0.003939	0.372682	0.005828	0.157043	0.004355
Brass	[HC _{1im}]Cl	70	98	0.522982	0.006116	0.529098	0.004087	0.527933	0.003591	0.22537	0.002636
Brass	[HC _{1im}]Cl	120	0	31.87216	3.162545	35.0347	0.131486	30.97942	0.323137	13.73476	1.362844
Brass	[HC _{1im}]Cl	120	75	13.19597	4.204793	17.40076	0.050542	9.574926	2.137368	5.686574	1.811983
Brass	[HC _{1im}]Cl	120	98	0.219083	0.007212	0.226295	0.018103	0.212891	0.003698	0.09441	0.003108
Brass	[N ₄₁₁₀][HSO ₄]	20	75	0.022958	0.003752	0.02671	0.001451	0.020402	0.002747	0.009893	0.001617
Brass	[N ₄₁₁₀][HSO ₄]	20	98	0.182072	0.009285	0.191356	0.001048	0.187445	0.007572	0.078461	0.004001
Brass	[N ₄₁₁₀][HSO ₄]	70	0	0.035647	0.008066	0.043713	0.000349	0.040582	0.00638	0.015361	0.003476
Brass	[N ₄₁₁₀][HSO ₄]	70	75	0.122758	0.000225	0.122983	0.001653	0.122927	0.000149	0.0529	9.70E-05
Brass	[N ₄₁₁₀][HSO ₄]	70	98	0.388647	0.016429	0.405076	0.002064	0.401341	0.01043	0.167481	0.00708

Metal	Solvent	Temp. [°C]	Water conc. [mol%]	MCR [RAVE]	MCR_error [RAVE]	MCR [RMAX]	MCR_error [RMAX]	MCR [RO]	MCR_error [RO]	CR [RAVE]	CR_error [RAVE]
Brass	[N ₄₁₁₀][HSO ₄]	120	0	0.137732	0.013773	0.137732	0.000988	0.137732		0.059353	0.005935
Brass	[N ₄₁₁₀][HSO ₄]	120	75	0.03053	0.007911	0.038441	0.002046	0.023824	0.004198	0.013156	0.003409
Brass	[N ₄₁₁₀][HSO ₄]	120	98	0.288765	0.149033	0.437798	0.001705	0.414311	0.080307	0.124438	0.064223
Cu	H ₂ O	20	100	0.000763	0.005273	-0.00451	0.000744	0.000113	0.002983	0.000311	0.002148
Cu	H ₂ O	70	100	-0.00819	0.006101	-0.0143	0.002143	-0.0034	0.003769	-0.00334	0.002485
Cu	H ₂ O	120	100	0.049272	0.029925	0.079197	0.003871	0.033773	0.025598	0.020072	0.01219
Cu	[C ₄ C ₁ im]Cl	20	75	0.061291	0.002814	0.064105	0.000485	0.062253	0.002645	0.024968	0.001146
Cu	[C ₄ C ₁ im]Cl	20	98	0.110371	0.008251	0.118623	0.000737	0.104798	0.006085	0.044961	0.003361
Cu	[C ₄ C ₁ im]Cl	70	0	0.048455	0.004845	0.048455	0.000652	0.048455		0.019739	0.001974
Cu	[C ₄ C ₁ im]Cl	70	75	0.219043	0.058002	0.277045	0.002416	0.169358	0.029926	0.089231	0.023628
Cu	[C ₄ C ₁ im]Cl	70	98	0.480114	0.065768	0.545882	0.001556	0.539086	0.029117	0.195582	0.026792
Cu	[C ₄ C ₁ im]Cl	120	0	0.346623	0.124801	0.471424	0.001393	0.38318	0.119327	0.141202	0.05084
Cu	[C ₄ C ₁ im]Cl	120	75	0.670326	0.187601	0.857928	0.006113	0.528255	0.122515	0.273068	0.076422
Cu	[C ₄ C ₁ im]Cl	120	98	0.031956	0.009276	0.041232	0.001787	0.031994	0.009276	0.013018	0.003779
Cu	[C ₄ C ₁ im][NTf ₂]	70	0	0.005848	0.00351	0.009357	0.000623	0.002406	0.000689	0.002382	0.00143
Cu	[C ₄ C ₁ im][NTf ₂]	150	0	0.176595	0.017659	0.176595	0.000546	0.176595		0.071939	0.007194
Cu	[HC ₁ im]Cl	20	75	0.099329	0.000725	0.100054	0.001232	0.099203	0.000714	0.040463	0.000295
Cu	[HC ₁ im]Cl	20	98	0.916441	0.023404	0.939845	0.002636	0.912377	0.023049	0.373327	0.009534
Cu	[HC ₁ im]Cl	70	75	0.421895	0.093242	0.515137	0.004196	0.497898	0.054016	0.171866	0.037984
Cu	[HC ₁ im]Cl	70	98	1.157504	0.457812	1.615316	0.005937	1.527586	0.269501	0.471528	0.186497
Cu	[HC ₁ im]Cl	120	0	67.90529	1.446172	69.35146	0.211192	68.73859	1.181956	27.66231	0.589121
Cu	[HC ₁ im]Cl	120	75	12.6885	0.968437	13.65693	0.043696	11.8523	0.488513	5.168862	0.394508
Cu	[HC ₁ im]Cl	120	98	0.971635	0.001251	0.972885	0.006536	0.972711	0.000637	0.395811	0.00051
Cu	[N ₄₁₁₀][HSO ₄]	20	75	0.016643	0.001765	0.018408	0.001515	0.016547	0.001763	0.00678	0.000719
Cu	[N ₄₁₁₀][HSO ₄]	20	98	0.198548	0.004	0.202548	0.002789	0.196547	0.003464	0.080882	0.00163
Cu	[N ₄₁₁₀][HSO ₄]	70	0	0.048486	0.002971	0.051457	0.000362	0.050304	0.002349	0.019752	0.00121
Cu	[N ₄₁₁₀][HSO ₄]	70	75	0.159678	0.016031	0.175709	0.002364	0.168497	0.013387	0.065047	0.00653
Cu	[N ₄₁₁₀][HSO ₄]	70	98	0.412443	0.098391	0.510835	0.002316	0.48661	0.064655	0.168015	0.040081
Cu	[N ₄₁₁₀][HSO ₄]	120	0	0.32064	0.249525	0.570165	0.002665	0.27609	0.245515	0.130618	0.101648

Metal	Solvent	Temp. [°C]	Water conc. [mol%]	MCR [RAVE]	MCR_error [RAVE]	MCR [RMAX]	MCR_error [RMAX]	MCR [RO]	MCR_error [RO]	CR [RAVE]	CR_error [RAVE]
Cu	[N ₄₁₁₀][HSO ₄]	120	75	0.119188	0.010764	0.129952	0.00079	0.128314	0.005709	0.048553	0.004385
Cu	[N ₄₁₁₀][HSO ₄]	120	98	0.774968	0.431146	1.206113	0.005387	0.411626	0.232098	0.315695	0.175634
Fe	H ₂ O	20	100	0.003572	0.001626	0.005197	0.003257	0.002596	0.0013	0.001659	0.000755
Fe	H ₂ O	70	100	0.13732	0.13667	0.224608	0.003628	0.162014	0.051941	0.063768	0.063466
Fe	H ₂ O	120	100	0.658492	0.121974	0.780465	0.003419	0.721307	0.104556	0.305788	0.056642
Fe	[C ₄ C ₁ im]Cl	20	75	0.035283	0.000161	0.035444	0.000599	0.035228	0.000151	0.016385	7.47E-05
Fe	[C ₄ C ₁ im]Cl	20	98	0.151587	0.017464	0.169051	0.00082	0.139236	0.012348	0.070393	0.00811
Fe	[C ₄ C ₁ im]Cl	70	0	0.026705	0.00267	0.026705	0.000585	0.026705	inf	0.012401	0.00124
Fe	[C ₄ C ₁ im]Cl	70	75	0.286349	0.02683	0.31318	0.001062	0.309333	0.013842	0.132974	0.012459
Fe	[C ₄ C ₁ im]Cl	70	98	0.508883	0.103751	0.612634	0.002231	0.579568	0.075947	0.236313	0.04818
Fe	[C ₄ C ₁ im]Cl	120	0	0.221392	0.204717	0.426109	0.001534	0.161342	0.195712	0.102809	0.095066
Fe	[C ₄ C ₁ im]Cl	120	75	2.463368	0.079099	2.542467	0.024378	2.445426	0.077037	1.14393	0.036732
Fe	[C ₄ C ₁ im]Cl	120	98	1.708543	0.423088	2.131632	0.015538	1.808032	0.411225	0.793407	0.196472
Fe	[C ₄ C ₁ im][NTf ₂]	70	0	0.001218	0.000122	0.001218	0.000611	0.001218		0.000566	5.66E-05
Fe	[C ₄ C ₁ im][NTf ₂]	150	0	-0.00198	0.000198	-0.00198	0.000141	-0.00198		-0.00092	9.19E-05
Fe	[HC ₁ im]Cl	20	75	0.290728	0.011336	0.302064	0.003733	0.284343	0.009366	0.135007	0.005264
Fe	[HC ₁ im]Cl	20	98	0.284271	0.008033	0.292303	0.003723	0.279743	0.006635	0.132009	0.00373
Fe	[HC ₁ im]Cl	45	98	4.831554	2.997091	7.828645	0.047633	2.017506	1.031354	2.24366	1.391779
Fe	[HC ₁ im]Cl	70	75	4.609816	0.161584	4.7714	0.110001	4.452368	0.036325	2.140691	0.075036
Fe	[N ₄₁₁₀][HSO ₄]	20	0	0.03613	0.014335	0.050466	0.000152	0.049009	0.006297	0.016778	0.006657
Fe	[N ₄₁₁₀][HSO ₄]	20	75	0.979835	0.043709	1.023544	0.01142	0.948617	0.030593	0.455012	0.020297
Fe	[N ₄₁₁₀][HSO ₄]	20	98	1.531582	0.035302	1.566884	0.012773	1.500299	0.016359	0.711231	0.016394
Fe	[N ₄₁₁₀][HSO ₄]	45	98	12.1951	0.205552	12.40065	0.031736	12.31688	0.165592	5.66312	0.095454
Fe	[N ₄₁₁₀][HSO ₄]	70	0	3.435125	2.746453	6.181578	0.015505	2.453103	2.564886	1.595192	1.275389
Fe	[N ₄₁₁₀][HSO ₄]	70	75	7.123516	2.911089	10.03461	0.026232	5.20027	2.185307	3.307994	1.351842
Fe	[N ₄₁₁₀][HSO ₄]	70	98	87.26673	6.51102	93.77775	0.407636	89.82241	5.988481	40.52463	3.023565
Fe	[N ₄₁₁₀][HSO ₄]	120	0	4.410423	0.595017	5.00544	0.018557	4.130318	0.524963	2.048097	0.276312
Fe	[N ₄₁₁₀][HSO ₄]	120	75	16.1366	0.071217	16.20782	0.033599	16.16102	0.066902	7.49346	0.033072
Mo	H ₂ O	20	100	0.006824	0.002852	0.009675	0.000152	0.009494	0.001002	0.002423	0.001013

Metal	Solvent	Temp. [°C]	Water conc. [mol%]	MCR [RAVE]	MCR_error [RAVE]	MCR [RMAX]	MCR_error [RMAX]	MCR [RO]	MCR_error [RO]	CR [RAVE]	CR_error [RAVE]
Mo	H ₂ O	70	100	0.069948	9.92E-05	0.070047	0.000867	0.070026	6.13E-05	0.024836	3.52E-05
Mo	H ₂ O	120	100	0.030457	0.003046	0.030457	0.001474	0.030457	inf	0.010814	0.001081
Mo	[C ₄ C ₁ im]Cl	20	75	0.000576	2.97E-05	0.000606	0.000117	0.000601	1.63E-05	0.000204	1.06E-05
Mo	[C ₄ C ₁ im]Cl	20	98	0.001527	0.000572	0.002099	0.000392	0.001049	0.000315	0.000542	0.000203
Mo	[C ₄ C ₁ im]Cl	70	0	0.000541	5.41E-05	0.000541	0.000542	0.000541		0.000192	1.92E-05
Mo	[C ₄ C ₁ im]Cl	70	75	0.019692	0.005373	0.025064	0.000217	0.024333	0.002706	0.006992	0.001908
Mo	[C ₄ C ₁ im]Cl	70	98	0.036508	0.003599	0.040107	0.000712	0.038974	0.002621	0.012962	0.001278
Mo	[C ₄ C ₁ im]Cl	120	0	-0.001	0.000479	-0.00148	0.00082	-0.00058	0.000221	-0.00036	0.00017
Mo	[C ₄ C ₁ im]Cl	120	75	0.008172	0.006079	0.014251	0.00042	0.012186	0.004566	0.002902	0.002158
Mo	[C ₄ C ₁ im]Cl	120	98	0.015855	0.006438	0.022294	0.000908	0.011604	0.004835	0.00563	0.002286
Mo	[C ₄ C ₁ im][NTf ₂]	70	0	0.000559	5.59E-05	0.000559	0.00035	0.000559	inf	0.000198	1.98E-05
Mo	[C ₄ C ₁ im][NTf ₂]	150	0	0.002208	0.000221	0.002208	0.000148	0.002208		0.000784	7.84E-05
Mo	[HC ₁ im]Cl	70	75	0.000954	0.001676	0.00263	0.001466	0.002159	0.001165	0.000339	0.000595
Mo	[HC ₁ im]Cl	70	98	0.022095	0.00184	0.023935	0.000366	0.020946	0.001437	0.007845	0.000653
Mo	[HC ₁ im]Cl	120	0	0.0079	0.001148	0.009048	0.000554	0.008816	0.000691	0.002805	0.000408
Mo	[HC ₁ im]Cl	120	75	0.031768	0.009478	0.041246	0.001532	0.024607	0.006208	0.01128	0.003365
Mo	[HC ₁ im]Cl	120	98	0.009165	0.003932	0.013097	0.00366	0.00536	0.000995	0.003254	0.001396
Mo	[N ₄₁₁₀][HSO ₄]	20	75	0.000541	0.001137	0.001678	0.001401	0.000612	0.001135	0.000192	0.000404
Mo	[N ₄₁₁₀][HSO ₄]	20	98	0.004747	0.006206	0.010953	0.001423	0.001169	0.005071	0.001685	0.002204
Mo	[N ₄₁₁₀][HSO ₄]	70	0	0.010895	0.009485	0.02038	0.000268	0.017411	0.006892	0.003869	0.003368
Mo	[N ₄₁₁₀][HSO ₄]	70	75	0.009444	0.003308	0.012752	0.001471	0.011925	0.002187	0.003353	0.001174
Mo	[N ₄₁₁₀][HSO ₄]	70	98	0.027891	0.005399	0.03329	0.001516	0.031951	0.003559	0.009903	0.001917
Mo	[N ₄₁₁₀][HSO ₄]	120	0	0.009548	0.000351	0.009899	0.000303	0.009717	0.000308	0.00339	0.000125
Mo	[N ₄₁₁₀][HSO ₄]	120	75	0.01914	0.007559	0.026699	0.002037	0.012733	0.004011	0.006796	0.002684
Mo	[N ₄₁₁₀][HSO ₄]	120	98	0.019952	0.011305	0.031257	0.000623	0.030611	0.003769	0.007084	0.004014
Ni	H ₂ O	20	100	0.000257	0.000407	0.000663	0.000208	0.000606	0.000208	0.000105	0.000167
Ni	H ₂ O	70	100	0.000922	0.004822	0.005201	0.002176	0.001561	0.000972	0.000378	0.001976
Ni	H ₂ O	120	100	-0.00313	0.000313	-0.00313	0.001418	-0.00313		-0.00128	0.000128
Ni	[C ₄ C ₁ im]Cl	20	75	0.002311	0.001284	0.003595	0.000397	0.001237	0.000704	0.000947	0.000526

Metal	Solvent	Temp. [°C]	Water conc. [mol%]	MCR [RAVE]	MCR_error [RAVE]	MCR [RMAX]	MCR_error [RMAX]	MCR [RO]	MCR_error [RO]	CR [RAVE]	CR_error [RAVE]
Ni	[C ₄ C ₁ im]Cl	20	98	0.000292	0.000176	0.000468	0.000391	0.000146	9.65E-05	0.00012	7.19E-05
Ni	[C ₄ C ₁ im]Cl	70	0	0.006056	0.000606	0.006056	0.000551	0.006056		0.002481	0.000248
Ni	[C ₄ C ₁ im]Cl	70	75	0.051521	0.020634	0.072155	0.000291	0.070105	0.008966	0.021111	0.008454
Ni	[C ₄ C ₁ im]Cl	70	98	0.005644	0.001516	0.00716	0.001504	0.004605	0.001104	0.002313	0.000621
Ni	[C ₄ C ₁ im]Cl	120	0	0.02955	0.011099	0.040649	0.000584	0.0344	0.009984	0.012108	0.004548
Ni	[C ₄ C ₁ im]Cl	120	75	0.029409	0.016798	0.046207	0.001987	0.014631	0.007986	0.01205	0.006883
Ni	[C ₄ C ₁ im]Cl	120	98	0.042171	0.038708	0.080879	0.002044	0.008134	0.018433	0.017279	0.01586
Ni	[C ₄ C ₁ im][NTf ₂]	70	0	0	0	0		0		0	0
Ni	[HC ₁ im]Cl	70	75	0.957305	0.077448	1.034753	0.005397	0.933962	0.073847	0.39225	0.031734
Ni	[HC ₁ im]Cl	70	98	0.479894	0.032514	0.512408	0.010729	0.44921	0.010756	0.196634	0.013322
Ni	[HC ₁ im]Cl	120	0	6.575083	0.867062	7.442145	0.084316	6.009146	0.656895	2.694101	0.355273
Ni	[HC ₁ im]Cl	120	75	9.721116	0.366441	10.08756	0.022448	10.03202	0.193957	3.983169	0.150147
Ni	[HC ₁ im]Cl	120	98	2.103655	0.477954	2.581609	0.008038	1.857994	0.409988	0.86196	0.195839
Ni	[N ₄₁₁₀][HSO ₄]	20	75	0.025749	0.002649	0.028398	0.000659	0.027539	0.001952	0.01055	0.001085
Ni	[N ₄₁₁₀][HSO ₄]	20	98	0.158628	0.002377	0.161005	0.001001	0.16	0.001941	0.064997	0.000974
Ni	[N ₄₁₁₀][HSO ₄]	70	0	0.033572	0.01027	0.043842	0.000616	0.026517	0.007462	0.013756	0.004208
Ni	[N ₄₁₁₀][HSO ₄]	70	75	0.126524	0.006599	0.133123	0.004075	0.121565	0.004354	0.051842	0.002704
Ni	[N ₄₁₁₀][HSO ₄]	70	98	0.357921	0.021276	0.379197	0.002097	0.373918	0.014027	0.146656	0.008718
Ni	[N ₄₁₁₀][HSO ₄]	120	0	0.79713	0.63546	1.43259	0.002879	1.326109	0.202896	0.326619	0.260376
Ni	[N ₄₁₁₀][HSO ₄]	120	75	0.901863	0.098101	0.999964	0.002242	0.972138	0.068449	0.369533	0.040196
Ni	[N ₄₁₁₀][HSO ₄]	120	98	0.611888	0.061189	0.611888	0.010412	0.611888	inf	0.250717	0.025072
SS304	H ₂ O	20	100	0.000581	0.000581	0.001163	0.000971	5.67E-05	0.00025	0.000271	0.000271
SS304	H ₂ O	70	100	0.000977	0.000116	0.001093	0.000609	0.001076	6.04E-05	0.000456	5.41E-05
SS304	H ₂ O	120	100	-0.00113	0.000113	-0.00113	0.001413	-0.00113		-0.00053	5.28E-05
SS304	[C ₄ C ₁ im]Cl	20	75	-0.0004	0.000553	-0.00095	0.000114	-0.00086	0.000303	-0.00019	0.000258
SS304	[C ₄ C ₁ im]Cl	20	98	0.001652	0.002452	0.004105	0.000394	0.000415	0.002117	0.000771	0.001145
SS304	[C ₄ C ₁ im]Cl	70	0	-0.00172	0.000172	-0.00172	0.000535	-0.00172	inf	-0.0008	8.03E-05
SS304	[C ₄ C ₁ im]Cl	70	75	0.000378	0.000525	0.000903	0.000646	-9.53E-05	0.000228	0.000176	0.000245
SS304	[C ₄ C ₁ im]Cl	70	98	0.000742	0.000742	0.001484	0.001486	0.000234	0.000541	0.000346	0.000346

Metal	Solvent	Temp. [°C]	Water conc. [mol%]	MCR [RAVE]	MCR_error [RAVE]	MCR [RMAX]	MCR_error [RMAX]	MCR [RO]	MCR_error [RO]	CR [RAVE]	CR_error [RAVE]
SS304	[C ₄ C ₁ im]Cl	120	0	0.007566	0.000757	0.007566	0.000835	0.007566		0.003532	0.000353
SS304	[C ₄ C ₁ im]Cl	120	75	0.004381	0.003212	0.007593	0.001911	0.001567	0.001548	0.002045	0.001499
SS304	[C ₄ C ₁ im]Cl	120	98	0.005525	0.00313	0.008655	0.000801	0.00409	0.002782	0.002579	0.001461
SS304	[C ₄ C ₁ im][NTf ₂]	70	0	0.000903	9.03E-05	0.000903	0.000349	0.000903	inf	0.000422	4.22E-05
SS304	[C ₄ C ₁ im][NTf ₂]	150	0	-0.00011	1.14E-05	-0.00011	0.000142	-0.00011	inf	-5.32E-05	5.32E-06
SS304	[HC ₁ im]Cl	70	75	0.820146	0.027121	0.847267	0.004059	0.82826	0.025879	0.382805	0.012659
SS304	[HC ₁ im]Cl	70	98	-0.00066	9.98E-05	-0.00076	0.000422	-0.00059	6.47E-05	-0.00031	4.66E-05
SS304	[HC ₁ im]Cl	120	0	6.98608	0.911346	7.897426	0.046216	7.432509	0.794514	3.260766	0.425373
SS304	[HC ₁ im]Cl	120	75	14.47569	1.800857	16.27655	0.047948	12.94428	0.947564	6.756556	0.840554
SS304	[HC ₁ im]Cl	120	98	0.078531	0.034399	0.11293	0.002236	0.096259	0.029479	0.036654	0.016056
SS304	[N ₄₁₁₀][HSO ₄]	20	0	-7.10E-05	1.08E-06	-7.21E-05	5.14E-05	-7.16E-05	9.42E-07	-3.32E-05	5.03E-07
SS304	[N ₄₁₁₀][HSO ₄]	20	75	0.000843	9.34E-06	0.000853	0.000611	0.00085	6.86E-06	0.000394	4.36E-06
SS304	[N ₄₁₁₀][HSO ₄]	20	98	0.001575	0.000458	0.002033	0.00073	0.001839	0.000374	0.000735	0.000214
SS304	[N ₄₁₁₀][HSO ₄]	70	0	-0.00055	0.000321	-0.00087	0.001085	-0.00023	3.53E-05	-0.00026	0.00015
SS304	[N ₄₁₁₀][HSO ₄]	70	75	0.002879	0.000579	0.003458	0.001447	0.003314	0.000382	0.001344	0.00027
SS304	[N ₄₁₁₀][HSO ₄]	70	98	-0.00051	0.001059	-0.00157	0.003915	0.00053	0.00021	-0.00024	0.000494
SS304	[N ₄₁₁₀][HSO ₄]	120	0	0.000824	0.001101	0.001925	0.000484	0.000476	0.001045	0.000385	0.000514
SS304	[N ₄₁₁₀][HSO ₄]	120	75	1.975236	0.444344	2.419579	0.006329	1.836219	0.422037	0.921945	0.207398
SS304	[N ₄₁₁₀][HSO ₄]	120	98	0.024634	0.012789	0.037423	0.005262	0.012789	0.004822	0.011498	0.005969
Ti	H ₂ O	20	100	-0.00067	0.000379	-0.00105	0.000746	-0.00034	0.000194	-0.00054	0.000307
Ti	H ₂ O	70	100	0.00031	0.000554	0.000864	0.002162	-0.00016	0.000289	0.000251	0.000448
Ti	H ₂ O	120	100	0	0	0	0	0	0	0	0
Ti	[C ₄ C ₁ im]Cl	20	0	-0.00022	2.16E-05	-0.00022	0.000539	-0.00022		-0.00017	1.75E-05
Ti	[C ₄ C ₁ im]Cl	20	75	0.000284	0.000191	0.000475	0.000397	0.000124	0.000105	0.00023	0.000155
Ti	[C ₄ C ₁ im]Cl	20	98	0.000815	0.000815	0.00163	0.000391	0.000404	0.000704	0.00066	0.00066
Ti	[C ₄ C ₁ im]Cl	70	75	0.002853	0.002982	0.005835	0.000158	0.005539	0.001296	0.002311	0.002416
Ti	[C ₄ C ₁ im]Cl	70	98	0.000228	0.001122	0.00135	0.000967	0.000688	0.001024	0.000185	0.000909
Ti	[C ₄ C ₁ im]Cl	120	0	-9.60E-05	0.00059	-0.00069	0.000201	-0.00062	0.000273	-7.77E-05	0.000478
Ti	[C ₄ C ₁ im]Cl	120	75	5.68E-06	0.000704	0.00071	0.000396	0.000471	0.000529	4.60E-06	0.000571

Metal	Solvent	Temp. [°C]	Water conc. [mol%]	MCR [RAVE]	MCR_error [RAVE]	MCR [RMAX]	MCR_error [RMAX]	MCR [RO]	MCR_error [RO]	CR [RAVE]	CR_error [RAVE]
Ti	[C ₄ C ₁ im]Cl	120	98	-0.00063	0.001108	-0.00174	0.000869	9.67E-05	0.000832	-0.00051	0.000898
Ti	[C ₄ C ₁ im][NTf ₂]	70	0	0.000139	1.39E-05	0.000139	0.000349	0.000139		0.000113	1.13E-05
Ti	[C ₄ C ₁ im][NTf ₂]	150	0	-0.00031	3.15E-05	-0.00031	0.000143	-0.00031		-0.00026	2.55E-05
Ti	[HC ₁ im]Cl	70	75	-0.00288	0.002877	-0.00575	0.003587	-0.00081	0.001999	-0.00233	0.00233
Ti	[HC ₁ im]Cl	70	98	-0.00034	9.18E-06	-0.00034	0.000156	-0.00034	7.17E-06	-0.00027	7.44E-06
Ti	[HC ₁ im]Cl	120	0	0.016155	0.014753	0.030909	0.001662	0.004375	0.008881	0.013086	0.011951
Ti	[HC ₁ im]Cl	120	75	0.000678	0.000492	0.001169	0.001464	0.000277	0.000285	0.000549	0.000398
Ti	[HC ₁ im]Cl	120	98	-0.00166	0.00269	-0.00435	0.00362	0.000939	0.000681	-0.00135	0.002179
Ti	[N ₄₁₁₀][HSO ₄]	20	75	-0.00033	0.001064	-0.0014	0.001395	0.00039	0.000781	-0.00027	0.000862
Ti	[N ₄₁₁₀][HSO ₄]	20	98	0.001554	0.000973	0.002527	0.001408	0.000994	0.000795	0.001259	0.000788
Ti	[N ₄₁₁₀][HSO ₄]	70	0	9.32E-05	9.32E-05	0.000186	0.000233	0.000157	6.77E-05	7.55E-05	7.55E-05
Ti	[N ₄₁₁₀][HSO ₄]	70	75	0.003401	0.001955	0.005356	0.003835	0.001934	0.001292	0.002755	0.001583
Ti	[N ₄₁₁₀][HSO ₄]	70	98	0.001028	0.003345	0.004373	0.001465	0.003542	0.002206	0.000832	0.002709
Ti	[N ₄₁₁₀][HSO ₄]	120	0	-0.00045	0.000105	-0.00056	0.000695	-0.00039	8.37E-05	-0.00037	8.48E-05
Ti	[N ₄₁₁₀][HSO ₄]	120	75	0.00917	0.000917	0.00917	0.002009	0.00917		0.007428	0.000743
Ti	[N ₄₁₁₀][HSO ₄]	120	98	18.04358	7.654981	25.69856	0.053881	12.40701	5.17956	14.61586	6.200773
Zn	H ₂ O	20	100	-0.01251	0.006659	-0.01916	0.003217	-0.00851	0.005325	-0.00639	0.003404
Zn	H ₂ O	70	100	-0.02467	0.019468	-0.04413	0.00155	-0.03635	0.015571	-0.01261	0.009952
Zn	H ₂ O	120	100	-0.03419	0.030387	-0.06458	0.00365	-0.01845	0.025992	-0.01748	0.015534
Zn	[C ₄ C ₁ im]Cl	20	75	0.047234	0.004794	0.052028	0.000628	0.045594	0.004505	0.024146	0.002451
Zn	[C ₄ C ₁ im]Cl	20	98	0.088909	0.095959	0.184868	0.001924	0.037847	0.012762	0.045451	0.049054
Zn	[C ₄ C ₁ im]Cl	70	0	0.025353	0.002535	0.025353	0.000735	0.025353	inf	0.012961	0.001296
Zn	[C ₄ C ₁ im]Cl	70	75	0.571713	0.331069	0.902783	0.003193	0.622045	0.327221	0.292262	0.169244
Zn	[C ₄ C ₁ im]Cl	70	98	0.061237	0.02444	0.085677	0.002909	0.039285	0.010745	0.031304	0.012494
Zn	[C ₄ C ₁ im]Cl	120	0	0.491778	0.003725	0.495503	0.001651	0.490688	0.003562	0.251399	0.001904
Zn	[C ₄ C ₁ im]Cl	120	75	7.208319	0.301126	7.509445	0.028892	7.090393	0.277075	3.684925	0.153937
Zn	[C ₄ C ₁ im]Cl	120	98	0.44503	0.421721	0.866752	0.011486	0.609684	0.38825	0.227502	0.215586
Zn	[C ₄ C ₁ im][NTf ₂]	70	0	0.002379	0.002249	0.004628	0.000617	0.000172	0.000433	0.001216	0.00115
Zn	[C ₄ C ₁ im][NTf ₂]	150	0	0.0029	0.00029	0.0029	0.00015	0.0029		0.001482	0.000148

Metal	Solvent	Temp. [°C]	Water conc. [mol%]	MCR [RAVE]	MCR_error [RAVE]	MCR [RMAX]	MCR_error [RMAX]	MCR [RO]	MCR_error [RO]	CR [RAVE]	CR_error [RAVE]
Zn	[HC ₁ im]Cl	20	75	6.960175	0.965098	7.925273	0.016455	6.559088	0.877806	3.558073	0.493362
Zn	[HC ₁ im]Cl	20	98	0.409655	0.05803	0.467685	0.002711	0.433779	0.052778	0.209418	0.029665
Zn	[HC ₁ im]Cl	45	75	484.5862	482.9587	967.545	7.022856	430.5337	479.9244	247.7227	246.8907
Zn	[HC ₁ im]Cl	45	98	2.076894	0.366472	2.443365	0.031626	2.276307	0.307467	1.061717	0.187342
Zn	[N ₄₁₁₀][HSO ₄]	20	0	0.117368	0.02222	0.139588	0.000531	0.097406	0.00976	0.059999	0.011359
Zn	[N ₄₁₁₀][HSO ₄]	20	75	8.864079	0.850157	9.714236	0.020424	9.488274	0.57719	4.531357	0.434604
Zn	[N ₄₁₁₀][HSO ₄]	20	98	15.50673	8.923503	24.43023	0.054067	20.64137	7.298242	7.927108	4.561735
Zn	[N ₄₁₁₀][HSO ₄]	45	98	7.068104	6.187863	13.25597	0.180231	0.930707	0.78867	3.613247	3.163263
Zn	[N ₄₁₁₀][HSO ₄]	70	0	8.637192	0.756089	9.393281	0.021048	8.367223	0.706249	4.415371	0.386516
Zn	[N ₄₁₁₀][HSO ₄]	70	75	45.04424	30.37812	75.42236	0.359646	14.72566	1.901045	23.02682	15.52943
Zn	[N ₄₁₁₀][HSO ₄]	70	98	51.47674	59.52441	111.0012	0.326633	18.81569	4.14569	26.31514	30.42915
Zn	[N ₄₁₁₀][HSO ₄]	120	0	37.27206	29.29625	66.56831	0.15437	8.705455	6.497631	19.05365	14.97637
Zn	[N ₄₁₁₀][HSO ₄]	120	75	37.64121	7.980862	45.62207	0.146255	43.43972	5.483744	19.24236	4.079852

Appendix 7 – High-level techno-economic analysis for the Oxidative Ionothermal Process

A7.1. Motivation

It has been shown in Chapter 3 that metals can be oxidized in Ionic Liquids (ILs) and water solution to yield nano- and micro-sized particles with controlled morphology. It has been noticed that there is a diversity of synthetic methods for ZnO synthesis which are being developed. This attests the importance of developing increasingly facile, inexpensive, environmentally friendly, and scalable approaches for ZnO fabrication. Critically, barriers also include improved morphological control and uniformity, good throughput and high yields for large-scale synthesis. ZnO particles, and other metals, with homogenous morphologies produced in a cost-effective way, could enable the development of new applications that can range from electronics to medicine.

A7.1.1. Objectives

The aim of this section is to explore the benefits of the Oxidative Ionothermal Synthesis (OIS) for zinc oxide (ZnO) production at large scale and to compare the OIS to other synthesis methods in terms of production cost, process safety and environmental impact. As the OIS concept is at an early stage of development, and there are several technical uncertainties which could not be validated at lab scale due to time constraints, several assumptions were made to develop the process. Therefore, the analysis and conclusions presented in this section are preliminary and should be further validated. The main objective is to establish on a high-level basis if the OIS concept is a valid synthetic route for ZnO and if further work toward developing this process should be undertaken.

A7.2. Introduction

Zinc oxide (ZnO) is a water-insoluble white powder that is used as an additive in numerous materials and products. The main application of ZnO includes cosmetics, food supplements, rubbers, plastics, ceramics, glass, cement, paints and batteries.

The ZnO market share by applications for nanoparticles (2013) and bulk (2019) is shown in Figure 191 shows. From a market perspective, the largest application of ZnO nanoparticles is

for the cosmetic and sunscreen industries, while tyre manufacturing has the highest market share for bulk ZnO.

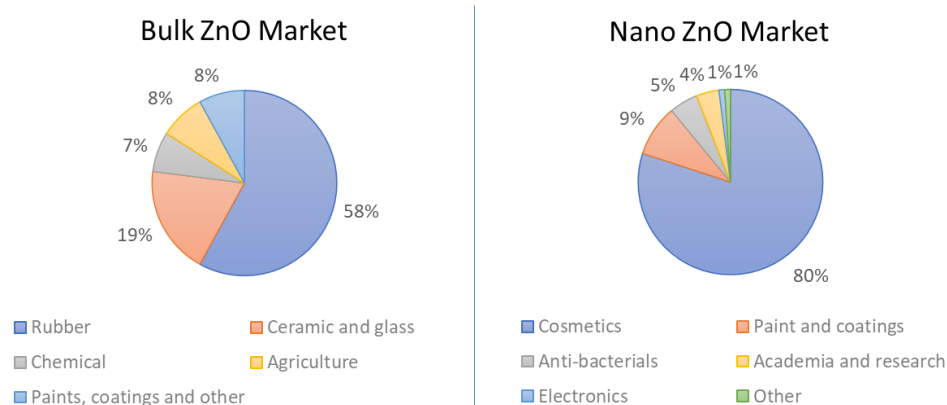


Figure 191. Bulk ZnO (IHS Markit - Zinc Oxide Market Overview) and nano-ZnO ⁴⁵² market share by applications in 2019 and 2013 respectively.

The variability of particle size, dimensions, and morphologies available for ZnO is beneficial for the wide array of applications and is, in fact, one of the greatest assortments of different particle structures among all known materials ⁴⁵³. Most common nano-ZnO materials have one-dimensional structures with different morphologies, such as rods, needles, helices, springs and rings, ribbons, tubes, belts, wires and combs. Two-dimensional crystals are also generally on the nanoscale, though fewer types of structures have been observed, *e.g.*, nanoplate/nanosheet and nanopellets. Three-dimensional ZnO crystals have been observed for a broad range of structures including flower, dandelion, snowflakes, coniferous urchin-like, etc. Details on ZnO toxicology are given in Appendix 7.

A7.2.1. Toxicology

Zinc oxide is generally categorized as a non-toxic material. Zinc oxide does not cause skin and eye irritation and there is no evidence of carcinogenicity, genotoxicity and reproduction toxicity in humans ²¹¹.

However, in the European Chemical Agency (ECHA) website, consulted the 18th of January 2020 ⁴⁵⁴, ZnO is labelled as very toxic to aquatic life and is very toxic to aquatic life with long-lasting effects, according to the harmonised classification and labelling (CLP00) approved by the European Union. Additionally, some companies indicated to ECHA in Registration, Evaluation, Authorisation and Restriction of Chemicals (REACH) registrations that this substance may damage fertility or the unborn child, is harmful if swallowed, is harmful if inhaled and may cause damage to organs through prolonged or repeated exposure. Also, at

least one company has indicated that the substance classification is affected by impurities or additives.

According to the Food and Drugs Administration (FDA), ZnO is generally recognized as safe when used in accordance with good manufacturing practices. Some applications include food for human consumption (21CFR182.8991), for sunscreen applications up to the concentration of 25% (21CFR352.50) and cosmetic as a colour additive (21CFR73.2991).

It has been shown that the ecotoxicity of ZnO to the model aquatic protozoan *Tetrahymena thermophila* is caused entirely by its solubilized fraction, *i.e.* the Zn²⁺ ion and that the toxicities of bulk ZnO, nano-ZnO and soluble Zn²⁺ are similar once their different solubilities are taken into account, with 4-h effect concentration (EC50) values of about 4 or 5 mg bio-available Zn/L (5 ppm), which is an order of magnitude lower than for soluble Cu²⁺ ⁴⁵⁵. By comparison, the naturally occurring amount of Zn ions in seawater is three orders of magnitude smaller (5 ppb).

ZnO has a long history of use in sunscreen compositions to block UV radiation, with the nanoparticulate form having been introduced for this application in the late 1990s. Sunscreen represents the major use of nano-ZnO (Figure 191). There have been occasional concerns voiced about possible adverse effects on human health or the environment. However, the current evidence shows that ZnO particles or nanoparticles do not penetrate viable skin cells and remain on the outer layer of undamaged skin (the stratum corneum) with low systemic toxicity ^{456–458}. Toxicity to the aquatic environment would depend on whether any ZnO washed off sunbathers was solubilized in, for example, the seawater, and whether the local environmental concentration of Zn²⁺ could thereby exceed the roughly 5 ppm threshold mentioned earlier ²¹¹.

A7.2.2. Industrial grades

There are many industrial grades of ZnO in use. Differentiation between the grades is based on the purity, composition and specific surface area of the powder, and sometimes the process through which it is made. Although some grades are covered in national or international standards, many of the companies producing ZnO have their own nomenclature, and slightly different purity requirements are applied to the ZnO grades by different manufacturers. Therefore, the minimum content of ZnO and/or maximum heavy metal impurity levels are probably a more reliable guide to quality. Moreover, standards regarding ZnO, cover purity and surface area (m²/g) but not ZnO morphology, average particle size or particle size distribution. For reference, surface areas typically used for commercial grades of ZnO (ASTM

D4295-89 ⁴⁵⁹) have been transformed to equivalent particle sizes (non-porous spheres) (Eq. 189 in Appendix 9) and the results shown in Table 58.

Table 58. Typical properties of different grades of zinc oxide according to ASTM D4295-89 ⁴⁵⁹. The Equivalent particle size for non-porous spheres has been calculated using Eq. 189 in Appendix 9.

Fabrication Method		Surface area [m ² /g]	Equivalent Particle Diameter [nm]
American (direct) type		3.5	306
	Class 1	9	119
French (indirect) type	Class 2	5	214
	Class 3	3.5	306
	Chemical	40	27
Secondary types	Metallurgical - Class 1	5	214
	Metallurgical - Class 2	3.5	306

According to ISO Technical Specification 80004, the nanoscale is defined as a length range from approximately 1 nm to 100 nm, as properties that are not extrapolations from a larger size are predominantly exhibited in this length range. A nano-object is defined as a discrete piece of material with one (nanofiber), two (nanoplate) or three (nanoparticle) external dimensions in the nanoscale. Nanoparticles have all external dimensions in the nanoscale where the lengths of the longest and the shortest axes of the nano-object do not differ significantly (typically by more than 3 times). In other words, If the dimensions differ significantly, terms such as nanofiber or nanoplate may be preferred to the term nanoparticle. Nanoparticles can exhibit size-related properties significantly different from those of either fine particles or bulk materials ⁴⁶⁰. The EU adopted a definition of a nanomaterial in 2011 (Recommendation on the definition of a nanomaterial (2011/696/EU). According to this recommendation, a "nanomaterial" means a natural, incidental or manufactured material containing particles, in an unbound state or as an aggregate or as an agglomerate and where, for 50 % or more of the particles in the number size distribution, one or more external dimensions is in the size range 1 nm - 100 nm. According to these definitions, it can be seen from Table 58 that chemical methods are the ones which typically yield nanoparticles. The boundary of 100 nm that separates nanomaterials from micromaterials, assuming perfect non-porous spheres of ZnO, corresponds to a specific area of 10.7 m²/g (calculated using Eq. 189 in Appendix 9).

A7.2.3. Different production methods

A diversity of methods to produce ZnO nanoparticles can be found in the scientific literature, such as mechanochemical processes, precipitation processes, precipitation in the presence of

surfactants, sol-gel, solvothermal, hydrothermal and microwave techniques, emulsion, microemulsion, Chemical Vapour Deposition (CVD), plasma, laser-based and other methods⁴⁵³. Unfortunately, methods that work in the laboratory cannot always be applied on an industrial scale, where it is important for the process to be economically effective⁴⁵³. At an industrial scale, there are 3 main fabrication methods: two of them are thermal processes and the third one is wet chemistry processes.

One of the thermal processes is called the indirect process, or French process, in which zinc oxide is obtained by vaporizing metallic zinc at 1000-1400 °C with further oxidation with atmospheric oxygen^{211,453}. This is the main fabrication method at industrial scale. A simplified process scheme is shown in Figure 192.

The other thermal process is the direct process, or American process, which involves the reduction of zinc ore by heating with coal (such as anthracite), followed by the oxidation of zinc vapour in the same reactor, in a single production cycle⁴⁵³.

The third family of methods for ZnO production is the wet chemical processes. Typically, ZnO is produced by the precipitation of zinc carbonate, basic carbonate, or zinc hydroxide, which is purified, filtered and dried, followed by calcination of the precipitate.

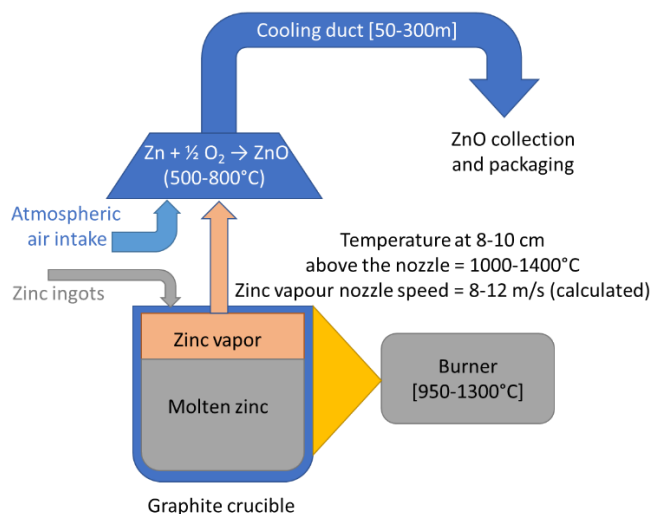


Figure 192. A basic process scheme for the French process furnace. Adapted from ref²¹¹.

According to the ISO 9298:2017 standard (Rubber compounding ingredients — Zinc oxide — Test methods), ZnO is classified either as type A, obtained by a direct process (the American process); type B, obtained by an indirect process (the French process) and type C, obtained by wet process method⁴⁶¹. Typical properties of different grades of ZnO are also defined in the standard ASTM D4295-89⁴⁵⁹.

A7.2.3.1 The American (Direct) Process

The American (Direct) Process involves the reduction of zinc ore by heating it with coal (such as anthracite), followed by the oxidation of zinc vapour in the same reactor, in a single production cycle. The resulting ZnO (of type A) contains impurities in the form of compounds of other metals from the zinc ore. In the ISO 9298:2017 standard, it is acknowledged that the purity of the ZnO obtained by the direct method, is less than the purity of the ZnO produced by the indirect method or wet processes, which can yield extremely high purity ZnO with low cadmium content, which is required in some countries where special regulations apply. Additionally, Standard D4295 – 89 Standard Classification for Rubber Compounding Materials—Zinc Oxide, also shows the same results ⁴⁵⁹. Moreover, Standard ASTM D79-86, which defines the properties expected for ZnO use as a pigment, specifies that ZnO produced from the French process has higher minimum purity (>99%) than material produced by the American process (>98.5%) ⁴⁶².

The specific surface area of direct process ZnO is generally 1 – 3 m²/g. The resulting ZnO particles are mainly needle-shaped, and sometimes spheroidal (nodular). The nodular-type particle shape is generally preferred for rubber compounding. To obtain a product with permanent white colour, the oxides of lead, iron and cadmium that are present are converted to sulfates. Increasing the permanence of the colour is linked to increasing the content of water-soluble substances, and also increasing the acidity of the product. Acidity is desirable in the case of rubber processing technology since it lengthens pre-vulcanization time and ensures the safe processing of the mixtures ^{211,453,461}.

In general, direct process ZnO is used in the paint and ceramic industries rather than for rubber ²¹¹. The direct method will not be further discussed, as it is not the main process to produce ZnO.

Table 59. Typical ZnO properties produced by the direct method according to industrial standards.

	ASTM D4295-89 ⁴⁵⁹	ISO 9298:2017 ⁴⁶¹
% Zinc oxide	99.0	98.5
% Lead	0.10	0.25
% Cadmium	0.05	0.02
% Sulfur	0.15	N.A.
% Heat loss at 105°C	0.25	N.A.
% Sieve residue, 45 µm	0.10	0.05
Surface area, m ² /g	3.5	3.5
% Volatile matter	N.A.	0.3
Acidity/alkalinity (g H ₂ SO ₄ /100 gr)	N.A.	0.07
% Copper	N.A.	0.005
% Manganese	N.A.	0.005
% Acid-insoluble matter	N.A.	0.1
% Water-soluble matter	N.A.	0.1

A7.2.3.2 The French (Indirect) Process

Most of the world's ZnO is manufactured via the indirect or French process, in which metallic zinc is melted in a graphite crucible and vaporized at high temperatures (above 907 °C). Zinc vapour reacts with atmospheric oxygen to give ZnO, accompanied by a drop in its temperature and bright luminescence (greenish-white flame). Zinc oxide particles are transported into a cooling duct and collected in a baghouse. This indirect method was popularized by LeClaire and Barruel (France) between 1840 and 1850 and therefore is commonly known as the French process. Its product normally consists of agglomerated ZnO particles with an average size of 0.1 to a few micrometres, with no morphological control. *i.e.* particles with different morphologies coexist^{453,463}.

In a typical French Process plant, a heated crucible containing zinc is covered with a lid to channel the zinc vapour through a central orifice. In the temperature range of 1230 – 1270 °C, zinc vapour has a pressure of 0.2 – 1.1 MPa. When the orifice cover (if used) is removed, zinc vapour streams into the atmosphere with a calculated nozzle speed of 8 – 12 m/s resulting in rapid oxidation in a length of ~30 cm and a temperature between 1000 – 1400 °C. There is a temperature drop from the combustion temperature to between 500 and 800 °C within ~5 s between the crucible and suction hood, which seems the main cause of non-uniform growth conditions²¹¹. The ZnO powder formed by this method enters a cooling duct of between 50 and 300 m long before it is collected in the bag-house at a temperature below 100 °C by a system of vertical fabric bags. After collection, the powder is fractionated according to particle size using vibrating hopper sieves. The French Process is widely considered to be the fastest and most productive industrial method to produce ZnO. However, as mentioned before, the particles produced by this are not optimum for all applications due to lack of controlled morphology and sizes²¹¹. For this reason, some modifications to the French process have been explored to provide controlled oxidation of zinc vapour and agglomeration of ZnO nucleates. For example, it has been proposed that the natural quenching of the vapour phase would result in the polydispersity of the synthesized ZnO nanoparticles which would uncontrollably grow to larger agglomerates with a typical size in the micrometre scale. Therefore, it has been recommended to control the oxidation of zinc vapour by controlling the supply of O₂ and N₂ into the synthesis system⁴⁶⁴.

The quality and purity of the ZnO obtained by this method will depend on the precursors used, *i.e.* high purity (>99%) can be obtained if high purity zinc is used as feedstock. However, the product may contain traces of zinc metal that may render it unsuitable for some applications or will require additional separation techniques. If low purity zinc sources are used, zinc

purification processes need to be applied first to eliminate Cd, Pb, Fe, and Al before the Zn is oxidized. The quality of some zinc sources is discussed in section A7.2.4.2.

Theoretically, the maximum yield of ZnO in the French process is 1.245 tons per ton of zinc used, but in practice, ZnO recovery of around 1.2 tons is obtained when using high purity zinc as the raw material. This yield drops when zinc with lesser purities are used, such as zinc dross (85 – 95% zinc content) or zinc ash (up to 30% metallic zinc with the balance composed of ZnO and zinc hydroxy-chloride). If zinc ash is used, the metallic content must first be separated from the ash by physical separation processes such as rotary mills and sieving before it can be used in the French process ²¹¹.

The ZnO particles obtained by the French process are generally nodular in shape, with the individual primary ZnO crystallites 30–2000 nm in size with surface areas ranging from 3 – 5 m²/g but can reach 12 m²/g by carefully controlling several parameters. For example, the combustion conditions such as airflow and flame turbulence or the distance between the suction hood and nozzle (which affects the air velocity). If the flame temperature increases, the specific surface area will drop. By increasing the excess of reactant air (oxygen) by making a better circulation of air or forced flow of compressed air in the combustion zone, ZnO quenching becomes faster and finer particles can be achieved, resulting in higher specific surface area ²¹¹. Tetrapodal ZnO nanoparticles have been obtained through the French Process by controlling the O₂/N₂ feed ratios ⁴⁶⁴.

There are various implementations of the French process. Older technologies principally use a batch process that takes place in a crucible with a long cooling duct, most of which is horizontal. Newer technologies use a semi-continuous process with a vertical cooling duct to save space. A basic process scheme of a batch French process furnace is depicted in Figure 192. A batch is recharged with zinc ingots at approximately 4 h intervals whereas in the semi-continuous process a zinc ingot (often 25 kg) is added to the furnace every 6 min. The productivity of the semi-continuous process is often higher than that of the batch process. The semi-continuous system is rarely shut down unless for an overhaul and it is generally very compact. There are several other variations to the process, the selection of which depends on the feedstock material and local conditions. More details can be found on a review article ²¹¹.

Table 60. Typical ZnO properties produced by the indirect method according to industrial standards.

Class	ASTM D4295-89 ⁴⁵⁹			ISO 9298:2017 ⁴⁶¹							
	1	2	3	B1a	B2a	B2b	B2c	B3b	B4a	B4b	B4c
% Zinc Oxide	99.5	99.5	99.5	99.5	99.5	99.5	99.5	99.00	99.00	99.00	99.00
% Lead	0.002	0.002	0.002	0.004	0.005	0.005	0.005	0.10	0.25	0.25	0.25
% Cadmium	0.005	0.005	0.005	0.001	0.005	0.005	0.005	0.05	0.05	0.05	0.05
% Sulfur	0.02	0.02	0.02	N.A.	N.A.	N.A.	N.A.	N.A.	N.A.	N.A.	N.A.
% Heat Loss at 105°C	0.30	0.30	0.30	N.A.	N.A.	N.A.	N.A.	N.A.	N.A.	N.A.	N.A.
% Sieve residue, 45 µm	0.05	0.05	0.05	0.01	0.05	0.05	0.05	0.05	0.05	0.05	0.05
Surface area, m ² /g	9.0	5.0	3.5	4.0	3.5	6.0	9.0	5.0	3.5	6.0	9.0
% Volatile matter	N.A.	N.A.	N.A.	0.25	0.25	0.25	0.25	0.25	0.3	0.3	0.3
Acidity/alkalinity (g H ₂ SO ₄ /100 gr)	N.A.	N.A.	N.A.	0.05	0.05	0.05	0.05	0.05	0.12	0.12	0.12
% Copper	N.A.	N.A.	N.A.	0.0005	0.0005	0.0005	0.0005	0.0005	0.001	0.001	0.001
% Manganese	N.A.	N.A.	N.A.	0.0005	0.0005	0.0005	0.0005	0.0005	0.001	0.001	0.001
% Acid-insoluble matter	N.A.	N.A.	N.A.	0.01	0.01	0.01	0.01	0.01	0.1	0.1	0.1
% Water-soluble matter	N.A.	N.A.	N.A.	0.01	0.2	0.2	0.2	0.2	0.2	0.2	0.2

A7.2.3.3 Wet-process zinc oxide

ZnO can also be manufactured by a wet chemistry process. Zinc is typically precipitated from zinc solutions (for example, as the carbonate or hydroxide) and then calcined at high temperatures to ZnO. Wet-process ZnO can yield very fine particle size and high purity, with surface areas from 5 m²/g to 40 m²/g. Zinc oxide can be coated with organic materials such as fatty acids (most commonly propionic acid) in order to improve dispersion in rubber. It can be supplied in the form of pellets manufactured with or without organic binders ⁴⁶¹.

It is known that particle properties relate to particle morphology, therefore, for novel applications, such as those relating to electronics and biomedical, particles with a high degree of morphological homogeneity are required. To overcome the poor degree of particle homogeneity by the direct or indirect process previously mentioned, a large array of approaches in ZnO fabrication with good control of particle morphology, size and spatial structure, have been developed, most based in solution ⁴⁵³.

Low-temperature synthesis of ZnO and Zn(OH)₂ nanoparticles is generally reported to use a Zn salt precursor, such as Zn(CH₃COO)₂, ZnCl₂, Zn(NO₃) and ZnSO₄. It has been proposed that the structural organization of ILs can be used as an “entropic driver” for the spontaneous formation of high-quality nanostructures ⁴⁶⁵. A wide spectrum of preparation routes using ILs had been developed, including precipitation, sol-gel technique, hydrothermal method, nanocasting, and microwave or ultrasound-mediated methods, which had been reviewed ^{196,466,467}. ILs had been used in the synthesis of ZnO nanomaterials from zinc-containing salts, such as Zn(CH₃COO)₂ ^{468–470}. In 2005 Zhou *et al.* ⁴⁷⁰ demonstrated, for the first time, that a protic

IL (oleic acid and ethylenediamine) mixed with $\text{Zn}(\text{CO}_2\text{CH}_3)_2$ at 286 °C for 1 h produced ZnO hexagonal micro-pyramids. Other studies had used IL containing zinc for ZnO formation⁴⁶⁸ or IL-ZnO nanocrystal⁴⁷¹. Another example employing an IL, by Liu *et al.*⁴⁷¹, reports the synthesis of IL-ZnO nanocrystal formed directly from an IL containing Zn^{2+} . Zhu *et al.*⁴⁶⁸ performed ionothermal synthesis of ZnO hierarchical structures of various morphologies using Zn-based ILs which serve as both solvents and precursors. Movahedi *et al.*⁴⁶⁹ formed a flower-like ZnO structure through a hydrothermal route using zinc acetate and a task-specific dicationic, dibasic ionic liquid. Li *et al.*¹⁹⁴ prepared ZnO spherical nanoparticles, with diameters of 15–20 nm, by one-step solid-state reaction at room temperature by mixing ground $\text{Zn}(\text{CH}_3\text{COO})_2 \cdot 2\text{H}_2\text{O}$, NaOH and the IL 1-butyl-3-methyl-imidazolium chloride [$\text{C}_1\text{C}_4\text{im}$]Cl for 50min at room temperature. The utilization of ILs as synthetic media for nanomaterials is discussed in detail by Kang *et al.*⁴⁶⁷.

A7.2.3.4 Other methods

The formation of ZnO using a metallic Zn substrate employs, in most cases, gas-phase approaches such as metal-organic chemical vapour deposition, chemical vapour transport and pulsed laser deposition. These techniques employ complex equipment, where stringent reaction conditions are essential and difficulties in control have been reported^{472,473}. Zinc oxide nanowires and nanoparticles using direct oxidation of micron-sized metal particles, in a high-throughput, atmospheric pressure microwave plasma jet reactor, have been reported by Kumar *et al.*⁴⁷⁴ Petzold *et al.*⁴⁷⁵ have also successfully used micron-scale zinc metal powder (1 – 45 μm) to synthesize ZnO nanowires (length: 1 – 30 μm , diameter: 5 – 50 nm) in a microwave plasma jet reactor at 900 °C. Other synthesis methods which do not require vaporization of metallic zinc had been reported. Vostrikov *et al.*⁴⁷⁶ synthesized ZnO nanostructures by oxidising solid and liquid zinc with sub- and supercritical water in a series of experiments ranging from 546 K to 921 K in a process called Chemical Supercondensation by Water (CSW). Dang *et al.*⁴⁷⁷ used direct oxidation of metallic Zn in O_2/Ar atmosphere by heating the Zn powder above its melting point, 550 °C for 30 min, and obtained white wool-like products. Yu *et al.*⁴⁷⁸ prepared ZnO nanostructures by directly heating metal-foil- or metal-film-coated substrates in air (375 °C for 12 h) using a hotplate.

Over the last decade, synthesis of ZnO nanomaterials from Zn foils, under moderate conditions, has been reported^{192,193,473,479}. In 2009, Cho *et al.*⁴⁷⁹ obtained ZnO nanorods (~250 nm long and ~18 nm in diameter) when Zn sheets were immersed in an aqueous ammonia solution containing Al_3^+ ion at 25 °C (and atmospheric pressure). In 2014, Ji⁴⁷³ reported a one-

step method for growing large scale ZnO NW with hexagonal wurtzite structure on Zn foils using a hydrothermal method. The Zn foils were exposed to aqueous ethylenediamine solutions (3.5 mol/L) at 140 °C for 10 h and observed ZnO crystals with wire-like structures randomly distributed on the surface of the zinc foil. The particles ranged from 300 nm to 1 µm in size, with an estimated layer thickness of 15 µm. Most recently, in 2017, Balela *et al.*¹⁹³ achieved the synthesis of ZnO nanostructures by oxidation of etched Zn foil in water at 90 °C. The morphology of these ZnO nanostructures evolved with the treatment time from nanorods to hexagonal nanotubes finally to flower-like structures.

A7.2.4. Metallic zinc feedstocks

The OIS process uses metals and alloys as feedstock for the production of micro or nano metallic oxide particles.

There are 2 zinc qualities used industrially for the production of ZnO. Namely Special High Grade Zinc (SHG), normally supplied as ingots for industrial processes, but other forms, granular zinc, wires or sheets, can be used. Low purity zinc sources, such as Secondary Zinc could be used as well for the production of ZnO micro/nano particles. As shown in section A5.8, even zinc-containing alloys, such as brass, could be used to generate ZnO nano-objects via OIS. Some applications require SHG zinc as source material, but about 93% of the ZnO market can be supplied using less expensive secondary zinc feed material²²⁸.

A7.2.4.1 Special High Grade (SHG) zinc

SHG zinc offers the highest purity but is the most expensive form of zinc. It does not require further treatment to remove impurities that would affect the purity of French Process ZnO. Some industries that typically require SHG zinc as source material for the production of ZnO include electronics, pharmaceutical and cosmetics. SHG zinc can be used with the OIS process.

A7.2.4.2 Secondary zinc

Secondary zinc is also known as hard zinc, scrap zinc, or zinc residues. Secondary zinc sources suitable for the French Process includes:

- **Top Dross:** One of the best sources of secondary zinc for the French Process due to its typically low lead and consistent iron levels. Top dross can be as high as 98% zinc and is usually uniformly shaped making handling and assay testing easier²²⁸.

- **Die Caster Dross:** Typically a good quality source of secondary dross generated from aluminium and zinc operations ²²⁸.
- **Bottom Dross:** Although it can be processed via de French Process, it tends to be a poor source of secondary zinc due to its varying quality. Bottom dross can contain solid iron and high lead levels. It is often supplied as irregular shapes and even scraps, making it more difficult to handle ²²⁸.
- **Zinc Blow-off Fines:** Very poor source of zinc for the French Process due to its potentially high contamination and its usually low metallic zinc content. Fines have a high surface area making them more prone to oxidation and high metal loss during melting ²²⁸.
- **Zinc Ash & Skimmings:** Not recommended for the French Process. Very low metallic zinc content. Already oxidized zinc will not yield metallic zinc in this process ²²⁸.

As mentioned before, ZnO can be produced even from brass, so it would be expected that secondary zinc can be used in the OIS. However, this awaits experimental validation, to establish the quality of the particles obtained.

Some considerations regarding secondary zinc sources for the French Process highlighted by a furnace manufacturer includes the following points ²²⁸:

- The total amount of metallic zinc should be determined to establish if the extra processing cost will not offset the reduced cost of these materials.
- The total zinc numbers may be misleading as they may include zinc ash. Zinc ash cannot be converted back into pure zinc by the French Process.
- For the French Process, high iron content materials are more expensive to process as they require more reagent and labour to purify. High lead content materials may be suitable feeds for the French Process. Typical production rates will be 90% of the SHG zinc production rate due to the additional downtime for lead removal and recovery. The effect of metallic contaminants in the OIS should be addressed experimentally.

A7.3. From laboratory to commercial scale

Most technologies are born in a laboratory set-up. Evaluating the techno-economic feasibility of a new process at large scale requires a great deal of time and resources. Even when implementing very well-established processes for new projects, companies generally start by

a high-level assessment called, conceptual study or basic engineering, to validate and justify further work. If the outcome of this preliminary work is favourable, then detailed engineering documents are produced to finetune the estimations, this phase is known as Front End Engineering Design (FEED). After FEED completion, the economic potential of a project can be assessed with a greater degree of accuracy and if favourable, then the project continues into a detailed engineering phase, called Engineering, Procurement and Construction (EPC).

A similar approach could be used to test new technologies developed in the lab. The first step to evaluate their potential could be to benchmark the new technology against other laboratory procedures. For the OIS process, this has been done and is shown in section A7.4.

If the technology offers clear benefits over existing ones, and from a high-level analysis it makes economic sense, then process modelling can be done to make a more realistic assessment. The new technology can be then compared to other industrial processes using alternative technologies. This has been done for the OIS process and is detailed and explained in section A7.5.

After the high-level assessment, if the technology shows clear benefits, it can be decided to do a more detailed analysis, for example, collect all experimental data required to validate, size and determine equipment cost with the help of vendors and suppliers. Doing this would provide a clear vision of the potential of the process and help decide if the technology should go to the pilot trial phase. This is essential to validate process parameters and obtained scaled-up data that will be required for detailed equipment sizing for commercial plants. This detailed evaluation was outside the scope of this study, due to time and resources.

If at any stage of this process it is shown that the technology is not performing better than other alternatives, it should be analysed to determine if it can be improved. If the answer is yes, then more work will be required to validate the technology, if the answer is no, the technology should be abandoned, and other solutions investigated. Figure 193 shows a schematic of the validation process to commercialize a technology developed in the lab.

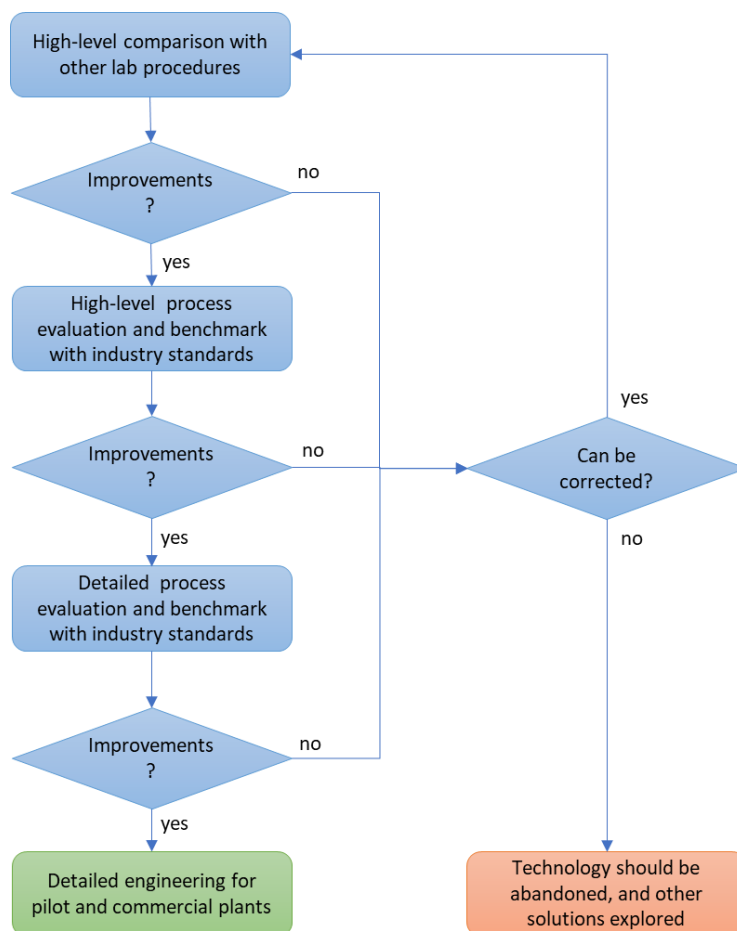


Figure 193. Schematic of the validation process of a new process from the lab to industrial applications.

A7.4. High-level laboratory assessment

The following section explores the cost to produce ZnO nanoparticles at lab scale using commercially available chemicals (Sigma-Aldrich) for different synthetic methods. Isolation cost, instrument costs, labour, and other direct and indirect cost are not taken into consideration at this stage. Additionally, the energy consumption and waste generated for each method are analysed and discussed. The safety and hazards of zinc precursors are reviewed.

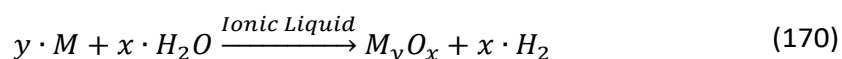
A7.4.1. Oxidative Ionothermal Synthesis (OIS)

This process consists of the oxidation of metals with an oxidant (typically water) in ILs to yield metal oxides and hydrogen, according to Eq. 170. Other metal-based compounds, such as hydroxides, could also be synthesised with this method. It is suspected that in the oxidation process to form a metal oxide or hydroxide species, the IL is not consumed and therefore can be recovered and reused. A strong indicator of this is the lack of chloride-containing species

when ZnO is formed by exposure of metallic zinc to aqueous [C₄C₁im]Cl solutions with water content below 75 mol%. However, the quality of the IL (degradation and accumulation of impurities) and the particles (purity and morphology) obtained upon recycling of the solvent should be verified experimentally.

As shown in Chapter 3, the particles obtained with this method can have homogeneous morphologies depending on the process conditions used. In this process, water is used as an oxidant for the metal and to modify the structure of the solvent as discussed in Chapter 2 (section 2.2.5), which is believed to provide a template for particle growth with controlled morphology. The lack of agglomeration observed in ZnO formation at low water contents, compared to the high water content and water control cases, might originate from the higher viscosity of the IL compared to water, which will limit diffusion rate of the metal cations (Chapter 3 – section 3.5.4.6). It has been suggested that the imidazolium cation (of ILs) are instrumental in the preferential growth of ZnO 1D nanostructures. One proposed mechanism is where the cation adsorbs onto the surface of the growing particle by electrostatic forces and/or hydrogen bonds (between the hydrogen atom attached to the carbon at position 2 in the imidazolium ring and the oxygen atoms of the ZnO crystal [C(2)-H···O-Zn]); this then results in the preferential growth⁴⁸⁰.

The proposed overall equation for the OIS process is given below:



Where M is a metal (*e.g.* Al, Fe, Cu, Zn, Ti and Ni) or an alloy, such as steels or brass. They can be ingots, sheets, scrap pieces, powders, granular, wires or other forms.

Some process parameters that can be used to tune particle chemistry, size and morphology include water concentration, temperature, exposure time, as shown in Chapter 3. Other parameters that could be used for this purpose are the use of catalysts, pH control, electric currents, surfactants, microwave or ultrasounds, other oxidants such as O₂, O₃, H₂O₂, blends of ILs or other molecular solvents. However, these other techniques await experimental validation.

The ILs can be protic or aprotic, such as [C₄C₁]Cl, [HC₁im]Cl, [N₄₂₂₀][HSO₄] and [C₄C₁im][NTf₂].

A7.4.2. ZnO nanoparticles synthesis methods

As mentioned, there are many different approaches to produce ZnO nanoparticles. Herein, a more limited focus will address 3 technologies on a high-level basis: I) The OIS process, II) the

French Process, which is the industrial standard for ZnO production at large scale, and III) other wet chemistry methods, which commonly found in the scientific literature

Table 61 summarizes the chemical reactions of the different wet chemistry methods and Table 62 provides the details on the synthetic routes evaluated in this section.

Table 61. Summary of chemical reactions from different ZnO nanoparticle synthesis methods

M	Name	Reaction	Ref
1	OIS - Metallic Zinc	$Zn + H_2O \rightarrow ZnO + H_2$	
2	Hydrothermal - Zn Sulfate	$ZnSO_4 \cdot 7H_2O + 2 NaOH \rightarrow Zn(OH)_2 + Na_2SO_4 + 7H_2O$ $Zn(OH)_2 \rightarrow ZnO(s) + H_2O$	481
3	Hydrothermal - Zn Acetate	$Zn(CH_3CO_2)_2 \cdot 2H_2O + 2 NaOH \rightarrow Zn(OH)_2 + 2CH_3COONa + 2H_2O$ $Zn(OH)_2 \rightarrow ZnO(s) + H_2O$	482
4	Hydrothermal - Zn Nitrate	$Zn(NO_3)_2 \cdot 6H_2O + 2 NaOH \rightarrow Zn(OH)_2 + 2NaNO_3 + 6H_2O$ $Zn(OH)_2 \rightarrow ZnO + H_2O$	483
5	IL - ZnCl ₂	$ZnCl_2 + 2 NaOH \rightarrow Zn(OH)_2 + 2NaCl$ $Zn(OH)_2 \rightarrow ZnO + H_2O$	484
6	IL - Zn Acetate	Similar to method 3	194
7	IL - Zn Acetate - Microwave	Similar to method 3	485
8	Sol-Gel - Zn Acetate	Similar to method 3	486

Table 62. Detailed experimental methods as reported in literature ^{194,481-486}.

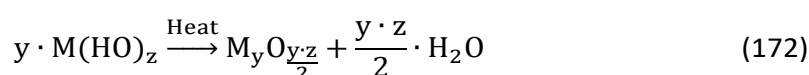
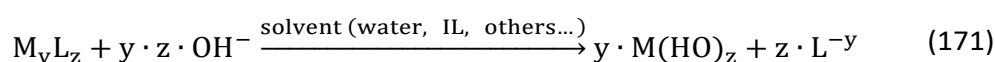
M	Description	Remarks
1	Oxidative Ionothermal Synthesis (refer to Chapter 3 Section 3.5.4)	
2	Sodium hydroxide solution (100 mM) was added dropwise to a 50 mM zinc sulfate solution and the reaction was carried out under vigorous stirring for 12 h at room temperature. The obtained precipitate was washed several times with Milli-Q grade water by centrifugation at 3000 rpm for 5 min. Finally, the precipitate was dried in an oven at 100 °C for 6 h ⁴⁸¹ .	The ZnO nanocrystals have an average diameter $\langle d \rangle = 24$ nm with a standard deviation $\sigma = 8$ nm
3	NaOH 0.25 M was added dropwise to 0.05 M zinc acetate maintained in a conical flask under vigorous mechanical agitation at room temperature; the cloudy viscous sediment thus obtained was filtered using vacuum filtration, dried overnight at 50 °C, and calcined at 200 °C for 2 h in a muffle furnace to obtain white fine powdered ZnO ⁴⁸² .	18.67 ± 2.2 nm

M	Description	Remarks
4	<p>The ZnO nanoparticles were prepared by the precipitation method using zinc nitrate and sodium hydroxide as precursors and soluble starch as a stabilizing agent. 0.3 g of starch was dissolved in 100 ml of distilled water at 27 °C. 10 ml of 0.1 M zinc nitrate was added to the starch solution. The obtained solution was stirred constantly using the magnetic stirrer for 2 h until the complete dissolution occurs. Subsequently, 10 ml of 0.2 M sodium hydroxide solution was added dropwise to the above solution from the sidewalls. The reaction was allowed to proceed for 2 h after the complete addition of sodium hydroxide solution. After the completion of the reaction, the solution was allowed to settle down for 24 h. The supernatant solution was discarded carefully and the remaining solution was centrifuged. In order to remove the by-products and excessive starch bound to the nanoparticles, the precipitate was washed with ethanol repeatedly. The powder of the ZnO nanoparticles was obtained after drying at 100 °C for 2 h ⁴⁸³.</p>	
5	<p>The synthesis was carried out in a Schlenk flask without an argon atmosphere. Initially, the ionic adducts were prepared from the reaction of RC₁im·Cl (R = butyl, decyl) and ZnCl₂ to form the RC₁im·ZnCl₃ compounds. In a typical reaction, 5 mmol of BC₁im·Cl and 5 mmol of ZnCl₂ were introduced into the Schlenk flask. The reaction was placed at 80 °C for 1 h. Then, 1 mL of aqueous NaOH 10 M was added dropwise with a syringe, observing immediately the formation of a white dispersion. The reaction was left under stirring at 80 °C for different times (5 and 20 h). At the end of the reaction, the Schlenk flask was cooled and the ZnO washed with acetonitrile, water, and acetone, twice for each solvent. After each washing, the ZnO was decanted by centrifugation at 3500 rpm during 10 min and the supernatant was removed. The isolated product was dried under vacuum for 3 h at 25 °C to yield a white powder. These hybrid ZnO materials were stable and all the manipulations for the characterization and photocatalytic processes were made under air without degradation/decomposition of the compounds ⁴⁸⁴.</p>	
6	<p>Starting materials are zinc acetate (Zn(CH₃COO)₂·2H₂O), sodium hydroxide (NaOH) and 1-butyl-3-methylimidazolium chloride ([C₄C₁im]Cl). Among them, Zn(CH₃COO)₂·2H₂O and NaOH were analytically pure and [C₄C₁im]Cl was prepared according to the literature. In a typical synthesis, 0.439 g of Zn(CH₃COO)₂·2H₂O (2 mmol) was ground for 5 min in agate mortar, followed by the addition of 0.35 g [C₄C₁im]Cl (2 mmol) and 0.24 g NaOH (6 mmol) flake. The mixture was ground for 50 min to obtain a white batter. It was then washed with distilled water and alcohol several times, and dried in vacuum at 60 °C for 6 h, yield: 78–83% ¹⁹⁴.</p>	<p>It indicates that the nanoparticles have spherical morphology with diameters 15–20 nm</p>
7	<p>IL [C₄C₁im]Cl was synthesized by the reaction of 1-butylchloride and N-methylimidazole. For synthesizing ZnO, 2.2 g of zinc acetate dihydrate was dissolved in 1.9 g [C₄C₁im]Cl using microwave heating. Then 1.2 g of sodium hydroxide was added to the solution, the mixture was manually homogenized and further irradiated with micro-wave radiation for 1 min under power radiations of 400 using a microwave oven (DAEWOO model KOC-1B3KP, Korea). Afterwards the mixture was washed with distilled water and centrifuged (Hettich Rotina, Germany) at 4000 rpm for 5 min for several times in order to remove IL and unreacted precursors. Finally, the product was dried at 100 °C for 2 h in a vacuum oven model WiseVen WOV (Wisd laboratory equipment, Germany) and the product was then calcined at 500 °C for 3 h in a furnace (Nabertherm B 180, Germany). The control sample was synthesized at the same conditions without using any IL ⁴⁸⁵.</p>	<p>grain size in the range of 15–25 nm</p>

M	Description	Remarks
8	ZnO powder was prepared by sol-gel method from zinc acetate dihydrate, oxalic acid (H ₂ C ₂ O ₄) using ethanol as solvent. ZnO gel was obtained by dissolving 50.1 mmole of zinc acetate (CH ₃ COO) ₂ Zn•2H ₂ O in 300 ml ethanol (CH ₃ CH ₂ OH) and refluxing at 60 °C under vigorous stirring for 30 min. 140 mmole of oxalic acid was mixed with 200 ml of ethanol and added to the previous solution slowly. The final mixture was refluxed at 50 °C for 60 min before left to cool down to room temperature. Finally, the ZnO gel was dried at 80 °C for 20 h (Xerogel), and the powder calcined under flowing air (0.1 mmol/s) for 4 h at 650 °C ⁴⁸⁶ .	

A7.4.2.1 Chemical precipitation

Chemical precipitation is the most popular method for ZnO nanoparticle preparation, which usually involves two reagents: a highly purified zinc source, such as zinc acetate (Zn(CH₃COO)₂•2H₂O), zinc nitrate (Zn(NO₃)₂), or zinc sulfate (ZnSO₄) and a solution of precipitator such as sodium hydroxide (NaOH) or ammonium hydroxide (NH₄OH). Typically, the precipitator is added dropwise to the dissolved zinc precursor under agitation until the pH level reaches about 10 to form a white intermediate of zinc hydroxide (Zn(OH)₂) (Eq. 171). Ultimately, samples of zinc hydroxide are converted to ZnO through calcination at high temperatures (Eq. 172). Control parameters for this method mainly include the concentration of zinc source and precipitator, the molar ratio of the two reagents, and the reaction and calcination temperature. Some examples of these synthesis routes are the methods 2 - 7 shown in Table 61 and Table 62.



Were M is a metal, L is an anion such as (halogen, acetate, sulfate, etc and OH⁻ is the hydroxide ion.

Table 63. Pros and cons of common hydrothermal methods for ZnO production compared to the OIS process.

Pros	Cons
<ul style="list-style-type: none"> Fast reactions 	<ul style="list-style-type: none"> Zn precursors (salts) are more expensive than metallic zinc (section A7.4.3). Waste salts containing the anion of the Zn precursors and the cation of the precipitator are generated, potentially increasing waste management cost and the environmental footprint.

- Calcination step required at high temperatures to convert Zn(OH)₂ into ZnO increasing the environmental impact.

A7.4.2.2 Sol-gel method

This chemical procedure involves a series of steps. First step in a typical sol-gel synthesis for ZnO is the formation of a "sol" (a colloidal solution) by dissolving the metal precursors (zinc salts) in ethanol. Then a gel-like diphasic system containing both a liquid phase and solid phase is formed by the addition of additives, such as oxalic acid. The gel is finally formed by removal of solvent (drying). Afterwards, a thermal treatment, or calcination at 500 – 600 °C, is often necessary to destroy the gel and produce the ZnO nanoparticles⁴⁵³. The sol-gel method is the subject of much interest as it can be used to obtain both nanoparticles and films with an excellent morphological control⁴⁵³. An example of a sol-gel synthesis is the method 8 shown in Table 61 and Table 62.

Table 64. Pros and cons of common Sol-Gel methods for ZnO production compared to the OIS process.

Pros	Cons
<ul style="list-style-type: none"> • Fast reactions • Excellent morphological control which allows the formation of powders and films. 	<ul style="list-style-type: none"> • Zn precursors (salts) are more expensive than metallic zinc (section A7.4.3). • Use of chemicals for the gel formation, which are eventually calcined. This increases the cost and produces CO₂ emissions from the combustion of the organic additives to form the gel. • Waste salts containing the anion of the Zn precursors and the cation of the precipitator are generated, potentially increasing waste management cost and the environmental footprint. • Calcination step required at high temperatures to convert Zn(OH)₂ into ZnO increasing the environmental impact.

A7.4.3. Production cost – raw materials

The cost of producing ZnO nanoparticles at lab scale, for each of the methods presented in Table 61 and Table 62, was evaluated based on the cost of raw materials. All chemical prices were taken from Sigma-Aldrich website (www.sigmaaldrich.com), accessed the 29th of November 2019. Minimum purity has been fixed to 98%. When the price for substances with

higher purities were within the order of magnitude of the lower purities, they were selected for the estimation. The price of bulk chemicals taken the same day from different suppliers on Alibaba's website (www.alibaba.com) are roughly 2 orders of magnitude less than the price of small quantities used for research.

Table 65. Metal content normalized cost for metal precursors used in the synthesis of ZnO nanoparticles.

Chemical	Small Quantities (A)	Bulk Quantities (B)	
	[£/g Zn]	[£/g Zn]	RSD (C)
Zinc	0.0685 (D)	0.0017 (E)	±41%
Zinc sulfate heptahydrate	0.2007	0.0028	±75%
Zinc chloride	0.2297	0.0016	±15%
Zinc nitrate hexahydrate	0.3272	0.0032	±26%
Zinc acetate dihydrate	0.6212	0.0047	±23%

A. Small quantities refer to the price for research purposes from Sigma-Aldrich website (www.sigmaaldrich.com, accessed the 29th of November 2019). Details provided in Table 66.

B. Bulk quantities were obtained as the average price from different bulk suppliers found online (www.alibaba.com, accessed the 29th of November 2019). The average value and the relative standard deviation are reported.

C. Relative Standard Deviation (RSD).

D. Granular. Cost is the average of 4 products (Table 66). RSD = 13%.

E. Ingots.

Table 66. Chemicals used in the synthesis of ZnO nanoparticles at lab scale from Sigma-Aldrich website (www.sigmaaldrich.com, accessed the 29th of November 2019).

Chemical (Product Code)	Molecular Formula	Purity [%]	Cost [£]	MW [g/mol]	Metal Content Normalized Cost	
					[£/mol Zn]	[£/g Zn]
Zinc acetate dihydrate (96459-250G)	Zn(CH ₃ COO) ₂ · 2H ₂ O	99.00	45.8	219.51	40.6204	0.6212
Zinc sulfate heptahydrate (31665-1KG)	ZnSO ₄ · 7H ₂ O	99.50	45.4	287.56	13.1208	0.2007
Zinc (31653-1KG)	Zn	99.90	80.3	65.39	5.2561	0.0804
Zinc - granular, 30-100 mesh, 99% (565148-1KG)	Zn	99	61.5	65.39	4.0621	0.0621
Zinc - granular, 20-30 mesh, ACS reagent, ≥99.8% (243469-2KG)	Zn	99.80	123	65.39	4.0295	0.0616
Zinc - pieces, 2-14 mesh, 99.9% trace metals basis (266353-500G)	Zn	99.90	35	65.39	4.5819	0.0701
ZnCl ₂ - anhydrous, free-flowing, Redi-Dri™, reagent grade, ≥98% (793523-1KG)	ZnCl ₂	98	108	136.3	15.0208	0.2297
Zinc nitrate hexahydrate (purum p.a., crystallized, ≥99.0% (KT)) (996482-500G)	Zn(NO ₃) ₂ · 6H ₂ O	99	35.6	297.49	21.3952	0.3272
Sodium Hydroxide - reagent grade, ≥98%, pellets (anhydrous) (S5881-5KG)	NaOH	98	172	40	-	-
1-Butyl-3-methylimidazolium chloride (≥98.0% (HPLC)) (94128-250G)	C ₈ H ₁₅ ClN ₂	98	234	174.67	-	-
Oxalic acid (puriss. p.a., anhydrous, ≥99.0% (RT)) (75688-250G)	HO ₂ CCO ₂ H	≥99.0	31.3	90.03	-	-

Chemical (Product Code)	Molecular Formula	Purity [%]	Cost [£]	MW [g/mol]	Metal Content Normalized Cost [£/mol Zn] [£/g Zn]	
Starch (puriss. p.a., from potato, reag. ISO, reag. Ph. Eur., soluble) (33615-1KG)	(C ₆ H ₁₀ O ₅) _n	≥99.3	192	n.a.	-	-
Etanol (denatured with about 1% methyl ethyl ketone for analysis EMSURE®) (1.00974)	C ₂ H ₆ O	99	2870	46.07	-	-
Sulfuric Acid (30743-2.5L-M)	H ₂ SO ₄	95-97	65.3	98.08	-	-

Zinc is a commodity and its price fluctuates in the markets. According to the London Metal Exchange website, the zinc price per ton was 2340.00 US\$ (1£ = 1.3031 US\$) on the 22nd of December 2019. (1795.72 £/ton).

To estimate the chemical cost for each of the methods shown in Table 62, the stoichiometric relationships for each synthetic route (Table 61) and the prices shown in Table 66 were used. The purity of the chemicals was considered for costing. For this high-level assessment, the chemical cost was normalized per gram or mol of ZnO produced, assuming 100% yields for all the methods, as the yields are not systematically reported. Water cost was not included. The results are shown in Figure 194 and examples of the calculations are provided in Appendix 8.

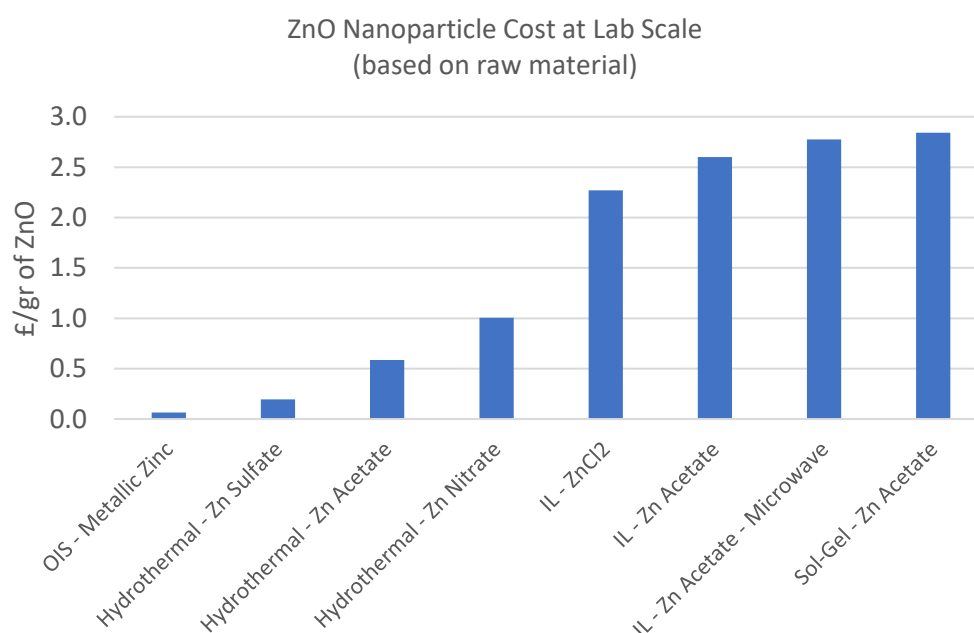


Figure 194. ZnO nanoparticle cost based on raw materials. OIS cost includes 1% IL loss (1:1 solid loading, with 25 wt% water).

Based on the price of raw materials, method using metallic zinc to produce ZnO, such as OIS process and the French Process, would be the most cost-effective ones. Compared to other hydrothermal and Ionothermal methods, the OIS appears to be the most cost-effective way

of producing ZnO, even assuming 1% IL losses. The sol-gel method evaluated was even more expensive per gram of nanomaterial than other IL-based methods. Other variations of the hydrothermal methods, for example those using emulsions, should have a higher production cost than simple hydrothermal methods not using surfactants. Thermal energy consumption and CO₂ emissions

For the initial assessment of the thermal energy consumption, only the energy input required to reach and maintain the reaction temperature (if applicable) and/or calcination were considered. The electric power needed for the magnetic stirring required in some methods was not considered for this assessment as details of the equipment used for this purpose is not provided in the references. Additionally, the electric power consumption should be less than the thermal energy as it will be shown in section A7.5.4.2.

To determine the energy requirements for both the reaction and calcination processes, two thermal events were considered: 1) heating from room temperature (25 °C) to reaction (or calcination) temperature, calculated by integration of the C_p of the components present in the mixture. and 2) heat losses from the oven to the environment by keeping the reaction (or calcination) temperature for a given amount of time. The heat losses for wet chemistry processes have been calculated assuming the same thermal loss from a laboratory convection oven, which were experimentally determined. Briefly, the oven was heated to a given temperature, and when the temperature was stable for 10 minutes, the power was shutoff. With the help of thermocouples, the temperature inside the oven was measured over time. From the internal volume of the oven, and the C_p and density of air, the energy loss equivalent to cooling down the mass of air within the oven over time gave the energy losses to the environment. Details on this procedure are given in Appendix 8 – section A8.1.1. This approach to estimate the heat losses is based on one convection oven, as such, it is expected that the thermal losses will be different for different heating devices. Even though the numerical values for the heat losses would be different for different experimental setups, the trends should be similar. For the thermal methods, the heat losses values were taken from literature²²⁸. The experimental procedures, values and formulae to calculate the energy and equivalent CO₂ emissions are detailed in Appendix 8 – section A8.1.

The results for the thermal energy consumption for different ZnO production methods are depicted in Figure 195. For the OIS process, it has been assumed a reaction temperature of 75 °C for 7 days. Under these assumptions, the OIS consumes more energy than other hydrothermal methods, mainly because of the way thermal losses are calculated. However, in an industrial installation these losses can be minimized by adding thermal insulators to the

reactors. Moreover, the OIS process allows the recovery of thermal energy through combustion of H₂. A more detailed assessment is performed in section A7.5.4.2.

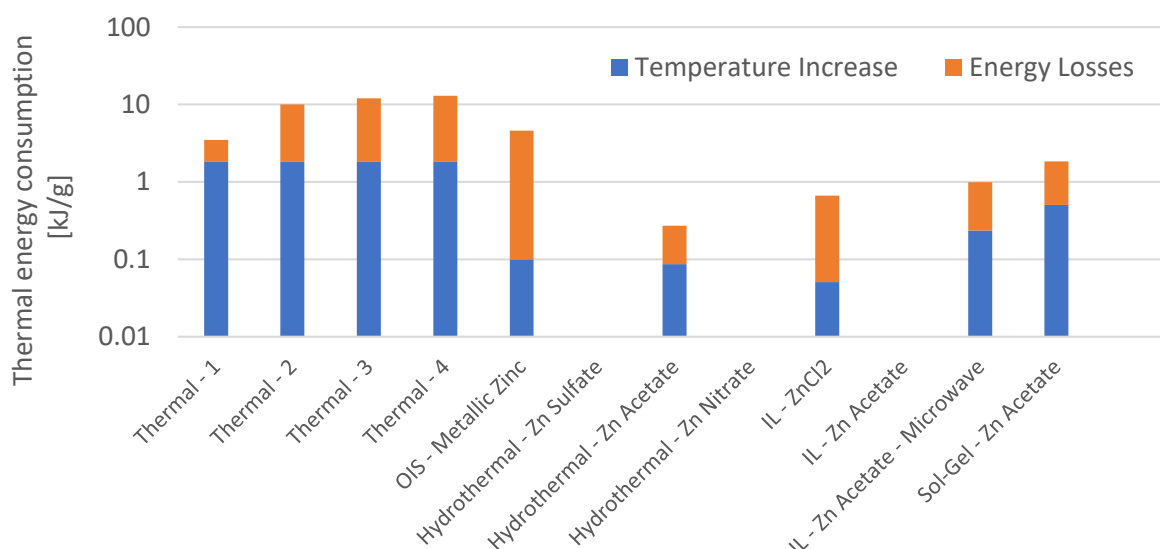


Figure 195. Energy consumption for different methods. Temperature increase corresponds to the energy required to heat the reaction medium to the required temperature. Temperature losses correspond to the energy to maintain the temperature for the length of the reaction. For thermal methods, it corresponds to the overall efficiency of the process. Thermal methods efficiency was taken from a furnace manufacturer ²²⁸, from Thermal 1 to 4: BURNS 3-crucible vaporizer, typical single crucible (200L) vaporizer, typical muffle type vaporizer, typical multi-crucible (200L) vaporizer.

The energy cost for the thermal requirements of the different methods has been calculated assuming the energy is supplied by natural gas. The energy cost and CO₂ equivalent emissions for each method are depicted in Figure 196. Calculation details are given in the Appendix 8.

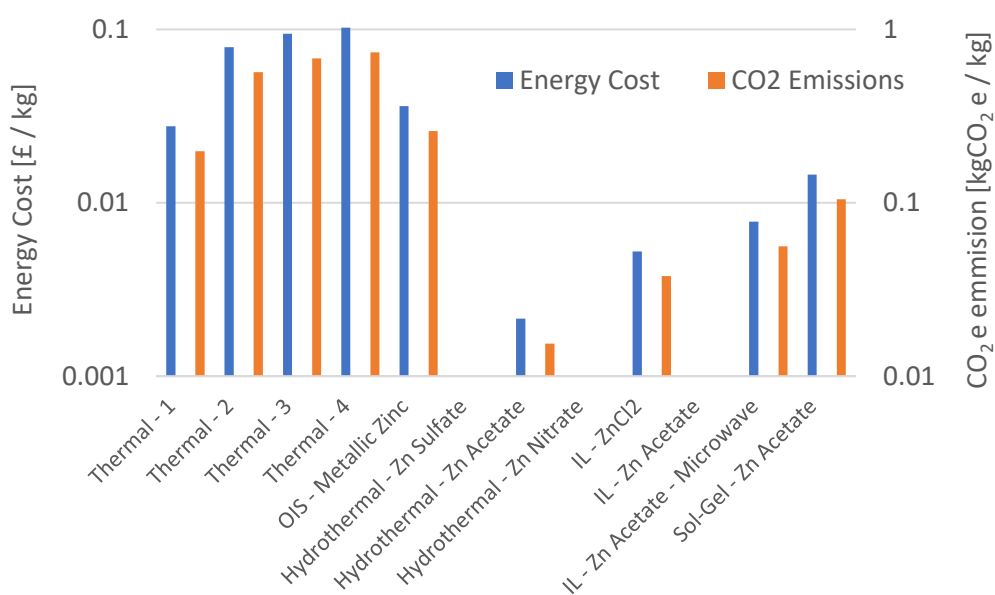


Figure 196. Energy cost for different synthesis methods of ZnO nanoparticles. Thermal methods from Thermal 1 to 4: BURNS 3-crucible vaporizer, typical single crucible (200L) vaporizer, typical muffle type vaporizer, typical multi-crucible (200L) vaporizer ²²⁸. Calculation details are given in the Appendix 8.

From Figure 195 and Figure 196 it can be seen that the thermal methods are up to 2 orders of magnitude higher than hydrothermal methods, mainly for the energy needed to melt and vaporize the Zn. The energy consumption of OIS will depend on the exact conditions at which the reaction needs to be run to achieve a desired particle size and shape. The energy requirements for OIS seem equivalent to other hydrothermal methods considering only the temperature rise of the reaction medium, and lower than thermal methods. The high thermal loss of the OIS process arises from the assumption that the reaction needs to be carried out for 7 days. However, even if this is the case, thermal energy losses could be minimized by insulating the reactors. Additionally, thermal energy can be produced from the hydrogen generated in the reaction. A sensitivity analysis regarding this point is given section A7.5.4.2.

A7.4.4. Environmental assessment

To assess the nature of the waste generated for each of the synthesis routes, the amount of water required to dilute the salts to a concentration suitable for discharge to the environment was calculated. There are different standards to regulate the water quality that can be rejected to the environment, depending on the region, the nature of the receiving water body, type of industry, etc. Additionally, not all chemicals are covered in all the standards. Therefore, Table 67 summarizes the limits for each chemical covered in different standards. It is noteworthy to mention that this method is a high-level approach to assess the environmental impact of the generated waste. A detailed life cycle assessment needs to be performed.

Most wet chemistry methods use a basic pH for the precipitate the $\text{Zn}(\text{OH})_2$ which is calcined to ZnO. There are multiple ways to neutralize any excess of sodium hydroxide to reduce the pH to below 9.0 for safe discharge. Neutralization by dilution will require a great amount of water, therefore chemical neutralization will be considered for the assessment. Commonly used chemicals for NaOH neutralization are carbon dioxide gas to make carbonic acid or sulfuric acid. To comply with the pH requirements, the addition of sulfuric acid will be considered. As sodium acetate is not a regulated substance, it is going to be dealt with as a contributor to the Biological Oxygen Demand (BOD) (Table 68). As no data for the BOD for sodium acetate was available, the Chemical Oxygen Demand (COD) will be used for the assessment.

Table 67. Water quality standards.

Compound	AA-EQS (µg/litre) ^A	Guidelines for Drinking-water Quality World Health Organization ⁴⁸⁷ (mg/litre)	FAO Recommended maximum concentration ^{B 488} (mg/litre)	Jordanian Standard (JS: 893/2002) ⁴⁸⁸ (mg/litre)	Reclaimed water standards for unrestricted irrigation in Saudi Arabia ⁴⁸⁸ (mg/litre)	Selected Value (mg/litre)
Chloride	250 000	250 ^C	106.5 ^F	350	100	100
Nitrate	-	50	9.5 ^F	30 – 45	10	10
Sulfate	400 000	250 ^D	-	300	600	250
Acetate	-	-	-	-	-	-
Zinc	10.9 (bioavailable) ^B	4 ^E	2.0	5	2	2
pH	-	-	Normal range 6.5 – 8.4	6.0 – 9.0	6.0 – 8.5	6.0 – 9.0
BOD	-	-	240 ^G	15 – 60	10	10

A. Hazardous pollutants listed in Fresh_waters_specific_pollutants_and_operational_EQS.CSV <https://www.gov.uk/guidance/surface-water-pollution-risk-assessment-for-your-environmental-permit>

B. Dissolved plus ambient background concentration.

C. No health-based guideline value is proposed for chloride in drinking-water. However, chloride concentrations more than about 250 mg/litre can give rise to detectable taste in water (see chapter 10).

D. No health-based guideline is proposed for sulfate. However, because of the gastrointestinal effects resulting from ingestion of drinking-water containing high sulfate levels, it is recommended that health authorities be notified of sources of drinking water that contain sulfate concentrations more than 500 mg/litre.

F. Not of health concern at concentrations normally observed in drinking water, but may affect the acceptability of water

G. The permitted limit for greywater reuse according to the use type.

Table 68. Biodegradability parameters of some organic substances (G-Biosciences, Safety Data Sheet, Cat. # R010, Sodium acetate, pH 5.2 [3M]).

	Acetic acid	Sodium acetate
CAS	64-19-7	127-09-3
Persistence and degradability	Readily biodegradable in the soil. Readily biodegradable in water.	Readily biodegradable in water.
Biochemical oxygen demand (BOD) [g O ₂ /g substance]	0.6 – 0.74	No data available
Chemical oxygen demand (COD) [g O ₂ /g substance]	1.03	0.675
ThOD [g O ₂ /g substance]	1.07	No data available

Regarding the environmental footprint of the IL [C₄C₁im]Cl, it has been reported that this substance is poorly biodegradable, in either the presence or the absence of an extra carbon source (*i.e.* glucose), however, it has low toxicity ⁴⁸⁹. In another study, the potential toxicity of the IL in the liver cells of zebrafish (*Danio rerio*) was reported. The 50% lethal concentration (LC₅₀) values after a 96-h exposure the IL was 632.8 ± 67.4 ppm, which indicated that this substance is practically harmless ⁴⁹⁰. To estimate the water needed for the OIS, 1% IL losses

have been considered (1:1 solid loading, with 25 wt% water) with a dilution factor have of the lower interval measured for the (LC₅₀) values after a 96-h exposure, *i.e.* 282.7 mg/L.

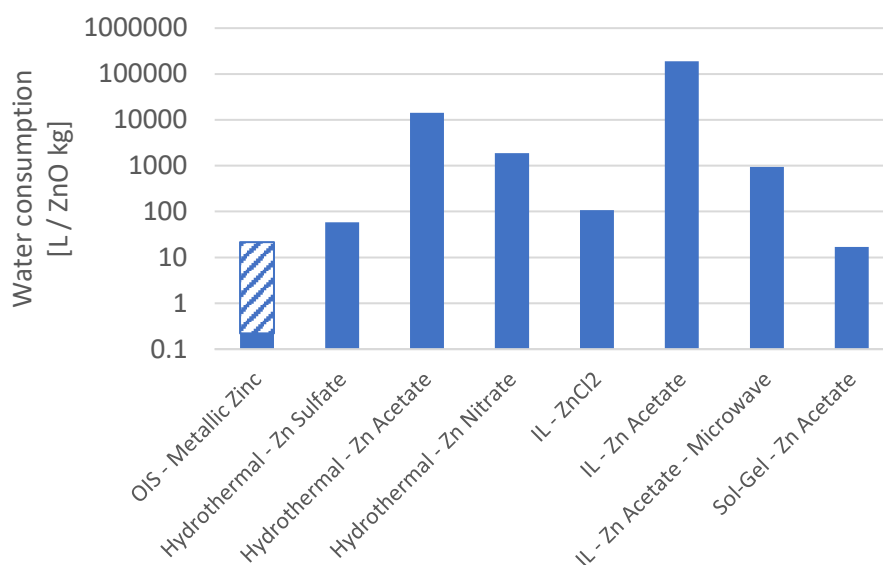










Figure 197. Water consumption to dilute by-products in order to meet maximum discharge limit as per Table 67. For method 1 (OIS – Metallic Zinc), the solid bar represents the water consumed in the oxidation process of the metal and the stripped section represents the water needed to dilute 1% IL losses down to 283 mg/L.

It can be seen from Figure 197 that the lowest water consumption is for the OIS process. If water is used to dilute the IL losses, the water consumption is slightly higher than the Sol-Gel method (method 8) but still orders of magnitude lower than other methods. Other hydrothermal methods require high amounts of water to dilute the anions of the precursors to acceptable levels and salts generated after pH neutralization. This suggests that the OIS process shows promise as a more environmentally friendly option when compared to other hydrothermal methods, due to a reduction to the aqueous waste stream generated. However, this needs to be further validated with a more detailed environmental assessment.

A7.4.4.1 Safety aspects of zinc precursors

The safety aspects of the raw materials were consulted from the supplier Material Safety Data Sheet MSDS (Sigma-Aldrich) and the information summarised in Table 69. From the information provided in the MSDS, it appears that metallic zinc is the safer precursor for ZnO nanoparticles among the substances considered.

Table 69. Safety aspects of materials used in ZnO nanoparticle synthesis. Obtained from the MSDS from the supplier website.

Compound	Symbol	Hazard statements	Precautionary statements	Personal Protective Equipment
Zn	 GHS09	H410	P273-P501	Eyeshields, Gloves
ZnCl ₂	  	H302- H314-H410	P260-P280- P301 + P312 + P330-P303 + P361 + P353- P304 + P340 + P310-P305 + P351 + P338	Eyeshields, Faceshields, full-face particle respirator type N100 (US), Gloves, respirator cartridge type N100 (US), type P1 (EN143) respirator filter, type P3 (EN 143) respirator cartridges
Zn(CH ₃ COO) ₂ · 2H ₂ O		H302- H318-H411	P280-P301 + P312 + P330- P305 + P351 + P338 + P310	dust mask type N95 (US), Eyeshields, Gloves
ZnSO ₄ · 7H ₂ O	GHS05, GHS07, GHS09	H302- H318-H410	P273-P280- P305 + P351 + P338-P501	None indicated
Zn(NO ₃) ₂ · 6H ₂ O	   GHS03, GHS07, GHS09	H272- H302- H315- H319- H335-H410	P210-P220- P261-P273- P370 + P378- P391	None indicated

A7.4.4.2 Overall considerations

This high-level assessment of the cost and environmental impact of different methods suggest that the OIS process is an interesting alternative for the production of ZnO. It uses metallic zinc as metal precursors, which appears to be the cheapest (Table 66) and safer (Table 69) raw material for ZnO production. Additionally, the energy consumption is in the order of magnitude

of other hydrothermal methods and much lower than thermal methods. In light of these results, it is justified to perform a high-level process evaluation.

A7.5. High-level OIS process evaluation

This section shows the results for the process design of ZnO manufacture *via* OIS. The base case plant is designed to produce 20 kton/year of ZnO operating 8000 hours per year. This will be compared with the French Process.

A7.5.1. CAPEX and OPEX estimations

The Capital Expenditure (CAPEX) and Operating Expenditure (OPEX) estimations for each process unit will be detailed in the following section. Equipment cost has been estimated using Mache's correlations⁴⁹¹, purchased equipment cost 2014 F.O.B. Gulf Coast U.S.A. The costs have been corrected to 2018 \$US using the Plant Cost Index from Chemical Engineering Magazine³⁶⁷ (2014 = 576.1 and 2018-June = 605.2) and Eq. 1 in Appendix 14. All results from Mache's correlations⁴⁹¹ have been expressed in 2018-June \$US. The electricity cost has been calculated using a value of 0.166 \$US/kWh (12.73 pence/kWh⁴⁹²) and the natural gas cost using a value of 0.037 \$US/kWh (2.84 pence/kWh⁴⁹²).

A7.5.2. Process description for particles production

The block flow diagram to produce ZnO nanoparticles via the OIS is given in Figure 198. In this case, the feedstock is metallic Zn and the solvent is the ionic liquid [C₄C₁im]Cl and water.

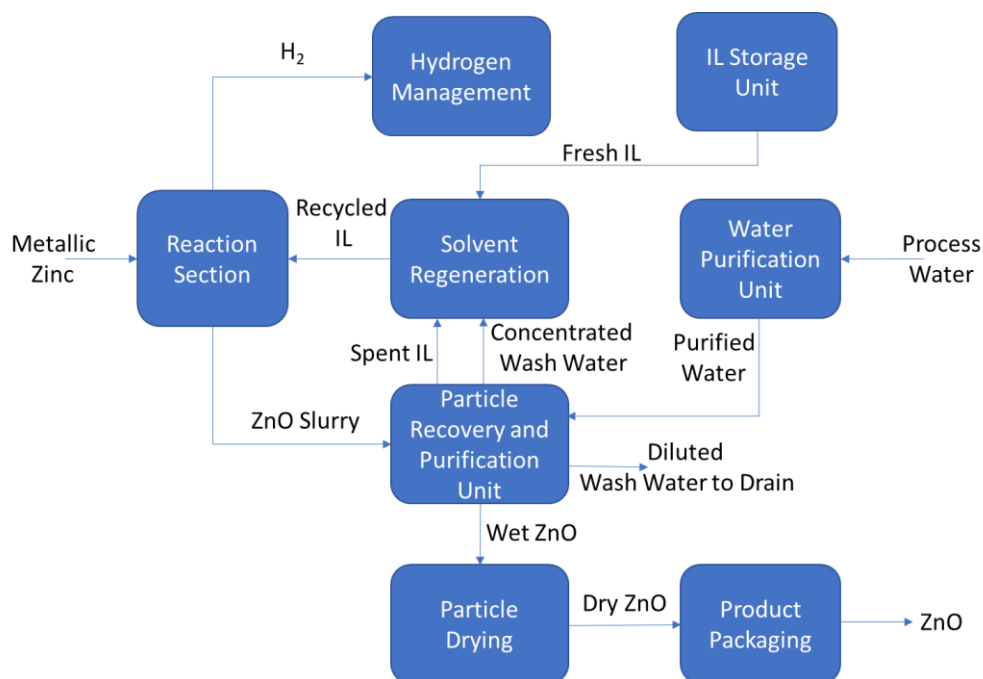


Figure 198. Block flow diagram of the OIS applied to ZnO production as powders.

The main process assumptions for the evaluation are:

- Overall ZnO production 20 kton/year
- SHG zinc will be used as feedstock
- The ionic liquid is $[C_4C_1im]Cl$
- Ultra-pure water is needed for the process
- Zinc conversion 100%
- The solid:liquid mass ratio in the reactor is 1:1
- The water content in the IL for the reaction is 25 wt%.
- Hydrogen is used as fuel in the process
- IL losses are 1% of the recirculating loop
- Moisture content in the ZnO after water washing 100% (assumed, needs to be validated experimentally).
- Final moisture content 0.5% (Table 60, the specification for volatile matter content for wet processes).

A7.5.2.1 Reaction unit

Metallic Zn is fed into a reactor and it is brought into contact with the ionic liquid water solution. The mixture is heated to the desired temperature and kept for a specified amount of time to achieve the desired particle morphology. The liquid can be agitated or not depending on the properties of the particles that are required.

After the reaction is completed, the spent solvent and the metal oxide particles are sent to the Particle Recovery and Purification Unit. The hydrogen generated (if water is used as the oxidant) is sent to the Hydrogen Management Unit.

The reactor design will depend on the reaction temperatures, volumes and residence times. For low temperatures, plastic tanks could be used. For higher temperatures, pressure vessels would be employed. To avoid particle contamination with metals and safety issues due to corrosion problems, careful selection of construction materials is required. Material suitability for hydrogen service should be evaluated carefully before it can be used in a large-scale process. In general, a material should not be used unless data is available to prove that it is suitable for the planned service conditions. As data is not available for H₂-IL-water systems, the material can be subjected to hydrogen embrittlement susceptibility testing (*e.g.* ISO 11114-4). According to the information included in the ISO/TR 15916:2015 “Basic considerations for the safety of hydrogen systems /Technical Report”⁴⁹³ most of the metallic materials present a certain degree of sensitivity to hydrogen embrittlement. However, there are some that can be used without any specific precautions as for example brass and most of the copper alloys or aluminium and its alloys. However, as shown in sections A5.1 and A5.8, brass and aluminium may react with the ionic liquid [C₄C₁im]Cl, and therefore should be avoided for this application. Nickel and high nickel alloys or titanium and its alloys are known to be sensitive to hydrogen embrittlement. For steels, the sensitivity may depend on several factors as the exact chemical composition, heat or mechanical treatment, microstructure, impurities and strength. ISO/TR 15916:2015 also provides information concerning the use of non-metallic materials which could be used for hydrogen handling.

The total reaction volume to meet production was estimated to 503 m³. The average flow rate for zinc and [C₄C₁im]Cl solution is 2500 kg/h each, which results in a total volumetric flow of 2.85 m³/h. With a 7 days residence time, the total working volume is 479 m³. As water is consumed in the process, the reaction volume will contract as the reaction takes place, with a total reduction of 17%. A 5% margin has been added to account for the thermal expansion of the reactants. The maximum reactor volume covered in the costing correlations used is 36.4 m³ (8000 gal)⁴⁹¹. This reactor volume was selected to minimize the number of vessels, and therefore, the CAPEX. This leads to a total of 16 reactors working in parallel, 14 in operation, 1 in loading mode and 1 in off-loading mode. .

The reactor material is carbon steel with a rubber liner rated for 150 psi. There is a significant difference in terms of CAPEX if agitators are added to the reactor, therefore, 2 cases were developed, one in which agitation is not required (optimistic case) and one in which agitation

is required (pessimistic case). The overall power includes the loading and discharging pumps and the agitators in all the reactors excluding the one being loaded and the one being discharged. The results for the CAPEX and OPEX for the reaction unit as a function of capacity is shown in Figure 199. The number of reactors was optimized to minimize the CAPEX without exceeding the maximum reactor volume. Details on the CAPEX and OPEX calculations for this unit are given in the Appendix 8.

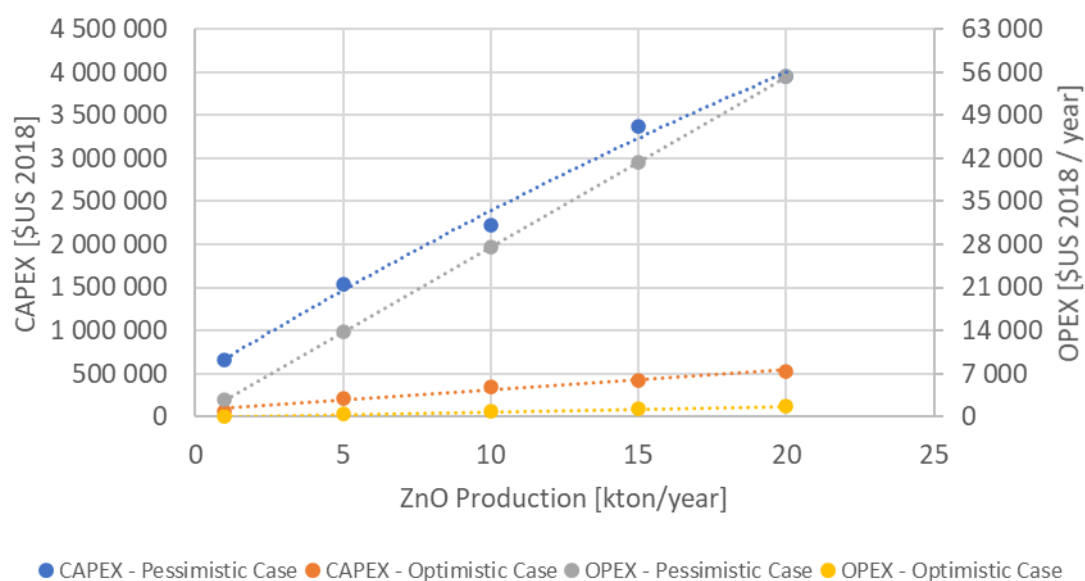


Figure 199. CAPEX and OPEX for the reaction unit. Pessimistic case considers that agitation is required and a residence time of 7 d. Optimistic case considered that agitation is not required and a residence time of 1 d.

Heat losses of a tank will depend on many factors such as tank geometry, ambient temperature, wind speed, exposure to solar radiation, the thickness and thermal properties of the material of construction used for the tank, liners and insulation. At this stage, such details are not available. Therefore, performing detailed heat losses calculation does not seem appropriate. In contrast, modelling the process as an adiabatic system, which is a non-realistic assumption, will underestimate the energy consumption and will not allow a fair estimation for the energy needed for the process. Therefore, a simplified approach to estimate heat losses was developed based on the heat losses of an insulated pipe (Appendix 8).

The overall heat consumption of the reaction unit includes the heating of the medium to the reaction temperature and the heat losses from the reactors. The heat needed to elevate the reaction medium temperature has been calculated integrating the C_p of the reactants (Appendix 8) while the heat losses of the reactors have been calculated using Eq. 180 (Appendix 8) and reactor number and geometry. Figure 200 shows the results as a function of production considering a residence time of 7 days. Under these assumptions, the heat required to reach the reaction temperature is greater than the heat losses by natural convection.

Reactor insulation could be further optimized to reduce the heat losses to the environment. A reduction of the residence time will also lead to a reduction of the heat losses. Further, a dedicated heater has not been added to this unit as it has been assumed that the heat is transferred via the reactor jacket due to the long filling time. During detailed engineering, this assumption will need to be validated. Thermal integration could also be considered.

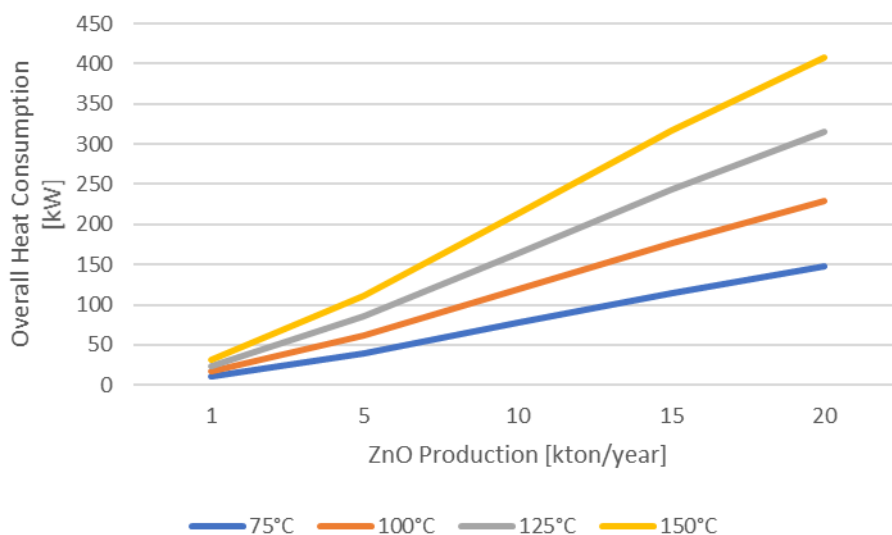


Figure 200. Overall heat consumption for the Reaction Unit as a function of production considering a residence time of 7 days.

A7.5.2.2 Hydrogen management unit

If water is used as the oxidant, hydrogen is generated as a by-product of the oxidation process (0.0248 kg / kg ZnO). This causes safety issues as hydrogen is a flammable gas and can cause metal embrittlement, which can lead to equipment and pipework failure. There are several options to manage the hydrogen produced, but the two main approaches considered in this work will be hydrogen venting or hydrogen burning for energy production.

As hydrogen has a propensity to ignite it is essential to perform detailed safety assessments. Some options for hydrogen disposal, such as dilution below the lower flammable limit, inerting, dispersion of flammable concentrations and flaring, are discussed in the scientific literature; along with the potential for ignition of releases⁴⁹⁴. Even though dilution of hydrogen with air is not considered the best practice from a safety point of view, as there is always a risk of the formation of flammable atmospheres, it will be evaluated from a CAPEX and OPEX perspective only, as this might be a cost-effective solution for pilot and demonstration plants. The amount of air was calculated based on a hydrogen density of 0.06731 kg/m³ (1 bar and 86.9°C⁴⁹⁵ and a dilution factor below 25% of the lower flammable limit, which is 4% v/v for hydrogen, meaning a dilution of 100-fold to reach 1% v/v⁴⁹⁴. Additionally, 2x100% fan

arrangement is considered. For the cost estimation, Mache's correlations⁴⁹¹ were used for centrifugal blower (1 psi carbon steel).

The fan power has been calculated with Eq. 173, assuming an overall fan efficiency of 0.8 and a ΔP of 8000 Pa.

$$P [kW] = \frac{Q \left[\frac{m^3}{s} \right] \cdot \Delta P [Pa]}{1000 \cdot \mu} \quad (173)$$

The Lower Heating Value (LHV) is based on the assumption that the latent heat of vaporization of water vapour produced during combustion is not released whereas the Higher Heating Value (HHV) represents the total energy in the fuel. Hydrogen has a LHV of 119.96 MJ/kg and a HHV of 141.8 MJ/kg⁴⁹⁵. Many modern boilers burning natural gas or other hydrogen-containing fuels already include the capability to recover heat from the water vapour. This capability will be of greater importance for appliances burning hydrogen alone than for those firing natural gas as the mass of water vapour produced from hydrogen is ~1.6 times that from natural gas²²⁷. Operating the hydrogen burner in "condensing mode" would maximize heat recovery from the flue gas and might also generate water that could be used in the process. However, this would lead to a very large heat transfer area and would limit boiler return temperature to around 50 °C²²⁷. For the purpose of the evaluation, an efficiency of 85% based on the LHV will be considered. During detailed engineering, the techno-economic feasibility of implementing burners in "condensing mode" should be explored with vendors. For the CAPEX estimation of the burners, Mache's correlations⁴⁹¹ were used to evaluate a cylindrical fired heater in stainless steel 316 and rated for 300 psi.

Figure 201, shows the CAPEX and OPEX results for the air blower system and the hydrogen burner. The CAPEX for the hydrogen burners is around 2.5 times the investment for the air fans. However, from an OPEX, sustainability and safety perspective it is better to use the H₂ as a fuel and recover energy. Therefore, this option is retained for the evaluation.

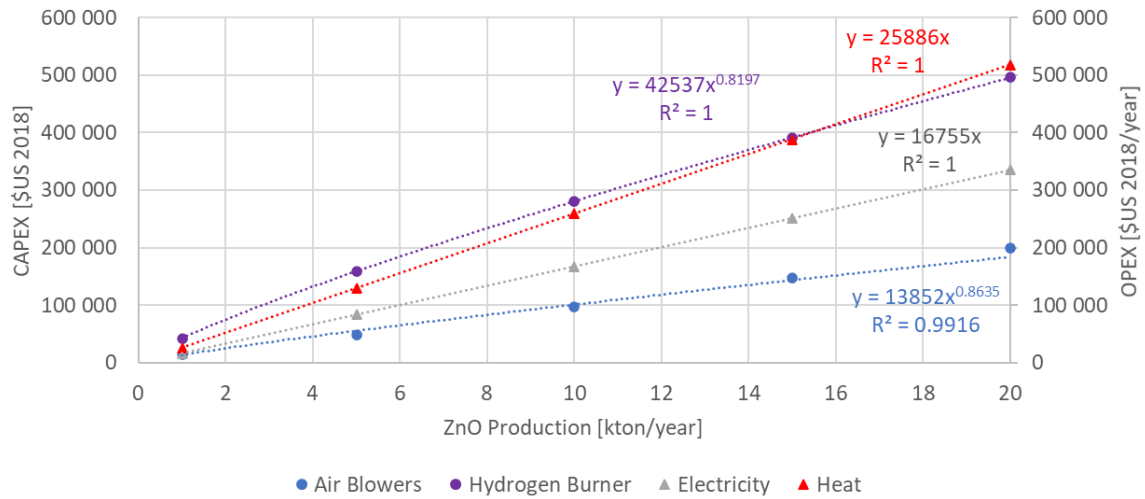


Figure 201. CAPEX and OPEX for different options for the hydrogen management unit.

Other alternatives such as fuel cells, or even recovering the hydrogen for export, could be considered at a later stage. The best alternative will need to take into account the size of the plant and the context of a specific project.

A7.5.2.3 Particle recovery and purification unit

In this unit, solid particles are separated from the ionic liquid solution. Further, the solid particles are washed with water to remove the IL, in order to produce high purity solid and to minimize IL losses. The IL solution and a fraction of wash water containing IL is sent to the IL Conditioning Unit. This is done to replenish the water fraction consumed in the process. Excess wash water containing excess IL is sent to the drain, as recovering IL from diluted aqueous solutions through thermal methods is not economically or sustainable, due to the large amount of energy required to evaporate water. Methods to re-concentrate the waste stream to minimize IL losses, such as reverse osmosis or membrane separations, could be explored at a later stage.

Solid:liquid separations are a very well established process. The bigger the particle, the easier the separation is. Figure 202 shows relative particle sizes and different pressure driven membrane process operations.

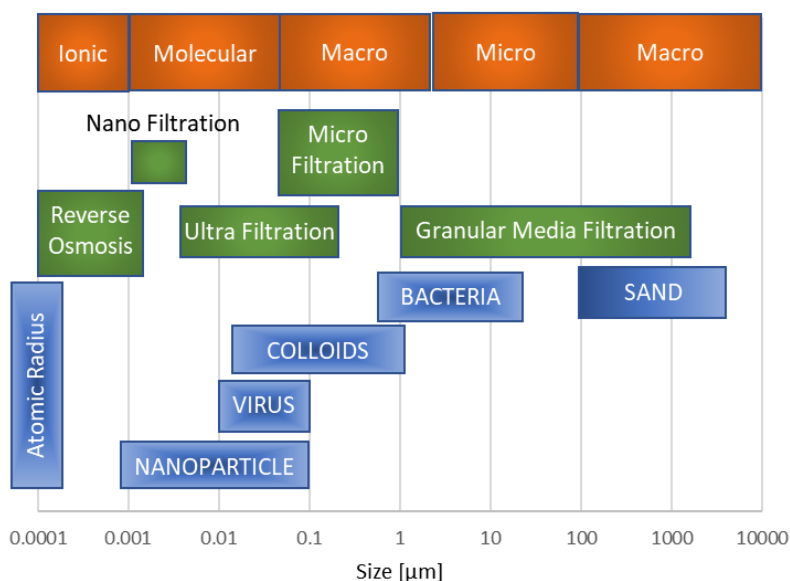


Figure 202. General particle size distribution of particulate contaminants with various treatment options. Adapted from ref ⁴⁹⁶.

Separation of particles with diameters of $\sim 1 \mu\text{m}$ and above is easy. It is known that nanomaterials have a different behaviour than bulk materials, which might lead to difficulties during separation processes. For example, the greater surface reactivity of nanoparticles due to changes in local electronic structure could lead to differences in the attachment of nanoparticles to filter surfaces in comparison to that of larger particles. The filtration mechanisms (attachment and transport) of nanoparticles in granular media filtration had been studied, as well as the influence of the physical and chemical conditions of the filter media, the nanoparticles, and the filter operation ⁴⁹⁷. It was shown that this technique could be used for nanoparticle removal.

As mentioned previously, producing monodisperse nanoparticles is essential to ensure consistency in final products for different applications. Even though it is technically possible to separate particles according to their shape and size, it would be better to ensure consistency in particle morphology during the synthesis process to avoid these post-synthesis classification steps, that will increase the overall production and investment costs.

A number of techniques have previously been employed to separate nanoparticles by size and shape, and several methods have been developed to purify subpopulations of particles after their assembly. Methods for nanoparticle purification by size include magnetic field flow fractionation filtration ⁴⁹⁸, size exclusion chromatography ⁴⁹⁹, size selective precipitation ⁵⁰⁰, density gradient centrifugation ⁵⁰¹, membrane filtration ⁵⁰², dimethyldioctadecylammonium bromide treated microporous polypropylene filters ⁵⁰³, supramolecular membrane ⁵⁰⁴ and

cross-flow filtration ⁵⁰⁵. Similarly, methods for purifying nanoparticles by shape include centrifugation ⁵⁰⁶, gel electrophoresis ⁵⁰⁷, and density gradient centrifugation ⁵⁰⁸. However, these reports have predominantly focused on “hard” nanoparticles such as gold nanoparticles and carbon nanotubes. Moreover, many of these methods cannot be applied to “soft” nanoparticles of tens to hundreds of nanometres in diameter ⁵⁰⁹. Some of these methods (filtration, centrifugation, Gel Permeation Chromatography (GPC) and density gradient centrifugation) were tested and validated at lab scale for polymersomes separation into monodisperse fractions ⁵⁰⁹.

Experiments and modelling of liquid filtration of nanoparticles through track-etched membrane filters under unfavourable and different ionic strength conditions has been studied to develop a basic understanding of surface interactions between nanoparticles and membranes in micro- and ultra-filtration applications for drinking water production, wastewater treatment and particle free water production in industries ⁵¹⁰. Filtration of engineered nanoparticles using porous membranes has been investigated in hollow fibre membranes ⁵¹¹ and it was shown that nanoparticle separation is possible and the exact fouling behaviour along the hollow fibre membrane is strongly influenced by the applied feed flow rate. It is noteworthy that manufacturers of such membranes were contacted and confirmed that it is technically possible to recover nanoparticles with these membranes. However, these systems are mainly used to remove the turbidity of water rather than to recover the nanoparticles. Additionally, some membranes do not withstand the presence of cationic surfactants. Therefore, the lifetime of the membranes exposed to IL would need to be validated. Regarding the scalability of this technology, it was mentioned that it is very easy to scale-up and to adapt the number of membrane units to meet production. Vendors also mentioned that 6 m³/h (approximate flow rate for a 20 kton/year ZnO production plant) is actually a very small capacity for membranes. Other alternatives to membranes will be the use of porous ceramics, again, for these systems, vendors focus on water purification systems but mentioned that they are starting to look at material recovery with this technology at scale.

As the above technologies are not validated for ILs, the CAPEX and OPEX estimation for this unit will be based on a centrifugation system. As a pessimistic approach, Mache’s correlations ⁴⁹¹ was used to evaluate a 70” vertical centrifugal separator (Auto Batch) in Hastelloy, which is the most expensive material for centrifuges according to the correlations used. Material factors for the centrifuge are as follows: Carbon steel = 1, carbon steel – rubber covered = 1.35, SS 316L = 1.80, Monel = 2.35 and Hastelloy = 4.34) ⁴⁹¹. The cost of the centrifuge is 9307000 \$US for a plant producing 20kton/year of ZnO. For other capacities, it has been scaled using

Eq. 2 in Appendix 14 with an exponent equal to 0.94. Details on the CAPEX estimation for the centrifuge are given in Appendix 8.

The power required for the centrifugation process will depend on the nature of the system being separated and centrifuge design and operation. Some of these factors include rotor speed, centrifuge type, motors efficiency, centrifugation time which in turn will depend on particle sedimentation behaviour, which is a function of particle shape, size, density, density and viscosity of the solution. For example, there are four components of the power consumption in a decanter centrifuge: friction during product transport, viscous and kinetic losses during feed acceleration, inefficiencies in power transmission components, and aerodynamic losses, known as windage ⁵¹². It has been shown that energy consumption for high-speed centrifuge could be reduced by 50% with proper centrifuge design ⁵¹³. At this stage, it is going to be assumed that a standard electric motor of 75 HP (55 kW) is required for the operation. The overall CAPEX and OPEX for the Particle Separation and Purification unit is shown in .

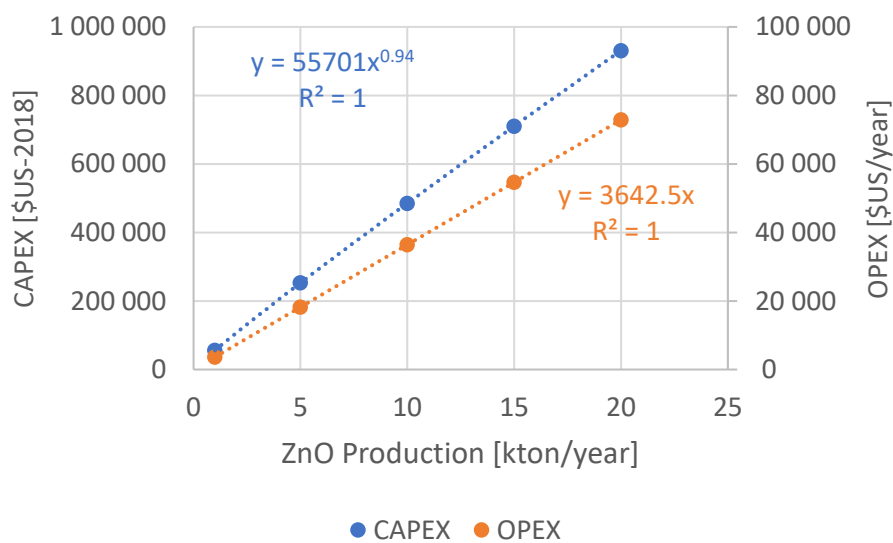


Figure 203. CAPEX and OPEX for the Particle Recovery and Purification Unit (Based on Centrifugation).

At a later stage, the best type of centrifuge and detailed power consumption for the ZnO particles needs to be addressed as a function of particle size and shape. Additionally, the use of filtrations systems should be considered and evaluated.

A7.5.2.4 Ionic liquid conditioning

The spent IL from the Particle Recovery and Purification unit is sent to a system of 3 receiving vessels (IL buffer tanks) working in parallel while the fraction of the water used for the washing step is sent to a water recovery buffer tank. One of the vessels of the IL buffer tanks receives the spent liquid, once its capacity has been reached, water from the recycled water tank is added to replenish the water consumed in the reaction process. The quality of the batch, in terms of concentration, is monitored before it can be used in the reaction section. The monitoring could be carried out through conductivity measurements, infrared and or refractive index. A second vessel is in stand-by mode full of on-spec solution. The third vessel, containing on-spec solution is used to feed the reactors. This configuration allows to operate the process in continuous mode. Other arrangements can be explored during detailed engineering.

Details on the sizing and costing for the equipment within this unit are given on Appendix 8. The material selected for the vessels is Hastelloy. For smaller capacities than the base case, the vessel size is small, therefore, piping elements could be used. Further, to reduce the cost, the material could be downgraded to CS with PTFE or glass liners. For these reasons, the CAPEX shown in Figure 204 should be a conservative estimate.

Agitator power has been assumed to be 3 HP (2.24 kW) for the 20 kton/year plant and scaled linearly with capacity. The pump power has been calculated with Eq. 174, assuming an overall pump efficiency of 0.6 and a head of 150 ft (45.7m) and a liquid density of 1200 kg/m³. The total OPEX as a function of capacity is given in Figure 204.

$$P [kW] = \frac{Q \left[\frac{m^3}{h} \right] \cdot \rho \left[\frac{kg}{m^3} \right] \cdot h [m] \cdot 9.81}{3.6 \cdot 10^6 \cdot \mu} \quad (174)$$

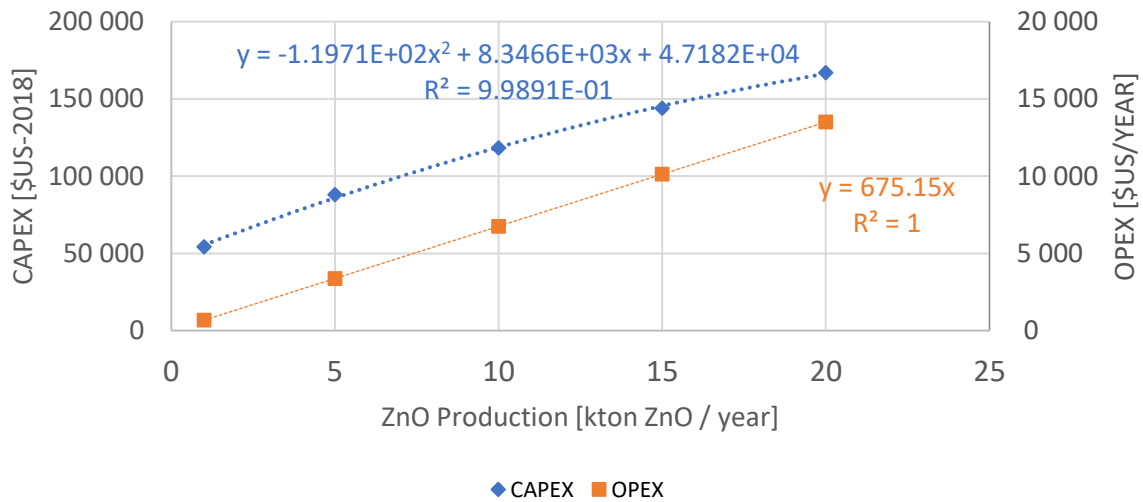


Figure 204. Total CAPEX and OPEX for IL Conditioning Unit.

A7.5.2.5 Water production unit

There are several technologies to produce pure water, such as distillation, membranes and reverse osmosis. The inorganic salts present in conventional municipal water would accumulate in the system and might lead to product contamination. Even though the quality of water required for the process is unknown at this stage, for conservative purposes it is going to be assumed that high quality water is required.

A comparative study of different technologies to produce very pure water (Water for Injection (WFI) grade) was performed by MECO ⁵¹⁴. Risk, reliability and sustainability are important factors in the evaluation of any systems cost but were not included in this study for simplicity. The analysis of total cost includes the capital cost, the operating utilities, including steam, electricity, feed water, cooling water and wastewater. Replacement parts, consumables and labour are also included ⁵¹⁴. The systems used by MECO for the assessment are relatively basic, yet typically sufficient. Table 70 summarizes the CAPEX/OPEX for different WFI production technologies.

Table 70. Comparison of different systems for ultra-pure water production (1500 L/h, 5600 h/year (8.4 MML/year).

System	CAPEX (US-2019)	OPEX (US-2019)	Power [kW]	Steam [kg/h]	Total Cost (US/L)
1	735921	194335	9.25	561	0.0275
2	560737	110514	9.5	0	0.0165
3	664720	82012	25.6	0	0.0137
4	786264	97955	25.6	55	0.0163

• System 1 - Water Softening / Carbon Filtration / Reverse Osmosis (not hot water sanitizable) and Multiple Effect (ME) Distillation.

- System 2 – Hot Water Sanitizable Reverse Osmosis / Electrodeionization/ Ultrafiltration/ Ultraviolet light / Ozonation.
- System 3 – Vapour Compression Distillation with Water Softening and Carbon Filtration as Pretreatment.
- System 4 – Vapour Compression Distillation with Water Softening, Carbon Filtration and Ultrafiltration as Pretreatment.

In Table 70 it can be seen that vapour-compression (VC) based WFI production has a total cost of ownership that is less than or equivalent to that of a membrane-based system and significantly less than that of a typical multiple-effect-based system.. The designs depicted in that work yield a capital cost savings of 15%–28% for a membrane-based system relative to a distillation system. However, the operating costs are 35% greater than that of a VC-based system ⁵¹⁴.

A chlorinated municipal feed water supply is assumed in each case, meeting drinking water standards. Each system under evaluation begins treatment with softening, although it is acknowledged that in many cases, there may be a need for additional particulate filtration ⁵¹⁴. In any case, a specific feed water analysis will influence the ultimate system design. Product water recovery rates may be adjusted for any number of factors. The presence of chloramines, silica or other constituents within the feed water may dictate different configurations than the ones shown in the study ⁵¹⁴. Reverse osmosis (RO) is used to remove dissolved ions that would otherwise promote scale or corrosion within the distiller. The RO unit effectively removes dissolved ions, bacteria, viruses and suspended solids. It is important to note that while the feed water quality is improved by RO, the improvement is not necessary to provide WFI quality, but only to protect the distiller from scale formation and corrosion. Scale formation will accumulate on the feed water side of the heat transfer surface, and its detrimental effect is to reduce the quantity of distillate produced, not the quality.

Vapour compression (VC) is the most energy efficient means to distil water. Producing hot WFI (82 °C), a multiple effect distiller will require eight–10 effects to compete with the energy consumption of a VC plant ⁵¹⁴. Although there have been assertions that a membrane-based system offers a lower cost of WFI production, this is not necessarily the case ⁵¹⁴. The study indicates that while a membrane-based system offers CAPEX and OPEX advantages over a multiple-effect-based system, the same is not necessarily true for a VC-based system. The VC-based systems have a lower operating cost than both the membrane-based system and the multiple-effect-based system. However, a membrane-based WFI system offers the advantages of a low capital cost and low energy consumption ⁵¹⁴.

The CAPEX estimation is based on the VC compression system (1500 L/h, 5600 h/year (8.4 MML/year) and scales with capacity using a Eq. 2 in Appendix 14 with an exponent equal to 0.6. OPEX has been scaled linearly with capacity.

The CAPEX and OPEX cost of the ultra-purified water ranges from 8-15 more expensive than municipal water. For reference, a typical value for the cost of water in England for households is 140.01 pence/m³ (0.00182 \$US/L) and waste water is 86.72 (0.00113 \$US/L). Assuming that the ultra-pure water generation unit required 2 volumes of water per volume of purified water and that the diluted stream containing IL could be sent to the drain, the total water cost (supply and discharge) per year of a 20 kton plant is 81800 US\$/year. Other capacities have been scaled linearly.

A7.5.2.6 Particle drying unit

After the particles are recovered and washed with water, the slurry is transferred to a dryer to reduce the moisture content. As seen in Figure 205, the volatile matter content ranges from 0.25-0.5 depending on the synthesis method. For wet chemistry methods, the standard value is 0.5%. Therefore, this value will be used for the specification. There are many types of dryers available for this purpose such as open flash drying systems, vacuum dryers and thermal dryers. The selection will depend on many factors, such as capacity, maximum temperatures that the product can withstand, nature of the wet and dry particles, for example, if particles can be broken mechanically or if they tend to agglomerate during the drying process. Vendors have recommended that maximum dewatering via mechanical methods should be performed prior to thermal drying, to reduce both CAPEX and OPEX of this unit. Materials of construction for these units should take into account the possibility of abrasion for the solid particles and duplex alloy is often used for this reason. A ballpark estimate for the main components of an open flash system capable of evaporating 2500 kg/h of water is 2.53 MM \$US. This unit requires a 55kW motor, that has been scaled linearly with production. The heat of vaporization of water used for OPEX calculations is 2258 kJ/kg (HYSYS V8.8 thermodynamic package ASME Steam).

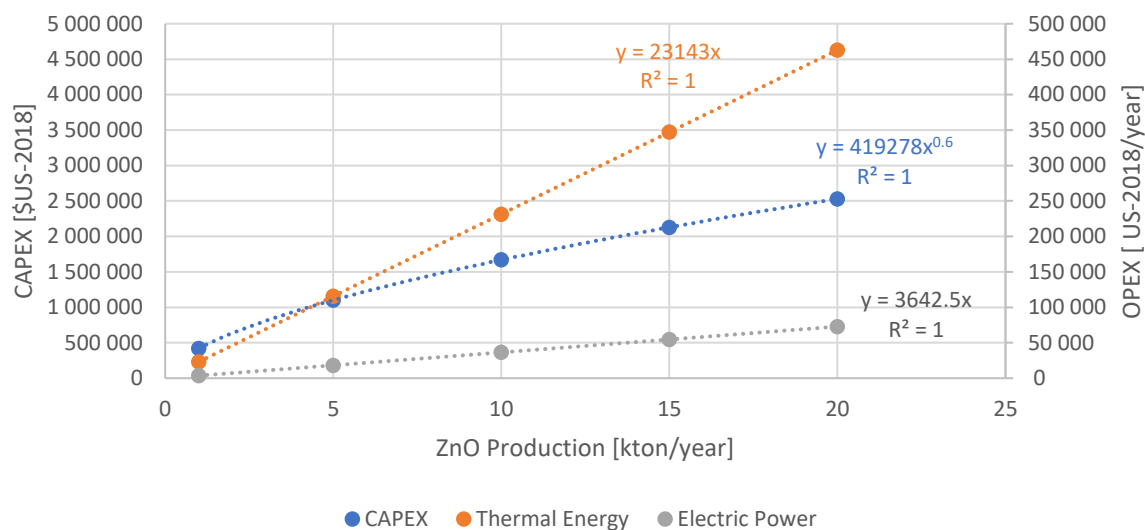


Figure 205. Total CAPEX and OPEX for the Particle Drying Unit as a function of capacity.

A7.5.2.7 IL storage unit

The aim of this unit is to supply Fresh IL to compensate for continuous IL losses (assumed to be 1% of recirculating loop) and store some IL for contingencies. This unit also contains an off-spec draining tank that serves to store the IL inventory in case of maintenance or during inspection of the facility.

The cost for the tanks was calculated using Mache's correlations⁴⁹¹ for horizontal tank, fuel storage, made of fiberglass reinforced plastic. The capacity of the Fresh IL tank was estimated to contain the average IL losses for 6 months operation (4000 h). The IL drain storage tank has been sized for the entire IL inventory (excluding fresh IL). Details on the CAPEX estimation for tanks are given in Appendix 8.

For the fresh IL injection pumps (2x100%), the same price for the pumps used in the IL Conditioning Unit have been used. An additional pump with the same capacity has been added, without spare, for the IL draining tank to transfer the inventory back to the process units to resume operation after draining. The OPEX was calculated using Eq. 174 for the continuous operation. Power consumption for intermittent operation was not included. The total CAPEX and OPEX for the IL Storage Unit is shown Figure 206.

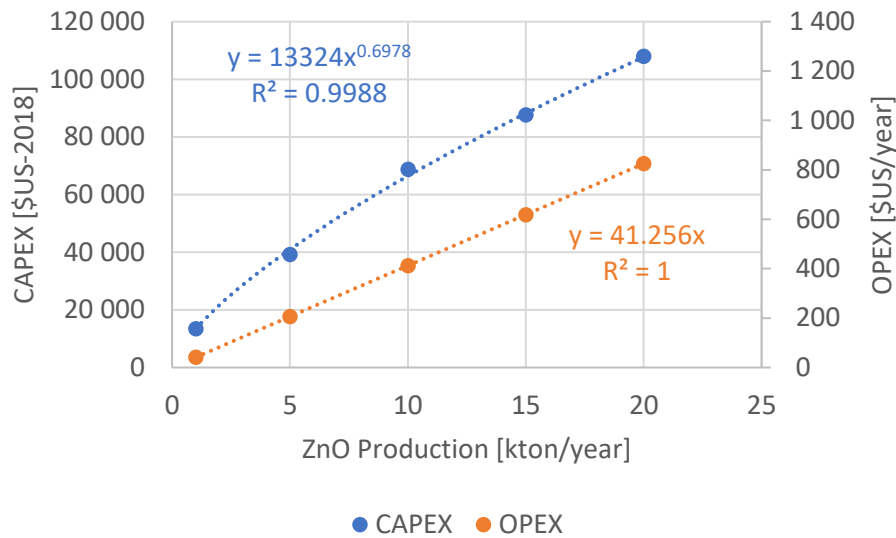


Figure 206. CAPEX and OPEX for the IL Storage Unit.

A7.5.2.8 Packaging unit

The objective of this unit is to put the ZnO power in packages for export. From different ZnO suppliers, it has been noticed that different containers can be used to store and transport ZnO powder, such as bulk, paper or plastic bags (25 kg or 50 lb), fibre drums, drums, 20-inches and 40-inches Export Container, UN/Reach approved bulk bags, paper bags and drums.

The cost of the packaging machines will depend on many factors, such as the degree of automation, type of packing, capacity (bpm, bags per minute), labelling options, etc. Ballpark estimates from different suppliers mentioned that fully automated machines able to handle 12 bpm ranges between 55000-110000 \$US. For estimation purposes, the highest value has been taken as a conservative approach and scaled with capacity according to Eq. 2 in Appendix 14 with an exponent of 0.6.

A7.5.2.9 Other systems

Other systems which are required but not evaluated in detail at this stage include solid handling and storage areas for import/export, administrative buildings, laboratory and utilities. For total investment cost, a Lang factor of 3 have been used, which should cover the cost of these systems.

Solid handling and storage: In this unit, the metal is received and stored, cleaned (if needed) and conveyed to the reaction unit. For pilot and small plants, this operation can be done manually. For large plants, automatic conveyors and feeders can be used. ZnO inventory

storage should also be considered. Commercial zinc plants generally use tagging systems for traceability purposes of the metal sources.

Utilities: The utilities required for the plant include the following systems:

- Plant air and instrument air: These units are commonly supplied as a packed skid with air compressors and air drying units. Due to the size of the plant, it is expected these units will be small.
- Nitrogen: It would be required for venting hydrogen containing systems for inspection and maintenance. Due to the size of the plant, nitrogen could be supplied in cylinders.
- Heating system: Heat from the hydrogen burner needs to be recovered to be used in the reaction section and particle drying operations. Steam systems are complex, therefore hot water or hot oil could be used as thermal transfer fluids. As the plant already has facilities to produce high purity water, water could be a cost-effective option. The best strategy for the heating system could be evaluated during detailed engineering.

Administrative building and laboratory: A laboratory for product quality compliance and for process monitoring would be required. Typical equipment will include XRD and XRF facilities

A7.5.3. Process description for metal-nanoparticle composites

For metal-nanoparticle composites, *i.e.* nanoparticles grown directly over metals, as discussed in Chapter 3, the process will be similar to the particle production process. For this option, the reactor is loaded with metallic sheets or wires followed by the IL/water solution. The system is heated to the desired temperature for a given amount of time. When the reaction is completed, the liquid could be drained and the coated metallic sheets or wire could be easier recovered and cleaned. This process should be easier to operate than the particle production as there is no need to recover and clean fine powers. This case will not be further explored, but it is expected to be significantly less expensive than the particle production plant, as the particle recovery and purification unit will be significantly simplified.

A7.5.4. Overall CAPEX and OPEX estimations

A7.5.4.1 CAPEX

The overall CAPEX has been calculated adding the total purchased equipment cost for all process units. The Lang Factor is an estimated ratio of the total cost of a plant to the cost of all major technical components. For the estimation of the Total CAPEX a Lang factor of 3 has been

considered. The IL inventory cost was added after (was not multiplied by the Lang Factor). Two scenarios have been evaluated to define a range for the Total CAPEX. A pessimistic scenario, in which a total residence time of 7 days with agitation have been assumed with an IL cost of 20000 US/ton and an optimistic scenario in which 1 day residence time without agitation with an IL cost of 10000 US/ton. The relative contribution of the equipment can be seen in Figure 207.

Further, the values were compared with a value provided by a French Process equipment manufacturer, which is 950 \$US / ton ZnO produced for a 20 kton/year plant²²⁸. This value was scaled with capacity using Eq. 2 in Appendix 14 and an exponent of 0.6 (Figure 208). The total CAPEX is given in Figure 209.

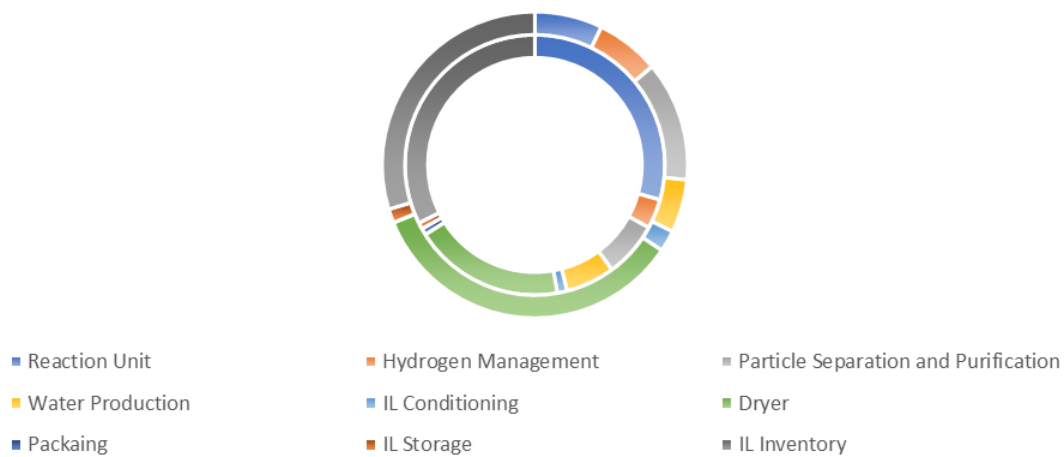


Figure 207. Total purchased equipment cost per process unit. Inner ring: pessimistic Scenario. Outer ring: optimistic scenario.

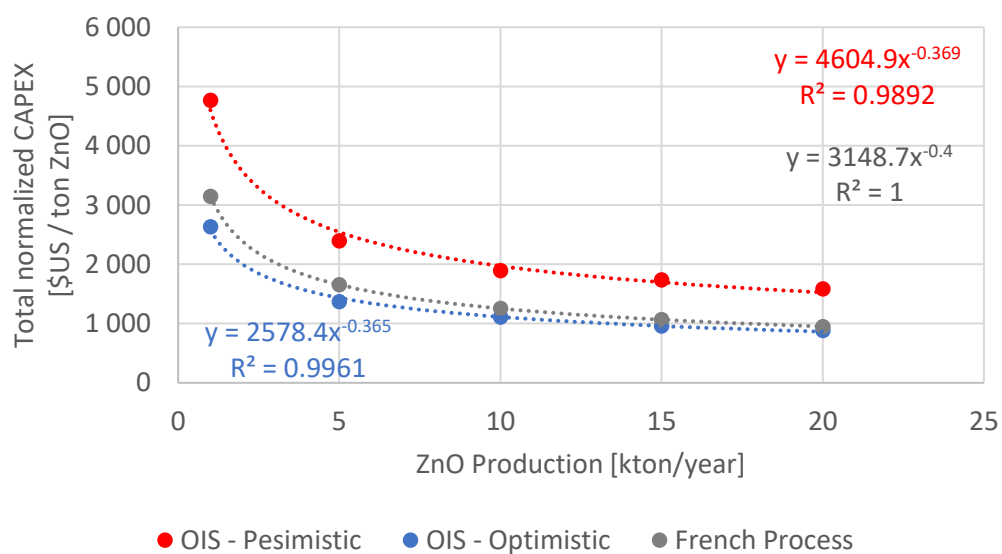


Figure 208. Total CAPEX per ton of ZnO for the OIS synthesis and French Process as a function of capacity.

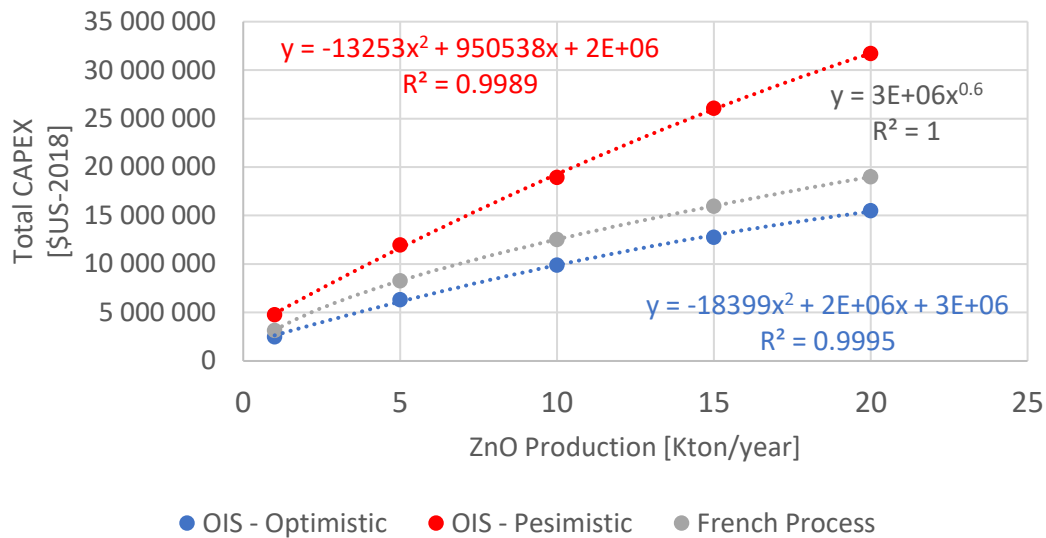


Figure 209. Total CAPEX for the OIS synthesis and French Process as a function of capacity.

From the CAPEX contribution for each process unit (Figure 207) it can be seen that the reactor system is heavily impacted by the residence time and the need of agitation, and on a relative basis, it can be the most expensive unit operation to a marginal one. The next most expensive unit in the pessimistic case is the drying unit. There are different dryer technologies with different costs. During detailed engineering, it has to be analysed which will be the best and most cost-efficient drying technology. In terms of overall CAPEX, it can be seen from Figure 208 that overall CAPEX per ton of ZnO ranges between 884 and 1590 \$US. When compared to the total CAPEX for a French Process (950 \$US/ton ZnO), the value ranges between -7% and +65%. This shows that the order of magnitude of an OIS plant is comparable to the French Process. It needs to be stressed that the CAPEX estimation for OIS had been performed on a high-level basis and with conservative assumptions and there is room for optimization of process to further reduce the cost. Further, no showstopper has been identified for the scale-up of the laboratory procedure to produce ZnO *via* OIS.

A7.5.4.2 Overall OPEX - Variable cost

The relative electrical power contribution per unit is shown in Figure 210. The electrical consumption of the packaging unit was not included as this unit will also exist in a French Process Plant. For comparison purposes, the electric consumption of the French Process has been assumed negligible. The variable cost is shown in Figure 211.

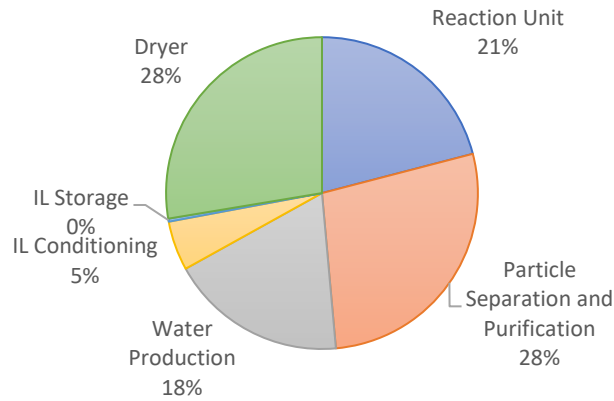


Figure 210. Power consumption per process unit (pessimistic case).

The electrical consumption could be significantly reduced if a filtration system is used instead of centrifuges for the particle recovery and purification. Additionally, if no agitation is needed, the power consumption can be further reduced.

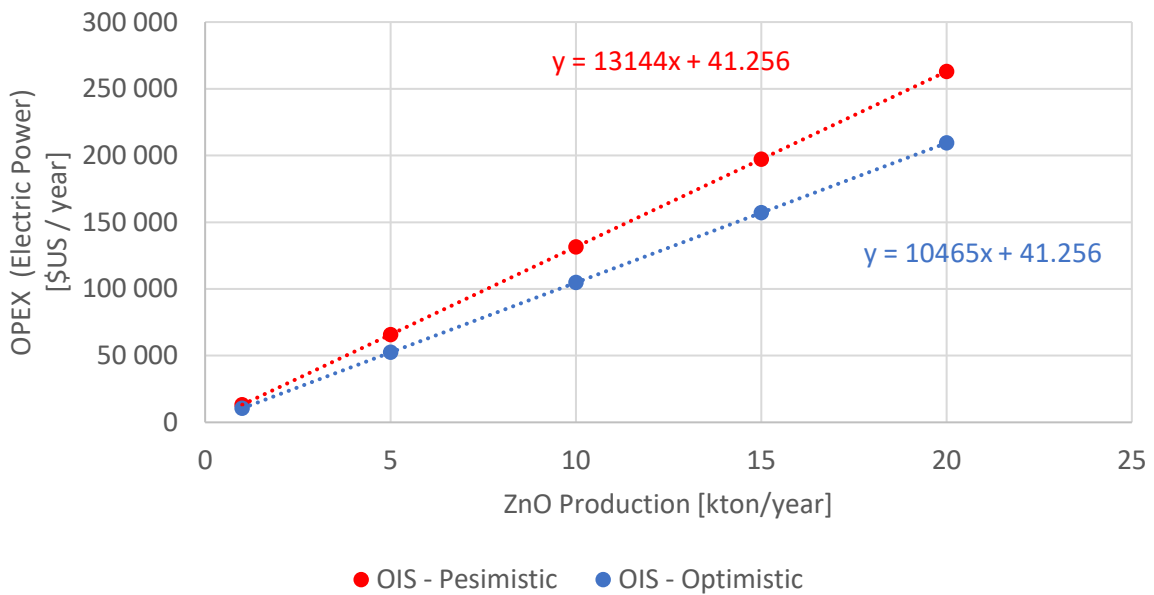


Figure 211. Estimated electric power cost per year for the OIS process.

The heat consumption of the OIS process originates from the energy required for the reaction and the drying of the particles. The particle drying is the major contributor to the heat consumption of the process and therefore it is important to experimentally measure the water retention of the ZnO particles and try to reduce the water content of the slurry as much as possible with mechanical means (if particle size allows for it). This is illustrated in Figure 212 where it can be seen that energy change by performing the reaction at 75 °C and 150 °C is minor, as the overall thermal energy consumption is driven by particle drying. Under these assumptions and considering that 85% of the hydrogen energy could be recovered, it can be

seen that the process can be energy-sufficient at a temperature of 75 °C. Reduction of the moisture content would allow higher reaction temperatures without energy import.

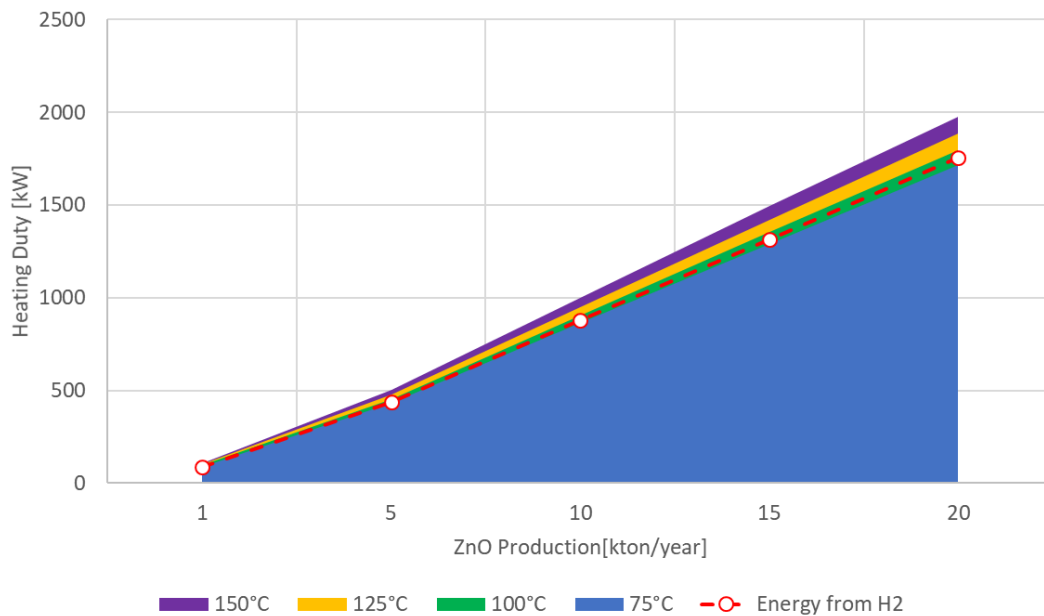


Figure 212. Total heating duty and energy produced by hydrogen burning.

A7.5.4.3 Overall OPEX - Fixed cost

Other fixed costs, such as insurance and labour are not included at this stage and assumed to be the same for the OIS process and the French Process.

A7.5.4.4 Zinc oxide production cost

The ZnO production cost for the OIS process was estimated considering the total CAPEX of the plant, normalized by the plant life, assumed to be 20 years. OPEX includes only the variable cost (electricity and thermal energy). Other costs (variable and fixed) are not taken into account as at this stage they are assumed the same for a French Process Plant. The cost for the French Process have been taken as 950 US\$/ton ZnO (green field development) with an energy consumption for this process ranges from 3.5G J/ton ZnO for a very performant system (BURNS 3-Crucible Vaporizer) to 13 GJ for typical multi-crucible (200L) vaporizers, as reported for a major ZnO production furnaces BURNS²²⁸.

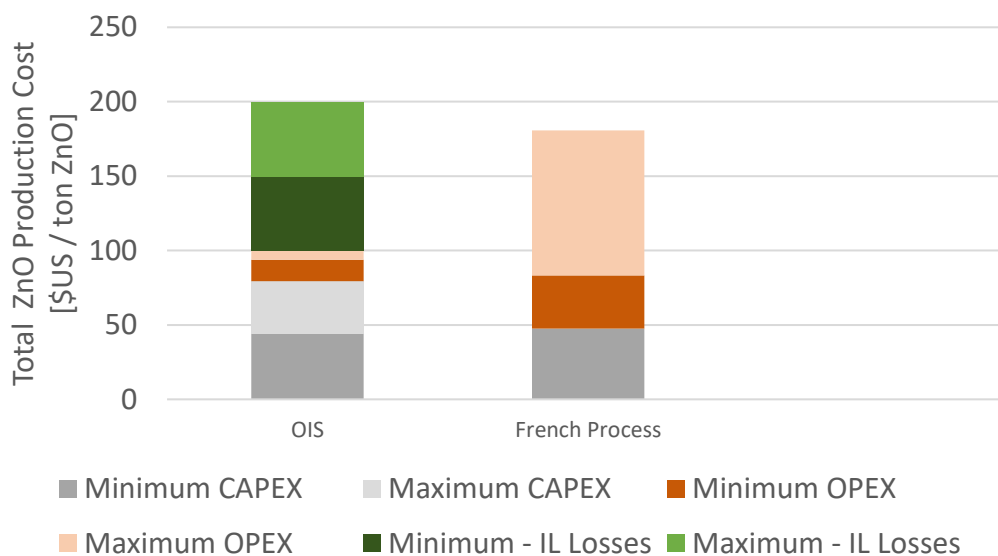


Figure 213. Total ZnO production cost per ton.

The maximum contributor to the OPEX for OIS is IL losses. As mentioned before, it has been considered 1% of the recirculating loop. Lowering the IL to solid ratio or implementing systems to minimize IL losses, such as re-concentration with membranes, would significantly reduce the OPEX. In Figure 213 it can be seen that the minimum production cost (minimum CAPEX and OPEX) for the OIS process have been estimated at 100 \$US/ton of ZnO produced vs. 83.4 \$US/ton for the French Process (based in a high efficient ZnO production system by BURNS), which represents a 17% production cost increased when compared to the French Process. The more pessimistic scenario leads to a production cost of 188.8 \$US/ton (maximum CAPEX and OPEX), which is a 126% more expensive than the highly efficient ZnO production system by BURNS and 4.5% more expensive compared to the performance of typical (200L) vaporizers.

The production costs of the OIS system are in the same order of magnitude of the French Process but there is a clear advantage in terms of energy savings. However, with the pessimistic assumption of 1% IL losses, the savings due to energy reduction are offset by the IL losses. Nonetheless, the OIS system allows control to particle morphology, which can improve existing products and open the door to new applications. The market price of ZnO nanoparticles with controlled morphologies is extremely high compared to bulk zinc, which can range up to 60000 / ton vs. 2000 / ton, therefore, even if the processing costs are higher for the OIS process than the French process, the increase in the value of the produced material will make an OIS plant economically viable. The OPEX will likely be reduced after process optimization.

The CO₂ emissions for kWh of energy used will depend on the energy source. The Department for Business, Energy and Industry Strategy ²²⁹ recommends the following conversion rates: Natural Gas – 0.20428 kgCO₂e/kWh and UK Grid Electricity – 0.2556 kgCO₂e/kWh, other organisations may use other conversion factors. Total equivalent CO₂ emissions per ton of ZnO is given in Figure 214. It can be seen an important reduction of the CO₂ emissions of almost 2 orders of magnitude, estimated in the range of 199 - 738 kgCO₂e/ton ZnO for the French Process and in the range of 16-20 kgCO₂e/ton ZnO for the OIS Process, which could be further reduced once the process is optimized. This represents a significant improvement for sustainability purposes that would off-set the water consumption of the OIS process and the wastewater stream containing traces of IL. A more detailed environmental assessment should be performed to quantify both effects.

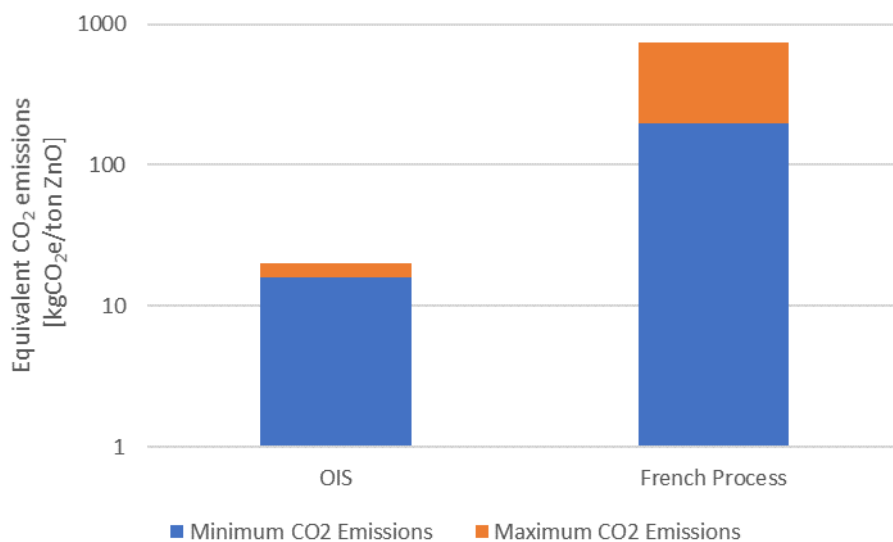


Figure 214. Total equivalent CO₂ emissions per ton of ZnO.

A7.6. Process uncertainties

This section summaries the process uncertainties in order of relevance:

- IL Recyclability:** IL losses is the main OPEX contributor for the OIS process. Even at 1% losses of the recirculating loop for a 1:1 solid:liquid ratio process (25% water content), the total OPEX for the OIS process can be higher than the OPEX for the French Process. IL degradation and the number of cycles that can be achieved without the need to change the IL inventory must be determined. One important thing to monitor is the formation of [C₄C₁im] zincates, and other impurities that might build up in the system and affect process performances.

- **Particle Properties:** It needs to be assured that particle morphology is consistent after recycling the IL.
- **Zinc Conversion:** If the conversion is not 100% and there is metallic zinc remaining after the reaction, means to recover the zinc from the ZnO should be implemented. For example, metallic zinc can be removed from zinc ash by physical separation processes such as rotary mills and sieving before it can be used in the French process ²¹¹. A similar strategy could be used for OIS. The formation of a stable film of particles on the surface of the metal, inhibiting the oxidation process, may become the major hurdle to realizing continuous ZnO generation through oxidation of this metal.
- **IL Losses:** This needs to be addressed in detail for the two technologies that have been considered for solid:liquid separation, *i.e.* filtration or centrifugation. The use of membranes (or other technologies) to re-concentrate the IL in the waste streams to minimize IL losses should be considered as per to reduce the OPEX.
- **Materials of construction:** The most cost-effective solution for the material of construction needs to be further investigated, taking into account the presence of hydrogen and the possibility of abrasion from the solid particles.
- **IL draining:** It needs to be confirmed if IL can be drained directly into commercial sewage or if it needs to be treated prior to discharge.
- **Water content of the slurry:** The water content in the slurry after the washing steps should be measured experimentally to size the dryers.
- **Drying behaviour of ZnO particles:** This needs to be addressed to select and size the dryers. If particles agglomerate, grinding equipment could be provided with the dryers.
- **Quality of the water needed:** This is needed to avoid overdesigning the water generation units.
- **Solid:Liquid separations:** Further investigate the best technology available to recover and wash the particles according to their size, and the production scale. For example, investigate if cyclones or hydro-cyclones could be used.
- **Further process optimizations:** The batch nature of the process allows the possibility to overdesign equipment and work in shifts rather than 24 h operation. This could be optimized according to the cost and number of operators vs. CAPEX to maximize revenues.

- **Methods to improve zinc conversion and particle morphology:** Other techniques to improve zinc conversion or to generate new morphologies should be investigated at lab scale. These parameters may include agitation, ultrasounds, microwave, other ILs, use of molecular solvents or blends of ILs, pH, electrical currents, catalysers, surfactants and other oxidants such as O₂, O₃ or H₂O₂.

A7.7. Overall considerations

The OIS process was compared to the French Process, which is the main method for ZnO production at large scale, and other hydrothermal methods. The results of the assessment are given in Table 71.

Table 71. Qualitative comparison of the main methods for ZnO production. The best process per criteria have been highlighted in green while the worst was highlighted in red. The symbol +?/-? were used to indicate that more research/analysis is needed to reach a conclusion.

Criteria	French Process	OIS	Hydrothermal Methods
Particle Quality	[-] Morphology not controlled.	[+?] It appears that morphology, size and chemical composition can be controlled.	[+] Morphology, size and chemical composition can be controlled.
Energy consumption (Environmental footprint)	[-] High temperatures required to vaporize metallic zinc.	[+?] Reaction can be carried out at low temperatures (no phase changes). Hydrogen produced can be used as a fuel. However, some process conditions will result in Zn(OH) ₂ (or others), which will require calcination for ZnO production.	[-] Reactions can be carried out at low temperatures but in most cases calcination of Zn(OH) ₂ at high temperatures is required.
Safety	[-] Risk of explosions and fires due to the high temperatures and the use of fossil fuels.	[+?] Ionic liquid/water mixtures are not flammable and have negligible vapour pressure. However, ILs can be dangerous if consumed or if released to the environment.	[-] Precursors used in hydrothermal methods are in general more dangerous than metallic zinc (section A7.4.4.1).
Operating Cost	[-] High energy demand.	[+?] Ionic liquid is not consumed in the process and can be recycled. No regeneration needed. ILs used in this process are commercially available at large scale. IL losses will significantly impact the OPEX.	[-?] These methods were not modelled in detail. However, it would be expected high energy demand due to the calcination step and increased cost to process aqueous waste streams.

Capital Investment	[-?] In general, furnaces are expensive (to be confirmed by a detailed Techno-Economic analysis TEA).	[+?] The CAPEX for the OIS is within the order of magnitude of the French Process. It is suspected that after a detailed process optimization, the overall CAPEX can be lower than the French Process.	[+?] Not modelled but should be similar to the OIS process excluding wastewater treatment plants.
Process	[+] Well established technology.	[-] Novel process. Large scale separation of nanoparticles from the IL/water mixtures needs to be validated.	[+] Industrial experience for the production of ZnO via wet chemistry methods.

After reviewing the Technology Readiness Levels (TRLs) summarised in Figure 215, it seems that the OIS process is at early stage 3 as lab experiments and techno-economic analysis show that it is possible to oxide metals with ionic liquids to produce metal oxides particles in a cost-effective and in a more sustainable way.

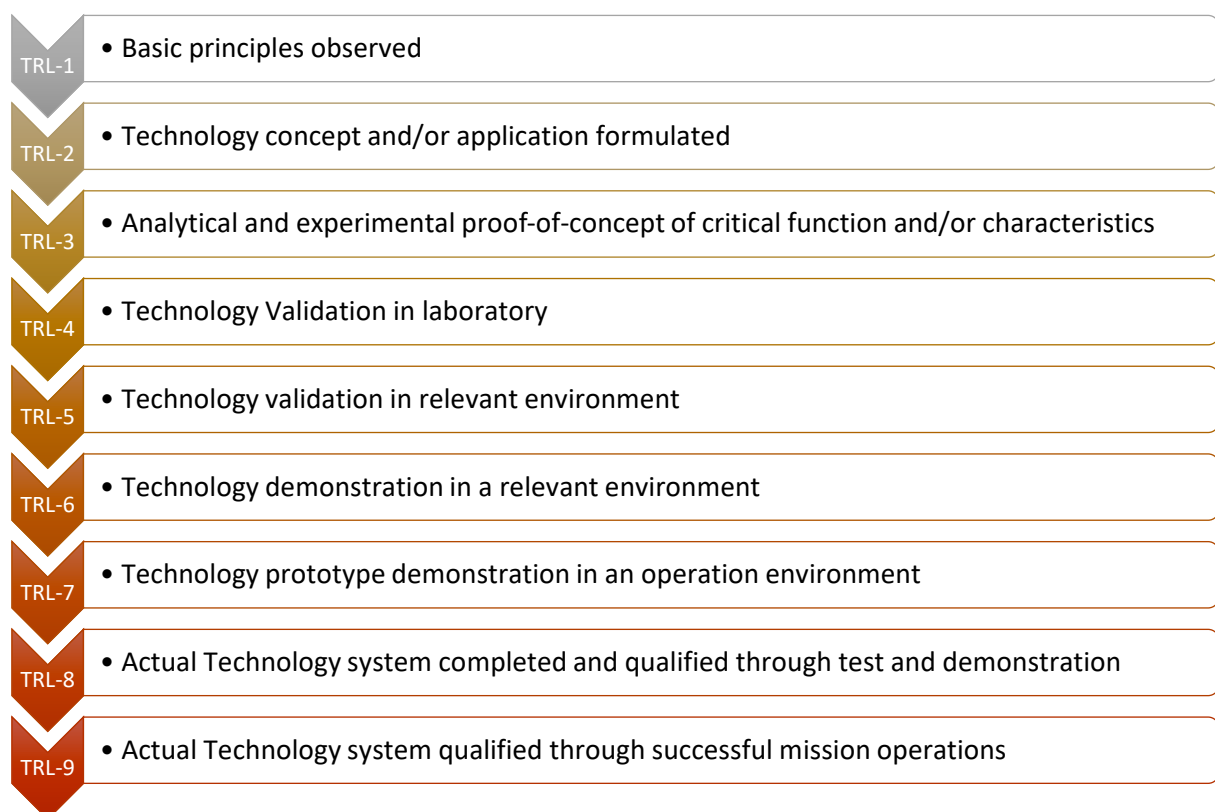


Figure 215. Technology Readiness Level – TLR ⁵¹⁵.

A7.8. Conclusions

The high-level assessment shows that in terms of CAPEX, the process should be the same order of magnitude than hydrothermal processes, due to similarities in the synthesis method, and similar or less expensive than the French Process. In terms of OPEX, OIS offers significant energy savings compared to the French Process and should be similar to other hydrothermal processes, depending on process conditions. However, the IL losses off-set the energy savings and the overall OPEX of OIS might be higher than the French Process. It appears that particle morphology can be controlled in the OIS process by adjusting the process conditions (e.g. temperature, water concentration and reaction time). Finally, from an environmental point of view, OIS offers clear advantages in terms of waste generated and energy consumption when compared to other processes.

The above suggests that the OIS process is an interesting alternative for ZnO particle production, and therefore, further research should be conducted to establish the feasibility of this concept as a viable synthesis route for advanced materials.

A7.8.1. Future research

The points mentioned in section A7.6 should be addressed at laboratory scale to collect data that will allow to bring the technology to commercial stage. They should cover both applications, *i.e.* particle formation and particle growth over metallic substrates. The next step should be to scale-up the process to the kg scale.

Once the experimental points have been confirmed, a more detailed process evaluation should be performed, in collaboration with vendors, to validate different technologies. Also, other hydrothermal processes should be modelled, and the overall environmental impact assessed through more detailed methods, such as Life Cycle Analyses (LCA), to establish the benefits of the OIS process vs. other technologies.

In parallel to the process development, products based on particles obtained *via* OIS should be explored to further justify the efforts of scaling-up the technology.

Appendix 8 – Supplementary information on the high-level TEA for the OIS Process

A8.1. Energy calculations for OIS evaluation

A8.1.1. Laboratory heat losses – Convection oven

The oven was heated to a given temperature, and when the temperature was stable for 10 minutes, the power was shut off. Using a chronometer and thermocouples, the time to cool down the mass of air inside the oven 1 °C was measured. From the internal volume of the oven (0.106 m³), the C_p and the density of the air, the energy equivalent to cool down the mass of air inside the oven can be calculated. Finally, the heat losses to the environment can be calculated by dividing this energy by the cool downtime. The numerical results are given in Table 72 and the graphical results, with a linear fit, in Figure 216.

Table 72. Heat losses from convection oven calculations.

Temp [C]	C _p Air [A] [kJ/Kg.°C]	Density Air [A] [kg/m ³]	Time [B] [s]	Mass Air [kg]	Energy [B] [kJ]	Heat Transfer [B] [kW]
50	0.9969	1.09214	432	0.1157	0.1153	0.0003
75	1.0015	1.01354	164	0.1074	0.1075	0.0007
100	1.0062	0.94552	104	0.1002	0.1008	0.0010
125	1.0110	0.88607	86	0.0939	0.0949	0.0011
150	1.0158	0.83366	60	0.0883	0.0897	0.0015
175	1.0208	0.78711	48	0.0834	0.0851	0.0018
200	1.0259	0.74550	38	0.0790	0.0810	0.0021

A. Taken from ref ³⁷.

B. Change in temperature of 1 °C.

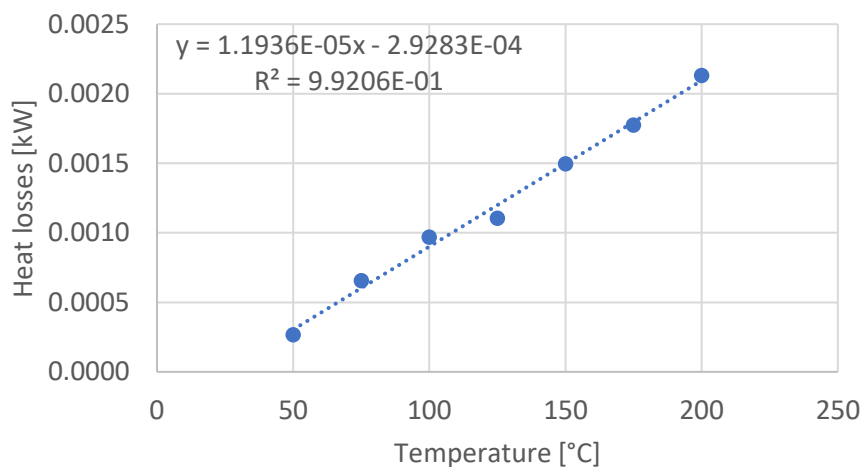


Figure 216. Heat losses from convection oven calculations.

A8.1.2. Energy cost and CO₂ emissions

The energy cost was calculated using the average values reported in the website (https://www.ukpower.co.uk/home_energy/tariffs-per-unit-kwh, access the 4th of January 2020). The values reported per kWh and were converted per kJ using Eq. 175. Emission conversion factors for 2019 in the UK taken from <https://www.gov.uk/government/publications/greenhouse-gas-reporting-conversion-factors-2019> (Conversion factors 2019: condensed set (for most users)). Energy cost and emissions equivalents are reported in Table 73.

Table 73. Average energy cost and CO₂ emissions equivalents in the UK.

	Energy Cost		CO ₂ emissions	
	[Pence / kWh]	[£ / kJ]	[kgCO ₂ e/ kWh]	[kgCO ₂ e/ kJ]
Electricity	12.736143	3.538x10 ⁻⁰⁵	0.20428	5.67x10 ⁻⁰⁵
Gas	2.838286	7.88x10 ⁻⁰⁶	0.2556	7.10x10 ⁻⁰⁵

$$Energy\ Cost\ \left[\frac{\pounds}{kJ}\right] = Energy\ Cost\ \left[\frac{pence}{kWh}\right] \cdot \frac{1\pounds}{100\ pence} \cdot \frac{1\ kWh}{3600\ kJ} \quad (175)$$

A8.1.3. Energy calculations

The heat required to elevate the temperature of a system has been calculated by integrating the C_p (Eq. 178) calculated with the Shomate Equation (Eqs.177 and Table 74). For some compounds shown in Table 75 the temperature dependence of the heat capacity was not found, and therefore, the C_p was considered constant.

$$t = \frac{T}{1000} \quad (176)$$

$$C_p^\circ = A + B \cdot t + C \cdot t^2 + D \cdot t^3 + \frac{E}{t^2} \quad (177)$$

$$\overline{C_p} = \int_{T_1}^{T_2} C_p^\circ dT \quad (178)$$

Where:

T Temperature (K)

t temperature (K) / 1000

C_p heat capacity (J/mol·K)

Table 74. Shomate equation parameters ¹⁷⁴.

Compound →	Water		Solid	Zinc	
	liquid	Gas		Liquid	Gas
State →					
Temp. [K] →	298 - 500	500 - 1700	298- 692.73	692.73 - 1180.173	1180.173 - 6000
Parameters ↓					
A	-203.6060	30.092	25.60123	31.38004	18.20166
B	1523.290	6.832514	-4.405292	-9.647635e-09	2.313999
C	-3196.413	6.793435	20.42206	6.798541e-09	-0.736547
D	2474.455	-2.53448	-7.399697	-1.574453e-09	0.07995
E	3.855326	0.082139	-0.045801	-3.249003e-10	1.073557
F	-256.5478	-250.881	-7.755964	-3.590873	126.9388
G	-488.7163	223.3967	72.91373	86.6816	184.6977
H	-285.8304	-241.8264	0.0	6.519007	130.4203

Table 75. Heat capacities for chemical compounds typically used in ZnO nanoparticle productions ¹⁴¹.

Compound	Heat Capacity [J/K·mol]
Zinc Oxide	40.3
Sodium Hydroxide	59.5
Zinc Acetate	153.6
Ethanol	112.4

The energy consumption to raise the temperature from 25 °C to a given temperature for zinc and water was plotted against the final temperature and the results are shown in Figure 217 and Figure 218 respectively. The vertical increments correspond to phase changes. The C_p for the IL [C₄C₁im]Cl (neat and aqueous) was taken from the literature (Figure 219) and correlations were fitted (Figure 220) to develop a numerical expression to calculate the C_p of aqueous [C₄C₁im]Cl solutions as a function of water content (molar fraction) and temperature (Eq. 179). A python script was developed to plot the energy consumption as a function of water content and temperature according to Eq. 179 and the result is shown in Figure 221.

$$C_p = (-0.7209X_{H_2O}^2 + 0.3301X_{H_2O} + 0.3956)T + 226.9378X_{H_2O}^2 - 351.7047X_{H_2O} + 199.3035 \quad (179)$$

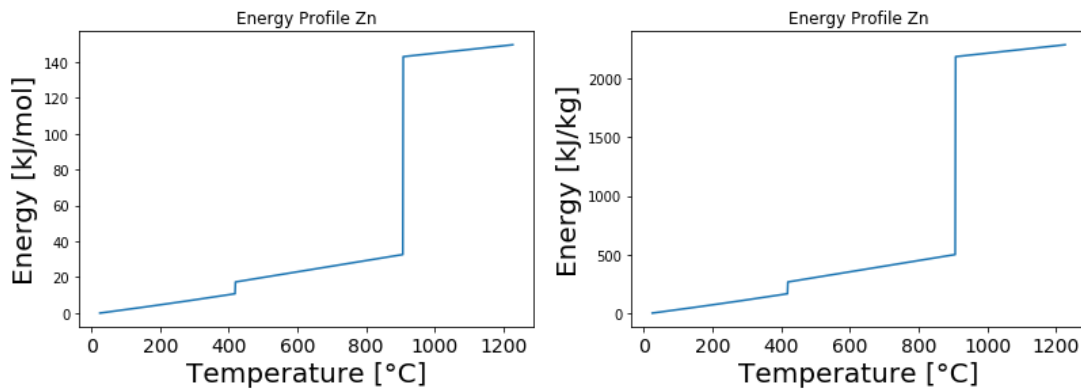


Figure 217. Energy consumption to raise the temperature of metallic zinc from 25 °C to a given temperature. Zinc melts at 420 °C and boils at 907 °C.

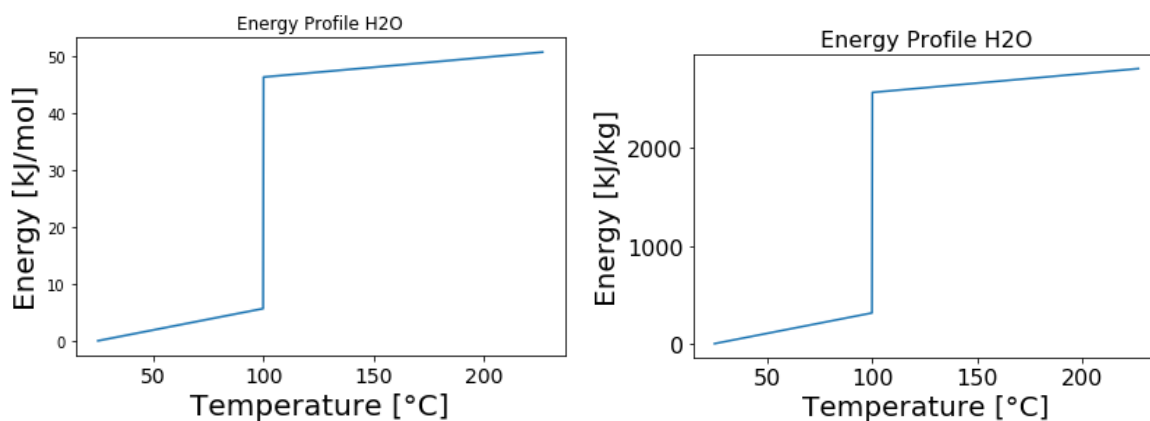


Figure 218. Energy consumption to raise the temperature of water from 25 °C to a given temperature. Water boils at 100 °C.

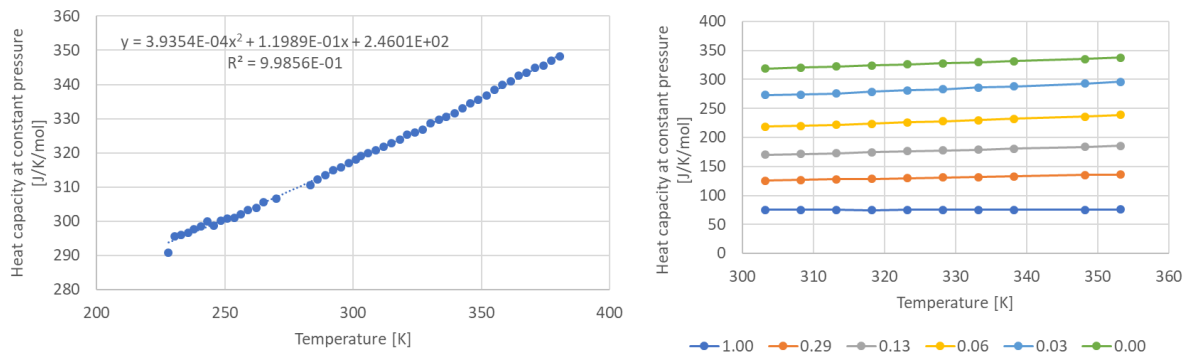


Figure 219. Heat capacity at constant pressure. Left: $[C_1C_4im]Cl$ metastable liquid⁵¹⁶. Right: $[C_1C_4im]Cl$ solutions as a function of water mol fraction⁵¹⁷. Water liquid phase heat capacity was calculated using Shomate Equation (Table 74). Metastable liquid data was used for Pure $[C_1C_4im]Cl$ ⁵¹⁶.

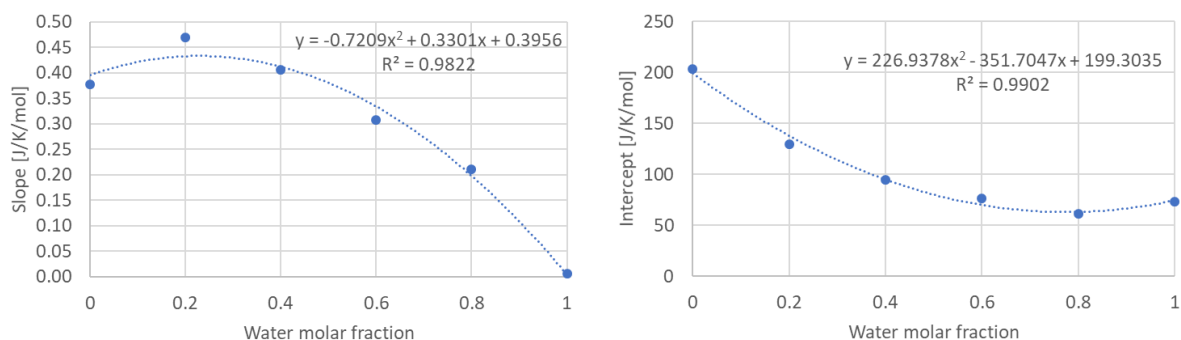


Figure 220. Fit parameters for the heat capacity at constant pressure for $[C_1C_4im]Cl$ solutions as a function of the water molar fraction.

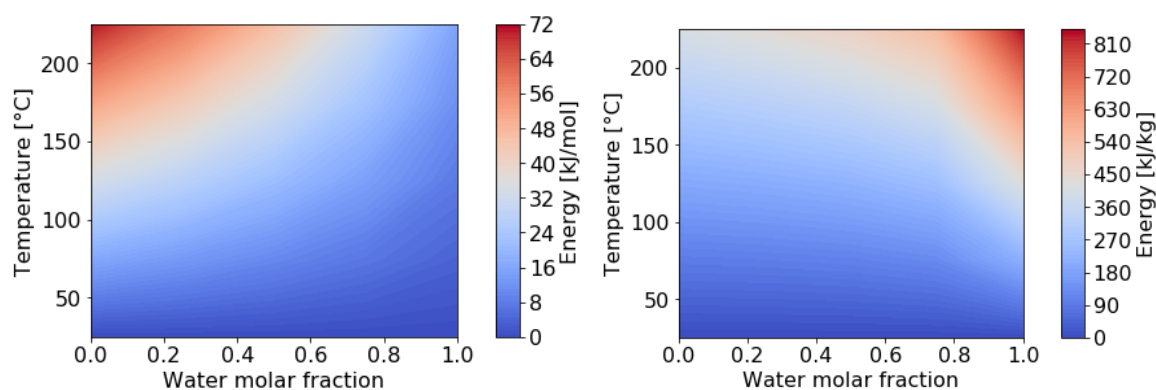


Figure 221. Energy consumption to raise the temperature of $[C_4C_1im]Cl$ solutions from 25 °C to a given temperature calculated with Eq. 179.

A8.2. ZnO laboratory-scale cost

The cost of producing ZnO nanoparticles at laboratory scale have been calculated by determining the quantities of the chemicals needed for the synthesis methods described in the literature (Table 62 and Table 61) and the chemical costs from a chemical supplier (Sigma-Aldrich) (Table 65 and Table 66). An example of these calculations was performed for the OIS Process (Table 76 and Table 77) and for a method based on zinc nitrate (method 4) (Table 62 and Table 61).

Table 76. Cost calculation example to produce 1 mol of ZnO via the OIS Process. Chemical purity taken into account. Chemical cost taken from Table 65 and Table 66. IL losses are assumed to 1% using a 1:1 solid:solvent ration (wt:wt) of a $[C_4C_1im]Cl$ solution 25 wt% water.

Chemical	Mol	Mass [g]	Cost [£]
Zn	1	66.05051	4.57
1-Butyl-3-methylimidazolium chloride ($\geq 98.0\%$ (HPLC))	0.003	0.490	0.47
		Total	5.04
		Total £ / g ZnO	0.06

Table 77. Cost calculation example to produce 1 mol of ZnO using zinc nitrate as metal precursor. Chemical purity taken into account. Chemical cost taken from Table 65 and Table 66.

Chemical	Mol	Mass [g]	Cost [£]
Zinc nitrate hexahydrate (purum p.a., crystallized, ≥99.0% (KT))	1	297.49	21.40
Sodium Hydroxide - reagent grade, ≥98%, pellets (anhydrous)	2	80	2.81
Starch	n.a	300	57.60
		Total	81.80
		Total / g ZnO	1.01

A8.3. CAPEX and OPEX estimations – OIS process

The following section describes the correlations used for CAPEX and OPEX estimations.

A8.3.1. Reactor

For the CAPEX evaluation, Mache’s correlations ⁴⁹¹ were used to evaluate a jacketed reactor, in carbon steel with a rubber liner rated for 150 psi, with and without agitation (Figure 222).

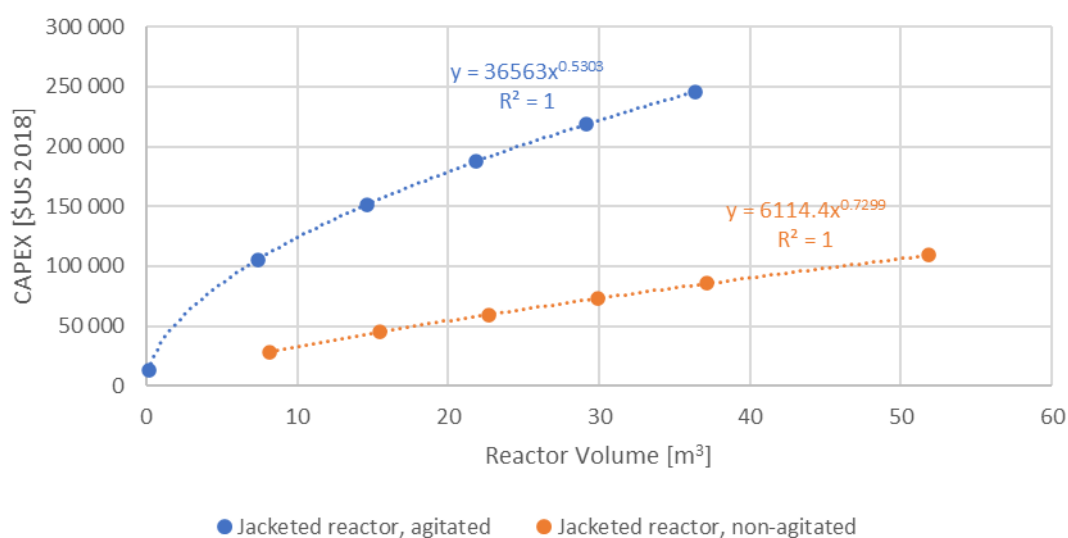


Figure 222. CAPEX for jacketed reactor as a function of the volume.

The electric power consumption has been calculated based on a 36.4 m³ reactor, with pitched blades, D/T ratio of 0.4 (Figure 223), scale of agitation 4, liquid density of 1200 kg/m³ and viscosity 50 cP ⁵¹⁸.

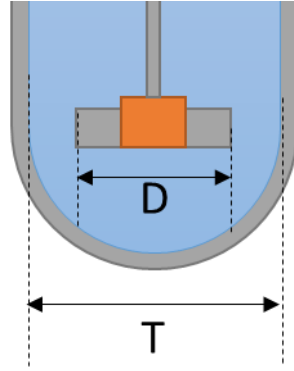


Figure 223. Agitator scheme for power calculation. Adapted from ref ⁵¹⁸

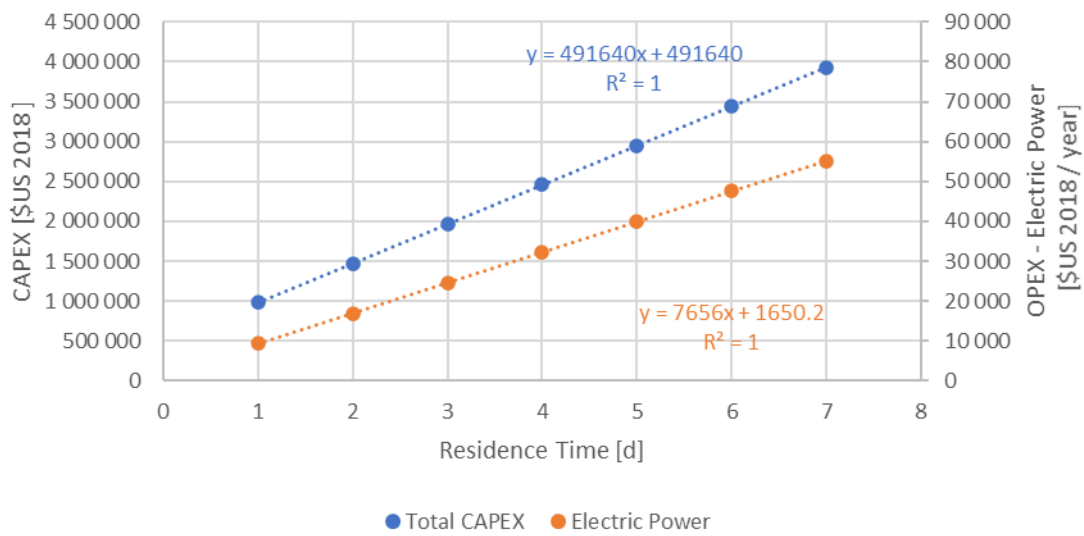


Figure 224. Total reactor CAPEX and OPEX as a function of residence time. The CAPEX is based on reactors of 8000 gal (36.4 m³) capacity. OPEX includes electric consumption for the loading/unloading pumps.

A8.3.1.1 Heat losses (reactor)

Therefore, a simplified approach to estimate heat losses was developed here based on the heat losses of an insulated pipe assuming an ambient temperature of 25 °C, a wind speed of 12.87 km/h and 1.5 inches thick insulator made of mineral wood ⁵¹⁹. As seen in Figure 225, the heat losses is a linear function of the diameter. Figure 226 shows the slope and intercept for a range of temperatures. The total heat loss calculated with Eq. 180 will be increased by 20% to account the tank/vessel head. Eq. 181 provides the estimated heat losses of a tank under these assumptions of 90 inches (2.3 m) diameter (D) extrapolated from Eq. 180 and 8.86 m height (L) (total volume 8000 gal or 36.4 m³ and L/D = 4).

$$Heat\ Loss_{pipe} \left[\frac{kw}{m} \right] = (4.01 \cdot 10^{-6} \cdot D[inches] + 7.12 \cdot 10^{-6}) \cdot T[^\circ C]^{1.58} \quad (180)$$

$$Heat\ Loss_{tank}[kw] = 0.391 \cdot T[^\circ C]^{1.58} \quad (181)$$

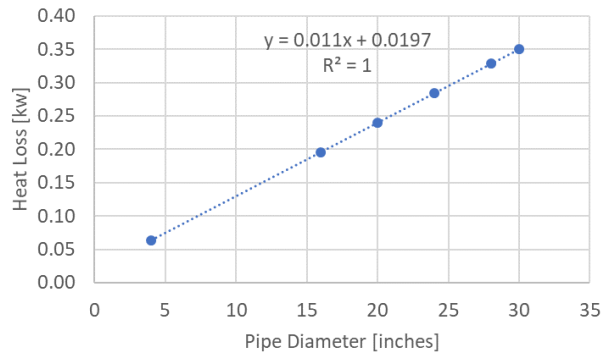


Figure 225. Heat loss estimates from an Insulated horizontal steel pipe (1.5 inches insulation thickness, mineral wood) ⁵¹⁹.

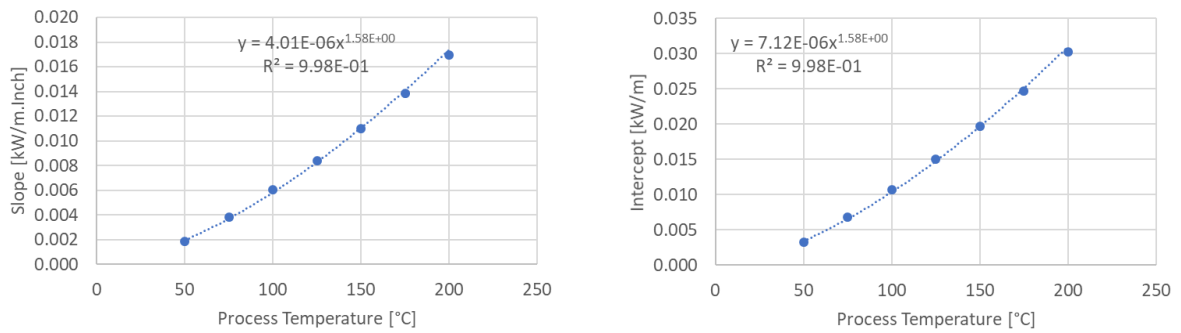


Figure 226. Correlations for insulated pipe heat loss calculations as a function of the process temperature.

A8.3.2. Centrifuge

The centrifuge cost scales with the diameter following a power law with exponent equals 0.94 as shown in Figure 227.

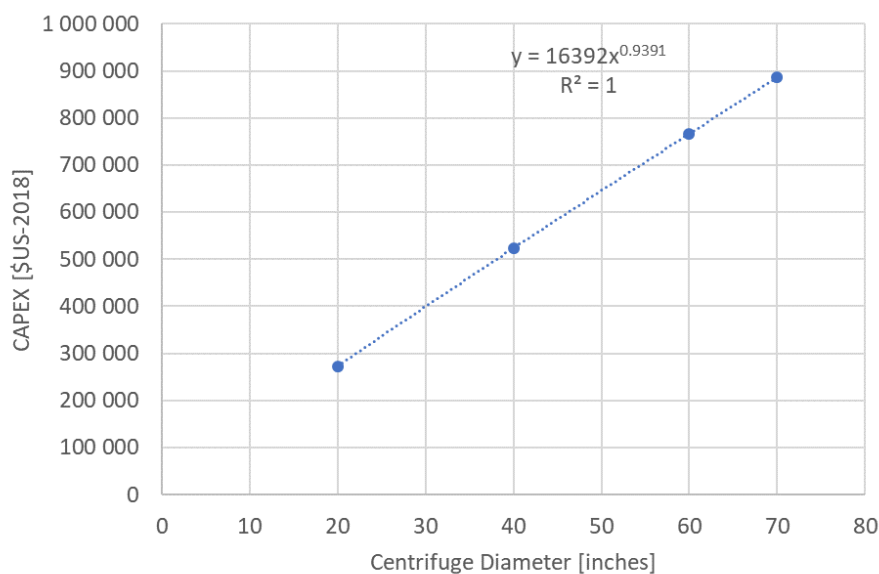


Figure 227. CAPEX for Hastelloy vertical centrifugal separator (Auto Batch) ⁴⁹¹.

A8.3.3. Vessels and tanks

The sizing of the vessels has been done assuming 3 h hold-up. The L/D ratio has been assumed 4, a thickness of 3 mm and a metal density of 7850 kg/m³ have been used to estimate the mass of metal. For the estimation, Hastelloy has been assumed for conservatives. All vessels are summed identical and 50% margin on the volume has been considered to account for the heads and vapour space. The cost of pressure vessels constructed in Hastelloy has been calculated using Mache's correlations ⁴⁹¹ (Figure 228). The cost of the pumps has been calculated assuming 2x100% configuration for water and IL pumps. The cost of a centrifugal pump (inline, 1-stage with a motor, 150 ft head, 1.5 inches, seal type: packing, fibreglass-reinforced plastic) is 10000 \$US and the agitators (propeller, top entering, 3 HP, carbon steel - rubber lined, atmospheric pressure) is 7100 \$US according to Mache's correlations ⁴⁹¹. This equipment cost for the pump and agitator corresponds to the 20 kton ZnO/year plant, for other capacities, the cost has been adjusted using Eq. 2 in Appendix 14 and an exponent of 0.5 for agitators and 0.8 for pumps (Table S2 in Appendix 15). CAPEX for horizontal tanks (fuel storage) made of fibreglass-reinforced plastic is given in Figure 229.

It is noteworthy that after scale correction, some pieces of equipment are smaller than the lower range for which the correlations were developed.

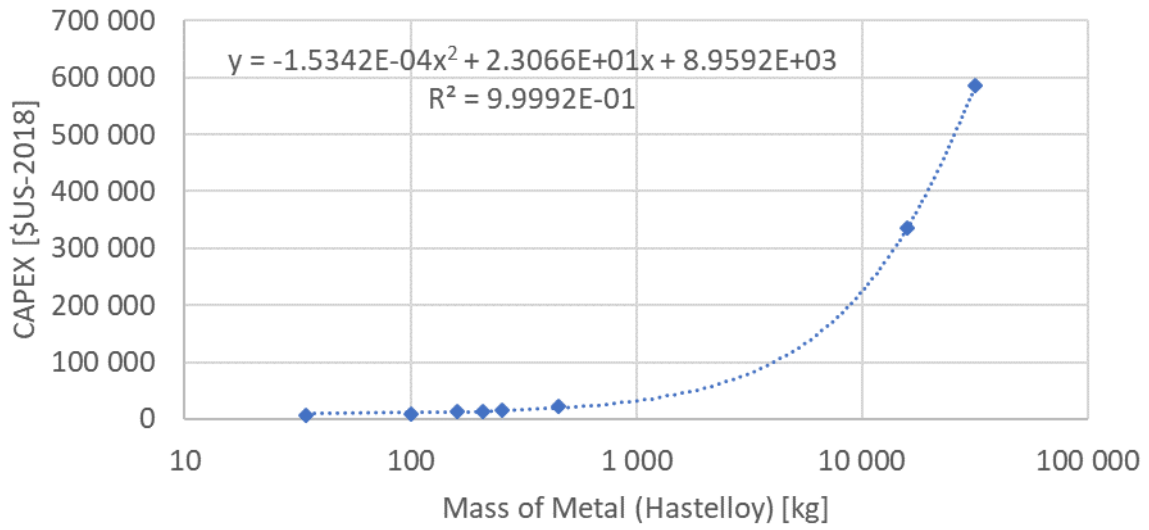


Figure 228. Vessel cost as a function of metal weight (Hastelloy).

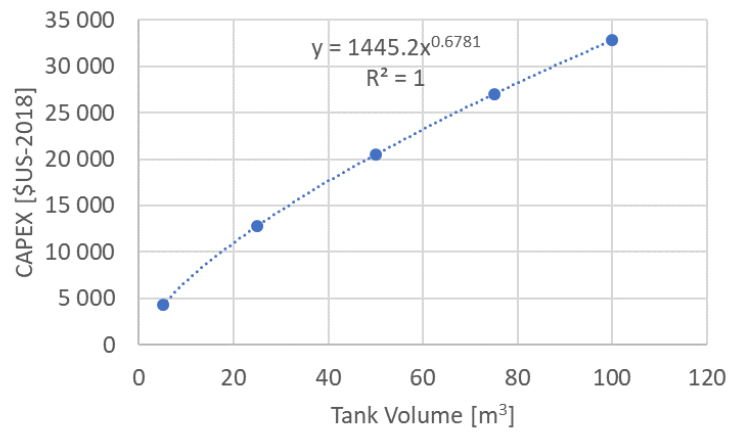


Figure 229. CAPEX for horizontal tank, fuel storage, made of fiberglass reinforced plastic ⁴⁹¹.

Appendix 9 - Specific area and equivalent particle size relationships

Equations 182 to 189 show the relationship between specific area and the equivalent particle size, assuming the particles are homogeneous non-porous spheres of equal diameter.

$$\text{Total Particles Eq. Area [m}^2\text{]} = N \cdot \pi D_{eq}^2 [\text{nm}^2] \cdot 10^{-18} \frac{\text{m}^2}{\text{nm}^2} \quad (182)$$

$$\text{Total Particles Eq. Volume} = N \cdot \frac{\pi D_{eq}^3}{6} \quad (183)$$

$$\text{Total Particles Eq. Mass} = \text{density} \cdot \text{Total Particles Eq. Volume} \quad (184)$$

$$\text{Total Particles Eq. Mass [g]} = \rho \left[\frac{\text{gr}}{\text{cm}^3} \right] \cdot N \cdot \frac{\pi D_{eq}^3}{6} [\text{nm}^3] \cdot 10^{-21} \frac{\text{cm}^3}{\text{nm}^3} \quad (185)$$

$$\text{Specific Area} \left[\frac{\text{m}^2}{\text{g}} \right] = \frac{\text{Total Particles Eq. Area [m}^2\text{]}}{\text{Total Particles Eq. Mass [g]}} \quad (186)$$

$$\text{Specific Area} \left[\frac{\text{m}^2}{\text{g}} \right] = \frac{N \cdot \pi D_{eq}^2 [\text{nm}^2] \cdot 10^{-18} \frac{\text{m}^2}{\text{nm}^2}}{\rho \left[\frac{\text{gr}}{\text{cm}^3} \right] \cdot N \cdot \frac{\pi D_{eq}^3}{6} [\text{nm}^3] \cdot 10^{-21} \frac{\text{cm}^3}{\text{nm}^3}} \quad (187)$$

$$\text{Specific Area} \left[\frac{\text{m}^2}{\text{g}} \right] = \frac{6 \cdot 10^3 \frac{\text{m}^2 \cdot \text{nm}}{\text{cm}^3}}{\rho \left[\frac{\text{g}}{\text{cm}^3} \right] \cdot D_{eq} [\text{nm}]} \quad (188)$$

$$D_{eq} [\text{nm}] = \frac{6 \cdot 10^3 \frac{\text{m}^2 \cdot \text{nm}}{\text{cm}^3}}{\rho \left[\frac{\text{g}}{\text{cm}^3} \right] \cdot \text{Specific Area} \left[\frac{\text{m}^2}{\text{g}} \right]} \quad (189)$$

Where:

N Number of particles

D_{eq} Equivalent particle diameter

ρ Density

Appendix 10 – Additional information on eucalyptus pretreatment

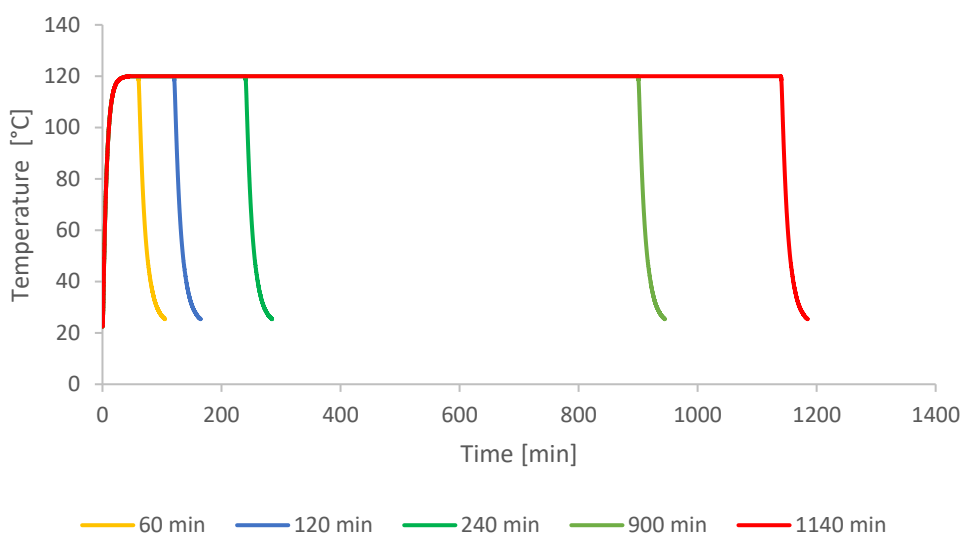


Figure 230. Typical reaction medium temperature inside an unstirred reaction tube (15 ml) at an oven temperature of 120 °C for different pretreatments times. Published by The Royal Society of Chemistry ³².

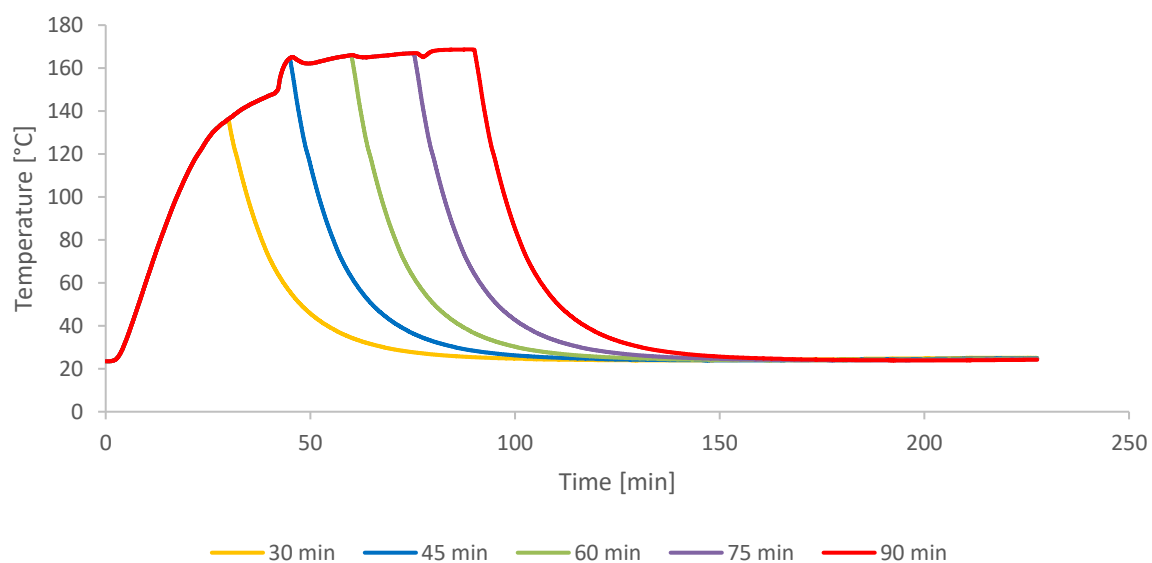


Figure 231. Typical reaction medium temperature inside an unstirred reaction tube (120 ml) at an oven temperature of 170 °C for different pretreatments times. Published by The Royal Society of Chemistry ³².

Table 78. Pulp composition, as determined by compositional analysis. Average of replicates ³².

Pretreatment conditions	Composition wt%						Extractive
	%Glucan	%Xylan	%ASL	%AIL	%Lignin	%Ash	
Untreated	50.3	10.0	5.2	28.1	33.3	-	0.7
120 °C - 60 min	74.9	10.6	4.0	24.8	28.8	-	-
120 °C - 120 min	79.3	3.8	3.4	20.9	24.3	-	-
120 °C - 240 min	89.9	2.2	2.3	16.2	18.5	-	-
120 °C - 900 min	98.3	-	1.5	11.8	13.3	-	-
120 °C - 1140 min	112.2	-	1.1	14.2	6.5	-	-
150 °C - 60 min	105.4	-	1.6	4.9	6.5	-	-
150 °C - 90 min	91.9	-	1.2	5.1	6.3	-	-
150 °C - 120 min	91.9	-	1.2	5.4	6.6	-	-
150 °C - 246 min	99.4	-	1.3	11.2	12.5	-	-
150 °C - 422 min	78.6	-	1.2	29.1	30.3	-	-
L0	56.9	8.1	4.5	25.0	29.5	-	-
LL	56.4	7.8	4.4	25.5	29.8	-	-
LH	54.2	8.6	4.5	25.2	29.7	-	-
H0	70.3	-	1.3	7.1	8.3	-	-
HL	88.8	-	1.0	8.0	9.0	-	-
HH	87.8	-	1.0	7.3	8.2	-	-

Table 79. Normalized average pulp composition ³².

Pretreatment conditions	Composition wt%						Extractive
	%Glucan	%Xylan	%ASL	%AIL	%Lignin	%Ash	
Untreated	53.4	10.6	5.5	29.8	35.3	-	0.7
120 °C - 60 min	65.5	9.3	3.5	21.7	25.2	-	-
120 °C - 120 min	73.9	3.5	3.1	19.5	22.6	-	-
120 °C - 240 min	81.3	2.0	2.1	14.6	16.7	-	-
120 °C - 900 min	88.1	-	1.3	10.6	11.9	-	-
120 °C - 1140 min	88.0	-	0.9	11.2	5.1	-	-
150 °C - 60 min	94.2	-	1.4	4.4	5.8	-	-
150 °C - 90 min	93.6	-	1.2	5.2	6.4	-	-
150 °C - 120 min	93.3	-	1.2	5.5	6.7	-	-
150 °C - 246 min	88.8	-	1.1	10.0	11.2	-	-
150 °C - 422 min	72.2	-	1.1	26.7	27.8	-	-
L0	60.2	8.6	4.8	26.4	31.2	-	-
LL	60.0	8.3	4.7	27.1	31.7	-	-
LH	58.6	9.3	4.8	27.3	32.1	-	-
H0	89.4	-	1.6	9.0	10.6	-	-
HL	90.8	-	1.0	8.1	9.2	-	-
HH	91.4	-	1.0	7.6	8.6	-	-

Table 80. Standard deviation in pulp composition determined by compositional analysis ³².

Pretreatment conditions	Composition errors (wt%)						
	%Glucan	%Xylan	%ASL	%AIL	%Lignin	%Ash	Extractive
Untreated	0.3	0.04	0.1	0.4	0.5	-	0.05
120 °C - 60 min	1	0.06	0.1	6	6	-	-
120 °C - 120 min	3	0.8	0.07	0.5	0.6	-	-
120 °C - 240 min	3	0.8	0.1	0.5	0.5	-	-
120 °C - 900 min	3	0.8	0.1	0.5	0.5	-	-
120 °C - 1140 min	4	-	0.1	0.5	0.5	-	-
150 °C - 60 min	4	-	0.1	1.0	1	-	-
150 °C - 90 min	0.2	-	0.01	1	1	-	-
150 °C - 120 min	4	-	0.1	0.1	0.1	-	-
150 °C - 246 min	4	-	0.1	0.3	0.3	-	-
150 °C - 422 min	4	-	0.1	5	5	-	-
L0	0.4	0.04	0.05	0.1	0.1	-	-
LL	2	0.6	0.06	0.7	0.8	-	-
LH	0.8	0.8	0.04	0.4	0.4	-	-
H0	2	0	0.4	1	2	-	-
HL	0.2	0	0.02	0.3	0.3	-	-
HH	0.6	0	0.03	0.3	0.3	-	-

Table 81. Pretreatment performance ³².

Pretreatment conditions	Pulp Yield (%)		Delignification (%)		Glucan Recovery (%)		Hemicellulose Removal (%)		Lignin Recovery (%) [A]		Lignin Yield (%) [B]	
	Value	Error	Value	Error	Value	Error	Value	Error	Value	Error	Value	Error
120 °C - 60 min	72.9	0.3	48	9	89	3	35.8	0.8	11.4	0.5	4.0	0.2
120 °C - 120 min	64	2	59	2	89	6	79	7	24	1	8.3	0.4
120 °C - 240 min	55	2	74	2	83	6	90	7	60	6	21	1
120 °C - 900 min	49.9	0.7	83	2	82	6	100	-	85	3	30	1
120 °C - 1140 min	49.6	0.7	83	2	82	7	100	-	92	2	32.5	0.7
150 °C - 60 min	48.1	0.7	92	3	85	7	100	-	66	4	23	1
150 °C - 90 min	45.9	0.4	92	3	80.5	0.8	100	-	77	3	27	1
150 °C - 120 min	45.1	0.2	91.5	0.5	79	7	100	-	86	14	31	5
150 °C - 246 min	40	2	87	1	67	7	100	-	73	3	26	1
150 °C - 422 min	41	3	67.9	6.9	55	7	100	-	66	13	23	5
L0	86.5	0.6	8.3	0.1	97	1	29.7	0.3	5.2	0.4	1.9	0.1
LL	87	2	7.6	0.4	98	5	31	3	5.4	0.1	1.89	0.02
LH	87.6	0.7	7.2	0.2	96	2	23	2	3.8	0.8	1.35	0.26
H0	51.2	0.3	30	5	86	2	100	-	56	5	20	1
HL	50.8	0.4	31	1	86.4	0.9	100	-	55	2	19.6	0.6
HH	52	2	31	2	88	3	100	-	56	2	19.6	0.3

A. Relative to the total lignin amount in untreated biomass.

B. Relative to the total biomass (dry basis).

Appendix 11 - ANOVA analysis (saccharification yields of IL pretreatment under CO₂ atmosphere)

The tables below were published by The Royal Society of Chemistry³²

	Saccharification Yield (% of theoretical maximum)	
	Experiment 1	Experiment 2
	H0	82.59
HL	84.78	85.46
HH	86.89	82.48
L0	7.56	7.28
LL	7.77	7.40
LH	6.93	7.12

ANOVA – High severity (pretreatment time 240 min)

<i>Groups</i>	<i>Count</i>	<i>Sum</i>	<i>Average</i>	<i>Variance</i>
H0	2	165.0966	82.54831	0.002841
HL	2	170.2453	85.12267	0.229667
HH	2	169.3778	84.68892	9.719482

<i>Source of Variation</i>	<i>SS</i>	<i>df</i>	<i>MS</i>	<i>F</i>	<i>P-value</i>	<i>F crit</i>
Between Groups	7.598446	2	3.799223	1.145265	0.427005	9.552094
Within Groups	9.951991	3	3.31733			
Total	17.55044	5				

ANOVA – High severity (pretreatment time 30 min)

<i>Groups</i>	<i>Count</i>	<i>Sum</i>	<i>Average</i>	<i>Variance</i>
L0	2	14.84474	7.42237	0.040372
LL	2	15.17159	7.585795	0.069103
LH	2	14.04833	7.024163	0.017522

<i>Source of Variation</i>	<i>SS</i>	<i>df</i>	<i>MS</i>	<i>F</i>	<i>P-value</i>	<i>F crit</i>
Between Groups	0.333804	2	0.166902	3.942683	0.144683	9.552094
Within Groups	0.126996	3	0.042332			
Total	0.4608	5				

Appendix 12- FTIR *Eucalyptus red grandis* pulps and lignin

Fourier transform infrared (FTIR) spectroscopy is can be used for wood characterization to determine cellulose or lignin content in the pulp, paper, and wood⁵²⁰. In this work, it has been used to address qualitatively the chemical changes of *Eucalyptus red grandis* wood during IL pretreatment. The FTIR spectra of the studied samples have been split into two information-rich regions, namely, the fingerprint region between 800 - 1800 cm^{-1} (call now onwards region I) and the range between 2600 - 4000 cm^{-1} (call now onwards region II). Usually, quantitative work requires recording the spectra on solid samples in KBr pellets. Additionally, the average of the spectra from several samples of the specimen is required for accurate determinations. As the FITR spectra are meant for qualitative analysis, only the spectra of 1 sample were recorded unless otherwise specified. In Figure 232, it can be seen the 2 spectra of the same specimen (untreated biomass). In the fingerprint region, the intensities of the 2 spectra match at wavenumbers higher than 1023 cm^{-1} and diverge at lower wavenumbers. In region II, the intensities form these 2 spectra match at wavenumbers greater than 3332 cm^{-1} and diverges al lower wavenumber. Unfortunately, these results show that quantitative analysis based on the intensities cannot be performed.

The spectrum in region II for all of the samples shows 4 peaks 2895, 2941, 3209 and 3332 cm^{-1} . It has been shown for *Eucalyptus globulus*, that the overall spectrum is the convolution of seven bands at 3567, 3423, 3342, 3278, 3106, 2921, and 2851 cm^{-1} , some of which are evidenced only by deconvolutions. The “fingerprint” region from 800 to 1800 cm^{-1} is very complicated, showing clearly 14 signals. However, for *Eucalyptus globulus*, it has been shown through deconvolution that there are twenty-seven bands. The deconvolution of the spectra were not performed as they are going to be used for quantitative assessment of the pretreatment. The assignments of these bands are presented in Table 83.

A comparison of FTIR spectra of the raw biomass and the ethanol extracted biomass shows no significant differences (Figure 232), most likely due to the low concentration of extractive present in the biomass and the fact that these substances might have bands that overlap with those of the main biomass components. In the region I, there is a reduction in the intensity of the bands at 1364 and 1428 cm^{-1} . In region II, It can be seen a change in the shape of the strong signal between 3000 and 3600 cm^{-1} is distorted due to changes in the intensities of the different bands encompasses this signal due to material removal.

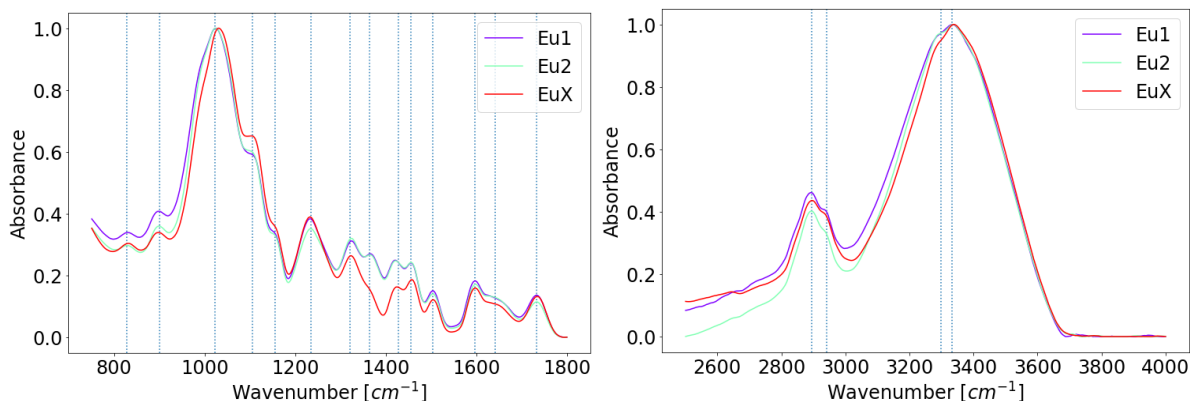


Figure 232. Normalized FTIR spectra of Eucalyptus Red Grandis (absorbance in arbitrary units). Eu1: untreated biomass. Eu2: untreated biomass. EuX. Ethanol-extracted biomass.

In Figure 233, the FTIR spectra of cellulose and Isolated lignin from *Eucalyptus red grandis* pretreatment with IL (120 °C and 60 min), the mildest pre-treatment conditions studied, had been overlapped with the FTIR spectra of the raw biomass. This clearly confirms the contributing signals from these biopolymers to the over biomass spectrum. The strong band at 1235 cm^{-1} has been attributed mainly to the C-O stretching in xylan, as it is not present in the cellulose nor the lignin spectra.

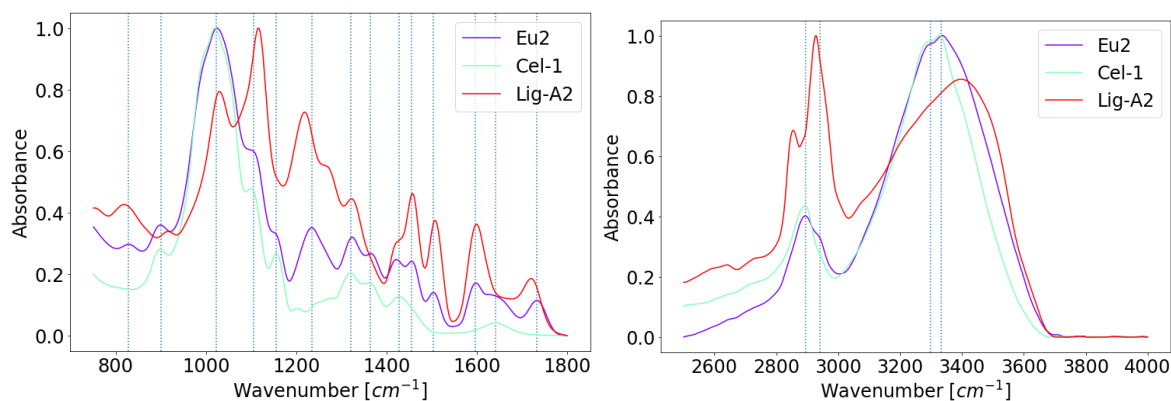


Figure 233. Normalized FTIR spectra of *Eucalyptus red grandis*, cellulose and lignin (absorbance in arbitrary units). Eu2: untreated biomass. Cel-1: cellulose. Lig-A2. Isolated lignin from *Eucalyptus red grandis* Pretreatment with IL (120 °C and 60 min).

Figure 234 and Figure 235 show the FTIR spectra of the pretreated biomass. It can be seen in Region I, the strong band at 1235 cm^{-1} that can be seen in the untreated biomass decreases with pretreatment severity, and it is no longer apparent in the spectra after 900 min pretreatment at 120 °C and it disappeared for all pretreated pulps at 150 °C. It is clear from the compositional analysis of the pre-treated pulp, that this trends in the intensity of this band, follow the overall xylene content of the pulp, and its further confirmation of the band assignment and that hemicellulose can be easily removed from the biomass. The band at 1734

cm^{-1} , assigned to C=O stretch in unconjugated ketones, follows a similar trend, therefore, must be a result of the xylan units. These bands can be used to identify the presence of hemicelluloses in the *Eucalyptus red grandis* pulps.

The maxima in the pulps FTIR spectra associated with lignin occurs at 827, 1428 and 1456 and 1597 cm^{-1} . The signal at 827 cm^{-1} also weakens at increasing pretreatment severities, and is no longer visible after 900 min pretreatment at 120 °C and it disappears for all pretreated pulps at 150 °C. In the spectra of the raw biomass, 2 maxima can be seen in the region 1400-1460 cm^{-1} , as the lignin removal takes place at high severities, it can be seen a decrease in the intensity in the peak at 1456 cm^{-1} but the peak at 1428 cm^{-1} remain, as cellulose also contain a band in that region (Figure 233). This modification results in a distortion of the spectra in that region to the point that the 2 maxima are no longer distinguishable. The band at 1597 cm^{-1} also decreases with severity, reaches a minimum, and increases at high severities. The decrease in the signals originating from lignin is expected due to the delignification process, however, the most severe pretreatment (150 °C and 422 min) yielded a pulp with high lignin content due to precipitation of condensed lignin and pseudo-lignins. This pulp does not show the band at 827 cm^{-1} . Additionally, there is a band at 1700 cm^{-1} that appears in the pretreated samples at higher severities, and it is most evident in the sample subjected to the highest severity, in which, the lignin content increased. We attribute this band to the precipitation of condensed lignin and pseudo-lignins back into the biomass. This proves that the molecular structure of the decondensed lignin is not the same as the native lignin. This recondensed lignin has an adverse effect in enzymatic saccharification as shown in Chapter 4.

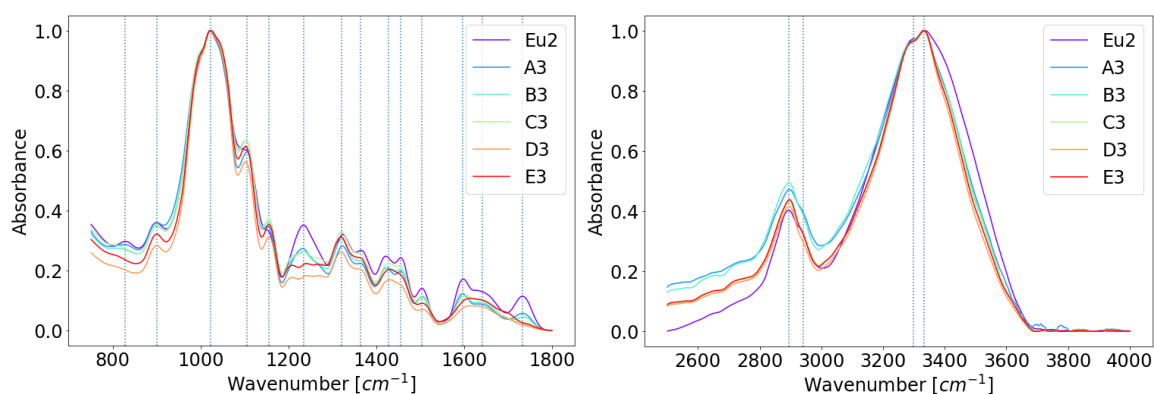


Figure 234. Normalized FTIR spectra of *Eucalyptus red grandis* pretreated with IL at 120 °C (absorbance in arbitrary units). Eu2: untreated biomass. A3: 60 min, B3: 120 min, C3: 240 min, D3: 900 min and E3: 1140 min.

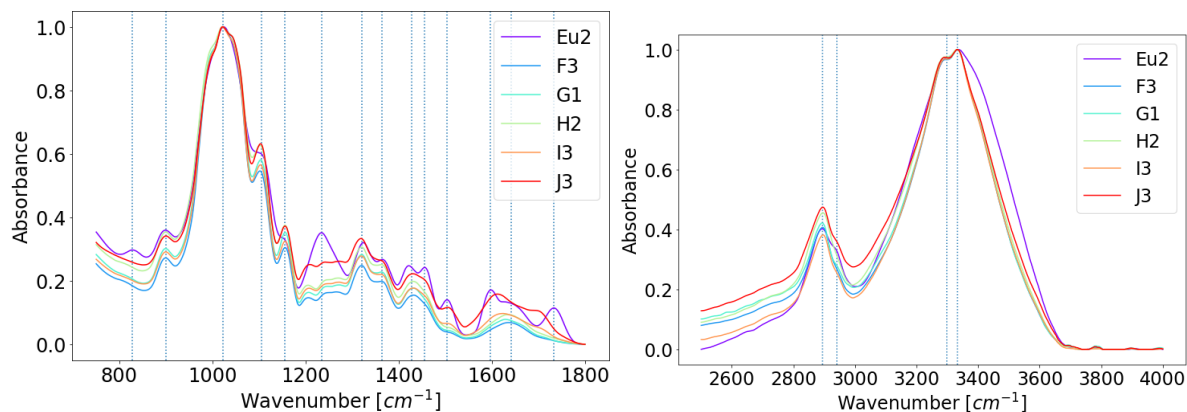


Figure 235. Normalized FTIR spectra of *Eucalyptus red grandis* pre-treated with IL at 150 °C (absorbance in arbitrary units). Eu2: untreated biomass, F3: 60 min, G1: 90 min, H2: 120 min, I3: 246 min and J2: 422 min.

There is less information in region II, however, it can be seen that the half-width at half maximum (HWHM) of the strong signal at $>3000\text{ cm}^{-1}$ has a maximum value for lignin and a minimum value for cellulose (Figure 233). It has been noticed that the position of the HWHM at high wavenumbers shifts to lower wavenumbers in samples with less lignin content. A plot of the lignin content vs the HWHM is shown in and shows a good degree of correlation, this approach can be used for a quick estimation of the lignin content within 5%.

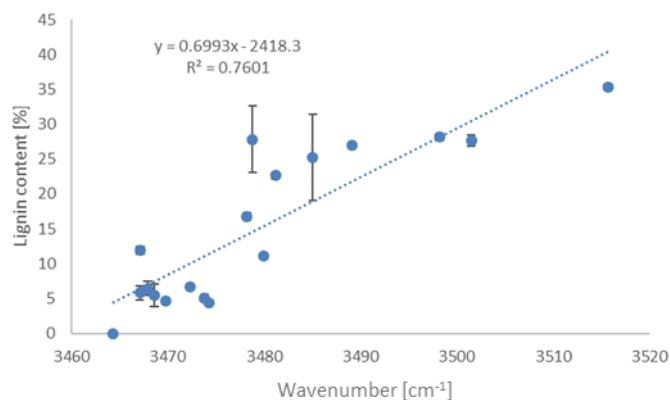


Figure 236. Total lignin content [%] in *Eucalyptus red grandis* pulps vs. wavenumber of the half-width at half maximum (HWHM) of the signal at 3332 cm^{-1} .

From Figure 237, it can be seen that the FTIR spectrum of *Eucalyptus red grandis* pretreated at 150 °C for 60 min is similar to the cellulose FTIR spectrum, further confirming the high cellulose contents of this pulp ($94 \pm 4\text{ wt}\%$).

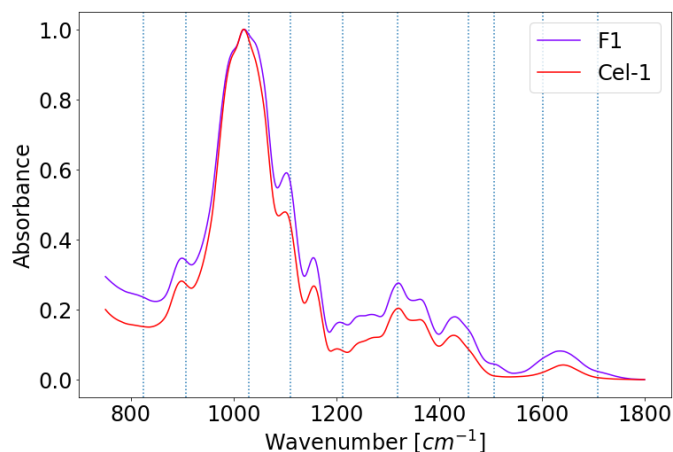


Figure 237. Pretreated *Eucalyptus red grandis* (150 °C and 60 min) (F1) vs. cellulose (Cel-1).

The FTIR spectra of the pulps pretreated under CO₂ atmosphere (Figure 238), shows 2 sets of signals corresponding to the low severity and the high severity experiments. Overall, there are no significant differences within the samples of each severity level (Lx and Hx), and as expected, the spectra of the low severity series are close to the one of the raw biomass due to very low pretreatment conditions. In region I, the signals from hemicelluloses disappear in the high severity cases, confirming complete xylene removal. The signals from lignin are significantly reduced. In region II, it can be seen the shift to lower wavenumbers of the HWHM of the signal at 3332 cm⁻¹ as severity increases.

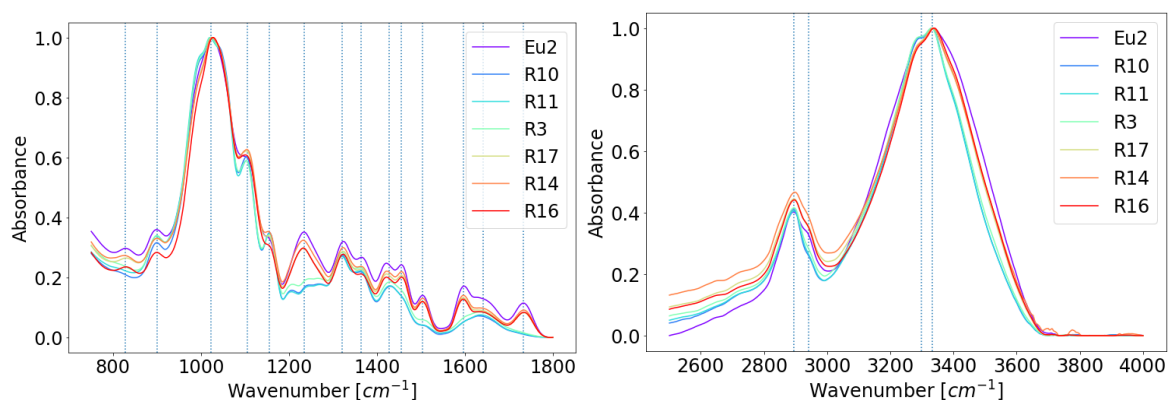


Figure 238. Normalized FTIR spectra of *Eucalyptus red grandis* pretreated with IL under CO₂ atmospheres (absorbance in arbitrary units). Eu2: untreated biomass. R10: H0, R11: HL, R3: HH, R17: L0, R14: LL, R16: LH.

The assignment of the bands of the FTIR spectra from the lignins isolated from the IonoSolv process is given in Table 82. Overall, the spectra do not show significant differences (Figure 239, Figure 240 and Figure 241). In region II, lignins from IonoSolv *Eucalyptus* shows a broad band at 3393 ± 8 cm⁻¹, attributed to the hydroxyl groups in phenolic and aliphatic structures, and two strong sharp bands centred around 2936 ± 4 and 2848 ± 4 cm⁻¹, predominantly arising from CH stretching in aromatic methoxyl groups and in methyl and methylene groups of side

chains⁵²¹. In the carbonyl/carboxyl region, weak to medium bands are found at $1710 \pm 7 \text{ cm}^{-1}$, originating from unconjugated carbonyl/carboxyl stretching. In some samples, a shoulder at around 1680 cm^{-1} , is apparent and can be associated with the conjugated carbonyl–carboxyl stretching. Aromatic skeleton vibrations at 1602 ± 1 , 1506.0 ± 0.9 and around 1426 cm^{-1} (as a shoulder) and the C–H deformation combined with aromatic ring vibration at $1457.8 \pm 0.7 \text{ cm}^{-1}$ are common for all lignins, although the intensity of the bands may differ. These aromatic bands show less dispersion in their wavenumbers compared to the other vibrations. The spectral region below 1400 cm^{-1} is more difficult to analyse since most bands result from the contribution from various vibration modes. However, this region contains vibrations that are specific to the different monolignol units and allows the structural characterisation of lignins⁵²².

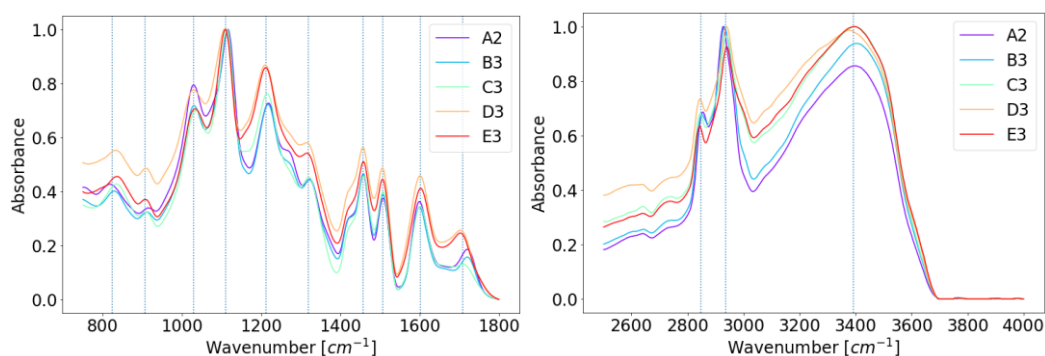


Figure 239. FTIR spectra from Eucalyptus-IonoSolv lignins isolated after pretreatment at $120 \text{ }^\circ\text{C}$ (absorbance in arbitrary units). A3: 60 min, B3: 120 min, C3: 240 min, D3: 900 min and E3: 1140 min.

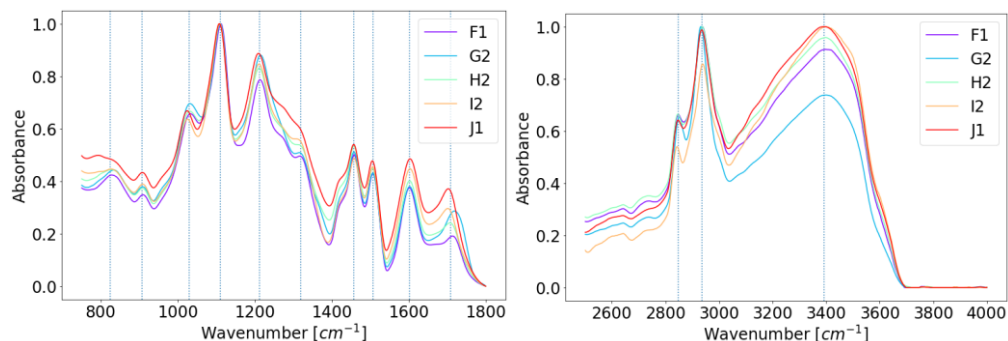


Figure 240. FTIR spectra from Eucalyptus-IonoSolv lignins isolated after pretreatment at $150 \text{ }^\circ\text{C}$ (absorbance in arbitrary units). F3: 60 min, G1: 90 min, H2: 120 min, I3: 246 min and J2: 422 min.

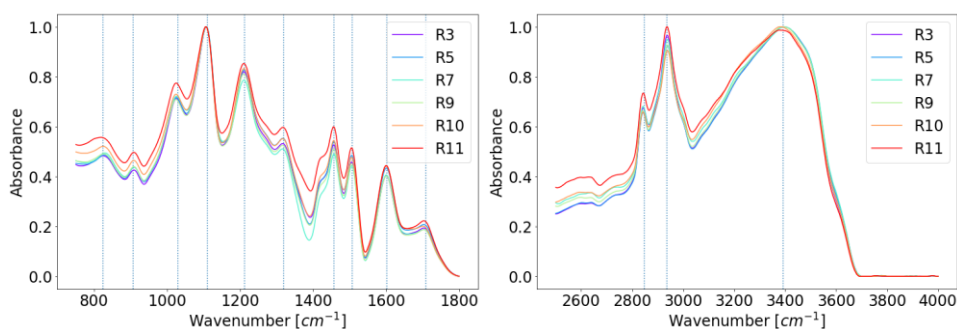


Figure 241. FTIR spectra from Eucalyptus-IonoSolv Lignins isolated after pre-treated with IL under CO₂ atmospheres (absorbance in arbitrary units). Eu2: untreated biomass. R10:bH0, R11: HL, R3:bHH, R17:bL0, R14:bLL , R16: LH.

Table 82. Lignin FTIR band assignment.

Band assignment ⁵²²	Wavenumber [cm ⁻¹]		
	<i>Eucalyptus red grandis</i>	<i>Acacia auriculaeformis</i> 522	<i>Pinus roxburghii</i> 522
O—H stretch (hydrogen-bonded)	3393 ± 8	3419	3414
C—H stretching	2936 ± 4	2919	2935
C—H stretching	2848 ± 4	2850	2842
C=O stretch (unconjugated)	1710 ± 7	1711	1714
Aromatic skeletal vibration + C=O stretching	1602 ± 1	1610	1606
Aromatic skeletal vibration	1506.6 ± 0.9	1502	1502
C—H deformation (methyl and methylene)	1457.8 ± 0.7	1462	1462
C—H in-plane deformation with aromatic ring stretching	Shoulder ~1426	1425	1425
C—O of syringyl ring	1319 ± 3	1315	-
C—O of guaiacyl ring	-	1267	1268
C—O of guaiacyl ring	1213 ± 3	1218	1214
Guaiacyl C—H and syringyl C—H	1110 ± 3	1113	1140
C—O of secondary alcohols		-	1086
C—O of primary alcohol, guaiacyl C—H	1030 ± 4	1026	1030
C—H out-of-plane	908 ± 17	912	866
C—H out-of-plane ⁵²³	825 ± 13		

Table 83. Eucalyptus FTIR band assignment.

Wavenumber [cm ⁻¹]	Band assignment ^[A]	<i>Eucalyptus</i>					
		<i>red grandis</i>	<i>renangs</i> 523		<i>globulus (chips)</i> ⁵²⁰	<i>globulus (BSP)</i> ^{520[B]}	<i>globulus (CBP)</i> ^{520[C]}
3580-3550	Free OH(6) and OH(2), weakly absorbed water				3568	3561	3557
3460-3405	O(2)H...O(6) intramolecular hydrogen bonds	3332			3423	3419	3421
3375-3340	O(3)H...O(5) intramolecular hydrogen bonds in cellulose		3300		3342	3344	3342
3310-3230	O(6)H...O(3) intermolecular hydrogen bonds in cellulose				3278	3277	3271
3175	-OH stretching intramolecular hydrogen bonds in cellulose II	3298			3106	3111	3106
2938-2920	Symmetric CH stretching in aromatic methoxyl groups and in methyl and methylene groups of side chains	2941			2921	2916	2911
2840-2835	Asymmetric CH stretching in aromatic methoxyl groups and in methyl and methylene groups of side chains	2895	2900		2852	2854	2852
1770-1760	C=O stretching in conjugated ketones				1757	-	-
1740-1720	C=O stretch in unconjugated ketones	1734	1730	1740	1740	-	-
1650-1640	Water associated with lignin or cellulose	1633	1650	0	1647	1637	1641
1610-1590	C=C stretching of the aromatic ring (S)	1597	1595	1595	1593	1594	1596
1515-1505	C=C stretching of the aromatic ring (G)	1505	1505	1505	1508	1510	1510
1470-1455	C-H asymmetric deformation in -OCH ₃ , CH ₂ in pyran ring symmetric scissoring	1456	1455 ^[d]	1464	1463	1455	1454
1430-1422	C-H asymmetric deformation in -OCH ₃	1428	1425 ^[e]	1424	1426	1427	1427
1375-1365	CH bending in cellulose I and cellulose II and hemicellulose	1364	1370	1375	1376	1373	1373
1335-1320	C1-O vibrations in S derivatives, CH in-plane bending in cellulose I and cellulose II	1322	1325	1329	1331	1338	1337
1315	CH ₂ wagging in cellulose I and cellulose II				1315	1317	1316
1282-1277	CH deformation in cellulose I and cellulose II				-	1283	1282
1268	Guaiacyl ring breathing, C-O linkage in guaiacyl aromatic methoxyl groups				1259	1263	1259
1235-1230	Syringyl ring breathing and C-O stretching in lignin and xylan	1235	1235	1239	1231	1234	1234
1205-1200	OH in-plane bending in cellulose I and cellulose II				1205	1203	1203
1162-1125	C-O-C asymmetric stretching in cellulose I and cellulose II	1156	1160	1157	1162	1166	1166
1140	Aromatic C-H in-plane deformation; typical for G units, where G condensed. G etherified			1122	1127	1130	1128
1128-1110	Aromatic C-H in-plane deformation (typical for S units), C=O stretch	1105	1110 ^[f]		1108	1111	1113

Wavenumber [cm ⁻¹]	Band assignment ^[A]	<i>Eucalyptus</i>					
		<i>red grandis</i>	<i>renangs</i> ⁵²³		<i>globulus (chips)</i> ⁵²⁰	<i>globulus (BSP)</i> ^{520[B]}	<i>globulus (CBP)</i> ^{520[C]}
1086-1075	C-O deformation in secondary alcohols and aliphatic ethers				1081	1079	-
1060-1015	C-O valence vibration mainly from C(3)-O(3)H3	0	1050 ^[G]	1047	1056	1060	1060
1047-1004	C-O stretching in cellulose I and cellulose II	1023	1030	0	1034	1029	1027
996-985	C-O valence vibration		990		988	987	994
970	=CH out-of-plane deformation (trans) ^b				959	961	957
930-915	Aromatic C-H out-of-plane deformations, pyran ring vibration				932	928	933
	C-H deformation in cellulose	900	895	897			
	Out of plane deformation Vibration of hydrogen atoms attached to 1,3,4,5- substituted benzene ring, as in a syringyl linkage ⁵²³	827	835	0			

- A. Band assignment as per "Spectral Characterization of Eucalyptus Wood"⁵²⁰ unless otherwise stated. S: syringyl; G: guaiacyl.
 B. BSP: brown stock pulp.
 C. CBP: chlorite-bleached pulp.
 D. Band assigned as CH₂ deformation vibn. in lignin and xylan + Aromatic skeletal vibn. in lignin in reference ⁵²³.
 E. Band assigned as CH₂ scissor vibn. in cellulose + CH₃ bending vibn. in lignin in reference ⁵²³.
 F. Band assigned as O — H association band in cellulose and hemicellulose in reference ⁵²³.
 G. C=O stretching vibn. In cellulose and hemicellulose in reference ⁵²³

Appendix 13 - Supplementary information on the bioenergy assessment

A12.1. Process description - Reference project

The following sections provide a brief description of the process units. For more details refers to the original reference ²³⁷.

A12.1.1. Section 1000 - Feedstock handling

The feedstock handling system receives chipped wood from the eucalyptus tree farm, removes metal and oversized material, contains 14 days of storage, and supplies a product to the process with the correct chip size ²³⁷.

A12.1.2. Section 100 – Pretreatment

The processed chips are conveyed to the pretreatment section where the wood chips are impregnated with a 0.2 wt% concentration of sulfuric acid. This pretreatment step enhances the desirable effects of the steam explosion treatment (higher glucose yields) while minimizing the severity of the steam explosion conditions ²³⁷.

A12.1.3. Section 200 - Steam explosion/wash

The acid-soaked wood chips are fed into the steam explosion guns where high-pressure steam is injected to raise the temperature and pressure to 240 °C (464 °F) and 32.4 barg (470 psig), respectively. The wood chips are cooked for 5 seconds at temperature and exploded into a medium pressure flash vessel. The steam explosion treatment enhances the accessibility of the wood to enzyme hydrolysis by disrupting the cellulose microfibrils, detaching the lignin, and increasing the surface area of the cellulose. The energy of the steam explosion is recovered as 4.14 barg (60 psig) steam in the HP flash vessel for process use. The exploded pulp is cooled in a vacuum flash and then washed in the counter-current water/ alkali wash to remove soluble hemicellulose (pentose) sugars and extract lignin with sodium hydroxide ²³⁷.

The water wash is essential to remove the water-soluble degradation products that are inhibitors of yeast fermentation and the production and activity of the enzyme complex. Lignin is removed prior to hydrolysis because of its potential interference with the enzyme recovery and hydrolysis performance ²³⁷.

The recovered lignin is combusted as boiler fuel for the production of process steam. 8% of the washed cellulose stream is conveyed to the enzyme production section where the total hydrolysis makeup enzyme requirement is produced ²³⁷.

A12.1.4. Section 300 - Enzyme production

The total hydrolysis makeup enzyme requirement is provided by this unit. The enzyme production section consists of two trains of three batch-fed fermenters. The system design utilizes the Rut-C-30 strain of *Trichoderma reesei* and was modelled with experimental data developed at the University of California, in Berkeley. Corn steep liquor (30 g/l at 54% solids) is added to supplement the media nutrients. In addition to the corn steep liquor, a supplemental nitrogen source and pH regulator, ammonia, is added in the amount of 23 g/l. This amount was based on the quantity required to maintain nitrogen balance for enzyme production and cell synthesis ²³⁷.

A12.1.5. Section 400 - Hydrolysis

In this Unit, fermentable sugars are formed by enzymatic hydrolysis on the remaining washed cellulose stream. The glucose concentration in hydrolysis was chosen as 5.7 wt% with an anticipated yield of 84% of cellulose conversion within 48 hours. This information was based on data generated from a steam-exploded corn stover at the University of California, Berkeley, since information on steam-exploded eucalyptus was not available at the time of the study ²³⁷.

Enzyme recovery was included as part of the base case design, which assumed a 50% recovery of enzyme filter paper activity ²³⁷.

A12.1.6. Section 500 - Evaporation

The hydrolysate stream is concentrated in a five-stage, multi-effect evaporator from 5.7 wt% to 14.7 wt% which is readily adaptable to commercial fermentation and alcohol recovery technologies at the time the study was performed (1987) ²³⁷.

A12.1.7. Section 600 - Fermentation

The hydrolysate stream is fermented in an immobilized yeast, fluidized bed, continuous fermentation system. Test results indicated that about 95% of theoretical conversion is possible when operating at 30-32 °C (86 – 90 °F). For mass balance purposes, all of the sugars

were assumed to ferment at the rate, with 2% of the sugar used for yeast production and 3% for by-product formation ²³⁷.

A small quantity of oxygen is added by an air sparge compressor to maintain yeast productivity. The fermenters are maintained below 32 °C (90 °F) by internal fermenter coolers. The plant cooling water supply temperature is too high to provide adequate cooling of the fermenters: therefore, a package chilled water system is provided. It was mentioned in the report that approximately 80% of the CO₂ could be recovered as a saleable by-product. Recovery equipment was not included in the base case design ²³⁷.

A12.1.8. Section 700 – Distillation

The resultant ethanol is recovered in a standard beer distillation system is designed to produce 99.98% ethanol. The beer distillation takes place in a conventional atmospheric column used to produce an azeotropic ethanol/water product. The azeotropic mixtures (95% ethanol and 5% water by volume), is sent to the anhydrous system which consists of two distillation columns for furtherer drying. In this system, cyclohexane is used to separate the near azeotropic ethanol ²³⁷.

A12.1.9. Section 800 - Anaerobic digestion

The digester is a 3.5-million-gallon anaerobic filter packed with corrugated plastic media which supports a film of active microorganisms. The organic components from the feed stream are biologically converted to a 50 to 60% methane gas stream which is burned as boiler fuel. The COD (Chemical Oxygen Demand) reduction is about 80%. The wastewater from the plant first enters the digester hold tank. The wastewater is then cooled in the digester feed cooler prior to entry into the anaerobic digester. The liquid overflow from the digester is sent to the wastewater treating system for final treating. The methane-rich gas is compressed in the methane gas compressor for use as boiler fuel. A gas storage sphere is included for plant storage capacity ²³⁷.

A12.1.10. Other units

The plant includes other process units that will not be further described. For more information, refer to the original reference ²³⁷. The other units are 900 – Boiler, 1100 - Cooling Water, 1200 – Waste treatment/Vent Scrubbing, 1300 - Chemical Handling, 1400 - Product Storage and Unloading, and 1500 Instrument Air/Fire Protection (buildings and miscellaneous auxiliaries).

A12.2. Process description - ionoSolv process

A12.2.1. Unit 100 - Fractionation

Prepared feedstock feeds a series of Batch Reactors working in parallel, where it is mixed with the pre-heated ionic liquid-water mixture. During the fractionation step, the majority of the lignin and hemicelluloses are dissolved in the ionic liquid, whilst cellulose and a small fraction of the hemicellulose and lignin remain in the solid phase, referred as pulp. A heating jacket keeps the content of the reactors at a constant temperature. The reactor operating conditions used for the estimation are given in Table 84. These values correspond to the maximum sugar recovery as shown in Chapter 6. It is noteworthy to mention that there are other parameters that could be optimized to boost production, such as water content, base:acid ratio and type of ionic liquid, but experimental data needs to be developed.

Table 84. Pretreatment conditions.

Parameter	Value
Temperature	150 °C
Pressure	7 bar
Residence Time	60 min
Glucose Yield	86%
Pulp composition after pretreatment	Refer to Table 80

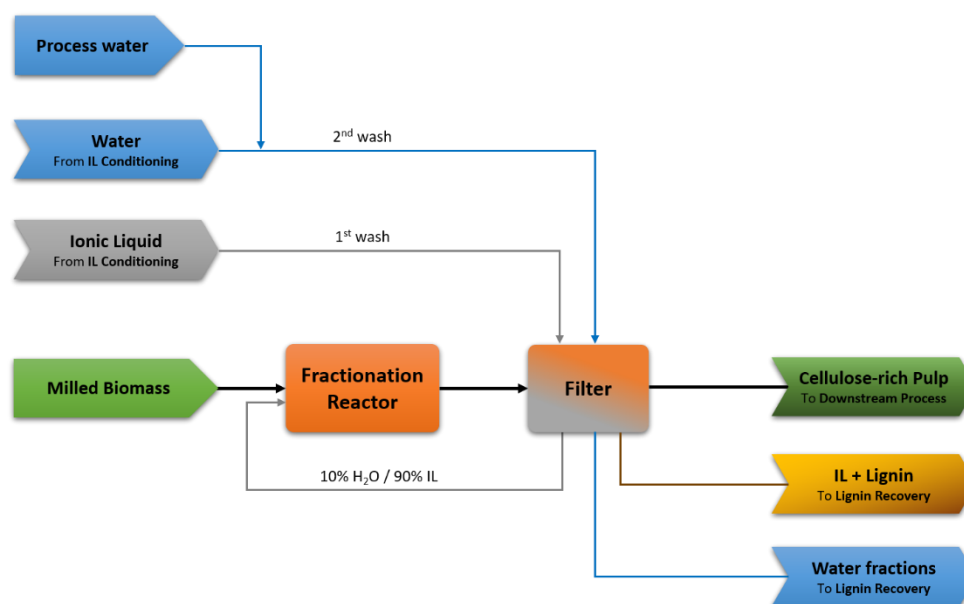


Figure 242. Fractionation Unit Block Flow Diagram.

At the end of the Fractionation step the slurry obtained is sent to the IL Preheater (H-101) to preheat the ionic liquid entering the reactor. Once cooled, the slurry enters the Slurry Buffer Vessel. The additional heating of the ionic liquid is supplied by the IL Heater (H-102) (Figure 242).

The Treated Pulp Pump (P-101 A/B) sends the slurry from the Slurry Buffer Vessel to the Cellulose Filter (F-101). In this filtration step, the pulp (solid cellulose fraction) is separated from the filtrate which contains hemicellulose, lignin and organic molecules such as acetic acid, oils, extractives, furfurals and other hemicellulose degradation products.

During the filtration (Figure 243), the slurry is fed to the filter and the pulp forms a cake on the filter element whilst the liquid phase passes through. This filtrate is pumped to the IL/Lignin Buffer Tank (V-201) in the Lignin Recovery Unit with the Cellulose Filter Pump (P-102 A/B). The pulp stays in the filter system for two subsequent wash steps.

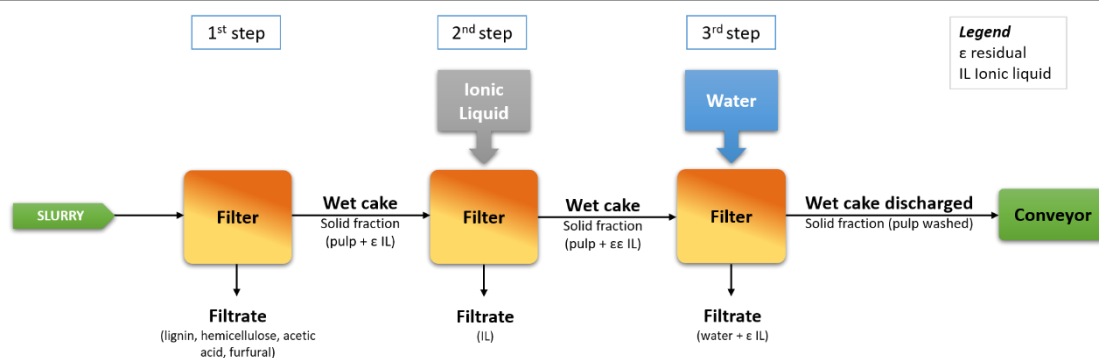


Figure 243. Filter operating sequence.

Regenerated IL from the Ionic Liquid Conditioning unit is used for the first wash. After the wash step, the recovered IL is routed to the IL Buffer Tank (V-101). From there, the IL Pump (P-103 A/B) transfers it through the heat recovery system to the Fractionation Reactor. The aim of this first wash with IL is to maximise the removal of solubilised lignin from the wet filter cake as it might otherwise precipitate during the water wash.

The second and final wash is performed with water and it is performed in order to remove IL from the pulp to minimize IL losses in the process and to generate an IL-free pulp suitable as a cellulose-rich product or used for biofuel production. The water exiting the filter is divided into two fractions. The first fraction, the most concentrated, passes through the filter cake and is sent with the Cellulose Filter Pump (P-102 A/B) to the Lignin recovery unit. The second fraction finishes the wash and is sent with the same pump to the Water Buffer Tank (V-202). For different downstream applications and as a function of the targeted cellulose purity, this second wash can be adapted. The pulp cake is discharged to the Cellulose Screw Conveyor (C-101). If required, cellulose can be further air-dried or bone-dried in an additional specific dryer.

A12.2.2. Unit 2000 – Lignin recovery

Contrary to the cellulose which remains solid throughout Fractionation, the lignin is mostly dissolved into the ionic liquid solution however becomes insoluble upon dilution of the ionic liquid with water. Therefore, in the Lignin Recovery unit, lignin is precipitated by mixing water with the ionic liquid solution in the Lignin Precipitation Vessel (V-203).

A continuous flow of IL/Lignin mixture and water is achieved in the IL/Lignin/Water Mixer (M-201). The IL/Lignin Buffer Pump (P-201 A/B) supplies IL/Lignin while water comes from either the first fraction of the pulp water wash or from the Water Buffer Tank (V-202) flowed by the Water Buffer Pump (P-202 A/B). Good mixing of the ionic liquid containing dissolved lignin with water is necessary to maximise lignin recovery. The mixed solution flows into the Lignin Precipitation Vessel (V-203) which provides residence time for the precipitated lignin to reach sufficient particle size for the filtration and minimise the amount of water required.

The mixture exiting the vessel through the Lignin Slurry Pump (P-203 A/B) is composed of solid lignin, water, ionic liquid and other minor components and it is sent to the Lignin Filter (F-201), where the precipitated lignin is separated. The lignin remains in the filter while the filtrate, which contains ionic liquid and water, is transferred to the Ionic Liquid Conditioning (Unit 3000) with the Lignin Filter Pump (P-204 A/B). Then, a water wash is used to minimise ionic liquid loss. The filtrate of the water wash is recycled back to the Water Buffer Tank (V-202) with the Lignin Filter Pump (P-204 A/B).

The Water Buffer Pump (P-202 A/B) distributes water for the lignin wash, the precipitation and to the drain.

After being air-dried and discharged, lignin is sent with the Lignin Screw Conveyor (C-201) to a boiler to be combusted to provide the energy required for the process. It is noteworthy mentioning that if applications are found for lignin, it would positively impact the economy of the plant if it can be sold at a higher price than the equivalent HHV.

A12.2.3. Unit 3000 - Ionic liquid conditioning

The purpose of this unit is to concentrate the ionic liquid solution by removing the excess of water and return to the initial ratio of 10 wt% water (or higher, if the feedstock has lower moisture content).

The Diluted IL Buffer Tank (V-301) receives an intermittent flow of dilute ionic liquid from the Lignin Filter (F-201). The Evaporator Feed Pump (P-301 A/B) continuously feeds a multiple-effect evaporation system, the Evaporator Package (Z-301).

In the first effect, steam is injected at a set pressure. Then, in each following effect, the pressure is decreased so that part of the duty is reused, and no additional steam is injected. Ionic liquid is increasingly concentrated while water is being removed.

All streams of water from each effect are collected and recycled back for the wash after pulp filtration with the Post-Evaporator Water Pump (P-302 A/B). Organic compounds are concentrated in the water stream. Therefore, a purge is necessary to avoid their accumulation in the recycle loop.

The recovered ionic liquid stream is pumped with the Concentrated IL Pump (P-303 A/B) into the IL Mixing Tank (V-302). Any loss of ionic liquid which happens on the course of the process is compensated by the injection of fresh ionic liquid into this tank (V-302). The fresh ionic liquid is stored in the Fresh IL Storage Tank (T-301) and injected with the Fresh IL Pump (P-305 A/B). If the ionic liquid molar ratio (acidity or pH) needs to be adjusted, sulfuric acid can be introduced from the Sulfuric Acid Storage Tank (T-302) with the Sulfuric Acid Injection Pump (P-306) and mixed using the agitator. After the mixing tank, the Recycled IL Pump (P-304 A/B) sends the ionic liquid to the Cellulose Filter (F-101) in the Fractionation unit.

The IL Draining Tank (T-303) is used for disposal or temporary storage of ionic liquid during maintenance operations.

A12.3. Biomass fractionation modelling in HYSYS

A12.3.1. Model parameters

The IonoSolv process modelled as solids in HYSYS V8.8. and the thermodynamic package “glycol package”.

Table 85. Simulation parameters.

Parameter	Value	Remarks
Pre-treatment Temperature	150 °C	Biomass dependent. To be adjusted.
Pre-treatment Time	30 min	Biomass dependent. To be adjusted.
Solid Loading	1:5	Calculated as dry biomass divided by the sum of the IL solution plus moisture content. Solubilised components not taken into account.
Water content in IL	20 wt%	For high moisture content biomass (50 wt%) the IL is dried to 10 wt%.
Water for lignin precipitation	1 equivalent	Calculated as the total water mass in the precipitation vessel divided by IL mass
Wash Water	10 kg H ₂ O / 1kg of solid (dry basis)	Water from the first solid washes is recovered and used to precipitate the lignin to minimize IL losses and water

Parameter	Value	Remarks
Equivalents of water to recover IL	2	usage. Water at the end of the washes is sent to the drain, as it will be too diluted in IL to be recovered.
Equivalents of water for the final wash	8	
IL recovery from cake	98.7722	Adjusted manually to meet overall IL losses specification
IL to Wash Pulp	100% of conditioned IL from Unit 300	
Moisture content in Solids	35 wt%	
IL content in solids	0.1 wt%	
Overall IL Loss	0.5%	As a percentage of the recirculating flowrate. IL not loss into the solids, sent to the drain.

Table 86. Steady state concentration in recycled ionic liquid ³⁵⁵.

Component	kg / kg of IL
Glucose	0.0075
Xylose	0.015
Arabinose	0
HMF	0.005
Levulinic Acid	0.003

Table 87. Pressure drops.

Item	Pressure drop [bar]
Pipe, fittings and elevation	1
Control Valve	1
Static mixers	1
Heat Exchanger	0.5
Filter	7 (conservative figure)
Evaporator	6 (to be confirmed by vendor)

A12.3.2. Ionic liquid modelling

The ionic liquid have been modelled as triethylene glycol (TEG). This compound has been chosen as it has a very high normal boiling point 289.5 °C. The heat capacity for TEG is 3.052 kJ/kg°C, which is in the same order of magnitude for a similar ionic liquid triethylammonium hydrogen sulfate [N₂₂₂₀][HSO₄] 3.792 kJ/kg°C determined experimentally ⁹⁰. The calculated VBT value is 1.73 kJ/kg°C (section 2.4.2).

A12.3.3. Chemical reactions

The following table summarizes the chemical reactions taking place in the biomass fractionation process.

Table 88. Chemical reactions.

Chemical Reaction	Equation	Conversion	Pretreatment Performance
Cellulose _(solid) + H ₂ O _(liquid) → Glucose _(solution)	1	α ₁	[C]
Hemicellulose _(solid) + H ₂ O _(liquid) → Xylose _(solution)	2	α ₂	[C]
Lignin _(solid) → Lignin _(solution)	3	α ₃	[C]
Other C ₆ -polymers _(solid) + H ₂ O _(liquid) → C ₆ sugar _(solution)	4	α ₄	100%
Other C ₅ -polymers _(solid) + H ₂ O _(liquid) → C ₅ sugar _(solution)	5	α ₅	100%
Acetate _(solid) → Acetic acid _(solution) [A]	6	α ₆	100%
Ash _(solid) → Ash _(solution)	7	α ₇	100%
Extractives _(solid) → Extractives _(solution)	8	α ₈	100%
C ₆ _(solution) → HMF _(solution) + 3 H ₂ O _(liquid)	9	α ₉	100%
HMF + H ₂ O → levulinic acid + formic acid	10	α ₁₀	100%
levulinic acid + 2 H ₂ O _(liquid) → pseudo-lignin [B]	11	α ₁₁	100%
C ₅ _(solution) → furfural _(solution) + 3 H ₂ O _(liquid)	12	α ₁₂	25%
C ₅ _(solution) → pseudo-lignin _(solution)	13	α ₁₃	75%

- A. Water has not been modelled.
 B. Chemical reaction assumed in order to keep the water content constant.
 C. Refer to Table 81.

The conversions of reactions 1 - 5 are dependent on the biomass type and pre-treatment conditions, however, in most cases, other C₅ - C₆ sugars contained in the hemicellulosic fraction are easily removed, therefore equations 4 - 5 are assumed to proceed to completion (100%), as well as the acetate groups, extractives and ash content. In steady state conditions, it is assumed that all the C₆ going into solution will generate pseudo-lignins. The C₅ fraction is transformed into furfural (Eq. 12 in Table 88) and pseudo-lignin. The exact amount of furfural production is still unknown and has been assumed to 25%.

A12.3.4. Components

The following components were modelled as solids in HYSYS V8.8. The temperature dependence for the density of the solids has not been taken into account.

Table 89. Properties for compound definition.

Component	Density [kg/m ³]	MW [g/mol]	Remarks
Cellulose	1500 ^[A]	162.14 ^[C,D]	Cellulose heat capacity is a function of the crystallinity
Hemicellulose	1500 ^[B]	132.11 ^[C,D]	
Ash	2196	60.08	Modelled as SiO ₂ .
Glucose	1540	180.1559 ³⁷⁴	
C ₆	1540	180.1559 ³⁷⁴	Assumed the same as glucose
Xylose	1520	150.1300 ³⁷⁴	
C ₅	1520	150.1300 ³⁷⁴	Assumed the same as xylose
Soluble Ash	2196	60.08	
Soluble Lignin	1300	1000	

Component	Density [kg/m ³]	MW [g/mol]	Remarks
Lignin	1300	1000	
Other C ₆ (solid)	1500	162.14 ^[C,D]	
Other C ₅ (solid)	1500	132.11 ^[C,D]	
Extractive (solid)	1042	152.15	Modelled as vanillin.
Acetate(solid)	1050	60.052	Modelled as acetic acid. No anhydrous correction was applied.

- A. The density value is larger for the crystalline cellulose structures than for the amorphous ones. The literature density of a perfect cellulose crystal is 1.582 and 1.599 g/cm³ for alpha and beta polymorphs⁵²⁴, whereas for the amorphous cellulose, the density values range from 1.34 to 1.48^[59,525]. As native cellulose of plants is a mixture of crystalline and amorphous cellulose, a value of 1.5 g/cm³ has been considered.
- B. Same as cellulose.
- C. Per monomeric unit. Calculated by subtracting water from the corresponding sugar.
- D. Per monomeric unit.

Heat of formation and combustion

Table 90. Heat of formation and combustion.

Component	Heat of Form (25°C) [kJ/mol]	Heat of Comb (25°C) [kJ/mol]	Enthalpy Basis Offset [kJ/mol]
Cellulose			
Hemicellulose			
Ash			
Glucose	-1271.0 ³⁷⁴	-2805.0 ³⁷⁴	5131.1 ^[A]
C ₆	-1271.0 ^[B]	-2805.0 ^[B]	5131.1 ^[B]
Xylose	-1054.5 ⁵²⁶	-2342.2 ⁵²⁶	-27852.6 ^[A]
C ₅	-1054.5 ^[C]	-2342.2 ^[C]	-27852.6 ^[C]
Other C ₆ (solid)	-1271.0 ^[B]	-2805.0 ^[B]	5131.1 ^[A]
Other C ₅ (solid)	-1054.5 ⁵²⁶	-2342.2 ⁵²⁶	-27852.6 ^[A]
Extractive (solid)	-369000	-3660000	-430697
Acetate(solid)	-483.88–483.16	-875.50–874.82	

- A. Calculated by HYSYS.
- B. Assumed as the same as glucose.
- C. Assumed as the same as xylose.

The energy that could be obtained from lignin if used as a fuel was calculated assuming 100% efficiency in the boiler (24.6 ± 0.9 MJ/kg, average HHV value for *ionoSolv Miscanthus* lignins)

⁸⁸.

Heat Capacity

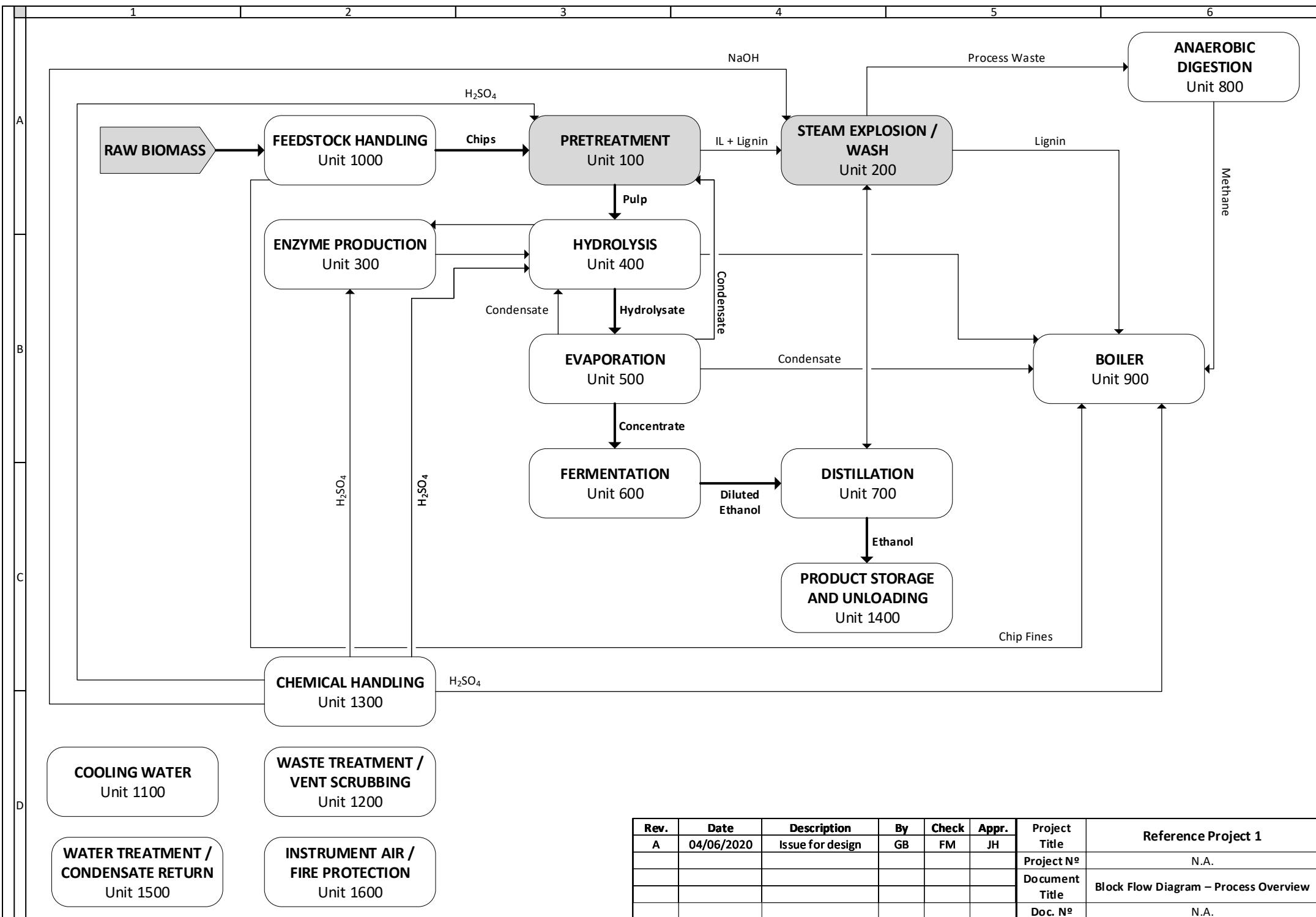
$$C_p = a + bT + cT^2 + dT^3$$

C_p in kJ/kg.K T in K

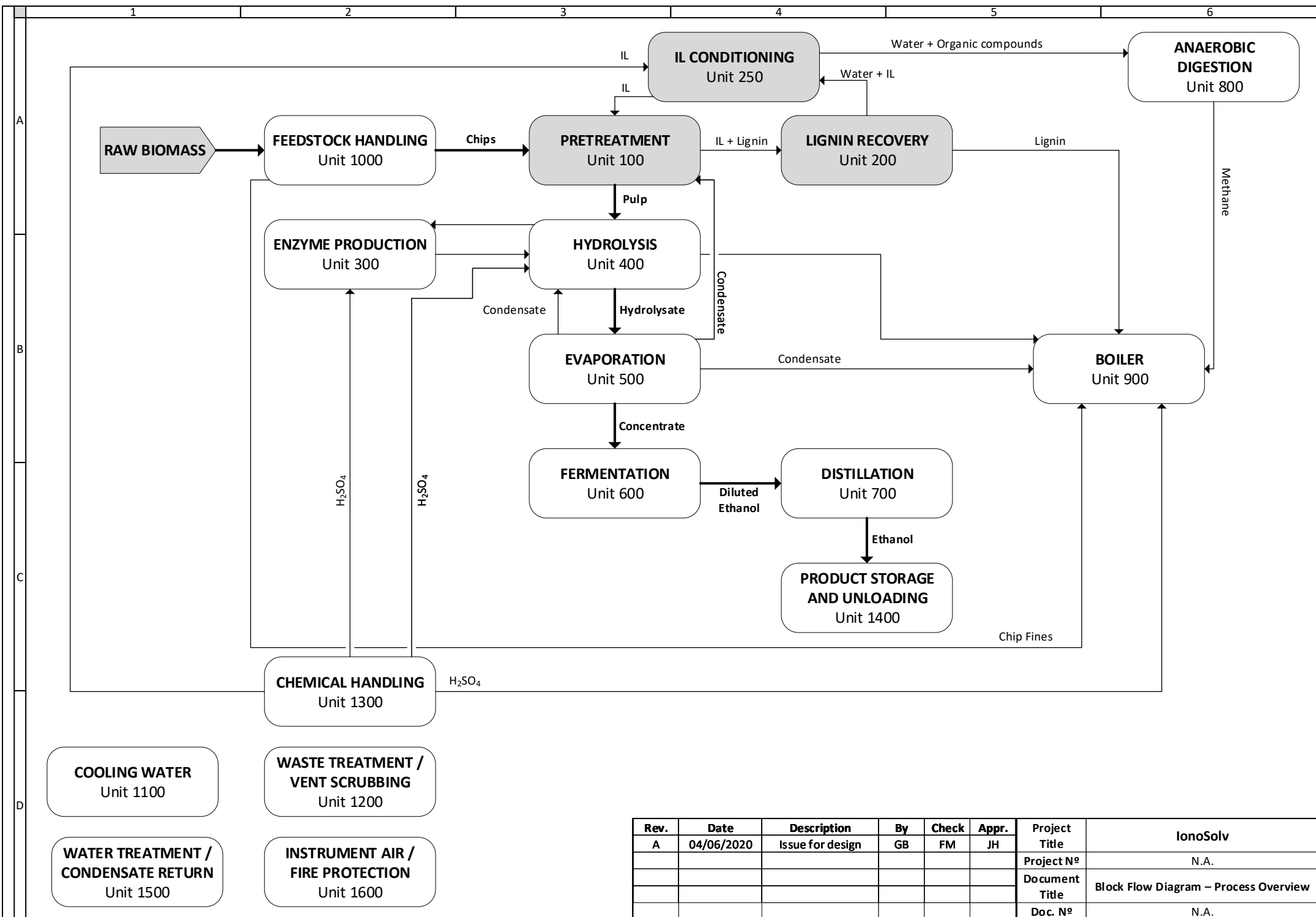
Table 91. Polynomial parameters for heat capacity calculations (biomass).

Component	a	b	c	d	ref
Cellulose	-0.407	5.10E-03			
Hemicellulose	-0.407	5.10E-03			
Ash	-9.87E-02	4.20E-03	-5.00E-06	3.00E-09	
Glucose ^[B]	-1.4527997	8.95E-03			
Other C ₆ ^[D]	-1.4527997	8.95E-03			
Xylose ^[C]	-8.79E-03	4.07E-03			
Other C ₅ ^[E]	-8.79E-03	4.07E-03			
Soluble Ash	-9.87E-02	4.20E-03	-5.00E-06	3.00E-09	
Soluble Lignin	-0.407	5.10E-03			
Lignin	-0.407	5.10E-03			
Other C ₆ (solid)	-4.07E-01	5.10E-03			
Other C ₅ (solid)	-0.407	5.10E-03			
Extractive (solid)	0.9491582	2.76E-03			[A]
Acetate(solid)					

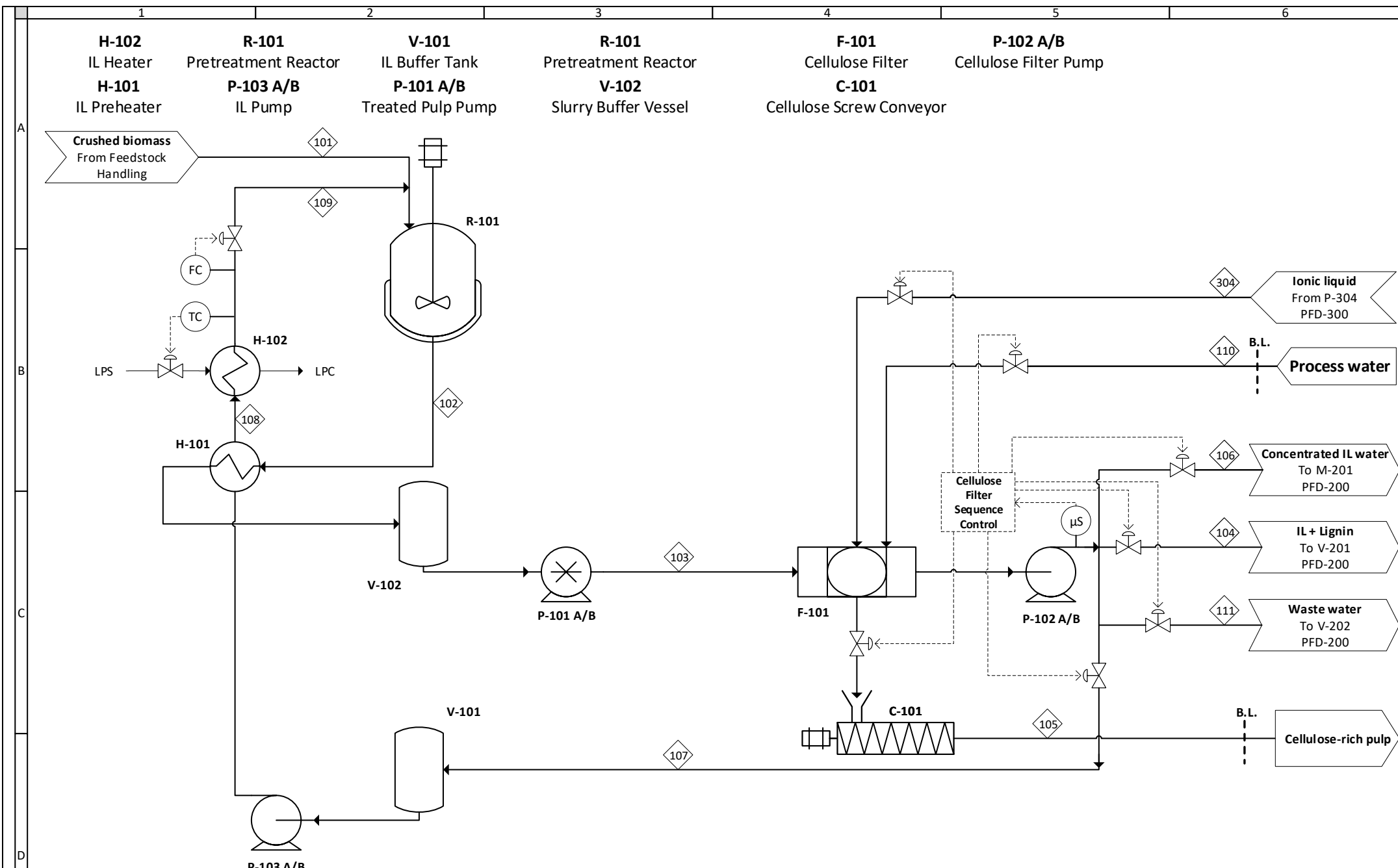
- A. Parameters obtained by fitting the liquid C_p of vanillin.
 B. Fitted from data available in NIST ³⁷⁴.
 C. Fitted from data ⁵²⁶.
 D. Same as glucose.
 E. Same as xylose.



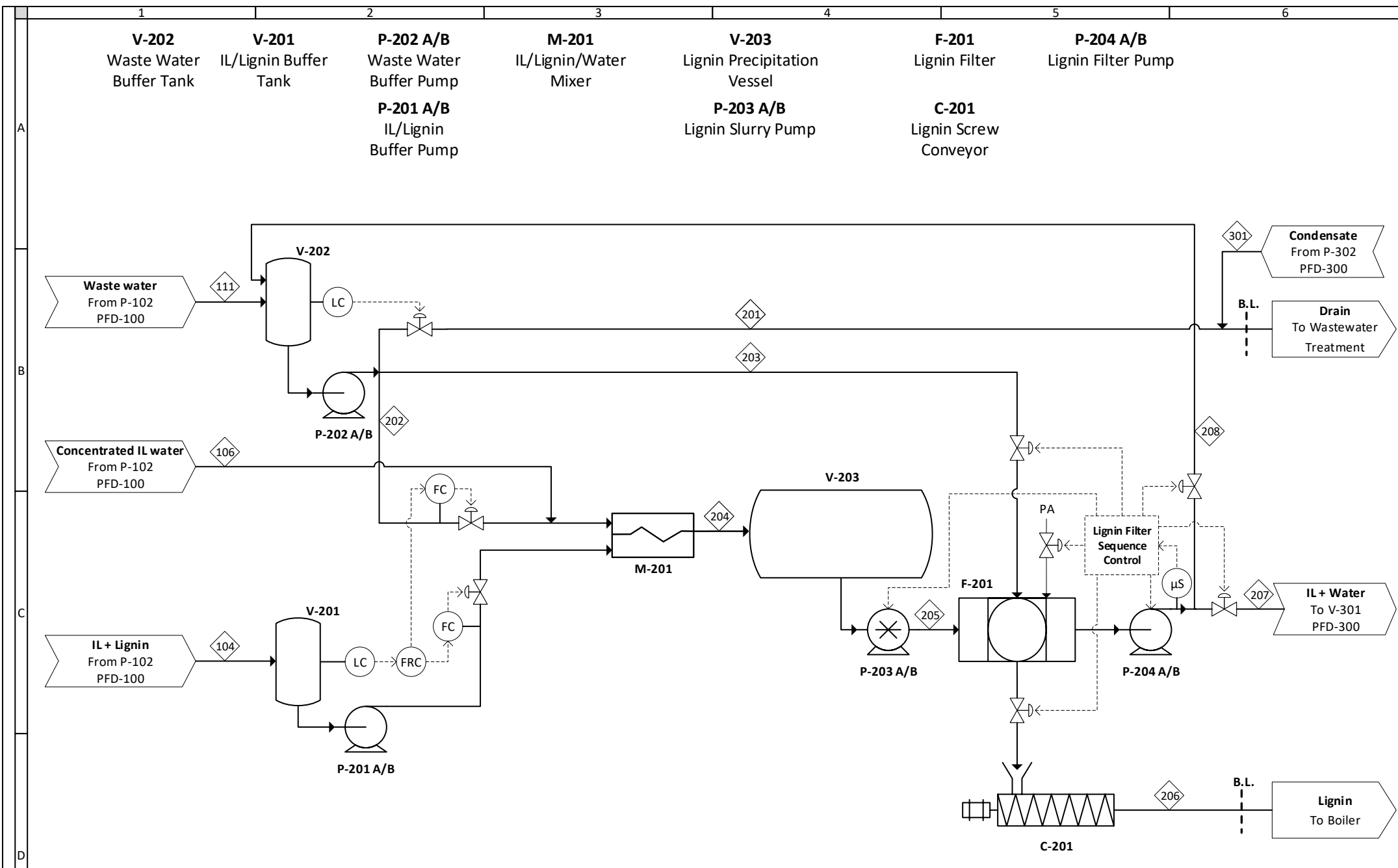
Rev.	Date	Description	By	Check	Appr.	Project Title	Reference Project 1
A	04/06/2020	Issue for design	GB	FM	JH	Project N°	N.A.
						Document Title	Block Flow Diagram – Process Overview
						Doc. N°	N.A.



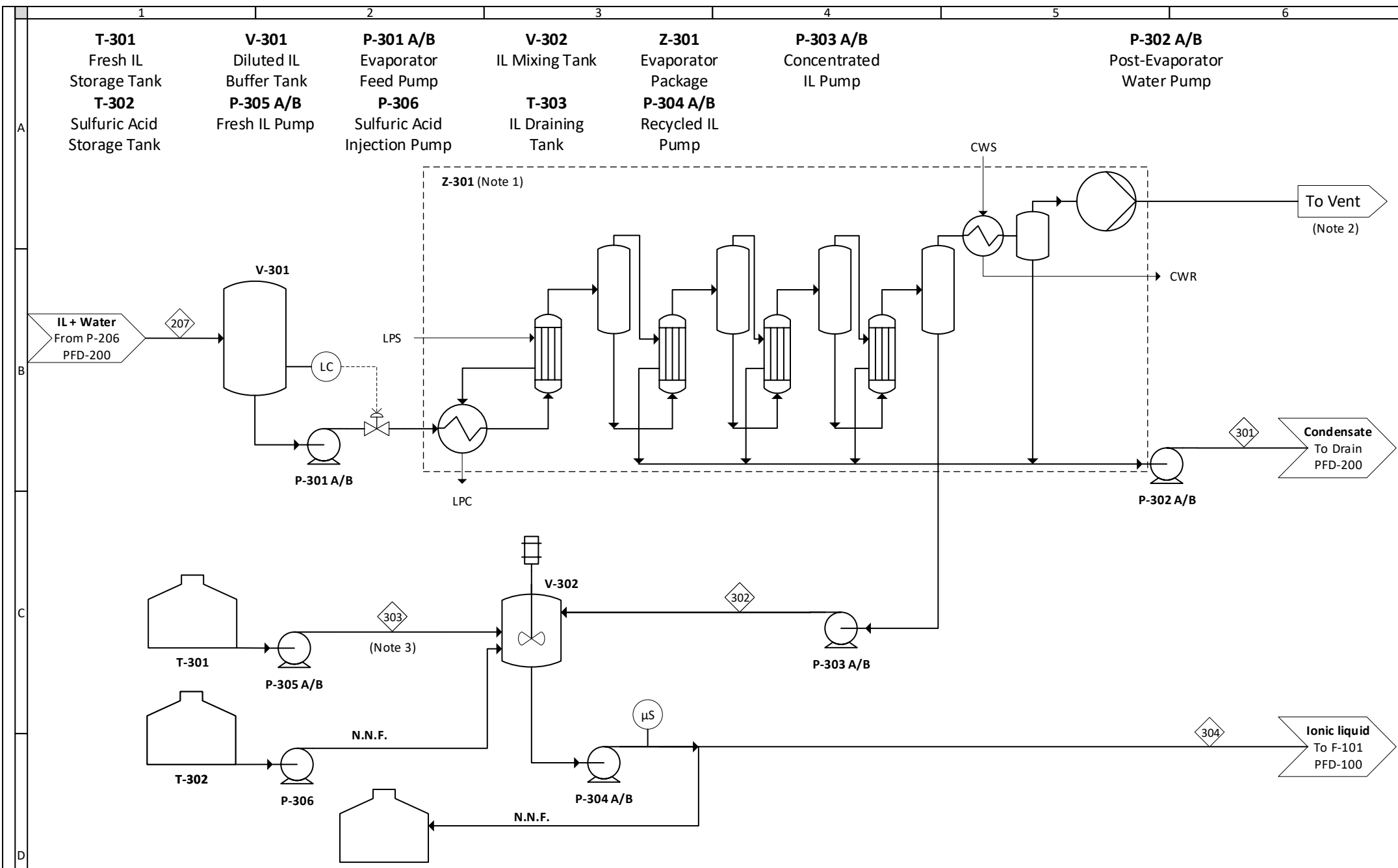
Rev.	Date	Description	By	Check	Appr.	Project Title	IonoSolv
A	04/06/2020	Issue for design	GB	FM	JH	Project N°	N.A.
						Document Title	Block Flow Diagram – Process Overview
						Doc. N°	N.A.



Rev.	Date	Description	By	Check	Appr.	Project Title	IonoSolv – Unit 100 Pretreatment
A	04/06/2020	Issue for design	GB	FM	JH	Project N ^o	N.A.
						Document Title	Process Flow Diagram
						Doc. N ^o	N.A.



Rev.	Date	Description	By	Check	Appr.	Project Title	IonoSolv – Unit 200 Lignin Recovery Unit
A	04/06/2020	Issue for design	GB	FM	JH	Project N ^o	N.A.
						Document Title	Process Flow Diagram
						Doc. N ^o	N.A.



Notes:

- Internal details of the Evaporator Package to be provided by the vendor.
- Vent routed to the site's vent scrubber.
- Manual operation. Intermittent flow.

Rev.	Date	Description	By	Check	Appr.	Project Title	IonoSolv – Unit 300 Ionic Liquid Conditioning
A	04/06/2020	Issue for design	GB	FM	JH	Project N ^o	N.A.
						Document Title	Process Flow Diagram
						Doc. N ^o	N.A.

Biorefinery equipment list

Unit	Tag	Item name	Type / description	Material (1)	Items	Cost estimation	Purchased cost per item	Year	Total purchased cost (2019 USD)	Total installed cost (2019 USD)
100	R-101 A/B/C	Fractionation Reactor	Glass-lined CS stirred and jacketed batch reactor	Glass-lined CS	3	Correlation (4).	158 815	2003	720 001	1 440 002
100	P-101 A/B	Treated Pulp Pump	Positive displacement pump (piston or screw pump)	SS316 (3)	2	Correlation (4)	8 863	2003	26 788	61 613
100	P-102 A/B	Cellulose Filter Pump	Centrifugal pump - one-stage - 1750 rpm	SS316 (3)	2	Correlation (4)	12 080	2003	36 509	83 971
100	P-103 A/B	IL Pump	Centrifugal pump - one-stage - 3550 rpm	SS316 (3)	2	Correlation (4)	11 019	2003	33 303	76 597
100	H-101	IL Preheater	Heat exchanger (calculations based on shell & tube counter current)	SS316	3	Correlation (4)	509 799	2003	2 311 214	5 084 670
100	H-102	IL Heater	Heat exchanger (calculations based on shell & tube counter current)	SS316	1	Correlation (4)	35 834	2003	54 152	119 134
100	F-101	Cellulose Filter	<i>Outotec's quote.</i> Horizontal vacuum belt filter	SS316	N/A	Vendor's quotes	1 509 724	2019	1 509 724	2 566 531
100	V-101	IL Buffer Tank	Vertical vessel	SS316 (2)	1	Correlation (4)	69 778	2003	105 448	210 897
100	V-102	Slurry Buffer Vessel	Vertical vessel	SS316 (2)	1	Correlation (4)	68 628	2003	103 710	207 421
100	C-101	Cellulose Screw Conveyor	Screw conveyor	SS316	1	Correlation (4)	18 215	2003	18 215	36 430
200	V-201	IL/Lignin Buffer Tank	Vertical vessel	SS316 (2)	1	Correlation (4)	68 482	2003	103 489	206 978
2000	V-202	Water Buffer Tank	Vertical vessel	SS316 (2)	1	Correlation (4)	71 900	2003	108 654	217 309

Unit	Tag	Item name	Type / description	Material (1)	Items	Cost estimation	Purchased cost per item	Year	Total purchased cost (2019 USD)	Total installed cost (2019 USD)
2000	V-203	Lignin Precipitation Vessel	Horizontal vessel	SS316 (2)	1	Correlation (4)	101 284	2003	153 060	306 120
2000	P-201 A/B	IL/Lignin Buffer Pump	Centrifugal pump - one-stage - 3550 rpm	SS316 (3)	2	Correlation (4)	8 104	2003	24 495	56 338
2000	P-202 A/B	Water Buffer Pump	Centrifugal pump - one-stage - 3550 rpm	SS316 (3)	2	Correlation (4)	9 145	2003	27 641	63 574
2000	P-203 A/B	Lignin Slurry Pump	Positive displacement pump (piston or screw pump)	SS316 (3)	2	Correlation (4)	9 995	2003	30 208	69 478
2000	P-204 A/B	Lignin Filter Pump	Centrifugal pump - one-stage - 3550 rpm	SS316 (3)	2	Correlation (4)	9 879	2003	29 859	68 675
2000	M-201	IL/Lignin/Water Mixer	Static mixer	SS316	1	Correlation (4)	6 325	2019	6 325	12 649
2000	F-201	Lignin Filter	<i>Dr M's quote.</i> Candle filter	SS316	1	Vendor's quotes	2 908 437	2019	2 908 437	4 944 343
2000	C-201	Lignin Screw Conveyor	Screw conveyor	SS316	1	Correlation (4)	18 223	2003	18 223	36 446
3000	Z-301	Evaporator Package	Multiple effect evaporator (vendor's package)	Various	1	Correlation (4)	2 869 815	2019	2 869 815	4 591 704
3000	V-301	Diluted IL Buffer Tank	Vertical vessel	SS316 (2)	1	Correlation (4)	80 229	2003	121 242	242 484
3000	V-302	IL Mixing Tank	Vertical vessel with agitator	SS316 (2)	1	Correlation (4)	61 021	2003	92 214	184 428
3000	P-301 A/B	Evaporator Feed Pump	Centrifugal pump - one-stage - 3550 rpm	SS316 (3)	2	Correlation (4)	12 969	2003	39 196	90 151
3000	P-302 A/B	Post-Evaporator Water Pump	Centrifugal pump - one-stage - 3550 rpm	SS316 (3)	2	Correlation (4)	8 008	2003	24 204	55 668
3000	P-303 A/B	Concentrated IL Pump	Centrifugal pump - one-stage - 3550 rpm	SS316 (3)	2	Correlation (4)	9 570	2003	28 924	66 525
3000	P-304 A/B	Recycled IL Pump	Centrifugal pump - one-stage - 3550 rpm	SS316 (3)	2	Correlation (4)	10 235	2003	30 933	71 146
3000	P-305 A/B	Fresh IL Pump	Centrifugal pump - one-stage - 3550 rpm	SS316 (3)	2	Correlation (4)	8 535	2003	25 795	59 328

Unit	Tag	Item name	Type / description	Material (1)	Items	Cost estimation	Purchased cost per item	Year	Total purchased cost (2019 USD)	Total installed cost (2019 USD)
3000	T-301	Fresh IL Storage Tank	Flat-bottom storage tank	SS316 (2)	1	Correlation (4)	172 072	2003	260 034	520 068
3000	T-303	IL Draining Tank	Flat-bottom storage tank	SS316 (2)	1	Correlation (4)	172 072	2003	260 034	520 068

(1) For economic evaluation.

(2) Manufactured in glass-lined CS. Conservative assumption as material factor for SS316 is greater than glass-lined CS.

(3) Manufactured in PTFE or other inert material. For cost evaluation purposes, material factor of SS316 is selected.

(4) Cost correlations taken from: James R. Couper W. Roy Penney James R. Fair W. Roy Penney Stanley M. Walas James R. Fair Stanley M. Walas. Chemical Process Equipment. (Elsevier, 2005). doi:10.1016/B978-0-7506-7510-9.X5000-1

Appendix 14 - Quick investment and operating cost estimation method for second generation bioethanol production plants

BACKGROUND

The rising concerns over Greenhouse Gas (GHG) emissions and oil dependency have driven recent research towards bioethanol production as a replacement for petroleum-based fuels. First-generation (1G) biofuels are obtained from fermentable sugars or vegetable oils found in food crops. As these feedstocks are edible, the production of 1G biofuels has been subjected to the food vs. fuel dilemma: there is a perceived risk of diverting farmland or crops towards biofuel production to the detriment of food supply [1,2]. Second-generation (2G) bioethanol production avoids this issue as it uses non-edible feedstocks from agricultural and forestry wastes. In this approach, lignocellulosic biomass is fractionated into fermentable sugars through a process called biomass pre-treatment (or biomass fractionation) followed by enzymatic hydrolysis. The resulting sugars from the enzymatic hydrolysis are then fermented into bioethanol [3]. There are different biomass pre-treatment strategies for 2G bioethanol production, such as chemical, physical, thermophysical, thermochemical and biological methods. Recent developments also include low-cost ionic liquids (ionoSolv Process) [4,5]. Many of these methods have been recently reviewed in the scientific literature [6,7]. Biorefineries have long offered promise for reducing our dependence on petroleum for transport fuels, chemicals and materials. Biorefineries based on 2G lignocellulosic feedstocks, such as wood or agricultural residues, offer the opportunity to create a carbon-neutral fuel and chemical industry without creating undue pressure on food supply. Major advances have been made to improve the efficiency of sugar release from feedstocks (variety of novel pre-treatment technologies) for 2G ethanol production.

Most of the Techno-Economic Analysis (TEA) for 2G bioethanol plants express the results in terms of Minimum Ethanol Selling Price (MESP) [8,9], which encompasses capital investment cost (or capital expenditure, CAPEX), operating costs (or operating expenditure, OPEX) and other economic parameters, such as income tax, interest, equipment depreciation costs, etc.

There are some methods to estimate plant costs at early stages, developed mainly for chemical plants in the oil and gas sector. These methods include Wilson's main plant item method; Taylor's process step scoring method; Bridgwater's correlations; Klumpar, Brown, and Fromme's process module method; and Petley's functional unit correlation (1997). However, it has been recently shown that these estimation methods tend to overestimate the actual CAPEX of bioethanol plants and that the largest deviations were reported for this process when compared to biodiesel and syngas ethanol plants [10]. Another estimation procedure proposed by Lange in 2001 for petrochemical plants seems valid for bio-based processes [11], however, this estimation is based on the overall rated power of electrical equipment, which requires a more detailed process modelling and sizing effort.

Therefore, an easy and simple CAPEX and OPEX estimation method for bioethanol plants was developed. The method is based on the biochemical conversion pathway developed by the United States National Renewable Energy Laboratory (NREL) [12]. This work has been selected as reference as it includes

complete technical and economic data. Additionally, data from NREL documentation had already been used for reference for other TEAs [13–15]. The CAPEX and OPEX estimation method shown herein is based on plant capacity and other process parameters commonly reported in early-stage scientific work exploring different (or novel) pre-treatment methods for 2G bioethanol, such as pulp yields, pulp composition and enzymatic digestibility.

RESULTS

Process description

The NREL process [12] (2011) uses co-current dilute-acid pre-treatment of corn stover, followed by enzymatic hydrolysis and fermentation of glucose and xylose into ethanol. In this model, lignin is used as a solid fuel and electricity is cogenerated. The process design (Figure 1A) includes other process units required for ethanol production, namely, feedstock handling and storage, product purification, wastewater treatment, lignin combustion for heat and electricity generation, product and chemicals storage, and required utilities. The as-received corn stover feed requirement for the plant is 104200 kg/h including moisture and it produces 232.5 MML/year (ethanol density 0.789 kg/L 20 °C (68 °F)) (61.0 MMgal/yr). The theoretical plant production at 100% ethanol yield is 303 MML/year (80.3 MMUSGAL/year) of ethanol.

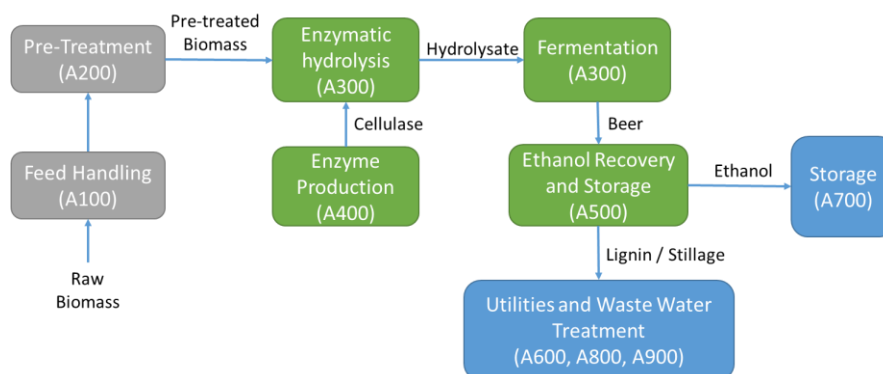


Figure 1A. Simplified block diagram of the NREL 2011 bioethanol plant [12].

In this section, a brief process description is presented. For more information on each process areas (process descriptions, process flow diagrams, heat and material balances, cost estimations) refer to the original NREL documentation [12]. Further details on how the CAPEX and OPEX correlation models were derived for each process area are given in Appendix 15.

AREA 100 - Feedstock storage and handling. The biomass is delivered to the biorefinery with a uniform format, resulting in minimum storage and feed handling. From this area, the biomass is conveyed into the pre-treatment reactors in Area 200.

Area 200 - Pre-treatment and conditioning. In this area, the biomass is treated with dilute sulfuric acid at high temperature to enhance its enzymatic hydrolysis and to liberate the hemicellulose sugars. Ammonia is then

added to the pre-treated slurry to raise the pH for enzymatic hydrolysis. This unit can be altered or omitted to evaluate other pre-treatment technologies.

Area 300 - Enzymatic hydrolysis and fermentation. Cellulose hydrolysis is performed using a cellulase enzyme cocktail prepared on-site. This reaction is started in a continuous reactor and finalized in a batch bioreactor. Once the hydrolysis is completed, the medium is cooled and inoculated with the co-fermenting microorganisms, in order to convert most of the glucose and xylose into ethanol. The resulting beer is sent to the product recovery facilities in Area 500.

Area 400 - Cellulase enzyme production. In this area, the enzymes required for cellulose hydrolysis in area 300 are produced. The enzyme-producing fungus is fed mainly with corn syrup, and it is grown aerobically in fed-batch bioreactors. This unit can be omitted from the calculation to evaluate a scenario in which the enzymes are outsourced.

Area 500 - Product, solids, and water recovery. The beer is separated into ethanol, water, and residual solids. Ethanol is produced at 99.5% purity by distillation followed by vapour-phase molecular sieve adsorption. Solids recovered from the distillation bottoms after filtration are sent to the combustor (Area 800) while the liquid is sent to wastewater treatment (Area 600).

Area 600 - Wastewater treatment (WWT). Wastewater streams are treated by anaerobic and aerobic digestion. The methane-rich biogas and the sludge formed are sent to the combustor in Area 800. The treated water is suitable for recycling and is re-used in the process.

Area 700 - Product and feed chemical storage. This area provides storage for chemicals used and produced in the process.

Area 800 - Combustor, boiler, and turbogenerator. Biogas and sludge from Area 600 are combusted to produce steam, which is used as the heating medium and for electricity generation. Electric power not consumed in the process is exported to the grid.

Area 900 - utilities. This area includes the utilities required for the process, such as cooling and chilling water systems, plant and instrument air and Cleaning in Place (CIP) system.

Methodology

Generally speaking, for projects at an early stage of development and in particular for innovative industrial processes, there are many technical uncertainties and limited data is available (*e.g.* suitable construction materials or detailed equilibrium or thermophysical data). This lack of information may lead to the wrong choice of equipment type and size, which will significantly impact any CAPEX/OPEX

estimations and therefore any TEA, as standard approaches for determining CAPEX and OPEX rely on equipment sizing. The strategy presented in this work does not require detailed process modelling or equipment sizing to estimate the CAPEX and OPEX for a 2G bioethanol plant.

The correlations shown for capital expenditure are expressed in US dollars (June 2018) and have been developed based on the reference project using Eq. 1 and Eq. 2. Costs associated with material streams are calculated on yearly basis using Eq. 3. Further details on how the different correlations were developed are given in the methodology section and in Appendix 15. The explanation and units for symbols used in all the equations presented in this work are given in the symbol section at the end of the article.

$$Cost_{2018} = Base\ Cost_{year} \cdot \left(\frac{2018\ Cost\ Index}{Base\ Year\ Index} \right) \quad Eq. 1$$

$$Cost_{new} = Cost_{Base\ case} \cdot \left(\frac{New\ Capacity}{Base\ Capacity} \right)^n \quad Eq. 2$$

$$VOC = F \cdot MC \cdot Oh \cdot 10^{-6} \quad Eq. 3$$

Heat and material balance

For CAPEX estimation, not all the material streams are required. The material streams required for this purpose are, raw biomass on a dry basis (F_{rb}), pre-treated biomass on a dry basis (F_{pb}), ethanol produced (F_{ETOH-P}), enzymes (F_e), untreated solids (F_s), chemicals (sulfuric acid ($F_{H_2SO_4}$), ammonia ($F_{ammonia}$), corn steep liquor (F_{CSL}) and diammonium phosphate (F_{DAP})) and steam (F_{steam}). In addition, the electric power (E_p) produced and cooling duty (Q_c) are required. In the following section, a way to approximate the heat and material balance for a bioethanol plant is described.

Plant capacity

The first step is to determine the plant capacity. Most of the scientific literature reports pre-treatment performance in terms of pulp yield, which is defined as the quantity of solid remaining after the pre-treatment. This value will depend on the feedstock and the nature and severity of the pre-treatment step [5].

In some pre-treatment methods, such as the IonoSolv Process, the solvent is recycled and reused. It has been noted that the pulp yield is different for each cycle [5]. In such situations, the steady-state values should be used for the estimation if available.

In a continuous process, the relationship between the mass flow of raw input biomass and of pre-treated biomass is also given by the pulp yield.

$$P_{yield} = \frac{F_{pb}}{F_{rb}} \cdot 100\% \quad Eq. 4$$

In the NREL base case, the raw biomass flow rate on a dry basis [kg/h] is 83367 kg/h and the pre-treated biomass flow rate on a dry basis is 46296 kg/h, which gives a pulp yield of 55.53%. The overall ethanol

production can be fixed as per the reference project, and the incoming biomass flowrates back-calculated.

Ethanol production

The amount of ethanol produced can be calculated from the amount of cellulose present in the biomass after pre-treatment, the enzymatic hydrolysis efficiency and the fermentable sugar in the hydrolysate (glucose and xylose). In the base case, the enzymatic hydrolysis of cellulose yields 91.2% of fermentable glucose. During the fermentation step, glucose and xylose are converted to ethanol with 95% and 85% efficiency respectively (Figure 2A). The fermentation performance cannot be changed in the model.

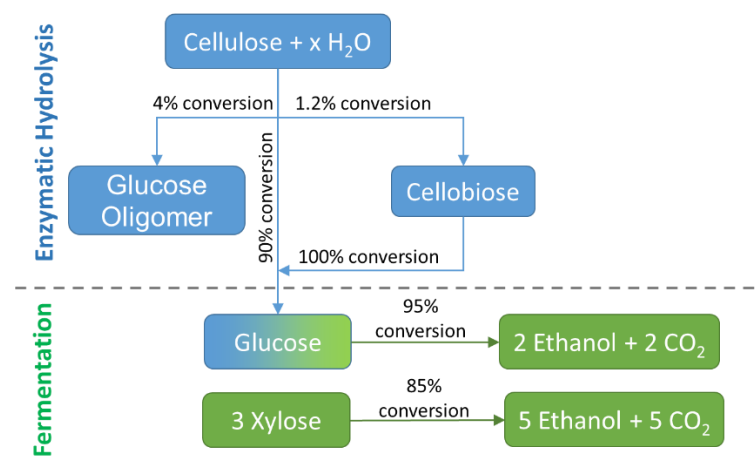


Figure 2A. Summary of main chemical reactions. Conversions based on the reference case are shown between brackets.

There are several degradation pathways for the sugars during the pre-treatment, hydrolysis and fermentation steps. Also, some of the sugars are used to feed the microorganisms for enzyme generation. Therefore, by assuming the same yields of all parallel reactions and ethanol losses, the overall ethanol mass flow rate after the bioreactor can be approximated by Eq. 5. For more information about all the parallel chemical reactions refer to the original NREL documentation [12].

$$F_{ET-F} = 0.516 (0.95 F_g + 0.85 F_x) + 0.544 F_{pb} X_c (E_s - E_m) \quad \text{Eq. 5}$$

The actual ethanol produced after the purification unit is given by Eq. 6:

$$F_{ET-P} = 0.994 F_{ET-F} \quad \text{Eq. 6}$$

The NREL base case anhydrous ethanol production (water content 0.5 wt% and 0.12 wt% CO₂) is 21808 kg/h of ethanol or 232.5 MML/year. Additives can be added to the ethanol (denatured ethanol) to make it poisonous, bad-tasting, foul-smelling, or nauseating in order to discourage recreational consumption

and avoid taxes applicable for edible ethanol. In the reference project, gasoline is used as an additive for this purpose (Eq. 38).

Enzyme flowrate

The enzyme flowrate can be calculated using Eq. 7. It can be set to zero if enzymes are not produced on-site.

$$F_e = 0.001185 F_{pb} \cdot X_c \cdot E_L \quad \text{Eq. 7}$$

Solid residue

During enzymatic hydrolysis, the cellulose will follow several chemical transformations into glucose and oligomers. In the NREL process, 4.8% in mass of the cellulose will remain in the solids, as well as other solid components, such as xylan, lignin, and other sugar polymers. The amount of unreacted solids after enzymatic hydrolysis can be calculated with Eq. 8 (dry basis), assuming that there are no solids in the enzymatic cocktail. For general processes, it can be assumed that the remaining solids from biomass can be calculated from the glucose yields. After the fermentation process, the solid mass will increase due to the addition of fermenting microorganisms (8.4% in the reference case). In the reference project, 98% the overall unreacted solid is recovered through filtration and sent to a burner. For simplicity, the correlations herein are developed in terms of F_s .

$$F_s = F_{pb} \cdot (1 - E_s \cdot X_c) \quad \text{Eq. 8}$$

Biogas and sludge

Biogas and sludge flowrates produced in the wastewater treatment can be approximated from the base case by scaling their flowrate with production.

$$F_{bg} = 0.472 F_{pb} \quad \text{Eq. 9}$$

$$F_{sl} = 0.211 F_{pb} \quad \text{Eq. 10}$$

Steam

The amount of steam generated in the boiler can be modelled using Eq. 11. In some pre-treatment methods such as the IonoSolv Process [4,5], lignin is removed prior to the enzymatic hydrolysis. If this is the case, and lignin is going to be used as a fuel, the quantity of lignin should be included in the term F_s to calculate the steam generated in Eq. 11. This applies to any other solid materials that are going to be incinerated for steam generation.

$$F_{Steam} = 4.187 F_{bg} + 0.745 F_{sl} + 6.35 F_s \quad \text{Eq. 11}$$

A fraction of the steam is used as a heating medium while the rest is used for electricity generation. The quantity of steam used as the heating medium can be calculated using Eq. 12. The term dependent on F_{pb} represents the heat consumed in the pre-treatment and can be corrected as a function of pre-treatment conditions using Eq. S1 (see Appendix 15). The term F_{ETOH-P} corresponds to the amount of steam consumed in the distillation column to separate water from ethanol and the term F_{rb} represents the steam consumption for the utilities.

$$F_{heat} = 0.605 F_{pb} + 0.365 F_{rb} + 3.434 F_{ET-P} \quad \text{Eq. 12}$$

Electric power

The electric power that can be generated can be model with Eq. 13.

$$P_p = 4.073 \cdot 10^{-4} (F_{Steam} - F_{heat}) \quad \text{Eq. 13}$$

The electric power consumption per unit area based on the same performance as the NREL report can be approximated with Eq 14- Eq 21. The electrical consumption of Area 700 is marginal and therefore is not considered for the calculations.

$$P_{A100} = \frac{F_{rb}}{101667} \quad \text{Eq. 14}$$

$$P_{A200} = \frac{F_{rb}}{14524} \quad \text{Eq. 15}$$

$$P_{A300} = \frac{F_{pb}}{18820} \quad \text{Eq. 16}$$

$$P_{A400} = \frac{F_e}{116} \quad \text{Eq. 17}$$

$$P_{A500} = \frac{F_{pb}}{22583} \quad \text{Eq. 18}$$

$$P_{A600} = \frac{F_{pb}}{6273} \quad \text{Eq. 19}$$

$$P_{A800} = \frac{F_{pb}}{37639} \quad \text{Eq. 20}$$

$$P_{A900} = \frac{F_{pb}}{14115} \quad \text{Eq. 21}$$

$$P_c = \sum^{Areas} P_{Axxx} \quad \text{Eq. 22}$$

It is not clear from the NREL report if the electrical balance takes into consideration losses in electrical distribution networks, the efficiency of electrical motors and consumption of non-process users, such as lighting. All of these factors need to be considered when establishing a detail electrical balance, which

can only be achieved after detailed engineering studies have been completed. Therefore, the electrical balance given in the NREL report might be optimistic if those factors are not considered.

Another factor to consider is that, in general, the efficiency of electrical motors is capacity-dependent: larger electrical motors tend to have higher efficiencies. The electrical consumption given by Eq. 14- Eq. 21 does not consider any corrections due to electrical motor efficiency changes due to capacity changes. However, for a high-level estimation, the above equations can be used.

The excess power that can be exported to the grid is the difference of the power produced and the power consumed (Eq. 23).

$$P_e = P_p - P_c \quad \text{Eq. 23}$$

Cooling duty:

The cooling duty for the plant can be estimated using Eq 24. The term based on F_{rb} represents the consumption of A200 while the term based on F_{pb} represent the overall duty of the rest of the plant.

$$Q_c = \frac{F_{rb}}{9327} + \frac{F_{pb}}{446} \quad \text{Eq. 24}$$

Chemical consumption

The chemical consumption has been scaled up with production keeping all other assumption constant. They can be approximated by the following equations given in Table 1A.

To evaluate the OPEX for the purchased enzyme scenario, the cost of the enzymatic cocktail needs to be considered. Several values are found in the literature for the cost of the enzymes, which depend on their enzymatic activity. For reference, the value used by the NREL in the 2000 design [16] is 1.327 US/kg cellulase.

Only the chemical material streams for sulfuric acid, ammonia, corn steep liquor (CSL) and ammonium phosphate (DAP) are needed for CAPEX estimation. Ammonia and CSL are used in two different process areas, the term F_e represents the fraction used in Area 400. The chemical consumption has not been corrected for changes in residence time required for the enzymatic hydrolysis of the cellulose. For other process schemes that require chemicals not listed here, the consumption of such chemicals needs to be estimated and costed (Eq. 3).

Table 1A. Chemical consumption for CAPEX and OPEX estimations (Eq. 3). Chemicals required for CAPEX estimation have been highlighted in bold. [A] Taken from table 29 of the NREL report [12]. [B] Taken from Alibaba web site reported as follows: Overall minimum value – overall maximum value (Average value, num = number of suppliers). [C] Sulfuric acid concentration between 96 and 98%.

Chemical	Process Area	Consumption [kg/h]		NREL Cost ^A (2007US\$)		Online Suppliers
				US\$/lb	US\$/kg	Cost[25] ^B
						[2018US\$/kg]
Sulfuric acid (93%)	200	$F_{H_2SO_4} = 0.0238 F_{rb}$	Eq 25	0.0399	0.0880	0.2-0.3 (0.245, num = 2) ^C
Ammonia	200, 400	$F_{amonia} = 0.0126 F_{rb} + 0.1855 F_E$	Eq 26	0.1993	0.4394	0.5-2 (0.925, num = 4)
Corn steep liquor	300, 400	$F_{CSL} = 0.025 F_{pb} + 0.2661 F_e$	Eq 27	0.0252	0.0556	0.43-0.7 (0.537, num = 4)
Diammonium phosphate	300	$F_{DAP} = 0.0163 F_{pb}$	Eq 28	0.4385	0.9667	0.3-0.52 (0.404, num = 4)
Sorbitol	300	$F_{sor} = 0.00095 F_{pb}$	Eq 29	0.5005	1.1034	0.5-0.7 (0.586, num = 4)
Glucose	400	$F_{glu} = 3.9 F_e$	Eq 30	0.2579	0.5686	0.37-0.6 (0.465, num = 5)
SO ₂	400	$F_{SO_2} = 0.0258 F_e$	Eq 31	0.1378	0.3038	0.4-1.5 (0.713, num = 4)
Enzyme nutrients	400	$F_{EN} = 0.108 F_e$	Eq 32	0.3727	0.8217	-
Caustic	600	$F_{CA} = 0.0486 F_{pb}$	Eq 33	0.0678	0.1495	0.3-0.9 (0.425, num = 6)
Lime	800	$F_{lime} = 0.00381 F_{steam}$	Eq 34	0.0904	0.1993	0.06-0.149 (0.098, num = 5)
Boiler chemicals	800	$F_{bc} = 1.9 \cdot 10^{-6} F_{steam}$	Eq 35	2.2661	4.9959	-
Cooling tower chemicals	900	$F_{cc} = 0.0178 Q_c$	Eq 36	1.3580	2.994	-
Fresh water	900	$F_{FW} = 1304.3 Q_c$	Eq 37	0.0001	0.00026	-
Gasoline	700	$F_{Gasoline} = 0.0213 F_{ETOH-P}$	Eq 38	-	-	-
Waste Disposal (Ash)	-	$F_{ASH} = 0.1837 (F_s + F_{sl})$	Eq 39	0.01301	0.02886	-

CAPITAL COST ESTIMATION

The TIEC (2018US\$) for each process area can be calculated using Eq. 40 - Eq. 48. To calculate the cost at another year, Eq. 1 can be used.

$$TIEC_{A100} = 0.0246F_{rb}^{0.62} \quad \text{Eq. 40}$$

$$TIEC_{A200} = 0.039F_{rb}^{0.607} \quad \text{Eq. 41}$$

$$TIEC_{A300} = 0.0019F_{pb}^{0.85} + 10.87 \cdot 10^{0.0675 \cdot Ts} \cdot \left(\frac{F_{pb}}{46296} \right)^{-8.1 \cdot 10^{-4} \cdot Ts^2 + 0.011 \cdot Ts + 0.94} \quad \text{Eq. 42}$$

$$TIEC_{A400} = 0.0407F_e^{0.972} \quad \text{Eq. 43}$$

$$TIEC_{A500} = 0.0416F_{ET-P}^{0.604} + 0.0037F_s^{0.774} \quad \text{Eq. 44}$$

$$TIEC_{A600} = 0.0903F_{pb}^{0.6} \quad \text{Eq. 45}$$

$$TIEC_{A700} = 8.16 \cdot 10^{-4} F_{H2SO4}^{0.7} + 3.08 \cdot 10^{-3} F_{Amonia}^{0.7} + 1.99 \cdot 10^{-3} F_{CSL}^{0.66} + 5.82 \cdot 10^{-4} F_{ETOH-P}^{0.86} + 3.01 \cdot 10^{-3} F_{DAP}^{0.66} + 1.55 \quad \text{Eq. 46}$$

$$TIEC_{A800} = 0.0347F_{Steam}^{0.6} + 1.999E_p^{0.6} \quad \text{Eq. 47}$$

$$TIEC_{A900} = 0.3061Q_C^{0.642} + 0.0025F_{pb}^{0.6} \quad \text{Eq. 48}$$

The Total Direct Cost (TDC) is calculated using the same assumptions as of the NREL project. It is the sum of the TIEC for all process areas (Eq. 53) plus all the additional direct costs: warehouse (C_w), site development (C_{ST}) and additional piping (C_{AP}). The additional direct costs are based on the Inside Battery Limit (ISBL) which is the sum of the installed cost (TIEC) for all equipment within equipment for areas (200, 300, 400 and 500).

$$ISBL = C_{A200} + C_{A300} + C_{A400} + C_{A500} \quad \text{Eq. 49}$$

$$C_w = 0.04 ISBL \quad \text{Eq. 50}$$

$$C_{ST} = 0.09 ISBL \quad \text{Eq. 51}$$

$$C_{AP} = 0.045 ISBL \quad \text{Eq. 52}$$

$$TIEC = \sum^{Areas} TIEC_{Axxx} \quad \text{Eq. 53}$$

$$TDC = TIEC + C_w + C_{ST} + C_{AP} \quad \text{Eq. 54}$$

The Total Indirect Cost (TIC) is calculated based on the TDC as per the NREL project. They include pro-rateable costs (C_{pt}), field expenses (C_{FE}), home office and construction (C_{HC}), project contingency (P_{PC}) and other costs (C_o). For more information about what is included in each of these items, refer to Table S4 in Appendix 15.

$$C_{PT} = 0.1 TDC \quad \text{Eq. 55}$$

$$C_{FE} = 0.1 TDC \quad \text{Eq. 56}$$

$$C_{HC} = 0.2 TDC \quad \text{Eq. 57}$$

$$C_{PC} = 0.1 TDC \quad \text{Eq. 58}$$

$$C_O = 0.1 TDC \quad \text{Eq. 59}$$

$$TIC = C_{PT} + C_{FE} + C_{HC} + C_{PC} + C_O \quad \text{Eq. 60}$$

The Fixed Capital Investment (FIC) is calculated as the sum of the TDC plus TIC. Finally, the CAPEX is calculated as the sum of the FIC, the land cost (C_{land}) and the Working Capital (WC). The WC can be determined from the OPEX [17], with typical values for conventional chemical plants are between 15–20% of the FCI, i.e. about 13–17% of the CAPEX. For biorefineries, the NREL estimated a value of 5% of the FCI. The cost of land will depend on the size and the exact location of the plant, which might not be known at early stages of development. In the NREL project, the cost of Land is 1.8 MMUS\$ (2007), which is 0.7% of the TIEC. This proportion had been used to estimate the C_{land} .

$$FIC = TDC + TIC \quad \text{Eq. 61}$$

$$C_{LAND} = 0.007 TIEC \quad \text{Eq. 62}$$

$$WC = 0.05 FIC \quad \text{Eq. 63}$$

$$CAPEX = FIC + C_{LAND} + WC \quad \text{Eq. 64}$$

RESULTS AND DISCUSSION

The CAPEX estimation from our method including all process areas (from A_{100} to A_{900}) has been plotted as a function of the capacity and compared to values reported in the literature (Figure 3A) adjusted to 2018 US\$ with the overall Plant Index. The model has been plotted within the range 10% - 250% of the capacity of the reference project, as beyond this range, the choice of equipment and processes schemes from the reference project might need to be adjusted, leading to significant differences.

It must be stressed that the actual CAPEX will depend on many factors as mentioned previously. Therefore, CAPEX comparisons with other studies with their own underlying assumptions in the evaluations should be undertaken with great care. However, it can be seen from Figure 3A that the model including enzyme production is in agreement with the order of magnitude of what would be expected for 2G bioethanol plants. The predicted CAPEX at the same capacity of the reference project (Point 14) is higher as Area 100 has been included. The method seems to predict the CAPEX well for lower capacity plants, as the model goes through points 10 and 4, which are small plants. Projects with higher capacities were not found for comparison purposes. Points 18 - 21 represent 1G or 2G coupled with 1G bioethanol plants, thus the overall CAPEX appears lower than a 2G plant only. Interestingly, points 11 - 13 are quite far off the trend but from the information provided in the original reference [14] it is not possible to identify the reason.

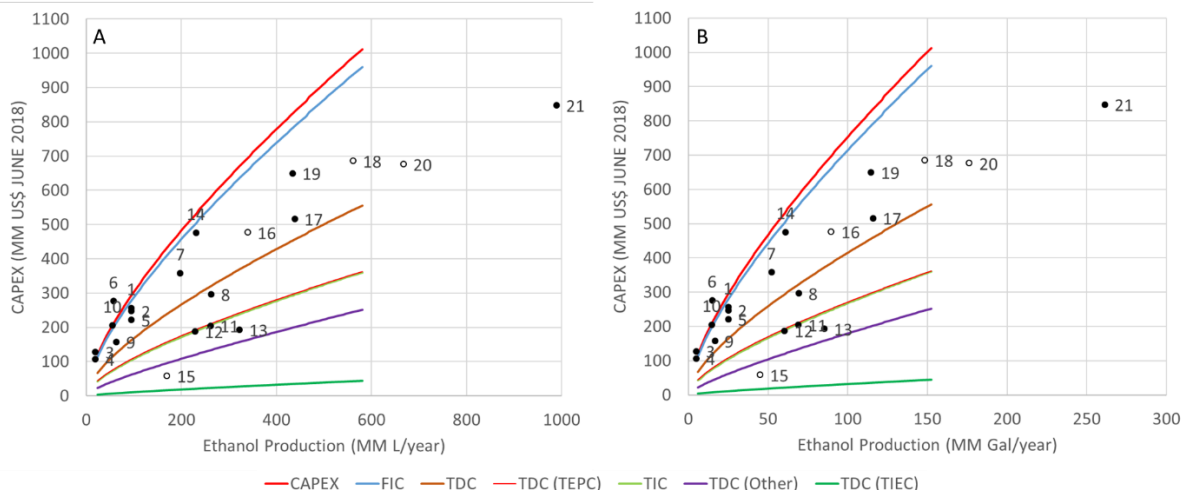


Figure 3A. CAPEX as a function of ethanol production based on NREL 2011 design (point 14) including Area 100. [A] The right chart is given in metric system units and the left chart [B] is given in imperial units. Full circles represent TEA reported in the literature for 2G or 1G2G plants. Empty circles represent TEA reported in the literature for 1G plants. The solids lines represent different costs estimated using the herein method.

It has been noticed from the calculations that the overall installation factor (defined as the ratio of TIEC / TEPC) depends on the capacity and has an average value of 1.5 if all the equipment is included and 1.73 if the equipment within Area 600 (WWT Unit) is excluded but provision for the WWT plant is still desired. The Lang factor, defined as the ratio of the CAPEX to the TEPC is also capacity dependant and has an average value of 2.57 if all equipment is included and 3.72 if equipment from Area 600 is excluded but provision for the WWT plant is still desired. This exclusion of the WWT equipment is proposed as in preliminary stages of development, the sizing of equipment is normally done for process equipment in main areas only.

As the method allows one to estimate each process area, different plant configurations can be studied. For example, a plant that received pre-treated biomass could be evaluated by removing A200 from the estimation. To illustrate this, two additional cases are investigated and discussed, namely the effect of the residence time required for the enzymatic saccharification and the effect of removing the Enzyme Production Area (A400) from the base case (purchased-enzyme scenario).

As expected, the overall CAPEX increases with increasing residence time. For smaller capacities, the relative difference is smaller than at higher capacities as economies of scale can be achieved by reducing the size of the tanks. As it has been assumed that the maximum tank size for this application is 1 million gallons (3785 m³), at higher capacities, the number of tanks needs to be increased, amplifying the CAPEX differences (Figure 4A[A]). Regarding enzyme logistics, it can be seen from Figure 4A[B] that the relative difference between taking into account the enzyme production unit (A400) or not is a function of the capacity. It is smaller at lower capacities and it is larger at a higher capacity. The reason for this is the way the CAPEX is calculated. Direct and indirect costs are based on the TIEC, and the multiplication factors (Eq. 55 - Eq. 59) have not been revised as a function of the capacity. Although the on-site enzyme cost contribution derived in our analysis leads to a higher CAPEX than a purchased-enzyme scenario, on-site production might result in a lower MESP, as a consequence of the OPEX reduction.

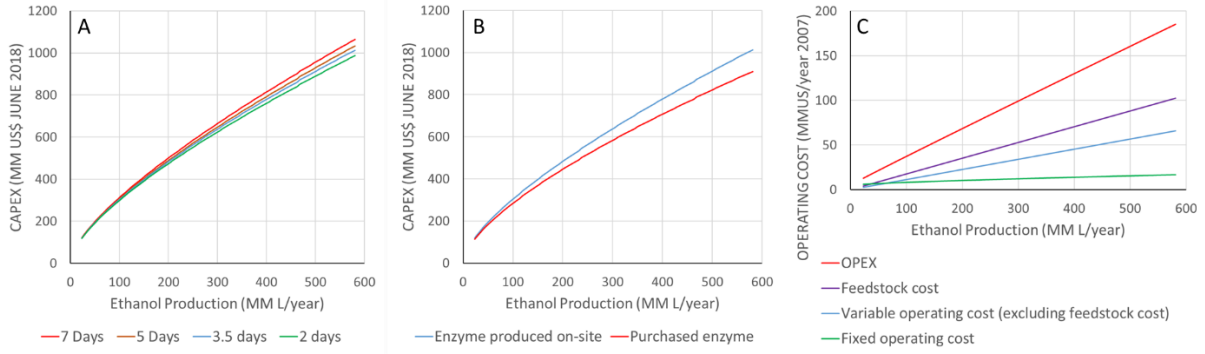


Figure 4A. Application of the method to study different cases. [A] Impact of the residence time required for the enzymatic saccharification. [B] Impact of A400: enzyme produced on-site vs. purchased enzyme case. [C] OPEX results (excluding feedstock cost).

The overall cost, assuming the same parameters as in the NREL case, can be approximated using Eq. 65 (Including all areas from A100 - A900) and Eq. 66 (Including all areas except A400). The scale exponents are slightly above 0.6, a typical value for this kind of estimation which is the origin of the six-tenths rule.

$$CAPEX_{\text{produced-enzyme}} = 0.644 F_{\text{ETOH-P}}^{0.67} \quad \text{Eq. 65}$$

$$CAPEX_{\text{purchased-enzyme}} = 0.744 F_{\text{ETOH-P}}^{0.65} \quad \text{Eq. 66}$$

The inputs required for OPEX estimation, such as the price and cost of chemicals, electricity, utilities, waste management, salaries, etc. as mentioned before, are strongly dependent on the location and year of evaluation. For accurate estimations, these parameters should be obtained from market research. For this reason, the results were not compared to other projects. The OPEX calculated using the assumptions as per the reference project as a function of the capacity is shown in Figure 4A[C]. Assuming that the chemicals and feedstock costs remain constant regardless of the quantities imported to the plant, the variable operating costs (including and excluding feedstock cost) are a linear function of the ethanol production (Eq. 67). The fixed operating cost can be also approximated as a linear function of the capacity (Eq. 68). It must be stressed that the personnel number and multiplication factors for fixed cost calculations have not been adjusted as a function of the size of the plant. The total OPEX (2007 MMUS/year) can be approximated with Eq. 69.

$$OPEX_{\text{Variable Cost (2007)}}^{(\text{without Feedstock})} = 0.00121 F_{\text{ETOH-P}} \quad \text{Eq. 67}$$

$$OPEX_{\text{Fixed Cost (2007)}} = 0.0002 F_{\text{ETOH-P}} + 6.468 \quad \text{Eq. 68}$$

$$OPEX_{\text{Total}}^{(2007)} = 0.00329 F_{\text{ETOH-P}} + 6.468 \quad \text{Eq. 69}$$

The feedstock costs, as another operating variable costs, is strongly dependent on the nature of the feedstock, its location and year of evaluation. In the reference project, it has been considered 0.0468 US\$/kg (wet basis). The feedstock cost should be included in the total OPEX (Eq. 3).

The global CAPEX and OPEX (Eq. 65 – Eq. 69) are given in terms of ethanol production flow rate but could be easily expressed in terms of biomass feedstock using global biomass to ethanol efficiency, on a dry or wet basis as needed.

Finally, the Minimum Ethanol Selling Price (MESP), determined at the breakeven point without any other financial considerations, can be calculated using (Eq. 70) (optimistic value). The term BC represents the income for any by-products generated in the plant (*e.g.* in the reference project electricity is exported to the grid). For a more detailed calculation, a discounted cash flow analysis should be used [16]. This approach consists of finding the MESP that will make the net present value of the project equal to zero, taking into consideration all economic parameters, such as discount rate (typically 10% [18]), depreciation method, income tax rates, plant life, and construction start-up duration [16]. In several NREL projects [12,16], the difference between the value obtained with Eq. 70 and the detailed discount cash flow analysis is around 50%. Therefore, for a more realistic MESP, the value obtained with Eq. 70 could be multiplied by 1.5.

$$MESP = \frac{\left(\frac{CAPEX}{Pl} + OPEX_{Total} - BC\right) \cdot 10^6 \cdot d_{ETOH}}{F_{ETOH-P} \cdot Oh} \quad \text{Eq. 70}$$

As expected, the MESP for a given project will depend on the capacity of the plant due to economies of scales: it decreases as capacity increases (Figure 5A). This method can be used to benchmark the ethanol production to meet a MESP target.

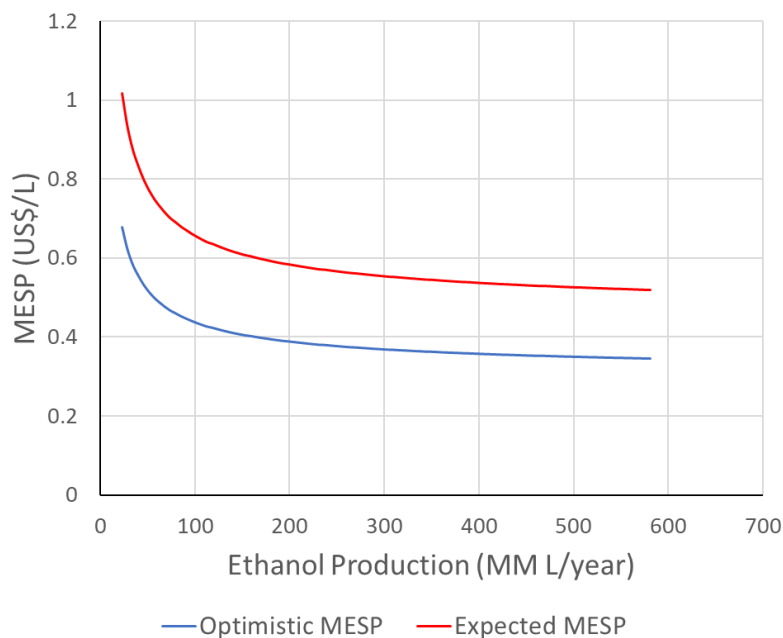


Figure 5A. Expected and optimistic MESP as a function of ethanol production calculated with Eq. 70.

Recommendations

For comparison purposes with other projects, the project CAPEX should be compared in the same year. For this, the CE INDEX for June 2018, the corresponding CE INDEX at the year of interest and Eq. 1 should be used. To allow meaningful comparisons, it is important to indicate the year of the estimate and the assumptions used.

The recommended average value for the installation factor (TIEC / TEPC) is 1.5 if all equipment is included, and 1.73 if the equipment from Area 600 (WWT Unit) is excluded but provision for the WWT plant is still required. The average Lang factor is 2.57 if all equipment is included, and 3.72 if equipment from Area 600 is excluded but provision for the WWT plant is still required.

The purpose of the estimation method is only to provide an order of magnitude of the cost to build a bioethanol plant. To determine the real cost of such a facility, the processes would need to be rigorously modelled and costed by an engineering contractor.

CONCLUSION

This study provides a quick and simple tool for estimating the capital and operating costs of a second-generation biorefinery at any scale, without the need to resort to complex process modelling nor detailed equipment sizing. This will enable early-stage researchers to evaluate the efficiency of their novel biorefinery advances and their impact on capital and operating costs at industrial scale; for process optimization, selecting best process schemes and technologies, or defining plant capacity to achieve a desired sugar or bioethanol selling price.

METHODS

CAPEX ESTIMATION

Process areas based on reference project

The costs for each piece of equipment from the NREL project (Design 2011) were used to compute the overall cost per process area. In the reference project, the quotations were obtained in 2009US\$ or 2010US\$ and expressed as 2007US\$ for comparison purposes with other NREL projects. In our case, the cost of each piece of equipment has been adjusted to June 2018US\$ (last value available at the moment the method was developed) using the Plant Cost Index from *Chemical Engineering Magazine* [19] and Eq. 1. The Plant Cost indices used are as follows: 525.4 (2007), 521.9 (2009), 550.8 (2010) and 605.2 (June 2018). The estimation is based on the Total Installed Equipment Cost (TIEC) rather than the Total Equipment Purchased Cost (TEPC). To calculate the TIEC, which includes everything required to install a given piece of equipment and make it operational (*e.g.* foundation, piping, wiring and instrumentation), the purchased cost of each piece of equipment has been multiplied by an index depending on the type of equipment and then added up. The TIEC is computed and fitted as a function of the main process variables driving the cost for each process area. This breakdown in process areas allows them to be

included or excluded in the overall estimation as required. The list of installation factors can be consulted in Table 25 the NREL report [12] or in Table S2 (Appendix 15).

The purchase cost for a given piece of equipment is related to its size or capacity. The quotes from the NREL report have been used as a baseline for cost estimation purposes. The actual cost of a given piece of equipment was then corrected by an exponential scaling expression (Eq. 2).

Where n is a characteristic scaling exponent (typically in the range of 0.6 to 0.7). The scale ratio is based upon some characteristic of the equipment related to production capacities, such as flow, power or heat duty. The scaling exponents can be consulted in Table 26 of the NREL report [12] or in Table S3 (Appendix 15).

In order to determine the Total Capital Investment (TCI) or CAPEX for the plant, other costs need to be taken into consideration besides total equipment cost in the year of interest. This includes site development, warehouse, project contingency, field expenses, home-office engineering and construction activities, and other costs related to construction. This is done by applying some factors to the total equipment purchased cost. For the method, the same assumptions and factors as per Table 27 in the NREL report [12] have been used and summarised in Table S4 in Appendix 15.

General case

General equations were developed to evaluate the cost of individual pieces of equipment for a general process based on the information provided in the reference project (Table S6 and S7 in Appendix 15). These simplified equations are based only on mass flow rate and construction material. Researchers using this simple approach need to bear in mind that the method does not take into consideration detailed equipment sizing and selection and therefore it only represents an order-of-magnitude for the equipment cost. These costs are helpful to compare different process schemes and to identify trends, during a project's early development stage. The actual cost of a piece of equipment depends upon many factors; therefore, for accurate budgeting, equipment needs to be properly sized and vendors should be consulted.

To evaluate a process with this approach, only the heat and material balance and process flow diagrams are needed. It is recommend to use the general equations to evaluate a new process or to compare different process schemes. To assess the impact of capacity, a base case should be computed with the general equations and then each piece of equipment should be corrected with the capacity using Eq. 2.

OPERATING COST ESTIMATIONS

Variable operating costs: These are incurred only when the process is operating, and they are a function of the production rate. They include raw materials, waste handling charges, and by-product credits.

The variable operating costs are obtained by multiplying the flow rate (normally expressed in units of mass per hour) by the market price. They are normally expressed on a yearly basis, thus it is necessary to multiply by the number of operating hours per year (Eq. 3). Industrial processes need to be periodically shut down for maintenance and inspection purposes. Additionally, random equipment

failures will contribute to plant downtime. For example, the NREL model assumed 8410 operating hours per year (96% uptime).

Chemical prices vary with time and location, depending on the available supply. Therefore, for a detailed study, local prices should be used. For reference, Table 1A summarises the price of the chemicals assumed by NREL. For comparison, the prices for some chemicals taken from www.alibaba.com (October 2018) have been included. Even though the chemical costs obtained for a given year could be indexed to the year of interest, similar to the equipment costs, this has not been performed as local market research would be the more accurate way to estimate the chemical costs when required. There exist several private databases (ICIS [20], IHS Markit [21]) and free databases (FRED [22]) that could be used for this purpose.

NREL used a wholesale electricity price of 5.71675 cents/kWh for 2007. Wholesale electricity price data is provided for the US market on the Energy Information Administration's website [23].

Fixed operating costs: These are generally incurred in full whether or not the plant is producing at full capacity. These costs include labour and various overhead items, such as safety, general engineering, general plant maintenance, payroll overhead, plant security, phone, light, heat, and plant communications. In the NREL report, it was assumed that there would be 60 employees and a total cost of 4.71 MM US\$ (2007) per year.

The number of personnel required for a given plant is mostly based on the level of automatization and the number and complexity of pieces of equipment. It has been noticed from available TEAs in the literature that the personnel number ranges from 50 - 73 for plants located in the US while lower figures (25 - 28) had been assumed for plants developed in Sweden. We believe that 60 employees, as per the reference project, could be assumed for early estimations without correction for plant size. Other fixed operating costs per year include maintenance, 3.0% of Inside Battery Limits (ISBL) and property insurance, 0.7% of FCI.

PRECISION OF THE METHOD

Our method is based on a conceptual study of bioethanol plants built in the US with quotations from vendors given between the years 2009 - 2010. In the NREL report [12] an accuracy of $\pm 25\%$ for the TCI estimate is reported. It should be noted that we did not change the design, choice of technologies and equipment, materials of construction, sizing and spearing criteria, applicable construction norms and regulations nor estimation and correction factors. All of these parameters will impact significantly the CAPEX of the plant. Additionally, the NREL equipment cost estimation is based on their engineering contractor and quotations from one vendor in the US. Equipment costs can vary significantly between different suppliers and in different countries.

We believe that the equations presented here are valid from a range of 10% - 250% of the production of the reference project. *i.e.* 58 - 580 MML/year (15 - 150 MMUSGAL/year) of ethanol. The uncertainty of the estimation beyond this range might be higher. Considering that there are many parameters

influencing the total CAPEX and that the method does not rely on detailed process simulation, equipment sizing and costing, we believe that the estimate uncertainty could be equivalent to a CAPEX estimation class 4 (-30% + 50%) as per AACE standards [24].

It should be noted that the following estimation method is not an optimized solution for each capacity. Advances in separation technologies, pre-treatment processes and biochemical processes (enzymes), process integration and technology changes due to capacity may lead to significant optimizations. Therefore, we believe that the estimate here is a conservative figure.

ABBREVIATIONS

1G	First generation bioethanol
2G	Second generation bioethanol
AACE	American Association of Cost Engineers
CAPEX	Capital expenditure (or capital investment cost)
CIP	Clean-in-place
CSL	Corn steep liquor
FCI	Fixed capital investment
GHG	Greenhouse gas
ISBL	Inside battery limits (of the plant)
MESP	Minimum ethanol selling price
MM	Millions
NREL	United States National Renewable Energy Laboratory
OPEX	Operating expenditure (or operating cost)
TCI	Total capital investment
TDC	Total direct cost
TEA	Techno-economic analysis
TEPC	Total equipment purchased cost
TIEC	Total installed equipment cost
US	United States
WWT	Wastewater treatment

SYMBOLS

BC	By-products credit (MMUS/year) (Eq. 70).
C _{AP}	Additional piping cost (MMUS\$) (Eq. 52).
CAPEX	CAPEX calculation (MMUS\$)(Eq. 64-Eq 66).
C _{FE}	Field expenses (MMUS\$)(Eq. 56).
C _{HC}	Home office and construction (MMUS\$)(Eq. 57).
C _{land}	Land cost (MMUS\$)(. 62).
C _O	Other Cost (MMUS\$)(Eq. 59).
C _{PC}	Project contingency (MMUS\$)(Eq. 58).
C _{PT}	Pro-rateable cost (MMUS\$)(Eq. 55).
C _{ST}	Site development cost (MMUS\$) (Eq.51).
C _w	Warehouse Cost (MMUS\$) (Eq. 50).
d _{ETOH}	Ethanol density 0.789 kg/L 20°C (Eq. 70).
E _L	Enzyme loading (mg of active enzyme/kg cellulose). NREL base case 20 mg/kg cellulose.
E _m	Glucose oligomer yield from saccharification. NREL base case 0.04.
E _s	Glucose yield or saccharification efficiency. NREL base case 0.952.
F	Mass flow rate (kg/h).
F _{ammonia}	Ammonia flow rate (kg/h). NREL base case 1166 kg/h (Eq. 26).
F _{ASH}	Ash flow rate for disposal (kg/h). NREL base case 5725 kg/h (Eq. 39).
F _{bc}	Boiler chemicals flow rate (kg/h). NREL base case 0.45 kg/h (Eq. 35).
F _{bg}	Biogas flow rate from WWT (kg/h). NREL base case 21860 kg/h (Eq. 9).
F _{CA}	Caustic Soda flow rate (kg/h). NREL base case 2252 kg/h (Eq. 33).
F _{cc}	Cooling tower chemicals flow rate (kg/h). NREL base case 2 kg/h (Eq. 36).

F_{CSL}	Corn steep liquor flow rate (kg/h). NREL base case 1322 kg/h (Eq. 27).
F_{DAP}	Diammonium phosphate flow rate (kg/h). NREL base case 142 kg/h (Eq. 28).
F_e	Enzyme protein flow rate (kg/h). NREL base case 620 kg/h (including margins) (Eq. 7).
F_{EN}	Enzyme nutrients flow rate (kg/h). NREL base case 67 kg/h (Eq. 32).
F_{ETOH-F}	Ethanol produced after fermentation flow rate (beer to distillation) (kg/h). NREL base case 21941 kg/h (Eq. 5).
F_{ETOH-P}	Total ethanol produced flow rate (kg/h). NREL base case 21808 kg/h (Eq. 6).
F_{fw}	Fresh water flow rate (kg/h). NREL base case 147140 kg/h (Eq. 37).
F_g	Dissolved glucose for fermentation flow rate (kg/h). NREL base case 3550 kg/h (Eq. 5).
$F_{gasoline}$	Gasoline flow rate (kg/h). NREL base case 465 kg/h (Eq. 38).
F_{glu}	Glucose flow rate (kg/h). NREL base case 2481 kg/h (Eq. 30).
$F_{H_2SO_4}$	Sulfuric acid flow rate (kg/h). NREL base case 1981 kg/h (Eq. 25).
F_{heat}	Steam flow rate used as the heating medium (kg/h). NREL base case 133331 kg/h (Eq. 12).
FIC	FIC Calculation (MMUS\$) (Eq. 61).
F_{lime}	Lime flow rate (kg/h). NREL base case 895 kg/h (Eq. 34).
F_{pb}	Pre-treated biomass flow rate on a dry basis (kg/h). NREL base case 46296 kg/h.
F_{rb}	Raw biomass flow rate on a dry basis (kg/h). NREL base case 83334 kg/h.
F_s	Unreacted solids flow rate (kg/h). NREL base case 21413 kg/h (Eq. 8).
F_{sl}	Solid Sludge form WWT flow rate (kg/h). NREL base case 9758 kg/h (Eq. 10).
F_{SO_2}	Sulfur dioxide flow rate (kg/h). NREL base case 16 kg/h (Eq. 31).
F_{sor}	Sorbitol flow rate (kg/h). NREL base case 44 kg/h (Eq. 29).
F_{steam}	Steam generated flow rate (kg/h). NREL base case 234784 kg/h (Eq. 11).
F_x	Dissolved xylose for fermentation flow rate (kg/h). NREL base case 16476 kg/h (Eq. 5).
$ISBL$	ISBL calculation (MMUS\$) (Eq. 49).
MC	Material cost (US\$/kg) (Eq. 3).
$MESP$	Minimum ethanol selling price (US\$/L) (Eq. 70).
n	Characteristic scaling exponent (typically in the range of 0.6 to 0.7). Values are given in Table S3 in Appendix 15.
Oh	Operating hours per year (hours/year). NREL base case 8410 operating hours per year (Eq. 3 and Eq. 70).
$OPEX$	OPEX Calculations (MMUS\$/YEAR) (Eq. 67-Eq 69).
P	Pulp yield. NREL base case 55.53% (Eq. 4).
P_{Axxx}	Electric power consumption per unit area (MWh). The subscript indicates the process area (Eq. 14 – Eq. 21).
P_c	Total electric power consumption (MWh). NREL base case 28.5 MWh (Eq. 22).
P_e	Electric power surplus to the grid (MWh). NREL base case 12.8 MWh (Eq. 23).
PI	Plant design life or lifetime in years (years). NREL base case 30 years (Eq. 70).
P_p	Electric power produced (MWh). NREL base case 41.3 MWh (Eq. 13).
Q_c	Cooling duty (MW). NREL base case 112.8 MW (Eq. 24).
TDC	TDC Calculation (MMUS\$) (Eq. 54).
TIC	TIC Calculation (MMUS\$) (Eq. 60).
$TIEC$	Overall TIEC (MMUS\$) (Eq. 53).
$TIEC_{Axxx}$	TIEC per area (MMUS\$). The subscript indicates the process area (Eq. 40 - Eq. 48).
T_s	Residence time for the saccharification reaction in days. The equations had been fitted for values between 1 and 7 days. NREL base case 3.5 days.
VOP	Variable operating cost (MMUS\$/year) (Eq. 3).
WC	Working capital (MMUS\$) (Eq. 63).
X_c	Cellulose mass fraction in pre-treated pulp. NREL base case 0.565.

REFERENCES

1. Sa, J. Trends in biotechnological production of fuel ethanol from different feedstocks. 99, 5270–5295 (2008).
2. Mandegari, M. A., Farzad, S. & Görgens, J. F. Recent trends on techno-economic assessment (TEA) of sugarcane biorefineries. 15, 704–712 (2017).
3. Rastogi, M. & Shrivastava, S. Recent advances in second generation bioethanol production: An insight to pretreatment, saccharification and fermentation processes. *Renew. Sustain. Energy Rev.* 80, 330–340 (2017).
4. Brandt, A., Gräsvik, J., Hallett, J. P. & Welton, T. Deconstruction of lignocellulosic biomass with ionic liquids. *Green Chem.* 15, 550 (2013).
5. Gschwend, F. J. V., Malaret, F., Shinde, S. & Hallett, J. P. Rapid pretreatment of *Miscanthus* using the low-cost ionic liquid triethylammonium hydrogen sulfate at elevated temperatures. 3486–3498 (2018). doi:10.1039/c8gc00837j
6. Putro, J. N., Soetaredjo, F. E., Lin, S., Ju, Y. & Ismajli, S. RSC Advances Pretreatment and conversion of lignocellulose biomass into valuable chemicals. 46834–46852 (2016). doi:10.1039/c6ra09851g

7. Mohapatra, S., Mishra, C., Behera, S. S. & Thatoi, H. Application of pretreatment , fermentation and molecular techniques for enhancing bioethanol production from grass biomass – A review. *Renew. Sustain. Energy Rev.* 78, 1007–1032 (2017).
8. Gnansounou, E. & Dauriat, A. Author ' s personal copy Bioresource Technology Techno-economic analysis of lignocellulosic ethanol : A review. doi:10.1016/j.biortech.2010.02.009
9. Tao, L. & Aden, A. The economics of current and future biofuels. 199–217 (2009). doi:10.1007/s11627-009-9216-8
10. Tsagkari, M., Couturier, J. L., Kokossis, A. & Dubois, J. L. Early-Stage Capital Cost Estimation of Biorefinery Processes: A Comparative Study of Heuristic Techniques. *ChemSusChem* 9, 2284–2297 (2016).
11. Piotrowski, S., Carus, M., Sibilla, F. & Raschka, A. New nova Methodology for Techno-Economic Evaluations of Innovative Industrial Processes (nTEE). 13 (2014).
12. Humbird, D. et al. Process Design and Economics for Biochemical Conversion of Lignocellulosic Biomass to Ethanol. *Renew. Energy* 303, 147 (2011).
13. Zhao, L. et al. Techno-Economic Analysis of Bioethanol Production from Lignocellulosic Biomass in China: Dilute-Acid Pretreatment and Enzymatic Hydrolysis of Corn Stover. 4096–4117 (2015). doi:10.3390/en8054096
14. Sassner, P., Galbe, M. & Zacchi, G. Techno-economic evaluation of bioethanol production from three different lignocellulosic materials. *Biomass and Bioenergy* 32, 422–430 (2008).
15. Wingren, A., Galbe, M. & Zacchi, G. Techno-economic evaluation of producing ethanol from softwood: Comparison of SSF and SHF and identification of bottlenecks. *Biotechnol. Prog.* 19, 1109–1117 (2003).
16. Aden, A. et al. Lignocellulosic Biomass to Ethanol Process Design and Economics Utilizing Co-Current Dilute Acid Prehydrolysis and Enzymatic Hydrolysis for Corn Stover Lignocellulosic Biomass to Ethanol Process Design and Economics Utilizing Co-Current Dilute Acid Prehyd. (2002).
17. Peters, M. S., Timmerhaus, K. D. & West, R. E. Plant Design and Economics. *Plant Design and Economics for Chemical Engineers* (1991).
18. Short, W. & Packey, D. J. A Manual for the Economic Evaluation of Energy Efficiency and Renewable Energy Technologies. (1995).
19. Chemical Engineering Magazine. Chemical Engineering Magazine Plant Cost Index. Available at: <http://www.che.com/pci/>.
20. ICIS. Available at: <https://www.icis.com/explore/>.
21. IHS Markit. Available at: <https://ihsmarkit.com/index.html>.
22. FRED Economic Data. Available at: <https://fred.stlouisfed.org/>.
23. North American Electric Reliability Corporation. "Wholesale Average Electricity Price Table." U.S. Energy Information Administration website,. Available at: <http://www.eia.doe.gov/cneaf/electricity/wholesale/wholesale.html>.
24. AACEI. 10S-90: Cost Engineering Terminology. 1–107 (2017).
25. Alibaba. Available at: www.alibaba.com.
26. Report, A. S. Economic Feasibility Study of an Acid Hydrolysis-Based Ethanol Plant. Subcontract Report SERI-STR-231-3142, Prepared under Subcontract ZX-3-03096-2. (1987).
27. Chem Systems, I. Economic Feasibility Study of an Enzymatic Hydrolysis based Ethanol Plant with Prehydrolysis Pretreatment. Subcontract Report SERISTR-231-3135, Prepared under Subcontract XX-3-03097-1. (1987).
28. Stone & Webster Engineering. Feasibility of an Enzyme-based Ethanol Plant. Subcontract Report SERI-STR-231-3138, Prepared under Subcontract ZX-3-03097-1. (1987).
29. Wooley, R. et al. Lignocellulosic Biomass to Ethanol Process Design and Economics Utilizing Co-Current Dilute Acid Prehydrolysis and Enzymatic Hydrolysis Current and Futuristic Scenarios Lignocellulosic Biomass to Ethanol Process Design and Economics Utilizing Co-Current D. (1999).
30. Junqueira, T. L. *et al.* Techno-economic analysis and climate change impacts of sugarcane biorefineries considering different time horizons. *Biotechnol. Biofuels* 10, 1–12 (2017).

Appendix 15 – ESI - Quick investment and operating cost estimation method for second generation bioethanol production plants

PROCESS DESCRIPTION

Area 100: Feedstock storage and handling

Area 100 handles the incoming biomass feedstock. It has been assumed that the feedstock (corn stover) was delivered according to certain specifications: particle size distribution (mean size of 0.4 or 0.6 cm or 0.16 – 0.23 in), moisture content (20% moisture) and bulk density (0.14 – 0.18 g/cm³ or 9 – 11 lb/ft³) [1]. The main equipment in this area consists of weighing and unloading stations for incoming biomass supply trucks, short-term queuing storage, and conveyors for feeding bulk feedstock to the pre-treatment section. The feedstock is not washed or dried in this model, but it has been mentioned that this might be required to reduce any incoming inorganics from fertilized feedstocks like corn stover. For the cost estimation of this unit, the number of truck scales had been kept constant. The number of truck-unloading stations has been calculated according to the plant capacity with no further corrections as it has been assumed that trucks need to be able to unload in the same time as per the reference project. The rest of the equipment had been scaled according to the capacity. It is noteworthy to mention that the cost of this unit was not included in the total cost of the NREL plant as they considered that its cost was included in the feedstock cost.

Area 200: Pre-treatment and conditioning

In general, the pre-treatment step is needed to enhance the activity of the biomass towards enzymatic saccharification. The pre-treatment process selected by NREL [1] is the co-current dilute-acid pre-treatment, which converts most of the hemicellulose carbohydrates in the feedstock to soluble sugars (xylose, mannose, arabinose, and glucose) and acetyl groups to acetic acid. Also, some lignin is solubilised. The remaining solid has a high enzymatic digestibility as the pre-treatment disrupts cell wall structures, reduces cellulose crystallinity and chain length. Costs for this area each piece of equipment had been scaled to the production capacity, keeping other parameters and assumptions constant.

Area 300: Enzymatic hydrolysis and fermentation

In this process area, the cellulose-rich pulp is first converted to glucose (and other sugars) using enzymes through a process known as enzymatic saccharification or enzymatic hydrolysis. To achieve this, a mixture of enzymes (catalytic proteins) that work together to break down cellulose fibres into glucose monomers is used. The resulting sugars are then fermented to ethanol using microorganisms. For this purpose, co-fermenting bacterium *Zymomonas mobilis* was selected by NREL, which is able to ferment glucose and xylose to ethanol. Another option is to use metabolically engineered strains of *Saccharomyces cerevisiae*. Finally, the ethanol-containing fermentation broth is emptied to the beer well (storage tank) before being pumped to distillation [1].

The process selected for the NREL plant is known as the Separate (or sequential) Hydrolysis and Fermentation (SHF) process. Another alternative is a Simultaneous Saccharification and Co-Fermentation (SSCF) process, in which the enzyme continues to hydrolyse cellulose even after fermentation is initiated. The SSCF is not considered for the TEA, but it might represent an opportunity for process optimization.

The feedstock for this unit is a slurry (total solids loading is 10.8 wt%) containing a cellulose-rich pulp. The first piece of equipment is a cooler to bring the temperature of the feed to the optimum saccharification temperature (49 °C). If the pre-treatment technology is changed, the incoming feed might be at different temperatures, so the cooler might need to be replaced by a heater or removed from the process. However, for simplicity, it has been kept in the model and no corrections with the inlet temperature have been performed, as its contribution to the total CAPEX is minor.

The main variables driving the cost of area 300 is the capacity and residence time for the saccharification. In the NREL case, it has been considered a total of 3.5 days residence time (1 day in the saccharification tank and the remaining time in the ethanol fermenters) to achieve 90% conversion of cellulose to glucose. This split in residence time for the saccharification had been kept the same for the estimation. It is important to mention that the residence time required for this enzymatic hydrolysis will

depend on the severity of the pre-treatment process [2], the feedstock and the enzyme loading, thus it has to be optimized for a given project. The residence time for fermentation (1.5 days) had been kept the same as the base case. Regarding the fermenters, the number of tanks has been adjusted according to the capacity and minimized without exceeding the 1 MM gal capacity (3785 m³) tanks used by NREL, as we consider this value as large.

Area 400: Cellulase enzyme production

This process area produces the cellulase enzyme mixture (catalytic proteins) that is used in Area 300 to hydrolyse cellulose into glucose. Cellulase is produced onsite using *Trichoderma reesei* (among other microorganisms), a filamentous fungus that secretes high levels of cellulase enzymes when grown aerobically in the presence of cellulose or other cellulase inducers [1]. Another alternative to on-site production of the enzyme is to purchase it from an external vendor. This approach will decrease the overall CAPEX and simplify the operation of the plant but will increase the OPEX of the plant, which might result in an overall increase in the MESP.

The amount of enzyme used (the enzyme loading) is determined by the amount of cellulose present in the hydrolysate and the specific activity of the enzyme. In the NREL design, the total cellulase loading is 20 mg enzyme protein/g cellulose to achieve a 90% conversion to glucose in 3.5 days. Enzyme loading has a significant and complex impact on process economics and therefore should be optimized for each project [1].

For the estimation method, the number of bio-reactors had been adjusted according to the capacity. It was mentioned in the NREL report that the on-site enzyme process was designed without input from enzyme companies or other protein production experts.

Area 500: Product, solids, and water recovery

Area 500 separates the fermentation broth from Area 300 into water, anhydrous ethanol (99.5%), and combustible solids. Two distillation columns and a molecular sieve adsorption unit were used by NREL to recover ethanol from the raw fermentation beer. The column bottoms (stillage) stream contains unconverted insoluble solids, which are recovered by a pressure filter and sent to the combustor in Area 800. The pressed stillage water cannot be recycled directly back to the process because it is loaded with contaminants and is therefore sent to the Waste Water Treatment (WWT) for clean-up [1].

For the cost estimation model, the ethanol recovery units had been scaled with the quantity of ethanol produced while the cost of the solid recovery units had been scaled with the amounts of solids to be removed.

Area 600: Wastewater treatment (WWT)

The WWT unit processes wastewater streams generated in the plant prior to recycling back to the process or released into the environment. It has been assumed that the quality of the water produced is suitable for the process, which reduces both the water makeup requirements and discharges to the environment.

The combined wastewater streams are processed by anaerobic digestion and aerobic digestion to digest organic matter in the stream. A methane-rich biogas stream and a sludge are routed to the combustor as fuels. It is noteworthy to mention that the WWT unit has been sized to handle the amount and nature of the waste streams, which are dependent on pre-treatment technology. For the NREL case, the use of ammonia is required in the pre-treatment unit to neutralize the pH from the sulfuric acid pre-treatment (ammonia conditioning). Therefore, the estimation of the cost of the WWT will be less accurate if the pre-treatment section is changed.

Area 700: Product and feed chemical storage

This portion of the plant provides bulk storage for process chemicals and the ethanol product.

For the NREL case, the chemicals stored in this area include ammonia, corn steep liquor (CSL), sulfuric acid, and gasoline (used as a denaturant for the ethanol product). Water for fire suppression is also stored here.

The chemical and quantities needed will depend on the technologies retained for the design. Also, the storage capacity will depend on the supply chains, for example, for chemicals that are easily available (common chemicals supplied by several vendors) or not critical for production, the storage capacity

might be reduced. For critical chemicals or chemicals which are more difficult to find, the storage capacity could be increased.

For cost estimation purposes, the same chemicals and storage capacities (based on production time) are retained. Fire water is assumed to be capacity independent.

Area 800: Combustor, boiler, and turbogenerator

The purpose of this process area is to burn various organic by-product streams (lignin and the unconverted biomass, biogas from anaerobic digestion and biomass sludge from WWT) to produce steam and electricity. In doing so, the plant can generate its own energetic requirements reducing the OPEX. Additionally, the solid waste disposal costs are reduced while the revenues are increased by exporting the excess electricity to the grid.

For estimation purposes, the cost of this process area had been modelled as a function of the steam and electrical power generated.

Area 900: Utilities

Area 900 supplies the utilities required by the facility, such as cooling water, chilled water, plant and instrument air, process water, and the Clean-In-Place (CIP) system.

For estimation purposes, the cost of this process area had been modelled as a function of the cooling duty, for all water storage and distribution facilities, and plant production capacity for plant and instrument air and the CIP system.

HEAT, COOLING AND STEAM CALCULATIONS

The heating or cooling duty for a process stream can be calculated with the equation:

$$Q = 2.78 \cdot 10^{-7} \cdot (F \cdot C_p \cdot \Delta T + F_{vap} \cdot H_{vap}) \quad \text{Eq. S1}$$

Where Q is the cooling or heating duty in MW, F is the mass flow rate in kg/h, C_p is the heat capacity in J/g.°C or kJ/kg.°C, ΔT is the difference in temperature in °C, F_{vap} is the evaporated mass flow rate in kg/h and H_{vap} is the enthalpy of vaporization in J/g.

Values for the heat capacity and heat of vaporization (enthalpy of vaporization) for pure substances can be easily found in literature, for example, in The NIST Chemistry WebBook [3]. As the C_p is a function of temperature, it needs to be integrated over the temperature range for accurate determinations. An easier approach is to determine the C_p at the mean temperature. For wet solids or slurries, the C_p of the material can be calculated as the sum of the C_p s of each compound multiplied by their mass fraction. Once the cooling or heating requirement is calculated with Eq. S1, the mass flow rate of the corresponding utility can be determined with the values given in Table S1.

Table S1. Thermophysical data of selected compounds.

Compound	Properties	Remarks
Biomass	$C_p = 0.00534 \cdot T - 0.299$ [4] Eq. S2	Temperature Range [313 K - 353 K (40 °C - 80 °C)]
Lignin	$C_p = 0.00405 \cdot T + 0.045$ [5] Eq. S3	Temperature Range [273.15 K - 380 K (0 °C - 107 °C)]
Wood Cellulose	$C_p = 0.00506 \cdot T + 0.407$ [6] Eq. S4	Temperature Range [350 K - 440 K (77 °C - 167 °C)]
Water	$F_{cooling\ water} = 95730 \cdot Q$ Eq. S5	Cooling Water - Temperature increase 288 K-353 K (28 °C - 33 °C)
	$F_{chilled\ water} = 78040 \cdot Q$ Eq. S6	Chilled Water - Temperature increase 277 K - 288 K (4 °C - 15 °C)
	$C_p = 4.19$ $C_p = 2258$	Heat capacity of liquid water at 70 °C (*) Enthalpy of vaporization of water at atmospheric pressure (*).

Compound	Properties	Remarks
Steam	$F_{steam} = 1673 \cdot Q$ $C_p = 2.50$	Eq. S7 Supersaturated steam flow rate (from 268 °C and 13 atm to saturated liquid at 13 atm (192 °C) (*)) Heat capacity of superheated steam at 220 °C and 13 atm (*)

(*) Values calculated with HYSYS V8.8 thermodynamic package ASME Steam.

Example – Steam consumption calculation in the pre-treatment reactor

From the steam table provided in the Process Flow Diagram (PFD-P120-A201) in the reference project [1], it can be seen that 104167 kg/h of wet biomass (20% water content in mass) enters the reactor at 25 °C and it is heated at 158 °C (stream 217). First, the C_p of the biomass is calculated at the mean temperature (91.5 °C). From Eq. S1 and the values provided in Table S1, the heating duty for the biomass is given below. Note that as there are no phase changes, F_{vap} and H_{vap} are equal to zero.

$$Q = 2.78 \cdot 10^{-7} \cdot (F \cdot (w_{water} \cdot C_{p_{water}} + w_{biomass} \cdot C_{p_{biomass}}) \cdot \Delta T)$$

$$Q = 2.78 \cdot 10^{-7} \cdot (104167 \cdot (0.2 \cdot 4.19 + 0.8 \cdot 1.68) \cdot (158 - 25)) = 8.31 \text{ MW}$$

Water is added to the process (stream 212: 140850 kg/h at 95 °C) as well as diluted sulfuric acid (stream 214: 38801 kg/h at 113 °C). The energy required to warm these streams to the reaction temperature (158 °C) needs to be calculated with Eq. S1 and the values provided in Table S1. For the diluted sulfuric acid, the C_p of the water is used. This leads to 10.34 MW and 2.03 MW respectively, thus the total energy required is 20.68 MW.

Ignoring the energy input due to mechanical equipment (conveyors, pumps, agitators, etc), the amount of steam required can be calculated using Eq. S7. In this instance, the steam is added directly to the process and mixed with the reaction media, therefore, the amount of energy from the condensation temperature of the steam (192 °C) to the reaction temperature needs to be taken into account.

$$Q = 2.78 \cdot 10^{-7} \cdot (F \cdot C_{p_{water}} \cdot \Delta T) = 2.78 \cdot 10^{-7} \cdot (F \cdot 4.19 \cdot (192 - 158))$$

$$Q = \frac{1}{1673} \cdot F$$

$$Q = 20.68 = 2.78 \cdot 10^{-7} \cdot (F \cdot 4.19 \cdot (192 - 158)) + \frac{1}{1673} \cdot F$$

Solving for F, the amount of steam is 32441 kg/h. The amount of steam calculated with these assumptions overestimates by 5% (4417 kg/h) the values are given in the NREL report (streams 215 and 216: 28024 kg/h), due to the energy input from the mechanical equipment and detailed C_p calculations by components and temperatures. In most situations, the energy input from mechanical equipment, such as pumps and agitators, are small and can be omitted for preliminary estimations. It needs to be highlighted that the process has been modelled by NREL as an adiabatic system, meaning that energy losses to the environment are not taken into account. The steam consumption estimated by the NREL is optimistic and will be higher in an actual plant.

To estimate changes in the steam flow rate as a function of pre-treatment temperature, the above methodology can be used subtracting the amount of steam equivalent to the energy input of mechanical equipment. However, the influence of residence time cannot be evaluated as the process has been modelled as an adiabatic system.

OTHER INFORMATION

Table S2. Installations factors taken from table 25 of the NREL report [1].

Equipment	Multiplier (*)
Agitators, carbon steel	1.6
Agitators, stainless steel	1.5
Boiler	1.8
Compressors, motor-driven	1.6
Cooling tower	1.5
Distillation columns, stainless steel	2.4
Heat exchangers, shell & tube, stainless steel	2.2
Heat exchangers, plate & frame, stainless steel	1.8
Heat exchangers, air-cooled	2.8
Inline mixers	1
Skidded equipment	1.8
Solids handling equipment (incl. filters)	1.7
Pressure vessels, carbon steel	3.1
Pressure vessels, stainless steel	2
Pre-treatment reactor system	1.5
Pumps, stainless steel	2.3
Pumps, carbon steel	3.1
Tanks, field-erected, carbon steel	1.7
Tanks, field-erected, stainless steel	1.5
Tanks, storage, plastic	3
Tanks, storage, carbon steel	2.6
Tanks, storage, stainless steel	1.8
Turbine/Generator	1.8

(*) Installed cost = (purchased equipment cost) x (multiplier).

Table S3. Scaling exponents taken from table 26 of the NREL report [1].

Equipment	Exponent
Agitators	0.5
Compressors, motor driven	0.6
Distillation columns	0.6
Heat exchangers	0.7
Inline mixers	0.5
Package quotes / Skidded equipment	0.6
Pressure vessels	0.7
Pumps	0.8
Tanks, atmospheric	0.7
Solids handling equipment	0.8

Table S4. Additional costs for determining Total Capital Investment (TCI) taken from table 27 of the NREL report [1].

Item	Description	Amount
Additional direct costs: Based on the Inside Battery Limit (ISBL) which is the sum of the installed cost (TIEC) for all equipment within equipment for areas (200,300, 400 and 500)		
Warehouse	On-site storage of equipment and supplies.	4.0% of ISBL
Site development	Includes fencing, curbing, parking lot, roads, well drainage, rail system, soil borings, and general paving. This factor allows for minimum site development assuming a clear site with no unusual problems such as right-of-way, difficult land clearing, or unusual environmental problems.	9.0% of ISBL
Additional piping	To connect ISBL equipment to storage and utilities outside the battery limits.	4.5% of ISBL
Indirect costs: Based on Total direct Cost (TDC), which is the sum of the installed cost (TIEC) (C_{IC}) for all areas plus all the additional direct costs (warehouse, site development and additional piping)		
Pro-rateable costs	This includes fringe benefits, burdens, and insurance of the construction contractor.	10% of TDC
Field expenses	Consumables, small tool and equipment rental, field services, temporary construction facilities, and field construction supervision.	10% of TDC
Home office and construction	Engineering plus incidentals, purchasing, and construction.	20% of TDC
Project contingency	Extra cash on hand for unforeseen issues during construction.	10% of TDC
Other costs	Start-up and commissioning costs. Land, rights-of-way, permits, surveys, and fees. Piling, soil compaction/dewatering, unusual foundations. Sales, use, and other taxes. Freight, insurance in transit, and import duties on equipment, piping, steel, instrumentation, etc. Overtime pay during construction. Field insurance. Project team. Transportation equipment, bulk shipping containers, plant vehicles, etc.	10% of TDC

Table S5. TEAs for 2G, 1G2G and 1G bioethanol plants.

Data Point	Year	Ethanol Production		Cost-Year	Cost-2018	Land included	Enzyme Production	WWT Included	Pre-treatment	Enzymatic Process	By-products	Feed-stock	Ref.
		MM Gal/year	MM L/year	MM US \$	MM US \$								
1		25	94.6	139.7	262.1					SHF	Furfural and electricity		
2	1984	25	94.6	134.8	252.9	Yes	No	Yes	Steam pre-treatment using H ₂ SO ₄ as catalyst	SHF	Furfural	Mixed of hardwood chips	7
3		5	18.9	69.7	130.8					SHF	Furfural and electricity		
4		5	18.9	58.1	109.0					SHF	Furfural		
5	1984	25	94.6	120.7	226.4	Yes	yes	yes	Dilute acid	SHF	Carbon dioxide and furfural	Hardwoods (57% aspen, 20% maple and 23% others)	8
6	1984	15	56.8	150.6	282.6	Yes	yes	yes	Steam pre-treatment using H ₂ SO ₄ as catalyst	SHF	n/a	eucalyptus wood chips	9
7	1997	80.3	197.6	233.8	366.1	Yes	Yes	Yes	Co-Current Dilute Acid Pre-hydrolysis	SHF	Electricity	hardwood chips	10
8	2000	69	262.3	197.4	303.1	Yes	No	Yes	Co-Current Dilute Acid Pre-hydrolysis	SHF	Electricity	Corn stover (comprised of stalks, leaves, cobs, and husks)	11
9	2003	60.4	63.0	107.1	161.2	known	No	known	SO ₂ -catalysed steam pre-treatment	SSCF	Solid fuel and CO ₂	Spruce	12
10	2003	85.2	55.0	139.3	209.7	known	No	known		SHF		Spruce	12
11	2006	25	261.2	172.5	209.0	known	No	Yes	SO ₂ -catalysed steam pre-treatment	SSCF	Solid fuel and CO ₂	Salix	13
12	2006	25	228.6	158.4	191.9	known	No	Yes		SSCF		corn stover	13
13	2006	5	322.5	162.7	197.1	known	No	Yes		SSCF		spruce	13
14	2007	5	304.0	422.5	486.7	yes	yes		co-current dilute-acid pre-treatment	SHF	Electricity	Corn Stover	1
15	2016	16.6	170.4	53.3	59.5				1G	SHF	-	sugar cane	
16	2016	14.5	339.7	436.4	487.6				1G	SHF		sugar cane	
17	2016	45.0	438.3	472.8	528.2				1G + steam pre-treated using H ₃ PO ₄ as catalyst	SHF		sugar cane bagasse and leaves	
18	2016	89.7	561.6	627.6	701.2	known	No	yes	1G	SHF		sugar cane	14
19	2016	115.8	433.9	595.1	664.9				1G + steam pre-treated using H ₃ PO ₄ as catalyst	SHF	Electricity	sugar cane bagasse and leaves	
20	2016	148.4	667.4	619.0	691.6				1G	SHF		sugar cane	
21	2016	114.6	989.1	776.5	867.5				1G + steam pre-treated using H ₃ PO ₄ as catalyst	SHF		sugar cane bagasse and leaves	

Table S6. Formulae to estimate the order-of-magnitude of the purchased costs (US\$ - June 2018) of different equipment commonly found in biorefineries. These costs are helpful during a project's early development and can be used to compare process schemes. The actual cost of a piece of equipment depends upon many factors, therefore, for accurate budgeting, equipment needs to be properly sized and vendors should be consulted.

Equipment	Formula	Eq.	Installation Factors	Remarks
Agitator	$PEC = 4452 \cdot F^{0.16} \cdot M_f$	Eq. S8	1.5	
Air compressor (for enzyme production)	$PEC = 8534 \cdot F_E^{0.6}$	Eq. S9	1.6	
Air compressor (utilities)	$PEC = 36 \cdot F_{rb}^{0.6}$	Eq. S10	1.6	
Air compressors (for press filter)	$PEC = 1397 \cdot F_{s-dry}^{0.6}$	Eq. S11	1.6	Includes pressing and drying compressors.
Beer rectification system	$PEC = 11450 \cdot F_{ETOH-P}^{0.6}$	Eq. S12	2.45	Includes distillations columns, all pumps, vessels, heat exchangers and air cooler.
Bels scale	$PEC = 12.9 \cdot F_{wb}^{0.6}$	Eq. S13	1.7	Total cost for 2 items.
Boiler	$PEC = 19012 \cdot F_{steam}^{0.6}$	Eq. S14	1.8	
Chilled water package	$PEC = 261300 \cdot Q_C^{0.6}$	Eq. S15	1.6	Water temperature from 4 °C to 15 °C
Cleaning in place system	$PEC = 930 \cdot F_{rb}^{0.6}$	Eq. S16	1.8	
Concrete feedstock storage dome	$PEC = 3921 \cdot F_{wb}^{0.6}$	Eq. S17	1.7	Including the reclaim system. Storage capacity based on ref project. Concrete dome has a 36 h buffer capacity.
Cooling tower system	$PEC = 101350 \cdot Q_C^{0.6}$	Eq. S18	1.5	Material fiberglass.
Dust collection system	$PEC = 335 \cdot F_{wb}^{0.6}$	Eq. S19	1.7	Total cost for 6 items.
Evaporator system	$PEC = 5353 \cdot F_{evap}^{0.6}$	Eq. S20	1	Mechanical Recompression. Materials SS316 / CS.
Filter (press)	$PEC = 1322 \cdot F_{s-dry}^{0.8}$	Eq. S21	1.7	Material SS306.
Heat exchanger	$PEC = (11700 \cdot \ln(Q) + 13200) \cdot M_f$	Eq. S22	Table S1	
Heat exchanger (gas-gas)	$PEC = (4300 \cdot \ln(Q) + 4500) \cdot M_f$	Eq. S23	Table S1	
Instrument air dryer	$PEC = 20 \cdot F_{rb}^{0.6}$	Eq. S24	1	
Mixer – inline with electric motor	$PEC = 108 \cdot F^{0.5} \cdot M_f$	Eq. S25	1.7	
Mixer – static	$PEC = 382 \cdot F^{0.17} \cdot M_f$	Eq. S26	1	
Molecular sieve package (ethanol drying)	$PEC = 7406 \cdot F_{ETOH-P}^{0.6}$	Eq. S27	1.8	Includes all items.
Pump	$PEC = 655 \cdot F^{0.26} \cdot M_f$	Eq. S28	Table S1	
Screw continuous reactor	$PEC = 25630 \cdot F_{dry}^{0.6}$	Eq. S29	1.5	Total cost for all items (including spare items as per reference project). Includes all conveyors, feeders, heaters. Reactor material: Incoloy 825-CLAD; CS.
Screw conveyor (wet cake)	$PEC = 31.5 \cdot F_{dry}^{0.6}$	Eq. S30	1.7	Screw conveyor cost is a function of the screw diameter and the length.
Storage tank	$PEC = (113000 \cdot \ln(F) - 615000) \cdot M_f$ (Minimum value 5500 US\$)	Eq. S31	Table S1	Minimum value 5500 US\$, which corresponds to a 650 gallons CS vertical tank.
Storage tank (process water)	$PEC = 32 \cdot F^{0.7}$	Eq. S32	1.7	Material CS
Transfer conveyor (general)	$PEC = 31 \cdot F_{dry}^{0.8}$	Eq. S33	1.7	Based on a Belt type, 100 ft. long x 24" wide and enclosed.
Transfer conveyor (inlet facilities)	$PEC = 3230 \cdot F_{wb}^{0.6}$	Eq. S34	1.7	System of transfers conveyors
Truck scale	$PEC = 68000 \cdot N$	Eq. S35	1.7	10' x 70', 200,000 lb Concrete. Per Scale
Truck unloading system	$PEC = \text{round}\left(\frac{F_{wb}}{52100}\right) \cdot 302700$	Eq. S36	1.7	Includes dumper and dumper hopper. Round function rounds a number to the next larger integer.
Turbine/Generator	$PEC = 1132600 \cdot Pp^{0.6}$	Eq. S37	1.8	
Vessel	$PEC = 54600 \cdot F^{0.15} \cdot M_f$	Eq. S38	Table S1	
Vessel (buffers for filter)	$PEC = 9650 \cdot F^{0.15} \cdot M_f$	Eq. S39	Table S1	

Table S7. Materials factors to be used with equations shown on Table S5. Carbon Steel (CS) = 1.

	CS – Glass Lined	CS-Rubber Liner	SS304	SS316	Shell:CS Tubes: SS304	Shell:CS Tubes: SS316
Agitator	1.1	-	1.2	1.25	-	-
Pump	-	1.1	1.3	1.4	-	-
Conveyor (general)	-	-	1.3	1.4	-	-
Mixer – Inline with electric motor	-	1.1	1.3	1.4	-	-
Static Mixer	-	-	1.7	1.9	-	-
Vessel	-	-	1.7	1.9	-	-
Tanks	1.6	1.65	2.7	3.4	-	-
Heat Exchanger	1.8	-	2.7	3.2	2.1	2.5

The correlations shown on table S6 and S7 are based on the reference project and are not a statistical average of many items. For equipment estimations based only on 1 item, the reference cost was taken from the NREL project (Design 2011), normalized with capacity using Eq. 2 and expressed in 2018 US\$ Eq. 1. For equipment based on several items, the cost as a function of capacity was plotted and fitted. The average utility consumption was computed in a similar way and given in Table S8. As per the range of validity, more accurate estimations are obtained for projects with similar capacities to the reference project. We evaluated a biorefinery plant with those equations and the difference in the CAPEX estimation was -5% compared to a more advanced sizing and costing method. For very small projects, such as pilot plants, higher deviations are expected.

To evaluate a process with this approach, only the heat and material balance and process flow diagrams are needed. The use of the general equations to evaluate a new process or to compare different process schemes is recommended. To assess the impact of capacity, a base case should be computed with the general equations and then each piece of equipment should be corrected with the capacity using Eq. 2.

Table S8. Utility consumption estimations. These values are for reference only. For accurate values, detailed equipment sizing and selection is required.

Equipment	Utility Consumption	
Agitator	$EP_C = 2.23 \times 10^{-4} \cdot F$	Eq. S40
Air compressor (for enzyme production)	$EP_C = 2.27 \cdot F_E$	Eq. S41
Air compressor (utilities)	$EP_C = 0.0125 \cdot F_{rb}$	Eq. S42
Air compressors (for press filter)	$EP_C = 0.0498 \cdot F_{dry}$	Eq. S43
	$EP_C = 0.023 \cdot F_{ETOH-P}$	Eq. S44
Beer rectification system	$Q_C = 2.46 \cdot 10^{-5} \cdot F_{ETOH-P}$	Eq. S45
	$Q_h = 2.06 \cdot 10^{-3} \cdot F_{ETOH-P}$	Eq. S46
Chilled water package	$EP_C = 151 \cdot Q_C$	Eq. S47
	$EP_C = 0.003 \cdot F_{rb}$	Eq. S48
Cleaning in place system	$Q_C = 3.85 \cdot 10^{-5} \cdot F_{rb}$	Eq. S49
	$Q_h = 1.27 \cdot 10^{-6} \cdot F_{rb}$	Eq. S50
Concrete feedstock storage dome	$EP_C = 1.08 \cdot 10^{-3} \cdot F_{wb}$	Eq. S51
Dust collection system	$EP_C = 1.42 \cdot 10^{-3} \cdot F_{wb}$	Eq. S52
Evaporator System	$EP_C = 0.0305 \cdot F_{vap}$	Eq. S53
Mixer – inline with electric motor	$EP_C = 1.69 \times 10^{-4} \cdot F$	Eq. S54
	$EP_C = 6.92 \times 10^{-3} \cdot F_{ETOH-P}$	Eq. S55
Molecular sieve package (ethanol drying)	$Q_C = 2.88 \cdot 10^{-4} \cdot F_{ETOH-P}$	Eq. S56
	$Q_h = 1.61 \cdot 10^{-5} \cdot F_{ETOH-P}$	Eq. S57
Pump	$EP_C = 6.3 \cdot 10^{-11} \cdot F^2 + 1.5 \cdot 10^{-4} \cdot F$	Eq. S58
Screw continuous reactor	$EP_C = 0.0576 \cdot F_{wb}$	Eq. S59
Screw conveyor (wet cake)	$EP_C = 1.92 \cdot 10^{-4} \cdot F$	Eq. S60
Transfer conveyor (general)	$EP_C = 3.01 \cdot 10^{-4} \cdot F$	Eq. S61
Transfer conveyor (inlet facilities)	$EP_C = 1.49 \cdot 10^{-3} \cdot F_{wb}$	Eq. S62
Truck unloading system	$EP_C = \text{round}\left(\frac{F_{wb}}{52100}\right) \cdot 337.5$	Eq. S63

SYMBOLS AND ABBREVIATIONS

1G	First generation bioethanol
2G	Second generation bioethanol
C _p	Heat capacity (J/g.°C or kJ/kg.°C)
CS	Carbon Steel
EPC	Electric power consumed (kWh)
F	Mass flow rate (kg/h)
F _{dry}	Mass flow rate in dry basis (kg/h)
F _e	Amount of enzyme. Mass flow rate (kg/h)
F _{ETOH-P}	Amount of ethanol produced. Mass flow rate (kg/h)
F _{rb}	Raw biomass mass flow rate (dry basis) (kg/h)
F _{s-dry}	Solids mass flow rate in dry basis (filter) (kg/h)
F _{steam}	Amount of steam generated. Mass flow rate (kg/h)
F _{vap}	Amount of water evaporated. Mass flow rate (kg/h)
F _{wb}	Raw biomass mass flow rate (web basis) (kg/h)
H _{vap}	Enthalpy of vaporization (kJ/kg.°C)
MESP	Minimum ethanol selling price (US/L)
Mf	Material factor
MM	Millions
N	Number of items
PEC	Purchased equipment Cost (US\$ - 2018 June)
Pp	Total electric power produced (MWh)
Q	Duty (MW)
Q _c	Cooling duty (MW)
Q _h	Heating Duty(MW)
SHF	Separate (or sequential) hydrolysis and fermentation
SS	Stainless Steel
SSCF	Simultaneous saccharification and fermentation
TEA	Techno-economic analysis
w	Mass fraction
ΔT	Temperature difference (°C or K)
OPEX	Operating expenditure (or operating cost)
CAPEX	Capital expenditure (or capital investment cost)
NREL	United States National Renewable Energy Laboratory
WWT	Wastewater treatment
CIP	Clean-in-place

REFERENCES

1. Humbird, D. et al. Process Design and Economics for Biochemical Conversion of Lignocellulosic Biomass to Ethanol. *Renew. Energy* 303, 147 (2011).
2. Gschwend, F. J. V., Malaret, F., Shinde, S. & Hallett, J. P. Rapid pretreatment of Miscanthus using the low-cost ionic liquid triethylammonium hydrogen sulfate at elevated temperatures. 3486–3498 (2018). doi:10.1039/c8gc00837j
3. NIST. NIST Standard Reference Database Number 69. NIST Chemistry WebBook (2016). doi:10.18434/T4D303
4. Dupont, C., Chiriac, R., Gauthier, G. & Toche, F. Heat capacity measurements of various biomass types and pyrolysis residues. *Fuel* 115, 644–651 (2014).
5. Voitkevich, O. V., Kabo, G. J., Blokhin, A. V., Paulechka, Y. U. & Shishonok, M. V. Thermodynamic properties of plant biomass components. Heat capacity, combustion energy, and gasification equilibria of lignin. *J. Chem. Eng. Data* 57, 1903–1909 (2012).
6. Hatakeyama, T., Nakamura, K. & Hatakeyama, H. Studies on heat capacity of cellulose and lignin by differential scanning calorimetry. *Polymer (Guildf)*. 23, 1801–1804 (1982).
7. Report, A. S. Economic Feasibility Study of an Acid Hydrolysis-Based Ethanol Plant. Subcontract Report SERI-STR-231-3142, Prepared under Subcontract ZX-3-03096-2. (1987).
8. Chem Systems, I. Economic Feasibility Study of an Enzymatic Hydrolysisbased Ethanol Plant with Prehydrolysis Pretreatment. Subcontract Report SERISTR-231-3135, Prepared under Subcontract XX-3-03097-1. (1987).
9. Stone & Webster Engineering, C. omic Feasibility of an Enzyme-based Ethanol Plant. Subcontract Report SERI-STR-231-3138, Prepared under Subcontract ZX-3-03097-1. (1987).
10. Wooley, R. et al. Lignocellulosic Biomass to Ethanol Process Design and Economics Utilizing Co-Current Dilute Acid Prehydrolysis and Enzymatic Hydrolysis Current and Futuristic Scenarios Lignocellulosic Biomass to Ethanol Process Design and Economics Utilizing Co-Current D. (1999).
11. Aden, A. et al. Lignocellulosic Biomass to Ethanol Process Design and Economics Utilizing Co-Current Dilute Acid Prehydrolysis and Enzymatic Hydrolysis for Corn Stover Lignocellulosic Biomass to Ethanol Process Design and Economics Utilizing Co-Current Dilute Acid Prehyd. (2002).
12. Wingren, A., Galbe, M. & Zacchi, G. Techno-economic evaluation of producing ethanol from softwood: Comparison of SSF and SHF and identification of bottlenecks. *Biotechnol. Prog.* 19, 1109–1117 (2003).
13. Sassner, P., Galbe, M. & Zacchi, G. Techno-economic evaluation of bioethanol production from three different lignocellulosic materials. *Biomass and Bioenergy* 32, 422–430 (2008).
14. Junqueira, T. L. et al. Techno-economic analysis and climate change impacts of sugarcane biorefineries considering different time horizons. *Biotechnol. Biofuels* 10, 1–12 (2017).